Modeling of the Microstructural Effects on the Mechanical Response of Polycrystals

Von der Fakultät für Georessourcen und Materialtechnik der Rheinisch-Westfälischen Technischen Hochschule Aachen

zur Erlangung des akademischen Grades eines

Doktors der Ingenieurwissenschaften

genehmigte Dissertation

vorgelegt von

Seyed Amir Hossein Motaman, M.Sc.

aus Teheran, Iran

Berichter: Univ.-Prof. Dr.-Ing. Wolfgang Bleck
Prof. Dr.-Ing. Dierk Raabe
Univ.-Prof. Dr.-Ing. Ulrich Prahl

Tag der mündlichen Prüfung: 18 Januar 2021

The present cumulative dissertation consists of the following journal publications:

I. S.A.H. Motaman, U. Prahl: Microstructural constitutive model for polycrystal viscoplasticity in cold and warm regimes based on continuum dislocation dynamics.
Journal of the Mechanics and Physics of Solids 122 (2019): 205–243, ISSN: 0022-5096.
doi: 10.1016/j.jmps.2018.09.002.

II. S.A.H. Motaman, K. Schacht, C. Haase, U. Prahl: Thermo-micro-mechanical simulation of metal forming processes.
International Journal of Solids and Structures 178-179 (2019): 59–80, ISSN: 0020-7683.
doi: 10.1016/j.ijsolstr.2019.05.028.

III. S.A.H. Motaman, F. Roters, C. Haase: Anisotropic polycrystal plasticity due to microstructural heterogeneity - A multi-scale experimental and numerical study on additively manufactured metallic materials.
Acta Materialia 185 (2020): 340–369, ISSN: 1359-6454.
doi: 10.1016/j.actamat.2019.12.003.

IV. S.A.H. Motaman, F. Kies, P. Köhnen, M. Létang, M. Lin, A. Molotnikov, C. Haase: Optimal design for metal additive manufacturing - An integrated computational materials engineering (ICME) approach.
JOM 72 (2020): 1092–1104, ISSN: 1543-1851.
doi: 10.1007/s11837-020-04028-4.

D 82 (Diss. RWTH Aachen University, 2021)

Acknowledgments

First and foremost, I would like to express my sincere gratitude to my advisors, Univ.-Prof. Dr.-Ing. Wolfgang Bleck (Institut für Eisenhüttenkunde, RWTH Aachen University, Aachen), Univ.-Prof. Dr.-Ing. Ulrich Prahl (Institute of Metal Forming, TU Bergakademie Freiberg, Freiberg) and Prof. Dr.-Ing. Dierk Raabe (Max-Planck-Institut für Eisenforschung, Düsseldorf) for their invaluable support, guidance, and encouragement.

I would also like to thank all my colleagues at IEHK, especially Konstantin Schacht and Patrick Köhnen. It would not have been possible to conduct this thesis without their precious support. I would also like to send my special thanks to Dr.-Ing. Christian Haase for his instrumental support and guidance throughout the dissertation work. The fruitful discussions and valuable comments made by PD Dr. Franz Roters are also deeply appreciated.

Finally, my heartfelt thanks to my lovely mother, father, and two brothers for their encouragement, strong support, and inspiration all these years.

S. Amir H. Motaman

Aachen, June 2020

Abstract

The modeling and hence exploitation of the connection between the microstructure and the mechanical response of polycrystals is and continues to be at the forefront of the longstanding challenges in the materials science and metallurgical engineering. The macroscopic mechanical response of polycrystalline materials is intricately governed by the propensity of the micro-mechanisms of crystal plasticity, which are controlled by the instantaneous hierarchical microstructure and its evolution. Therefore, the microstructure almost exclusively controls the macroscopically observable mechanical response of polycrystalline aggregates in terms of the stress response and its variation (the stress rate or strain hardening). In this thesis, the microstructural effects on the mechanical response/properties of polycrystals are classified into four groups: the polarity, size, composite, and porosity effects. The historical background as well as the research on the modeling of the microstructural effects, which has so far lasted almost a century, are concisely reviewed.

The primary microstructural effects, the size and polarity effects, are modeled for different polycrystalline metallic materials at various length scales. First, the size effect was modeled at the macro-scale using a nonlocal (physics-based) microstructural model for polycrystal plasticity to simulate the behavior of a ferritic-pearlitic steel during large deformation in the cold and warm regimes. Then, the model was applied to simulate industrial cold and warm forging processes of a bevel gear shaft and predict its final microstructure and properties (process-microstructure-properties linkage). Second, the polarity effect was modeled at the meso-scale using a physics-based crystal plasticity model to simulate the (macroscopic) anisotropic mechanical response of an additively manufactured austenitic high-Mn steel (microstructure-properties linkage). It was, then, demonstrated that the meso-scale model can be applied for the optimal computational design of an additively manufactured lattice structure.

Zusammenfassung

Die Modellierung und die gezielte Ausnutzung des Zusammenhangs zwischen Mikrostruktur und mechanischem Verhalten von Polykristallen ist eine bestehende Herausforderungen in den Werkstoffwissenschaften und der Metallurgie. Die makroskopische mechanische Reaktion polykristalliner Materialien wird auf komplizierte Weise durch die Mikromechanismen der Kristallplastizität bestimmt, welche wiederum durch die ausgebildete hierarchische Mikrostruktur und deren Entwicklung gesteuert werden. Daher beeinflusst die Mikrostruktur fast ausschließlich die makroskopisch beobachtbare mechanische Reaktion von Polykristallen in Bezug auf die Spannungsantwort und ihrer Variation (Spannungsrate oder Verfestigung) während plastischer Verformung. In dieser Arbeit werden die mikrostrukturellen Effekte auf die mechanische Reaktion/Eigenschaften von Polykristallen eindeutig in vier Gruppen eingeteilt: Polaritäts-, Größen-, Komposit- und Porositätseffekte. Der historische Kontext und die fast einhundert Jahre andauerde Forschung und Entwicklung in der Modellierung der mikrostrukturellen Effekte werden kurz aufgearbeitet.

Darüber hinaus werden die grundlegenden Mikrostruktureffekte, die Größen- und Polaritätseffekte, für verschiedene polykristalline metallische Werkstoffe auf verschiedenen Längenskalen modelliert. Zunächst wurde der Größeneffekt auf der Makroskala mithilfe eines nicht lokalen (physikbasierten) Mikrostrukturmodells für polykristalline Plastizität modelliert, um das Verhalten eines ferritisch-perlitischen Stahls bei großer Verformung in kalten und warmen Temperaturbereichen zu simulieren. Das Modell wurde angewandt, um industrielle Kalt- und Warmschmiedeprozesse einer Kegelradwelle zu simulieren und ihre endgültige Mikrostruktur und mechanische Eigenschaften (Verbindung zwischen Prozess, Mikrostruktur und Eigenschaften) vorherzusagen. Zweitens wurde der Polaritätseffekt auf der Mesoskala mithilfe eines physikbasierten Kristallplastizitätsmodells modelliert, um die anisotrope mechanische Reaktion/Eigenschaften eines additiv hergestellten austenitischen Hochmanganstahls zu simulieren (Mikrostruktur-Eigenschaften-Korrelation). Anschließend wurde dargestellt, wie das mesoskalige Modell für ein optimales rechnerisches Design für die additive Herstellung von Metallen angewendet werden kann.

Contents

1. Introduction

The modeling of the microstructural effects plays the central role in the computational design of polycrystalline materials/components with respect to predicting their in-process and in-service behavior, and thus the quantitative linkages of [1]:

- Process-microstructure: Simulation of the (macroscopic) mechanical response and microstructure evolution under complex thermo-mechanical loading during the deformation-based material processing, i.e., metal forming and metal cutting processes.

- Microstructure-properties/performance: Prediction of the mechanical properties and microstructure evolution under complex thermo-mechanical service load, and thus the performance of the final component (given its microstructure after the last step in the manufacturing process chain).

The mechanical properties of polycrystals reflect their performance under particular loading conditions: (initial) yield stress/strength, ultimate tensile stress, uniform elongation, maximum elongation, post-uniform elongation, hardness, fatigue strength/life, Lankford coefficients/R-values, creep resistance, Charpy impact energy, fracture toughness, hole-expansion ratio, and so on. Almost all the mechanical properties of polycrystals, including the aforementioned properties, are not fundamental and are, in fact, indices for reduced-order representations of certain aspects of polycrystal plasticity under specific deformation parameters (strain rate and temperature). Moreover, the mechanical response of polycrystals during deformation-based material processing is also governed by the aspects of polycrystal plasticity.

It is well established that the polycrystal plasticity is highly sensitive to the polycrystalline microstructure. Microstructure (here, the term *micro* does not signify a specific length scale) is generally defined as the internal/underlying structure, and thus depends on the length scale at which the material is probed. A polycrystalline microstructure consists of the following *microstructural elements*, which span across different length scales:

- Meso-scale: Meso-structural elements (i.e., grains/crystallites) are mesoscopic crystals with (intra-granular) orientation/symmetry/composition gradient less than a certain threshold.

- Submeso-scale(s): Possible submeso-structural/constitutive elements are dislocation (submeso-) structure, particulate/lamellar dispersoids (nano-precipitates and nano-phases), nano-twins, elemental segregation, and/or voids.

In the above classification, the meso-scale/(intermediate length scale) is selected as the reference length scale due to its enormous importance in polycrystal materials science as it represents a bridge between the macro-scale and all the fundamental length scales, the submeso-scale(s). Henceforth, the terms *meso-structure* [2], and *submeso-structure* refer to the microstructure, and its associated elements and features specifically on the meso- and submeso-scales, respectively. Furthermore, the microstructural elements with respect to their heterogeneities own the following main distinctive statistical attributes known as the *microstructural features*:

- Fraction: A (polycrystalline) microstructure may consist of multiple constituents, the primary/matrix/parent constituent, and secondary constituents (phases, precipitates, and/or voids). The elements of a microstructural constituent have the *same* (elemental) composition and crystal symmetry, which are different from those of the elements of other microstructural constituents. For instance, the composition and/or crystal symmetry of grains of each meso-structural constituent are different from those of the other (if existent) meso-structural constituents. Moreover, to be consistent in definitions, let the void as a microstructural constituent to have the zero/void composition and infinite crystal symmetry. Each microstructural constituent occupies a certain volumetric fraction of the corresponding polycrystal satisfying $\sum_{i=1}^{n} f_i = 1$, where $f_i > 0$ denotes the volume fraction associated with the i-th microstructural constituent, and $n \geq 1$ represents the total number of microstructural constituents. $n = 1$ ($\Leftrightarrow f_1 = 1$) corresponds to a single-constituent polycrystal.

- Polarity/texture: There are morphological (shape and shape-axis orientation) and crystallographic (crystallographic orientation and interface misorientation) features associated with the elements of each microstructural constituent. Generally, the polarity of a microstructural constituent has two distinct aspects: crystallographic and morphological. The crystallographic polarity is a measure for the deviation of crystallographic orientation and misorientation distributions of microstructural elements from a corresponding fully random/non-polarized case [3–7]. On the other hand, a polarized morphology constitutes high frequency of asymmetric elements whose (ellipsoidal) semi-axes are dominantly orientated with low angle along specific axes/poles in the reference/global/sample/lab Cartesian frame [8–10]. It should be noted

that void as a microstructural constituent (owing to its postulated infinite crystal symmetry) does not have crystallographic polarity, but it may be morphologically polarized.

- Size/spacing: Each 3D microstructural element is associated with a volume and a corresponding (microstructural) size parameter. Therefore, when referred to a specific microstructural element type, the (elemental) size is the (scalar) effective equivalent sphere diameter of the elements of the same type. Therefore, an effective size and a size variance/heterogeneity can be assigned to each microstructural element type based on the statistical distribution of its elemental size. Moreover, the spacing among the elements of the same type and their size are closely related. The elemental spacing is a function of the size, shape, and spatial distribution of the elements of the same type.

The polycrystal mechanical response is governed by the micro-mechanisms that accommodate crystal plasticity, including the micro-mechanisms of slip, twinning, interface motion, phase transformation, void evolution, and fracture. From an irreversible/non-equilibrium thermodynamics point of view [11–23], the frequency and amplitude of those competitive micro-mechanisms depend on their activation/barrier energy and their dissipation/relaxation efficiency (maximizing the specific entropy production rate, and thus minimizing the rate of the stored elastic/free energy density). The micro-mechanisms of some processes such as recrystallization often require thermal assistance to be activated, but once activated they reduce the stored elastic energy, and increase dissipation. Some processes such as twinning have a relatively high stress threshold (corresponding to a surface energy density barrier, e.g., stacking fault energy), but they are highly efficient in dissipation. There are micro-mechanisms such as those of the fracture process have a high stress threshold (associated with a surface energy density barrier, e.g., Griffith surface energy), and at the same time are highly inefficient in dissipation. Given this premise, the prevalence of the fracture micro-mechanisms is the last resort for the polycrystal.

Under a certain set of deformation parameters and thermo-chemo-mechanical boundary conditions, the mechanical response (stress and stress rate) of a polycrystal depends on its instantaneous microstructure as well as the microstructure evolution, which is a functional of the energetic-dissipative micro-mechanisms. Therefore, to study the microstructural effects on the mechanical response of polycrystals, the interactive effects of the micro-mechanisms of plasticity and polycrystalline microstructure on its evolution must be understood as well. Assuming

a displacement-controlled load, let the microstructural effects on the instantaneous stress response be expressed by an explicit function:

$$\boldsymbol{\sigma} = \mathbf{f}(T, \dot{\boldsymbol{\varepsilon}}, \boldsymbol{s}); \quad \boldsymbol{s} \equiv \{s_1, s_2, s_3, \ldots\}; \tag{1}$$

where $\boldsymbol{\sigma}$ and $\dot{\boldsymbol{\varepsilon}}$ are the macroscopic/homogenized true stress and strain rate tensors, respectively; T is the absolute temperature; $\boldsymbol{s}$ represents the microstructural state (configuration of micro-state variables); and s_i denotes the i-th statistical microstructural state variable or simply the i-th micro-state variable (MSV). The stress response (macroscopic stress tensor homogenized over the polycrystalline aggregate) is a function ($\mathbf{f}$) of deformation parameters (temperature and strain rate) and the microstructural state (a thermo-micro-mechanical function). The microstructural evolution can be represented by the explicit function $\boldsymbol{g}$, which is also a thermo-micro-mechanical function:

$$\dot{\boldsymbol{s}} = \boldsymbol{g}(T, \dot{\boldsymbol{\varepsilon}}, \boldsymbol{s}). \tag{2}$$

With the known stress response ($\mathbf{f}$) and microstructure evolution ($\boldsymbol{g}$), the stress rate response can be formally expressed as follows:

$$\dot{\boldsymbol{\sigma}} = \frac{\partial \mathbf{f}}{\partial T}\dot{T} + \frac{\partial \mathbf{f}}{\partial \dot{\boldsymbol{\varepsilon}}}\ddot{\boldsymbol{\varepsilon}} + \frac{\partial \mathbf{f}}{\partial \boldsymbol{s}}\dot{\boldsymbol{s}}. \tag{3}$$

In fact, if the stress response ($\mathbf{f}$), and one of the microstructure evolution ($\boldsymbol{g}$) or the stress rate response are known, the other one can be dependently represented using them. Further, in the case of a non-singular strain rate tensor, the stress rate response can be normalized by the strain rate, and represented by the notion of strain hardening or tangent modulus ($\boldsymbol{\Theta}$) as well, which is generally a fourth-order tensor:

$$\boldsymbol{\Theta} \equiv \frac{\partial \boldsymbol{\sigma}}{\partial \boldsymbol{\varepsilon}} = \dot{\boldsymbol{\sigma}}\dot{\boldsymbol{\varepsilon}}^{-1}. \tag{4}$$

Generally, there are two approaches for the continuum modelling of the microstructural effects on the mechanical response of polycrystals, corresponding to two different length scales:

- Meso-scale computational polycrystal homogenization: The polycrystalline meso-structure is explicitly modeled, and a crystal plasticity constitutive

model is used to calculate the constitutive response (and the submeso-structure evolution). The meso-scale fields (stress, strain, and MSVs) are then homogenized incrementally to give the macroscopic response.

- Macro-scale nonlocal microstructural modeling: The hierarchical polycrystalline microstructure and its evolution are nonlocally and constitutively modeled with sufficient detail directly at the macro-scale using a microstructural constitutive model, which also renders the macroscopic mechanical response of the polycrystal. Such kind of modeling is performed using the notion of micro-state variables.

In this thesis, the origins, modeling of the microstructural effects on the mechanical response of polycrystals are comprehensively reviewed. The primary/basic microstructural effects, the size and polarity effects, are modeled for different polycrystalline metallic materials using the macro- and meso-scale modeling approaches. Subsequently, it is shown that how the aforementioned modeling methods can be used for the simultaneous optimal (computational) design of polycrystalline metallic materials and manufacturing processes.

2. Origins and a Century of Research

The microstructural effects on the mechanical response of polycrystals can be classified into the following interdependent aspects: the primary (size and polarity) and secondary (composite and porosity) effects. Secondary effects appear in the presence of multiple microstructural constituents. Accordingly, from a novel perspective, the crucial historical findings and modeling developments related to the microstructural effects are concisely reviewed in this section.

2.1. Polarity effect

The anisotropic mechanical response of single-constituent polycrystalline materials is exclusively due to their meso-structural polarity (i.e., meso-polarity) [24]. A sufficiently strong deviatoric mechanical boundary condition on a polycrystal results in a macroscopic plasticity entailing the evolution of the meso-polarity state, which in turn affects the anisotropic mechanical response of the material. The meso-polarity has two distinct aspects: crystallographic and morphological. The crystallographic polarity is a measure for deviation of crystallographic orientation and misorientation distributions from a corresponding fully random/non-polarized case. A non-polarized meso-structural morphology usually comprises equiaxed grains, whereas a polarized morphology constitutes high frequency of elongated grains whose (ellipsoidal) semi-axes are dominantly orientated with low angle along specific axes in the reference frame. Therefore,

the morphological meso-polarity effect can be regarded as an anisotropic size effect (directional grain size or various grain boundary spacing along different directions) [24]. The constitutive mechanical response of an intra-granular meso-scale material point (i.e., meso-point) is almost always anisotropic. In the absence of submeso-structural elements, the polarity state of a meso-point (submeso-structural polarity, i.e., submeso-polarity) depends only on its crystal symmetry/structure. However, the presence of submeso-structural elements underlying the meso-point alters its submeso-polarity state and hence its constitutive (anisotropic) elastic stiffness tensor.

Due to the high dimensionality of the polarity space, extraction of the polarity effect is much more difficult than the other microstructural effects, and requires advanced continuum modeling and numerical methods, i.e., computational polycrystal homogenization/approximation. It began with the pioneering analytical models of Reuss [25], Hill [26], Hershey [27], and Eshelby [28,29], for mean-field approximation of macroscopic elastic properties as well as the analytical estimates of Sachs [30], Taylor [31], Bishop and Hill [32,33], Lin [34], Kröner [35], Kocks [36], and Bunge [37], for capturing the anisotropic mechanical response of polycrystalline aggregates due to their meso-polarity, all based on simplified linearization assumptions. Thereafter, more sophisticated numerical homogenization methods were developed to capture the anisotropic polycrystal plasticity as an implicit function of the meso-polarity.

2.1.1. Computational polycrystal homogenization

The derivation of the macroscopic mechanical response of polycrystalline aggregates from those of their grains is a long-standing (meso-scale) problem in the materials science. An accurate derivation requires the knowledge of the crystal properties of the grains, the geometrical specifications (shape, size, orientation, and arrangement) of the grains, and a physically consistent mathematical/algorithmic method, which can properly account for the grain interactions. Such a mathematical scheme belongs to a class of methods known as computational polycrystal homogenization (CPH). The CPH methods were originally introduced in attempts to capture the meso-polarity effect on the anisotropic (macroscopic) mechanical response of polycrystalline aggregates [38–41]. However, they have been developing during the past six decades to capture the other meso-structural effects as well, since they explicitly model the polycrystalline microstructure on the reference scale, the meso-scale. CPH currently rules the mainstream of the scientific research on the microstructural effects. In CPH, a meso-scale continuum model for crystal finite strain [42–53], which is coupled with a crystal plasticity

constitutive model is numerically solved and homogenized over the polycrystalline aggregate to render the macroscopic mechanical response. The CPH methods are divided into the mean- and full-field schemes.

2.1.1.1. Mean-field CPH schemes

In the mean-field methods for CPH, usually three-dimensional (3D) meso-structural constituents (grains), which are assigned certain idealized shape features, are immersed in a homogenous matrix/medium (self-consistent approach) or arranged with respect to one another (cluster approach). Moreover, there exist mean-field CPH methods based on model order reduction. In the following, the main characteristics of the mean-field CPH approaches are briefly described:

- *Self-consistent approximations* are based on the ellipsoid/Eshelby inclusion formalism [27–29,54–101]. In the self-consistent (mean-field) approximations, the meso-structural constituents are embedded as isolated *equivalent ellipsoidal inclusions* in an *infinite homogenous equivalent matrix* (linear comparison polycrystal). In the first-order self-consistent estimates (secant, tangent, affine, and variational), as formally shown by Eshelby [28], the mechanical (stress and strain rate) fields are uniform in the ellipsoidal inclusion, and related to the uniform mechanical far-fields (infinitely far mechanical fields of the matrix) by the fourth-order Eshelby tensor. However, more accurate higher-order self-consistent estimates, which are based on variational methods for general nonlinear heterogenous/composite media [73,102–119], also account for intra-granular field fluctuations using higher-order statistical moments. In general, the self-consistent methods account for the morphological polarity through the ellipsoid simplification. Nonetheless, since each ellipsoid is treated as an isolated inclusion within a *homogeneous* matrix, among the aspects of the crystallographic polarity, self-consistent methods do not consider the direct neighbor interactions or interface effects (i.e., the effect of meso-structural crystallographic misorientation).

- *Cluster approximations* (also known as grain cluster or relaxed constraint methods) approximately account for the crystallographic polarity including the neighbor interactions (interface misorientation) by partial fulfillment of the meso-structural interface mechanical (stress equilibrium and strain compatibility) conditions, but they neglect the morphological polarity [120–134]. Weak enforcement of the equilibrium and compatibility conditions between

the contiguous *grains* in the cluster is performed by partial relaxation of Taylor/isostrain (uniform strain field in the entire polycrystal) constraints/assumptions [31].

- *Order reduction schemes* (commonly known as transformation field analysis) often use the notions of macroscopic internal state variables and thermodynamics potentials [135–148]. Such mean-field schemes systematically reduce the number of macroscopic internal variables by decomposing the plastic strain within each grain to a finite set of *plastic modes*, which can represent large deviations from uniformity.

Mean-field approximations enable (computationally) efficient transfer of the (evolving) meso-polarity effects to the macro-scale material points (i.e., macro-points) during macro-scale simulations, e.g., finite element (FE) simulation of sheet metal forming process.

2.1.1.2. Full-field CPH schemes

Numerical full-field methods were developed to overcome the deficiencies of the mean-field methods by considering a higher level of meso-structural detail with the expense of computational power/time. In the full-filed schemes, external/far-field displacement/traction boundary conditions on the polycrystalline material translates as a homogenous periodic boundary conditions on a synthetic periodic (often cubic) meso-structural ensemble as a statistically representative volume element (SRVE). The main criterion for an SRVE is that its (statistical) *meso-structural descriptors* must match (within a tolerance) the meso-structural descriptors of the respective polycrystalline material. In the last two decades, considerable development has been made in the synthetic generation of SRVEs of polycrystals [9,149–160]. The aforementioned boundary value problem can be numerically solved to spatially resolve the fields by the finite element method (FEM) [38,161–171], or schemes based on the fast Fourier transform (FFT) algorithm [172–197], which take advantage of the periodicity of the boundary conditions imposed on the SRVE.

2.2. Size effect

All the mechanical properties of polycrystalline materials are affected by the intrinsic microstructural size parameters at various length scales [198–200]. Size effect is the most significant microstructural effect. The morphological polarity effect can be regarded as an anisotropic size effect. The secondary microstructural effects, each impose their own size effect. The size effects are divided into meso-

scale size (i.e., meso-size) and submeso-scale/constitutive size (i.e., submeso-size) effects. In this context, the meso-size represents the effective spacing among the boundaries of contiguous grains.

Orowan [201], Taylor [202], Bragg [203], and Zener [204], were the first to propose (in the 1930s based on rudimentary rationales) that the stress response (or strength) has an inverse relationship with a scalar microstructural size. However, the meso-size/(grain size)/Hall-Petch effect, which is one of the most investigated microstructural effects, is best known by the empirical studies of Hall [205,206], and Petch [207,208] (in the 1950s), shortly after the supportive theoretical calculations of Eshelby et al. [209], and Leibfried [210], on the stress field in the vicinity of dislocation pileups. Thereafter, many attempts have been made to derive/justify/modify/extend the so-called Hall-Petch relation based on physically motivated elastic/plastic incompatibilities at grain boundaries and/or dislocation-grain-boundary interactions (grain boundary dislocation pileups and sources), which result in a composite consisting of a hard boundary layer (impenetrable or opaque for dislocations) and a soft interior/bulk region [36,211–252]. This leads to stress concentration at the reinforced boundaries contributing to the macroscopic yield stress/strength of the polycrystalline aggregate.

The classical Hall-Petch and Taylor relations inspired proposals for describing the submeso-size effect as a (scaling) function of the effective/characteristic spacing/wavelength of the self-organized dislocation walls/pileups and/or subgrain boundaries (a scalar submeso-scale parameter) [221,222,233,239,241,249,253–286]. More fundamentally, the submeso-size effect on the instantaneous stress response of a meso-point is a function of dislocation junction/lock strengths and spacings, and thus dislocation density (defined in the meso-scale control volume surrounding the meso-point) according to the generalized Taylor relation [202,212,286–300].

The submeso-size and its evolution are governed by various sources of submeso-scale crystal discontinuities acting as both dislocation sources and obstacles for dislocation slip, e.g., dispersoids, nano-twins, and most importantly forest dislocations. These discontinuities can be constitutively homogenized using the harmonic superposition/mixture/mean law to render the (effective) submeso-size through the notion of mean free path for dislocation slip [290,301–309]:

$$\Lambda = \left(\sum\nolimits_i c_i \, \lambda_i^{-1} \right)^{-1} ; \tag{5}$$

where Λ represents the submeso-size at a given meso-point (at all the slip systems in average or at a specific slip system); λ_i denotes the effective spacing among the elements of the i-th submeso-structural obstacle/source type at the meso-point; and $c_i > 0$ (absorbable in λ_i) is a dimensionless constant controlling the relative strength of the i-th obstacle/source type. Notice that the smallest term in the right-hand side of Eq. (5) has the strongest impact on Λ^{α}. The spacing of forest dislocations (λ_f) is often the smallest among λ_i. The submeso-size (Λ) controls the effective length/curvature of dislocation sources and thereby the rate of dislocation generation/multiplication (source), consequent accumulation/storage (obstacle), and ultimately the constitutive strain hardening response. It is worth noting that (obstacle-type) relationships analogous to Eq. (5) can be envisaged for the other carriers of crystal plasticity such as twinning and stress-induced phase propagation.

In addition, decreasing the meso-size generally gives rise to the proliferation of dislocation multiplication through increasing the number density of grain boundary sources (at boundary dislocations and disconnections such as ledges, steps, kinks, and trijunctions), which in turn leads to surging the macroscopic strain hardening response of undeformed polycrystals [212–214,221–223,232,233,237,239,240,256,262,269,310–344]. However, the strain hardening response will undergo a relatively abrupt drop after exhaustion of the boundary sources and formation of dislocation pileups. Therefore, in nonlocal constitutive modeling either at macro- or meso-scale, the meso-size should be one of the λ_i in Eq. (5), since given a certain grain shape distribution, the grain boundary area density is inversely proportional to the effective grain size.

The submeso-size effects on the constitutive mechanical response of meso-points lead to the evolution of meso-structure and its associated effects, which will collectively reveal themselves on the macroscopic mechanical response. In this context, seemingly distinct (on the meso-scale) subgrain boundaries also known as geometrically necessary boundaries (GNBs) or dense dislocation walls (DDWs) [255,345–360], emerge on the meso-scale due to a detectable *low angle* misorientation stemming from a rich underlying dislocation submeso-structure/substructure corresponding to a relatively high density of geometrically necessary dislocations (GNDs) [221,361–367]. Therefore, as an emergent cross-scale microstructural feature, the (low-angle) subgrain (diffuse) boundaries and their spacing should be considered through their underlying submeso-structural features (e.g., submeso-size). Nevertheless, in this setting, the sharp meso-structural/grain boundaries, as pure rotational defects with relatively low free energy density (in the undeformed state under free macroscopic boundary conditions)

can be described by a certain underlying disclination (density) field [368–384], as opposed to interface-dislocations/Frank-Bilby/Read-Shockley models of grain boundaries [385–394]. This suggests that at a sufficiently small submeso-size and large meso-size, the meso-size effect will vanish (associated with a zero Hall-Petch constant/slope). To capture this phenomenologically, modified/generalized Hall-Petch relations augmented with a submeso-size parameter were recently proposed, which couple the meso- and submeso-size effects [329–331,395,396].

Even though there is a large body of data in the literature supporting the Hall-Petch relation in capturing the meso-size effect in a wide variety of polycrystalline materials, it is not free of controversy [211,214,397–401]. At a constant relatively low dislocation density (and thus a constant relatively large submeso-size), a nonlinearity is often observed in the Hall-Petch plots (initial yield stress versus the inverse squareroot of the effective grain size), corresponding to a transition from a coarse-grained to a fine-grained regime. This bi-linear regime change is relatively sharp, usually observed in the grain sizes in the order of 1-10 μm, and typically is associated with the appearance of macroscopic discontinuous (initial) yielding [333,402–416]. The pronounced discontinuous yielding, yield point or Lüders phenomenon [206,417–423], which is due to the inhomogeneous inter- and intra-granular (elasto-plastic) deformation, dominates in the early stage of fine-grained polycrystal deformation until the average intra-granular shear resistance reaches the mean threshold for plasticity of grain boundaries (the equivalence of meso- and submeso-size effects).

The Hall-Petch relation also fails where the effective grain size falls below a (submicron) threshold corresponding to the transition from the meso- to submeso-scale. Such transition is usually correlated with an abrupt decrease in the Hall-Petch constant (often to negative values). The aforementioned nonlinearities in the Hall-Petch constant, which mark different meso-size regimes [424–427], are associated with switches in domination of different competitive energetic-dissipative micro-mechanisms of plasticity. The negative Hall-Petch constant (inverse Hall-Petch effect or grain size softening), which is often accompanied by superplasticity in polynanocrystals (nano-grained/nano-structured/ultrafine-grained polycrystals) [236,250,251,424–458], is due to the prevalence of the stress-induced/shear-coupled/athermal grain boundary migration, sliding, and rotation-coalescence [370,371,388,427,454,455,457,459–552]. The anomalous deviations from the Hall-Petch trend associated with relatively small and large meso-sizes are known as the Hall-Petch break-down/collapse phenomena.

The dynamics of submeso-size is governed by (continuous) dislocation density evolution stemming from dislocation multiplication/accumulation/storage as well as recovery/annihilation mechanisms, which have been extensively modeled at various length/time scales often by compartmentalizing the dislocation population [24,258,276,281,307,316,317,333,340,553–623]. Despite the highly dynamic nature of submeso-size, the meso-size usually undergoes negligible changes during plastic deformation. On the other hand, the meso-polarity is highly dynamic during polycrystal plasticity. Meso-structural size (and polarity) and the associated meso-structural effects evolve under the following *extreme meso-structural processes*:

- Deformation and annealing twinning due to twin formation (nucleation and propagation) and thickening/growth [305,624–680].
- Stress-induced grain boundary migration, sliding, and rotation-coalescence.
- Continuous/discontinuous/geometric recrystallization by grain nucleation, growth (curvature-driven/capillarity-driven/thermally-activated/diffusion-induced/spontaneous grain boundary migration), and stagnation [388,681–797].
- Phase transformation (see Section 2.3).

In the framework of phenomenological (isotropic) strain gradient plasticity [798–835], attempts have been made to capture both the meso- and submeso-size effects at the macro-scale using constitutive modeling in a semi-physics-based fashion (still with the accumulated plastic strain as an internal state variable) [799,817,818,836–877]. Nevertheless, the meso- and submeso-size effects can be coupled though the (physics-based) microstructural constitutive modeling (nonlocally [878–881]) at the macro-scale [553], which can be implemented in a thermo-micro-mechanical formalism [882], to simulate the macroscopic response of (macro-scale) polycrystal volumes based on the underlying (meso- and submeso-) structural sizes. In the (nonlocal) microstructural constitutive modeling, the key postulate is that a differential meso-structural singularity (infinitesimal meso-interface associated with a disorientation) in the *polycrystal continuum* can be replaced by a fictitious *equivalent GND density* (tensor) as a diffuse interface (GNB) [883], that smoothly resolves the effective geometrical features and mechanical properties of the meso-interface. Accordingly, the microstructural size features at different length scales and their associated (meso- and submeso-size) effects can be unified. Nonetheless, there is a need for a generalized microstructural constitutive model that in addition to the size effects also accounts for the

other microstructural effects, most importantly the polarity effect through the polarity/tensorial feature of GNDs.

As mentioned earlier, CPH schemes may simultaneously capture multiple meso-structural effects. The unique advantage of the full-field schemes is that they allow for gradient-based crystal plasticity constitutive treatments [884–897], to account for strong field contrasts in the vicinity of grain boundaries. Plasticity (slip/twin) transmission across interfaces as a function of interface opacity/penetrability/transferability/transmissivity/hardness [648,898–929], can be conveniently incorporated in the meso-scale (particularly gradient-based) full-field crystal plasticity formulations to simultaneously account for the size and polarity effects [189,193,329–331,334–336,338,340–344,371,552,570,609,842,865,866,883,930–969]. It should be noted that besides the mean values of the microstructural sizes, their heterogeneities/distributions/variances also affect the mechanical response of polycrystals. In particular, the meso-size heterogeneity effect has been already investigated/modeled [396,970–983].

It is worth noting that the stress-reversal/strain-reversal/(strain-path change)/Bauschinger/(kinematic hardening) effect [984–1013], is intrinsically a submeso-size effect. This effect is intimately related to the collective curvature and the associated short-range back stress state of statistically stored dislocations (SSDs) [196,337], and GNDs at meso-points, as well as the long-range/nonlocal internal stresses induced due to their associated submeso-structural dislocation walls/boundaries [258,260,1011,1014–1025]: incidental dislocation boundaries (IDBs) and GNBs [255,345–360][255,345–360], respectively. The stress-reversal effect caused by the sign change of resolved shear stress and plastic shear strain rate (reverse dislocation slip [1000,1023,1026–1029], and/or detwinning/retwinning [1030–1037]) at deformation systems of meso-points arising from the change of macroscopic boundary conditions and/or mesoscopic lattice rotation can be incorporated in physics-based crystal plasticity constitutive models [562,572,577,578,590,600–608,610,611,613,615,618,619,935,1034,1038–1054]. The stress-reversal effect is stronger where the submeso-structural dislocation boundaries have a higher frequency and amplitude (misorientation of GNBs and thickness of IDBs). Cyclic polycrystal plasticity (with sufficiently low amplitude, high frequency, and long duration) in the presence of adequate cross-slip activity often leads to the formation of thick submeso-structural IDBs (containing relatively high density of edge dislocation dipoles) with particular vein/ladder/labyrinth arrangement, and the associated channels or the persistent slip bands [258,286,577,587,615,993,999,1018,1019,1021,1055–1082].

2.3. Composite effect

A composite polycrystalline microstructure comprises a matrix/primary/parent constituent and at least a (non-void) secondary constituent (phase and/or precipitate). The inherent geometrical features of crystal structure (crystal symmetry and lattice constants) and the elemental composition of each grain/dispersoid belonging to a single constituent are identical (within a tolerance) but sufficiently different from those of the other constituents. Consequently, the physical/energetic properties of each constituent are different from those of the other constituents. These intrinsic crystal properties, which can be calculated using submeso-scale simulations/calculations (ab initio calculations, atomistic simulations, discrete dislocation dynamics simulations, and/or phase-field micro-elasticity simulations), are the elastic constants and moduli, dislocation junction strengths, maximum short-range slip resistance (also known as Peierls stress or solid solution strength), activation volumes for slip, climb, and cross-slip, self-diffusion thermal activation energy, self-diffusion coefficient, stacking fault energy, anti-phase boundary energy, and so on. Moreover, the aforementioned submeso-scale simulations/calculations can be invoked to derive the (constitutive) parameters associated with the interactions of the submeso-structural elements (e.g., dispersoids, voids, and nano-twins) with the matrix, grain boundaries, dislocations, and/or each other.

The fractions of different secondary constituents are known to have strong impacts on many mechanical properties. Nevertheless, depending on the size, morphological, and crystallographic features of the secondary constituents, they impose their own size and polarity effects on the mechanical response. Therefore, if a secondary constituent has an effective/mean meso-scale size, its associated microstructural effects is classified as meso-scale composite (i.e., meso-composite) effects. Likewise, if the dispersoids of a secondary component have an effective submeso-scale size, their associated microstructural effects are categorized as submeso-scale composite (i.e., submeso-composite) effects. The meso-composite effect can be explicitly modeled using the CPH methods so that the constitutive response of the meso-points of each meso-structural constituent is calculated using different constitutive models and/or constitutive parameters [152,155,1044,1083–1101]. In contrast, in meso-scale CPH or macro-scale microstructural modeling, the submeso-composite effect can only be implicitly accounted for in the corresponding constitutive model.

Thermo-chemo-mechanical boundary conditions and the respective evolving fields may lead to evolution of the secondary constituents, which thus will *compositely* affect the mechanical response. Diffusional/diffusion-controlled (solid-state) phase transformation by nucleation, growth, and impingement [692,759,1102–1148], the stress-induced/strain-induced/displacive/diffusionless/martensitic phase transformation by nucleation, propagation, and termination [657,680,1102,1107,1122,1149–1282], and diffusional continuous/discontinuous precipitate evolution by nucleation, growth, aggregation/coalescence, coarsening/ripening, and dissolution [759,1102,1147,1283–1379], impose combined (meso-/submeso-) composite, size, and polarity effects.

Mott and Nabarro [1380], Orowan [1381], Fisher et al. [1382], Friedel [1383,1384], Kocks [301,1385], Ashby [1386–1388], Foreman and Makin [1389,1390], Hirsch and Humphreys [1391–1393], and Brwon and Stobbs [1394], were the first (1940-1970) followed by other researchers [1395–1420], to model the submeso-composite and -size effects associated with (plastically) non-shearable/non-deformable/shear-resistant/impenetrable/strong/rigid/hard spherical particles (particulate nano-precipitates/phases) submesoscopically dispersed in a deformable/soft matrix. The aforementioned non-shearable particle dispersoids were assumed to be incoherent and/or sufficiently large and thus looped by mobile dislocations through the Orowan/Hirsch bypassing mechanisms [1381,1392,1393]. Nevertheless, if the mean size of dispersoids is larger than a certain threshold (comparable to average length of dislocation segments), dislocation bypassing/looping can no longer be a viable dislocation-dispersoid interaction mechanism. Therefore, in the presence of (eutectic/eutectoid) lamellar/multilayered/nanolayered/nanolaminate dispersoids, the constitutive response is governed by the interface-driven/dominated plasticity: the competition between the confined layer plasticity and the slip transmission across the matrix-dispersoid interfaces [929,1421–1445]. The combined submeso-composite, -size, and -polarity effects associated with the lamellar dispersoids can be constitutively modeled [1425–1427,1437,1439,1442,1446–1465].

In contrast, shearable/deformable/penetrable/weak/soft coherent particles with adequately small size may be sheared by the slipping dislocations. Such coherent particles give rise to the following submeso-size and -composite (strengthening) effects [1378,1379,1466–1472]:

- *Chemical effect* [1470,1473,1474], which arises from the energy required to create an additional particle-matrix interface when the particle is sheared by a mobile dislocation.

- *Stacking fault effect* [1475], occurs when the stacking fault energy of the coherent particle is different from that of the matrix. This results in different separation width of the passing partial dislocations in the matrix and in the particle, which will lead to a short-range stacking fault strengthening effect.

- *Modulus effect* [1476–1480], occurs when a dislocation enters a coherent particle having a shear modulus different from that of the matrix, leading to a change in the dislocation line tension and thus the Peierls stress, which typically leads to a short-range hardening effect.

- *Coherency effect* [1481–1483], occurs when the lattice parameter of the coherent particle is different from that of the matrix. A non-zero matrix-particle interface energy ensuing the lattice misfit generates a relatively long-range stress field in the matrix (through a grid of geometrically necessary misfit dislocations) that interacts with nearby dislocations.

- *Order effect* [1484–1488], which is due to the additional work required to generate an antiphase boundary in the case of dislocations passing through particles which have an ordered lattice.

The (submeso-structural) dispersoids impose a submeso-size effect on the strain hardening (or stress rate) response due to their effective size and spacing [307–309,1378,1383,1385,1389,1402,1405,1469,1489–1493], which can be integrated through the harmonic superposition law (Eq. (5)) together with the other sources of crystal singularities. They enforce a submeso-size effect on the instantaneous stress response as well, which can be constitutively homogenized with the submeso-size effect due to dislocation junctions to give the effective constitutive critical shear stress using the general superposition/mixture law [1043,1390,1395,1406,1468,1490,1494–1510]:

$$\tau_{\text{intra sl cr}} = \left(\sum\nolimits_i \tau_i^q\right)^{1/q}; \tag{6}$$

where $\tau_{\text{intra sl cr}}$ is the effective intra-granular critical shear stress for dislocation slip at a given meso-point (at all the slip systems in average or at a specific slip system); τ_i is the contribution of the i-th submeso-size/-composite effect on the dislocation slip resistance; $\tau_\rho \equiv \tau_i|_{i=1}$ denotes the effective critical shear stress for dislocation slip due to dislocation junctions; and q represents a constant exponent ($q \geq 1$). Typically, it is assumed that $q = 2$, corresponding to the quadratic/geometric/Pythagorean superposition; and sometimes $q = 1$ is taken, corresponding

to the linear superposition. Notice that the harmonic and the general superposition laws for the constitutive strain hardening and stress responses (Eqs. (5) and (6), with $c_i = 1$ and $q = -1$) share obvious similarities.

2.4. Porosity effect

As a submeso-structural constituent, the porosity and its evolution mechanisms have a dominant effect on the strain/stress localization, and hence ultimately govern the damage-induced macroscopic softening/(negative strain hardening) response and the ductile failure-related mechanical properties of polycrystals (e.g., ultimate tensile stress, uniform/post-uniform/maximum elongation). McClintock et al. [1511], McClintock [1512], Rice and Tracy [1513], Tracey [1514], Green [1515], Rudnicki and Rice [1516], McMeeking [1517], Hancock and Mackenzie [1518], Shima and Oyane [1519], Gurson [1520], Yamamoto [1521], and Needleman and coworkers [1522,1523], were the first (1966-1978) to formally model the pressure-dependent porosity effect by postulating certain idealized void shapes embedded in isotropic (porous) matrices with rigid plastic properties.

Subsequently, the void evolution mechanisms [1524–1572] (nucleation [1573–1582], growth [1583–1606], and coalescence/collapse/sheet [1607–1644]) during plastic deformation and the associated porosity effects have been extensively studied and modeled for various void shapes and polarity [1525,1607,1645–1654] (spherical [1589,1655–1673], cylindrical [1659,1674–1681], spheroidal [1534,1599,1600,1624,1682–1696], and ellipsoidal [1555,1697–1719]) under different loading modes (stress triaxiality and lode parameter). Furthermore, the porosity evolution and effects have been investigated/modeled for different effective void (submeso-) size and distributions [1531,1551,1559,1562,1583,1594–1596,1604,1605,1614,1633,1634,1649,1654,1660,1687,1694,1695,1720–1734], in viscoplastic matrices with effective orthotropic and/or asymmetric properties [1607,1614,1643,1650,1652,1653,1669,1688–1690,1692,1702,1713,1735–1743], and more recently in single crystals [1553,1556,1557,1572,1583,1588,1593,1594,1596–1598,1601–1603,1621,1623,1679,1680,1706,1707,1714,1715,1718,1743–1747].

Nevertheless, in certain regimes of deformation parameters and microstructure, polycrystalline materials may undergo (inter/trans -granular cleavage) brittle fracture (crack nucleation and propagation), which operate in lower time scales compared to their ductile counterparts [215,247,248,1748–1782]. In such cases, localized voids and particles and their associated stress/strain localization are usually the precursor of the brittle crack nucleation [1764,1766,1775,1776,1783–1786].

3. Papers

In this section, the primary microstructural effects, the size and polarity effects, are modeled for different polycrystalline metallic materials at various length scales. In Paper I, the size effect was modeled at the macro-scale using a nonlocal microstructural model for polycrystal plasticity to simulate the behavior of a ferritic-pearlitic steel during deformation in the cold and warm regimes. Then, in Paper II, the same model was used to simulate industrial cold and warm forging processes of a bevel gear shaft and predict its final microstructure and properties (process-microstructure-properties linkage). In Paper III, the polarity effect was modeled at the meso-scale using a physics-based crystal plasticity model to simulate the anisotropic mechanical response of a highly (meso-structurally) polarized additively manufactured austenitic high-Mn steel (microstructure-properties linkage). Subsequently, in Paper IV, it was shown that the meso-scale model can be applied for the optimal computational design of an additively manufactured component (lattice structure).

3.1. Paper I

S.A.H. Motaman, U. Prahl: Microstructural constitutive model for polycrystal viscoplasticity in cold and warm regimes based on continuum dislocation dynamics.
Journal of the Mechanics and Physics of Solids 122 (2019): 205–243, ISSN: 0022-5096.
doi: 10.1016/j.jmps.2018.09.002.

Journal of the Mechanics and Physics of Solids 122 (2019) 205–243

Contents lists available at ScienceDirect

Journal of the Mechanics and Physics of Solids

journal homepage: www.elsevier.com/locate/jmps

Microstructural constitutive model for polycrystal viscoplasticity in cold and warm regimes based on continuum dislocation dynamics

S. Amir H. Motaman*, Ulrich Prahl

Department of Ferrous Metallurgy, RWTH Aachen University, Intzestr. 1, Aachen D-52072, Germany

ARTICLE INFO

Article history:
Received 6 March 2018
Revised 5 August 2018
Accepted 3 September 2018
Available online 6 September 2018

Keywords:
Continuum dislocation dynamics
Microstructural constitutive modeling
Dislocation density
Thermo-micro-mechanical modeling
Polycrystal viscoplasticity
Nonlocal theory
Warm metal forming

ABSTRACT

Viscoplastic flow of polycrystalline metallic materials is the result of motion and interaction of dislocations, line defects of the crystalline structure. In the microstructural/physics-based constitutive model presented in this paper, the main underlying microstructural processes influencing viscoplastic deformation and mechanical properties of metals in cold and warm regimes are statistically described by the introduced sets of postulates/axioms for continuum dislocation dynamics (CDD). Three microstructural (internal) state variables (MSVs) are used for statistical quantifications of different types/species of dislocations by the notion of dislocation density. Considering the mobility property of dislocations, they are categorized to mobile and (relatively) immobile dislocations. Mobile dislocations carry the plastic strain (rate), while immobile dislocations contribute to plastic hardening. Moreover, with respect to their arrangement, dislocations are classified to cell and wall dislocations. Cell dislocations are those that exist inside cells/subgrains, and wall dislocations are packed in (and consequently formed) the subgrain walls/boundaries. Therefore, the MSVs incorporated in this model are cell mobile, cell immobile and wall immobile dislocation densities. The evolution of these internal variables is calculated by means of adequate equations that characterize the dislocation processes dominating material behavior during cold and warm monotonic viscoplastic deformation. The constitutive equations are then numerically integrated; and the constitutive parameters are determined/fitted for a widely used ferritic-pearlitic steel (20MnCr5).

1. Introduction

Nowadays, finite element (FE) simulation of manufacturing processes such as metal forming is an important part of process and product design and development in the industry. Correct and accurate description of material behavior and properties is always the biggest challenge in simulation of industrial manufacturing processes that are based on viscoplastic deformation. Dislocation-density-dependent physics-based constitutive models of metal plasticity while are computationally efficient and history-dependent, can accurately account for varying process parameters such as strain rate and temperature. Since these models are founded on essential phenomena dominating the deformation, they have a wide range of usability and validity. Moreover, they are suitable for manufacturing chain simulations as they can efficiently compute the cumulative

* Corresponding author.
E-mail address: seyedamirhossein.motaman@iehk.rwth-aachen.de (S. Amir H. Motaman).

https://doi.org/10.1016/j.jmps.2018.09.002
0022-5096/

Nomenclature

Symbol description		
b	Burgers length (magnitude of Burgers vector)	[m]
c	Material coefficient associated with probability amplitude (or frequency) of a dislocation process	[-]
d	Critical distance for dislocation processes	[m]
e	Relative error, residual/objective/fitness function	[%]
f	Volume fraction	[-]
G	Shear modulus	[Pa]
H	Viscoplastic tangent modulus	[Pa]
l	Length of a dislocation segment	[m]
m	Strain rate sensitivity parameter	[-]
n	Number of active slip/glide systems	[-]
M	Taylor factor	[-]
p	Probability amplitude (or frequency) of a dynamic dislocation process	[-]
q	Volumetric heat generation	[J·m^{-3}]
r	Temperature sensitivity coefficient	[-]
R	Dislocation radius	[m]
s	Temperature sensitivity exponent	[-]
$\boldsymbol{S}$	Stochastic/nonlocal microstructural state	[a set containing all MSVs]
t	Time	[s]
T	Temperature	[K]
u	Volumetric stored energy	[J·m^{-3}]
v	Velocity vector	[m·s^{-1}]
w	Volumetric work	[J·m^{-3}]
α	Dislocation interaction strength/coefficient	[-]
β	Dissipation factor, efficiency of plastic dissipation, or Taylor–Quinney coefficient	[-]
γ	Shear strain in slip system, mean shear strain	[-]
ε	Mean/nonlocal true (normal) strain	[-]
θ	Plastic/strain hardening	[Pa]
φ	Viscous/strain-rate hardening	[Pa.s]
κ	Material constant associated with dissipation factor	[-]
Λ	Dislocation spacing	[m]
ρ	Dislocation density	[m^{-2}]
σ	Mean/nonlocal true (normal) stress	[Pa]
τ	Resolved shear stress	[Pa]

Index description	
ac	Accumulation
an	Annihilation
d	Dynamic
gn	Generation
GN	Geometrically necessary
i	Immobile
loc	Local
m	Mobile, melt
(n)	Time step index, previous time increment
$(n+1)$	Current time increment
nc	Nucleation
c	Cell
p	Plastic
pn	Pinning
rm	Remobilization
s	Static
sat	Saturated
SS	Statistically stored
t	Total (subscript), time (superscript)
tr	Trapping
$\boldsymbol{v}$	Viscous

w	Wall
x	Cell, wall, or total ($x = c, w, t$)
y	Mobile, immobile, or total ($y = m, i, t$), yield/flow
z	Dislocation process ($z = \mathrm{gn}, \mathrm{an}, \mathrm{ac}, \mathrm{tr}, \mathrm{nc}, \mathrm{rm}, \mathrm{spn}, \mathrm{srm}$)
0	Reference, initial/undeformed state
$+$	Increase/production
-	Decrease/elimination
$\hat{}$	Normalized/dimensionless ($\hat{x} = \frac{x}{x_0}$)
$\check{}$	Function
$\sim$	Statistical mean/average
$\bar{}$	Equivalent

Abbreviation	*description*
CB	Cell block
CDD	Continuum dislocation dynamics
CMD	Continuum microstructure dynamics
DDD	Discrete dislocation dynamics
DDW	Dense dislocation wall
DSA	Dynamic strain aging
DTH	Dynamic thermal hardening
DTS	Dynamic thermal softening
EBSD	Electron backscatter diffraction
EVP	Elasto-viscoplastic
FE	Finite element
FEMU	Finite element model updating
GB	Grain boundary
GNB	Geometrically necessary boundary
GND	Geometrically necessary dislocation
IDB	Incidental dislocation boundary
MB	Micro-band
MD	Molecular dynamics
MSV	Microstructural (internal) state variable
RMV	Representative material volume
RVE	Representative volume element
SC	Sub-cell
SMS	Stochastic microstructural state
SFE	Stacking fault energy
TMM	Thermo-micro-mechanical/thermal-microstructural-mechanical
TWIP	Twinning-induced plasticity

effect of the various manufacturing processes by following the microstructure state through the entire manufacturing chain including interpass periods and give a realistic prediction of material behavior and final product properties. The constitutive models are mainly divided into the following main categories (Lin and Chen, 2011; Rusinek et al., 2010):

1.1. Empirical constitutive models

Empirical constitutive models provide description of the yield/flow stress based on empirical observations, and consist of some mathematical functions that lack the physical background. In these models, yield stress is usually an explicit function of accumulated plastic strain, strain rate and temperature, which makes empirical models not history dependent. Moreover, the problem with the accumulated plastic strain is that it is a non-measurable virtual variable. Furthermore, empirical constitutive models are normally characterized by reduced number of material constants and easy calibration. However, due to their empirical characteristics, they are usually covering limited range of applicability and flexibility and offer low accuracy. Empirical models are determined by fitting parameters of model equations to experimental data without considering the physical processes causing the observed material behavior. Empirical or phenomenological models are also named engineering models as they are more common in engineering applications than the physics-based material models. A number of common empirical constitutive models of metals viscoplasticity are usually incorporated in commercial FE programs (Follansbee and Kocks, 1988; Hockett and Sherby, 1975; Johnson and Cook, 1983; Khan and Liang, 1999; Rusinek and Klepaczko, 2001; Sung et al., 2010).

1.2. Microstructural constitutive models

Microstructural or physics-based constitutive models account for microstructural/physical aspects of the material behavior. These are the models where knowledge about the underlying microstructural processes including dislocation processes, is applied to formulate the thermo-micro-mechanical (TMM)/thermal-microstructural-mechanical constitutive equations. In addition, since microstructural material models simulate the main microstructural phenomena influencing the overall mechanical response of the material to plastic deformation, they can be used in wide range of deformation parameters (strain rate and temperature) and loading/deformation modes (tension, compression, creep, and relaxation). Additionally, since in industrial metal forming processes, material usually undergoes variety of loading types and parameters, history-dependent microstructural constitutive models are much more suitable and robust for comprehensive simulations of complex industrial metal forming processes. Physics-based models may follow different approaches to describe microstructure evolution/kinetics in polycrystalline materials under plastic deformation:

- *Discrete dislocation dynamics (DDD)* in which slip/glide/motion and interaction of individual dislocations are considered; and thereby, the stress-strain response of the material is a result of direct simulation of a huge assemble of dislocations in a very small representative volume element (RVE). Some good examples can be found in works of van der Giessen and Needleman (1995), Zbib et al. (1998), Devincre et al. (2001), Zbib and La Diaz de Rubia (2002), Arsenlis et al. (2007), Groh et al. (2009), Zhou et al. (2010), Huang et al. (2012) and Chandra et al. (2018). The algorithms based on DDD are extremely costly in terms of computation time, they do not account for size effect, and cannot be readily implemented in standard FE software for industrial application. Nevertheless, DDD simulations are more efficient than those of molecular dynamics (MD) because the RVEs in DDD are much bigger in size than those used in MD which run in atomistic level. DDD simulations provide insights into larger scale behavior (mesoscale). Therefore, models based on MD and DDD are very helpful for studying of dislocation processes and construction of statistical continuum models based on dislocation density (Kubin, 2013; Li et al., 2014; Monavari et al., 2016).
  Furthermore, DDD and MD have proven to be very useful tools for stochastic modeling of microplasticity experiments such as micro-pillar/column compression, micro-bending and nano-indentation, that together with (in-situ) electron microscopy provide a deep understanding into collective behaviors of dislocations such as dislocation sources, arrangements, configurations and interactions (Csikor et al., 2007; Cui et al., 2017, 2016a, 2016b; Derlet and Maaß, 2013; El-Awady et al., 2009; Greer et al., 2008; Lee et al., 2016; Miller et al., 2004; Motz et al., 2008; Ng and Ngan, 2008; Oh et al., 2009; Papanikolaou et al., 2018; Parthasarathy et al., 2007; Po et al., 2014; Shiari et al., 2005; Yamakov et al., 2002; Zaiser, 2013; Zhang et al., 2015; Zhu, 2004).
- *Continuum dislocation dynamics (CDD)* describe the microstructure indirectly, so that the effects of the micro level processes are accounted for, in an average way on the macro level. Such type of approach is the subject of this study using the notion of dislocation density which unlike (accumulated) plastic strain, is measurable to some extent by electron microscopy and X-ray techniques. Due to their physical nature, besides plastic/strain/work hardening, constitutive models based on different types of dislocation densities have the potential of predicting many other important processes such as creep, relaxation, dynamic strain aging, static aging, and bake hardening.

Opposite to the DDD approach, constitutive models based on CDD are formulated at the macro level, i.e. the microstructural (internal) state variables (MSVs) are calculated for a mesoscale representative material volume (RMV). In macroscale simulation of plastic deformation, material/integration points are considered to be RMVs. Additionally, an ideal test sample under homogenous uniaxial normal load (tension or compression) which is used for obtaining flow curve is assumed to be a RMV.

With indirect approach of CDD, dislocation density-dependent constitutive models provide a bridge between the micro-level phenomena and macro-level continuum quantities, such as stress and strain rate. Furthermore, simulations performed using these constitutive models are much less costly (in the same range of common empirical constitutive models) and less complicated compared to the algorithms based on discrete dislocation dynamics. Hence, they can be easily implemented in standard FE software and are suitable for industrial applications. This study is limited to the isotropic case meaning that Bauschinger, asymmetrical and anisotropic effects are not included in the presented TMM constitutive model. However, the constitutive relations developed in this context can be applied in the crystal plasticity framework in order to account for anisotropic effects caused by nonuniform dislocation density evolution on each slip system which is negligible in steel alloys.

Viscoplastic deformation of crystalline materials with respect to temperature may occur in one of the following regimes/domains:

- cold regime: the maximum temperature in cold regime is normally characterized by temperatures above which diffusion controlled dislocation mechanisms such as dislocation climb and pinning become dominant (approximately $T < 0.3\,T_m$, where T is the absolute temperature; and T_m is the melting absolute temperature) (Galindo-Nava and Rae, 2016);
- warm regime: warm viscoplastic deformation of crystalline materials occur above cold but below hot temperature regime (approximately $0.3\,T_m < T < 0.5\,T_m$) (Doherty et al., 1997; Sherby and Burke, 1968); and
- hot regime: hot viscoplastic deformations are carried out above warm temperature regime. Hot metal forming processes are characterized by at least one of the hot/extreme microstructural processes such as recrystallization, phase transformation, notable precipitate processes, etc. (roughly $0.5\,T_m < T < T_m$).

Strain rate has different regimes as well, however, relatively independent from the material (Field et al., 2004):

- creep or static: $\dot{\varepsilon} < 10^{-4}\ s^{-1}$ (where $\dot{\varepsilon}$ is the strain rate);
- quasi-static: $10^{-4}\ s^{-1} \leq \dot{\varepsilon} < 10^{-2}\ s^{-1}$;
- intermediate-rates: $10^{-2}\ s^{-1} \leq \dot{\varepsilon} \leq 10\ s^{-1}$;
- dynamic: $10\ s^{-1} < \dot{\varepsilon} \leq 10^{3}\ s^{-1}$; and
- shock/highly-dynamic: $\dot{\varepsilon} > 10^{3}\ s^{-1}$.

In the present paper, the focus is on monotonic viscoplastic deformation of polycrystalline metallic materials in cold and warm temperature regimes with quasi-static to intermediate strain rate levels. Nevertheless, further studies must be conducted for generalization to hot regime probably in the framework of continuum micro-dynamics (CMD) which its scope encompasses CDD. Microstructural constitutive models based on CDD and CMD can be coupled with finite element method as microstructural solvers (in addition to the regular thermal and mechanical FE solvers) to simulate not only metal forming processes but also the entire material processing chain including casting, heat treatment, interpass periods, etc., one after the other. However, the microstructural constitutive model based on CMD are characterized with application of extra MSVs in addition to different types of dislocation density. These additional statistical MSVs can be phase volume fractions, void volume fraction, recrystallized volume fraction, twinned volume fraction, transformed volume fraction, precipitate concentrations, etc. In this paper, postulates of CDD are listed. Based on these postulates, a microstructural constitutive model for polycrystal isotropic viscoplasticity in cold and warm regimes is derived. Model's kinetics differential equations are then numerically integrated and subsequently its parameters are determined for a case-hardenable ferritic-pearlitic steel alloy 20MnCr5 which is widely used in industrial forging of automotive components such as bevel gears.

2. Background

The foundation of CDD was formed in 1930's when the pioneers of the theory, Orowan (1934) and Taylor (1934) introduced the concept of dislocation density and its relationship with plastic strain rate and yield stress. They considered the mean effect rather than individual aspects of dislocations motion and interactions in an attempt to describe macroscopic plastic flow. Johnston and Gilman (1959) were the first to propose an evolutionary equation for dislocation density, which was simply the superposition of a multiplication term and a recovery term. Webster (1966) applied an analogous methodology to creep by assuming that the time rate of change of dislocation density is due to multiplication, immobilization and annihilations processes. Later, widespread adoption of this approach was established by the works of Bergström (1970), Kocks (1976), Mecking and Kocks (1981).

Subsequently, many physics-based constitutive models were proposed with more than one type of dislocation density (multi-MSV models). Ananthakrishna and Sahoo (1981), Bammann and Aifantis (1982), Estrin and Kubin (1986) and Hähner and Zaiser (1999) classified dislocations with respect to their mobility feature. They predicted the flow curve by constitutive models based on two MSVs, mobile/glissile/glide and immobile/sessile dislocation densities. 2-MSV models of mobile and immobile dislocation densities are still being developed and applied in different frameworks (Austin and McDowell, 2011; Hansen et al., 2013; Li et al., 2014). Mughrabi (1983), Nix et al. (1985) and Estrin et al. (1998) differentiated dislocations with regard to their arrangement in the dislocation network; and introduced models with two MSVs, cell and wall dislocation densities. Estrin et al. (1996) and Roters et al. (2000) proposed models with three MSVs, cell mobile, cell immobile, and wall immobile dislocation densities. These models appreciate different dislocations based on their mobility property and their arrangement. Likewise, Blum et al. (2002) approached the creep problem in metals by using a 2-MSV constitutive model that decomposed dislocations with respect to their singularity property, namely singular and dipolar dislocations. There exist models that account for dislocation character (edge and screw dislocations) (Cheong and Busso, 2004) and dislocation polarity (right-hand and left-hand) (Arsenlis and Parks, 2002; Roters, 2011). Ma and Roters (2004) classified dislocations further by allocating extra MSVs to their model for parallel and forest dislocation densities. Moreover, Estrin and Mecking (1992) incorporated effective grain size to the classical single variable Kocks-Mecking model Mecking and Kocks (1981).

Sandström and Lagneborg (1975), Busso (1998), Mukherjee et al. (2010) and Babu and Lindgren (2013) all developed multi-MSV microstructural constitutive models to characterize metals behavior under hot deformation by introduction of an additional statistical MSV, recrystallized fraction, with its corresponding kinetics equation. Fan and Yang (2011) and Bok et al. (2014) went further by allocating additional MSVs for each phase fraction to build a microstructural constitutive model for hot sheet metal forming.

Many researchers including Fleck et al. (1994), Fleck and Hutchinson (1997), Nix and Gao (1998), Gao et al. (1999), Gao (1999), Qiu et al. (2001), Gao and Huang (2001), Bhushan and Nosonovsky (2003), Huang et al. (2004), Abu Al-Rub and Voyiadjis (2004), Voyiadjis and Al-Rub (2005), Voyiadjis and Abed (2005), Brinckmann et al. (2006), Bardella (2006), Ardeljan et al. (2014), Lyu et al. (2015) and Nguyen et al. (2017b) distinguished between geometrically necessary dislocations (GNDs) and statistically stored dislocations (SSDs) to formulate strain (rate) gradient plasticity models. Furthermore, Busso (2000), Arsenlis and Parks (2002), Arsenlis (2004), Evers et al. (2004), Clayton et al. (2006), Ma et al. (2006), Beyerlein and Tomé (2008), Lim et al. (2011), Askari et al. (2013), Li et al. (2014), Hochrainer et al. (2014), Sandfeld et al. (2015),

and Askari et al. (2015) among many other authors applied the multi-MSV dislocation density-based approach in crystal plasticity framework.

Recently, some microstructural constitutive models have been developed for special purposes. Viatkina et al. (2007), Kitayama et al. (2013), Pham et al. (2013), Knezevic et al. (2013) and Zecevic and Knezevic (2015) proposed multi-MSV models for strain path dependent evolution of dislocation structures during cyclic plastic deformation to account for kinematic hardening and Bauschinger effect. Austin and McDowell (2011), Lloyd et al. (2014), Luscher et al. (2017) and Nguyen et al. (2017a) utilized dislocation density-based constitutive modeling for viscoplastic deformation of metals at dynamic and shock regimes. Patra and McDowell (2012) developed a physics–based constitutive model for inelastic deformation of irradiated bcc ferritic-martensitic steels by introduction of an extra statistical MSV, namely number of interstitial loops that are formed due to irradiation. Bouaziz and Guelton (2001), Allain et al. (2004) and Steinmetz et al. (2013) incorporated twinned volume fraction as an additional MSV to existing dislocation density-based models in order to reflect plastic hardening behavior of twinning-induced plasticity (TWIP) steels. These models were further developed and implemented in crystal plasticity framework by Wong et al. (2016) to account also for transformation-induced plasticity (TRIP) effect by incorporating one more MSV, namely transformed volume fraction. In addition, Kubin et al. (2002) and Ananthakrishna (2007) have published reviews on theoretical approaches for modeling of collective behavior of dislocations which are recommended for the readers.

In the microstructural state variable approach, the mechanical state at a macroscale nonlocal material point in a continuum body is characterized in terms of internal/hidden variables that statistically represent the stochastic/nonlocal microstructural state (SMS) in addition to the observable statistical external variables such as temperature, strain rate and mean yield stress. To date, many statistical physics-based approaches have been applied for constitutive modeling of metals. Even though extensive work has been conducted in this area, there is not a universal agreement on the number and kind of MSVs to be used (Horstemeyer and Bammann, 2010) as well as the influencing microstructural processes and their associated kinetics equations that determine the values of corresponding MSVs. This study is an attempt for unification and completion of the previous works in the field of continuum dislocation dynamics, by gathering and modifying some of the most important postulates of the CDD theory. In the following section, it is argued that the statistical state of microstructure of polycrystalline materials under monotonic and isotropic viscoplastic deformation in cold and warm regimes is fully defined by three MSVs that are cell mobile, cell immobile and wall immobile dislocation densities. For the first time, evolution of these MSVs with respect to time (or plastic strain) are described considering every statistically notable dislocation process/interaction affecting values of the aforementioned dislocation densities. Without comprehensive decomposition of dislocation types and processes as suggested in this paper, accurately capturing the mechanical response of complex metal alloys such as steels particularly in warm regime is not achievable.

3. Postulates and the constitutive model

To construct a constitutive model based on microstructural processes, first a set of postulates/axioms must be established as the basis for reasoning and subsequent derivation of constitutive relations. In the framework of CDD, the following postulates are introduced, although not all of them are independent. Additionally, for derivation of the constitutive equations, the consequences of each postulate in combination with the earlier ones (or the results of earlier postulates) are provided as well.

3.1. Fundamental postulates

(1) *Stochastic/nonlocal microstructural state*: the mean/nonlocal yield/flow/critical shear stress resolved at slip systems ($\tilde{\tau}_y$) as the nonlocal mechanical response of material is an implicit function of temperature, shear strain rate, and statistical state of microstructure, given by the following equation (Mecking and Kocks, 1981):

$$\tilde{\tau}_y \equiv \overset{\vee}{\tilde{\tau}}_y\left(T,\ \boldsymbol{S}, \dot{\tilde{\gamma}}_p\right) ; \tag{1}$$

where $\dot{\tilde{\tau}}_y$ is the TMM constitutive function; $\dot{\tilde{\gamma}}_p$ is mean plastic shear strain rate at slip systems; T is temperature, and $\boldsymbol{S}$ is a set containing all MSVs and is referred to as stochastic microstructural state (SMS) since it represents the statistical state of microstructure:

$$\boldsymbol{S} \equiv \{S_1\ ,\ S_2\ ,\ S_3\ ,\ \ldots\} ; \tag{2}$$

where S_i is the ith nonlocal MSV which can be various types of dislocation density, grain size, phase fractions, recrystallized fraction, precipitate concentration and size, etc. The evolution of each MSV which is often expressed as time rate of change of MSV, is a function of thermo-mechanical loading and $\boldsymbol{S}$ (Nadgornyi, 1988):

$$\dot{S}_k \equiv \overset{\vee}{\dot{S}}_k\left(T,\ \boldsymbol{S}, \dot{\tilde{\gamma}}_p\right) = \overset{\vee}{\dot{S}}_k\left(T,\ S_1\ ,\ S_2\ ,\ S_3\ ,\ \ldots, \dot{\tilde{\gamma}}_p\right) ; \tag{3}$$

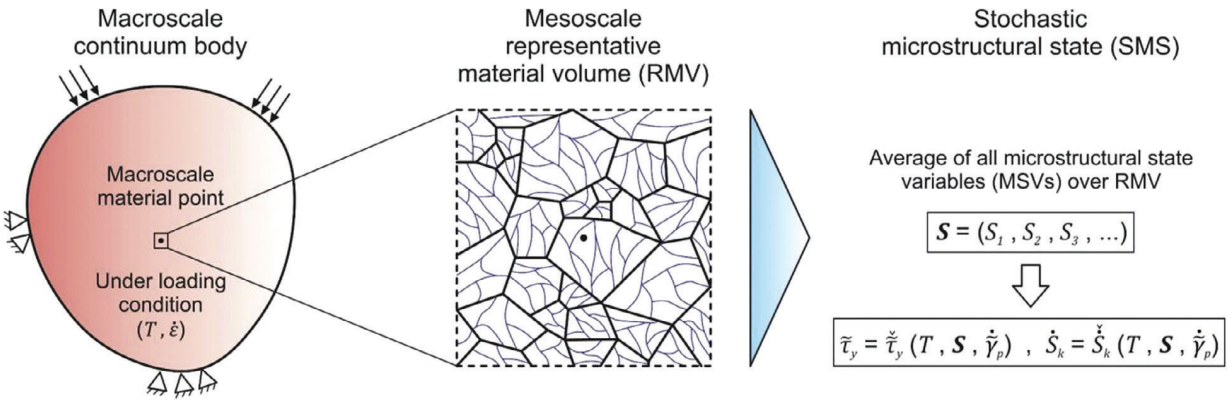

Fig. 1. Multiscale framework of CDD: schematic relation among macroscale continuum body under thermo-mechanical loading, mesoscale representative material volume, and stochastic microstructural state.

where $\overset{\vee}{\dot{S}}_k$ is the function that determines evolution of S_k with respect to time. As shown in Fig. 1, $\boldsymbol{S}$ statistically and nonlocally represents the microstructural state of a material point on a macroscale continuum body. As deformation proceeds, the microstructure state $\boldsymbol{S}$ evolves towards a saturation/steady state $\boldsymbol{S}^{\text{sat}}$ (Estrin and Mecking, 1984).

Furthermore, it is emphasized that in this description, the SMS set and its components (MSVs) are treated based on the nonlocal principle/treatment (Eringen, 1983; Gao and Huang, 2001) as they are averaged over a mesoscale RMV. The mesoscale RMV must be a polycrystalline aggregate that represents the bulk material properly at the considered macroscale continuum material point. Hence, it must consist of sufficient number of constituent single crystal grains in order to capture the size effect Adams and Olson, 1998). This implies that inside the mesoscale RMV, locally the values of MSVs are not necessarily equal to their integral average over RMV due to their heterogeneous (local) distribution. For instance, some MSVs are highly concentrated at small regions while some are statistically distributed inside the grains of RMV (postulate ((3)).

It should be noted that accumulated plastic strain is not an MSV but a mechanical internal state variable and due to its virtual characteristic, it cannot be measured directly. Two identical material samples that are plastically (uniaxially) deformed to an equal amount of accumulated plastic strain but with different histories of temperature and strain rate (e.g. in cold or warm regime), if again deformed under an equal temperature and strain rate condition, do not necessarily yield the same stress response.

Furthermore, the mean//nonlocal normal yield/flow stress (σ_y) (or simply the yield stress) nonlocally applied on a polycrystalline aggregate is related to the mean yield shear stress resolved at its slip systems ($\tilde{\tau}_y$) by Taylor factor (Kocks, 1970; Taylor, 1938):

$$M \equiv \frac{\sigma_y}{\tilde{\tau}_y} = \frac{\dot{\tilde{\gamma}}_p}{\dot{\varepsilon}_p} = \frac{\mathrm{d}\tilde{\gamma}_p}{\mathrm{d}\varepsilon_p} \; ; \tag{4}$$

where $\dot{\varepsilon}_p$ is the mean/nonlocal normal plastic strain rate (or simply the plastic strain rate). It is safe to assume constant $M \cong 3$ for a random orientation distribution of texture for bcc and fcc polycrystalline aggregates. Nevertheless, Taylor factor evolves as plastic strain accumulate; and it is also dependent on the deformation mode but for sufficiently random-textured polycrystals (weak texture or textureless) with random loading during deformation (isotropic case), these dependencies can be neglected (Kocks and Mecking, 2003).

(2) *Dislocation mobility*: with respect to their mobility property, dislocations are divided into mobile and immobile dislocations. While mobile dislocations carry plastic strain, immobile dislocations contribute to plastic hardening (Estrin and Kubin, 1986; Hunter and Preston, 2015). Upon confronting obstacles, mobile dislocation segments may become fully or partially immobilized. Partial immobilization of a (prior) mobile dislocation segment and consequently its division to mobile and immobile dislocation segments is schematically shown in Fig. 2. As illustrated in Fig. 2, an individual dislocation which is typically curved (mixed character), might be consisted of several mobile and immobile dislocation segments. During movement, statistically speaking, the mean length and bow-out radius of bowed-out mobile segments which are always bounded by adjacent immobile segments are reduced while the lengths of the bounding immobile dislocation segments are increased proportionally, as long as the immobile segments are not remobilized by remobilization mechanisms. As pointed out in postulate (1), according to the non-locality principle, mobile and immobile dislocation densities at each macroscale material point are defined as follows:

$$\rho_{cm} \equiv \frac{1}{V}\sum_j l_{cm}^{(j)} \; ; \qquad l_{cm}^{(j)} \equiv \int_{l_{cm}^{(j)}} \mathrm{d}l_{cm}^{(j)} \; ; \tag{5}$$

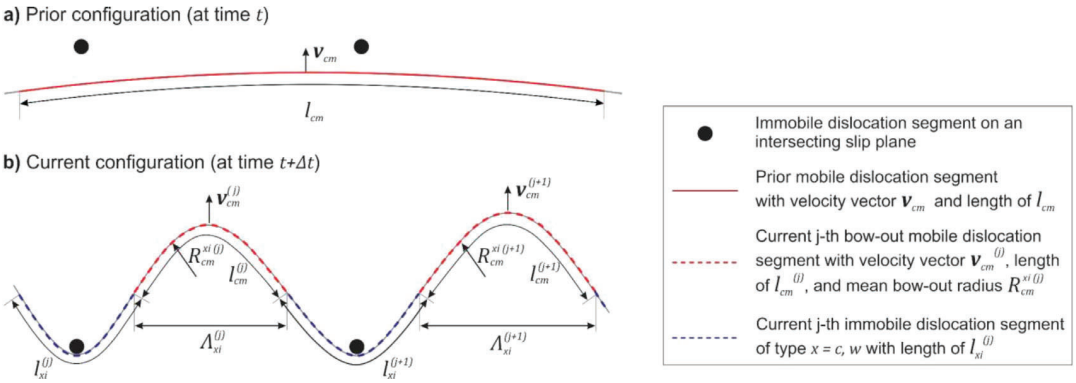

Fig. 2. Schematic of a mobile dislocation segment that is partially immobilized by immobile dislocations intersecting its slip plane (adopted from Hunter and Preston (2015)).

$$\rho_{xi} \equiv \frac{1}{V}\sum_{j} l_{xi}^{(j)} \; ; \qquad l_{xi}^{(j)} \equiv \int_{l_{xi}^{(j)}} \mathrm{d}l_{xi}^{(j)} \; ; \qquad x = c, w \; ; \tag{6}$$

where V is the considered volume which in nonlocal case, is the volume of mesoscale RMV; $l_{cm}^{(j)}$ and $l_{xi}^{(j)}$ are respectively lengths of jth mobile dislocation segment and immobile dislocation segment of type x; $\mathrm{d}l_{cm}^{(j)}$ and $\mathrm{d}l_{xi}^{(j)}$ are infinitesimal elements of arc length along the dislocation segments $l_{cm}^{(j)}$ and $l_{xi}^{(j)}$, respectively; and ρ_{cm} and ρ_{xi} are (nonlocal) mobile dislocation density and immobile dislocation densities (of type x), respectively. x can be c or w that respectively stand for cell and wall (see postulate (3)).

As shown in Fig. 2, it is postulated that motion of bowed out mobile dislocation segments moving on slip systems is always restricted at their both ends by immobile dislocation segments (either cell or wall immobile dislocations). Moving a bowed-out mobile dislocation segment requires a certain amount of shear stress acting on it which is inversely related to the mean radius of bowed-out segment Hull and Bacon, 2011). In postulate ((8), a statistical relation between bow-out radius and immobile dislocation density is derived. Hence, only the collection of immobile dislocations determines the required mean shear stress acting on bowed-out mobile dislocation segments to move them in order to accommodate plastic straining.

(3) *Dislocation arrangement*: due to heterogeneous distribution of dislocations in crystal grains, dislocations with regard to their arrangement are categorized to cell dislocations that exist inside the cell/subgrain blocks/interiors and wall dislocations that form the cell walls/boundaries (Mughrabi, 1983). Wall dislocations are immobile and closely clustered (dense dislocation walls); and statistically, their Burgers vector is very similar to their surrounding wall dislocations. As such, they cause considerable lattice torsion/warp/twist/bending that is manifested by measurable misorientation angle across wall regions that can be detected and measured by electron backscatter diffraction (EBSD) (Gardner et al., 2010; Jiang et al., 2013) and X-ray methods. These dislocations are often referred to as geometrically necessary dislocations (GNDs) (Ashby, 1970; Nye, 1953) as they accommodate lattice curvature (incompatibility of plastic deformation) that arises by geometry change due to local gradient of plastic strain (Arsenlis and Parks, 1999; Gao and Huang, 2003) through formation of semi-planar geometrically necessary boundaries (GNBs) or dense dislocation walls (DDWs) (Kuhlmann-Wilsdorf and Hansen, 1991). Consequently, GNDs are in fact wall dislocations that contribute the most to plastic hardening due to the long range internal stress produced by them (Kassner et al., 2013; Mughrabi, 2006). As plastic straining proceeds, the degree of misorientation angle between adjacent cells or cell blocks (CBs) increases.

Physically, GNBs containing a high local dislocation density with a net Burgers vector are very different than spatially relatively random distributions of cell dislocations (Hughes et al., 2003). Cell dislocations that can be either mobile or immobile do not necessarily adopt any considerable particular semi-stable arrangement unless they become part of walls. Thus, cell dislocations are assumed to be statistically/homogenously distributed inside the CB structure (subgrain); and hence are known as statistically stored dislocations (SSD) (Ashby, 1970). However, stationary cell immobile dislocations form another type of semi-temporary accumulates/clusters/ pile-ups/bundles/tangles/nets named incidental dislocation boundaries (IDBs) (Kuhlmann-Wilsdorf and Hansen, 1991), or forest dislocations with relatively negligible misorientation angle. IDBs form secondary dislocation cells or sub-cells (SCs) inside subgrains. Moreover, the cell volumes bounded by GNBs may form tiny channel-shaped shear/deformation bands such as micro-bands (MBs) and lamellar bands (LBs) (Bay et al., 1992,1989; Hughes, 1993; Hughes and Hansen, 1993). Fig. 3 schematically illustrates cell-wall substructure inside crystal grains. Therefore, there are three main independent types of dislocation density, cell mobile dislocation density (ρ_{cm}), cell immobile dislocation density (ρ_{ci}) and wall immobile dislocation density (ρ_{wi}):

$$\boldsymbol{S} \equiv \{\rho_{cm} \; , \; \rho_{ci}, \rho_{wi}\} \; ; \tag{7}$$

$$\rho_{ct} \equiv \rho_{cm} + \rho_{ci} \equiv \rho_{SS} \; ; \qquad \rho_{wt} \equiv \rho_{wi} \equiv \rho_{GN} \; ; \tag{8}$$

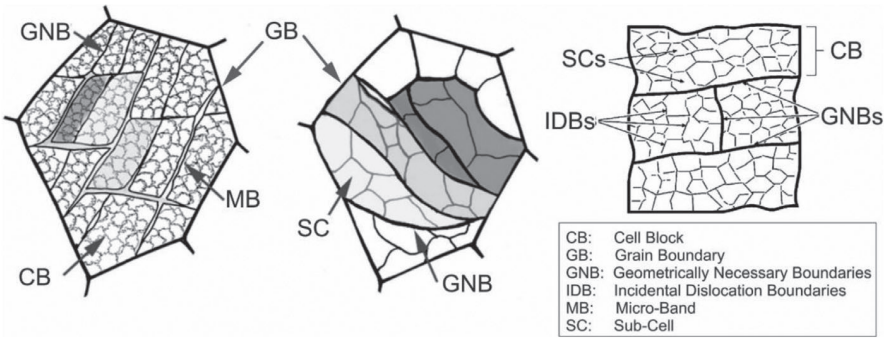

Fig. 3. Schematic of grain subdivision to cell-wall dislocation microstructure (Clayton et al., 2006; Hughes et al., 1998).

$$\rho_{ti} \equiv \rho_{ci} + \rho_{wi} \; ; \qquad \rho_{tm} \equiv \rho_{cm} \; ; \tag{9}$$

$$\rho_t \equiv \rho_{tt} \equiv \rho_{ct} + \rho_{wt} = \rho_{tm} + \rho_{ti} = \rho_{cm} + \rho_{ci} + \rho_{wi} \; ; \tag{10}$$

where ρ denotes dislocation density; subscripts *t, i, m, c*, and *w* respectively stand for total, immobile, mobile, cell and wall; and SS and GN represent statistically stored and geometrically necessary, respectively.

To sum up, wall immobile dislocations are locally (inside the RMV) highly concentrated/compacted at GNBs. Thus, local density of wall immobile dislocations at GNBs is much higher than density of cell immobile dislocations at IDBs or sub-cell interiors. Mobile dislocations are nearly homogeneously distributed in sub-cells. Consequently, local density of (cell) mobile dislocations is much lower than immobile dislocations.

Initial cell immobile dislocation density is determined by density of trapped and accumulated cell dislocations. Wall immobile dislocation density of an undeformed polycrystal is determined by the area of grain boundaries, phase and precipitate interfaces and other two-dimensional crystal defects. Even though grain boundaries and interfaces do not fit in classical definition of dislocations, as they are two-dimensional crystal defects like dislocations and because they interact with dislocations (acting as relatively impenetrable obstacles), technically, they can be included in undeformed wall immobile dislocation density. The equivalent dislocation density of these interfaces is relatively small enough that does not lead to a considerable error in the calculated initial yield stress, although they largely influence the initial plastic hardening. On the other hand, their equivalent density is not affected by plastic straining in cold and warm regime (constant during deformation). Since the interfaces are stable and strictly immobile in cold and warm regime, at the earliest stage of deformation they quickly transform to walls due to the misorientation (relative to undeformed configuration) they inflict, and hence are considered as sources of walls. Therefore, in the undeformed material state, (initial) wall immobile dislocation density depends on the effective grain size which includes the influence of all the interfaces (size effect). Furthermore, in some dual phase metals (e.g. ferritic-martensitic DP steels), due to phase transformation associated expansion during quenching, softer phase (ferrite) becomes plastically deformed by the harder phase (martensite) which results in formation of wall immobile dislocations (GNDs) in the softer phase. In such cases, initial wall immobile dislocation density has a relatively high value.

(4) *Viscoplastic decomposition*: the mean yield shear stress at slip systems ($\tilde{\tau}_y$) has two major contributions that obeys the linear superposition rule (Kumar et al., 1968; Mecking and Kocks, 1981):

$$\tilde{\tau}_y = \tilde{\tau}_v + \tilde{\tau}_p \; ; \tag{11}$$

where $\tilde{\tau}_p$ is plastic/athermal/rate-independent/internal/back shear stress; and $\tilde{\tau}_v$ is referred to as viscous/rate-dependent/thermal/effective shear stress/drag, mean Peierls-Nabarro stress, or overstress which is the mean viscous lattice resistance to move mobile dislocations in a nearly obstacle/dislocation-free lattice (with relatively very low dislocation density) (Nabarro, 1997,1952; Peierls, 1940). Viscous shear stress is affected by point defects such as vacancies, alloying elements and solute atoms (interstitial and substitutional). Additionally, plastic shear stress needs to be overcome to move the bowed-out mobile dislocations Fig. 2). As mentioned in postulate ((2), the lower the bow-out radius, the lower the required (extra) plastic shear stress to move it.

The viscoplastic decomposition can be depicted by the rheological model shown in Fig. 4, similar to Perzyna-type formulation (Perzyna, 1966), which consists of a parallel set of nonlinear dashpot/damper and nonlinear friction elements that are in series linkage with a linear spring element.

Furthermore, given Eq. (4), Eq. (11) may take the following form:

$$\sigma_y = \sigma_v + \sigma_p \; ; \qquad \sigma_v \equiv \tilde{M}\tilde{\tau}_v \; ; \qquad \sigma_p \equiv \tilde{M}\tilde{\tau}_p \; . \tag{12}$$

(5) *Cell-wall decomposition*: as emphasized in postulate (2), only immobile dislocations contribute to plastic hardening. The total surface density (total surface area per unit volume) of cells and walls are equal, as dislocation walls (GNBs) encompass the cell volumes (subgrains). In other words, the cell-wall dislocation substructure can be treated as a cellular

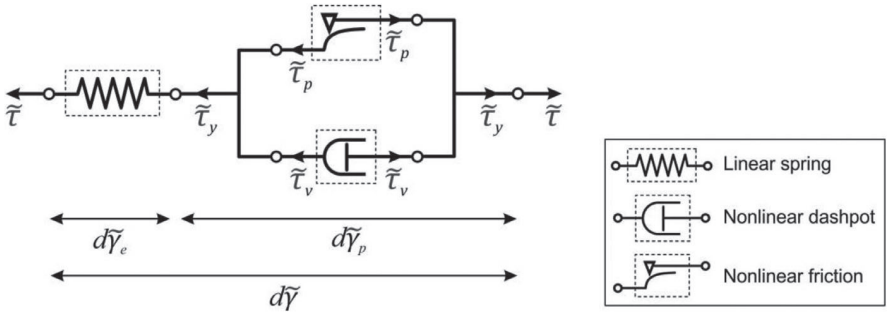

Fig. 4. Rheological model of polycrystal elasto-viscoplasticity; plastic flow occurs when the applied shear stress ($\tilde{\tau}$) becomes equal to the yield shear stress at slip systems ($\tilde{\tau} = \tilde{\tau}_y$).

composite. Hence, it is postulated that the two types of immobile dislocations contribute to plastic hardening in parallel (additive decomposition of plastic stress) in order to satisfy the compatibility for isochoric viscoplastic flow of material in which both cells and walls need to be deformed simultaneously at an equal rate (isostrain homogenization). Thus, mean plastic shear stress is linearly decomposed to its constituent internal stresses corresponding to cell immobile dislocations (immobile SSDs) and wall immobile dislocations (immobile GNDs) (Columbus and Grujicic, 2002; Mughrabi, 1987; Voyiadjis and Al-Rub, 2005):

$$\tilde{\tau}_p = \tilde{\tau}_{pc} + \tilde{\tau}_{pw} \ ; \tag{13}$$

where $\tilde{\tau}_{pc}$ and $\tilde{\tau}_{pw}$ are respectively contributions of cell and wall immobile dislocations to plastic shear stresses. $\tilde{\tau}_{pc}$ and $\tilde{\tau}_{pw}$ are axial and torsional plastic stress, respectively. In postulate (8), the relations of $\tilde{\tau}_{pc}$ and $\tilde{\tau}_{pw}$ with immobile dislocation densities are described. Considering Eq. (4), Eq. (13) is rewritten as follows:

$$\sigma_p = \sigma_{pc} + \sigma_{pw} \ ; \qquad \sigma_{pc} \equiv \tilde{M}\tilde{\tau}_{pc} \ ; \qquad \sigma_{pw} \equiv \tilde{M}\tilde{\tau}_{pw} \ . \tag{14}$$

(6) *Local dislocation density*: in saturation state, dislocation substructure and density is steady and statistically remain constant in a representative material volume. One can assume that the exact locations of walls (GNBs) inside RMV at saturation state are known prior to viscoplastic deformation. Hence, V_w is assumed to be the summation of immediate (local) surrounding volumes of GNBs in the saturation state (including mobile dislocations constrained by GNBs constituent wall immobile dislocations). Cell immobile dislocations and the mobile dislocations bounded by them are envisaged to be uniformly distributed in the rest of RMV's volume (V_c). Therefore,

$$V = V_c + V_w \ ; \qquad V_c \cap V_w = \emptyset \ . \tag{15}$$

Notice that V, V_c and V_w are virtual volumes. Moreover, V (volume of RMV) is constant during deformation. In monotonic viscoplastic deformation, it is known that GNBs are relatively sharp boundaries containing locally dense wall immobile dislocations (postulate (3)). This indicates that $V_w << V_c$ and $V_w << V$. However, in materials under long and high-amplitude cyclic viscoplastic deformation, V_w and V_c become closer but still often $V_w < V_c$. Thus, in monotonic viscoplastic deformation which is the subject of this study, one can assume that cell and wall immobile dislocations during the entire deformation are homogenously locally distributed over constant volumes of V_c and V_w, respectively. Therefore,

$$\rho_{xi}^{\mathrm{loc}} \equiv \frac{1}{V_x}\sum_j l_{xi}^{(j)} \ ; \qquad x = c, w \ . \tag{16}$$

According to Mughrabi (1983), constant cell volume fraction (f_c) and wall volume fraction (f_w) are defined as follows:

$$f_x \equiv \frac{V_x}{V} \ ; \qquad x = c, w \ . \tag{17}$$

Combining Eqs (6), (16) and (17) results in (Mughrabi, 1983):

$$\rho_{xi}^{\mathrm{loc}} = \frac{\rho_{xi}}{f_x} \ ; \qquad x = c, w \ ; \tag{18}$$

$$f_c + f_w = 1 \ . \tag{19}$$

From the view point of an observer who observes the macroscale material point shown in Fig. 1, viscoplastic deformation is homogenous. This leads to the assumption of nearly uniform local distribution of mobile dislocations which carry the plastic strain. Consequently, local and nonlocal mobile dislocation densities are almost equal ($\rho_{cm}^{\mathrm{loc}} = \rho_{cm}$). Combining this with Eq. (18) and the fact that f_x is constant gives:

$$\rho_{xy}^{\mathrm{loc}} \propto \rho_{xy} \ ; \qquad \begin{cases} x = c, w, t \\ y = m, i, t \end{cases} . \tag{20}$$

(7) *Dislocations characteristic spacing*: dislocations intersect each other and form dislocation network with characteristic average spacing of $\tilde{\Lambda}$. It can be easily shown that the average spacing among dislocations (also known as mean free path of dislocations) of type xy ($\tilde{\Lambda}_{xy}$) is inversely proportional to the square root of respective local dislocation density (Kocks, 1966; Nes, 1997; Seeger, 1955):

$$\tilde{\Lambda}_{xy} \propto \frac{1}{\sqrt{\rho_{xy}^{\text{loc}}}} \propto \frac{1}{\sqrt{\rho_{xy}}} \; ; \qquad \begin{cases} x = c, w, t \\ y = m, i, t \end{cases} . \tag{21}$$

It should be noted that $\tilde{\Lambda}_{xy}$ has a local character. Additionally, it can be also readily shown that the volumetric number of junctions/intersection/nodes of dislocation type xy or dislocation junction density of type xy (N_{xy}) is proportional to dislocation density ρ_{xy}^{loc} or ρ_{xy} (Eq. (20)) while inversely proportional to the average spacing $\tilde{\Lambda}_{xy}$ (Gottstein and Argon, 1987):

$$N_{xy} \propto \rho_{xy} \frac{1}{\tilde{\Lambda}_{xy}} \propto \rho_{xy}^{3/2} \; ; \qquad \begin{cases} x = c, w, t \\ y = m, i, t \end{cases} . \tag{22}$$

(8) *Plastic stress*: as pointed out in postulate (2), the average bow-out radius of cell mobile dislocations that are constrained at both ends by immobile dislocations of type $x = c,\ w, t$ ($\tilde{R}_{cm}^{xi}$) (Fig. 2) is proportional to average spacing of immobile dislocations of type x (Nes, 1997):

$$\tilde{R}_{cm}^{xi} \propto \tilde{\Lambda}_{xi} \; ; \qquad x = c, w, t \; . \tag{23}$$

On the other hand, the mean plastic resolved shear stress at slip systems is directly proportional to Burgers length (magnitude of Burgers vector) (b) and shear modulus (G) and inversely proportional to $\tilde{R}_{cm}^{xi}$ (Gao et al., 1999; Hull and Bacon, 2011; Nabarro, 1952):

$$\tilde{\tau}_{px} \propto \frac{bG}{\tilde{R}_{cm}^{xi}} \; ; \qquad x = c, w \; ; \tag{24}$$

where $\tilde{\tau}_{px}$ is the mean plastic resolved shear stress associated with immobile dislocations of type x. Given Eqs. (21) and (23), the Taylor relation (Bailey and Hirsch, 1960; Seeger et al., 1957; Taylor, 1934) is derived:

$$\tilde{\tau}_{px} = bG\tilde{\alpha}^{\text{loc}} \sqrt{\rho_{xi}^{\text{loc}}} \; ; \qquad x = c, w \; ; \tag{25}$$

where α^{loc} is a material constant known as local dislocation interaction strength/coefficient; and $\tilde{\alpha}^{\text{loc}}$ is statistical average of α^{loc} for different configurations of interacting mobile-immobile dislocations in various slip systems at the considered local point. Given Eq. (18):

$$\tilde{\tau}_{px} = bG\tilde{\alpha}_x \sqrt{\rho_{xi}} \; ; \qquad \tilde{\alpha}_x = \frac{\tilde{\alpha}^{\text{loc}}}{\sqrt{f_x}} \; ; \qquad x = c, w \; ; \tag{26}$$

where $\tilde{\alpha}_x$ is the nonlocal interaction strength related to local density and geometrical arrangement of immobile dislocations of cell and wall species ($x = c, w$). Variation of $\tilde{\alpha}_x$ with plastic strain is assumed to be negligible Kocks and Mecking, 2003). Since most of the plastic hardening is due to wall immobile dislocations, essentially $\tilde{\alpha}_w > \tilde{\alpha}_c$. Further, combining Eqs. (19) and ((26) yields:

$$f_c = \frac{\tilde{\alpha}_w^2}{\tilde{\alpha}_c^2 + \tilde{\alpha}_w^2} \; ; \qquad f_w = \frac{\tilde{\alpha}_c^2}{\tilde{\alpha}_c^2 + \tilde{\alpha}_w^2} \; ; \qquad \tilde{\alpha}^{\text{loc}} = \frac{\tilde{\alpha}_c \tilde{\alpha}_w}{\sqrt{\tilde{\alpha}_c^2 + \tilde{\alpha}_w^2}} \; . \tag{27}$$

Finally, given Eq. (4), Eq. (26) may be rewritten as:

$$\sigma_{px} = MbG\tilde{\alpha}_x \sqrt{\rho_{xi}} \; ; \qquad x = c, w \; . \tag{28}$$

(9) *Kinetics superposition*: dynamic evolution of dislocation density is described as the rate of change of dislocation density with respect to time or plastic strain which is linear superposition of increase/production (with positive sign) and decrease/elimination (negative sign) terms (Johnston and Gilman, 1959; Kocks, 1976; Webster, 1966):

$$\dot{\rho}_{xy} = \dot{\rho}_{xy}^{+} - \dot{\rho}_{xy}^{-} \; ; \qquad \begin{cases} x = c, w, t \\ y = m, i, t \end{cases} . \tag{29}$$

Therefore,

$$\partial_{\tilde{\gamma}_p} \rho_{xy} = \partial_{\tilde{\gamma}_p} \rho_{xy}^{+} - \partial_{\tilde{\gamma}_p} \rho_{xy}^{-} \; ; \qquad \partial_{\varepsilon_p} \rho_{xy} = \partial_{\varepsilon_p} \rho_{xy}^{+} - \partial_{\varepsilon_p} \rho_{xy}^{-} \; ; \qquad \begin{cases} x = c, w, t \\ y = m, i, t \end{cases} ; \tag{30}$$

where $\partial_{\tilde{\gamma}_p} \equiv \frac{\partial}{\partial \tilde{\gamma}_p}$ and $\partial_{\varepsilon_p} \equiv \frac{\partial}{\partial \varepsilon_p}$ are partial derivative operator with respect to mean shear plastic strain at slip systems and mean plastic strain, respectively. Static and overall (combination of static and dynamic) evolution of dislocation densities are represented by time derivative relations:

$$(\dot{\rho}_{xy})_s = \left(\dot{\rho}_{xy}^{+}\right)_s - \left(\dot{\rho}_{xy}^{-}\right)_s \; ; \qquad \begin{cases} x = c, w, t \\ y = m, i, t \end{cases} ; \tag{31}$$

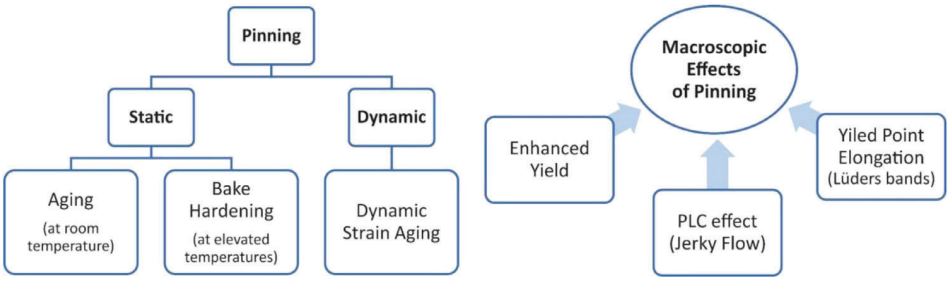

Fig. 5. Pinning phenomena and their macroscopic effects.

$$\left(\dot{\rho}_{xy}\right)_d = \dot{\tilde{\gamma}}_p \partial_{\tilde{\gamma}_p} \rho_{xy} = \dot{\varepsilon}_p \ \partial_{\varepsilon_p} \rho_{xy} \ ; \qquad \begin{cases} x = c, w, t \\ y = m, i, t \end{cases} ; \tag{32}$$

$$\dot{\rho}_{xy} = \left(\dot{\rho}_{xy}\right)_d + \left(\dot{\rho}_{xy}\right)_s = \dot{\varepsilon}_p \partial_{\varepsilon_p} \rho_{xy} + \left(\dot{\rho}_{xy}\right)_s \ ; \qquad \begin{cases} x = c, w, t \\ y = m, i, t \end{cases} ; \tag{33}$$

where subscripts *s* and *d* respectively represent static and dynamic states.

Furthermore, for convenience in calculations and dimensional balancing of equations, the normalized/dimensionless dislocation density of type *xy* ($\hat{\rho}_{xy}$) is defined as follows:

$$\hat{\rho}_{xy} \equiv \frac{\rho_{xy}}{\rho_0} \ ; \qquad \begin{cases} x = c, w, t \\ y = m, i, t \end{cases} ; \tag{34}$$

where the hat-sign (^) indicates the normalization; and ρ_0 is constant reference dislocation density. Therefore, in all the previous relations that are presented so far in this paper (except Eqs. (26) and (28)) ρ_{xy} can be replaced by $\hat{\rho}_{xy}$. Thereby, $\hat{\tilde{\Lambda}}_{xy}$ and $\hat{N}_{xy}$ are respectively normalized average spacing among dislocations of type *xy* and normalized dislocation junction density of type *xy*.

(10) *Dynamic dislocation processes*: there are six main classes of dynamic dislocation processes that are statistically considerable in constitutive modeling of metal viscoplasticity in cold and warm regimes:

- Generation/multiplication of mobile dislocations: Motion/displacement of mobile dislocations leads to their elongation.
- Annihilation of dislocations: Dislocations of all three types can be annihilated by mobile dislocations with opposite Burgers vector slipping on neighboring parallel slip plane.
- Accumulation of immobile dislocations: Mobile dislocations can be immobilized by immobile dislocations and produce accumulates of immobile dislocations.
- Trapping of mobile dislocations: Mobile dislocations interacting each other can be immobilized by trapping process. Trapping process has two underlying mechanisms/reactions that result in immobilization of infected parts of mobile dislocations: locking of mobile dislocations; and pinning of mobile dislocations by interstitial solute/impurity atoms. Dynamic strain aging (DSA) effect in part is associated with pinning of mobile dislocations. At macroscopic level, pinning process reveals itself in the existence of enhanced upper initial yield stress which is followed by yield point elongation associated with Lüders bands (Hahn, 1962; Hall, 1970) in stress-strain curves. Pinning phenomena and their macroscopic effects are classified in Fig. 5.
- Nucleation of wall dislocations: Cell immobile dislocations can become wall dislocations if the accumulates they belong to, while are being immobilized sufficiently strong, reach a critical size and local density.
- Remobilization/mobilization of immobile dislocations: Immobile dislocations can be mobilized and contribute to plastic straining.

(11) *Static dislocation processes*: there are two major static (at nonlocal $\dot{\tilde{\gamma}}_p \approx 0$) dislocation processes during viscoplastic deformation of metals in cold and warm regimes (Pham et al., 2015):

- Static pinning (Fig. 5) of cell dislocations by diffusion of interstitial solute atoms such as Carbon and Nitrogen to surroundings of dislocation cores and junctions (Cottrell cloud) which are statistically distributed (SSDs). This is due to higher stored elastic energy density of dislocation surroundings compared to defect-free regions of lattice (Cottrell and Bilby, 1949).
- Static remobilization of immobile dislocations by means of thermal mechanisms such as junction dissociation and dislocation climb (vacancy diffusion).

It should be noted that the aforementioned dynamic and static dislocation processes often consist of multiple individual underlying mechanisms. In the following sections, evolution of different types of dislocations by the above-listed dislocation processes is quantitatively and statistically described through several postulates.

3.2. Dynamic dislocation processes

(12) *Dynamic generation*: motion of bowing mobile dislocation segments that are held at both ends by immobile dislocations generates more mobile dislocations by different mechanisms (Stricker et al., 2018) such Frank-Read mechanism (Frank and Read, 1950), multiple cross-slip mechanism (Koehler, 1952), or mobile junctions mechanism (Stricker and Weygand, 2015; Weygand, 2014). Thus, the rate of dynamic generation rate of mobile dislocations in plastic shear increment ($\partial_{\tilde{\gamma}_p}\rho^{\mathrm{gn}}_{cm}$) is proportional to cell mobile dislocation density. The generation rate is higher where average bow-out radius of mobile dislocation segments bounded by immobile dislocations ($\tilde{R}^{ti}_{cm}$) and the average length of mobile dislocation segments ($\tilde{\Lambda}_{ti} \propto \tilde{R}^{ti}_{cm}$) is larger (Nadgornyi, 1988; Steif and Clifton, 1979):

$$\partial_{\tilde{\gamma}_p}\rho^{\mathrm{gn}}_{cm} \propto \rho_{cm}\ \tilde{R}^{ti}_{cm}\ . \tag{35}$$

Given Eqs. (4), (21), (23) and (34):

$$\partial_{\tilde{\gamma}_p}\rho^{\mathrm{gn}}_{cm} = p^{\mathrm{gn}}_{cm}\ \rho_{cm}\ ; \qquad p^{\mathrm{gn}}_{cm} = c^{\mathrm{gn}}_{cm}\ \frac{1}{\sqrt{\hat{\rho}_{ti}}}\ ; \tag{36}$$

$$\partial_{\varepsilon_p}\hat{\rho}^{\mathrm{gn}}_{cm} = M\ c^{\mathrm{gn}}_{cm}\ \frac{\hat{\rho}_{cm}}{\sqrt{\hat{\rho}_{ti}}}\ ; \tag{37}$$

where $\partial_{\varepsilon_p}\hat{\rho}^{\mathrm{gn}}_{cm}$ is normalized dynamic generation rate of cell mobile dislocation density with respect to plastic strain; p^{gn}_{cm} is probability amplitude of dynamic generation of cell mobile dislocations; and c^{gn}_{cm} is material coefficient associated with probability amplitude of dynamic generation of cell mobile dislocations. Frequency of occurrence of a dynamic dislocation process with probability amplitude of p is equal to $\nu = p\ \dot{\tilde{\gamma}}_p$. In addition, dynamic generation of mobile dislocations is an athermal dislocation process meaning that it is not directly dependent on the temperature.

(13) *Dynamic annihilation:* the annihilation process takes place between a mobile dislocation and another dislocation that can be of any type. Thus, there are three sorts of dislocation annihilation: mutual annihilation of cell mobile dislocations, mutual annihilation of cell mobile and cell immobile dislocations, and mutual annihilation of cell mobile and wall immobile dislocations. Hence, the magnitude of dynamic annihilation rate of mobile dislocations and dislocations of type xy with respect to plastic shear strain increment ($\partial_{\tilde{\gamma}_p}\rho^{an}_{xy}$) is proportional to cell mobile dislocation density and the dislocation density of type xy (Ananthakrishna and Sahoo, 1981):

$$\partial_{\tilde{\gamma}_p}\rho^{\mathrm{an}}_{xy} \propto \rho_{cm}\ \rho_{xy}\ ; \qquad xy = cm, ci, wi\ . \tag{38}$$

Given Eqs. (4) and (34):

$$\partial_{\tilde{\gamma}_p}\rho^{\mathrm{an}}_{xy} = p^{\mathrm{an}}_{xy}\ \rho_{xy}\ ; \qquad p^{\mathrm{an}}_{xy} = c^{\mathrm{an}}_{xy}\ \hat{\rho}_{cm}\ ; \qquad xy = cm, ci, wi\ ; \tag{39}$$

$$\partial_{\varepsilon_p}\hat{\rho}^{\mathrm{an}}_{xy} = M\ c^{\mathrm{an}}_{xy}\ \hat{\rho}_{cm}\ \hat{\rho}_{xy}\ ; \qquad xy = cm, ci, wi\ ; \tag{40}$$

where $\partial_{\varepsilon_p}\hat{\rho}^{\mathrm{an}}_{xy}$ is normalized dynamic annihilation rate of dislocation density of type xy with respect to plastic strain; p^{an}_{xy} is probability amplitude of dynamic annihilation of dislocation density of type xy; And c^{an}_{xy} are material coefficients related to frequency of dynamic annihilation of dislocation density of type xy. Annihilation events take place between a mobile dislocation and another dislocation with opposite/antiparallel Burgers vector on parallel planes when two dislocations are within a critical distance from each other. Two near-screw dislocations of opposite sign, slipping on two neighboring parallel slip planes can annihilate by cross slip of one of them (Brown, 2002; Essmann and Mughrabi, 1979; Nix et al., 1985; Oren et al., 2017; Pauš et al., 2013; Püschl, 2002; Seeger et al., 1957). Two near-edge dislocations may annihilate as well by spontaneous formation and disintegration of a very narrow unstable dislocation dipole which can be assisted by dislocation climb. (Eisenlohr and Blum, 2005; Monavari and Zaiser, 2018; Vegge and Jacobsen, 2002). Thus, thermally activated dislocation climb and cross-slip mechanisms facilitate dislocation annihilation. Therefore, dynamic annihilation of dislocations are thermal dislocation processes meaning that probability amplitudes associated with dislocation annihilation processes have temperature dependence (increase with increasing temperature). On the other hand, since at least dislocation climb as a contributing mechanism for dynamic annihilation processes is controlled by time-dependent diffusion of vacancies, annihilation processes have strain rate dependence with negative strain rate sensitivity. Besides, dislocation cross-slip can be as well considered a rate-controlled mechanism (Nes, 1997).

Thus, one might suggest that when a mobile dislocation and another dislocation (of type xy) are on the same slip system within the critical distance (some authors call it capture radius) for annihilation of dislocations of type xy (d^{an}_{xy}), they will likely annihilate each other, in case of having opposite Burgers vectors (Essmann and Mughrabi, 1979). In light of this, for instance, the dimensionless material parameter associated with frequency of dynamic annihilation among cell mobile dislocations (c^{an}_{cm}) can be decomposed as $c^{\mathrm{an}}_{cm} = \frac{d^{\mathrm{an}}_{cm}}{\tilde{n}b}$, where $\tilde{n}$ is the average number of active slip systems ($\tilde{n} \geq 3$). Statistically,

one can assume equal density of dislocations on all active slip systems (in isotropic case) which gives rise to normalization factor $\frac{1}{\tilde{n}}$ (Roters et al., 2000).

(14) *Dynamic accumulation:* immobilization of mobile dislocations by immobile dislocations produces or increases the size of immobile dislocation accumulates. This dislocation process is known as dislocation accumulation; and its magnitude with respect to plastic shear strain increment ($\partial_{\tilde{\gamma}_p}\rho_{xi}^{\mathrm{ac}}$) is proportional to cell mobile dislocation density. It is also inversely proportional to average spacing among immobile dislocations of type $x = c, w$ ($\tilde{\Lambda}_{xi}$) (Kocks, 1976) as well as the average radius of mobile dislocation segments bounded by immobile dislocations of type $x = c, w$ ($\tilde{R}_{cm}^{xi} \propto \tilde{\Lambda}_{xi}$):

$$\partial_{\tilde{\gamma}_p}\rho_{xi}^{\mathrm{ac}} \propto \rho_{cm}\ \frac{1}{\tilde{\Lambda}_{xi}}\ ; \qquad x = c, w\ . \tag{41}$$

Having Eqs. (4), (21) and (34):

$$\partial_{\tilde{\gamma}_p}\rho_{xi}^{\mathrm{ac}} = p_{xi}^{\mathrm{ac}}\ \rho_{cm}\ ; \qquad p_{xi}^{\mathrm{ac}} = c_{xi}^{\mathrm{ac}}\ \sqrt{\hat{\rho}_{xi}}\ ; \qquad x = c, w\ ; \tag{42}$$

$$\partial_{\varepsilon_p}\hat{\rho}_{xi}^{\mathrm{ac}} = M\ c_{xi}^{\mathrm{ac}}\ \sqrt{\hat{\rho}_{xi}}\ \hat{\rho}_{cm}\ ; \qquad x = c, w\ ; \tag{43}$$

where $\partial_{\varepsilon_p}\hat{\rho}_{xi}^{\mathrm{ac}}$ is normalized dynamic accumulation rate of immobile dislocations of type x with respect to plastic strain; p_{xi}^{ac} is probability amplitude of dynamic accumulation of immobile dislocations of type x; and c_{xi}^{ac} are material parameters associated with probability of dynamic accumulation of immobile dislocations of type x. Dynamic accumulation of immobile dislocations is an athermal process.

(15) *Dynamic trapping:* interaction between mobile dislocations moving in different intersecting slip systems results in the formation of dislocation junctions/intersections/nodes. These dislocation junctions can be lock junctions such as Lomer-Cottrell lock junctions (Cottrell, 1953; Lomer, 1951), Hirth lock junctions (Hirth, 1961), collinear (Madec et al., 2003) and coplanar lock junctions (Thompson, 1953). Lock junctions restrict movement of involved mobile dislocations by immobilizing parts of them near the formed lock junction, leading to latent hardening (Franciosi, 1985). In addition, some junctions formed due to interaction of mobile dislocation pairs are not lock junctions (depending on the configuration of respective slip systems and mobile dislocations). They can as well be mobile/glissile or temporal (temporary) junctions which do not lead to immediate immobilization directly.

Essentially, dislocation junctions due to their relative high energy density are attractive regions for diffusion and accumulation of interstitial solute atoms. Therefore, some of the mobile and temporal junctions become pinned/arrested/anchored due to diffusion and accumulation of interstitial solutes at their vicinity; which leads to subsequent immobilization of respective mobile dislocations or infected parts of them (Cottrell and Bilby, 1949; Mulford and Kocks, 1979; van den Beukel and Kocks, 1982). Density of potential junctions of interacting mobile dislocations, as mentioned in postulate (7), is proportional to density of mobile dislocations (ρ_{cm}) and inversely proportional to the average spacing among mobile dislocations ($\tilde{\Lambda}_{cm}$). Thus, frequency of occurrence of mobile dislocation trapping events comprised of two major underlying mechanisms (locking and pinning), must be proportional to junction density of cell mobile dislocations (N_{cm}). Henceforth,

$$\partial_{\tilde{\gamma}_p}\rho_{cm}^{\mathrm{tr}} \propto N_{cm}\ . \tag{44}$$

Given Eqs. (4), (22) and (34):

$$\partial_{\tilde{\gamma}_p}\rho_{cm}^{\mathrm{tr}} = p_{cm}^{\mathrm{tr}}\ \rho_{cm}\ ; \qquad p_{cm}^{\mathrm{tr}} = c_{cm}^{\mathrm{tr}}\ \sqrt{\hat{\rho}_{cm}}\ ; \tag{45}$$

$$\partial_{\varepsilon_p}\hat{\rho}_{cm}^{\mathrm{tr}} = M\ c_{cm}^{\mathrm{tr}}\ \hat{\rho}_{cm}^{3/2}\ ; \tag{46}$$

where superscript tr denotes the trapping process; $\partial_{\varepsilon_p}\hat{\rho}_{cm}^{\mathrm{tr}}$ is normalized dynamic trapping rate of cell mobile dislocations with respect to plastic strain; p_{cm}^{tr} is probability amplitude of dynamic trapping of cell mobile dislocations; and c_{cm}^{tr} is a material coefficient associated with probability amplitude of dynamic trapping of cell mobile dislocations. Since the pinning mechanism of trapping process is a diffusion controlled reaction, dynamic trapping of cell mobile dislocations is a thermal dislocation process that its magnitude increases with increasing temperature. In other words, by increasing temperature, particularly in metals with notable interstitial concentration, the rate of immobilization of dislocation junctions (trapping) becomes higher. Additionally, since pinning occurs due to diffusion of interstitial solute atoms to dislocation cores and junction, c_{cm}^{tr} is a function of concentration of interstitial solutes atoms such as Carbon and Nitrogen.

Moreover, one might argue that c_{cm}^{tr} has a negative strain rate sensitivity because the pinning process is associated with time-dependent diffusion of interstitial solute atoms. The DSA effect is observed when the interstitial atoms reorientation time is shorter than the waiting time of temporal and mobile junctions at the locations nearby interstitial solute complex (Kubin et al., 1988; Kubin and Estrin, 1990). Hence, there exist a critical strain rate beyond which the intensity of mobile dislocation pinning abruptly drops. That strain rate belongs to the dynamic regime.

(16) *Dynamic wall nucleation*: accumulates of cell immobile dislocations that are immobile sufficiently strong (meaning that their remobilization requires higher stress than mean yield resolved shear stress) will grow and become denser by immobilizing more mobile dislocations at their vicinity (cell immobile accumulation process). These cell immobile pile-ups

that reach a critical size and local density, subsequently become adequately stable to produce sufficient local stress concentration which results in necessary lattice curvature in their vicinity to make them part of walls. This process is called wall nucleation. From this point of view, wall nucleation process converts some cell immobile to wall immobile dislocations. As such, its rate is proportional to cell immobile dislocation density. On the other hand, the accumulation of cell immobile dislocations increases the probability of wall nucleation process. Hence, statistical magnitude of dynamic nucleation rate of wall immobile dislocations with respect to plastic shear strain increment ($\partial_{\tilde{\gamma}_p}\rho_{wi}^{\mathrm{nc}}$) is proportional to cell immobile dislocation density (ρ_{ci}) and the rate of cell immobile dislocation accumulation ($\partial_{\tilde{\gamma}_p}\rho_{ci}^{\mathrm{ac}}$):

$$\partial_{\tilde{\gamma}_p}\rho_{wi}^{\mathrm{nc}} \propto \ \rho_{ci}\ \partial_{\tilde{\gamma}_p}\rho_{ci}^{\mathrm{ac}}\ . \tag{47}$$

Given Eqs. (4), (21), (34) and (41):

$$\partial_{\tilde{\gamma}_p}\rho_{wi}^{\mathrm{nc}} = p_{wi}^{\mathrm{nc}}\ \rho_{ci}\ ; \qquad p_{wi}^{\mathrm{nc}} = c_{wi}^{\mathrm{nc}}\ \sqrt{\hat{\rho}_{ci}}\ \hat{\rho}_{cm}\ ; \tag{48}$$

$$\partial_{\varepsilon_p}\hat{\rho}_{wi}^{\mathrm{nc}} = M\ c_{wi}^{\mathrm{nc}}\ \hat{\rho}_{ci}^{3/2}\ \hat{\rho}_{cm}\ ; \tag{49}$$

where $\partial_{\varepsilon_p}\hat{\rho}_{wi}^{\mathrm{nc}}$ is normalized dynamic nucleation rate of wall immobile dislocations with respect to plastic strain; p_{wi}^{nc} is probability amplitude of dynamic nucleation of wall immobile dislocations; and c_{wi}^{nc} is a material coefficient associated with probability amplitude of dynamic nucleation of wall immobile dislocations. Pinning of cell immobile dislocations at their junctions by solute atoms contributes to stronger immobilization of cell immobile accumulates and consequently enhances the stability of the respective IDBs which are about to transform to GNBs. This is also suggested by existence of the factor $\hat{\rho}_{ci}^{3/2}$ in Eq. (49) which is proportional to junction density of cell immobile dislocations ($N_{ci} \propto \rho_{ci}^{3/2}$), considering that the pinning process occurs mainly at dislocation junctions. From another perspective, given Eq. (26), presence of the factor $\sqrt{\hat{\rho}_{ci}}$ in Eq. (48) is proportional to the average plastic shear stress concentration at IDBs.

With this approach, twin formation can be considered as a wall nucleation mechanism, in case of slip-dominated metals. Regular dislocation walls are formed by high local stress concentration that causes local elastic bending of crystal in metals with relatively high stacking fault energy (SFE). Analogously, twins are also boundaries of lattice misorientation (GNBs) that plastically nucleate due to local stress concentration at sufficiently stable dislocation pile-ups (IDBs) (Christian and Mahajan, 1995; Kibey et al., 2007; Venables, 1964) in metals with adequately low SFE. Each stacking fault that nucleates a twin is bounded by partial dislocations such as Shockley and Frank partial dislocations (Hirth and Lothe, 1982; Hull and Bacon, 2011) that are geometrically necessary (Mahajan and Chin, 1973) and hence are treated as wall dislocations. Therefore, c_{wi}^{nc} also reflects frequency of twin nucleation which in turn depends on the mean SFE at the nonlocal material point under consideration. Twin forming dislocations must overcome the intrinsic SFE barrier to nucleate twin's associated stacking fault. Further, most of the energy required for twinning is spent on creating its associated stacking fault. Thus, especially in relatively low SFE metals such as high manganese TWIP steels, c_{wi}^{nc} has a relatively high value. It is emphasized that pinning of cell immobile dislocations facilitates twin nucleation by increasing stress concentration in the cells to reach the critical shear stress for dislocation separation/dissociation/splitting mechanism (Byun, 2003; Koyama et al., 2015). In slip dominated plastic deformation in which twinning occurs, the share of TWIP effect in total accumulated plastic strain is negligible compared to that of slip. However, as already highlighted, twinning has a remarkable influence on plastic hardening by facilitating the formation of dislocation walls.

As mentioned before, pinning is a diffusion-controlled mechanism that its magnitude increases by increasing temperature in metals with adequate interstitial solute content. Moreover, the rate of stacking fault formation due to dislocation separation mechanism depends on SFE which in turn is generally an increasing function of temperature. In view of this, dynamic nucleation of wall immobile dislocations is a thermal dislocation process that its statistical magnitude by increasing temperature might increase or decrease depending on the metal structure and composition.

Further, since in nucleation of wall immobile dislocations, time-dependent diffusion-controlled pinning mechanism is partly involved, one might argue that c_{wi}^{nc} has negative strain rate sensitivity. On the other hand, wall and twin nucleation can be amplified by increasing strain rate provoking positive strain rate sensitivity of c_{wi}^{nc}. Therefore, overall strain rate sensitivity of c_{wi}^{nc} can be negative, zero or positive (Yang et al., 2017).

(17) *Dynamic remobilization*: probability of recurrence of remobilization of cell or wall immobile dislocations depends on their density (Bergström, 1970):

$$\partial_{\tilde{\gamma}_p}\rho_{xi}^{\mathrm{rm}} \propto \rho_{xi}\ ; \qquad x = c, w\ ; \tag{50}$$

where $\partial_{\tilde{\gamma}_p}\rho_{xi}^{\mathrm{rm}}$ is the statistical magnitude of remobilization rate of immobile dislocations of type x with respect to plastic shear strain increment. Given Eqs. (4) and (34):

$$\partial_{\tilde{\gamma}_p}\rho_{xi}^{\mathrm{rm}} = p_{xi}^{\mathrm{rm}}\ \rho_{xi}\ ; \qquad p_{xi}^{\mathrm{rm}} = c_{xi}^{\mathrm{rm}}\ ; \qquad x = c, w\ ; \tag{51}$$

$$\partial_{\varepsilon_p}\hat{\rho}_{xi}^{\mathrm{rm}} = M\ c_{xi}^{\mathrm{rm}}\ \hat{\rho}_{xi}\ ; \qquad x = c, w\ . \tag{52}$$

where $\partial_{\varepsilon_p}\hat{\rho}_{xi}^{\mathrm{rm}}$ is normalized dynamic remobilization rate of immobile dislocations of type x with respect to plastic strain; p_{wi}^{rm} is probability amplitude of dynamic remobilization of immobile dislocations of type x; and c_{xi}^{rm} are material

parameters associated with probability amplitude of dynamic remobilization of immobile dislocations of type x. Dislocation remobilization process is performed by different underlying mechanisms such as climb, cross-slip, bow-out, junction dissociation/unzipping, etc. (Hunter and Preston, 2015). Owing to the involvement of thermal mechanisms in the remobilization processes, such as dislocation climb and cross-slip, they are treated as thermal dislocation processes. At low and medium temperatures, dynamic dislocation remobilization and annihilation processes (together known as dynamic recovery) are mainly governed by the cross-slip mechanism while at high temperatures dislocation climb is the dominant mechanism of dynamic recovery processes (Essmann and Mughrabi, 1979; Galindo-Nava et al., 2012; Kubin et al., 1992; Nix et al., 1985; Püschl, 2002; Rivera-Díaz-del-Castillo and Huang, 2012). Essentially, by definition inherently $\partial_{\varepsilon_p}\hat{\rho}^{\mathrm{rm}}_{wi}$ should be much lower than $\partial_{\varepsilon_p}\hat{\rho}^{\mathrm{rm}}_{ci}$ ($\partial_{\varepsilon_p}\hat{\rho}^{\mathrm{rm}}_{wi} << \partial_{\varepsilon_p}\hat{\rho}^{\mathrm{rm}}_{ci}$).

Finally, since dislocation climb as an underlying mechanism for dynamic remobilization processes is controlled by time-dependent diffusion of vacancies, remobilization processes might have strain rate dependence with negative strain rate sensitivity. On the other hand, by increasing strain rates, the viscous stress is also increased which assists the remobilization process. This provokes positive strain rate sensitivity of remobilization parameters. Therefore, c^{rm}_{xi} might have negative, zero or positive strain rate sensitivities.

By approaches analogous to the one adopted in postulate (13) (dynamic annihilation), one may also physically interpret the constitutive parameters associated with frequency of other dislocation processes (c^{z}_{xy}) by defining various mean critical distances, local densities, shear stresses, etc. Nevertheless, the mean critical physical parameters have virtual characters (like probability amplitude), as they are extremely difficult and mostly even impossible to be determined accurately enough by means of independent experimental measurements.

Now that every main dynamic dislocation process is statistically and quantitatively characterized, the approach first introduced by Ananthakrishna and Sahoo (1981), and Estrin and Kubin (1986) is applied to construct the overall kinetics equations for dynamic evolution of each dislocation type.

(18) *Kinetics of wall immobile dislocations*: dynamic nucleation and accumulation of wall immobile dislocations, contribute to dynamic increase of wall immobile dislocation density while dynamic decrease of wall immobile dislocations occurs as the consequence of annihilation and remobilization of wall immobile dislocations:

$$\partial_{\varepsilon_p}\hat{\rho}^{+}_{wi} = \partial_{\varepsilon_p}\hat{\rho}^{\mathrm{nc}}_{wi} + \partial_{\varepsilon_p}\hat{\rho}^{\mathrm{ac}}_{wi} \; ; \tag{53}$$

$$\partial_{\varepsilon_p}\hat{\rho}^{-}_{wi} = \partial_{\varepsilon_p}\hat{\rho}^{\mathrm{an}}_{wi} + \partial_{\varepsilon_p}\hat{\rho}^{\mathrm{rm}}_{wi} \; . \tag{54}$$

Combining Eqs. (30), (53), and (54) yields:

$$\partial_{\varepsilon_p}\hat{\rho}_{wi} = \partial_{\varepsilon_p}\hat{\rho}^{\mathrm{nc}}_{wi} + \partial_{\varepsilon_p}\hat{\rho}^{\mathrm{ac}}_{wi} - \left(\partial_{\varepsilon_p}\hat{\rho}^{\mathrm{an}}_{wi} + \partial_{\varepsilon_p}\hat{\rho}^{\mathrm{rm}}_{wi}\right) . \tag{55}$$

Eq. (55) is the dynamic evolutionary/kinetics equation of wall immobile dislocation density.

(19) *Kinetics of cell immobile dislocations*: dynamic increase of cell immobile dislocation density is the result of dynamic trapping of cell mobile dislocations and accumulation of cell immobile dislocations, whereas dynamic decrease of cell immobile dislocations takes place by means of annihilation and remobilization of cell immobile dislocations and also nucleation of wall immobile dislocations:

$$\partial_{\varepsilon_p}\hat{\rho}^{+}_{ci} = \partial_{\varepsilon_p}\hat{\rho}^{\mathrm{tr}}_{cm} + \partial_{\varepsilon_p}\hat{\rho}^{\mathrm{ac}}_{ci} \; ; \tag{56}$$

$$\partial_{\varepsilon_p}\hat{\rho}^{-}_{ci} = \partial_{\varepsilon_p}\hat{\rho}^{\mathrm{an}}_{ci} + \partial_{\varepsilon_p}\hat{\rho}^{\mathrm{rm}}_{ci} + \partial_{\varepsilon_p}\hat{\rho}^{\mathrm{nc}}_{wi} \; . \tag{57}$$

Combining Eqs. (30), (56), and (57) reads:

$$\partial_{\varepsilon_p}\hat{\rho}_{ci} = \partial_{\varepsilon_p}\hat{\rho}^{\mathrm{tr}}_{cm} + \partial_{\varepsilon_p}\hat{\rho}^{\mathrm{ac}}_{ci} - \left(\partial_{\varepsilon_p}\hat{\rho}^{\mathrm{an}}_{ci} + \partial_{\varepsilon_p}\hat{\rho}^{\mathrm{rm}}_{ci} + \partial_{\varepsilon_p}\hat{\rho}^{\mathrm{nc}}_{wi}\right) . \tag{58}$$

Eq. (58) is the dynamic evolutionary equation of cell immobile dislocation density.

(20) *Kinetics of cell mobile dislocations*: dynamic generation of cell mobile dislocations and remobilization of cell and wall immobile dislocations contribute to dynamic increase of cell mobile dislocations, while dynamic decrease of cell mobile dislocations occurs through dynamic annihilation of cell mobile, cell immobile, and wall immobile dislocations, accumulation of cell and wall immobile dislocations, and pinning of mobile dislocations:

$$\partial_{\varepsilon_p}\hat{\rho}^{+}_{cm} = \partial_{\varepsilon_p}\hat{\rho}^{\mathrm{gn}}_{cm} + \partial_{\varepsilon_p}\hat{\rho}^{\mathrm{rm}}_{ci} + \partial_{\varepsilon_p}\hat{\rho}^{\mathrm{rm}}_{wi} \; ; \tag{59}$$

$$\partial_{\varepsilon_p}\hat{\rho}^{-}_{cm} = 2\;\partial_{\varepsilon_p}\hat{\rho}^{\mathrm{an}}_{cm} + \partial_{\varepsilon_p}\hat{\rho}^{\mathrm{an}}_{ci} + \partial_{\varepsilon_p}\hat{\rho}^{\mathrm{an}}_{wi} + \partial_{\varepsilon_p}\hat{\rho}^{\mathrm{ac}}_{ci} + \partial_{\varepsilon_p}\hat{\rho}^{\mathrm{ac}}_{wi} + \partial_{\varepsilon_p}\hat{\rho}^{\mathrm{tr}}_{cm} \; . \tag{60}$$

The term $\partial_{\varepsilon_p}\hat{\rho}^{\mathrm{an}}_{cm}$ is considered twice in dynamic decrease of cell mobile dislocations because two mobile dislocations annihilate each other in the process of dynamic annihilation of cell mobile dislocations. Combining (30), (59), and (60) gives:

$$\partial_{\varepsilon_p}\hat{\rho}_{cm} = \partial_{\varepsilon_p}\hat{\rho}^{\mathrm{gn}}_{cm} + \partial_{\varepsilon_p}\hat{\rho}^{\mathrm{rm}}_{ci} + \partial_{\varepsilon_p}\hat{\rho}^{\mathrm{rm}}_{wi} - \left(2\;\partial_{\varepsilon_p}\hat{\rho}^{\mathrm{an}}_{cm} + \partial_{\varepsilon_p}\hat{\rho}^{\mathrm{an}}_{ci} + \partial_{\varepsilon_p}\hat{\rho}^{\mathrm{an}}_{wi} + \partial_{\varepsilon_p}\hat{\rho}^{\mathrm{ac}}_{ci} + \partial_{\varepsilon_p}\hat{\rho}^{\mathrm{ac}}_{wi} + \partial_{\varepsilon_p}\hat{\rho}^{\mathrm{tr}}_{cm}\right). \tag{61}$$

Eq. (61) is the dynamic evolutionary equation of cell mobile dislocation density. Considering Eqs. (10) and (30), dynamic evolution of total dislocation density reads:

$$\partial_{\varepsilon_p}\hat{\rho}^{+}_{t} = \partial_{\varepsilon_p}\hat{\rho}^{\mathrm{gn}}_{cm} \; ; \tag{62}$$

$$\partial_{\varepsilon_p}\hat{\rho}_t^{-} = 2\left(\partial_{\varepsilon_p}\hat{\rho}_{cm}^{\mathrm{an}} + \partial_{\varepsilon_p}\hat{\rho}_{ci}^{\mathrm{an}} + \partial_{\varepsilon_p}\hat{\rho}_{wi}^{\mathrm{an}}\right); \tag{63}$$

$$\partial_{\varepsilon_p}\hat{\rho}_t = \partial_{\varepsilon_p}\hat{\rho}_{cm}^{\mathrm{gn}} - 2\left(\partial_{\varepsilon_p}\hat{\rho}_{cm}^{\mathrm{an}} + \partial_{\varepsilon_p}\hat{\rho}_{ci}^{\mathrm{an}} + \partial_{\varepsilon_p}\hat{\rho}_{wi}^{\mathrm{an}}\right) . \tag{64}$$

Eq. (64) is the dynamic evolutionary equation of total dislocation density.

3.3. Static dislocation processes

(21) *Static pinning*: nonlocal static pinning of cell (mobile and immobile) dislocations is very similar to dynamic pinning (postulate (15) and (16)) with the difference that it occurs at very low local strain rates in relatively long durations. Time rate of static pinning of cell dislocations ($\dot{\rho}_{cy}^{\mathrm{spn}}$) by diffusion of solute atoms at their junctions is proportional to their junction density (N_{cy}):

$$\dot{\rho}_{cy}^{\mathrm{spn}} \propto N_{cy} \ ; \qquad y = m, i \ . \tag{65}$$

Given Eqs. (22) and (34):

$$\dot{\hat{\rho}}_{cy}^{\mathrm{spn}} = c_{cy}^{\mathrm{spn}}\hat{\rho}_{cy}^{3/2}; \quad y = m, i \ ; \tag{66}$$

where c_{cy}^{spn} is a material coefficient associated with frequency of static pinning of cell dislocations of type $y = m, i$. Since pinning is a diffusion-controlled process, static pinning of cell dislocations is a thermal dislocation process that its magnitude increases with increasing temperature. As mentioned in postulate (15), since pinning process occurs due to diffusion of interstitial solute atoms to dislocation surrounding, c_{cy}^{spn} is a function of interstitial solute content.

(22) *Static remobilization*: nonlocal static remobilization process consists of the same contributing mechanisms of its dynamic counterpart. Time rate of static remobilization of immobile dislocations of type $x = c, w$ ($\dot{\rho}_{xi}^{\mathrm{srm}}$) is proportional to density of them:

$$\dot{\rho}_{xi}^{\mathrm{srm}} \propto \rho_{xi} \ ; \qquad x = c, w \ . \tag{67}$$

Given Eqs. (22) and (34):

$$\dot{\hat{\rho}}_{xi}^{\mathrm{srm}} = c_{xi}^{\mathrm{srm}}\hat{\rho}_{xi}; \quad x = c, w; \tag{68}$$

where c_{xi}^{srm} is a material parameter associated with frequency of static remobilization of immobile dislocations of type $x = c, w$. Moreover, static remobilization is a thermal dislocation process due to thermal character of its underlying mechanisms such as dislocation climb and junction dissociation.

(23) *Static kinetics*: static pinning of cell mobile dislocations reduces cell mobile and increases cell immobile dislocation density, while static remobilization processes of immobile dislocations increase cell mobile and decrease immobile dislocation density. Thus, given Eq. (31), static evolution of dislocation densities reads:

$$\left(\dot{\hat{\rho}}_{cm}\right)_s = \dot{\hat{\rho}}_{ci}^{\mathrm{srm}} + \dot{\hat{\rho}}_{wi}^{\mathrm{srm}} - \dot{\hat{\rho}}_{cm}^{\mathrm{spn}}; \tag{69}$$

$$\left(\dot{\hat{\rho}}_{ci}\right)_s = \dot{\hat{\rho}}_{cm}^{\mathrm{spn}} - \dot{\hat{\rho}}_{ci}^{\mathrm{srm}} - \dot{\hat{\rho}}_{ci}^{\mathrm{spn}}; \tag{70}$$

$$\left(\dot{\hat{\rho}}_{wi}\right)_s = \dot{\hat{\rho}}_{ci}^{\mathrm{spn}} - \dot{\hat{\rho}}_{wi}^{\mathrm{srm}} \ . \tag{71}$$

Notice that pinning of already immobilized cell dislocations (cell immobile dislocations), strengthens their immobilization (resistance to remobilization). Consequently, upon application of external stress, just prior to local yielding, some of those pinned cell immobile dislocations will convert to GND due to elastic bending of their surrounding lattice to a sufficient mean misorientation angle.

3.4. Temperature and strain rate dependencies

(24) *Temperature dependence of dislocation processes*: as pointed out earlier, each thermal dislocation process comprised of at least one underlying thermally-activated mechanism. Temperature is a statistical variable (representative of mean amplitude of atomic fluctuations) as well, which directly affects probability amplitude of different thermal dislocation processes. It is postulated that the change in probability amplitude of a thermal dislocation process with respect to temperature in constant strain rate is proportional to a power of temperature change:

$$\Delta p_{xy}^{z} \propto (\Delta T)^{s_{xy}^{z}} \ ; \qquad xy = cm, ci, wi \ . \tag{72}$$

Therefore,

$$\frac{\Delta c_{xy}^{z}}{c_{xy0}^{z}} = r_{xy}^{z}\left(\frac{\Delta T}{T_0}\right)^{s_{xy}^{z}}; \qquad \Delta T = T - T_0 \ ; \qquad \Delta c_{xy}^{z} = c_{xy}^{z} - c_{xy0}^{z} \ ; \qquad xy = cm, ci, wi \ ; \tag{73}$$

where T is absolute temperature; T_0 is reference absolute temperature; p^z_{xy} is probability amplitude associated with thermal dislocation process z that involves dislocations of type xy; c^z_{xy} and c^z_{xy0} are respectively, current (at current temperature) and reference (at reference temperature and strain rate) material parameters associated with probability amplitude of dislocation process z of dislocations of type xy; r^z_{xy} and s^z_{xy} are respectively temperature sensitivity coefficient and exponent associated with dislocation process z of dislocations of type xy. Reference temperature is assumed to be the minimum temperature in the temperature regime under consideration. Thus, in case of cold and warm regimes, reference temperature is the room temperature. Likewise, the reference strain rate is assumed to be the lowest strain rate in the investigated strain rate regime. The reference strain rate must be lower than the maximum/critical strain rate beyond which the viscoplastic deformation cannot be considered isothermal anymore because of adiabatic heat generation.

Referring to the postulates of dynamic and static dislocation processes (Sections 3.2 and 3.3), thermal dislocation processes are dynamic annihilation of dislocations, dynamic trapping of cell mobile dislocation, dynamic nucleation of wall immobile dislocations, dynamic remobilization of immobile dislocation, static pinning of cell mobile dislocations, and static remobilization of immobile dislocations:

$$r^z_{xy}\begin{cases} > 0: \ z = \text{an}, \ \text{tr}, \text{rm}, \text{spn}, \text{srm} \\ \gtrless 0: \ z = \text{nc} \\ = 0: \ z = \text{gn}, \text{ac} \end{cases}; \qquad s^z_{xy}\begin{cases} > 0: \ z = \text{an}, \text{tr}, \text{nc}, \text{rm}, \text{spn}, \text{srm} \\ = 0: \ z = \text{gn}, \text{ac} \end{cases}. \tag{74}$$

Temperature dependencies of frequency of different thermal dislocation processes characterized via Eq. (73) are the general monotonically increasing or decreasing functions of temperature ($\partial c/\partial T \geq 0$ or $\partial c/\partial T \leq 0$) with unchanging concavity ($\partial^2 c/\partial T^2 \geq 0$ or $\partial^2 c/\partial T^2 \leq 0$) throughout the entire temperature domain (in cold and warm regimes). The temperature dependence of dislocation mobility (stress dependence of velocity of mobile dislocations) and underlying mechanisms of thermal dislocation processes, e.g. dislocation climb (speed), are often much more complex than that can be described purely by Arhenius relation and the respective activation energy barriers (Amodeo and Ghoniem, 1990; Argon and Moffatt, 1981; Blum et al., 2002; Eisenlohr and Blum, 2005; Gu et al., 2015; Hirth and Lothe, 1982; Yuan et al., 2018). In addition, the temperature dependence of some of the involved thermal mechanisms has not been properly understood yet. Therefore, it is reasonable to assume a phenomenological power-law description for temperature dependence of constitutive parameters associated with probability amplitude of different thermal dislocation processes.

(25) *Strain-rate dependence of dislocation processes*: the strain rate dependence of probability amplitude of rate-dependent dynamic dislocation processes is suggested to be described by power-law relation as:

$$p^z_{xy} \propto \dot{\tilde{\gamma}}_p^{\,m^z_{xy}}; \qquad xy = cm, ci, wi; \tag{75}$$

where m^z_{xy} is strain rate sensitivity associated with dislocation process z of dislocations of type xy. Therefore, at reference temperature:

$$\tilde{c}^z_{xy} = \dot{\hat{\tilde{\gamma}}}_p^{\,m^z_{xy}}; \qquad \dot{\hat{\tilde{\gamma}}}_p \equiv \frac{\dot{\tilde{\gamma}}_p}{\dot{\gamma}_0}; \qquad \tilde{c}^z_{xy} \equiv \frac{c^z_{xy}}{c^z_{xy0}}; \qquad xy = cm, ci, wi; \tag{76}$$

where $\dot{\gamma}_0$ is reference shear strain rate; and $\dot{\hat{\tilde{\gamma}}}_p$ is normalized mean plastic shear strain rate. Combination of Eqs. (73) and (76) produce:

$$\tilde{c}^z_{xy} = \left[1 + r^z_{xy}\left(\hat{T} - 1\right)^{s^z_{xy}}\right]\dot{\hat{\tilde{\gamma}}}_p^{\,m^z_{xy}}; \quad \hat{T} \equiv \frac{T}{T_0}; \quad xy = cm, ci, wi; \tag{77}$$

where $\hat{T}$ is normalized absolute temperature; $\tilde{c}^z_{xy}$ is normalized material coefficient associated with frequency of dislocation process z that involves dislocations of type xy. Moreover, given Eqs. (4) and (76), and owing to Taylor factor (M) being constant in the isotropic case:

$$\dot{\hat{\varepsilon}}_p \equiv \frac{\dot{\varepsilon}_p}{\dot{\varepsilon}_0} = \frac{\dot{\tilde{\gamma}}_p}{\dot{\gamma}_0} \equiv \dot{\hat{\tilde{\gamma}}}_p; \qquad \dot{\varepsilon}_0 \equiv \frac{\dot{\gamma}_0}{M}; \tag{78}$$

where $\dot{\varepsilon}_0$ is reference strain rate. Furthermore, as pointed out earlier, material coefficients associated with probability amplitudes of dynamic thermal dislocation processes depend on strain rate, although their rate sensitivity in quasi-static and intermediate regimes is often negligible. Therefore,

$$m^z_{xy}\begin{cases} < 0: \ z = \text{an}, \text{tr} \\ \gtrless 0: \ z = \text{nc}, \text{rm} \\ = 0: \ z = \text{gn}, \text{ac}, \text{spn}, \text{srm} \end{cases}; \qquad xy = cm, ci, wi. \tag{79}$$

(26) *Temperature dependence of plastic stress*: strain rate sensitivity of mean dislocation interaction strengths ($\tilde{\alpha}_x$) are reportedly negligible compared to strain rate sensitivity of viscous stress Mecking and Kocks, 1981). Nonetheless, mean interaction strengths decrease with increasing temperature for each material in a characteristic way (Kassner, 2015; Kocks and Mecking, 2003). Shear modulus (G) has a mild temperature dependence (decreasing with increasing temperature) as

well which can be expressed by power-law relation (Argon, 2012; Galindo-Nava and Rae, 2016; Ghosh and Olson, 2002). Variation of temperature-dependent factors in Eqs. (26) and ((28), $\tilde{\alpha}_x$ and G, with respect to temperature can be described simultaneously similar to temperature dependence relation of frequency of thermal dislocation processes:

$$\hat{G\tilde{\alpha}}_x = 1 + r^G_{\alpha x}\left(\hat{T}-1\right)^{s^G_{\alpha x}}\ ; \qquad \hat{G\tilde{\alpha}}_x \equiv \frac{G\tilde{\alpha}_x}{G_0\tilde{\alpha}_{x0}}\ ; \qquad r^G_{\alpha x}<0\ ; \qquad s^G_{\alpha x}>0\ ; \qquad x=c,w\ ; \tag{80}$$

where G_0 and $\tilde{\alpha}_{x0}$ are respectively reference (at reference temperature) shear modulus and mean dislocation interaction strength associated with immobile dislocations of type x; $\hat{G\tilde{\alpha}}_x$ is normalized $G\tilde{\alpha}_x$; and $r^G_{\alpha x}$ and $s^G_{\alpha x}$ are temperature sensitivity coefficient and exponent associated with $G\tilde{\alpha}_x$.

(27) *Viscous stress and its temperature dependence*: as shown in Fig. 4, the viscous contribution of yield shear stress at slip systems is represented by a nonlinear dashpot in rheological representation of the elasto-viscoplastic (EVP) constitutive model. Stress response of the nonlinear dashpot is:

$$\tilde{\tau}_v = \tilde{\tau}_{v0}\,\hat{\dot{\gamma}}_p^{\,m_v}\ ; \quad m_v>0\,; \tag{81}$$

where $\tilde{\tau}_{v0}$ is mean viscous shear stress at reference strain rate; and m_v is strain rate sensitivity parameter of viscous stress. At constant reference strain rate, by the assumption of $\Delta\tilde{\tau}_v \propto (\Delta T)^{s_v}$, temperature dependence of viscous resistance can be expressed as:

$$\tilde{\tau}_{v0} = \tilde{\tau}_{v00}\left[1 + r_v\left(\hat{T}-1\right)^{s_v}\right]\ ; \quad r_v<0\ ; \quad 0<s_v\le 1\,; \tag{82}$$

where $\tilde{\tau}_{v00}$ is the reference viscous shear stress (at reference temperature and strain rate); and r_v and s_v are respectively viscosity's temperature sensitivity coefficient and exponent. Eq. (82) is similar to the relations proposed by Kocks et al. (1975) and Argon (2012) for temperature dependence of viscous stress. Substituting Eq. (82) into Eq. (81) leads to:

$$\hat{\tilde{\tau}}_v = \left[1 + r_v\left(\hat{T}-1\right)^{s_v}\right]\hat{\dot{\gamma}}_p^{\,m_v}\ ; \qquad \hat{\tilde{\tau}}_v \equiv \frac{\tilde{\tau}_v}{\tilde{\tau}_{v00}}\ ; \tag{83}$$

where $\hat{\tilde{\tau}}_v$ is normalized mean viscous shear stress. Considering Eqs. (12) and (83), with constant Taylor factor (in isotropic case):

$$\hat{\sigma}_v \equiv \frac{\sigma_v}{\sigma_{v00}} = \frac{\tilde{\tau}_v}{\tau_{v00}} \equiv \hat{\tilde{\tau}}_v\,; \qquad \sigma_{v00} \equiv M\tau_{v00}\,; \tag{84}$$

where σ_{v00} is the reference viscous stress (at reference temperature and strain rate); and $\hat{\sigma}_v$ is normalized viscous stress. The reason for assuming an ambiguous phenomenological description for temperature dependence of viscous stress is that the temperature dependence of mean (mixed/curved) dislocations mobility function is extremely complex and has not been yet properly understood (Argon, 2012; Fleischer, 1962; Gilbert et al., 2011; Gilman, 1965; Kocks et al., 1975; Li, 1967; Tang and Marian, 2014).

(28) *Rate dependence of strain rate sensitivities*: strain rate sensitivity of viscous drag increases with increasing temperature (Cereceda et al., 2016; Khan and Liu, 2012; Kocks, 1976; Rusinek and Rodríguez-Martínez, 2009) and is assumed to have a similar form as aforementioned temperature and strain rate dependence relations:

$$\hat{m}_v = \left[1 + r^m_v\left(\hat{T}-1\right)^{s^m_v}\right]\hat{\dot{\gamma}}_p^{\,m^m_v}\ ; \qquad \hat{m}_v \equiv \frac{m_v}{m_{v0}}\,; \quad r^m_v,\ s^m_v \ge 0\,; \tag{85}$$

where m_{v0} is reference strain rate sensitivity (at reference temperature and strain rate); $\hat{m}_v$ is normalized strain rate sensitivity of viscous stress; r^m_v and s^m_v are respectively temperature sensitivity coefficient and exponent associated with strain rate sensitivity of viscous stress; and m^m_v is strain rate sensitivity parameter associated with strain rate sensitivity of viscous stress. Moreover, strain rate sensitivity coefficients associated with dislocation processes are assumed to have similar form of temperature and strain rate dependencies:

$$\hat{m}^z_{xy} = \left[1 + r^m_{z_{xy}}\left(\hat{T}-1\right)^{s^m_{z_{xy}}}\right]\hat{\dot{\gamma}}_p^{\,m^m_{z_{xy}}}\ ; \quad \hat{m}^z_{xy} \equiv \frac{m^z_{xy}}{m^z_{xy0}}\,; \quad xy = cm, ci, wi\,; \tag{86}$$

where $m^m_{z_{xy}}$, m^z_{xy0} and $\hat{m}^z_{xy}$ are respectively, current, reference (at reference temperature) and normalized strain rate sensitivities associated with dislocation process z of dislocations of type xy; and $r^m_{z_{xy}}$ and $s^m_{z_{xy}}$ are temperature sensitivity coefficient and exponent associated with strain sensitivity of dislocation process z of dislocations of type xy, respectively. Further, m^m_v and $m^m_{z_{xy}}$ are very small compared to m_v and m^z_{xy}. Thus, only often shock regimes they have considerable impact.

(29) *Plastic dissipation/adiabatic heating*: volumetric adiabatic heat generation rate due to plastic work ($\dot{q}_p$) which is a fraction of volumetric plastic power ($\dot{w}_p$) (Taylor and Quinney, 1934), is obtained as follows:

$$\dot{q}_p = \beta\ \dot{w}_p = \dot{w}_p - \dot{u};\ \ \dot{w}_p = \dot{\tilde{\gamma}}_p\tilde{\tau}_c = \sigma_y\ \dot{\varepsilon}_p;\ \ \beta\ \equiv 1 - \frac{\dot{u}}{\dot{w}_p}\ ; \tag{87}$$

where $\dot{u}$ is volumetric stored elastic power which is a fraction of volumetric plastic power that is stored in material by dislocations; and β is referred to as dissipation/conversion factor, inelastic heat fraction, efficiency of plastic dissipation, or the Taylor–Quinney coefficient. In other words, β is the fraction of plastic power that is not stored elastically and consequently is converted to heat. Taylor and Quinney (1934) emphasized that the fraction β increases as plastic deformation progresses until saturation state where $\beta = 1$. In other words, in saturation state, the entire input volumetric plastic power is converted to heat ($\dot{q}_p = \dot{w}_p$). Moreover, Rosakis et al. (2000) and Zehnder (1991) proposed models for variation of β as a function of plastic strain and plastic hardening ($\theta \equiv \partial_{\varepsilon_p}\sigma_y$) where β approaches one by decreasing θ as plastic strain increases. At the beginning of plastic deformation of a nearly undeformed/annealed polycrystalline metallic material, large portion of the input plastic energy is stored in the crystal structure by generation of dislocations and dislocation structures. However, as the deformation progresses the generation rate of dislocations diminishes whereas the annihilation rate increases (annihilation releases the previously stored energy of dislocations in form of heat) until the saturation state where these two rates are equivalent. Therefore, one can assume:

$$\beta = \left(\frac{\partial_{\varepsilon_p}\hat{\rho}_t^-}{\partial_{\varepsilon_p}\hat{\rho}_t^+}\right)^{\kappa} \; ; \quad \kappa > 0 \; ; \tag{88}$$

where $\kappa > 0$ is a material constant associated with dissipation factor.

Furthermore, given Eqs. (12), (14), (28), (34), (78), (83) and (84), plastic/strain hardening (θ) can be calculated as follows:

$$\theta \equiv \partial_{\varepsilon_p}\sigma_y = \partial_{\varepsilon_p}\sigma_p = \theta_c + \theta_w \; ; \tag{89}$$

$$\theta_x \equiv \partial_{\varepsilon_p}\sigma_{px} = \frac{MbG\tilde{\alpha}_x}{2\sqrt{\rho_{xi}}}\; \partial_{\varepsilon_p}\rho_{xi} = \frac{\partial_{\varepsilon_p}\hat{\rho}_{xi}}{2\hat{\rho}_{xi}}\; \sigma_{px} \; ; \qquad x = c, w \; ; \tag{90}$$

where θ_x is plastic hardening associated with dislocations of type x. In addition, according to Eqs. (12), (14), (28), (34), (55), (58), (78), (83), (84) and (85) viscous/strain-rate hardening (φ) is obtained as follows:

$$\varphi \equiv \partial_{\dot{\varepsilon}_p}\sigma_y = \varphi_v + \varphi_p \; ; \tag{91}$$

$$\varphi_v \equiv \partial_{\dot{\varepsilon}_p}\sigma_v = \frac{m_v}{\dot{\varepsilon}_p}\left[1 + \; m_v^m \overset{\vee}{\ln}\left(\frac{\hat{}}{\dot{\varepsilon}_p}\right)\right]\sigma_v \; ; \tag{92}$$

$$\varphi_p \equiv \partial_{\dot{\varepsilon}_p}\sigma_p = \varphi_{pc} + \varphi_{pw} \; ; \quad \varphi_{px} \equiv \partial_{\dot{\varepsilon}_p}\sigma_{px} = \frac{\partial_{\dot{\varepsilon}_p}\hat{\rho}_{xi}}{2\hat{\rho}_{xi}}\sigma_{px} = \frac{\partial \varepsilon_p}{\partial \dot{\varepsilon}_p}\theta_x \; ; \quad x = c, w \; ; \tag{93}$$

where $\partial_{\dot{\varepsilon}_p} \equiv \frac{\partial}{\partial \dot{\varepsilon}_p}$ is partial derivative operator with respect to plastic strain rate ($\dot{\varepsilon}_p$); φ_v and φ_p are viscous hardenings respectively associated with viscous and plastic stress; and φ_{px} is viscous hardening associated with plastic stress of type x.

4. Numerical integration and parameter identification

4.1. Numerical integration

Since there is no analytical solution to overall evolution rate of dislocation densities, they must be solved numerically. Hence, the differential continuum equations expressed in previous sections must be numerically integrated with respect to time. Simulation time is discretized to small increments. Consider a (pseudo) time interval $[t^{(n)}, t^{(n+1)}]$, such that $\Delta t^{(n+1)} \equiv t^{(n+1)} - t^{(n)}$ is the time increment at $(n+1)$-th time step. Accordingly,

$$\Delta(\bullet)^{(n+1)} \equiv (\bullet)^{(n+1)} - (\bullet)^{(n)} \; ; \quad \dot{(\bullet)}^{(n+1)} \equiv \frac{\Delta(\bullet)^{(n+1)}}{\Delta t^{(n+1)}} \; ; \tag{94}$$

where $(\bullet)$ can be any time-dependent variable; and superscripts (n) and $(n+1)$ respectively, represent the value of corresponding time-dependent variable at the beginning and the end of $(n+1)$-th time step. Application of forward/explicit Euler method for numerical integration of dislocation densities gives:

$$\hat{\rho}_{xy}^{(n+1)} = \hat{\rho}_{xy}^{(n)} + \Delta\hat{\rho}_{xy}^{(n)} \; ; \quad \Delta\hat{\rho}_{xy}^{(n)} = \Delta\varepsilon_p^{n+1}\; \partial_{\varepsilon_p}\hat{\rho}_{xy}^{(n)} = \Delta t^{(n+1)}\; \dot{\hat{\rho}}_{xy}^{(n)} \; ; \quad \hat{\rho}_{xy}^{(n=0)} = \hat{\rho}_{xy0} \; ; \quad \begin{cases} x = c, w, t \\ y = m, i, t \end{cases} \; ; \tag{95}$$

where $\partial_{\varepsilon_p}\hat{\rho}_{xy}^{(n)}$ is computed by Eqs. (55), (58) and (61). Given Eqs. (12), (14), (28), (34), (77), (78), (80), (83), (84), (85) and (86):

$$\sigma_y^{(n+1)} = \sigma_v^{(n+1)} + \sigma_{pc}^{(n+1)} + \sigma_{pw}^{(n+1)} ; \tag{96}$$

$$\sigma_{px}^{(n+1)} = Mb(G\tilde{\alpha}_x)^{(n)}\sqrt{\rho_0\; \hat{\rho}_{xi}^{(n+1)}} \; ; \quad x = c, w \; ; \tag{97}$$

$$(G\tilde{\alpha}_x)^{(n)} = G_0\tilde{\alpha}_{x0}\left[1 + r^G_{\alpha x}\left(\hat{T}^{(n)} - 1\right)^{s^G_{\alpha x}}\right]; \quad \hat{T}^{(n)} \equiv \frac{T^{(n)}}{T_0}; \quad x = c, w; \tag{98}$$

$$\sigma_\nu^{(n+1)} = \sigma_{\nu 00}\left[1 + r_\nu\left(\hat{T}^{(n)} - 1\right)^{s_\nu}\right]\left(\hat{\varepsilon}_p^{(n+1)}\right)^{m_\nu^{(n)}}; \quad \hat{\dot{\varepsilon}}_p^{(n+1)} \equiv \frac{\dot{\varepsilon}_p^{(n+1)}}{\dot{\varepsilon}_0} = \frac{\Delta\varepsilon_p^{(n+1)}}{\Delta t^{(n+1)}\,\dot{\varepsilon}_0}; \tag{99}$$

$$m_\nu^{(n)} = m_{\nu 0}\left[1 + r_\nu^m\left(\hat{T}^{(n)} - 1\right)^{s_\nu^m}\right]\left(\hat{\varepsilon}_p^{(n+1)}\right)^{m_\nu^m}; \tag{100}$$

$$c_{xy}^{z\,(n)} = c_{xy0}^z\left[1 + r_{xy}^z\left(\hat{T}^{(n)} - 1\right)^{s_{xy}^z}\right]\left(\hat{\varepsilon}_p^{(n+1)}\right)^{m_{xy}^{z\,(n)}}; \quad xy = cm, ci, wi; \tag{101}$$

$$m_{xy}^{z\,(n)} = m_{xy0}^z\left[1 + r_{z_{xy}}^m\left(\hat{T}^{(n)} - 1\right)^{s_{z_{xy}}^m}\right]\left(\hat{\varepsilon}_p^{(n+1)}\right)^{m_{z_{xy}}^m}; \quad xy = cm, ci, wi. \tag{102}$$

In addition, discretized forms of Eqs. (87) and (88) in combination with Eqs. (62) and (63) read:

$$\Delta q_p^{(n+1)} = \beta^{(n)}\frac{\sigma_y^{(n)} + \sigma_y^{(n+1)}}{2}\Delta\varepsilon_p^{(n+1)}; \tag{103}$$

$$\beta^{(n)} = \left(\frac{2\left(\partial_{\bar{\varepsilon}_p}\hat{\rho}_{cm}^{\mathrm{an}\,(n)} + \partial_{\bar{\varepsilon}_p}\hat{\rho}_{ci}^{\mathrm{an}\,(n)} + \partial_{\bar{\varepsilon}_p}\hat{\rho}_{wi}^{\mathrm{an}\,(n)}\right)}{\partial_{\bar{\varepsilon}_p}\hat{\rho}_{cm}^{\mathrm{gn}\,(n)}}\right)^{\kappa}. \tag{104}$$

For FE implementation, in return mapping (using Newton-Raphson scheme) of EVP constitutive models as well as calculation of viscoplastic consistent tangent operator (implicit FE framework), the viscoplastic tangent modulus (H) is required. Given Eqs. (40), (46), (49), (52), (55), (58), (79), (95), (96), (97), (99), (100), (101) and (102):

$$\begin{aligned} H^{(n+1)} \equiv \frac{\mathrm{d}\sigma_y^{(n+1)}}{\mathrm{d}\Delta\bar{\varepsilon}_p^{(n+1)}} = {} & \frac{m_\nu^{(n)}\left[1 + m_\nu^m \overset{\vee}{\ln}\left(\hat{\varepsilon}_p^{(n+1)}\right)\right]}{\Delta\varepsilon_p^{(n+1)}}\sigma_\nu^{(n+1)} \\ & + \frac{\partial_{\varepsilon_p}\hat{\rho}_{ci}^{(n)} + m_{cm}^{\mathrm{tr}\,(n)}\left[1 + m_{\mathrm{tr}_{cm}}^m \overset{\vee}{\ln}\left(\hat{\varepsilon}_p^{(n+1)}\right)\right]\partial_{\varepsilon_p}\hat{\rho}_{cm}^{\mathrm{tr}\,(n)} - \sum_{\substack{\mathrm{an}_{ci} \\ z_{xy} = \mathrm{rm}_{ci} \\ \mathrm{nc}_{wi}}} m_{xy}^{z\,(n)}\left[1 + m_{z_{xy}}^m \overset{\vee}{\ln}\left(\hat{\varepsilon}_p^{(n+1)}\right)\right]\partial_{\varepsilon_p}\hat{\rho}_{xy}^{z\,(n)}}{2\hat{\rho}_{ci}^{(n+1)}}\sigma_{pc}^{(n+1)} \\ & + \frac{\partial_{\varepsilon_p}\hat{\rho}_{wi}^{(n)} + m_{wi}^{\mathrm{nc}\,(n)}\left[1 + m_{\mathrm{nc}_{wi}}^m \overset{\vee}{\ln}\left(\hat{\varepsilon}_p^{(n+1)}\right)\right]\partial_{\varepsilon_p}\hat{\rho}_{wi}^{\mathrm{nc}\,(n)} - \sum_{\substack{\mathrm{an}_{wi} \\ z_{xy} = \mathrm{rm}_{wi}}} m_{xy}^{z\,(n)}\left[1 + m_{z_{xy}}^m \overset{\vee}{\ln}\left(\hat{\varepsilon}_p^{(n+1)}\right)\right]\partial_{\varepsilon_p}\hat{\rho}_{xy}^{z\,(n)}}{2\hat{\rho}_{wi}^{(n+1)}}\sigma_{pw}^{(n+1)}. \end{aligned} \tag{105}$$

Details of FE implementation of the above discretized constitutive equations in the framework of hypo-EVP finite deformation/strain based on isotropic associative J_2 plasticity is planned to be published soon.

4.2. Identification of constitutive parameters

Generally, constitutive/material parameters/constants of constitutive models are directly derived from experimental flow curves (yield stress versus plastic strain) through parameter identification techniques. Here, as an important hypothesis, it is envisaged that having the flow curves of a material in various temperatures, strain rates, etc. in the considered regimes is sufficient for calibration of a properly devised microstructural constitutive model using a robust parameter identification procedure. After all, under viscoplastic deformation, the underlying microstructural processes statistically result in a specific material response that is macroscopically observable through flow curves. However, although due to their physical nature, some of the constitutive parameters can be obtained by independent characterization methods (other than flow curves), it is suggested that the most accurate and effective approach for finding them is the simultaneous parameter identification, given the flow curves as the reference of fitting. Identification of microstructural parameters is carried out in two steps:

(1) In the first step, isothermal uniaxial compression/upsetting or tensile tests are conducted in reference strain rate and various temperatures. Then, based on the measured experimental flow curves, most of the constitutive parameters are determined by means of pointwise parameter optimization using RMV-based analysis (RMVA).

(2) In the last step, nonisothermal uniaxial tests are performed with different strain rates (in intermediate strain rate regime) and various initial temperatures (in cold and warm regime). Subsequently, the remaining constants which are strain rate sensitivity parameters (m), temperature sensitivity coefficients (r) and exponents (s) associated with strain rate sensitivities, as well as the material parameter associated with dissipation factor (κ) are simultaneously calibrated by parameter optimization using finite element model updating (FEMU) method also known as finite element-based inverse strategy (Steenackers et al., 2007).

After conducting uniaxial tests, force-displacement data is processed to true stress-strain, and then to flow curves. Afterwards, noise of flow curve data is reduced (here, "smooth" function in MATLAB library is used for noise filtration) and interpolated for constant plastic strain intervals. For the first step of parameter identification by RMVA, the following mean relative error which is also called objective, fitness, or residual function, is constructed as follows to be optimized/minimized:

$$\tilde{e}(C) \equiv \frac{1}{p}\sum_{i=1}^{p}\frac{\omega_i}{q_i}\sum_{j=0}^{q_i}\varpi_j\frac{\left|\sigma_{ij}^{\mathrm{num}}\left(C, T_i, \Delta\varepsilon_p, S^j\right) - \sigma_{ij}^{\mathrm{exp}}\left(T_i, \varepsilon_p^j = j\Delta\varepsilon_p\right)\right|}{\sigma_{ij}^{\mathrm{exp}}\left(T_i, \varepsilon_p^j = j\Delta\varepsilon_p\right)}; \tag{106}$$

where $\boldsymbol{C}$ is the set containing constitutive constants for fitting; p is total number of experiments at different temperatures with constant reference strain rate $\dot{\varepsilon}_0$; q_i is total number of data points of isothermal experimental flow curve at temperature T_i; $\Delta\varepsilon_p$ is the constant plastic strain interval between data points; $\sigma_{ij}^{\mathrm{num}}$ is yield stress calculated numerically by the constitutive model at temperature T_i which is corresponding to $\varepsilon_p^j = j\Delta\varepsilon_p$; $\boldsymbol{S}^j$ is the set of MSVs of jth step; $\sigma_{ij}^{\mathrm{exp}}$ is yield stress in isothermal experimental flow curve at temperature T_i and plastic strain $\varepsilon_p^j = j\Delta\varepsilon_p$; ω_i and ϖ_j are weighting factors respectively for isothermal flow curve at temperature T_i, and data point j corresponding to $\varepsilon_p^j = j\Delta\varepsilon_p$. In default, $\omega_i = 1$ and $\varpi_j = 1$, unless some individual flow curve or ranges of plastic strain, have higher weight/importance ($\omega_i, \varpi_j > 1$) or lower importance ($\omega_i, \varpi_j < 1$) than the rest. For the example provided in the next section, $\Delta\varepsilon_p = 0.001$ and $\omega_i = \varpi_j = 1$.

For many cases, finding the global solution/minimum to this optimization problem is difficult and requires complex and robust mathematical optimization methods which follow the steepest descent with the crossover functionality. Many methods are available for searching for the global solution such as gradient-free minimization methods and evolutionary algorithms including genetic algorithm. These methods exist in literature and their corresponding computer codes are developed and embedded in many commercial mathematical software. For the example provided in the next section, minimization of Eq. (106) for calibration of material parameters is carried out by a script written in MATLAB software. The optimization script employs MATLAB's global search class "GlobalSearch" and genetic algorithm "ga" which are coupled with its local minimization solver for constrained nonlinear multivariate functions "fmincon". The local minimization solver optionally utilizes various robust optimization algorithms such as interior point and reflective trust region.

For the second step of fitting based on FEMU, firstly the constitutive model must be implemented and programmed as a material subroutine based on hypo-EVP finite deformation using the constitutive parameters derived in the first step of calibration and with an initial guess for the constitutive parameters yet to be determined in the second step. Then, depending on the type of conducted experimental uniaxial tests, an FE model of either uniaxial compression or tension test must be constructed and linked to the material subroutine. Next, optimization of remaining constitutive parameters is done by iterative running of FE simulation of uniaxial tests with consecutives correction and update of remaining parameters. Running of FE simulation of uniaxial tests with updated parameters can be done by an optimization script that controls the pre-processing and post-processing of FE simulation. However, with a good initial guess for the remaining material constants, the second step of optimization can be done manually as well. For the example provided in the next section, the presented constitutive model has been implemented as implicit and explicit user-defined material subroutines for hypo-EVP finite deformation in ABAQUS FE package based on isotropic associative J_2 plasticity.

5. Results, discussion and validation

In order to determine constitutive parameters, and also for validation of the constitutive model, uniaxial compression tests at various temperatures and strain rates using a deformation-type dilatometer (DIL-805A/D by TA Instruments) were conducted as dilatometer provides better precision than conventional compression test machines. Temperature measurement was done by thermocouple welded on the middle point in height direction at the lateral surface of the compression specimen. Temperature and strain rate were controlled by the dilatometer's integrated PID controller. Moreover, GND density measurements using high resolution EBSD for deformed compression specimens at different plastic strains are carried out. The material used in dilatometer compression is case-hardenable ferritic-pearlitic steel alloy 20MnCr5 (1.7147/1.7149) which is widely used in industrial forging of automotive components such as bevel gear. The chemical composition of 20MnCr5 used in experiments is presented in Table 1. The material constants required by the constitutive model that are independently measurable are also presented in Table 2.

As already mentioned, reference temperature and strain rate are selected as the minimum possible temperature and strain rate in the considered domain (Table 2). Since for the steel studied here, the minimum temperature for onset of dynamic recrystallization of ferrite is slightly above 600 °C, the maximum temperature for constitutive modeling in warm regime is selected to be 600 °C. For the first step of parameter identification, experimental dilatometer compression tests

Table 1
Chemical composition of the investigated steel 20MnCr5 [mass%].

C	Si	Mn	P	S	Cr	Mo	Ni	Cu	Al	N
0.210	0.191	1.350	0.014	0.025	1.270	0.074	0.076	0.149	0.040	0.010

Table 2
Reference parameters and independently measurable required material constants.

T_0 [°C]	$\dot{\boldsymbol{\varepsilon}}_0$ [s^{-1}]	ρ_0 [m^{-2}]	G_0 [GPa]	M [-]	b [m]
20	0.01	10^{12}	82.5	3.0	2.55×10^{-10}

Table 3
Constitutive parameters determined in the first step of parameter identification by RMVA scheme.

c^{gn}_{cm} [-]	c^{an}_{cm0} [-]	c^{an}_{ci0} [-]	c^{an}_{wi0} [-]	c^{ac}_{ci} [-]	c^{ac}_{wi} [-]	c^{tr}_{cm0} [-]	c^{nc}_{wi0} [-]
6.2970×10^2	0.1492	0.0133	0.0312	0.4989	0.1280	1.4184	1.5534×10^{-3}
c^{rm}_{ci0} [-]	c^{rm}_{wi0} [-]	$\tilde{\alpha}_{c0}$ [-]	$\tilde{\alpha}_{w0}$ [-]	$\hat{\rho}_{cm0}$ [-]	$\hat{\rho}_{ci0}$ [-]	$\hat{\rho}_{wi0}$ [-]	σ_{v00} [MPa]
0.2261	0.0217	0.1001	0.4725	2.2573×10^1	2.6427×10^1	0.9234	318.84

Table 4
Temperature sensitivity coefficients and exponents determined in the first step of parameter identification by RMVA scheme.

r^{an}_{cm} [-]	r^{an}_{ci} [-]	r^{an}_{wi} [-]	r^{tr}_{cm} [-]	r^{nc}_{wi} [-]	r^{rm}_{ci} [-]	r^{rm}_{wi} [-]	$r^{G}_{\alpha c}$ [-]	$r^{G}_{\alpha w}$ [-]	r_v [-]
0.0547	2.0581	0.2045	3.9680	6.1587	5.0910	2.0631	-0.0835	-0.0288	-0.3376
s^{an}_{cm} [-]	s^{an}_{ci} [-]	s^{an}_{wi} [-]	s^{tr}_{cm} [-]	s^{nc}_{wi} [-]	s^{rm}_{ci} [-]	s^{rm}_{wi} [-]	$s^{G}_{\alpha c}$ [-]	$s^{G}_{\alpha w}$ [-]	s_v [-]
8.6725	0.9988	4.0282	1.5593	4.8075	5.5999	3.4306	2.8735	2.5451	0.5115

Table 5
Constitutive parameters identified in the second step of parameter calibration by FEMU method.

m_{v0} [-]	r^m_v [-]	s^m_v [-]	m^m_v [-]	κ [-]
0.027	0.0785	5.0	0.0	2.0

at reference strain rate and 13 different temperatures (20, 50, 100, 150, ..., 600 °C) are performed. For each temperature at least two compression tests are carried out. Cylindrical dilatometer compression samples with diameter of 3.5 mm and height of 5 mm without lubrication pockets are used. However, lubricant is applied on contact surfaces. Subsequently, corresponding flow curves including yield point elongation are derived, smoothed, and interpolated in constant plastic strain intervals. Averages of the resultant flow curves that have the same nominal test parameters (temperature and strain rate) are calculated. These flow curves are then used for calculation of constitutive parameters using RMVA scheme. The constitutive constants that are determined in the first calibration step using RMVA method are presented in Table 3; and their corresponding temperature sensitivity coefficients and exponents are listed in Table 4.

Mean relative error of the fitting is $\tilde{e} = 0.39\%$ which is in the same range of experimental scatter/precision (around 0.43%). constitutive parameters identified in the second step of calibration procedure by FEMU technique using nonisothermal uniaxial compression tests at different strain rates and various initial temperatures are presented in Table 5.

Temperature dependencies of material coefficients associated with frequencies of various thermal dynamic dislocation processes are shown in Fig. 6. For discussing the temperature dependence of different dynamic dislocation processes demonstrated in Fig. 6, it is useful to consider an intermediate temperature regime as the transition between cold and warm regimes which in case of the investigated material ranges from 200 °C to 400 °C. As shown in Fig. 6, probability amplitudes associated with dynamic annihilation of cell mobile and wall immobile dislocations, dynamic nucleation of wall immobile dislocations and dynamic remobilization of immobile dislocations are nearly constant or have almost linear temperature dependencies in cold ($0\,°C < T < 200\,°C$) temperatures. However, they have appreciable nonlinear (exponential Arhenius-type) temperature dependencies in the intermediate ($200\,°C < T < 400\,°C$) and warm ($400\,°C < T < 600\,°C$) regimes. This is partly ascribed to different temperature dependencies of various thermal dislocation mechanisms in different temperature regimes that contribute unevenly to the aforementioned dynamic dislocation processes.

As Fig. 6 suggests, frequencies of annihilation of cell mobile and wall immobile dislocations as well as remobilization of immobile dislocations are intensified by transition from cold to intermediate and warm regimes. This can be in part explained by the well-accepted phenomenon that the principal recovery mechanism changes from cross-slip to climb by transition from cold to warm regime because climb is energetically more favorable in warm regime (Essmann and Mughrabi, 1979; Galindo-Nava et al., 2012; Kubin et al., 1992; Nix et al., 1985; Püschl, 2002; Rivera-Díaz-del-Castillo and Huang, 2012).

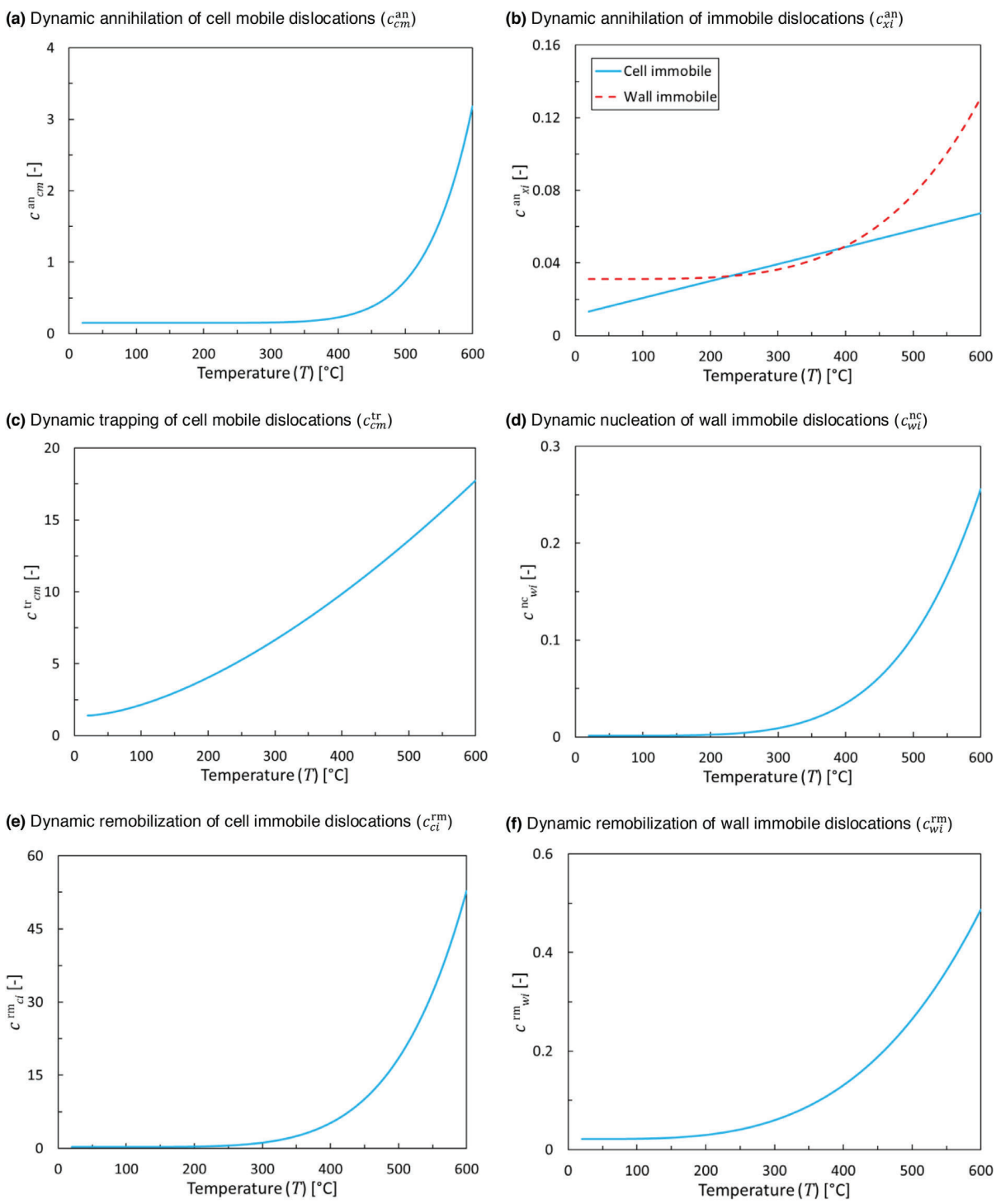

Fig. 6. Temperature dependencies of material coefficients associated with probability amplitudes of different thermal dynamic dislocation processes.

As plotted in Fig. 6(e), probability amplitude of dynamic remobilization of cell immobile dislocations has the strongest temperature dependence compared to the rest of thermal dynamic dislocation processes. At 600 °C, it is roughly 230 times higher than room temperature. However, dynamic annihilation of wall immobile dislocations at 600 °C is only about 10 times higher than that of room temperature.

As mentioned in postulates (13) and (17), dynamic annihilation and remobilization (dynamic recovery) processes share some of the underlying thermal mechanisms. Moreover, as shown in Fig. 6(b), probability amplitude of dynamic annihilation of cell immobile dislocations is almost linear in the entire temperature domain (cold and warm regimes) while the probability amplitude of the other dynamic annihilation processes have nonlinear temperature dependencies (Fig. 6(a) and (b)). The reason is that the thermally-activated and diffusion-controlled dislocation recovery mechanisms such as dislocation climb operating on a cell immobile dislocation in warm regime, more likely results in its remobilization than annihilation compared to its wall immobile counterpart. However, after being remobilized, this former cell immobile dislocation that is now another cell mobile dislocation can become annihilated by another cell mobile dislocation (dynamic annihilation of cell mobile dislocations). This also can partly explain why the frequency of cell mobile dislocation annihilation is more sensitive to temperature raise. Hence, the climb mechanism has much stronger effect on dynamic annihilation of wall immobile dislocations than dynamic annihilation of cell immobile dislocations. Combining this with the fact that the climb mechanism is controlled by vacancy diffusion which has a high nonlinear temperature dependence in warm regime, will explain the difference between forms of temperature dependencies of probability amplitudes of dynamic annihilation of different types of immobile dislocations. As inferred from Fig. 6(e), the climb mechanism substantially influences cell immobile dislocations because of their immobility and particular loose local arrangement compared to wall immobile dislocations. In cold regime, as shown in Fig. 6(e), the climb mechanism is not strong enough in order to notably impact the remobilization rate of cell immobile dislocations. However, as shown in Fig. 6(b), together with cross-slip, its intensity in cold regime is sufficient to linearly affect the annihilation rate of cell immobile dislocations.

Probability amplitude of remobilization of cell immobile dislocations for the investigated material, as mentioned, grows intensively in warm regime by increasing temperature, while it is almost constant in cold regime. Accordingly, cell immobile dislocations and their associated dislocation substructures (IDBs) have relatively high stability in cold regime. However, their stability diminishes abruptly by transition from cold to warm temperatures. Hence, cell immobile dislocation density must be much lower during plastic deformation at warm temperatures than that of cold temperatures. From this it can be inferred that the studied metal tends to formation of dislocation sub-cells (bounded by IDBs) in cold regime while in warm regime it leans toward formation of dislocation cells (bounded by dislocation walls or GNBs).

Furthermore, temperature dependencies of shear modulus, interaction strengths, viscous stress, and strain rate sensitivity are depicted in Fig. 7.

5.1. Isothermal uniaxial tests

Experimental and computational flow curves (after optimization by RMVA) at different temperatures (isothermal condition) for compressive deformation at reference strain rate ($\dot{\varepsilon}_0 = 0.01\ s^{-1}$) are shown in Fig. 8.

For the RMVA fitting, the experimental data are used only up to the accumulated plastic strain of $\varepsilon_p = 0.4$, because at larger strains the effect of friction between compression tools and specimen becomes dominant. This induces notable inhomogeneous distribution of MSVs and strain rate (in compression specimen) that is in contradiction with the assumptions of homogenous RMV and uniaxial deformation. Moreover, since experimental measurements carry notable amount of noise, for fitting of constitutive parameters as well as for comparison to corresponding computational curves, they have been smoothed. In each temperature regime (cold, intermediate and warm), one of the experimental flow curves plotted in Fig. 8 has not been used for parameter identification. Those experimental flow curves (isothermal condition at reference strain rate) that are associated with temperatures 150 °C, 350 °C and 550 °C, have been later compared to their computational predictions for validation.

Isothermal flow curves as shown in Fig. 8, are categorized in the aforementioned three temperature groups: cold, intermediate and warm regimes. As shown in Fig. 6 and Fig. 7, in cold temperature regime for the investigated material (20 to 200 °C), temperature dependent constitutive parameters are either almost constant or have approximately linear temperature dependence. However, in intermediate and warm regimes (200 to 600 °C), temperature dependence of most of the thermal material constants abruptly changes. Temperature dependence of flow curves is the result of two competing effects:

- *Dynamic thermal softening (DTS)* due to temperature dependence of viscous stress, shear modulus, interaction strength, dynamic annihilation of dislocations, and dynamic remobilization of immobile dislocations.
- *Dynamic thermal hardening (DTH)* because of DSA (by pinning mechanism), i.e. temperature dependence of dynamic trapping of cell mobile dislocations and dynamic nucleation of wall immobile dislocations.

According to Figs. 6–8, with respect to relative average difference among flow curves at different temperatures, in cold regime, DTS mostly due to temperature dependence of viscous stress, is clearly stronger than DTH. In cold regime by increasing temperature, DTS gradually decreases while DTH grows. This can be seen from the decreasing trend (by increasing temperature) of relative difference of yield stress in flow curves of cold regime. As shown in Fig. 8(a), in constant plastic strains by increasing temperature the yield stress decreases due to DTS. However, the amount of reduction by increasing temperature also decreases because the competing DTH becomes stronger as the temperature continues to rise. Thus, the

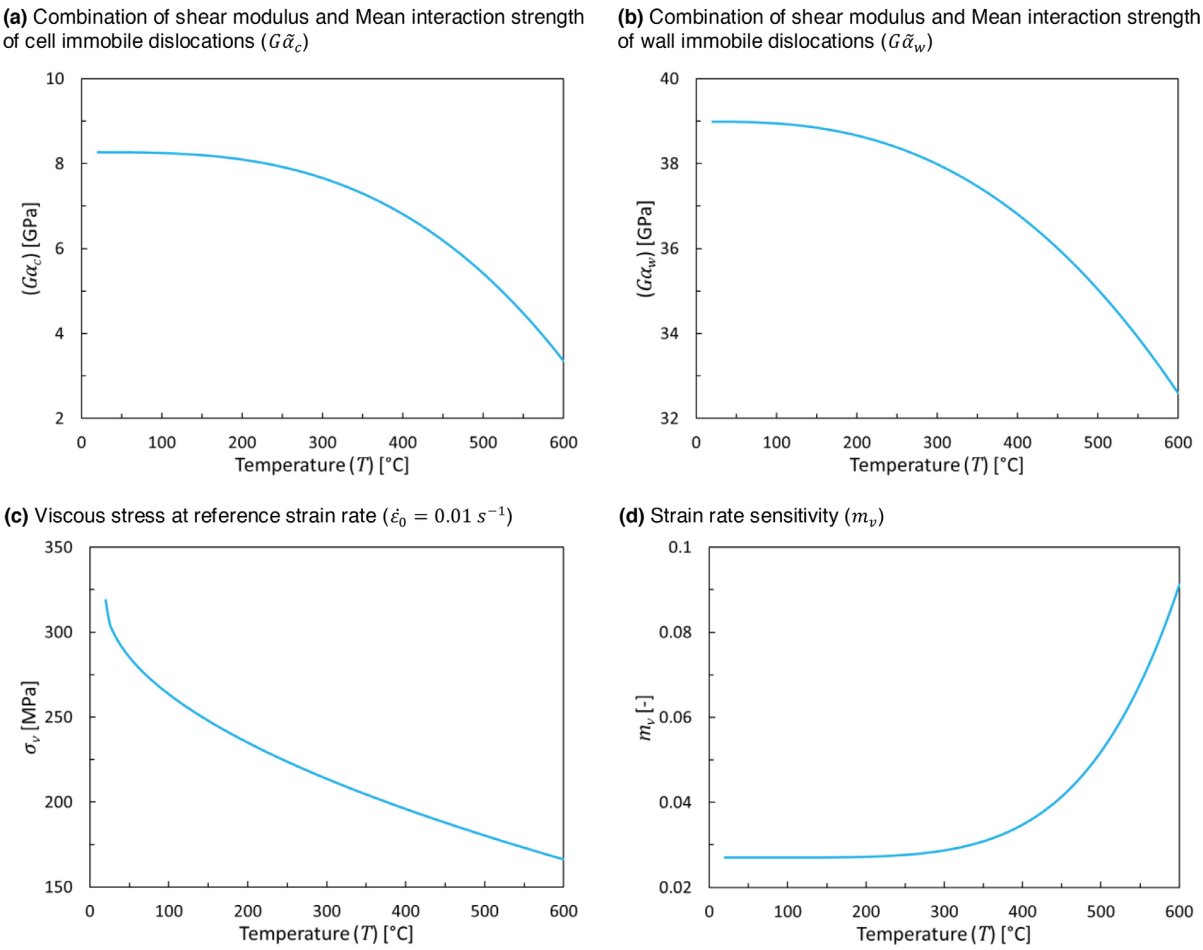

Fig. 7. Temperature dependencies of shear modulus, mean interaction strengths, viscous stress, and strain rate sensitivity.

transition between cold and intermediate regimes occurs in the temperature at which DTS and DTH almost neutralize each other.

In intermediate regimes, DTH is slightly more dominant than DTS. As shown in Fig. 8(b), in constant plastic strains by increasing temperature the yield stress increases as well due to stronger DTH in intermediate regime compared to DTS. Nonetheless, at the upper bound of intermediate regime, the amount of increase in yield stress by increasing temperature diminishes because this time the competing DTS is getting stronger as the temperature continues to grow. In warm regime, the dominant effect again becomes DTS which enhances more than DTH by increasing temperature, mainly due to dynamic annihilation and remobilization processes, mean interaction strengths and shear modulus. As shown in Fig. 8(c), in constant plastic strains by increasing temperature the yield stress decreases with an increasing rate due to very strong DTS in warm regime that cannot be competed by DTH effect. This implies that, in warm regime by increasing temperature, even though the pinning mechanism is amplified but the DTS impact becomes much greater that macroscopically results in an accelerated reduction of yield stress by increasing temperature. Experimental and computational plastic hardening curves (plastic hardening vs. yield stress or plastic strain) of compression tests in constant reference condition ($T = 20\ ^{\circ}C$ and $\dot{\varepsilon}_0 = 0.01\ s^{-1}$) are demonstrated in Fig. 9.

As plotted in Fig. 9, the plastic hardening increases abruptly at the beginning of deformation of the investigated material at reference temperature and strain rate. As shown in experimental flow curves depicted in Fig. 8, in cold regime and close to lower bound of intermediate regime, yield point elongation occurs which corresponds to this increasing domain in plastic hardening curves (Fig. 9) at small plastic strains. The proposed constitutive model has captured this effect. After reaching a maximum value, plastic hardening begins to decrease with a high rate. The rate of decrease of plastic hardening gradually decreases as the plastic strain continues to accumulate. As shown in Fig. 9(a), the model predict saturation ($\theta = 0$) at yield stress of $\sigma_y^{sat} \approx 900$ MPa which corresponds to (accumulated) plastic strain of $\varepsilon_p^{sat} \approx 1.1$. The lowest plastic strain at which saturation occurs (ε_p^{sat}) usually has a decreasing trend by increasing temperature. As shown in Fig. 8(c), for the investigated material in warm regime, the saturation starts at plastic strains of less than 0.4 ($\varepsilon_p^{sat} < 0.4$) which can be measured exper-

(a) Cold Temperatures ($0\ ℃ < T < 200\ ℃$)

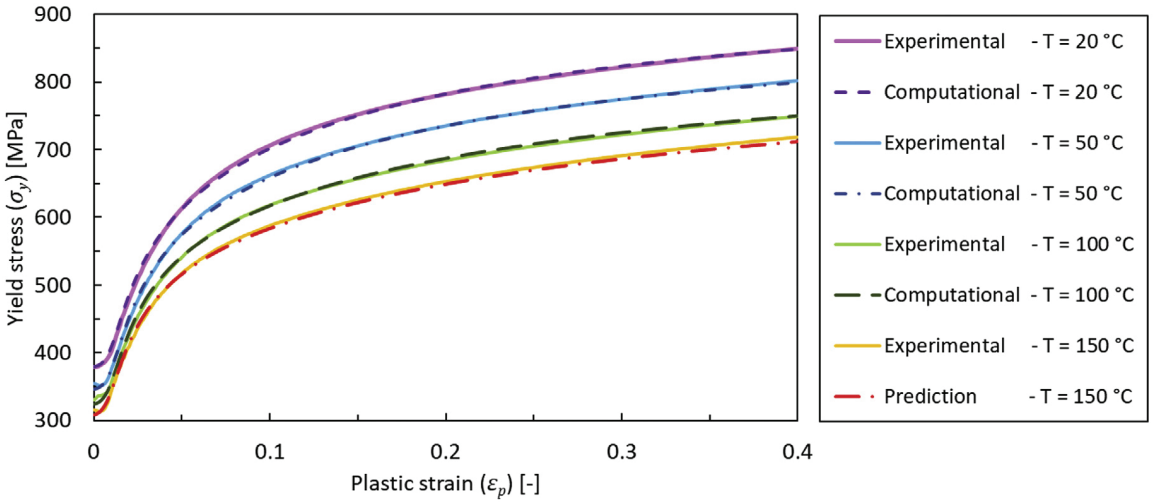

(b) Intermediate temperatures ($200\ ℃ \leq T < 400\ ℃$)

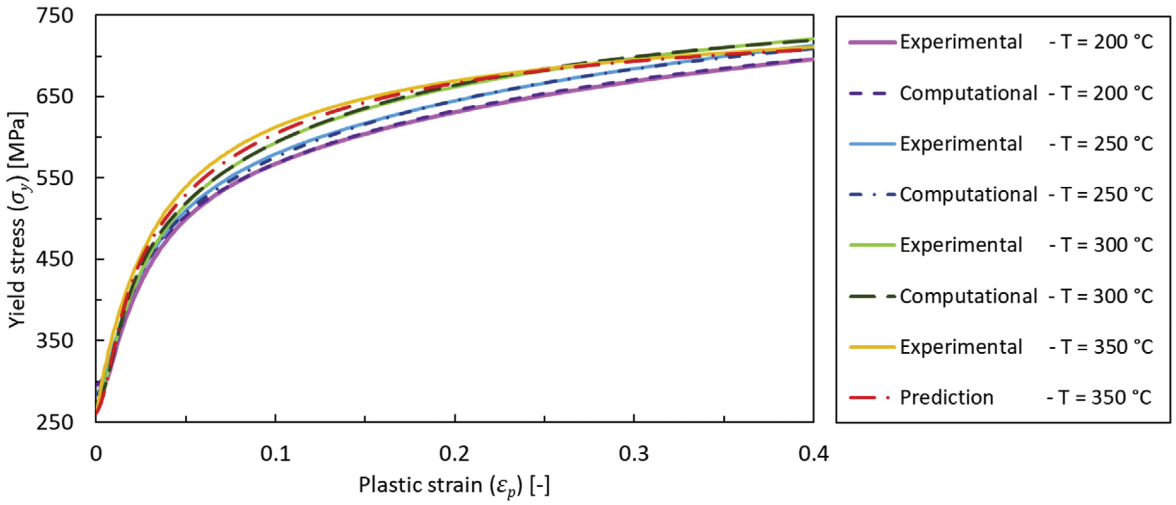

(c) Warm temperatures ($400\ ℃ \leq T \leq 600\ ℃$)

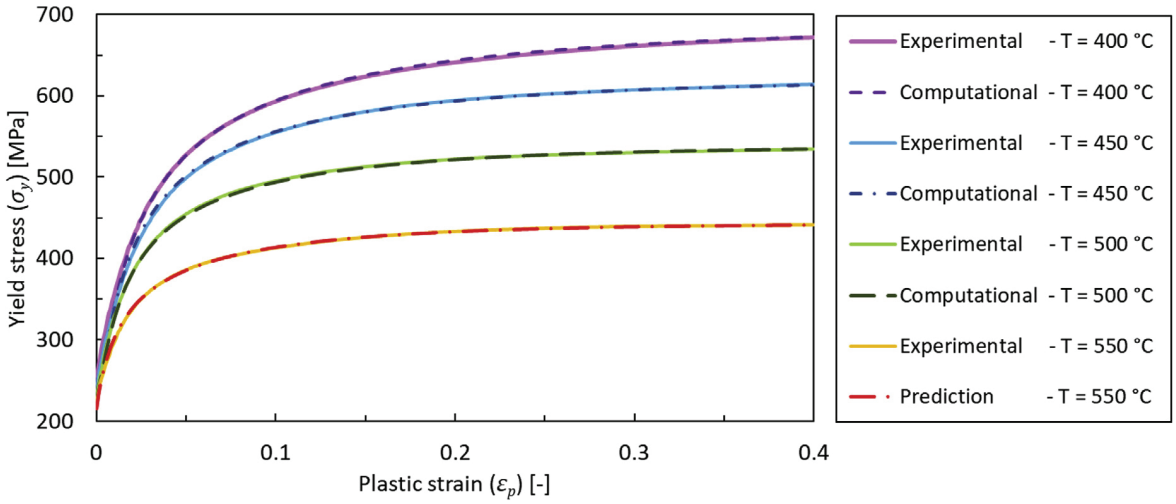

Fig. 8. Comparison between experimental and computational flow curves at different temperatures (isothermal condition) for compressive deformation at reference strain rate ($\dot{\varepsilon}_0 = 0.01\ s^{-1}$).

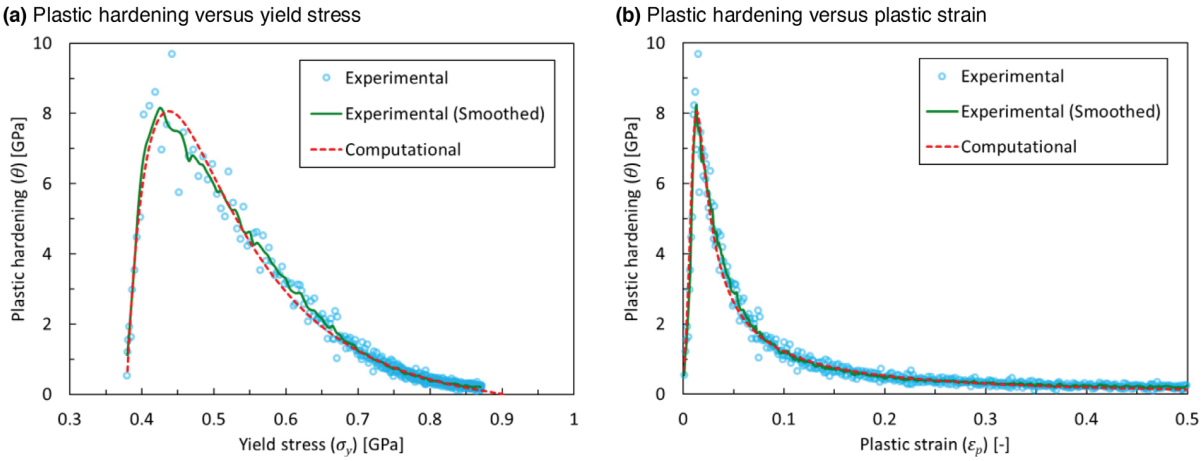

Fig. 9. Comparison between experimental and RMV-based computational plastic hardening curves of compression tests at constant reference temperature and strain rate ($T = 20\ ^{\circ}C$ and $\dot{\varepsilon}_0 = 0.01\ s^{-1}$).

imentally. However, for materials similar to the one investigated in the present paper (nearly all steel grades), in cold and intermediate regimes, generally it is not possible to experimentally measure the flow curves until the point of saturation with acceptable accuracy (using uniaxial tests). Therefore, in order to perform FE simulation of metal forming processes in cold and warm regimes with adequate precision, one has to predict/extrapolate the flow curves generally for relatively very large plastic strains (until saturation) for which there are not experimental measurements available. The microstructural constitutive model proposed in this paper can be trusted for such predictions because it can reproduce the experimental flow curves very accurately in the plastic strain range for which the experimental data is available. On the other hand, it has a comprehensive (statistical) physical background that covers all the major dislocation types and processes in cold and warm regimes.

5.2. Evolution of dislocation densities at constant strain rate

Numerically calculated evolution of dislocation densities based on RMV versus plastic strain in isothermal condition at various temperatures and reference strain rate ($\dot{\varepsilon}_0 = 0.01\ s^{-1}$) are plotted in Fig. 10.

It is emphasized that by increasing temperature in cold and warm regimes, there is trend of reduction in cell mobile, cell immobile and total dislocation densities. However, similar to flow curves of intermediate temperature regime Fig. 8(b)), by increasing temperature wall immobile dislocation density increases, but again in warm regime it decreases. This is reasonable because the plastic stress associated with wall (immobile) dislocations (σ_{pw}) has the largest contribution to the yield stress (postulates ((5) and (8)).

As demonstrated in Fig. 10(b) and (c), in cold regime ($0\,^{\circ}C < T < 200\,^{\circ}C$), generally (nonlocal) cell immobile dislocation density is higher than wall immobile dislocation density ($\rho_{ci} > \rho_{wi}$). In other words, as mentioned earlier in this section, this material tends to formation of cell immobile dislocation tangles (IDBs) at cold regime (sub-cell forming material). Nevertheless, by increasing temperature from 200 °C to 300 °C (intermediate regime), there is a sudden drop in cell immobile dislocation density and a (increasing) jump in wall immobile dislocation density. In this material, in the intermediate regime, (nonlocal) wall immobile dislocations have higher density than their cell immobile counterparts ($\rho_{ci} < \rho_{wi}$). This implies that, in warm regime, dislocation walls (GNDs) are becoming more frequent in the microstructure (of the investigated material) than cell dislocation pile-ups (IDBs). Temperature-dependent dynamic pinning associated with DSA as an underlying mechanism facilitating wall nucleation process (transforming cell dislocations to wall dislocations), is responsible for this effect. Due to contribution of dynamic pinning, as shown in Fig. 6 (d), at around 200 °C, frequency of wall nucleation process in the investigated material increases exponentially by increasing temperature. This results in transformation of more cell immobile to wall immobile dislocations. As Fig. 10 (d) suggests by increasing temperature, total dislocation density always decreases during plastic deformation at constant temperature and strain rate. At 600 °C which is close to the upper bound of warm regime for the investigated steel and therefore very close to the temperature of the onset of dynamic recrystallization (DRX), total dislocation density during deformation is almost constant. Furthermore, as shown in Fig. 10(a), at the beginning of viscoplastic deformation, the undeformed/annealed material (low initial dislocation density), generates (cell) mobile dislocations with a remarkably high rate. High generation rate of mobile dislocations subsequently will lead to a maximum cell mobile dislocation density which occurs at relatively low accumulated plastic strains. This maximum is followed by a rapid drop in cell mobile dislocation density, very similar to the plastic hardening behavior (Fig. 9(b)). As the plastic deformation proceeds, the rate of production of cell mobile dislocations becomes gradually lower until the saturation state at which the rate of production of cell mobile dislocations becomes equal to the rate of their reduction.

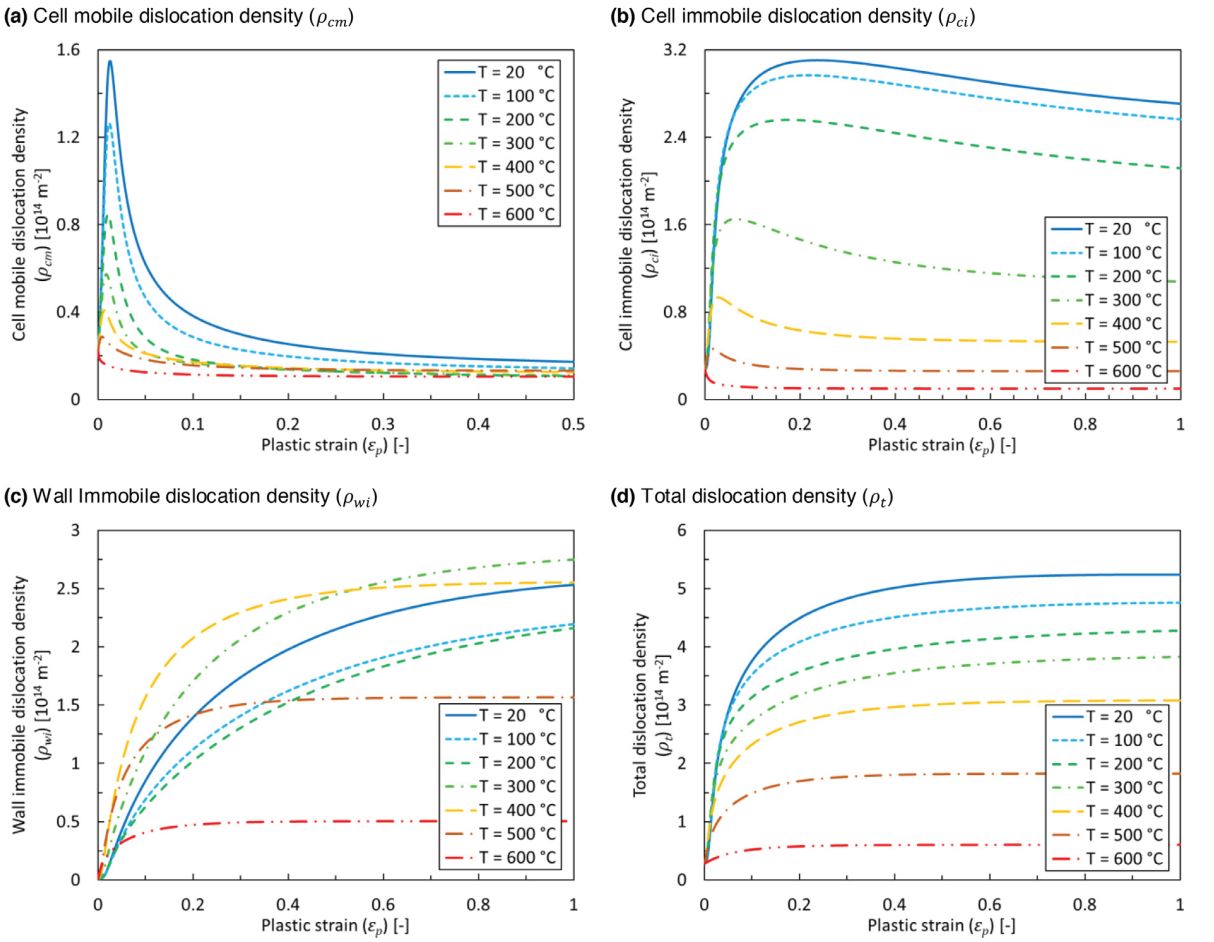

Fig. 10. RMV-based computational cell mobile, cell immobile, wall immobile, and total dislocation densities versus plastic strain in isothermal condition at various temperatures and reference strain rate ($\dot{\varepsilon}_0 = 0.01$ s^{-1}).

5.3. GND density measurements

In order to examine and validate the model's prediction of GND density which as mentioned in postulate (3) is equal to wall immobile dislocation density (ρ_{wi}), several compression specimens are deformed to different plastic strain at constant reference temperature and strain rate. Along the symmetry axis of a deformed compression specimen, there is a gradient of accumulated (equivalent) plastic strain ranging from a near zero value at the contact surface to a maximum of more than mean/macroscopic/true accumulated plastic strain of the deformed specimen at its center point. Hence, along the symmetry axis there is always a point at which local equivalent plastic strain is equal to the mean plastic strain of the deformed specimen. For each of those deformed specimens, coordinates of such points are derived through corresponding FE simulations. It must be noted that there are other points with this property in the cross section of deformed compression specimens; however, the strain state at those points are much more complex (triaxial) compared to the points on the symmetry axis which are almost under uniaxial strain state. Moreover, it can be easily shown that those local points with the aforementioned property ($\bar{\varepsilon}_p = \varepsilon_p$), have also the same average and instantaneous local equivalent plastic strain rate as the (constant) prescribed mean/macroscopic/true plastic strain rate of the deforming specimen ($\dot{\bar{\varepsilon}}_p = \dot{\varepsilon}_p$).

For each specimen, around the vicinity of such points (RMV), an EBSD sample is prepared. Sample preparation for EBSD involved standard mechanical polishing to 0.05 μm, followed by electropolishing in a 5% perchloric acid and 95% acetic acid solution (by volume) with an applied voltage of 35 V. Measurements are performed using a field emission gun scanning electron microscope (FEG-SEM), JOEL JSM 7000F, at 20 KeV beam energy, approximately 30 nA probe current, and 100-300 nm step size. A Hikari EBSD camera by Ametek-EDAX, in combination with the OIM software suite (OIM Data Collection and OIM Analysis V7.3) by EDAX-TSL, is used for data acquisition and analysis. Subsequently, at each point, GND density is calculated from kernel average misorientation (KAM) which is the average angular deviation between a point and its neighbors in a distance twice the step size as long as their misorientation does not exceed 5° (Calcagnotto et al., 2010).

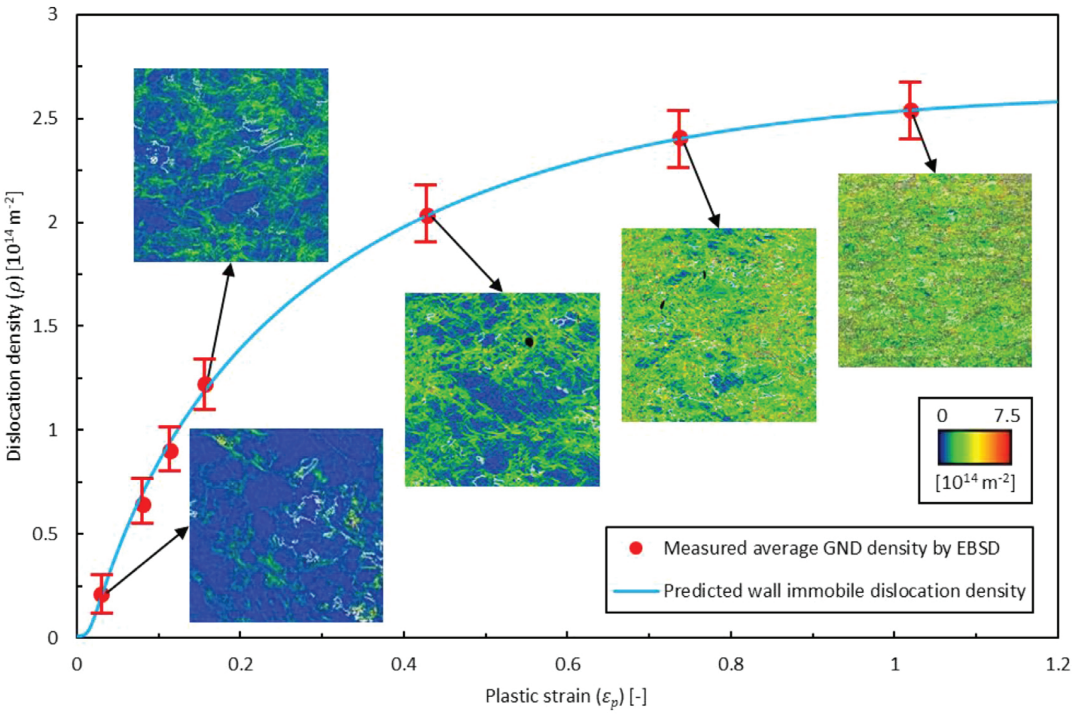

Fig. 11. Comparison between computationally predicted wall immobile dislocation density and measured GND density using high resolution EBSD in different compressive plastic strains at reference condition ($T = 20$ °C and $\dot{\varepsilon}_0 = 0.01$ s^{-1}) along with corresponding EBSD images with GND density distribution (calculated from KAM data) over the representative area.

After mapping KAM values to GND density, over a representative area with the size of $100 \times 100\,\mu$m, the average GND density is calculated.

Comparison between computationally predicted wall immobile dislocation density and the measured average GND density using high resolution EBSD in different plastic strains at reference condition ($T = 20$ °C and $\dot{\varepsilon}_0 = 0.01$ s^{-1}) is shown in Fig. 11.

5.4. Multistep uniaxial tests

As mentioned in postulate (1), "*Two identical material samples that are plastically deformed to an equal amount of accumulated plastic strain but with different histories of temperature and strain rate, if again deformed under an equal temperature and strain rate condition, do not necessarily yield the same stress response*". In order to test this statement and further validate the history dependence of the presented microstructural constitutive model, the multistep compression tests are devised. In these tests, first, previously undeformed compression specimens are plastically deformed to a predefined plastic strain in constant temperature T_i with low reference strain rate to make sure temperature remains almost constant during compression (initial compression step). In the next step (final compression step), they are cooled down and again deformed in constant room temperature at the reference strain rate to a certain plastic strain. This cycle is illustrated in the schematic time-temperature diagram shown in Fig. 12(a). The initial compression step is performed at three constant temperatures, $T_i = 20,\ 300$ and 400 °C until the accumulated plastic strain $\varepsilon_p = 0.2$. In Fig. 12(b), flow curves derived from the final compression steps are compared to their corresponding RMV-based computational flow curves predicted by the constitutive model.

All three flow curves shown in Fig. 12(b) are material responses (yield stress) under plastic deformation at identical constant reference temperature and strain rate with the same initial accumulated plastic strain $\varepsilon_{p0} = 0.2$. However, for each of them, the initial plastic strain was accumulated in different temperatures (different histories of plastic strain accumulation). As shown in Fig. 12(b), initial yield stress is slightly higher while plastic hardening is considerably much lower for $T_i = 300$ and 400 °C compared to those of $T_i = 20$ °C. The flow curves related to $T_i = 300$ and 400 °C in the investigated plastic strain domain exhibit yield point elongation (Lüders bands) as they are convex ($\theta' \equiv {\partial^2 \sigma_y}/{\partial \varepsilon_p^2} \geq 0$) instead

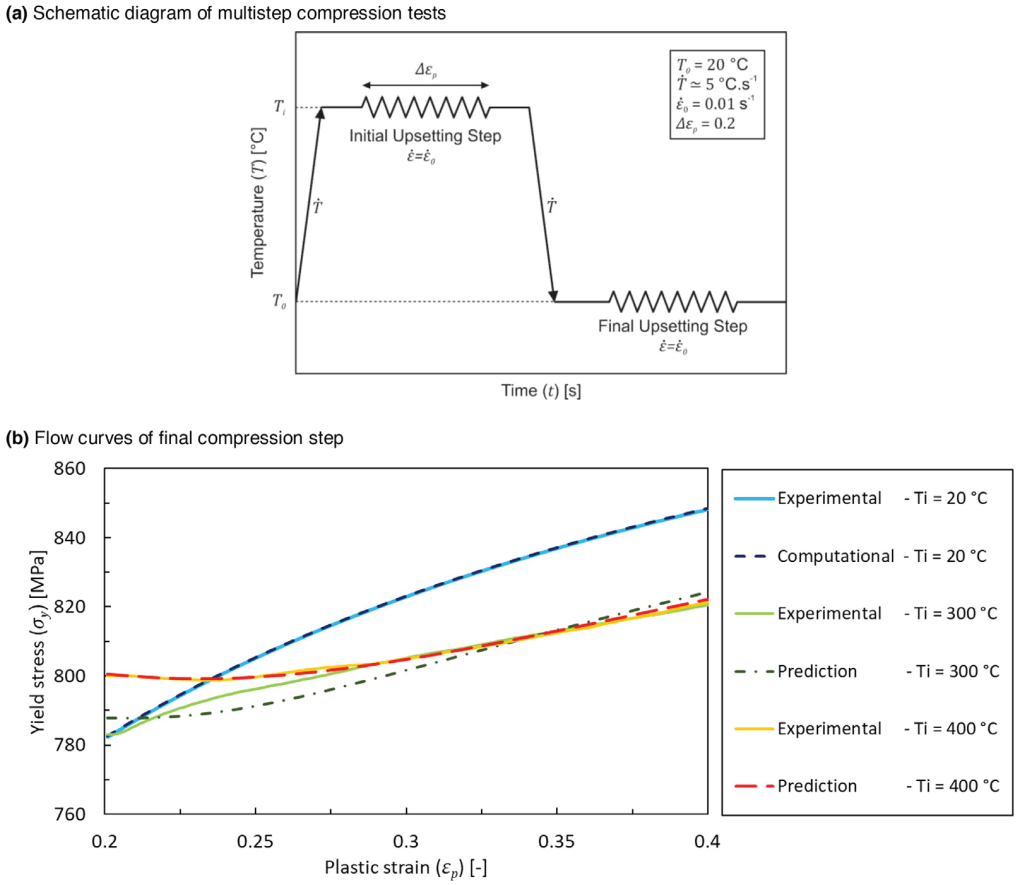

Fig. 12. Schematic time-temperature diagram of multistep compression tests and comparison between corresponding experimental and RMV-based computationally predicted flow curves of final compression step.

of typical concave flow curves ($\theta' \equiv {}^{\partial^2\sigma_y}/_{\partial\varepsilon_p^2} \leq 0$), and they have relatively large domain of nonpositive plastic hardening ($\theta \equiv {}^{\partial\sigma_y}/_{\partial\varepsilon_p} \leq 0$) or low plastic hardening (Pham et al., 2015).

5.5. Nonisothermal uniaxial tests

Nonisothermal compression tests and their respective FE simulations at various strain rates (in intermediate-rate regime) and different initial temperatures (in cold and warm regimes) are conducted for the second step of parameter identification to determine constitutive parameters associated with strain rate sensitivity and dissipation factor. In order to do so, first the presented constitutive model is implemented as a user-defined material subroutine UMAT in ABAQUS/Standard with the material constants identified in the RMV-based fitting step with an initial guess for the parameters yet to be determined in the second step of parameter identification using FEMU technique. Then, thermo-mechanical FE model of compression test with the nominal dimensions of experimental specimens and tools has been created in the implicit ABAQUS/Standard software. Mechanical and physical properties of compression material and tools such as elastic modulus, poisson's ratio, mass density, specific heat capacity, thermal conductivity, and thermal expansion are inputted to the FE model as functions of temperature. Convection and radiation along with thermal contact conductance as a function of pressure of contact interface of compression specimen and tools are also considered. In addition, simple coulomb friction model with friction coefficient of 0.05 corresponding to the experimental condition was used. As mentioned, details of FE implementation of the constitutive model and thermo-mechanical FE simulation of an industrial multistep warm forging of a bevel gear for the same material investigated here are planned to be published later.

Fig. 13 shows FE-simulated distribution of statistical TMM variables, equivalent stress ($\bar{\sigma}$), temperature (T), equivalent plastic strain rate ($\dot{\bar{\varepsilon}}_p$), cell mobile dislocation density (ρ_{cm}), cell immobile dislocation density (ρ_{ci}), and wall immobile

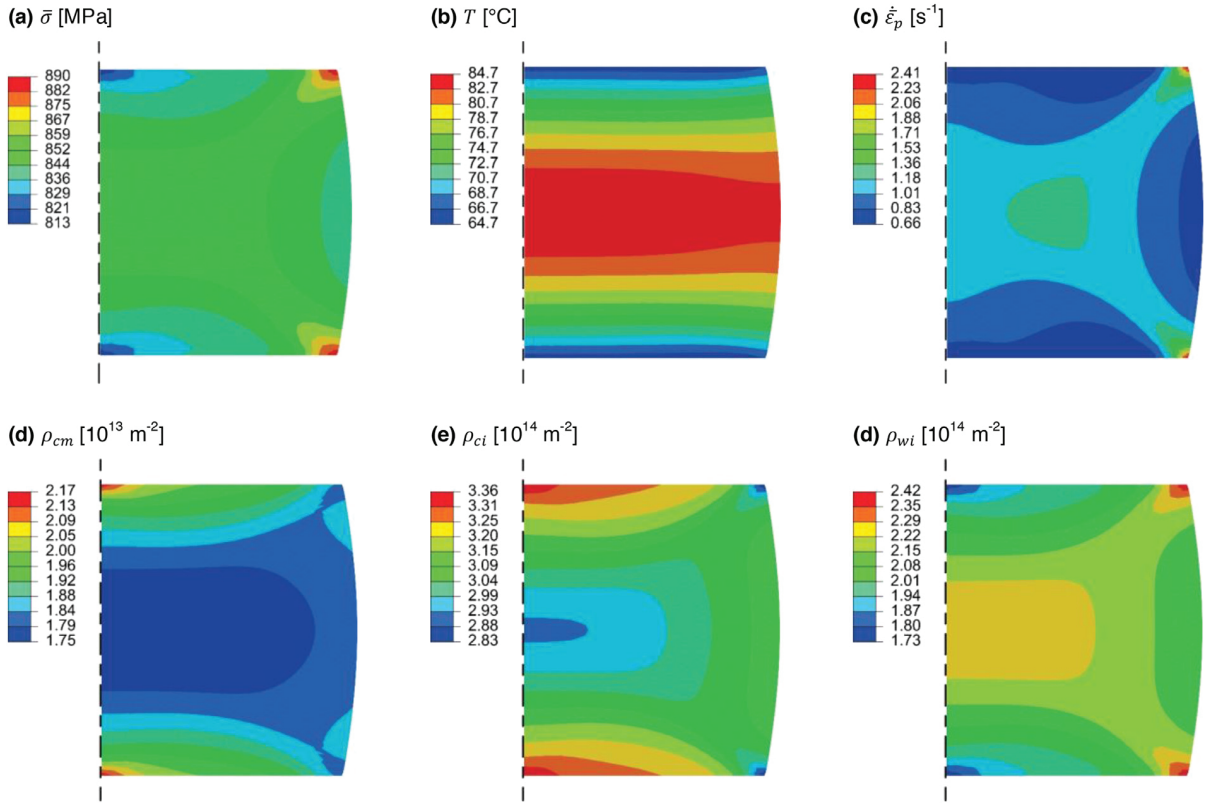

Fig. 13. FE-simulated distribution of statistical TMM variables including MSVs in a radial section of compression specimen during deformation at mean plastic strain of $\varepsilon_p = 0.6$ and mean strain rate of $\dot{\varepsilon} = 1\ s^{-1}$ with initial temperature of $T_0 = 20\ ^\circ C$.

dislocation density (ρ_{wi}), in radial cross section of compression specimen during compressive plastic deformation at mean plastic strain of $\varepsilon_p = 0.6$ and strain rate of $\dot{\varepsilon} = 1\ s^{-1}$ with initial temperature of $T_0 = 20\ ^\circ C$. Experimental and FE-simulated yield stress and temperature change ($\Delta T = T - T_0$) due to plastic work for compression tests at different strain rates and initial room temperature are shown in Fig. 14.

In each experimental compression test corresponding to Fig. 14, temperature is measured via a thermocouple welded on the middle point in height direction at the lateral surface of the compression specimen. Likewise, in FE simulation the temperature is read from the respective point. The experimental data (force and temperature versus displacement) obtained from the nonisothermal compression tests at constant strain rates of 0.1, 1.0 and 10.0 s^{-1} are supplied to the second step of parameter identification by FEMU procedure. As shown in Fig. 14, for validation of the model's rate-dependent features, the experimental data corresponding to the nonisothermal compression test at constant strain rate of 3.0 s^{-1} is compared to its counterpart predicted by the FE simulation.

As inferred from Fig. 14, at relatively high strain rates in the investigated rate regimes, since there is not enough time for the generated adiabatic heat to dissipate completely, it remain in the material; and as a result elevates the temperature which in turn leads to spontaneous DTS. Nonisothermal FE simulations of metal forming processes highly depend on the input thermo-physical properties of billet/blank and tools, their pressure-dependent friction and thermal contact conductance, as well as convection and radiation heat transfer with the ambient environment which all of them are temperature-dependent. Hence, large portion of the difference in temperature readings from these FE-simulated nonisothermal compression (virtual) tests compared to their experimental counterparts is attributed to the complexity of the thermomechanical FE simulation of metal forming that is independent from the constitutive model. In addition, the accuracy of experimental temperature measurement with welded thermocouples is highly dependent on the weld quality and position, as well as the thermocouple delay. However, the discrepancy between FE-simulated and experimental temperature increase is much less than expected.

6. Outlook

As every continuum plasticity model has limitations, despite its vast scope and outstanding accuracy, the presented constitutive model in this paper is not an exception:

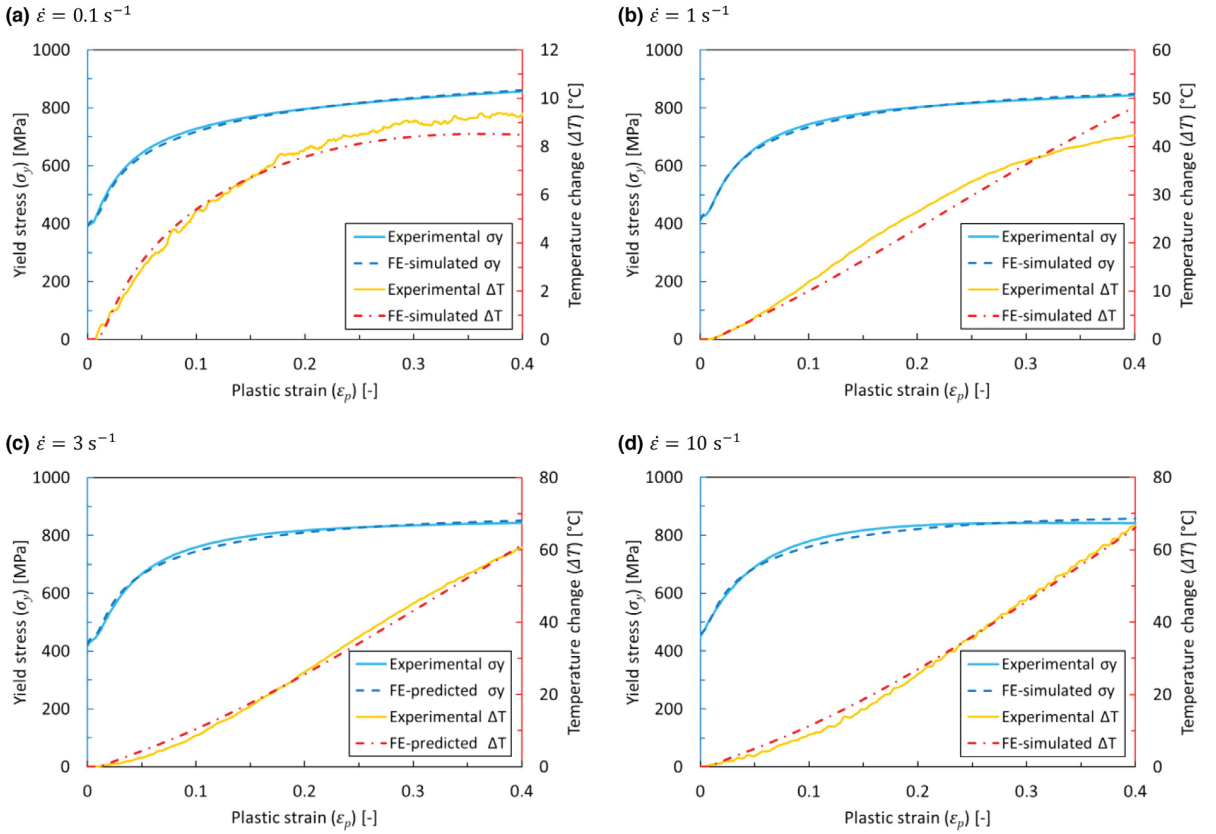

Fig. 14. Comparison between experimental and FE-simulated yield stress and temperature change due to plastic work ($\Delta T = T - T_0$) for compression tests at different strain rates ($\dot{\varepsilon} = 0.1,\ 1,\ 3,\ 10\ s^{-1}$) and initial room temperature ($T_0 = 20\ ^\circ C$).

- In its current state, the model does not account for anisotropy and strain path dependence. In order to generalize it to account for such effects, some new postulates need to be added while probably some of the existing ones require slight modification. Subsequently, for validation, the model must be implemented in the crystal plasticity framework.
- It has been tested thus far only for cold and warm regimes. Therefore, application or extension of it to hot temperature regime demands further research.
- It has been validated up to now, merely for the intermediate-rate regime. Its validity for other strain rate regimes as well as static state must be verified. Moreover, its overall strain rate dependence needs more tests.

Furthermore, the proposed microstructural constitutive model requires further validation using different alloys with various compositions, microstructures and grain size distributions.

7. Conclusion

A fully coupled thermo-micro-mechanical constitutive model for viscoplasticity of polycrystalline metallic materials was proposed based on continuum dislocation dynamics. The constitutive model was developed in such a way to statistically capture and quantify all statistically-considerable microstructural phenomena influencing dislocations in cold and warm regimes and hence accurately describe macroscopic viscoplastic response of material. The following conclusions are drawn from the present approach:

- The mechanical response of a macroscale material point under viscoplastic deformation is an implicit function of its stochastic microstructural state, plastic strain rate, and temperature. The presented constitutive model is history dependent and it does not depend on accumulated plastic strain. Multistep compression tests were conducted for verification of the accuracy of model's history dependence features.
- Dynamic and static evolutions of different types of dislocations are functions of dynamic and static pinning of dislocations by interstitial solute atoms. Hence, the proposed constitutive model accounts for the effects associated with pinning such as yield point elongation, dynamic strain aging, static aging and bake hardening. However, validation of static evolution of dislocation densities suggested by four postulates is a subject of another paper.

- The constitutive model predicts flow curves at various temperatures and strain rates in cold and warm regimes with an exceptionally high accuracy (mean error of less than 0.4% which is in the same range of experimental scatter). Moreover, the evolution of measured GND density (by EBSD) is very close to that of predicted by the model.
- Comparison of FE simulations of nonisothermal compression tests at various strain rates with their corresponding compression experiments verifies that the postulates suggested for model's rate sensitivity and varying dissipation factor in adiabatic heat generation (due to plastic work) are realistic.
- Implementation of the presented constitutive model as user-defined material subroutines UMAT and VUMAT respectively, in ABAQUS/Standard and ABAQUS/Explicit based on associative isotropic J_2 hypoelasto-viscoplasticity, has revealed that the constitutive model is computationally efficient (simulation costs are in the same level as empirical models) in thermo-mechanical FE simulations of cold and warm metal forming processes.

Acknowledgements

The authors appreciate the support received under the project "IGF-Vorhaben 18531N" in the framework of research program of "Integrierte Umform und Wärmebehandlungssimulation für Massivumformteile (InUWäM)" funded by the German federation of industrial research associations (AiF). The authors also wish to express their gratitude for the support received from the project "Laserunterstütztes Kragenziehen hochfester Bleche" by the research association EFB e.V. funded under the number 18277N by AiF. The help of Mr. Konstantin Schacht with experiments and valuable suggestions of Prof. Wolfgang Bleck and Prof. Wolfgang Blum are gratefully acknowledged.

References

Abu Al-Rub, R.K., Voyiadjis, G.Z., 2004. Analytical and experimental determination of the material intrinsic length scale of strain gradient plasticity theory from micro- and nano-indentation experiments. Int. J. Plast. 20, 1139–1182. doi:10.1016/j.ijplas.2003.10.007.
Adams, B.L., Olson, T., 1998. The mesostructure—properties linkage in polycrystals. Prog. Mater Sci. 43, 1–87. doi:10.1016/S0079-6425(98)00002-4.
Allain, S., Chateau, J.-P., Bouaziz, O., 2004. A physical model of the twinning-induced plasticity effect in a high manganese austenitic steel. Mater. Sci. Eng.: A 387-389, 143–147. doi:10.1016/j.msea.2004.01.060.
Amodeo, R.J., Ghoniem, N.M., 1990. Dislocation dynamics. I. A proposed methodology for deformation micromechanics. Phys. Rev. B 41, 6958–6967. doi:10.1103/PhysRevB.41.6958.
Ananthakrishna, G., 2007. Current theoretical approaches to collective behavior of dislocations. Phys. Rep. 440, 113–259. doi:10.1016/j.physrep.2006.10.003.
Ananthakrishna, G., Sahoo, D., 1981. A model based on nonlinear oscillations to explain jumps on creep curves. J. Phys. D: Appl. Phys. 14, 2081–2090. doi:10.1088/0022-3727/14/11/015.
Ardeljan, M., Beyerlein, I.J., Knezevic, M., 2014. A dislocation density based crystal plasticity finite element model: application to a two-phase polycrystalline HCP/BCC composites. J. Mech. Phys. Solids 66, 16–31. doi:10.1016/j.jmps.2014.01.006.
Argon, A.S., 2012. Strengthening Mechanisms in Crystal Plasticity. Oxford University Press, Oxford 404 S.
Argon, A.S., Moffatt, W.C., 1981. Climb of extended edge dislocations. Acta Metall. 29, 293–299. doi:10.1016/0001-6160(81)90156-5.
Arsenlis, A., 2004. On the evolution of crystallographic dislocation density in non-homogeneously deforming crystals. J. Mech. Phys. Solids 52, 1213–1246. doi:10.1016/j.jmps.2003.12.007.
Arsenlis, A., Cai, W., Tang, M., Rhee, M., Oppelstrup, T., Hommes, G., Pierce, T.G., Bulatov, V.V., 2007. Enabling strain hardening simulations with dislocation dynamics. Model. Simul. Mater. Sci. Eng. 15, 553–595. doi:10.1088/0965-0393/15/6/001.
Arsenlis, A., Parks, D., 1999. Crystallographic aspects of geometrically-necessary and statistically-stored dislocation density. Acta Mater. 47, 1597–1611. doi:10.1016/S1359-6454(99)00020-8.
Arsenlis, A., Parks, D.M., 2002. Modeling the evolution of crystallographic dislocation density in crystal plasticity. J. Mech. Phys. Solids 50, 1979–2009. doi:10.1016/S0022-5096(01)00134-X.
Ashby, M.F., 1970. The deformation of plastically non-homogeneous materials. Philos. Mag. 21, 399–424. doi:10.1080/14786437008238426.
Askari, H., Maughan, M.R., Abdolrahim, N., Sagapuram, D., Bahr, D.F., Zbib, H.M., 2015. A stochastic crystal plasticity framework for deformation of micro-scale polycrystalline materials. Int. J. Plast. 68, 21–33. doi:10.1016/j.ijplas.2014.11.001.
Askari, H., Young, J., Field, D., Kridli, G., Li, D., Zbib, H., 2013. A study of the hot and cold deformation of twin-roll cast magnesium alloy AZ31. Philos. Mag. 94, 381–403. doi:10.1080/14786435.2013.853884.
Austin, R.A., McDowell, D.L., 2011. A dislocation-based constitutive model for viscoplastic deformation of FCC metals at very high strain rates. Int. J. Plast. 27, 1–24. doi:10.1016/j.ijplas.2010.03.002.
Babu, B., Lindgren, L.-E., 2013. Dislocation density based model for plastic deformation and globularization of Ti-6Al-. Int. J. Plast. 50, 94–108. doi:10.1016/j.ijplas.2013.04.003.
Bailey, J.E., Hirsch, P.B., 1960. The dislocation distribution, flow stress, and stored energy in cold-worked polycrystalline silver. Philos. Mag. 5, 485–497. doi:10.1080/14786436008238300.
Bammann, D.J., Aifantis, E.C., 1982. On a proposal for a continuum with microstructure. Acta Mech. 45, 91–121. doi:10.1007/BF01295573.
Bardella, L., 2006. A deformation theory of strain gradient crystal plasticity that accounts for geometrically necessary dislocations. J. Mech. Phys. Solids 54, 128–160. doi:10.1016/j.jmps.2005.08.003.
Bay, B., Hansen, N., Hughes, D.A., Kuhlmann-Wilsdorf, D., 1992. Overview no. 96 evolution of f.c.c. deformation structures in polyslip. Acta Metall. Mater. 40, 205–219. doi:10.1016/0956-7151(92)90296-Q.
Bay, B., Hansen, N., Kuhlmann-Wilsdorf, D., 1989. Deformation structures in lightly rolled pure aluminium. Mater. Sci. Eng.: A 113, 385–397. doi:10.1016/0921-5093(89)90325-0.
Bergström, Y., 1970. A dislocation model for the stress-strain behaviour of polycrystalline α-Fe with special emphasis on the variation of the densities of mobile and immobile dislocations. Mater. Sci. Eng. 5, 193–200. doi:10.1016/0025-5416(70)90081-9.
Beyerlein, I.J., Tomé, C.N., 2008. A dislocation-based constitutive law for pure Zr including temperature effects. Int. J. Plast. 24, 867–895. doi:10.1016/j.ijplas.2007.07.017.
Bhushan, B., Nosonovsky, M., 2003. Scale effects in friction using strain gradient plasticity and dislocation-assisted sliding (microslip). Acta Mater. 51, 4331–4345. doi:10.1016/S1359-6454(03)00261-1.
Blum, W., Eisenlohr, P., Breutinger, F., 2002. Understanding creep—a review. Metall. Mater. Trans. A 33, 291–303. doi:10.1007/s11661-002-0090-9.
Bok, H.-H., Choi, J., Barlat, F., Suh, D.W., Lee, M.-G., 2014. Thermo-mechanical-metallurgical modeling for hot-press forming in consideration of the prior austenite deformation effect. Int. J. Plast. 58, 154–183. doi:10.1016/j.ijplas.2013.12.002.
Bouaziz, O., Guelton, N., 2001. Modelling of TWIP effect on work-hardening. Mater. Sci. Eng.: A 319-321, 246–249. doi:10.1016/S0921-5093(00)02019-0.
Brinckmann, S., Siegmund, T., Huang, Y., 2006. A dislocation density based strain gradient model. Int. J. Plast. 22, 1784–1797. doi:10.1016/j.ijplas.2006.01.005.

Brown, L.M., 2002. A dipole model for the cross-slip of screw dislocations in fee metals. Philos. Mag. A 82, 1691–1711. doi:10.1080/01418610208235684.
Busso, E., 2000. Gradient-dependent deformation of two-phase single crystals. J. Mech. Phys. Solids 48, 2333–2361. doi:10.1016/S0022-5096(00)00006-5.
Busso, E.P., 1998. A continuum theory for dynamic recrystallization with microstructure-related length scales. Int. J. Plast. 14, 319–353. doi:10.1016/S0749-6419(98)00008-4.
Byun, T.S., 2003. On the stress dependence of partial dislocation separation and deformation microstructure in austenitic stainless steels. Acta Mater. 51, 3063–3071. doi:10.1016/S1359-6454(03)00117-4.
Calcagnotto, M., Ponge, D., Demir, E., Raabe, D., 2010. Orientation gradients and geometrically necessary dislocations in ultrafine grained dual-phase steels studied by 2D and 3D EBSD. Mater. Sci. Eng.: A 527, 2738–2746. doi:10.1016/j.msea.2010.01.004.
Cereceda, D., Diehl, M., Roters, F., Raabe, D., Perlado, J.M., Marian, J., 2016. Unraveling the temperature dependence of the yield strength in single-crystal tungsten using atomistically-informed crystal plasticity calculations. Int. J. Plast. 78, 242–265. doi:10.1016/j.ijplas.2015.09.002.
Chandra, S., Samal, M.K., Chavan, V.M., Raghunathan, S., 2018. Hierarchical multiscale modeling of plasticity in copper: from single crystals to polycrystalline aggregates. Int. J. Plast. 101, 188–212. doi:10.1016/j.ijplas.2017.10.014.
Cheong, K.-S., Busso, E.P., 2004. Discrete dislocation density modelling of single phase FCC polycrystal aggregates. Acta Mater. 52, 5665–5675. doi:10.1016/j.actamat.2004.08.044.
Christian, J.W., Mahajan, S., 1995. Deformation twinning. Prog. Mater Sci. 39, 1–157. doi:10.1016/0079-6425(94)00007-7.
Clayton, J.D., McDowell, D.L., Bammann, D.J., 2006. Modeling dislocations and disclinations with finite micropolar elastoplasticity. Int. J. Plast. 22, 210–256. doi:10.1016/j.ijplas.2004.12.001.
Columbus, D., Grujicic, M., 2002. A comparative discrete-dislocation/nonlocal crystal-plasticity analysis of plane-strain mode I fracture. Mater. Sci. Eng.: A 323, 386–402. doi:10.1016/S0921-5093(01)01397-1.
Cottrell, A.H., 1953. Dislocations and Plastic Flow in Crystals. Clarendon Press, Oxford.
Cottrell, A.H., Bilby, B.A., 1949. Dislocation theory of yielding and strain ageing of iron. Proc. Phys. Soc. A 62, 49–62. doi:10.1088/0370-1298/62/1/308.
Csikor, F.F., Motz, C., Weygand, D., Zaiser, M., Zapperi, S., 2007. Dislocation avalanches, strain bursts, and the problem of plastic forming at the micrometer scale. Science (New York, N.Y.) 318, 251–254. doi:10.1126/science.1143719.
Cui, Y., Po, G., Ghoniem, N., 2016a. Controlling strain bursts and avalanches at the nano- to micrometer scale. Phys. Rev. Lett. 117, 155502. doi:10.1103/PhysRevLett.117.155502.
Cui, Y., Po, G., Ghoniem, N., 2016b. Temperature insensitivity of the flow stress in body-centered cubic micropillar crystals. Acta Mater. 108, 128–137. doi:10.1016/j.actamat.2016.02.008.
Cui, Y., Po, G., Ghoniem, N., 2017. Influence of loading control on strain bursts and dislocation avalanches at the nanometer and micrometer scale. Phys. Rev. B 95. doi:10.1103/PhysRevB.95.064103.
Derlet, P.M., Maaß, R., 2013. Micro-plasticity and intermittent dislocation activity in a simplified micro-structural model. Model. Simul. Mater. Sci. Eng. 21, 35007. doi:10.1088/0965-0393/21/3/035007.
Devincre, B., Kubin, L., Lemarchand, C., Madec, R., 2001. Mesoscopic simulations of plastic deformation. Mater. Sci. Eng.: A 309-310, 211–219. doi:10.1016/S0921-5093(00)01725-1.
Doherty, R.D., Hughes, D.A., Humphreys, F.J., Jonas, J.J., Jensen, D., Kassner, M.E., King, W.E., McNelley, T.R., McQueen, H.J., Rollett, A.D., 1997. Current issues in recrystallization: a review. Mater. Sci. Eng.: A 238, 219–274. doi:10.1016/S0921-5093(97)00424-3.
Eisenlohr, P., Blum, W., 2005. Bridging steady-state deformation behavior at low and high temperature by considering dislocation dipole annihilation. Mater. Sci. Eng.: A 400-401, 175–181. doi:10.1016/j.msea.2005.01.069.
El-Awady, J.A., Wen, M., Ghoniem, N.M., 2009. The role of the weakest-link mechanism in controlling the plasticity of micropillars. J. Mech. Phys. Solids 57, 32–50. doi:10.1016/j.jmps.2008.10.004.
Eringen, A., 1983. Theories of nonlocal plasticity. Int. J. Eng. Sci. 21, 741–751. doi:10.1016/0020-7225(83)90058-7.
Essmann, U., Mughrabi, H., 1979. Annihilation of dislocations during tensile and cyclic deformation and limits of dislocation densities. Philos. Mag. A 40, 731–756. doi:10.1080/01418617908234871.
Estrin, Y., Braasch, H., Brechet, Y., 1996. A dislocation density based constitutive model for cyclic deformation. J. Eng. Mater. Technol. 118, 441. doi:10.1115/1.2805940.
Estrin, Y., Kubin, L.P., 1986. Local strain hardening and nonuniformity of plastic deformation. Acta Metall. 34, 2455–2464. doi:10.1016/0001-6160(86)90148-3.
Estrin, Y., Mecking, H., 1984. A unified phenomenological description of work hardening and creep based on one-parameter models. Acta Metall. 32, 57–70. doi:10.1016/0001-6160(84)90202-5.
Estrin, Y., Mecking, H., 1992. A remark in connection with 'direct versus indirect dispersion hardening'. Scr. Metall. Mater. 27, 647–648. doi:10.1016/0956-716X(92)90355-I.
Estrin, Y., Tóth, L.S., Molinari, A., Bréchet, Y., 1998. A dislocation-based model for all hardening stages in large strain deformation. Acta Mater. 46, 5509–5522. doi:10.1016/S1359-6454(98)00196-7.
Evers, L., Brekelmans, W., Geers, M., 2004. Scale dependent crystal plasticity framework with dislocation density and grain boundary effects. Int. J. Solids Struct. 41, 5209–5230. doi:10.1016/j.ijsolstr.2004.04.021.
Fan, X.G., Yang, H., 2011. Internal-state-variable based self-consistent constitutive modeling for hot working of two-phase titanium alloys coupling microstructure evolution. Int. J. Plast. 27, 1833–1852. doi:10.1016/j.ijplas.2011.05.008.
Field, J.E., Walley, S.M., Proud, W.G., Goldrein, H.T., Siviour, C.R., 2004. Review of experimental techniques for high rate deformation and shock studies. Int. J. Impact Eng. 30, 725–775. doi:10.1016/j.ijimpeng.2004.03.005.
Fleck, N.A., Hutchinson, J.W., 1997. Strain Gradient Plasticity. In: vol. 33. Elsevier, pp. 295–361.
Fleck, N.A., Muller, G.M., Ashby, M.F., Hutchinson, J.W., 1994. Strain gradient plasticity: theory and experiment. Acta Metall. Mater. 42, 475–487. doi:10.1016/0956-7151(94)90502-9.
Fleischer, R.L., 1962. Rapid solution hardening, dislocation mobility, and the flow stress of crystals. J. Appl. Phys. 33, 3504–3508. doi:10.1063/1.1702437.
Follansbee, P.S., Kocks, U.F., 1988. A constitutive description of the deformation of copper based on the use of the mechanical threshold stress as an internal state variable. Acta Metall. 36, 81–93. doi:10.1016/0001-6160(88)90030-2.
Franciosi, P., 1985. The concepts of latent hardening and strain hardening in metallic single crystals. Acta Metall. 33, 1601–1612. doi:10.1016/0001-6160(85)90154-3.
Frank, F.C., Read, W.T., 1950. Multiplication processes for slow moving dislocations. Phys. Rev. 79, 722–723. doi:10.1103/PhysRev.79.722.
Galindo-Nava, E.I., Rae, C., 2016. Microstructure-sensitive modelling of dislocation creep in polycrystalline FCC alloys: Orowan theory revisited. Mater. Sci. Eng.: A 651, 116–126. doi:10.1016/j.msea.2015.10.088.
Galindo-Nava, E.I., Sietsma, J., Rivera-Díaz-del-Castillo, P., 2012. Dislocation annihilation in plastic deformation: II. Kocks–Mecking Analysis. Acta Materialia 60, 2615–2624. doi:10.1016/j.actamat.2012.01.028.
Gao, H., 1999. Mechanism-based strain gradient plasticity: I. Theory. J. Mech. Phys. Solids 47, 1239–1263. doi:10.1016/S0022-5096(98)00103-3.
Gao, H., Huang, Y., 2001. Taylor-based nonlocal theory of plasticity. Int. J. Solids Struct. 38, 2615–2637. doi:10.1016/S0020-7683(00)00173-6.
Gao, H., Huang, Y., 2003. Geometrically necessary dislocation and size-dependent plasticity. Scr. Mater. 48, 113–118. doi:10.1016/S1359-6462(02)00329-9.
Gao, H., Huang, Y., Nix, W.D., 1999. Modeling plasticity at the micrometer scale. Naturwissenschaften 86, 507–515. doi:10.1007/s001140050665.
Gardner, C.J., Adams, B.L., Basinger, J., Fullwood, D.T., 2010. EBSD-based continuum dislocation microscopy. Int. J. Plast. 26, 1234–1247. doi:10.1016/j.ijplas.2010.05.008.
Ghosh, G., Olson, G.B., 2002. The isotropic shear modulus of multicomponent Fe-base solid solutions. Acta Mater. 50, 2655–2675. doi:10.1016/S1359-6454(02)00096-4.

Gilbert, M.R., Queyreau, S., Marian, J., 2011. Stress and temperature dependence of screw dislocation mobility in α -Fe by molecular dynamics. Phys. Rev. B 84, 1052. doi:10.1103/PhysRevB.84.174103.
Gilman, J.J., 1965. Dislocation Mobility in Crystals. J. Appl. Phys. 36, 3195–3206. doi:10.1063/1.1702950.
Gottstein, G., Argon, A.S., 1987. Dislocation theory of steady state deformation and its approach in creep and dynamic tests. Acta Metall. 35, 1261–1271. doi:10.1016/0001-6160(87)90007-1.
Greer, J.R., Weinberger, C.R., Cai, W., 2008. Comparing the strength of f.c.c. and b.c.c. sub-micrometer pillars: compression experiments and dislocation dynamics simulations. Mater. Sci. Eng.: A 493, 21–25. doi:10.1016/j.msea.2007.08.093.
Groh, S., Marin, E.B., Horstemeyer, M.F., Zbib, H.M., 2009. Multiscale modeling of the plasticity in an aluminum single crystal. Int. J. Plast. 25, 1456–1473. doi:10.1016/j.ijplas.2008.11.003.
Gu, Y., Xiang, Y., Quek, S.S., Srolovitz, D.J., 2015. Three-dimensional formulation of dislocation climb. J. Mech. Phys. Solids 83, 319–337. doi:10.1016/j.jmps.2015.04.002.
Hahn, G., 1962. A model for yielding with special reference to the yield-point phenomena of iron and related bcc metals. Acta Metall. 10, 727–738. doi:10.1016/0001-6160(62)90041-X.
Hähner, P., Zaiser, M., 1999. Dislocation dynamics and work hardening of fractal dislocation cell structures. Mater. Sci. Eng.: A 272, 443–454. doi:10.1016/S0921-5093(99)00527-4.
Hall, E.O., 1970. Yield point phenomena in metals and alloys. Plenum Press, New York, 1 online resource (viii, 296.
Hansen, B.L., Beyerlein, I.J., Bronkhorst, C.A., Cerreta, E.K., Dennis-Koller, D., 2013. A dislocation-based multi-rate single crystal plasticity model. Int. J. Plast. 44, 129–146. doi:10.1016/j.ijplas.2012.12.006.
Hirth, J.P., 1961. On dislocation interactions in the fcc Lattice. J. Appl. Phys. 32, 700–706. doi:10.1063/1.1736074.
Hirth, J.P., Lothe, J., 1982. Theory of dislocations, 2nd ed. Krieger Pub. Co, Malabar FL, xii, 857.
Hochrainer, T., Sandfeld, S., Zaiser, M., Gumbsch, P., 2014. Continuum dislocation dynamics: towards a physical theory of crystal plasticity. J. Mech. Phys. Solids 63, 167–178. doi:10.1016/j.jmps.2013.09.012.
Hockett, J.E., Sherby, O.D., 1975. Large strain deformation of polycrystalline metals at low homologous temperatures. J. Mech. Phys. Solids 23, 87–98. doi:10.1016/0022-5096(75)90018-6.
Horstemeyer, M.F., Bammann, D.J., 2010. Historical review of internal state variable theory for inelasticity. Int. J. Plast. 26, 1310–1334. doi:10.1016/j.ijplas.2010.06.005.
Huang, M., Zhao, L., Tong, J., 2012. Discrete dislocation dynamics modelling of mechanical deformation of nickel-based single crystal superalloys. Int. J. Plast. 28, 141–158. doi:10.1016/j.ijplas.2011.07.003.
Huang, Y., Qu, S., Hwang, K.C., Li, M., Gao, H., 2004. A conventional theory of mechanism-based strain gradient plasticity. Int. J. Plast. 20, 753–782. doi:10.1016/j.ijplas.2003.08.002.
Hughes, D., Hansen, N., Bammann, D., 2003. Geometrically necessary boundaries, incidental dislocation boundaries and geometrically necessary dislocations. Scr. Mater. 48, 147–153. doi:10.1016/S1359-6462(02)00358-5.
Hughes, D.A., 1993. Microstructural evolution in a non-cell forming metal: Al·Mg. Acta Metall. Mater. 41, 1421–1430. doi:10.1016/0956-7151(93)90251-M.
Hughes, D.A., Hansen, N., 1993. Microstructural evolution in nickel during rolling from intermediate to large strains. MTA 24, 2022–2037. doi:10.1007/BF02666337.
Hughes, D.A., Kassner, M.E., Stout, M.G., Vetrano, J.S., 1998. Metal forming at the center of excellence for the synthesis and processing of advanced materials. JOM 50, 16–21. doi:10.1007/s11837-998-0122-z.
Hull, D., Bacon, D.J., 2011. Introduction to Dislocations. Butterworth-Heinemann, Amsterdam 1 online resource (x, 257.
Hunter, A., Preston, D.L., 2015. Analytic model of the remobilization of pinned glide dislocations from quasi-static to high strain rates. Int. J. Plast. 70, 1–29. doi:10.1016/j.ijplas.2015.01.008.
Jiang, J., Britton, T.B., Wilkinson, A.J., 2013. Measurement of geometrically necessary dislocation density with high resolution electron backscatter diffraction: effects of detector binning and step size. Ultramicroscopy 125, 1–9. doi:10.1016/j.ultramic.2012.11.003.
Johnson, G.R., Cook, W.H., 1983. A constitutive model and data for metals subjected to large strains, high strain rates and high temperatures. In: Proceedings of the 7th International Symposium on Ballistics, 21, pp. 541–547.
Johnston, W.G., Gilman, J.J., 1959. Dislocation velocities, dislocation densities, and plastic flow in lithium fluoride crystals. J. Appl. Phys. 30, 129–144. doi:10.1063/1.1735121.
Kassner, M.E., 2015. Fundamentals of creep in Materials. Butterworth-Heinemann, Amsterdam 1 online resource (1 recurs en línia).
Kassner, M.E., Geantil, P., Levine, L.E., 2013. Long range internal stresses in single-phase crystalline materials. Int. J. Plast. 45, 44–60. doi:10.1016/j.ijplas.2012.10.003.
Khan, A.S., Liang, R., 1999. Behaviors of three BCC metal over a wide range of strain rates and temperatures: experiments and modeling. Int. J. Plast. 15, 1089–1109. doi:10.1016/S0749-6419(99)00030-3.
Khan, A.S., Liu, H., 2012. Variable strain rate sensitivity in an aluminum alloy: response and constitutive modeling. Int. J. Plast. 36, 1–14. doi:10.1016/j.ijplas.2012.02.001.
Kibey, S., Liu, J.B., Johnson, D.D., Sehitoglu, H., 2007. Predicting twinning stress in fcc metals: linking twin-energy pathways to twin nucleation. Acta Mater. 55, 6843–6851. doi:10.1016/j.actamat.2007.08.042.
Kitayama, K., Tomé, C.N., Rauch, E.F., Gracio, J.J., Barlat, F., 2013. A crystallographic dislocation model for describing hardening of polycrystals during strain path changes. Application to low carbon steels. Int. J. Plast. 46, 54–69. doi:10.1016/j.ijplas.2012.09.004.
Knezevic, M., Beyerlein, I.J., Brown, D.W., Sisneros, T.A., Tomé, C.N., 2013. A polycrystal plasticity model for predicting mechanical response and texture evolution during strain-path changes: application to beryllium. Int. J. Plast. 49, 185–198. doi:10.1016/j.ijplas.2013.03.008.
Kocks, U.F., 1966. A statistical theory of flow stress and work-hardening. Philos. Mag. 13, 541–566. doi:10.1080/14786436608212647.
Kocks, U.F., 1970. The relation between polycrystal deformation and single-crystal deformation. Metall. Mater. Trans. 1, 1121–1143. doi:10.1007/BF02900224.
Kocks, U.F., 1976. Laws for work-hardening and low-temperature creep. J. Eng. Mater. Technol. 98, 76. doi:10.1115/1.3443340.
Kocks, U.F., Argon, A.S., Ashby, M.F., 1975. Thermodynamics and kinetics of slip. Prog. Mater Sci. 19.
Kocks, U.F., Mecking, H., 2003. Physics and phenomenology of strain hardening: the FCC case. Prog. Mater Sci. 48, 171–273. doi:10.1016/S0079-6425(02)00003-8.
Koehler, J.S., 1952. The nature of work-hardening. Phys. Rev. 86, 52–59. doi:10.1103/PhysRev.86.52.
Koyama, M., Sawaguchi, T., Tsuzaki, K., 2015. Deformation twinning behavior of twinning-induced plasticity steels with different carbon concentrations – Part 2: Proposal of dynamic-strain-aging-assisted deformation twinning. ISIJ Int. 55, 1754–1761. doi:10.2355/isijinternational.ISIJINT-2015-070.
Kubin, L., 2013. Dislocations, Mesoscale Simulations and Plastic Flow. Oxford University Press.
Kubin, L.P., Canova, G., Condat, M., Devincre, B., Pontikis, V., Bréchet, Y., 1992. Dislocation microstructures and plastic flow: a 3D simulation. SSP 23-24, 455–472 10.4028/www.scientific.net/SSP.23-24.455.
Kubin, L.P., Chihab, K., Estrin, Y., 1988. The rate dependence of the portevin-Le chatelier effect. Acta Metall. 36, 2707–2718. doi:10.1016/0001-6160(88)90117-4.
Kubin, L.P., Estrin, Y., 1990. Evolution of dislocation densities and the critical conditions for the Portevin-Le Châtelier effect. Acta Metall. Mater. 38, 697–708. doi:10.1016/0956-7151(90)90021-8.
Kubin, L.P., Fressengeas, C., Ananthakrishna, G., 2002. Chapter 57 Collective behaviour of dislocations in plasticity. In: Nabarro, F.R.N., Duesbery, M.S., Hirth, J.P. (Eds.). In: Dislocations in Solids, vol. 11. North-Holland Pub. Co, Amsterdam, New York, pp. 101–192. https://doi.org/10.1016/S1572-4859(02)80008-0.

Kuhlmann-Wilsdorf, D., Hansen, N., 1991. Geometrically necessary, incidental and subgrain boundaries. Scr. Metall. Mater. 25, 1557–1562. doi:10.1016/0956-716X(91)90451-6.
Kumar, A., Hauser, F., Dorn, J., 1968. Viscous drag on dislocations in aluminum at high strain rates. Acta Metall. 16, 1189–1197. doi:10.1016/0001-6160(68)90054-0.
Lee, S., Jeong, J., Kim, Y., Han, S.M., Kiener, D., Oh, S.H., 2016. FIB-induced dislocations in Al submicron pillars: annihilation by thermal annealing and effects on deformation behavior. Acta Mater. 110, 283–294. doi:10.1016/j.actamat.2016.03.017.
Li, D., Zbib, H., Sun, X., Khaleel, M., 2014. Predicting plastic flow and irradiation hardening of iron single crystal with mechanism-based continuum dislocation dynamics. Int. J. Plast. 52, 3–17. doi:10.1016/j.ijplas.2013.01.015.
Li, J.C.M., 1967. Dislocation dynamics in deformation and recovery. Can. J. Phys. 45, 493–509. doi:10.1139/p67-043.
Lim, H., Lee, M.G., Kim, J.H., Adams, B.L., Wagoner, R.H., 2011. Simulation of polycrystal deformation with grain and grain boundary effects. Int. J. Plast. 27, 1328–1354. doi:10.1016/j.ijplas.2011.03.001.
Lin, Y.C., Chen, X.-M., 2011. A critical review of experimental results and constitutive descriptions for metals and alloys in hot working. Mater. Des. 32, 1733–1759. doi:10.1016/j.matdes.2010.11.048.
Lloyd, J.T., Clayton, J.D., Becker, R., McDowell, D.L., 2014. Simulation of shock wave propagation in single crystal and polycrystalline aluminum. Int. J. Plast. 60, 118–144. doi:10.1016/j.ijplas.2014.04.012.
Lomer, W.M., 1951. A dislocation reaction in the face-centred cubic lattice. London Edinburgh Dublin Philosophical Magazine J. Sci. 42, 1327–1331. doi:10.1080/14786444108561389.
Luscher, D.J., Addessio, F.L., Cawkwell, M.J., Ramos, K.J., 2017. A dislocation density-based continuum model of the anisotropic shock response of single crystal α -cyclotrimethylene trinitramine. J. Mech. Phys. Solids 98, 63–86. doi:10.1016/j.jmps.2016.09.005.
Lyu, H., Ruimi, A., Zbib, H.M., 2015. A dislocation-based model for deformation and size effect in multi-phase steels. Int. J. Plast. 72, 44–59. doi:10.1016/j.ijplas.2015.05.005.
Ma, A., Roters, F., 2004. A constitutive model for fcc single crystals based on dislocation densities and its application to uniaxial compression of aluminium single crystals. Acta Mater. 52, 3603–3612. doi:10.1016/j.actamat.2004.04.012.
Ma, A., Roters, F., Raabe, D., 2006. A dislocation density based constitutive model for crystal plasticity FEM including geometrically necessary dislocations. Acta Mater. 54, 2169–2179. doi:10.1016/j.actamat.2006.01.005.
Madec, R., Devincre, B., Kubin, L., Hoc, T., Rodney, D., 2003. The role of collinear interaction in dislocation-induced hardening. Science (New York, N.Y.) 301, 1879–1882. doi:10.1126/science.1085477.
Mahajan, S., Chin, G.Y., 1973. Formation of deformation twins in f.c.c. crystals. Acta Metall. 21, 1353–1363. doi:10.1016/0001-6160(73)90085-0.
Mecking, H., Kocks, U.F., 1981. Kinetics of flow and strain-hardening. Acta Metall. 29, 1865–1875. doi:10.1016/0001-6160(81)90112-7.
Miller, R.E., Shilkrot, L., Curtin, W.A., 2004. A coupled atomistics and discrete dislocation plasticity simulation of nanoindentation into single crystal thin films. Acta Mater. 52, 271–284. doi:10.1016/j.actamat.2003.09.011.
Monavari, M., Sandfeld, S., Zaiser, M., 2016. Continuum representation of systems of dislocation lines: A general method for deriving closed-form evolution equations. J. Mech. Phys. Solids 95, 575–601. doi:10.1016/j.jmps.2016.05.009.
Monavari, M., Zaiser, M., 2018. Annihilation and sources in continuum dislocation dynamics. Mater. Theory 2, 761. doi:10.1186/s41313-018-0010-z.
Motz, C., Weygand, D., Senger, J., Gumbsch, P., 2008. Micro-bending tests: a comparison between three-dimensional discrete dislocation dynamics simulations and experiments. Acta Mater. 56, 1942–1955. doi:10.1016/j.actamat.2007.12.053.
Mughrabi, H., 1983. Dislocation wall and cell structures and long-range internal stresses in deformed metal crystals. Acta Metall. 31, 1367–1379. doi:10.1016/0001-6160(83)90007-X.
Mughrabi, H., 1987. A two-parameter description of heterogeneous dislocation distributions in deformed metal crystals. Mater. Sci. Eng. 85, 15–31. doi:10.1016/0025-5416(87)90463-0.
Mughrabi, H., 2006. Deformation-induced long-range internal stresses and lattice plane misorientations and the role of geometrically necessary dislocations. Philos. Mag. 86, 4037–4054. doi:10.1080/14786430500509054.
Mukherjee, M., Prahl, U., Bleck, W., 2010. Modelling of microstructure and flow stress evolution during hot forging. Steel Res. Int. 81, 1102–1116. doi:10.1002/srin.201000114.
Mulford, R.A., Kocks, U.F., 1979. New observations on the mechanisms of dynamic strain aging and of jerky flow. Acta Metall. 27, 1125–1134. doi:10.1016/0001-6160(79)90130-5.
Nabarro, F., 1952. Mathematical theory of stationary dislocations. Adv. Phys. 1, 269–394. doi:10.1080/00018735200101211.
Nabarro, F., 1997. Fifty-year study of the Peierls-Nabarro stress. Mater. Sci. Eng.: A 234-236, 67–76. doi:10.1016/S0921-5093(97)00184-6.
Nadgornyi, E., 1988. Dislocation dynamics and mechanical properties of crystals. Prog. Mater Sci. 31, 1–530. doi:10.1016/0079-6425(88)90005-9.
Nes, E., 1997. Modelling of work hardening and stress saturation in FCC metals. Prog. Mater Sci. 41, 129–193. doi:10.1016/S0079-6425(97)00032-7.
Ng, K.S., Ngan, A., 2008. Stochastic nature of plasticity of aluminum micro-pillars. Acta Mater. 56, 1712–1720. doi:10.1016/j.actamat.2007.12.016.
Nguyen, T., Luscher, D.J., Wilkerson, J.W., 2017a. A dislocation-based crystal plasticity framework for dynamic ductile failure of single crystals. J. Mech. Phys. Solids 108, 1–29. doi:10.1016/j.jmps.2017.07.020.
Nguyen, T.N., Siegmund, T., Tomar, V., Kruzic, J.J., 2017b. Interaction of rate- and size-effect using a dislocation density based strain gradient viscoplasticity model. J. Mech. Phys. Solids 109, 1–21. doi:10.1016/j.jmps.2017.07.022.
Nix, W.D., Gao, H., 1998. Indentation size effects in crystalline materials: a law for strain gradient plasticity. J. Mech. Phys. Solids 46, 411–425. doi:10.1016/S0022-5096(97)00086-0.
Nix, W.D., Gibeling, J.C., Hughes, D.A., 1985. Time-dependent deformation of metals. MTA 16, 2215–2226. doi:10.1007/BF02670420.
Nye, J., 1953. Some geometrical relations in dislocated crystals. Acta Metall. 1, 153–162. doi:10.1016/0001-6160(53)90054-6.
Oh, S.H., Legros, M., Kiener, D., Dehm, G., 2009. In situ observation of dislocation nucleation and escape in a submicrometre aluminium single crystal. Nat. Mater. 8, 95–100. doi:10.1038/nmat2370.
Oren, E., Yahel, E., Makov, G., 2017. Kinetics of dislocation cross-slip: a molecular dynamics study. Comput. Mater. Sci. 138, 246–254. doi:10.1016/j.commatsci.2017.06.039.
Orowan, E., 1934. Zur Kristallplastizitaet. Z. Physik 89, 605–613. doi:10.1007/BF01341478.
Papanikolaou, S., Cui, Y., Ghoniem, N., 2018. Avalanches and plastic flow in crystal plasticity: An overview. Model. Simul. Mater. Sci. Eng. 26, 13001. doi:10.1088/1361-651X/aa97ad.
Parthasarathy, T.A., Rao, S.I., Dimiduk, D.M., Uchic, M.D., Trinkle, D.R., 2007. Contribution to size effect of yield strength from the stochastics of dislocation source lengths in finite samples. Scr. Mater. 56, 313–316. doi:10.1016/j.scriptamat.2006.09.016.
Patra, A., McDowell, D.L., 2012. Crystal plasticity-based constitutive modelling of irradiated bcc structures. Philos. Mag. 92, 861–887. doi:10.1080/14786435.2011.634855.
Pauš, P., Kratochvíl, J., Beneš, M., 2013. A dislocation dynamics analysis of the critical cross-slip annihilation distance and the cyclic saturation stress in fcc single crystals at different temperatures. Acta Mater. 61, 7917–7923. doi:10.1016/j.actamat.2013.09.032.
Peierls, R., 1940. The size of a dislocation. Proc. Phys. Soc. 52, 34–37. doi:10.1088/0959-5309/52/1/305.
Perzyna, P.Chernyi, G.G. (Ed.), 1966. Fundamental problems in viscoplasticity. Advances In Applied Mechanics, vol. 9 243–377.
Pham, M.S., Holdsworth, S.R., Janssens, K., Mazza, E., 2013. Cyclic deformation response of AISI 316L at room temperature: mechanical behaviour, microstructural evolution, physically-based evolutionary constitutive modelling. Int. J. Plast. 47, 143–164. doi:10.1016/j.ijplas.2013.01.017.
Pham, M.-S., Iadicola, M., Creuziger, A., Hu, L., Rollett, A.D., 2015. Thermally-activated constitutive model including dislocation interactions, aging and recovery for strain path dependence of solid solution strengthened alloys: application to AA5754-O. Int. J. Plast. 75, 226–243. doi:10.1016/j.ijplas.2014.09.010.

Po, G., Mohamed, M.S., Crosby, T., Erel, C., El-Azab, A., Ghoniem, N., 2014. Recent Progress in discrete dislocation dynamics and its applications to micro plasticity. JOM 66, 2108–2120. doi:10.1007/s11837-014-1153-2.
Püschl, W., 2002. Models for dislocation cross-slip in close-packed crystal structures: a critical review. Prog. Mater Sci. 47, 415–461. doi:10.1016/S0079-6425(01)00003-2.
Qiu, X., Huang, Y., Nix, W.D., Hwang, K.C., Gao, H., 2001. Effect of intrinsic lattice resistance in strain gradient plasticity. Acta Mater. 49, 3949–3958. doi:10.1016/S1359-6454(01)00299-3.
Rivera-Díaz-del-Castillo, P., Huang, M., 2012. Dislocation annihilation in plastic deformation: I. Multiscale irreversible thermodynamics. Acta Mater. 60, 2606–2614. doi:10.1016/j.actamat.2012.01.027.
Rosakis, P., Rosakis, A.J., Ravichandran, G., Hodowany, J., 2000. A thermodynamic internal variable model for the partition of plastic work into heat and stored energy in metals. J. Mech. Phys. Solids 48, 581–607. doi:10.1016/S0022-5096(99)00048-4.
Roters, F., 2011. Advanced Material Models for the Crystal Plasticity Finite Element Method: Development of a general CPFEM framework Habilitation thesis.
Roters, F., Raabe, D., Gottstein, G., 2000. Work hardening in heterogeneous alloys—a microstructural approach based on three internal state variables. Acta Mater. 48, 4181–4189. doi:10.1016/S1359-6454(00)00289-5.
Rusinek, A., Klepaczko, J.R., 2001. Shear testing of a sheet steel at wide range of strain rates and a constitutive relation with strain-rate and temperature dependence of the flow stress. Int. J. Plast. 17, 87–115. doi:10.1016/S0749-6419(00)00020-6.
Rusinek, A., Rodríguez-Martínez, J.A., 2009. Thermo-viscoplastic constitutive relation for aluminium alloys, modeling of negative strain rate sensitivity and viscous drag effects. Mater. Des. 30, 4377–4390. doi:10.1016/j.matdes.2009.04.011.
Rusinek, A., Rodríguez-Martínez, J.A., Arias, A., 2010. A thermo-viscoplastic constitutive model for FCC metals with application to OFHC copper. Int. J. Mech. Sci. 52, 120–135. doi:10.1016/j.ijmecsci.2009.07.001.
Sandfeld, S., Thawinan, E., Wieners, C., 2015. A link between microstructure evolution and macroscopic response in elasto-plasticity: Formulation and numerical approximation of the higher-dimensional continuum dislocation dynamics theory. Int. J. Plast. 72, 1–20. doi:10.1016/j.ijplas.2015.05.001.
Sandström, R., Lagneborg, R., 1975. A model for hot working occurring by recrystallization. Acta Metall. 23, 387–398. doi:10.1016/0001-6160(75)90132-7.
Seeger, A., 1955. The generation of lattice defects by moving dislocations, and its application to the temperature dependence of the flow-stress of F.C.C. crystals. London Edinburgh Dublin Philos. Mag. J. Sci. 46, 1194–1217. doi:10.1080/14786441108520632.
Seeger, A., Diehl, J., Mader, S., Rebstock, H., 1957. Work-hardening and work-softening of face-centred cubic metal crystals. Philos. Mag. 2, 323–350. doi:10.1080/14786435708243823.
Sherby, O.D., Burke, P.M., 1968. Mechanical behavior of crystalline solids at elevated temperature. Prog. Mater Sci. 13, 323–390. doi:10.1016/0079-6425(68)90024-8.
Shiari, B., Miller, R.E., Curtin, W.A., 2005. Coupled atomistic/discrete dislocation simulations of nanoindentation at finite temperature. J. Eng. Mater. Technol. 127, 358. doi:10.1115/1.1924561.
Steenackers, G., Devriendt, C., Guillaume, P., 2007. On the use of transmissibility measurements for finite element model updating. J. Sound Vib. 303, 707–722. doi:10.1016/j.jsv.2007.01.030.
Steif, P.S., Clifton, R.J., 1979. On the kinetics of a Frank-Read source. Mater. Sci. Eng. 41, 251–258. doi:10.1016/0025-5416(79)90145-9.
Steinmetz, D.R., Jäpel, T., Wietbrock, B., Eisenlohr, P., Gutierrez-Urrutia, I., Saeed-Akbari, A., Hickel, T., Roters, F., Raabe, D., 2013. Revealing the strain-hardening behavior of twinning-induced plasticity steels: theory, simulations, experiments. Acta Mater. 61, 494–510. doi:10.1016/j.actamat.2012.09.064.
Stricker, M., Sudmanns, M., Schulz, K., Hochrainer, T., Weygand, D., 2018. Dislocation multiplication in stage II deformation of fcc multi-slip single crystals. J. Mech. Phys. Solids 119, 319–333. doi:10.1016/j.jmps.2018.07.003.
Stricker, M., Weygand, D., 2015. Dislocation multiplication mechanisms – Glissile junctions and their role on the plastic deformation at the microscale. Acta Mater. 99, 130–139. doi:10.1016/j.actamat.2015.07.073.
Sung, J.H., Kim, J.H., Wagoner, R.H., 2010. A plastic constitutive equation incorporating strain, strain-rate, and temperature. Int. J. Plast. 26, 1746–1771. doi:10.1016/j.ijplas.2010.02.005.
Tang, M., Marian, J., 2014. Temperature and high strain rate dependence of tensile deformation behavior in single-crystal iron from dislocation dynamics simulations. Acta Mater. 70, 123–129. doi:10.1016/j.actamat.2014.02.013.
Taylor, G.I., 1934. The mechanism of plastic deformation of crystals. Part I. Theoretical. Proc. R. Soc. A: Math. Phys. Eng. Sci. 145, 362–387. doi:10.1098/rspa.1934.0106.
Taylor, G.I., 1938. Plastic strain in metals. J. Inst. Metals 307–325.
Taylor, G.I., Quinney, H., 1934. The latent energy remaining in a metal after cold working. Proc. R. Soc. A: Math. Phys. Eng. Sci. 143, 307–326. doi:10.1098/rspa.1934.0004.
Thompson, N., 1953. Dislocation nodes in face-centred cubic lattices. Proc. Phys. Soc. B 66, 481–492. doi:10.1088/0370-1301/66/6/304.
van den Beukel, A., Kocks, U.F., 1982. The strain dependence of static and dynamic strain-aging. Acta Metall. 30, 1027–1034. doi:10.1016/0001-6160(82)90211-5.
van der Giessen, E., Needleman, A., 1995. Discrete dislocation plasticity: a simple planar model. Model. Simul. Mater. Sci. Eng. 3, 689–735. doi:10.1088/0965-0393/3/5/008.
Vegge, T., Jacobsen, K.W., 2002. Atomistic simulations of dislocation processes in copper. J. Phys.: Condens. Matter 14, 2929–2956. doi:10.1088/0953-8984/14/11/309.
Venables, J., 1964. The nucleation and propagation of deformation twins. J. Phys. Chem. Solids 25, 693–700. doi:10.1016/0022-3697(64)90178-7.
Viatkina, E.M., Brekelmans, W., Geers, M., 2007. Modelling the evolution of dislocation structures upon stress reversal. Int. J. Solids Struct. 44, 6030–6054. doi:10.1016/j.ijsolstr.2007.02.010.
Voyiadjis, G.Z., Abed, F.H., 2005. Microstructural based models for bcc and fcc metals with temperature and strain rate dependency. Mech. Mater. 37, 355–378. doi:10.1016/j.mechmat.2004.02.003.
Voyiadjis, G.Z., Al-Rub, R.K.A., 2005. Gradient plasticity theory with a variable length scale parameter. Int. J. Solids Struct. 42, 3998–4029. doi:10.1016/j.ijsolstr.2004.12.010.
Webster, G.A., 1966. A widely applicable dislocation model of creep. Philos. Mag. 14, 775–783. doi:10.1080/14786436608211971.
Weygand, D., 2014. Mechanics and dislocation structures at the micro-scale: insights on dislocation multiplication mechanisms from discrete dislocation dynamics simulations. MRS Proc. 1651, 188. doi:10.1557/opl.2014.362.
Wong, S.L., Madivala, M., Prahl, U., Roters, F., Raabe, D., 2016. A crystal plasticity model for twinning- and transformation-induced plasticity. Acta Mater. 118, 140–151. doi:10.1016/j.actamat.2016.07.032.
Yamakov, V., Wolf, D., Phillpot, S.R., Mukherjee, A.K., Gleiter, H., 2002. Dislocation processes in the deformation of nanocrystalline aluminium by molecular-dynamics simulation. Nat. Mater. 1, 45–48. doi:10.1038/nmat700.
Yang, H.K., Zhang, Z.J., Tian, Y.Z., Zhang, Z.F., 2017. Negative to positive transition of strain rate sensitivity in Fe-22Mn-0.6C-x(Al) twinning-induced plasticity steels. Mater. Sci. Eng.: A 690, 146–157. doi:10.1016/j.msea.2017.02.014.
Yuan, S., Huang, M., Zhu, Y., Li, Z., 2018. A dislocation climb/glide coupled crystal plasticity constitutive model and its finite element implementation. Mech. Mater. 118, 44–61. doi:10.1016/j.mechmat.2017.12.009.
Zaiser, M., 2013. Statistical aspects of microplasticity: experiments, discrete dislocation simulations and stochastic continuum models. J. Mech. Behav. Mater. 22. doi:10.1515/jmbm-2012-0006.
Zbib, H.M., La Diaz de Rubia, T., 2002. A multiscale model of plasticity. Int. J. Plast. 18, 1133–1163. doi:10.1016/S0749-6419(01)00044-4.
Zbib, H.M., Rhee, M., Hirth, J.P., 1998. On plastic deformation and the dynamics of 3D dislocations. Int. J. Mech. Sci. 40, 113–127. doi:10.1016/S0020-7403(97)00043-X.

Zecevic, M., Knezevic, M., 2015. A dislocation density based elasto-plastic self-consistent model for the prediction of cyclic deformation: application to AA6022-T4. Int. J. Plast. 72, 200–217. doi:10.1016/j.ijplas.2015.05.018.
Zehnder, A.T., 1991. A model for the heating due to plastic work. Mech. Res. Commun. 18, 23–28. doi:10.1016/0093-6413(91)90023-P.
Zhang, J.-l., Zaefferer, S., Raabe, D., 2015. A study on the geometry of dislocation patterns in the surrounding of nanoindents in a TWIP steel using electron channeling contrast imaging and discrete dislocation dynamics simulations. Mater. Sci. Eng.: A 636, 231–242. doi:10.1016/j.msea.2015.03.078.
Zhou, C., Biner, S.B., LeSar, R., 2010. Discrete dislocation dynamics simulations of plasticity at small scales. Acta Mater. 58, 1565–1577. doi:10.1016/j.actamat.2009.11.001.
Zhu, T., 2004. Predictive modeling of nanoindentation-induced homogeneous dislocation nucleation in copper. J. Mech. Phys. Solids 52, 691–724. doi:10.1016/j.jmps.2003.07.006.

3.2. Paper II

S.A.H. Motaman, K. Schacht, C. Haase, U. Prahl: Thermo-micro-mechanical simulation of metal forming processes.
International Journal of Solids and Structures 178-179 (2019): 59–80, ISSN: 0020-7683.
doi: 10.1016/j.ijsolstr.2019.05.028.

International Journal of Solids and Structures 178–179 (2019) 59–80

Contents lists available at ScienceDirect

International Journal of Solids and Structures

journal homepage: www.elsevier.com/locate/ijsolstr

Thermo-micro-mechanical simulation of metal forming processes

S. Amir H Motaman[a,*], Konstantin Schacht[a], Christian Haase[a], Ulrich Prahl[a,b]

[a] Steel Institute, RWTH Aachen University, Intzestr. 1, D-52072 Aachen, Germany
[b] Institute of Metal Forming, TU Bergakademie Freiberg, Bernhard-von-Cotta-Str. 4, D-09599 Freiberg, Germany

ARTICLE INFO

Article history:
Received 5 March 2019
Revised 20 May 2019
Accepted 30 May 2019
Available online 31 May 2019

Keywords:
Thermo-micro-mechanical simulation
Finite element method
Finite strain
Polycrystal viscoplasticity
Continuum dislocation dynamics
Dislocation density
Metal forming simulation
Warm forging

ABSTRACT

The newly proposed microstructural constitutive model for polycrystal viscoplasticity in cold and warm regimes (Motaman and Prahl, 2019), is implemented as a microstructural solver via user-defined material subroutine in a finite element (FE) software. Addition of the microstructural solver to the built-in thermal and mechanical solvers of a standard FE package enabled coupled thermo-micro-mechanical or thermal-microstructural-mechanical (TMM) simulation of cold and warm metal forming processes. The microstructural solver, which incrementally calculates the evolution of microstructural state variables (MSVs) and their correlation to the thermal and mechanical variables, is implemented based on the constitutive theory of isotropic hypoelasto-viscoplastic (HEVP) finite (large) strain/deformation. The numerical integration and self-consistent algorithmic procedure of the FE implementation are explained in detail. Then, the viability of this approach is shown for (TMM-) FE simulation of an industrial multistep warm forging.

1. Introduction

Metal forming processes can be considered as large hypoelasto-viscoplastic deformation under complex varying thermo-mechanical boundary conditions. Moreover, viscoplastic flow of polycrystalline metallic materials is one of the long-standing challenges in classical physics due to its tremendous complexity; and for its accurate continuum description, complex microstructural constitutive modeling is essential.

Microstructural/physics-based material modeling offers the opportunity to enhance the understanding of complex industrial metal forming processes and thus provides the basis for their improvement and optimization. In our previous work (Motaman and Prahl, 2019), the significance of microstructural constitutive models for polycrystal viscoplasticity was pointed out. Application of microstructural state variables (MSVs) including different types of dislocation density was suggested rather than non-measurable virtual internal state variables (ISVs) such as accumulated plastic strain, which is not a suitable measure, particularly in complex thermo-mechanical loading condition (varying temperature, strain rate) where history effects are more pronounced (Follansbee and Kocks, 1988; Horstemeyer and Bammann, 2010). However, almost every metal forming simulation performed in industry for design and optimization purposes, apply empirical constitutive models that are based on the accumulated plastic strain as their main ISV. In the last two decades, extensive research in the field of numerical simulation of industrial bulk metal forming has been aimed towards investigation of (thermo-) mechanical aspects of the process such as tools shape and wear, forming force, preform shape, material flow pattern and die filling, etc. (Choi et al., 2012; Guan et al., 2015; Hartley and Pillinger, 2006; Kim et al., 2000; Lee et al., 2013; Ou et al., 2012; Sedighi and Tokmechi, 2008; Vazquez and Altan, 2000; Xianghong et al., 2006; Zhao et al., 2002).

Microstructure of the deforming material and its mechanical properties evolve extensively during metal forming processes. Evolution of microstructure and mechanical properties of the deforming metal directly affects its deformation behavior and consequently the forming process itself as well as in-service performance of the final product. Therefore, in addition to thermo-mechanical simulation of forming processes (simulation of evolution of continuous thermo-mechanical field variables), computation of microstructure and properties evolution of the deforming part by means microstructural state variables through a fully coupled thermo-micro-mechanical (TMM) simulation is of paramount importance. Since process, material, microstructure and properties are highly entangled, resorting to cost-effective simultaneous intercorrelated simulation of process, microstructure and properties facilitates and ensures their efficient and robust design. Currently the literature lacks TMM simulation of complex industrial metal forming processes. Nonetheless, a few instances can be found for TMM

* Corresponding author.
E-mail address: seyedamirhossein.motaman@iehk.rwth-aachen.de (S.A.H. Motaman).

https://doi.org/10.1016/j.ijsolstr.2019.05.028
0020-7683/

Nomenclature

Symbol	*Description*
b	Burgers length (magnitude of Burgers vector) [m]
$\mathbf{B}$	Left Cauchy-Green deformation tensor [-]
$\mathcal{B}$	Continuum body [-]
c	Constitutive parameter associated with probability amplitude of dislocation processes [-]
$\mathbf{C}$	Right Cauchy-Green deformation tensor [-]
$\mathbb{C}$	Fourth-order stiffness operator/tensor [Pa]
$\mathbf{D}$	Rate of deformation tensor [s^{-1}]
E	Elastic/Young's modulus [Pa]
$\mathbf{F}$	Deformation gradient tensor [-]
G	Shear modulus [Pa]
H	Tangent modulus [Pa]
$\mathbf{I}$	Unit/identity (second-order) tensor [-]
$\mathbb{I}$	Fourth-order unit tensor [-]
J	Jacobian of the deformation map [-]
K	Bulk modulus [Pa]
$\mathbf{L}$	Velocity gradient tensor [s^{-1}]
m	Strain rate sensitivity parameter [-]
M	Taylor factor [-]
$\mathbf{N}$	Yield surface normal tensor [-]
$\mathbf{O}$	Zero (second-order) tensor [-]
q	Volumetric heat generation [$J.m^{-3}$]
r	Temperature sensitivity coefficient [-]
R	Residual function in Newton-Raphson scheme
$\mathbf{R}$	Polar (rigid-body) rotation tensor [-]
s	Temperature sensitivity exponent [-]
$\boldsymbol{s}$	Stochastic/nonlocal microstructural state set (a set containing all MSVs)
t	Time [s]
T	Temperature [K]
$\boldsymbol{u}$	Displacement vector [m]
$\mathbf{U}$	Right stretch tensor [-]
$\boldsymbol{v}$	Velocity vector [$m.s^{-1}$]
$\mathbf{V}$	Left stretch tensor [-]
w	Volumetric work [$J.m^{-3}$]
$\mathbf{W}$	Spin tensor [s^{-1}]
$\boldsymbol{x}$	Position vector (spatial coordinate) [m]
α	Dislocation interaction strength/coefficient [-]
β	Dissipation factor, efficiency of plastic dissipation, or Taylor-Quinney coefficient [-]
ε	Mean/nonlocal (normal) strain [-]
$\boldsymbol{\varepsilon}$	Logarithmic/true strain tensor [-]
θ	Plastic/strain hardening [Pa]
ϕ	Viscous/strain-rate hardening [Pa.s]
φ	Yield function
χ	Tolerance [-]
ψ	Flow potential [Pa]
κ	Material constant associated with dissipation factor [-]
$\dot{\lambda}$	Consistency parameter or plastic multiplier [s^{-1}]
$\boldsymbol{\Lambda}$	Rotation tensor [-]
ν	Poisson's ratio [-]
ρ	Dislocation density [m^{-2}]
ϱ	Mass density [$kg.m^{-3}$]
σ	Mean/nonlocal (normal) stress [Pa]
$\boldsymbol{\sigma}$	Cauchy stress tensor [Pa]
$\boldsymbol{\omega}$	Spatial skew-symmetric tensor associated with the rotation tensor [s^{-1}]

Index	*Description*
ac	Accumulation
an	Annihilation
corr	Corrected
d	Deviatoric/isochoric
eff	Effective
gn	Generation
h	Hydrostatic
i	Immobile
{k}	Newton-Raphson iteration index, previous Newton-Raphson iteration step
{k+1}	Current Newton-Raphson iteration step
m	Mobile, melt
min	Minimum
(n)	Time increment index, previous time increment, beginning of the current time increment
(n+1)	Current time increment/step, end of the current time increment
nc	Nucleation
c	Cell
p	Plastic
rm	Remobilization
tr	Trapping (locking and pinning)
trial	Trial step
v	Viscous (subscript), volumetric (superscript)
w	Wall
x	Cell, wall, or total ($x = c, w, t$)
y	Mobile, immobile, or total ($y = m, i, t$), yield/flow
z	Dislocation process (z = gn, an, ac, tr, nc, rm)
0	Reference, initial/undeformed state
∇	Objective/material rate of a tensor
$\hat{}$	Normalized/dimensionless ($\hat{x} = \frac{x}{x_0}$)
$\vee$	Function
$\sim$	Statistical mean/average
–	Equivalent
—	Corotational representation of a tensor (rotated to the corotational basis)

simulation of laboratory scale metal forming processes using semi-physical models (Álvarez Hostos et al., 2018; Bok et al., 2014).

The microstructural constitutive models based on continuum microstructure dynamics (CMD), which encompass continuum dislocation dynamics (CDD) are formulated at macro level, so that the nonlocal MSVs at each macroscale material point in a continuum body are calculated for a (virtual) representative material volume (RMV) around the point based on the evolution/kinetics equations that have physical background, as shown in Fig. 1. The set $\boldsymbol{S}$ containing all the MSVs is known as the stochastic/nonlocal microstructural state (SMS).

The main objective of the present paper is to show how the microstructural constitutive models based on CDD (as a subset of CMD) can be practically invoked in actual industrial metal forming simulations. The cost of thermo-micro-mechanical (TMM) simulations performed using the applied microstructural constitutive model is in the same range that is offered by common empirical constitutive models. However, since the microstructural models account for the main microstructural processes influencing the material response under viscoplastic deformation, they have a wide range of usability and validity, and can be used in a broad spectrum of deformation parameters (strain rate and temperature). In industrial metal forming processes, polycrystalline materials usually undergo a variety of loading types and parameters; thus, history-dependent microstructural constitutive models are much more suitable and robust for comprehensive simulations of complex industrial metal forming processes. Hence, implementation of the microstructural solver as a user-defined material subroutine in

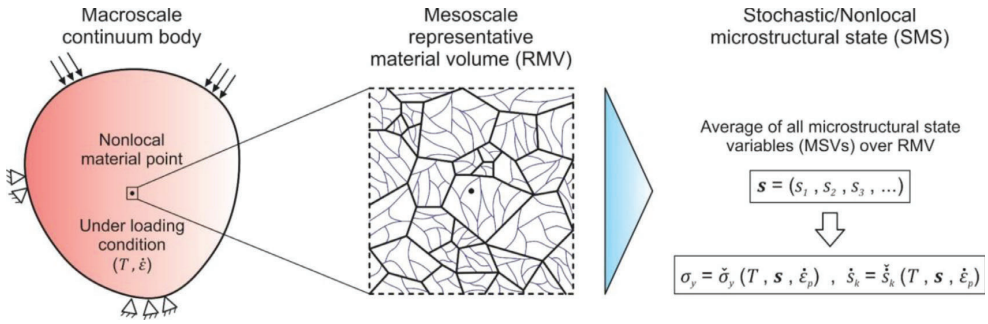

Fig. 1. Schematic relation among macroscale continuum body under thermo-mechanical loading, mesoscale representative material volume, and nonlocal microstructural state (Motaman and Prahl, 2019).

a commercial FE software package and coupling it with the FE software's built-in mechanical and thermal solvers enables performing realistic TMM simulations of the considered metal forming process chain in order to optimize the process parameters.

Industrial metal forming processes with respect to temperature are categorized in the following regimes/domains:

- Cold regime: Cold metal forming processes are conducted in the temperature range starting from room temperature to slightly above it; the maximum temperature in the cold regime is normally characterized by temperatures above which diffusion controlled dislocation mechanisms such as dislocation climb and pinning become dominant (approximately $T < 0.3T_m$, where T is the absolute temperature; and T_m is the melting absolute temperature) (Galindo-Nava and Rae, 2016).
- Warm regime: Warm viscoplastic flow of crystalline materials occurs above the cold but below the hot temperature regime (approximately $0.3T_m < T < 0.5T_m$) (Berisha et al., 2010; Doherty et al., 1997; Sherby and Burke, 1968); and
- Hot regime: Hot metal forming processes are carried out above the warm temperature regime. They are characterized by at least one of the hot/extreme microstructural processes such as recrystallization, phase transformation, notable precipitate processes, etc. (roughly $0.5T_m < T < T_m$).

Strain rate has different regimes as well, however, independent from the material (Field et al. (2004)):

- creep or static: $\dot{\varepsilon} < 10^{-4}$ s^{-1} (where $\dot{\varepsilon}$ is the strain rate);
- quasi-static: 10^{-4} s$^{-1} \leq \dot{\varepsilon} < 10^{-2}$ s^{-1};
- intermediate-rates: 10^{-2} s$^{-1} \leq \dot{\varepsilon} \leq 10$ s^{-1};
- dynamic: 10 s$^{-1} < \dot{\varepsilon} \leq 10^3$ s^{-1}; and
- shock/highly-dynamic: $\dot{\varepsilon} > 10^3$ s^{-1}.

The microstructural constitutive model proposed by Motaman and Prahl (2019), has been validated for cold and warm regimes. Moreover, its validity has been verified for the intermediate-rates regime as well, at which most of the industrial metal forming processes are being carried out. In this paper, that constitutive model has been utilized for FE simulation of an actual industrial warm forging process of a bevel gear for automotive applications, made of the ferritic-pearlitic case-hardenable steel 20MnCr5. This particular steel grade, which is currently used extensively in industrial bulk metal forming processes in different temperature regimes, has been investigated in hot regime by the recent works of Puchi-Cabrera et al. (2013, 2014) as well as in cold and warm regimes by Brnic et al. (2014) and Motaman and Prahl (2019).

The dynamic evolution of sophisticated dislocation substructure (cells and walls), and their associated densities is responsible for complex behavior of engineering metallic alloys such as steels during the viscoplastic deformation under thermo-mechanical loading in cold and warm regimes. The (immobile) dislocation walls (cell/subgrain boundaries) are mostly composed of unipolar dislocations with a non-zero net Burgers vector (geometrically necessary dislocations) accommodating lattice curvature that arises due to non-uniform plastic deformation in polycrystal constituents. On the other hand, the (immobile) cell dislocations that accumulate at and consequently form the random metastable subcell boundaries (dislocation boundaries inside subgrains) are particularly tangles/bundles of dislocations in dipolar configuration (statistically stored dislocations) which do not give rise to a substantial lattice rotation, i.e., their net Burgers vector is practically zero (Arsenlis and Parks, 1999; Ashby, 1970; Gao and Huang, 2003; Hughes et al., 2003). The immobile cell and wall dislocations, are respectively sources of short and long range plastic/back stress (Kassner et al., 2013; Mughrabi, 2006). Therefore, the plastic/strain hardening behavior of the material is only affected by the evolution of immobile cell and wall dislocations, that is highly influenced by thermal and rate-dependent diffusion-controlled dislocation processes, quite differently in cold, intermediate and warm regimes. The nucleation process of wall immobile dislocations is assisted by diffusion-controlled dislocation pinning mechanism (responsible for dynamic strain aging), while annihilation and remobilization processes of immobile cell dislocations are mainly affected by the diffusion-controlled dislocation climb mechanism (responsible for creep) (Motaman and Prahl, 2019). Hence, for accurately capturing the complex material behavior at different strain rates and temperatures (in cold and warm regimes), it is imperative to use a constitutive model that employs the state variables that their evolution is a functions of temperature and strain rate (as opposed to the empirical variable, accumulated plastic strain), taking the aforementioned thermal dislocation processes into account. This brings us to application of different dislocation densities as (microstructural) state variables, which their overall evolution is described by superposition of the underlying dislocation processes such as thermally activated dislocation pinning and climb.

Generally, bulk forming of textureless (randomly oriented equiaxed grains) undeformed/as-built/annealed polycrystalline metallic materials such as most of the forging and extrusion steel grades can be considered isotropic. Therefore, since deformation of metallic crystalline materials is categorized under isotropic hypoelasto-viscoplastic (HEVP) finite strain/deformation, in this paper first the continuum finite strain theory of isotropic HEVP is reformulated in the format of rate equations (without using accumulated strain scalars and tensors). The constitutive equations in corotational configuration are then numerically integrated using various schemes. The described algorithmic procedure is implemented as microstructural solver using user-defined material subroutines in

ABAQUS, that are naturally coupled to the software's built-in mechanical and thermal modules. Finally, the developed method is applied to TMM-FE simulation a bulk metal forming process: industrial multistep warm forging of a bevel gear shaft for automotive applications.

2. Continuum finite strain: isotropic hypoelasto-viscoplasticity (HEVP)

2.1. Basic kinematics

Consider $\mathcal{B}$ define the current configuration of a continuum body at time t, and $\mathcal{B}_0$ the reference, initial or undeformed configuration at the initial time $t=t_0$, where t is time. Let $\boldsymbol{x}_0 \in \mathcal{B}_0$ be the initial position of particle P in the reference configuration $\mathcal{B}_0$, and $\boldsymbol{x} \in \mathcal{B}$ the position of P in the current configuration $\mathcal{B}$. The motion and deformation of the body is defined by a smooth time-dependent mapping $\overset{\vee}{\mathrm{x}}_t : \mathcal{B}_0 \to \mathcal{B}$, so that $\boldsymbol{x} = \overset{\vee}{\boldsymbol{x}}(\boldsymbol{x}_0, t)$ Accordingly, the deformation gradient tensor ($\mathbf{F}$) is defined as:

$$\mathbf{F} \equiv \nabla_0 \boldsymbol{x} = \frac{\partial \boldsymbol{x}}{\partial \boldsymbol{x}_0} \;\Rightarrow\; \mathrm{d}\boldsymbol{x} = \mathbf{F}\,\mathrm{d}\boldsymbol{x}_0; \quad \mathrm{d}\boldsymbol{x}_0 \in \mathcal{B}_0; \quad \mathrm{d}\boldsymbol{x} \in \mathcal{B}; \tag{1}$$

where $\nabla_0 = \frac{\partial}{\partial \boldsymbol{x}_0}$ is the material gradient operator. Furthermore, the velocity gradient tensor ($\mathbf{L}$) is the spatial derivative of velocity vector, which is given by:

$$\mathbf{L} \equiv \nabla \boldsymbol{v} = \frac{\partial \boldsymbol{v}}{\partial \boldsymbol{x}} = \dot{\mathbf{F}}\mathbf{F}^{-1}; \quad \boldsymbol{v} \equiv \frac{\partial \boldsymbol{u}}{\partial t} = \frac{\partial \boldsymbol{x}}{\partial t}; \quad \boldsymbol{u} \equiv \boldsymbol{x} - \boldsymbol{x}_0; \tag{2}$$

where $\nabla \equiv \frac{\partial}{\partial \boldsymbol{x}}$ is the spatial gradient operator; $\boldsymbol{v}$ is the velocity vector; and $\boldsymbol{u}$ is the displacement vector. The velocity gradient is decomposed to its symmetric and skew-symmetric parts, that are respectively known as rate of deformation tensor ($\mathbf{D}$) and spin tensor ($\mathbf{W}$):

$$\mathbf{L} = \mathbf{D} + \mathbf{W}; \quad \mathbf{D} \equiv \overset{\vee}{\mathrm{sym}}(\mathbf{L}) = \frac{1}{2}\left(\mathbf{L} + \mathbf{L}^{\mathrm{T}}\right);$$
$$\mathbf{W} \equiv \overset{\vee}{\mathrm{skw}}(\mathbf{L}) = \frac{1}{2}\left(\mathbf{L} - \mathbf{L}^{\mathrm{T}}\right). \tag{3}$$

2.2. Polar decomposition

The polar decomposition theorem states that any non-singular, second-order tensor can be decomposed uniquely into the product of an orthogonal (rotation) tensor, and a symmetric (stretch) tensor. Since the deformation gradient tensor is a non-singular second-order tensor, the application of polar decomposition theorem to $\mathbf{F}$ implies:

$$\mathbf{F} = \mathbf{RU} = \mathbf{VR}; \quad \mathbf{R}^{-1} = \mathbf{R}^{\mathrm{T}}; \quad \mathbf{U} = \mathbf{U}^{\mathrm{T}}; \quad \mathbf{V} = \mathbf{V}^{\mathrm{T}}; \tag{4}$$

where $\mathbf{R}$ is the orthogonal polar (rigid-body) rotation tensor; and $\mathbf{U}$ and $\mathbf{V}$ are the right and left stretch tensors, respectively. Hence,

$$\mathbf{U}^2 = \mathbf{C} \equiv \mathbf{F}^{\mathrm{T}}\mathbf{F}; \quad \mathbf{V}^2 = \mathbf{B} \equiv \mathbf{F}\mathbf{F}^{\mathrm{T}}; \tag{5}$$

where $\mathbf{B}$ and $\mathbf{C}$ are left and right Cauchy–Green deformation tensors, respectively.

2.3. Elasto-plastic decomposition

The multiplicative elasto-plastic decomposition/split of deformation gradient tensor reads (Kröner, 1959; Lee, 1969; Lee and Liu, 1967; Reina et al., 2018):

$$\mathbf{F} = \mathbf{F}_e\mathbf{F}_p; \quad \overset{\vee}{\det}(\mathbf{F}_p) = 1; \quad J \equiv \overset{\vee}{\det}(\mathbf{F}) = \overset{\vee}{\det}(\mathbf{F}_e) > 0; \tag{6}$$

where $\mathbf{F}_e$ and $\mathbf{F}_p$ are elastic and plastic deformation gradients, respectively. Combining Eqs. (2) and (6) leads to:

$$\mathbf{L} = \mathbf{L}_e + \mathbf{F}_e\mathbf{L}_p\mathbf{F}_e^{-1}; \quad \mathbf{L}_e \equiv \dot{\mathbf{F}}_e\mathbf{F}_e^{-1}; \quad \mathbf{L}_p \equiv \dot{\mathbf{F}}_p\mathbf{F}_p^{-1}; \tag{7}$$

where $\mathbf{L}_e$ and $\mathbf{L}_p$ are elastic and plastic velocity gradients, respectively, that can be additively decomposed to their symmetric and skew-symmetric parts:

$$\mathbf{L}_e = \mathbf{D}_e + \mathbf{W}_e; \quad \mathbf{D}_e \equiv \overset{\vee}{\mathrm{sym}}(\mathbf{L}_e); \quad \mathbf{W}_e \equiv \overset{\vee}{\mathrm{skw}}(\mathbf{L}_e); \tag{8}$$

$$\mathbf{L}_p = \mathbf{D}_p + \mathbf{W}_p; \quad \mathbf{D}_p \equiv \overset{\vee}{\mathrm{sym}}(\mathbf{L}_p); \quad \mathbf{W}_p \equiv \overset{\vee}{\mathrm{skw}}(\mathbf{L}_p); \tag{9}$$

where $\mathbf{D}_e$ and $\mathbf{D}_p$ are the rates of elastic and plastic deformation gradient tensors, respectively; and $\mathbf{W}_e$ and $\mathbf{W}_p$ are elastic and plastic spin tensors, respectively. Commonly, the deformation of metallic materials is considered hypoelasto-viscoplastic. Thus, generally, it can be assumed that elastic strains (rates) are very small compared to unity and plastic strains (and rates). This restriction results in the following approximation (Nemat-Nasser, 1979):

$$\mathbf{F}_e \approx \mathbf{V}_e \approx \mathbf{U}_e \approx \mathbf{I}; \tag{10}$$

where $\mathbf{I}$ is the second-order unit/identity tensor. From this, Eq. (7) turns to (Green and Naghdi, 1965):

$$\mathbf{L} \approx \mathbf{L}_e + \mathbf{L}_p. \tag{11}$$

Therefore, considering Eqs. (3), (7), (8), (9), (10) and (11) (Dunne, 2011; Khan and Huang, 1995):

$$\mathbf{D} = \mathbf{D}_e + \mathbf{D}_p; \quad \mathbf{W} = \mathbf{W}_e + \mathbf{W}_p. \tag{12}$$

In this context, the strain rate measure is the power (work) conjugate of Cauchy stress tensor, and thus is the rate of deformation gradient tensor. Consequently,

$$\dot{\boldsymbol{\varepsilon}} = \dot{\boldsymbol{\varepsilon}}_e + \dot{\boldsymbol{\varepsilon}}_p; \quad \dot{\boldsymbol{\varepsilon}} \equiv \mathbf{D}; \quad \dot{\boldsymbol{\varepsilon}}_e \equiv \mathbf{D}_e; \quad \dot{\boldsymbol{\varepsilon}}_p \equiv \mathbf{D}_p; \tag{13}$$

where $\dot{\boldsymbol{\varepsilon}}$, $\dot{\boldsymbol{\varepsilon}}_e$, $\dot{\boldsymbol{\varepsilon}}_p$ are respectively total, elastic and plastic (logarithmic/true) strain rate tensors.

2.4. Corotational formulation

Physically motivated material objectivity/frame-indifference principle demands independence of material properties from the respective frame of reference or observer (Truesdell and Noll, 1965). Constitutive equations of HEVP are formulated in a rotation-neutralized configuration with the aid of local coordinate system/basis that rotates with the material. In this framework, the rotation of the neighborhood of a material point is characterized by orthogonal rotation tensor $\boldsymbol{\Lambda}$, which is subjected to the following evolutionary equation and initial condition (de-Souza Neto et al., 2008; Simo and Hughes, 1998):

$$\dot{\boldsymbol{\Lambda}} = \boldsymbol{\omega}\boldsymbol{\Lambda}; \quad \boldsymbol{\Lambda}_0 = \mathbf{I}; \quad \boldsymbol{\Lambda}^{-1} = \boldsymbol{\Lambda}^{\mathrm{T}}; \quad \boldsymbol{\omega} = -\boldsymbol{\omega}^{\mathrm{T}}; \tag{14}$$

where $\boldsymbol{\Lambda}_0$ is initial (at time $t=0$) $\boldsymbol{\Lambda}$; and $\boldsymbol{\omega}$ is a spatial skew-symmetric (second-order) tensor associated with the rotation tensor. Hence,

$$\boldsymbol{\omega} = \dot{\boldsymbol{\Lambda}}\boldsymbol{\Lambda}^{\mathrm{T}}. \tag{15}$$

Therefore, the (symmetric) Cauchy stress tensor ($\boldsymbol{\sigma} = \boldsymbol{\sigma}^{\mathrm{T}}$) is rotated to the rotation-neutralized configuration by multiplying it from the left and right with $\boldsymbol{\Lambda}^{\mathrm{T}}$ and $\boldsymbol{\Lambda}$, respectively:

$$\underline{\boldsymbol{\sigma}} = \boldsymbol{\Lambda}^{\mathrm{T}}\boldsymbol{\sigma}\boldsymbol{\Lambda} \;\Rightarrow\; \boldsymbol{\sigma} = \boldsymbol{\Lambda}\underline{\boldsymbol{\sigma}}\boldsymbol{\Lambda}^{\mathrm{T}}; \tag{16}$$

where _ denotes corotational representation of a tensor (rotated to the corotational basis). Moreover, the (symmetric) rate of deformation tensor in the corotational configuration reads:

$$\underline{\mathbf{D}} = \boldsymbol{\Lambda}^{\mathrm{T}}\mathbf{D}\boldsymbol{\Lambda} \;\Rightarrow\; \mathbf{D} = \boldsymbol{\Lambda}\underline{\mathbf{D}}\boldsymbol{\Lambda}^{\mathrm{T}}. \tag{17}$$

Given Eq. (14), time differentiation of the rotated Cauchy stress tensor (Eq. (16)) renders:

$$\dot{\underline{\boldsymbol{\sigma}}} = \boldsymbol{\Lambda}^{\mathrm{T}}\overset{\nabla}{\boldsymbol{\sigma}}\boldsymbol{\Lambda}; \quad \overset{\nabla}{\boldsymbol{\sigma}} = \boldsymbol{\Lambda}\dot{\underline{\boldsymbol{\sigma}}}\boldsymbol{\Lambda}^{\mathrm{T}} = \dot{\boldsymbol{\sigma}} + \boldsymbol{\sigma}\boldsymbol{\omega} - \boldsymbol{\omega}\boldsymbol{\sigma}; \tag{18}$$

where $\overset{\nabla}{\boldsymbol{\sigma}}$ is referred to as objective/frame-invariant/material rate of Cauchy stress tensor. In HEVP finite strain, depending on the FE formulation, commonly two members of the family of objective stress rates are considered (Doghri, 2000; Johnson and Bammann, 1984; Mourad et al., 2014):

- Green-Naghdi rate, corresponding to $\boldsymbol{\Lambda}=\mathbf{R}$ Green and Naghdi, 1971): the rotation is the same as orthogonal polar (rigid-body) rotation tensor $\mathbf{R}$, which can be calculated by tensor Eqs. (4), and (5), using the spectral decomposition (eigen-projection) method.
- Jaumann rate, corresponding to $\boldsymbol{\omega}=\mathbf{W}$: in this case, often the widely used Hughes–Winget approximation (Hughes and Winget, 1980) based on the midpoint rule is applied for calculation of the rotation tensor. The Hughes–Winget formula is valid if the increment of spin tensor ($\Delta t\,\mathbf{W}$) is sufficiently small (adequately small incremental rotations).

For the details of numerical update algorithms of incremental finite rotations associated with the Green–Naghdi and Jaumann rates, which are usually based on midpoint method (at the midpoint configuration), readers are encouraged to refer to Simo and Hughes (1998), de-Souza Neto et al. (2008), and/or Belytschko et al. (2014).

2.5. Constitutive relation of isotropic HEVP

In HEVP with plastic incompressibility, volume change during deformation is fully elastic and negligible. Therefore, according to the isotropic three-dimensional Hook's law and the material objectivity principle:

$$\boldsymbol{\sigma}^{\nabla}=\mathbb{C}_e:\dot{\boldsymbol{\varepsilon}}_e=\mathbb{C}_e:\left(\dot{\boldsymbol{\varepsilon}}-\dot{\boldsymbol{\varepsilon}}_p\right); \tag{19}$$

where $\mathbb{C}_e$ is the fourth-order (isotropic) elastic stiffness tensor, which is calculated according to:

$$\mathbb{C}_e=2G\mathbb{I}^d+K\mathbf{I}\otimes\mathbf{I}=2G\mathbb{I}+\left(K-\frac{2}{3}G\right)\mathbf{I}\otimes\mathbf{I};$$
$$G=\frac{1}{2(1+\upsilon)}E;\quad K=\frac{1}{3(1-2\upsilon)}E=\frac{2(1+\upsilon)}{3(1-2\upsilon)}G;$$
$$\mathbb{I}^d\equiv\mathbb{I}-\mathbb{I}^v;\quad \mathbb{I}^v\equiv\frac{1}{3}\mathbf{I}\otimes\mathbf{I}; \tag{20}$$

where E, G, K and υ are respectively elastic, shear and bulk moduli and poisson's ratio; and $\mathbb{I}$, $\mathbb{I}^d$ and $\mathbb{I}^v$ being the unit and unit deviatoric and unit volumetric fourth-order tensors, respectively.

2.6. Deviatoric-volumetric decomposition

The strain rate tensor can be additively decomposed to deviatoric/isochoric and volumetric parts:

$$\dot{\boldsymbol{\varepsilon}}=\dot{\boldsymbol{\varepsilon}}^v+\dot{\boldsymbol{\varepsilon}}^d;\quad \dot{\boldsymbol{\varepsilon}}^v\equiv\mathbb{I}^v:\dot{\boldsymbol{\varepsilon}}=\frac{1}{3}\dot{\varepsilon}^v\mathbf{I};\quad \dot{\varepsilon}^v=\mathbf{I}:\dot{\boldsymbol{\varepsilon}};$$
$$\dot{\boldsymbol{\varepsilon}}^d=\mathbb{I}^d:\dot{\boldsymbol{\varepsilon}}; \tag{21}$$

where superscripts d and v denote deviatoric and volumetric decomposition of the corresponding tensor, respectively. Moreover, the elastic and plastic strain rate tensors can be decomposed to their deviatoric and volumetric parts:

$$\dot{\boldsymbol{\varepsilon}}_e=\dot{\boldsymbol{\varepsilon}}_e^v+\dot{\boldsymbol{\varepsilon}}_e^d;\quad \dot{\boldsymbol{\varepsilon}}_p=\dot{\boldsymbol{\varepsilon}}_p^v+\dot{\boldsymbol{\varepsilon}}_p^d. \tag{22}$$

Hence, considering Eq. (13):

$$\dot{\boldsymbol{\varepsilon}}^v=\dot{\boldsymbol{\varepsilon}}_e^v+\dot{\boldsymbol{\varepsilon}}_p^v;\quad \dot{\boldsymbol{\varepsilon}}^d=\dot{\boldsymbol{\varepsilon}}_e^d+\dot{\boldsymbol{\varepsilon}}_p^d. \tag{23}$$

In pressure-independent plasticity, the volumetric elastic strain rate is responsible for the entire volume change during the elasto-plastic deformation (Aravas, 1987); meaning that:

$$\dot{\boldsymbol{\varepsilon}}_p^v=\mathbf{O}\ \Rightarrow\ \dot{\boldsymbol{\varepsilon}}_p=\dot{\boldsymbol{\varepsilon}}_p^d. \tag{24}$$

Thereby,

$$\dot{\boldsymbol{\varepsilon}}^v=\dot{\boldsymbol{\varepsilon}}_e^v=\frac{1}{3}\dot{\varepsilon}_e^v\mathbf{I}=\mathbb{I}^v:\dot{\boldsymbol{\varepsilon}}_e;\quad \dot{\varepsilon}_e^v=\mathbf{I}:\dot{\boldsymbol{\varepsilon}}_e=\dot{\varepsilon}^v=\mathbf{I}:\dot{\boldsymbol{\varepsilon}};$$
$$\dot{\boldsymbol{\varepsilon}}_e^d=\mathbb{I}^d:\dot{\boldsymbol{\varepsilon}}_e. \tag{25}$$

Thus, Eqs. (22) and (23) can be rewritten as:

$$\dot{\boldsymbol{\varepsilon}}_e=\dot{\boldsymbol{\varepsilon}}^v+\dot{\boldsymbol{\varepsilon}}_e^d;\quad \dot{\boldsymbol{\varepsilon}}^d=\dot{\boldsymbol{\varepsilon}}_e^d+\dot{\boldsymbol{\varepsilon}}_p. \tag{26}$$

Knowing that the hydrostatic/volumetric parts of objective/material and spatial time derivatives of stress tensor are equal, since they are proportional to the first invariant of stress rate tensors, the objective stress rate tensor is decomposed to its deviatoric and hydrostatic splits as follows:

$$\overset{\nabla}{\boldsymbol{\sigma}}=\dot{\boldsymbol{\sigma}}^h+\overset{\nabla}{\boldsymbol{\sigma}}^d; \tag{27}$$

so that,

$$\dot{\boldsymbol{\sigma}}^h\equiv\dot{\sigma}^h\mathbf{I}=\mathbb{I}^v:\dot{\boldsymbol{\sigma}}=\mathbb{I}^v:\overset{\nabla}{\boldsymbol{\sigma}}=\overset{\nabla}{\boldsymbol{\sigma}}^h;\quad \dot{\sigma}^h=\frac{1}{3}\mathbf{I}:\dot{\boldsymbol{\sigma}};$$
$$\overset{\nabla}{\boldsymbol{\sigma}}^d=\mathbb{I}^d:\overset{\nabla}{\boldsymbol{\sigma}}; \tag{28}$$

where superscript h denotes hydrostatic contribution of the corresponding tensor. Taking Eqs. (19), (20), (25), (27) and (28) into account results in:

$$\dot{\boldsymbol{\sigma}}^h=K\dot{\varepsilon}^v\mathbf{I}=K\dot{\varepsilon}_e^v\mathbf{I}\ ;\quad \overset{\nabla}{\boldsymbol{\sigma}}^d=2G\dot{\boldsymbol{\varepsilon}}_e^d;\ \Rightarrow$$
$$\overset{\nabla}{\boldsymbol{\sigma}}=2G\dot{\boldsymbol{\varepsilon}}_e^d+K\dot{\varepsilon}^v\mathbf{I}=2G\dot{\boldsymbol{\varepsilon}}_e+\left(K-\frac{2}{3}G\right)\dot{\varepsilon}^v\mathbf{I}. \tag{29}$$

Therefore, by time integration in a fixed arbitrary spatial coordinate system:

$$\boldsymbol{\sigma}=\boldsymbol{\sigma}^h+\boldsymbol{\sigma}^d;\quad \boldsymbol{\sigma}^h=\sigma^h\mathbf{I}=\mathbb{I}^v:\boldsymbol{\sigma};\quad \sigma^h=\frac{1}{3}\mathbf{I}:\boldsymbol{\sigma};$$
$$\boldsymbol{\sigma}^d=\mathbb{I}^d:\boldsymbol{\sigma}. \tag{30}$$

2.7. Associative isotropic J_2 plasticity

The (hydrostatic-) pressure-independent yield criterion for isotropic hardening is adopted through definition of the following yield function (φ) :

$$\phi\equiv\bar{\sigma}-\sigma_y;\quad \bar{\sigma}\equiv\breve{\bar{\sigma}}(\boldsymbol{\sigma})=\sqrt{3\breve{J}_2(\boldsymbol{\sigma})}=\sqrt{\frac{3}{2}}\|\boldsymbol{\sigma}^d\|;$$
$$\sigma_y\equiv\breve{\sigma}_y\left(T,\boldsymbol{s},\dot{\bar{\varepsilon}}_p\right); \tag{31}$$

where $\bar{\sigma}$ and σ_y are equivalent (J_2/von Mises) stress and (scaler) yield stress, respectively; T is the temperature; $\dot{\bar{\varepsilon}}_p$ is the equivalent (von Mises) plastic strain rate; $\|\mathbf{A}\|\equiv\sqrt{\mathbf{A}:\bar{\mathbf{A}}}$ denotes the Euclidean norm of second-order tensor $\mathbf{A}$; and $\breve{J}_2(\boldsymbol{\sigma})$ is the second invariant of deviatoric part of Cauchy stress tensor $\boldsymbol{\sigma}$:

$$\breve{J}_2(\boldsymbol{\sigma})=\frac{1}{2}\left\|\boldsymbol{\sigma}^d\right\|^2\ \Rightarrow\ \frac{\partial J_2}{\partial\boldsymbol{\sigma}}=\boldsymbol{\sigma}^d. \tag{32}$$

In addition, due to invariance of J_2, for an arbitrarily rotated Cauchy stress tensor $\underline{\boldsymbol{\sigma}}$:

$$\breve{J}_2(\underline{\boldsymbol{\sigma}})=\breve{J}_2(\boldsymbol{\sigma})\ \Rightarrow\ \bar{\sigma}\equiv\breve{\bar{\sigma}}(\boldsymbol{\sigma})=\breve{\bar{\sigma}}(\underline{\boldsymbol{\sigma}}). \tag{33}$$

In the associative plasticity, the flow potential (ψ) is taken as the yield function ($\psi=\varphi$), leading to the following associative flow rule (Rice, 1971, 1970):

$$\dot{\boldsymbol{\varepsilon}}_p=\dot{\lambda}\frac{\partial\psi}{\partial\boldsymbol{\sigma}}=\dot{\lambda}\frac{\partial\phi}{\partial\boldsymbol{\sigma}}=\dot{\lambda}\mathbf{N};\quad \mathbf{N}\equiv\frac{\partial\phi}{\partial\boldsymbol{\sigma}}; \tag{34}$$

where $\dot{\lambda}$ is the non-negative consistency parameter or viscoplastic multiplier (Simo and Hughes, 1998); and $\mathbf{N}$ is known as flow direction tensor, which represents the yield surface normal tensor ($\mathbf{N}$ is

not necessarily a unit tenor). Given Eqs. (31), (32) and (34):

$$\mathbf{N} = \frac{3}{2}\frac{\boldsymbol{\sigma}^d}{\bar{\sigma}} \;\Rightarrow\; \dot{\boldsymbol{\varepsilon}}_p = \frac{3}{2}\frac{\dot{\lambda}}{\bar{\sigma}}\boldsymbol{\sigma}^d; \tag{35}$$

which sometimes are referred to as the Prandtl–Reuss equations. Taking Euclidean norm from both sides of Eq. (35) leads to:

$$\dot{\lambda} = \sqrt{\frac{2}{3}}\|\dot{\boldsymbol{\varepsilon}}_p\|. \tag{36}$$

According to the power (work) equivalence principle, (scaler) volumetric plastic power ($\dot{w}_p$) in multiaxial state can be equally expressed by the equivalent stress and equivalent plastic strain rate ($\dot{\bar{\varepsilon}}_p$):

$$\dot{w}_p = \boldsymbol{\sigma}^d : \dot{\boldsymbol{\varepsilon}}_p = \bar{\sigma}\ \dot{\bar{\varepsilon}}_p \geq 0. \tag{37}$$

Combining Eqs. (35)–(37) results in:

$$\dot{\lambda} = \dot{\bar{\varepsilon}}_p \equiv \breve{\dot{\bar{\varepsilon}}}_p\left(\dot{\boldsymbol{\varepsilon}}_p\right) = \sqrt{\frac{2}{3}}\|\dot{\boldsymbol{\varepsilon}}_p\|; \quad \dot{\boldsymbol{\varepsilon}}_p = \dot{\bar{\varepsilon}}_p\mathbf{N}. \tag{38}$$

Substituting Eq. (38) into Eq. (35) yields the Levy–Mises flow rule:

$$\dot{\boldsymbol{\varepsilon}}_p = \frac{3}{2}\frac{\dot{\bar{\varepsilon}}_p}{\bar{\sigma}}\boldsymbol{\sigma}^d. \tag{39}$$

Finally, formulation is completed by introducing Kuhn–Tucker loading-unloading complementary conditions:

$$\dot{\lambda} \geq 0; \quad \phi \leq 0; \quad \dot{\lambda}\phi = 0; \tag{40}$$

and the consistency condition:

$$\dot{\lambda}\dot{\phi} = 0. \tag{41}$$

Therefore, during viscoplastic deformation ($\dot{\lambda} > 0$), $\dot{\lambda}\phi = 0$ reduces to $\varphi = 0$, which is identical to $\bar{\sigma} = \sigma_y$, given Eq. (31). Also, the consistency condition during viscoplastic deformation with isotropic hardening according to yield function defined by Eq. (31), becomes (de-Borst et al., 2014; Wang et al., 1997):

$$\begin{aligned}\dot{\phi} &= \frac{\partial\phi}{\partial\boldsymbol{\sigma}} : \dot{\boldsymbol{\sigma}} - \dot{\sigma}_y = \sqrt{\frac{3}{2}}\mathbf{N} : \dot{\boldsymbol{\sigma}} - \dot{\sigma}_y = 0;\\ \dot{\sigma}_y &= \frac{\partial\sigma_y}{\partial\lambda}\dot{\lambda} + \frac{\partial\sigma_y}{\partial\dot{\lambda}}\ddot{\lambda};\end{aligned} \tag{42}$$

where $\dot{\sigma}_y$ is the viscoplastic hardening rate. In case of associative isotropic J_2 plasticity ($\dot{\lambda} = \dot{\bar{\varepsilon}}_p$):

$$\dot{\sigma}_y = \theta\ \dot{\bar{\varepsilon}}_p + \varphi\ \ddot{\bar{\varepsilon}}_p; \quad \theta \equiv \frac{\partial\sigma_y}{\partial\bar{\varepsilon}_p}; \quad \varphi \equiv \frac{\partial\sigma_y}{\partial\dot{\bar{\varepsilon}}_p}; \tag{43}$$

where θ and ϕ are plastic/strain hardening and viscous/strain-rate hardening, respectively.

2.8. Corotational representation of constitutive equations

Taking advantage of corotational formulation (Section 2.4), the orthogonality of the rotation tensor ($\boldsymbol{\Lambda}^{-1} = \boldsymbol{\Lambda}^{\mathrm{T}}$), symmetry of Cauchy stress tensor ($\boldsymbol{\sigma} = \boldsymbol{\sigma}^{\mathrm{T}}$), and the isotropy of elastic stiffness tensor ($\mathbb{C}_e = \mathbb{C}_e$), the tensor equations described in Sections 2.5, 2.6 and 2.7 are form-identical in the corotational configuration but with the spatial tensor variables replaced with their corotational counterparts (Zaera and Fernández-Sáez, 2006). The corotational representation of some of those equations are:

$$\underline{\dot{\boldsymbol{\varepsilon}}} = \underline{\dot{\boldsymbol{\varepsilon}}}_e + \underline{\dot{\boldsymbol{\varepsilon}}}_p; \tag{44}$$

$$\underline{\dot{\boldsymbol{\varepsilon}}} = \underline{\dot{\boldsymbol{\varepsilon}}}^d + \frac{1}{3}\dot{\varepsilon}^v\mathbf{I}; \quad \dot{\varepsilon}^v = \mathbf{I} : \underline{\dot{\boldsymbol{\varepsilon}}} = \dot{\varepsilon}^v_e = \mathbf{I} : \underline{\dot{\boldsymbol{\varepsilon}}}_e; \tag{45}$$

$$\underline{\dot{\boldsymbol{\varepsilon}}}_e = \underline{\dot{\boldsymbol{\varepsilon}}}^d_e + \frac{1}{3}\dot{\varepsilon}^v\mathbf{I}; \tag{46}$$

$$\underline{\dot{\boldsymbol{\varepsilon}}}_p = \underline{\dot{\boldsymbol{\varepsilon}}}^d_p = \underline{\dot{\boldsymbol{\varepsilon}}}^d - \underline{\dot{\boldsymbol{\varepsilon}}}^d_e; \tag{47}$$

$$\underline{\dot{\boldsymbol{\sigma}}} = \underline{\dot{\boldsymbol{\sigma}}}^d + \dot{\sigma}^h\mathbf{I}; \quad \underline{\dot{\boldsymbol{\sigma}}}^d = 2G\underline{\dot{\boldsymbol{\varepsilon}}}^d_e; \quad \dot{\boldsymbol{\sigma}}^h = \frac{1}{3}\mathbf{I} : \underline{\dot{\boldsymbol{\sigma}}} = K\dot{\varepsilon}^v; \tag{48}$$

$$\underline{\dot{\boldsymbol{\sigma}}} = \mathbb{C}_e : \underline{\dot{\boldsymbol{\varepsilon}}}_e = 2G\underline{\dot{\boldsymbol{\varepsilon}}}_e + \left(K - \frac{2}{3}G\right)\dot{\varepsilon}^v\mathbf{I}; \tag{49}$$

$$\underline{\boldsymbol{\sigma}} = \underline{\boldsymbol{\sigma}}^d + \sigma^h\mathbf{I}; \quad \sigma^h = \frac{1}{3}\mathbf{I} : \underline{\boldsymbol{\sigma}}; \tag{50}$$

$$\bar{\sigma} \equiv \breve{\bar{\sigma}}(\boldsymbol{\sigma}) = \breve{\bar{\sigma}}(\underline{\boldsymbol{\sigma}}) = \sqrt{\frac{3}{2}}\left\|\underline{\boldsymbol{\sigma}}^d\right\|; \tag{51}$$

$$\dot{\bar{\varepsilon}}_p \equiv \breve{\dot{\bar{\varepsilon}}}_p\left(\dot{\boldsymbol{\varepsilon}}_p\right) = \breve{\dot{\bar{\varepsilon}}}_p\left(\underline{\dot{\boldsymbol{\varepsilon}}}_p\right) = \sqrt{\frac{2}{3}}\left\|\underline{\dot{\boldsymbol{\varepsilon}}}_p\right\|; \tag{52}$$

$$\underline{\mathbf{N}} = \frac{3}{2}\frac{\underline{\boldsymbol{\sigma}}^d}{\bar{\sigma}} = \frac{\underline{\dot{\boldsymbol{\varepsilon}}}_p}{\dot{\bar{\varepsilon}}_p} \;\Rightarrow\; \underline{\dot{\boldsymbol{\varepsilon}}}_p = \frac{3}{2}\frac{\dot{\bar{\varepsilon}}_p}{\bar{\sigma}}\underline{\boldsymbol{\sigma}}^d. \tag{53}$$

The numerical time integration of the above-mentioned corotational representation of constitutive equations and the resultant algorithmic procedure for finite element implementation is explained in Section 4.

3. Microstructural constitutive model

The microstructural constitutive model for metal isotropic viscoplasticity has the form $\sigma_y = \breve{\sigma}_y(T, \boldsymbol{s}, \dot{\bar{\varepsilon}}_p)$. In the case of cold and warm regimes, the stochastic/nonlocal microstructural state set is $\boldsymbol{s} = \{\rho_{cm}, \rho_{ci}, \rho_{wi}\}$, where ρ is nonlocal dislocation density defined as the summation of integral lengths of dislocation segments over the (virtual) RMV, which contains a sufficient number of crystallites to be a representative of the polycrystalline aggregate (Eringen, 1983; Gao and Huang, 2001); subscripts c and w denote cell and wall; and subscripts m and i represent mobile and immobile, respectively. Thus, ρ_{cm}, ρ_{ci} and ρ_{wi} are cell mobile, cell immobile and wall immobile dislocation densities, respectively. According to Motaman and Prahl (2019), the microstructural constitutive model for polycrystal viscoplasticity in cold and warm regimes based on continuum dislocation dynamics consists of the following main equations:

$$\sigma_y = \sigma_v + \sigma_p; \quad \sigma_p = \sigma_{pc} + \sigma_{pw}; \tag{54}$$

$$\sigma_{px} = MbG\tilde{\alpha}_x\ \sqrt{\rho_{xi}}; \quad x = c, w; \tag{55}$$

$$\begin{aligned}&\sigma_v = \sigma_{v0}\ \dot{\bar{\varepsilon}}_p^{\,m_v}; \quad \sigma_{v0} \equiv \sigma_{v00}\left[1 + r_v\ \left(\hat{T} - 1\right)^{s_v}\right];\\ &\hat{T} \equiv \frac{T}{T_0}; \quad \dot{\hat{\varepsilon}}_p \equiv \frac{\dot{\bar{\varepsilon}}_p}{\dot{\varepsilon}_0}; \quad r_v < 0; \quad 0 < s_v \leq 1;\end{aligned} \tag{56}$$

where subscripts v and p, respectively stand for viscous and plastic; M is the Taylor factor; b is the Burgers length (magnitude of Burgers vector); $\tilde{\alpha}_x$ is the nonlocal interaction strength related to local density and geometrical arrangement of immobile dislocations of cell and wall species ($x = c, w$); r and s are temperature sensitivity coefficient and exponent; m is the strain rate sensitivity parameter; the hat-sign ($\hat{}$) indicates normalization; T is absolute temperature; and here subscript 0 denotes the reference state. Moreover, as a rule of thumb, the reference temperature and strain rate are assumed to be the lowest temperature and strain rate in the corresponding investigated regimes, respectively.

According to Eq. (54), the overall yield stress is decomposed to viscous/rate-dependent/thermal/effective/over- stress and plastic/athermal/rate-independent/internal/back /critical stress

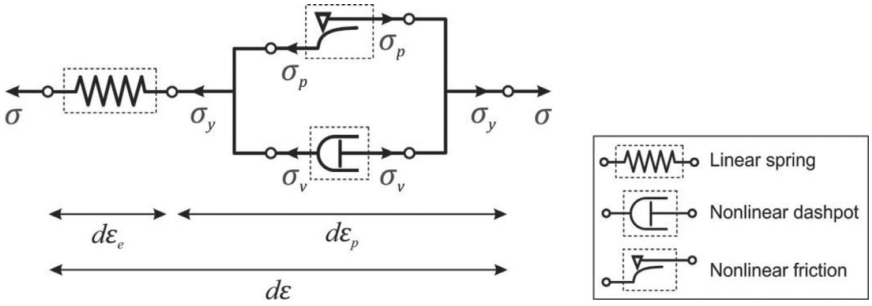

Fig. 2. Rheological model of polycrystal elasto-viscoplasticity. The plastic flow occurs once the applied stress ($\boldsymbol{\sigma}$) becomes equal to the yield stress ($\boldsymbol{\sigma} = \boldsymbol{\sigma_y}$).

contributions (Kumar et al., 1968; Mecking and Kocks, 1981). The plastic stress is the average (nonlocal) back stress that should be overcome for bowed-out mobile dislocations to initiate slip/glide; and hence related to the mean critical resolved shear stress for slip by the Taylor factor. Moreover, the viscous stress is the mean over-stress (the amount of additional stress exerted in average on the curved mobile dislocations) to move mobile dislocations forward. Therefore, due to temperature-dependent lattice viscosity, this mean effective stress applied on mobile dislocations should be a function (usually taken as a power law relation) of the average speed (norm of velocity vector) of mobile dislocations on slip systems which is proportional to plastic strain rate according to the Orowan relation. The viscoplastic decomposition can be depicted by the rheological illustration shown in Fig. 2, similar to Perzyna-type formulation (Perzyna, 1966), which consists of a parallel set of nonlinear dashpot/damper and nonlinear friction elements that are in series linkage with a linear spring element. In addition, it is postulated that (only) immobile dislocations contribute to plastic hardening (Estrin and Kubin, 1986) according to the Taylor relation, in parallel (additive decomposition of plastic stress) to satisfy the compatibility for isochoric viscoplastic flow of material, in which both cells and walls need to be deformed simultaneously at an equal rate (treated as cellular composite) (Columbus and Grujicic, 2002; Mughrabi, 1987; Voyiadjis and Al-Rub, 2005).

Combination of shear modulus and mean interaction strengths ($G\tilde{\alpha}_x$ factor in Eq. (55)) and strain rate sensitivity of viscous stress (m_v) depend on temperature and strain rate:

$$\widehat{G\tilde{\alpha}}_x = 1 + r^G_{\alpha x}\,\left(\hat{T}-1\right)^{s^G_{\alpha x}};\quad \widehat{G\tilde{\alpha}}_x \equiv \frac{G\tilde{\alpha}_x}{G_0\tilde{\alpha}_{x0}};$$
$$r^G_{\alpha x} < 0;\quad s^G_{\alpha x} > 0;\quad x = c, w; \tag{57}$$

$$\hat{m}_v = \left[1 + r^m_v\,\left(\hat{T}-1\right)^{s^m_v}\right]\dot{\hat{\varepsilon}}_p^{\,m^m_v};\quad \hat{m}_v \equiv \frac{m_v}{m_{v0}};\quad r^m_v, s^m_v \geq 0; \tag{58}$$

where $r^G_{\alpha x}$ and $s^G_{\alpha x}$ are temperature sensitivity coefficient and exponent associated with $G\tilde{\alpha}_x$; m_{v0} is the reference (at reference temperature and strain rate) strain rate sensitivity; r^m_v and s^m_v are respectively temperature sensitivity coefficient and exponent associated with strain rate sensitivity of viscous stress; and m^m_v is the strain rate sensitivity parameter associated with strain rate sensitivity of viscous stress. The following equations describe evolution of different types of dislocation densities:

$$\dot{\hat{\rho}}_{wi} = \dot{\hat{\rho}}^{\rm nc}_{wi} + \dot{\hat{\rho}}^{\rm ac}_{wi} - \left(\dot{\hat{\rho}}^{\rm an}_{wi} + \dot{\hat{\rho}}^{\rm rm}_{wi}\right);$$
$$\hat{\rho}_{xy} \equiv \frac{\rho_{xy}}{\rho_0};\quad \begin{cases} x = c, w \\ y = m, i \end{cases};$$
$$\hat{\rho}_{ci} = \dot{\hat{\rho}}^{\rm tr}_{cm} + \dot{\hat{\rho}}^{\rm ac}_{ci} - \left(\dot{\hat{\rho}}^{\rm an}_{ci} + \dot{\hat{\rho}}^{\rm rm}_{ci} + \dot{\hat{\rho}}^{\rm nc}_{wi}\right);$$
$$\hat{\rho}_{cm} = \dot{\hat{\rho}}^{\rm gn}_{cm} + \dot{\hat{\rho}}^{\rm rm}_{ci} + \dot{\hat{\rho}}^{\rm rm}_{wi} - \left(2\dot{\hat{\rho}}^{\rm an}_{cm} + \dot{\hat{\rho}}^{\rm an}_{ci} + \dot{\hat{\rho}}^{\rm an}_{wi} + \dot{\hat{\rho}}^{\rm ac}_{ci} + \dot{\hat{\rho}}^{\rm ac}_{wi} + \dot{\hat{\rho}}^{\rm tr}_{cm}\right); \tag{59}$$

so that,

$$\dot{\hat{\rho}}^{\rm gn}_{cm} = M\, c^{\rm gn}_{cm}\,\frac{\hat{\rho}_{cm}}{\sqrt{\hat{\rho}_{ci} + \hat{\rho}_{wi}}}\dot{\bar{\varepsilon}}_p;$$
$$\dot{\hat{\rho}}^{\rm an}_{xy} = M\, c^{\rm an}_{xy}\,\hat{\rho}_{cm}\,\hat{\rho}_{xy}\,\dot{\bar{\varepsilon}}_p;\quad xy = cm, ci, wi;$$
$$\dot{\hat{\rho}}^{\rm ac}_{xi} = M\, c^{\rm ac}_{xi}\,\sqrt{\hat{\rho}_{xi}}\,\hat{\rho}_{cm}\,\dot{\bar{\varepsilon}}_p;\quad x = c, w;$$
$$\dot{\hat{\rho}}^{\rm tr}_{cm} = M\, c^{\rm tr}_{cm}\,\hat{\rho}^{3/2}_{cm}\dot{\bar{\varepsilon}}_p;$$
$$\dot{\hat{\rho}}^{\rm nc}_{wi} = M\, c^{\rm nc}_{wi}\,\hat{\rho}^{3/2}_{ci}\,\hat{\rho}_{cm}\,\dot{\bar{\varepsilon}}_p;$$
$$\dot{\hat{\rho}}^{\rm rm}_{xi} = M\, c^{\rm rm}_{xi}\,\hat{\rho}_{xi}\,\dot{\bar{\varepsilon}}_p;\quad x = c, w; \tag{60}$$

where superscripts gn, an, ac, tr, nc and rm respectively denote dislocation generation, annihilation, accumulation, trapping, nucleation and remobilization processes; c^z_{xy} is the constitutive parameter associated with probability amplitude or frequency of occurrence of dislocation process z (z = gn, an, ac, tr, nc, rm) corresponding to dislocations of type xy ($xy = cm, ci, wi$).

The following equations describe the temperature and strain rate dependencies of constitutive parameters associated with different dislocation processes:

$$\hat{c}^z_{xy} = \left[1 + r^z_{xy}\,\left(\hat{T}-1\right)^{s^z_{xy}}\right]\dot{\hat{\varepsilon}}_p^{\,m^z_{xy}};\quad \hat{c}^z_{xy} \equiv \frac{c^z_{xy}}{c^z_{xy0}};$$
$$xy = cm, ci, wi; \tag{61}$$

$$\hat{m}^z_{xy} = \left[1 + r^m_{z_{xy}}\,\left(\hat{T}-1\right)^{s^m_{z_{xy}}}\right];\quad \hat{m}^z_{xy} \equiv \frac{m^z_{xy}}{m^z_{xy0}};$$
$$xy = cm, ci, wi; \tag{62}$$

where c^z_{xy0} is the reference (at reference temperature and strain rate) material constant associated with probability amplitude of dislocation process z that involves dislocations of type xy; r^z_{xy} and s^z_{xy} are respectively temperature sensitivity coefficient and exponent associated with probability amplitude of dislocation process z that involves dislocations of type xy; m^z_{xy} and m^z_{xy0} are current and reference (at reference temperature) strain rate sensitivities associated with dislocation process z corresponding to dislocations of type xy, respectively; and $r^m_{z_{xy}}$ and $s^m_{z_{xy}}$ are temperature sensitivity coefficient and exponent associated with strain sensitivity of dislocation process z of dislocations of type xy, respectively.

Moreover, among dislocation processes, only dislocation generation and accumulation are considered a thermal and therefore rate-independent dislocation processes, simply because their underlying mechanisms are not thermal. However, the rest of dislocation processes are thermal (temperature-dependent) and (strain) rate-dependent, as at least one of their underlying mechanisms is thermally activated, for example, annihilation and remobilization processes can be assisted by thermally activated cross-slip and diffusion-controlled climb mechanisms, while thermal pinning mechanism (diffusion of interstitial solute atoms to dislocation

cores and junctions) is one of the mechanisms assisting dislocation trapping and wall nucleation processes:

$$r^z_{xy}\begin{cases}>0: & z=\text{an, tr, rm, spn, srm}\\ \gtrless 0: & z=\text{nc}\\ =0: & z=\text{gn, ac}\end{cases};$$

$$s^z_{xy}\begin{cases}>0: & z=\text{an, tr, nc, rm}\\ =0: & z=\text{gn, ac}\end{cases};$$

$$m^z_{xy}\begin{cases}<0: & z=\text{an, tr}\\ \gtrless 0: & z=\text{nc, rm};\quad xy=cm, ci, wi.\\ =0: & z=\text{gn, ac}\end{cases} \tag{63}$$

Given Eqs. (31), (37) and (40), plastic power and generated heat rate due to plastic work are calculated as follows:

$$\dot{w}_p=\bar{\sigma}\ \dot{\bar{\varepsilon}}_p=\sigma_y\dot{\bar{\varepsilon}}_p;\quad \dot{q}_p=\beta\dot{w}_p=\beta\sigma_y\dot{\bar{\varepsilon}}_p; \tag{64}$$

where $\dot{q}_p$ is the volumetric heat generation rate due to plastic work; and β is known as dissipation/conversion factor, inelastic heat fraction, efficiency of plastic dissipation, or the Taylor-Quinney coefficient. In other words, β is the fraction of plastic power that is not stored elastically in the material by dislocations and consequently is converted to heat. Taylor and Quinney (1934) emphasized that the fraction β increases as plastic deformation progresses until the saturation state where $\beta=1$. In the saturation state, the entire input volumetric plastic power is converted to heat ($\dot{q}_p=\dot{w}_p$). In addition, Rosakis et al. (2000) and Zehnder (1991) proposed models for variation of β as a function of plastic strain and plastic hardening ($\theta\equiv\partial_{\bar{\varepsilon}_p}\sigma_y$) where β approaches unity by decreasing θ as plastic strain increases. At the beginning of plastic deformation of a nearly undeformed/annealed polycrystalline metallic material, large portion of the input plastic energy is stored in the crystal structure through generation of dislocations and dislocation substructures. Generation is the only dislocation process that increases the total population of dislocations, whereas the annihilation processes are the only class of dislocation processes that decrease the total dislocation density. However, as the plastic deformation proceeds, the generation rate of dislocations diminishes, while the annihilation rate increases (annihilation releases the previously stored energy of dislocations in form of heat) until the saturation state, where these two rates are equivalent. Therefore, one can assume the following physics-based relationship for description of the asymptotic behavior of dissipation factor:

$$\beta=\left(\frac{2\left(\dot{\hat{\rho}}^{\text{an}}_{cm}+\dot{\hat{\rho}}^{\text{an}}_{ci}+\dot{\hat{\rho}}^{\text{an}}_{wi}\right)}{\dot{\hat{\rho}}^{\text{gn}}_{cm}}\right)^{\kappa};\quad \kappa>0; \tag{65}$$

where κ is the material constant associated with dissipation factor. The factor 2 in Eq. (65) is due to annihilation of two dislocations in each annihilation event. The plastic/strain hardening (θ) is obtained by:

$$\theta\equiv\partial_{\bar{\varepsilon}_p}\sigma_y=\partial_{\bar{\varepsilon}_p}\sigma_p=\theta_c+\theta_w;$$

$$\theta_x\equiv\partial_{\bar{\varepsilon}_p}\sigma_{px}=\frac{MbG\tilde{\alpha}_x}{2\sqrt{\rho_{xi}}}\ \partial_{\bar{\varepsilon}_p}\rho_{xi}=\frac{\partial_{\bar{\varepsilon}_p}\hat{\rho}_{xi}}{2\hat{\rho}_{xi}}\ \sigma_{px};\quad x=c, w; \tag{66}$$

where $\partial_{\bar{\varepsilon}_p}\equiv\frac{\partial}{\partial\bar{\varepsilon}_p}$ is the partial derivative operator with respect to equivalent plastic strain ($\bar{\varepsilon}_p$); θ_x is plastic hardening associated with dislocations of type x. Further, viscous/strain-rate hardening (ϕ) is calculated as follows:

$$\varphi\equiv\partial_{\dot{\bar{\varepsilon}}_p}\sigma_y=\varphi_v+\varphi_p;$$

$$\varphi_v\equiv\partial_{\dot{\bar{\varepsilon}}_p}\sigma_v=\frac{m_v}{\dot{\bar{\varepsilon}}_p}\left[1+\ m^m_v\ \ln\left(\dot{\bar{\varepsilon}}_p\right)\right]\sigma_v;$$

$$\varphi_p\equiv\partial_{\dot{\bar{\varepsilon}}_p}\sigma_p=\varphi_{pc}+\varphi_{pw};\quad \varphi_{px}\equiv\partial_{\dot{\bar{\varepsilon}}_p}\sigma_{px}=\frac{\partial_{\dot{\bar{\varepsilon}}_p}\hat{\rho}_{xi}}{2\hat{\rho}_{xi}}\sigma_{px};\quad x=c, w; \tag{67}$$

where $\partial_{\dot{\bar{\varepsilon}}_p}\equiv\frac{\partial}{\partial\dot{\bar{\varepsilon}}_p}$ is the partial derivative operator with respect to equivalent plastic strain rate ($\dot{\bar{\varepsilon}}_p$); ϕ_v and ϕ_p are viscous hardening associated with viscous and plastic stresses, respectively; and ϕ_{px} is the viscous hardening associated with plastic stress of type $x=c$, w.

The equations related to the constitutive model are numerically integrated in the next section.

4. Numerical integration and algorithmic procedure

For finite element implementation, the differential continuum equations presented in Sections 2 and 3 must be numerically integrated with respect to time. Thus, the simulation time is discretized to relatively small increments/steps. Consider a (pseudo) time interval $[t^{(n)},t^{(n+1)}]$, so that $\Delta t^{(n+1)}\equiv t^{(n+1)}-t^{(n)}$ is the time increment at $(n+1)$-th time step. Accordingly,

$$\Delta(\bullet)^{(n+1)}\equiv(\bullet)^{(n+1)}-(\bullet)^{(n)};\quad(\dot{\bullet})^{(n+1)}\equiv\frac{\Delta(\bullet)^{(n+1)}}{\Delta t^{(n+1)}}; \tag{68}$$

where $(\bullet)$ can be any time-dependent scaler, vector or tensor (of any order) variable; and superscripts (n) and $(n+1)$ respectively represent the value of corresponding time-dependent variable at the beginning and the end of $(n+1)$-th time increment.

Furthermore, it is emphasized that all the tensor variables and equations in this section belong to the corotational/material frame, in which the basis system rotates with the material. Hence, calculation of rotation increments, and rotation of corresponding tensors are necessary before the algorithmic procedure provided in this section. Generally, the commercial FE software packages available today, upon user's request, handle the incremental finite rotations and pass the properly rotated stress and strain increment tensors to their user-defined material subroutine. For instance, the incrementally rotated stress and strain increment tensors passed to the user-defined material subroutines of ABAQUS Explicit (VUMAT) and ABAQUS Standard/implicit (UMAT) are based on the Green-Naghdi and Jaumann rates, respectively (ABAQUS, 2014). Moreover, at the end of the time increment computations, FE solver updates the spatial stress tensor ($\boldsymbol{\sigma}^{(n+1)}$) by rotating the corotational stress tensor ($\underline{\boldsymbol{\sigma}}^{(n+1)}$) back to the spatial configuration.

4.1. Trial (elastic predictor) step

In trial step, it is assumed that the deformation in time increment $[t^{(n)},t^{(n+1)}]$ is purely elastic:

$$\dot{\underline{\boldsymbol{\varepsilon}}}^{(n+1)}_{p\ \text{trial}}=\mathbf{O}\ \Rightarrow\ \dot{\lambda}^{(n+1)}_{\text{trial}}=\dot{\bar{\varepsilon}}^{(n+1)}_{p\ \text{trial}}\equiv 0; \tag{69}$$

where subscript trial denotes the trial step. Considering Eq. (44):

$$\dot{\underline{\boldsymbol{\varepsilon}}}^{(n+1)}_{e\ \text{trial}}=\dot{\underline{\boldsymbol{\varepsilon}}}^{(n+1)}. \tag{70}$$

Given Eq. (45):

$$\dot{\varepsilon}^{v\ (n+1)}=\dot{\varepsilon}^{v\ (n+1)}_{\text{trial}}=\mathbf{I}:\dot{\underline{\boldsymbol{\varepsilon}}}^{(n+1)}. \tag{71}$$

Accordingly, given Eqs. (49), (68) and (70), the trial stress tensor is calculated as follows:

$$\underline{\boldsymbol{\sigma}}^{(n+1)}_{\text{trial}}=\underline{\boldsymbol{\sigma}}^{(n)}+\Delta\underline{\boldsymbol{\sigma}}^{(n+1)}_{\text{trial}}; \tag{72}$$

$$\begin{aligned}\dot{\underline{\boldsymbol{\sigma}}}^{(n+1)}_{\text{trial}}&=\mathbb{C}_e:\dot{\underline{\boldsymbol{\varepsilon}}}^{(n+1)}_{e\ \text{trial}}=\mathbb{C}_e:\dot{\underline{\boldsymbol{\varepsilon}}}^{(n+1)}\\&=2G\dot{\underline{\boldsymbol{\varepsilon}}}^{(n+1)}+\left(K-\frac{2}{3}G\right)\dot{\varepsilon}^{v\ (n+1)}\mathbf{I}.\end{aligned} \tag{73}$$

Taking Eqs. (48), (50) and (71) into account gives:

$$\sigma^{h\ (n+1)}=\mathbf{I}:\underline{\boldsymbol{\sigma}}^{(n+1)}=\sigma^{h\ (n+1)}_{\text{trial}}=\mathbf{I}:\underline{\boldsymbol{\sigma}}^{(n+1)}_{\text{trial}}; \tag{74}$$

$$\underline{\boldsymbol{\sigma}}^{d\ (n+1)}_{\text{trial}}=\underline{\boldsymbol{\sigma}}^{(n+1)}_{\text{trial}}-\boldsymbol{\sigma}^{h\ (n+1)};\quad \boldsymbol{\sigma}^{h\ (n+1)}=\sigma^{h\ (n+1)}\mathbf{I}; \tag{75}$$

$$\underline{\boldsymbol{\sigma}}^{(n+1)} = \underline{\boldsymbol{\sigma}}^{d\ (n+1)} + \boldsymbol{\sigma}^{h\ (n+1)}. \tag{76}$$

Finally, considering Eq. (53), the trial flow direction reads:

$$\mathbf{N}_{\text{trial}}^{(n+1)} = \frac{3}{2}\frac{\underline{\boldsymbol{\sigma}}_{\text{trial}}^{d\ (n+1)}}{\bar{\sigma}_{\text{trial}}^{(n+1)}}. \tag{77}$$

4.2. Return mapping (plastic corrector)

Considering Eq. (70), rewriting Eqs. (47) and (48) for time increment $[t^{(n)},t^{(n+1)}]$ leads to:

$$\begin{cases} \underline{\dot{\boldsymbol{\sigma}}}^{d\ (n+1)} = 2G\underline{\dot{\boldsymbol{\varepsilon}}}_e^{d\ (n+1)} \\ \underline{\dot{\boldsymbol{\sigma}}}_{\text{trial}}^{d\ (n+1)} = 2G\underline{\dot{\boldsymbol{\varepsilon}}}_{e\ \text{trial}}^{d\ (n+1)} \end{cases};$$
$$\underline{\dot{\boldsymbol{\varepsilon}}}_{e\ \text{trial}}^{d\ (n+1)} = \underline{\dot{\boldsymbol{\varepsilon}}}^{d\ (n+1)} = \underline{\dot{\boldsymbol{\varepsilon}}}_e^{d\ (n+1)} + \underline{\dot{\boldsymbol{\varepsilon}}}_p^{(n+1)}. \tag{78}$$

Consequently,

$$\underline{\dot{\boldsymbol{\sigma}}}_{\text{trial}}^{d\ (n+1)} = \underline{\dot{\boldsymbol{\sigma}}}^{d\ (n+1)} + 2G\underline{\dot{\boldsymbol{\varepsilon}}}_p^{(n+1)} \Rightarrow$$
$$\Delta\underline{\boldsymbol{\sigma}}_{\text{trial}}^{d\ (n+1)} = \Delta\underline{\boldsymbol{\sigma}}^{d\ (n+1)} + 2G\Delta\underline{\boldsymbol{\varepsilon}}_p^{(n+1)}. \tag{79}$$

Given Eq. (72):

$$\underline{\boldsymbol{\sigma}}_{\text{trial}}^{d\ (n+1)} = \underline{\boldsymbol{\sigma}}^{d\ (n+1)} + 2G\Delta\underline{\boldsymbol{\varepsilon}}_p^{(n+1)}. \tag{80}$$

The following equations represent the incremental forms of Eqs. (51)–(53):

$$\bar{\sigma}^{(n+1)} = \sqrt{\frac{3}{2}}\left\|\underline{\boldsymbol{\sigma}}^{d\ (n+1)}\right\| \Rightarrow \bar{\sigma}_{\text{trial}}^{(n+1)} = \sqrt{\frac{3}{2}}\left\|\underline{\boldsymbol{\sigma}}_{\text{trial}}^{d\ (n+1)}\right\|; \tag{81}$$

$$\dot{\bar{\varepsilon}}_p^{(n+1)} = \sqrt{\frac{2}{3}}\left\|\underline{\dot{\boldsymbol{\varepsilon}}}_p^{(n+1)}\right\| \Rightarrow \Delta\bar{\varepsilon}_p^{(n+1)} = \sqrt{\frac{2}{3}}\left\|\Delta\underline{\boldsymbol{\varepsilon}}_p^{(n+1)}\right\|; \tag{82}$$

$$\mathbf{N}^{(n+1)} = \frac{3}{2}\frac{\underline{\boldsymbol{\sigma}}^{d\ (n+1)}}{\bar{\sigma}^{(n+1)}} = \frac{\underline{\dot{\boldsymbol{\varepsilon}}}_p^{(n+1)}}{\dot{\bar{\varepsilon}}_p^{(n+1)}} = \frac{\Delta\underline{\boldsymbol{\varepsilon}}_p^{(n+1)}}{\Delta\bar{\varepsilon}_p^{(n+1)}} \Rightarrow$$
$$\Delta\underline{\boldsymbol{\varepsilon}}_p^{(n+1)} = \frac{3}{2}\frac{\Delta\bar{\varepsilon}_p^{(n+1)}}{\bar{\sigma}^{(n+1)}}\underline{\boldsymbol{\sigma}}^{d\ (n+1)}. \tag{83}$$

Inserting $\Delta\underline{\varepsilon}_p^{(n+1)}$ from Eq. (83) into Eq. (80) results in:

$$\frac{\underline{\boldsymbol{\sigma}}_{\text{trial}}^{d\ (n+1)}}{\bar{\sigma}^{(n+1)} + 3G\Delta\bar{\varepsilon}_p^{(n+1)}} = \frac{\underline{\boldsymbol{\sigma}}^{d\ (n+1)}}{\bar{\sigma}^{(n+1)}}. \tag{84}$$

Given Eq. (81), taking the Euclidian norm of both sides of Eq. (84) leads to:

$$\bar{\sigma}_{\text{trial}}^{(n+1)} = \bar{\sigma}^{(n+1)} + 3G\Delta\bar{\varepsilon}_p^{(n+1)}; \quad \frac{\underline{\boldsymbol{\sigma}}_{\text{trial}}^{d\ (n+1)}}{\bar{\sigma}_{\text{trial}}^{(n+1)}} = \frac{\underline{\boldsymbol{\sigma}}^{d\ (n+1)}}{\bar{\sigma}^{(n+1)}}. \tag{85}$$

Combining Eqs. (77), (83) and (85) yields:

$$\mathbf{N}^{(n+1)} = \frac{3}{2}\frac{\underline{\boldsymbol{\sigma}}^{d\ (n+1)}}{\bar{\sigma}^{(n+1)}} = \frac{3}{2}\frac{\underline{\boldsymbol{\sigma}}^{d\ (n+1)}}{\sigma_y^{(n+1)}} = \mathbf{N}_{\text{trial}}^{(n+1)} = \frac{3}{2}\frac{\underline{\boldsymbol{\sigma}}_{\text{trial}}^{d\ (n+1)}}{\bar{\sigma}_{\text{trial}}^{(n+1)}}. \tag{86}$$

Since the flow direction and trial flow direction tensors are equal ($\mathbf{N}^{(n+1)} = \mathbf{N}_{\text{trial}}^{(n+1)}$), the yield surface normal is the same for elastic and plastic steps. Therefore, the return mapping in case of associative isotropic J_2 plasticity is also known as radial/classical return mapping. Given Eq. (85), the yield function defined by Eq. (31) becomes:

$$\phi^{(n+1)} = \bar{\sigma}^{(n+1)} - \sigma_y^{(n+1)} = \bar{\sigma}_{\text{trial}}^{(n+1)} - \sigma_y^{(n+1)} - 3G\Delta\bar{\varepsilon}_p^{(n+1)}. \tag{87}$$

Thereby, the trial yield function reads:

$$\phi_{\text{trial}}^{(n+1)} = \bar{\sigma}_{\text{trial}}^{(n+1)} - \sigma_{y\ \text{trial}}^{(n+1)}. \tag{88}$$

According to Kuhn–Tucker complementary conditions (Eq. (40)):

$$\phi_{\text{trial}}^{(n+1)}\begin{cases} \le 0: & \text{Elastic step} \\ > 0: & \text{Plastic step} \end{cases}. \tag{89}$$

In return mapping, stress and plastic strain can be updated by linearizing and solving stress and strain residual functions using an iterative method such as Newton–Raphson (NR). Therefore, there are two general types of return mapping:

- *Stress-based return mapping*, in which the nonlinear yield function in case of plastic step is being solved; and
- *Strain-based return mapping*, in which a nonlinear equation for plastic strain increment must be solved.

4.3. Numerical integration of constitutive model

Using forward/explicit Euler method for numerical integration of normalized dislocation densities gives:

$$\hat{\rho}_{xy}^{(n+1)} = \hat{\rho}_{xy}^{(n)} + \Delta\hat{\rho}_{xy}^{(n)};$$
$$\Delta\hat{\rho}_{xy}^{(n)} = \Delta t^{(n+1)}\ \dot{\hat{\rho}}_{xy}^{(n)} = \Delta\bar{\varepsilon}_p^{(n+1)}\ \partial_{\bar{\varepsilon}_p}\hat{\rho}_{xy}^{(n)};$$
$$\hat{\rho}_{xy}^{(n=0)} = \hat{\rho}_{xy0};\ \begin{cases} x = c, w \\ y = m, i \end{cases}. \tag{90}$$

Likewise, application of backward/implicit Euler method for numerical integration of normalized dislocation densities results in:

$$\hat{\rho}_{xy}^{(n+1)} = \hat{\rho}_{xy}^{(n)} + \Delta\hat{\rho}_{xy}^{(n+1)};$$
$$\Delta\hat{\rho}_{xy}^{(n+1)} = \Delta t^{(n+1)}\dot{\hat{\rho}}_{xy}^{(n+1)} = \Delta\bar{\varepsilon}_p^{(n+1)}\ \partial_{\bar{\varepsilon}_p}\hat{\rho}_{xy}^{(n+1)};$$
$$\hat{\rho}_{xy}^{(n=0)} = \hat{\rho}_{xy0};\ \begin{cases} x = c, w \\ y = m, i \end{cases}. \tag{91}$$

In empirical constitutive models where the equivalent accumulated plastic strain is the (mechanical) ISV, it is updated readily by $\bar{\varepsilon}_p^{(n+1)} = \bar{\varepsilon}_p^{(n)} + \Delta\bar{\varepsilon}_p^{(n+1)}$. For fully implicit constitutive integration, backward Euler Eq. (91)) or other implicit integration methods need to be applied for updating state variables (dislocation densities) that result in a system of coupled nonlinear equations that must be simultaneously solved along with the NR residual function in the return mapping procedure. However, even fully implicit FE simulations of HEVP in complex thermo-mechanical metal forming processes with high geometrical and material nonlinearities often have very low convergence rate. In order to overcome this convergence issue, time increments must be highly reduced. Therefore, in such cases, application of explicit finite element method with semi-implicit integration of constitutive equations is the most efficient approach. Nonetheless, more sophisticated implicit numerical time integration schemes such as generalized midpoint can improve convergence rate, stability, accuracy and performance of the implicit FE analysis (Ortiz and Popov, 1985). Application of implicit numerical integration schemes such as backward Euler and implicit midpoint methods coupled with the consistency approach (Eqs. (41)–(43)) in a fully implicit return mapping scheme will improve the convergence of implicit FE simulations through increasing computation cost of each time increment (de-Borst and Heeres, 2002; Heeres et al., 2002).

Incremental forms of Eqs. (54)–(58) are:

$$\sigma_y^{(n+1)} = \sigma_v^{(n+1)} + \sigma_p^{(n+1)}; \quad \sigma_p^{(n+1)} = \sigma_{pc}^{(n+1)} + \sigma_{pw}^{(n+1)}; \tag{92}$$

$$\sigma_{px}^{(n+1)} = Mb(G\tilde{\alpha}_x)^{(n+1)}\sqrt{\rho_0\ \hat{\rho}_{xi}^{(n+1)}}; \quad x = c, w;$$
$$(G\tilde{\alpha}_x)^{(n+1)} = (G\tilde{\alpha}_x)^{(n)} = G_0\tilde{\alpha}_{x0}\left[1 + r_{\alpha x}^{G}\left(\hat{T}^{(n)} - 1\right)^{s_{\alpha x}^{G}}\right];$$

$$\hat{T}^{(n)} \equiv \frac{T^{(n)}}{T_0}; \quad x = c, w; \tag{93}$$

$$\sigma_v^{(n+1)} = \sigma_{v0}^{(n+1)} \left(\hat{\dot{\varepsilon}}_p^{(n+1)}\right)^{m_v^{(n+1)}};$$
$$\sigma_{v0}^{(n+1)} = \sigma_{v0}^{(n)} = \sigma_{v00}\left[1 + r_v \left(\hat{T}^{(n)} - 1\right)^{s_v}\right]; \quad \hat{\dot{\varepsilon}}_p^{(n+1)} \equiv \frac{\dot{\bar{\varepsilon}}_p^{(n+1)}}{\dot{\varepsilon}_0};$$
$$m_v^{(n+1)} = m_{v0}\left[1 + r_v^m \left(\hat{T}^{(n)} - 1\right)^{s_v^m}\right]\left(\hat{\dot{\varepsilon}}_p^{(n+1)}\right)^{m_v^m}. \tag{94}$$

Given Eqs. (61) and (62), temperature and strain rate dependencies of material coefficients associated with probability amplitude of various dislocations processes are incrementally calculated according to:

$$c_{xy}^{z\ (n+1)} = c_{xy0}^z\left[1 + r_{xy}^z \left(\hat{T}^{(n)} - 1\right)^{s_{xy}^z}\right]\left(\hat{\dot{\varepsilon}}_p^{(n+1)}\right)^{m_{xy}^{z\ (n+1)}};$$
$$m_{xy}^{z\ (n+1)} = m_{xy}^{z\ (n)} = m_{xy0}^z\left[1 + r_{z_{xy}}^m \left(\hat{T}^{(n)} - 1\right)^{s_{z_{xy}}^m}\right];$$
$$xy = cm, ci, wi. \tag{95}$$

4.4. Stress-based return mapping

In stress-based return mapping, the residual function ($R^{(n+1)}$) to be solved ($R^{(n+1)} = 0$) using the NR scheme is usually the same as the yield function:

$$R^{(n+1)} \equiv \phi^{(n+1)} = \bar{\sigma}^{(n+1)} - \sigma_y^{(n+1)}$$
$$= \bar{\sigma}_{\text{trial}}^{(n+1)} - \sigma_y^{(n+1)} - 3G\Delta\bar{\varepsilon}_p^{(n+1)}. \tag{96}$$

According to Eqs. (88) and (89), in order to check for viscoplastic yielding, $\sigma_{y\ \text{trial}}^{(n+1)}$ must be computed first. In stress-based return mapping, considering Eq. (92):

$$\sigma_{y\ \text{trial}}^{(n+1)} = \sigma_{v\ \text{trial}}^{(n+1)} + \sigma_{p\ \text{trial}}^{(n+1)}; \ \sigma_{p\ \text{trial}}^{(n+1)} = \sigma_{pc\ \text{trial}}^{(n+1)} + \sigma_{pw\ \text{trial}}^{(n+1)}. \tag{97}$$

Given Eqs. (69), (90), (91) and (93):

$$\sigma_{px\ \text{trial}}^{(n+1)} = Mb(G\tilde{\alpha}_x)^{(n)}\sqrt{\rho_0\ \hat{\rho}_{xi\ \text{trial}}^{(n+1)}};$$
$$\hat{\rho}_{xi\ \text{trial}}^{(n+1)} = \hat{\rho}_{xi}^{(n)}; \quad x = c, w. \tag{98}$$

Since the viscous response associated with viscous stress is instantaneous, in order to calculate the trial viscous stress ($\sigma_{v\ \text{trial}}^{(n+1)}$), equivalent plastic strain rate at the beginning of the time increment $\dot{\bar{\varepsilon}}_p^{(n)}$ is taken into account. However, to avoid a vanishing of the trial viscous stress, for instance, at the beginning of loading (where $\dot{\bar{\varepsilon}}_p^{(n)} = 0$), instead of $\dot{\bar{\varepsilon}}_p^{(n)}$, a minimum equivalent plastic strain rate ($\dot{\bar{\varepsilon}}_p^{\min}$) determines the trial viscous stress. Accordingly, a corrected equivalent plastic strain rate ($\dot{\bar{\varepsilon}}_{p\ \text{corr}}^{(n)}$) at the beginning of current time increment is adopted:

$$\dot{\bar{\varepsilon}}_{p\ \text{corr}}^{(n)} \equiv \begin{cases} \dot{\bar{\varepsilon}}_p^{(n)}: & \dot{\bar{\varepsilon}}_p^{(n)} > \dot{\varepsilon}_p^{\min} \\ \dot{\varepsilon}_p^{\min}: & \dot{\bar{\varepsilon}}_p^{(n)} \le \dot{\varepsilon}_p^{\min} \end{cases}; \quad \dot{\varepsilon}_p^{\min} \equiv \xi^{\min}\dot{\varepsilon}_0; \quad 0 < \xi^{\min} < 1. \tag{99}$$

As suggested by Eq. (99), the minimum equivalent plastic strain rate is assumed to be a fraction ($\xi^{\min}$) of the reference strain rate ($\dot{\varepsilon}_0$). In case of having creep or relaxation deformation modes, $\xi^{\min}$ must be chosen adequately small. Nevertheless, for most of metal forming cases, a value of $10^{-3} \le \xi^{\min} \le 10^{-2}$ is generally recommended. Therefore, given Eq. (94):

$$\sigma_{v\ \text{trial}}^{(n+1)} = \sigma_{v00}\left[1 + r_v \left(\hat{T}^{(n)} - 1\right)^{s_v}\right]\left(\frac{\dot{\bar{\varepsilon}}_{p\ \text{corr}}^{(n)}}{\dot{\varepsilon}_0}\right)^{m_{v\ \text{trial}}^{(n+1)}};$$
$$m_{v\ \text{trial}}^{(n+1)} = m_{v0}\left[1 + r_v^m \left(\hat{T}^{(n)} - 1\right)^{s_v^m}\right]\left(\frac{\dot{\bar{\varepsilon}}_{p\ \text{corr}}^{(n)}}{\dot{\varepsilon}_0}\right)^{m_v^m}. \tag{100}$$

Thereby,

$$\begin{cases} \sigma_y^{(n+1)} \equiv \dot{\sigma}_y^{(n+1)}\left(T^{(n)}, \boldsymbol{s}^{(n)}, \Delta\bar{\varepsilon}_p^{(n+1)}, \Delta t^{(n+1)}\right) \\ \sigma_{y\ \text{trial}}^{(n+1)} \equiv \dot{\sigma}_{y\ \text{trial}}^{(n+1)}\left(T^{(n)}, \boldsymbol{s}^{(n)}, \dot{\bar{\varepsilon}}_{p\ \text{corr}}^{(n)}\right) \end{cases};$$
$$\boldsymbol{s}^{(n)} \equiv \left\{\rho_{cm}^{(n)}, \rho_{ci}^{(n)}, \rho_{wi}^{(n)}\right\}. \tag{101}$$

As mentioned earlier, in stress-based return mapping, in case of plastic step ($\phi_{\text{trial}}^{(n+1)} > 0$), the nonlinear implicit yield function is taken as the residual function, $R^{(n+1)} \equiv \varphi^{(n+1)} = 0$ (Eq. (96)), which must be solved for $\Delta\bar{\varepsilon}_p^{(n+1)}$ using a linearization solving scheme such as iterative Newton-Raphson method. The NR loop starts with an initial guess for $\Delta\bar{\varepsilon}_p^{(n+1)}$. Here, it has been taken from $\dot{\bar{\varepsilon}}_{p\ \text{corr}}^{(n)}$:

$$\Delta\bar{\varepsilon}_{p\ \{k=0\}}^{(n+1)} = \dot{\bar{\varepsilon}}_{p\ \text{corr}}^{(n)}\Delta t^{(n+1)}; \tag{102}$$

where subscript $\{k\}$ is the NR loop index. If the residual function $R_{\{k\}}^{(n+1)}$ is close enough to zero with the specified tolerance χ (e.g., $\chi = 10^{-6}$), the calculated $\Delta\bar{\varepsilon}_{p\ \{k\}}^{(n+1)}$ is taken as $\Delta\bar{\varepsilon}_p^{(n+1)}$:

$$\Delta\bar{\varepsilon}_p^{(n+1)} = \Delta\bar{\varepsilon}_{p\ \{k\}}^{(n+1)}; \quad \left|\hat{R}_{\{k\}}^{(n+1)}\right| < \chi; \quad \hat{R}_{\{k\}}^{(n+1)} \equiv \frac{R_{\{k\}}^{(n+1)}}{R_{\{y\,\text{trial}\}}^{(n+1)}}; \tag{103}$$

where $\hat{R}_{\{k\}}^{(n+1)}$ is the normalized NR residual function at k-th NR iteration. Otherwise ($|\hat{R}_{\{k\}}^{(n+1)}| \ge \chi$), $\Delta\bar{\varepsilon}_{p\ \{k\}}^{(n+1)}$ will be updated iteratively using NR linearization:

$$\Delta\bar{\varepsilon}_{p\ \{k+1\}}^{(n+1)} = \Delta\bar{\varepsilon}_{p\ \{k\}}^{(n+1)} - \left(\frac{\mathrm{d}R_{\{k\}}^{(n+1)}}{\mathrm{d}\Delta\bar{\varepsilon}_{p\ \{k\}}^{(n+1)}}\right)^{-1} R_{\{k\}}^{(n+1)}. \tag{104}$$

Given Eq. (96), Eq. (104) becomes:

$$\Delta\bar{\varepsilon}_{p\ \{k+1\}}^{(n+1)} = \Delta\bar{\varepsilon}_{p\ \{k\}}^{(n+1)} + \frac{R_{\{k\}}^{(n+1)}}{3G + H_{vp\ \{k\}}^{(n+1)}}; \quad H_{vp\ \{k\}}^{(n+1)} \equiv \frac{\mathrm{d}\sigma_{y\ \{k\}}^{(n+1)}}{\mathrm{d}\Delta\bar{\varepsilon}_{p\ \{k\}}^{(n+1)}}; \tag{105}$$

where $H_{vp}^{(n+1)}$ is the viscoplastic tangent modulus at the end of the current time increment $(n+1)$. After updating the equivalent plastic strain increment (calculation of $\Delta\bar{\varepsilon}_{p\ \{k+1\}}^{(n+1)}$), again the yield function (NR residual) must be calculated (Eq. (96)); and then the NR loop condition (Eq. (103)) needs to be checked with the updated residual. Given Eqs. (59), (60), (63), (90), (91), (92), (93), (94) and (95):

$$H_{vp}^{(n+1)} \equiv \frac{\mathrm{d}\sigma_y^{(n+1)}}{\mathrm{d}\Delta\bar{\varepsilon}_p^{(n+1)}} = H_v^{(n+1)} + H_p^{(n+1)}; \tag{106}$$

where $H_v^{(n+1)}$ and $H_p^{(n+1)}$ are viscous and plastic tangent moduli, respectively:

$$H_v^{(n+1)} \equiv \frac{\mathrm{d}\sigma_v^{(n+1)}}{\mathrm{d}\Delta\bar{\varepsilon}_p^{(n+1)}} = \frac{m_v^{(n+1)}\left[1 + m_v^m \ln\left(\hat{\dot{\varepsilon}}_p^{(n+1)}\right)\right]}{\Delta\bar{\varepsilon}_p^{(n+1)}}\sigma_v^{(n+1)}; \tag{107}$$

$$H_p^{(n+1)} \equiv \frac{\mathrm{d}\sigma_p^{(n+1)}}{\mathrm{d}\Delta\bar{\varepsilon}_p^{(n+1)}} = \frac{\partial_{\bar{\varepsilon}_p}\hat{\rho}_{ci}^{(n)/(n+1)} + m_{cm}^{\mathrm{tr}\ (n+1)}\partial_{\bar{\varepsilon}_p}\hat{\rho}_{cm}^{\mathrm{tr}\ (n)/(n+1)} - \sum_{z_{xy}=\substack{\mathrm{an}_{ci}\\ \mathrm{rm}_{ci}\\ \mathrm{nc}_{wi}}} m_{xy}^{z\ (n+1)}\partial_{\bar{\varepsilon}_p}\hat{\rho}_{xy}^{z\ (n)/(n+1)}}{2\hat{\rho}_{ci}^{(n+1)}}\sigma_{pc}^{(n+1)} + \frac{\partial_{\bar{\varepsilon}_p}\hat{\rho}_{wi}^{(n)/(n+1)} + m_{wi}^{\mathrm{nc}\ (n+1)}\partial_{\bar{\varepsilon}_p}\hat{\rho}_{wi}^{\mathrm{nc}\ (n)/(n+1)} - \sum_{z_{xy}=\substack{\mathrm{an}_{wi}\\ \mathrm{rm}_{wi}}} m_{xy}^{z\ (n+1)}\ \partial_{\bar{\varepsilon}_p}\hat{\rho}_{xy}^{z\ (n)/(n+1)}}{2\hat{\rho}_{wi}^{(n+1)}}\sigma_{pw}^{(n+1)}. \tag{108}$$

Notice that $\Delta\bar{\varepsilon}_{p\ \{k=0\}}^{(n+1)}$ must not be taken zero (Eq. (107)); otherwise, $H_{vp\ \{k=0\}}^{(n+1)}$ will be undefined. This is the reason behind taking $\Delta\bar{\varepsilon}_{p\ \{k=0\}}^{(n+1)} = \dot{\bar{\varepsilon}}_{p\ \mathrm{corr}}^{(n)}\ \Delta t^{(n+1)} > 0$.

4.5. Strain-based return mapping

According to Eqs. (87), (92), (93) and (94), in case of plastic step ($\phi_{\mathrm{trial}}^{(n+1)} > 0$):

$$\dot{\bar{\varepsilon}}_p^{(n+1)} = \dot{\varepsilon}_0\left(\frac{\sigma_v^{(n+1)}}{\sigma_{v0}^{(n+1)}}\right)^{\frac{1}{m_v^{(n+1)}}};\quad \sigma_v^{(n+1)} = \sigma_y^{(n+1)} - \sigma_p^{(n+1)} > 0;$$
$$\sigma_y^{(n+1)} = \bar{\sigma}_{\mathrm{trial}}^{(n+1)} - 3G\Delta\bar{\varepsilon}_p^{(n+1)}; \tag{109}$$

which is an implicit function for $\Delta\bar{\varepsilon}_p^{(n+1)}$. Considering Eq. (68), and Eq. (109) can be rearranged as follows to define the residual function in strain-based return mapping:

$$R^{(n+1)} \equiv \Delta\bar{\varepsilon}_p^{(n+1)} - \Delta t^{(n+1)}\dot{\bar{\varepsilon}}_p^{(n+1)} = \Delta\bar{\varepsilon}_p^{(n+1)} - \Delta t^{(n+1)}\dot{\varepsilon}_0\left(\frac{\sigma_v^{(n+1)}}{\sigma_{v0}^{(n+1)}}\right)^{\frac{1}{m_v^{(n+1)}}}; \tag{110}$$

which ought to be solved ($R^{(n+1)} = 0$) for $\Delta\bar{\varepsilon}_p^{(n+1)}$ using the iterative NR method.

Furthermore, in strain-based return mapping, considering Eqs. (69), (90), (91), (92) and (93):

$$\sigma_{y\ \mathrm{trial}}^{(n+1)} = \sigma_{p\ \mathrm{trial}}^{(n+1)} = \sigma_{pc\ \mathrm{trial}}^{(n+1)} + \sigma_{pw\ \mathrm{trial}}^{(n+1)};$$
$$\sigma_{px\ \mathrm{trial}}^{(n+1)} = Mb(G\tilde{\alpha}_x)^{(n)}\sqrt{\rho_0\ \hat{\rho}_{xi}^{(n)}};\ x = c, w. \tag{111}$$

In strain-based return mapping, depending on explicit or implicit finite elements, the following initial guess for $\Delta\bar{\varepsilon}_p^{(n+1)}$ is adopted to obtain the highest convergence rate and stability:

$$\Delta\bar{\varepsilon}_{p\ \{k=0\}}^{(n+1)} \equiv \begin{cases}\dot{\bar{\varepsilon}}_p^{(n)}\ \Delta t^{(n+1)} & : \quad \text{Implicit Finite Elements}\\ 0 & : \quad \text{Explicit Finite Elements}\end{cases}. \tag{112}$$

If the residual $R_{\{k\}}^{(n+1)}$ is close enough to zero with the specified tolerance χ (e.g., $\chi = 10^{-6}$), the calculated $\Delta\bar{\varepsilon}_{p\ \{k\}}^{(n+1)}$ is taken as $\Delta\bar{\varepsilon}_p^{(n+1)}$:

$$\Delta\bar{\varepsilon}_p^{(n+1)} = \Delta\bar{\varepsilon}_{p\ \{k\}}^{(n+1)};\quad \left|\hat{R}_{\{k\}}^{(n+1)}\right| < \chi;$$
$$\hat{R}_{\{k\}}^{(n+1)} \equiv \frac{R_{\{k\}}^{(n+1)}}{\Delta t^{(n+1)}\ \xi^{\mathrm{mean}}\ \dot{\varepsilon}_0};\quad \xi^{\mathrm{mean}} > 0; \tag{113}$$

where ξ^{mean} determines the approximate average of equivalent plastic strain rate. Otherwise ($|\hat{R}_{\{k\}}^{(n+1)}| \geq \chi$), $\Delta\bar{\varepsilon}_{p\ \{k\}}^{(n+1)}$ will be updated iteratively using the NR linearization using Eq. (104), with:

$$\frac{\mathrm{d}R_{\{k\}}^{(n+1)}}{\mathrm{d}\Delta\bar{\varepsilon}_{p\ \{k\}}^{(n+1)}} = 1 + \frac{3G + H_{p\ \{k\}}^{(n+1)}}{m_v^{(n+1)}\sigma_{v\ \{k\}}^{(n+1)}}\Delta t^{(n+1)}\dot{\bar{\varepsilon}}_{p\ \{k\}}^{(n+1)};$$
$$\dot{\bar{\varepsilon}}_{p\ \{k\}}^{(n+1)} = \dot{\varepsilon}_0\left(\frac{\sigma_{v\ \{k\}}^{(n+1)}}{\sigma_{v0}^{(n+1)}}\right)^{\frac{1}{m_v^{(n+1)}}}. \tag{114}$$

4.6. Consistent tangent stiffness operator in implicit finite elements

In implicit finite element method for global linearization, the HEVP consistent/algorithmic tangent stiffness operator/modulus/tensor ($\underline{\mathbb{C}}^{(n+1)}$) must be computed:

$$\underline{\mathbb{C}}^{(n+1)} \equiv \frac{\partial\Delta\underline{\boldsymbol{\sigma}}^{(n+1)}}{\partial\Delta\underline{\boldsymbol{\varepsilon}}^{(n+1)}} = 2G_{\mathrm{eff}}^{(n+1)}\mathbb{I} + \left(K - \frac{2}{3}G_{\mathrm{eff}}^{(n+1)}\right)\mathbf{I}\otimes\mathbf{I} + H_{\mathrm{eff}}^{(n+1)}\underline{\mathbf{N}}^{(n+1)}\otimes\underline{\mathbf{N}}^{(n+1)}; \tag{115}$$

so that,

$$H_{\mathrm{eff}}^{(n+1)} \equiv \frac{4}{3}\left(\frac{G}{1 + \frac{3G}{H_{vp}^{(n+1)}}} - G_{\mathrm{eff}}^{(n+1)}\right);$$
$$G_{\mathrm{eff}}^{(n+1)} \equiv \frac{\bar{\sigma}^{(n+1)}}{\bar{\sigma}_{\mathrm{trial}}^{(n+1)}}G = \frac{\sigma_y^{(n+1)}}{\bar{\sigma}_{\mathrm{trial}}^{(n+1)}}G; \tag{116}$$

where $H_{\mathrm{eff}}^{(n+1)}$ and $G_{\mathrm{eff}}^{(n+1)}$ are effective/elasto-viscoplastic tangent and shear moduli. In case of elastic step, in which $\bar{\sigma}^{(n+1)} = \bar{\sigma}_{\mathrm{trial}}^{(n+1)}$, given Eq. (116), $G_{\mathrm{eff}}^{(n+1)} = G$. Moreover, in elastic domain where the equivalent plastic strain increment tends to zero ($\Delta\bar{\varepsilon}_p^{(n+1)} = 0$), according to Eqs. (106)–(108) the viscoplastic tangent modulus approaches infinity ($H_{vp}^{(n+1)} \to \infty$) that leads to $H_{\mathrm{eff}}^{(n+1)} = 0$. Given Eqs. (20) and (115), this is compatible with the fact that for pure elastic deformation $\underline{\mathbb{C}}^{(n+1)} = \mathbb{C}_e$.

4.7. Objective stress update algorithm

The trial step and radial return mapping (elastic predictor-plastic corrector) scheme for objective stress update in associative isotropic J_2 plasticity with microstructural constitutive model are summarized in Box 1.

The presented self-consistent algorithm (Box 1) is programmed as various user-defined material subroutines in ABAQUS Explicit (VUMAT) and ABAQUS Standard/implicit (UMAT) with semi-implicit and fully-implicit constitutive integration schemes using both stress-based and strain-based return mapping algorithms, which are available as supplementary materials to this paper. The overall algorithmic procedure of such implementation is illustrated in the flowchart shown in Fig. 3. The presented consistent algorithm is sufficient for establishing the microstructural solver as well as its linkage to the mechanical and thermal solvers. The interaction among mechanical, thermal and microstructural solvers and their associated fields, together with the initial and boundary conditions and thermo-micro-mechanical properties in the proposed fully coupled TMM-FE simulation approach is shown in Fig. 4. It should be noted that in this framework, temperature-dependent thermal expansion coefficients, which are directly provided to the thermal solver (along with the other required thermo-physical material properties) are used to update the diagonal components of the strain increment tensor passed (from the mechanical solver) to the microstructural solver (user-defined material subroutine), using the computed values of volumetric thermal (elastic) strain increments.

Box 1
Trial step and radial return mapping (elastic predictor – plastic corrector) scheme for objective stress update in associative isotropic J_2 plasticity with microstructural constitutive model.

1) Trial step (elastic predictor):

$$\mathbb{C}_e = 2G\mathbb{I} + \left(K - \frac{2}{3}G\right)\mathbf{I}\otimes\mathbf{I}; \quad K = \frac{2(1+\upsilon)}{3(1-2\upsilon)}G; \tag{1.1}$$

$$\underline{\boldsymbol{\sigma}}_{\text{trial}}^{(n+1)} = \underline{\boldsymbol{\sigma}}^{(n)} + \mathbb{C}_e : \Delta\underline{\boldsymbol{\varepsilon}}^{(n+1)} = \underline{\boldsymbol{\sigma}}^{(n)} + 2G\Delta\underline{\boldsymbol{\varepsilon}}^{(n+1)} + \left(K - \frac{2}{3}G\right)\Delta\varepsilon^{\upsilon\ (n+1)}\mathbf{I}; \quad \Delta\varepsilon^{\upsilon\ (n+1)} = \mathbf{I} : \Delta\underline{\boldsymbol{\varepsilon}}^{(n+1)}; \tag{1.2}$$

$$\underline{\boldsymbol{\sigma}}_{\text{trial}}^{d\ (n+1)} = \underline{\boldsymbol{\sigma}}_{\text{trial}}^{(n+1)} - \boldsymbol{\sigma}^{h\ (n+1)}; \quad \boldsymbol{\sigma}^{h\ (n+1)} = \sigma^{h\ (n+1)}\mathbf{I}; \quad \sigma^{h\ (n+1)} = \mathbf{I} : \underline{\boldsymbol{\sigma}}_{\text{trial}}^{(n+1)}; \tag{1.3}$$

$$\phi_{\text{trial}}^{(n+1)} = \tilde{\sigma}_{\text{trial}}^{(n+1)} - \sigma_{y\ \text{trial}}^{(n+1)}; \quad \tilde{\sigma}_{\text{trial}}^{(n+1)} = \sqrt{\tfrac{3}{2}}\|\underline{\boldsymbol{\sigma}}_{\text{trial}}^{d\ (n+1)}\|. \tag{1.4}$$

2) Check viscoplastic yielding:
IF $\phi_{\text{trial}}^{(n+1)} \le 0$, THEN it is an elastic step:

$$\underline{\boldsymbol{\sigma}}^{(n+1)} = \underline{\boldsymbol{\sigma}}_{\text{trial}}^{(n+1)}; \quad \underline{\mathbb{C}}^{(n+1)} = \mathbb{C}_e; \quad \boldsymbol{s}^{(n+1)} = \boldsymbol{s}^{(n)}; \quad \Delta\bar{\varepsilon}_p^{(n+1)} = 0. \tag{1.5}$$

3) Return mapping ($\phi_{\text{trial}}^{(n+1)} > 0$): solving the stress or strain-based residual function ($R^{(n+1)} = 0$) for $\Delta\bar{\varepsilon}_p^{(n+1)}$ and $\sigma_y^{(n+1)}$ using the iterative Newton-Raphson method and updating the MSVs.

4) Update the stress and HEVP consistent tangent stiffness operator:

$$\underline{\boldsymbol{\sigma}}^{(n+1)} = \underline{\boldsymbol{\sigma}}^{d\ (n+1)} + \boldsymbol{\sigma}^{h\ (n+1)}; \quad \underline{\boldsymbol{\sigma}}^{d\ (n+1)} = \frac{2}{3}\sigma_y^{(n+1)}\ \underline{\mathbf{N}}^{(n+1)}; \quad \underline{\mathbf{N}}^{(n+1)} = \frac{3}{2}\frac{\underline{\boldsymbol{\sigma}}_{\text{trial}}^{d\ (n+1)}}{\tilde{\sigma}_{\text{trial}}^{(n+1)}} = \frac{\Delta\underline{\boldsymbol{\varepsilon}}_p^{(n+1)}}{\Delta\bar{\varepsilon}_p^{(n+1)}}; \tag{1.6}$$

$$H_{\text{eff}}^{(n+1)} \equiv \frac{4}{3}\left(\frac{G}{1+\frac{3G}{H_{\text{iso}}^{(n+1)}}} - G_{\text{eff}}^{(n+1)}\right); \quad G_{\text{eff}}^{(n+1)} = \frac{\sigma_y^{(n+1)}}{\tilde{\sigma}_{\text{trial}}^{(n+1)}}G; \tag{1.7}$$

$$\underline{\mathbb{C}}^{(n+1)} = 2G_{\text{eff}}^{(n+1)}\mathbb{I} + (K - \frac{2}{3}G_{\text{eff}}^{(n+1)})\mathbf{I}\otimes\mathbf{I} + H_{\text{eff}}^{(n+1)}\underline{\mathbf{N}}^{(n+1)}\otimes\underline{\mathbf{N}}^{(n+1)}\ . \tag{1.8}$$

5) Calculation of equivalent plastic strain rate, incremental plastic work and generated heat:

$$\dot{\bar{\varepsilon}}_p^{(n+1)} = \frac{\Delta\bar{\varepsilon}_p^{(n+1)}}{\Delta t^{(n+1)}}; \quad \Delta q_p^{(n+1)} = \beta^{(n)/(n+1)}\Delta w_p^{(n+1)}; \quad \Delta w_p^{(n+1)} = \sigma_y^{(n+1)}\Delta\varepsilon_p^{(n+1)}. \tag{1.9}$$

Table 1
Chemical composition of the investigated steel 20MnCr5 [mass%].

C	Si	Mn	P	S	Cr	Mo	Ni	Cu	Al	N
0.210	0.191	1.350	0.014	0.025	1.270	0.074	0.076	0.149	0.040	0.010

Table 2
Selected reference variables, mean Taylor factor and Burgers length of the investigated material.

T_0 [°C]	$\dot{\varepsilon}_0$ [s^{-1}]	ρ_0 [m^{-2}]	M [–]	b [m]
20	0.01	10^{12}	3.0	2.55×10^{-10}

Table 3
Elastic constants and their temperature sensitivity.

G_0 [GPa]	r^G [–]	s^G [–]	υ [–]	r^υ [–]	s^υ [–]
82.5	−0.095	1.460	0.2888	0.0385	1.0

5. Finite element modeling and simulation

5.1. Material and microstructure

The material used in this study is a case-hardenable steel, 20MnCr5 (1.7147, ASI 5120), which is widely used in industrial forging of automotive components such as bevel gears. The chemical composition measured by optical emission spectroscopy (OES) is presented in Table 1.

Furthermore, the microstructure of the undeformed (as-delivered) material consists of equi-axed ferritic-pearlitic grains. Electron backscatter diffraction (EBSD) was used to analyze the microstructure and the texture of undeformed material.[1] The inverse pole figure (IPF) orientation map of the undeformed material sample showing distribution of grain morphology and orientation is demonstrated in Fig. 5. The orientation and grain size distributions are shown in Fig. 6. Pole figures derived from EBSD measurements of a relatively large area in the plane normal to the symmetry axis of undeformed billet for different crystallographic poles/directions are shown in Fig. 6(a). Furthermore, the grain size distribution calculated based on analysis of EBSD data of the aforementioned large area is shown in Fig. 6(b). According to Fig. 6(b), the effective grain size, which here is defined as the average of mean grain sizes calculated using distribution of grain size number fraction and area fraction is 8.23 μm, for the investigated material. Furthermore, from the evaluated orientation map (Fig. 5) and pole figures (Fig. 6(a)), it can be concluded that the undeformed material has a very weak texture (almost random).

The selected reference variables, Taylor factor and Burgers length of the studied material are listed in Table 2.

[1] EBSD measurements were carried out using a a field emission gun scanning electron microscope (FEG-SEM), JOEL JSM 7000F equipped with an EDAX-TSL Hikari EBSD camera. The measurements are conducted at 20 KeV beam energy, approximately 30 nA probe current, and 100 nm step sInt. J. Plast.. OIM software suite (OIM Data Collection and OIM Analysis v7.3) was used to analyze the data.

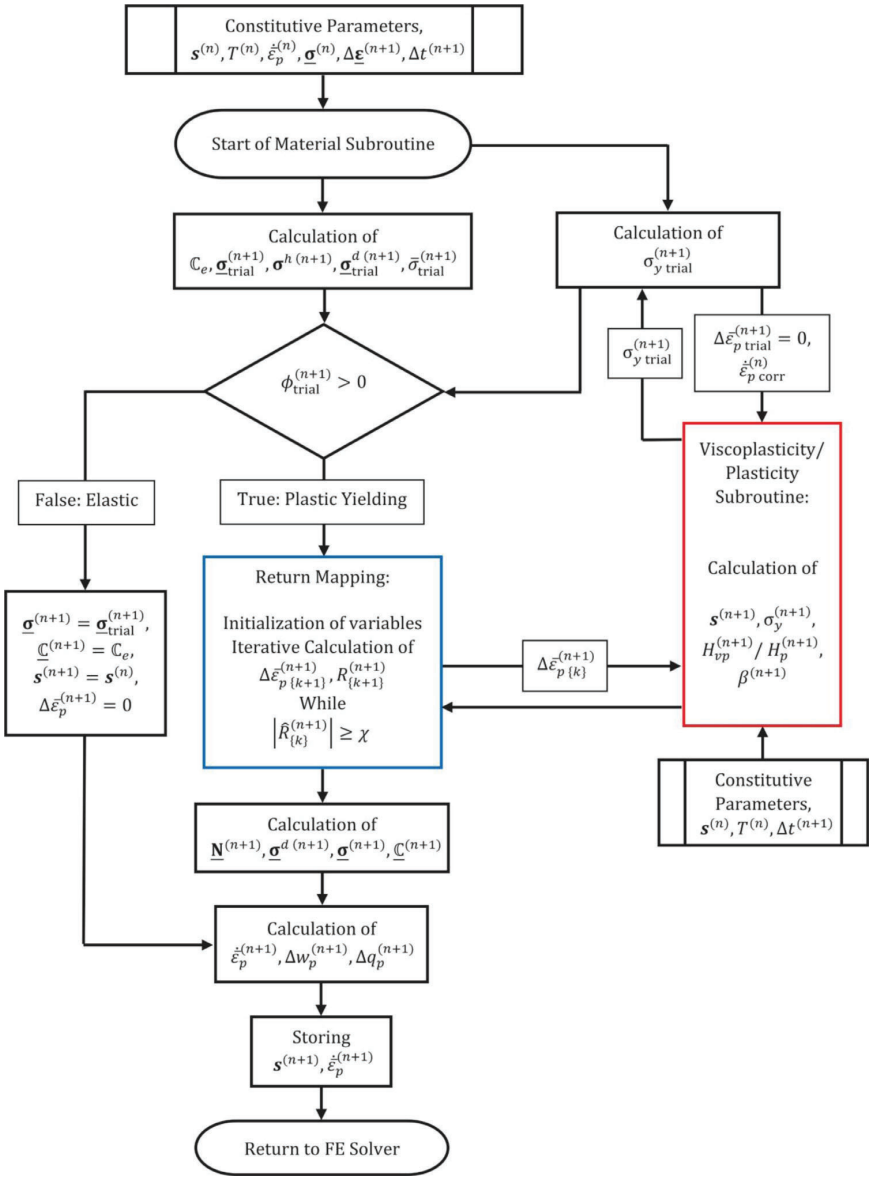

Fig. 3. Flowchart illustration of algorithmic procedure for implementation of microstructural material subroutine; the numerically integrated equations of microstructural constitutive model are programmed in the (visco)plasticity subroutine (red box); return mapping loop (blue box), which calls the (visco)plasticity subroutine iteratively, is implemented within the main material subroutine. (For interpretation of the references to color in this figure legend, the reader is referred to the web version of this article.)

In TMM simulation of HEVP, temperature dependent elastic constants (shear modulus and Poisson's ratio) are required as input. The values of elastic constants are calculated using the JMatPro software for the investigated steel with the composition presented in Table 1. The exported temperature-dependent shear modulus and Poisson's ratio versus temperature were fitted using the familiar temperature-dependence relations (Table 3):

$$\hat{G} = 1 + r^G \left(\hat{T} - 1\right)^{s^G}; \quad \hat{G} \equiv \frac{G}{G_0}; \quad r^G < 0; \quad s^G > 0; \tag{117}$$

$$\hat{\upsilon} = 1 + r^{\upsilon} \left(\hat{T} - 1\right)^{s^{\upsilon}}; \quad \hat{\upsilon} \equiv \frac{\upsilon}{\upsilon_0}; \quad r^{\upsilon} > 0; \quad s^{\upsilon} > 0; \tag{118}$$

where r^G and s^G are temperature sensitivity coefficient and exponent associated with shear modulus (G), respectively; υ is the Poisson's ratio; υ_0 is the Poisson's ratio at reference temperature; and r^{υ} and s^{υ} are temperature sensitivity coefficient and exponent of Poisson's ratio, respectively.

The micro-mechanical constitutive parameters of the studied material are taken from Motaman and Prahl (2019). Constitutive parameters associated with probability amplitude of different dislocation processes, interaction strengths, initial dislocation densities and reference viscous stress for the investigated material are presented in Table 4. The corresponding temperature sensitivity coefficients and exponents are listed Table 5. The constitutive

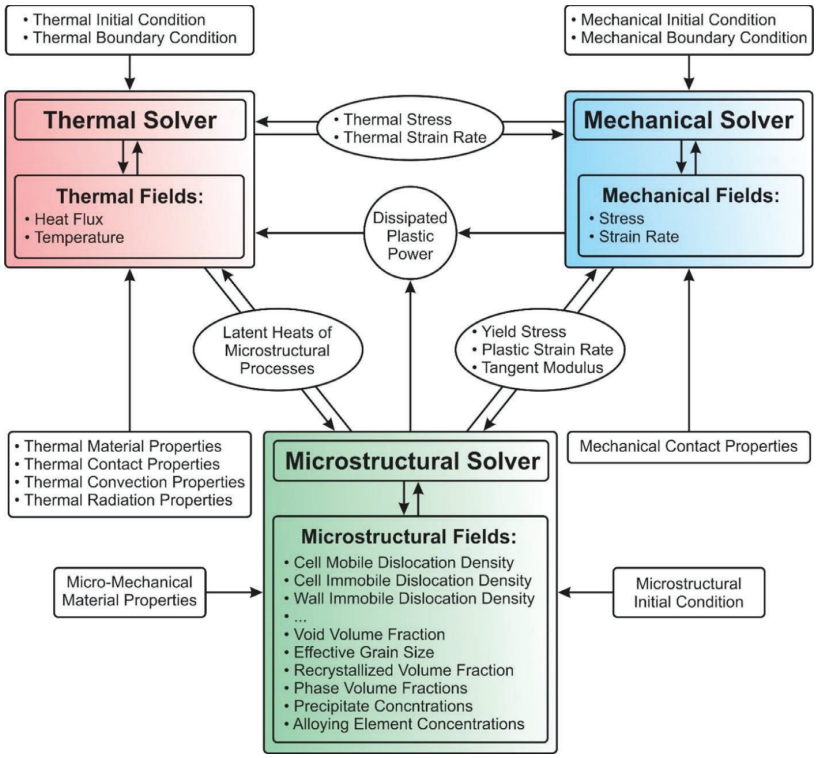

Fig. 4. Block diagram illustrating the interactions among mechanical, thermal and microstructural solvers and fields, initial and boundary conditions, and thermo-micro-mechanical properties in fully coupled TMM-FE simulations.

Table 4
Reference constitutive parameters associated with probability amplitude of different dislocation processes, reference interaction strengths, initial dislocation densities and reference viscous stress for the investigated material.

c_{cm}^{gn} [−]	c_{cm0}^{an} [−]	c_{ci0}^{an} [−]	c_{wi0}^{an} [−]	c_{ci}^{ac} [−]	c_{wi}^{ac} [−]	c_{cm0}^{tr} [−]	c_{wi0}^{nc} [−]
6.2970×10^2	0.1492	0.0133	0.0312	0.4989	0.1280	1.4184	1.5534×10^{-3}
c_{ci0}^{rm} [−]	c_{wi0}^{rm} [−]	$\tilde{\alpha}_{c0}$ [−]	$\tilde{\alpha}_{w0}$ [−]	$\hat{\rho}_{cm0}$ [−]	$\hat{\rho}_{ci0}$ [−]	$\hat{\rho}_{wi0}$ [−]	σ_{v00} [MPa]
0.2261	0.0217	0.1001	0.4725	22.573	26.427	0.9234	318.84

Table 5
Temperature sensitivity coefficients and exponents associated with probability amplitude of different dislocation processes, interaction strengths and viscous stress for the studied material.

r_{cm}^{an} [−]	r_{ci}^{an} [−]	r_{wi}^{an} [−]	r_{cm}^{tr} [−]	r_{wi}^{nc} [−]	r_{ci}^{rm} [−]	r_{wi}^{rm} [−]	$r_{\alpha c}^{G}$ [−]	$r_{\alpha w}^{G}$ [−]	r_v [−]
0.0547	2.0581	0.2045	3.9680	6.1587	5.0910	2.0631	−0.0835	−0.0288	−0.3376
s_{cm}^{an} [−]	s_{ci}^{an} [−]	s_{wi}^{an} [−]	s_{cm}^{tr} [−]	s_{wi}^{nc} [−]	s_{ci}^{rm} [−]	s_{wi}^{rm} [−]	$s_{\alpha c}^{G}$ [−]	$s_{\alpha w}^{G}$ [−]	s_v [−]
8.6725	0.9988	4.0282	1.5593	4.8075	5.5999	3.4306	2.8735	2.5451	0.5115

Table 6
Constitutive parameters associated with strain rate sensitivity of viscous stress and the parameter controlling the dissipation factor.

m_{v0} [−]	r_v^m [−]	s_v^m [−]	m_v^m [−]	κ [−]
0.027	0.0785	5.0	0.0	2.0

parameters associated with strain rate sensitivity of viscous stress together with the parameter controlling the dissipation factor (κ) are presented in Table 6.

Some thermo-physical material properties of the investigated material including specific heat capacity and thermal conductivity as functions of temperature are calculated using JMatPro software and supplied to the FE model. Moreover, temperature-dependent mass density and thermal expansion coefficient (with respect to room temperature, 20 °C) in cold and warm regimes is measured by dilatometry experiments. Thermo-physical properties of the studied 20MnCr5 steel grade as functions of temperature are plotted in Fig. 7.

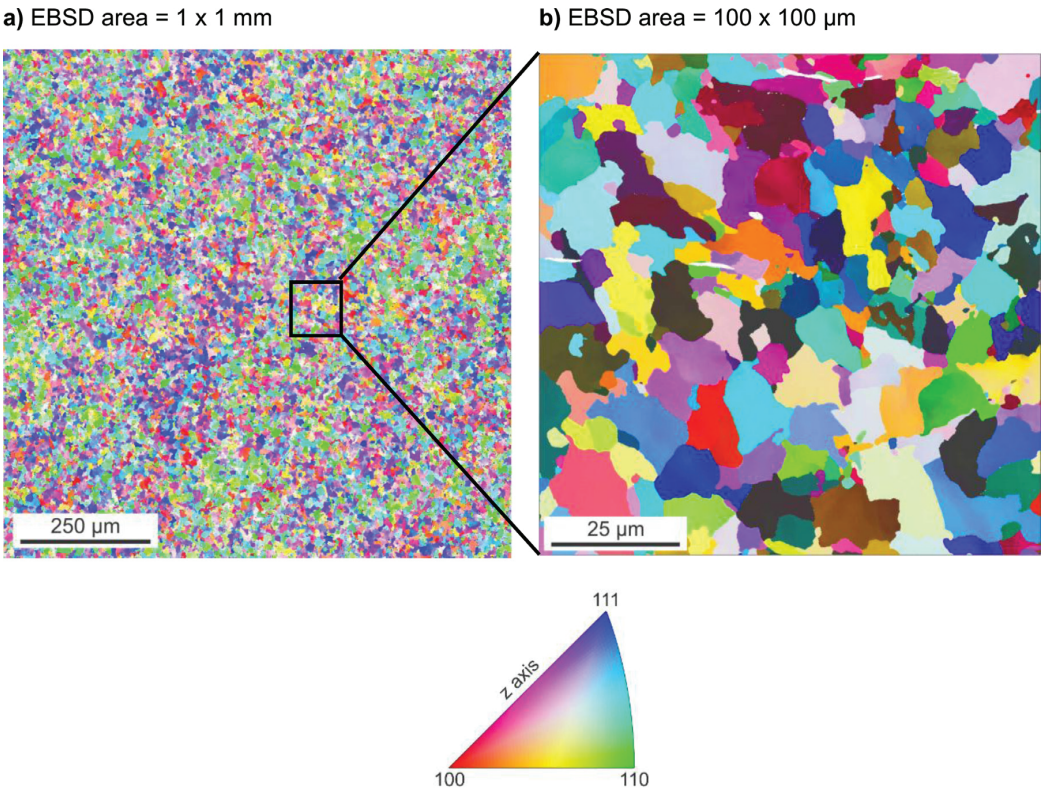

Fig. 5. IPF orientation map in the plane (*x*-*y*) normal to the symmetry axis (*z*) of undeformed cylindrical billet. Grain boundaries were identified as boundaries where the misorientation angle is above 5°. (For interpretation of the references to color in this figure legend, the reader is referred to the web version of this article.)

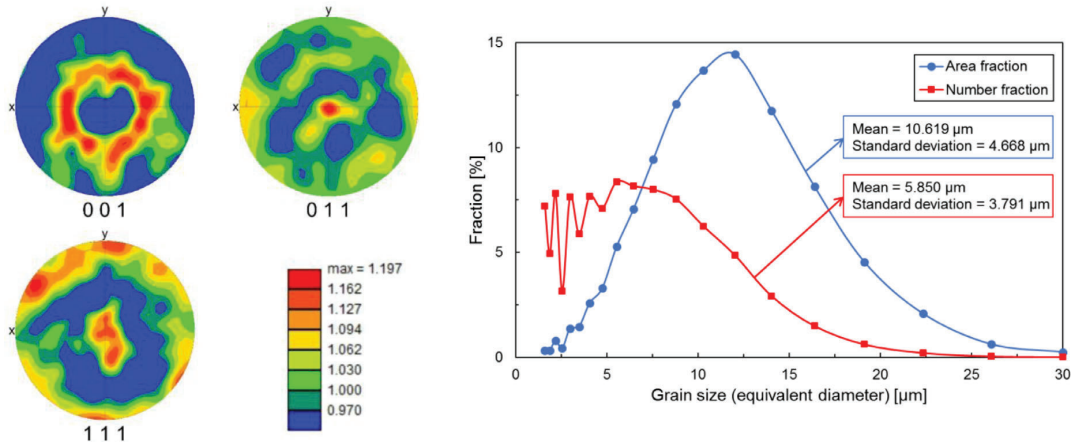

Fig. 6. (a) pole figures calculated from EBSD measurements (1 × 1 mm area) in the plane (*x*-*y*) normal to the symmetry axis (*z*) of undeformed cylindrical billet for different crystallographic directions (001, 011 and 111); (b) grain size distribution calculated based on analysis of the same EBSD data (the mean and standard deviation values are calculated by fitting to normal/lognormal distribution functions). (For interpretation of the references to color in this figure legend, the reader is referred to the web version of this article.)

5.2. Process

An industrial warm forging of a bevel gear shaft for automotive applications has been selected as the warm bulk metal forming process to be thermo-micro-mechanically simulated. The manufacturing process chain (MPC) consists of four steps including two forging hits:

(1) *Preform forging*: the cylindrical forging billet (approximate diameter and length of 54 mm and 112 mm, respectively) is forged in the first forging tool set (punch and die) during 2.5 s. The billet is slightly preheated to about 180 °C (cold regime) just before starting the preform forging operation;
(2) *Interpass*: this step is the short transfer time (2.5 s) between the end of preform forging and the next forging operation

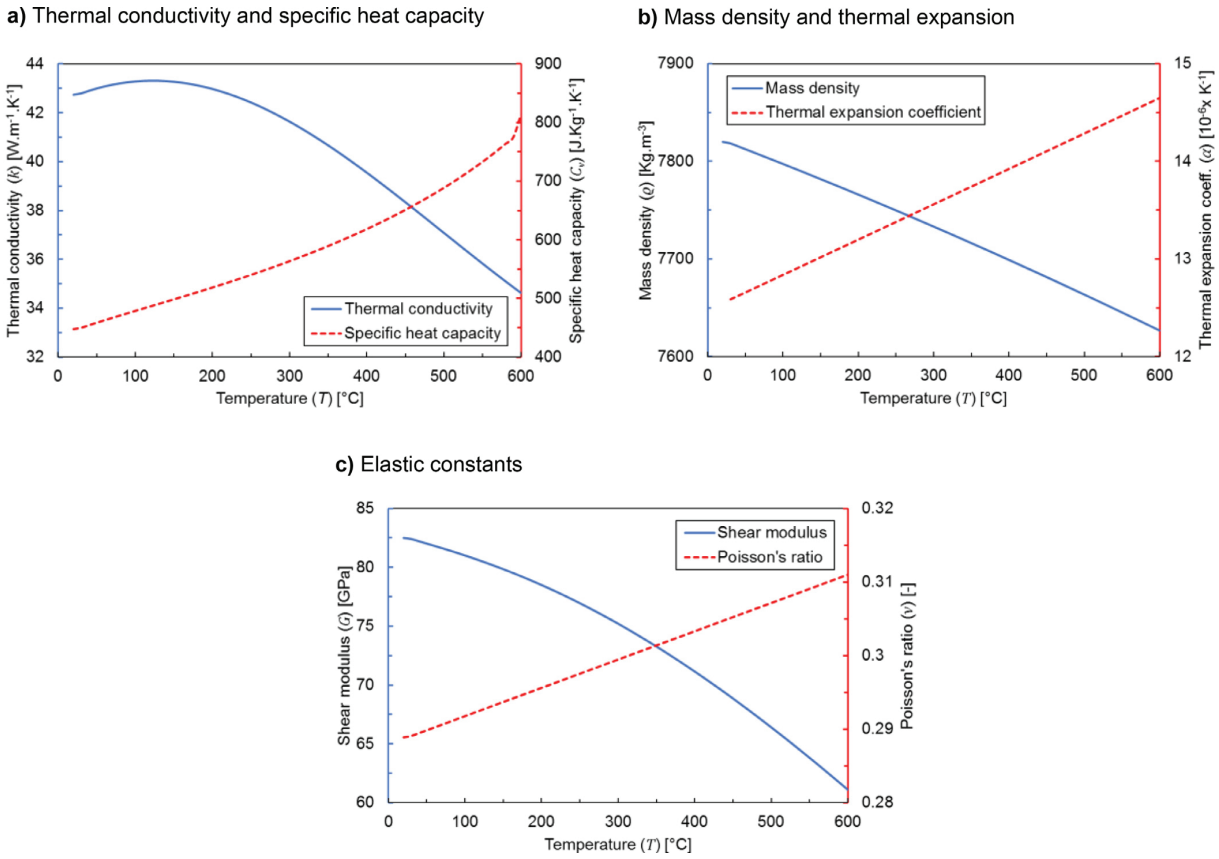

Fig. 7. Thermo-physical properties of the of the investigated 20MnCr5 steel grade as functions of temperature.

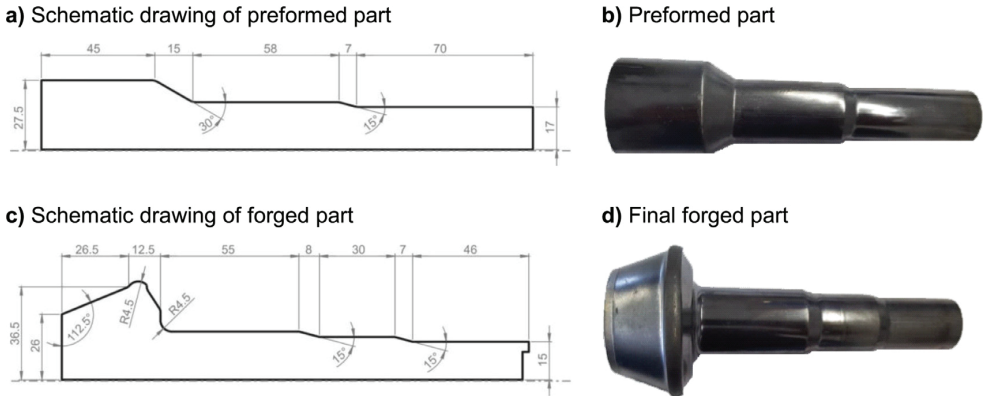

Fig. 8. Preformed and forged parts in production of bevel gear. Dimensions are approximate and in mm.

(final forging). The preformed billet, which is heated up by preheating as well as adiabatic heating and die-contact friction during preform forging, loses some of the absorbed heat and consequently temperature to the ambient environment mostly due to unforced convection and radiation;

(3) *Final forging*: after the interpass stage, the somewhat cooled down preformed billet is again forged in the second tool set during 2 s to reach its final shape; and

(4) *Air cooling*: before performing the subsequent manufacturing processes such as heat treatment and machining on the forged shaft, it is held and consequently reaches the thermal equilibrium at room temperature.

The drawings of radial sections of preformed and (final) forged parts and their images are shown in Fig. 8.

The following thermo-mechanical boundary conditions are imposed (values of properties are obtained by independent experimental measurements):

- Exploiting axisymmetry of all the parts as well as boundary conditions, only a (two-dimensional) radial section of their

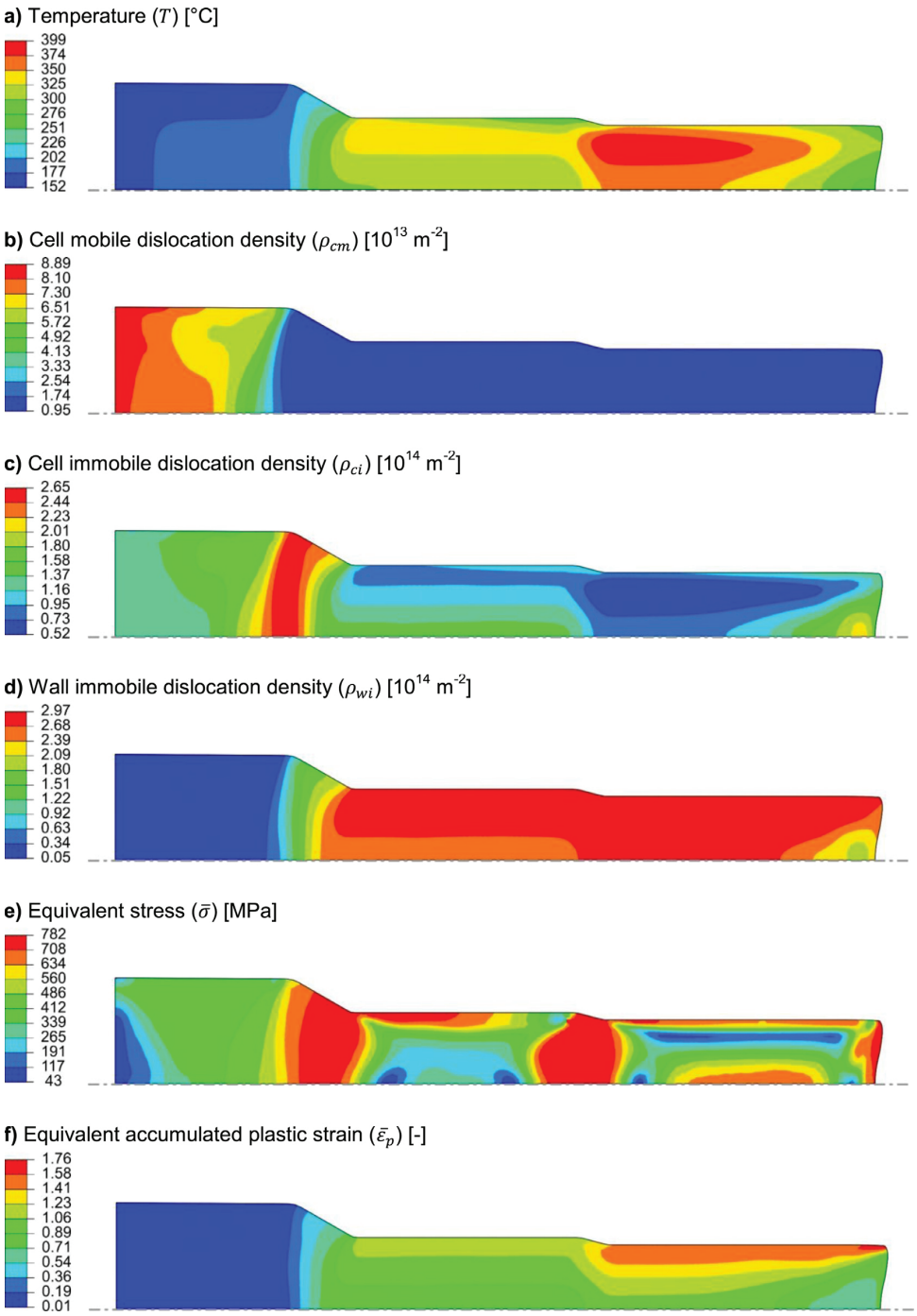

Fig. 9. Distribution of temperature, MSVs (different types of dislocation density), equivalent stress and equivalent accumulated plastic strain at the end of preform forging step (before unloading). (For interpretation of the references to color in this figure legend, the reader is referred to the web version of this article.)

assembly is modeled. Thus, appropriate boundary conditions are set to symmetry axes of all parts.

- Similar to its experimental/industrial counterpart, the forging simulation is displacement-controlled. A constant velocity (vertical) of 40 mm.s^{-1} is prescribed to the punches in both deformation steps. There are periods of acceleration and deceleration of punch, respectively, at the beginning and the end of each forging step, which last for 0.1 s.
- Constant coulomb friction coefficient of 0.05, considering the operation temperature regime and the solid lubricant MoS_2 applied on the actual industrial forging (Altan et al., 2004).
- Total generated heat in contact surfaces due to relative motion of contact master and slave surfaces under non-zero

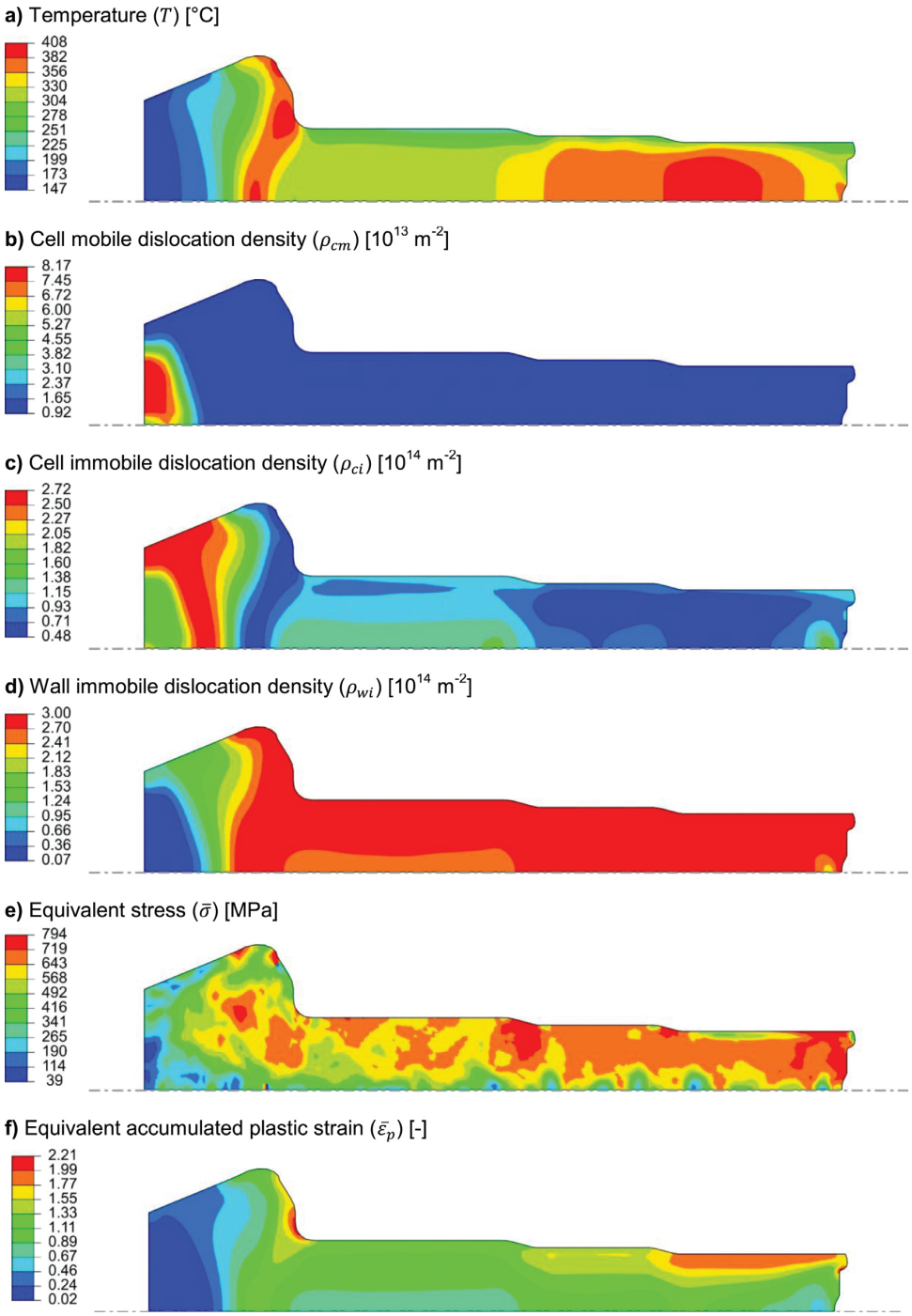

Fig. 10. Distribution of temperature, MSVs (different types of dislocation density), equivalent stress and equivalent accumulated plastic strain at the end of final forging step (before unloading). (For interpretation of the references to color in this figure legend, the reader is referred to the web version of this article.)

contact pressure is evenly divided between the engaged bodies.

- Thermal contact conductance between the billet and tools as a function of contact pressure and clearance.
- Thermal convection and radiation from forging billet's free surfaces to the ambient environment. Assuming constant convection heat transfer coefficient of 15 $Wm^{-2}K^{-1}$ and radiative emissivity coefficient of 0.8 provided an accurate

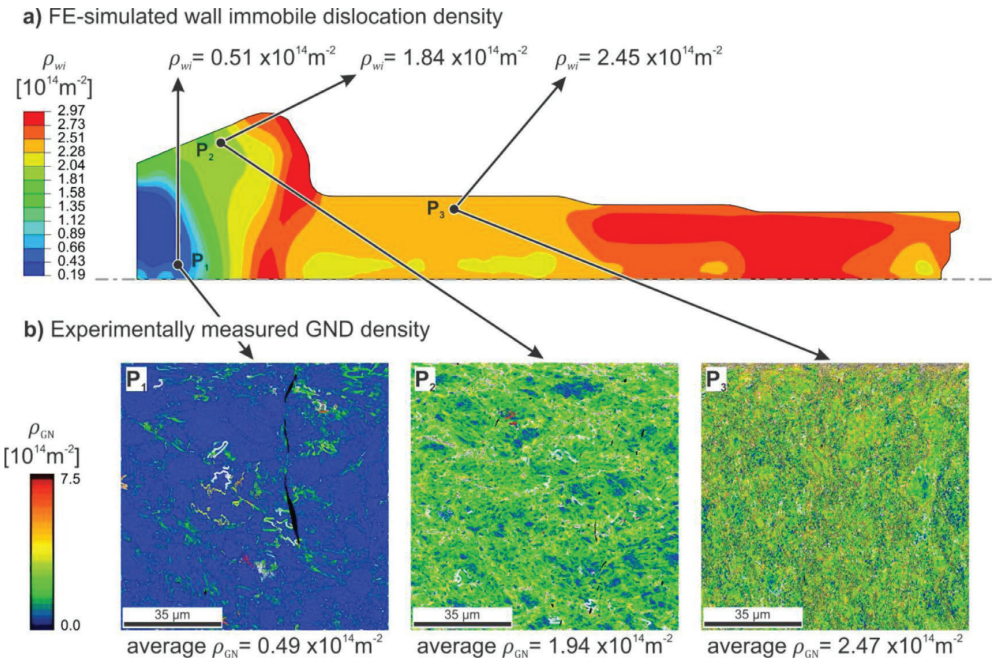

Fig. 11. Comparison between FE-simulated wall immobile dislocation density and the experimentally measured average GND density using high resolution EBSD at different points in the final forged part (the billet is not heated prior to preform forging). (For interpretation of the references to color in this figure legend, the reader is referred to the web version of this article.)

computational prediction of time-temperature loss from a homogenized temperature in warm regime during free cooling in laboratory conditions.

5.3. Results and validation

Given the aforementioned material model and properties as well as the introduced process details and assumptions, FE model of the multistep industrial warm forging of bevel gear is created using the ABAQUS CAE software. A fine biased mesh containing 2960 finite elements (explicit/implicit 4-node linear thermally coupled axisymmetric, bilinear displacement and temperature) is assigned to the billet. The adaptive Lagrangian–Eulerian remeshing (ALE) algorithm is employed in order to prevent severe element distortion and mesh degradation due to large deformation. In addition, for increasing the computational efficiency of the simulation, the mass-scaling factor of 10^3 was applied to the first three steps of the modeled warm forging MPC. Subsequently, the modeled forging MPC is simulated by the thermo-mechanical/temperature-displacement ABAQUS Explicit solver. The simulation was run using the domain-based computational parallelization method and threads-based multiprocessing mode on a single computer having AMD FX^{TM}–6300 6-core processor with the clock rate of 3.50 GHz. The duration of simulation of the first three steps of the warm forging MPC (without the air cooling step) was approximately 99 min. Distribution of temperature, MSVs (different types of dislocation density), equivalent stress and equivalent accumulated plastic strain at the end of preform and final forging steps (before unloading) are respectively shown in Figs. 9 and 10.

All the programmed microstructural solvers coupled with their corresponding explicit and implicit thermal and mechanical solvers of ABAQUS have shown a good convergence and stability in TMM-FE simulation of simple uniaxial compression (upsetting) tests. Nonetheless, many trials of explicit and implicit TMM-FE simulations of forging (of bevel gear) with various microstructural solvers revealed that, in case of proper mass scaling, the most efficient and robust microstructural solver is the one with semi-implicit constitutive integration using stress-based return mapping algorithm, implemented as user-defined material subroutines in ABAQUS Explicit (VUMAT). Nevertheless, quantitative comparison of the performance of different integration schemes, and comparison of the results of conventional thermo-mechanical simulations with those of thermo-micro-mechanical simulations are out of scope of the present paper; however, they will make interesting topics for future research.

Although the microstructural constitutive model is validated comprehensively through simple uniaxial compression experiments (Motaman and Prahl, 2019), it still required further validation using experimental deformation under much more complex loading condition (varying temperature, strain rate and stress state) such as the one exists in industrial bulk metal forming processes. TMM-FE simulation of bevel gear is validated by measurement of geometrically necessary dislocation (GND) density (ρ_{GN}) using high resolution EBSD, as well as experimental punch force. In order to examine the simulated GND density, which by definition is equal to the wall immobile dislocation density (ρ_{wi}), several samples are cut from different regions of the final forged product. From each specimen, an EBSD sample is prepared. Comparison between FE-simulated wall immobile dislocation density and the measured average GND density using EBSD in the final forged part,[2] which

[2] Sample preparation for EBSD involved standard mechanical polishing to 0.05 μm, followed by electropolishing in a 5% perchloric acid and 95% acetic acid solution (by volume) with an applied voltage of 35 V. Measurements are performed using a field emission gun scanning electron microscope (FEG-SEM), JOEL JSM 7000F, at 20 KeV beam energy, approximately 30 nA probe current, and 100-300 nm

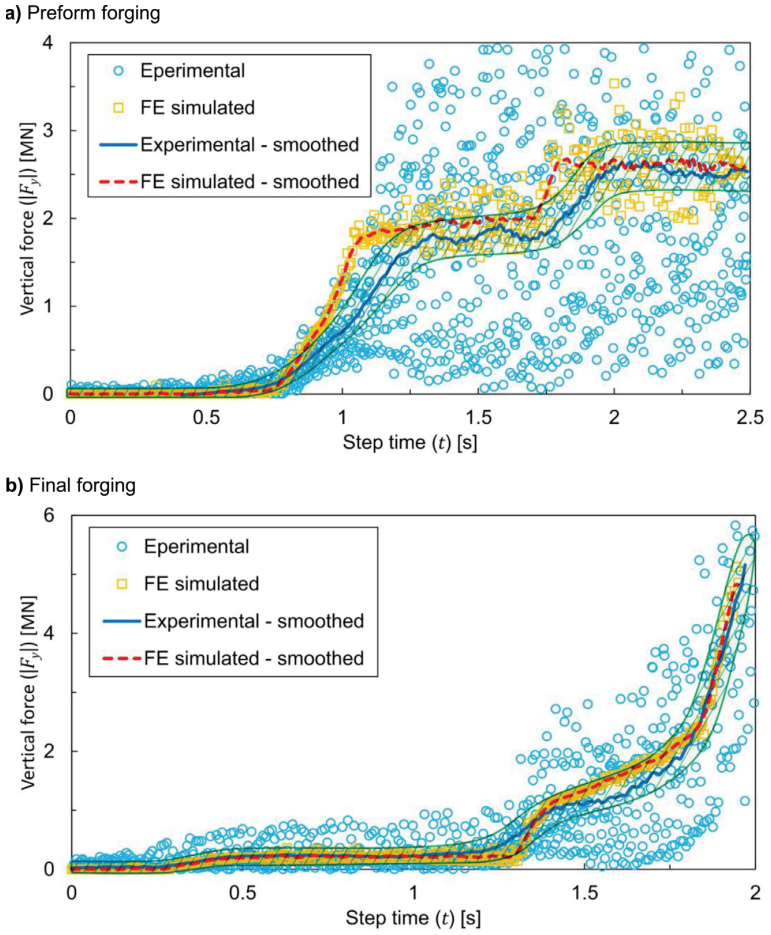

Fig. 12. FE-simulated and experimental punch normal force response versus time in the preform and final forging steps. The unavoidable noise existing in the experimental force plots is associated with the relatively high force and the trade-off between accuracy and stiffness of force measuring devices. The lower and upper bounds of the green hatched area (confidence interval) that surrounds the smoothed experimental curve are drawn based on the precision of the force measuring device as well as the maximum and minimum peaks of the applied various smoothing algorithms. (For interpretation of the references to color in this figure legend, the reader is referred to the web version of this article.)

is manufactured without preheating of the billet prior to preform forging step, is shown in Fig. 11.

Comparison of distribution of wall immobile dislocation density (ρ_{wi}) in the final forged parts manufactured with preheating (prior to preform forging) to 180 °C (Fig. 10(d)) and without preheating (Fig. 11(a)) reveals that preheating has a significant influence on the distribution of ρ_{wi} and its mean value. In the preheated case, the final forged product has a more homogenous distribution of ρ_{wi}; and the mean ρ_{wi} has a larger value. This will result in a more homogenous grain size distribution and finer grains after recrystallization annealing, which is one of the subsequent steps in the manufacturing process chain of the bevel gear. The reason is that $\rho_{wi} = \rho_{GN}$ is the principal driving force for recrystallization because it is the only source of micro-scale residual stresses due to crystal lattice distortions. There is another advantage in the preheating: it lowers the rate of damage accumulation since viscoplastic deformation of ferritic steels in warm regime is followed by a relatively high plastic hardening due to dynamic strain aging (DSA); and generally higher plastic hardening means lower rate of damage accumulation (nucleation and growth of micro-voids).

The FE-simulated normal force responses of the punches versus time in the preform and final forging steps are compared to their experimental counterparts in Fig. 12.

6. Concluding remarks

In the introduced method, addition of the microstructural solver, which computes the microstructure/properties evolution, to the main thermal and mechanical solvers enabled fully coupled thermo-micro-mechanical simulation. Since in the cold and warm regimes, (by definition) the microstructure variables are solely the dislocation structures and their associated dislocation densities, by the assumption of isotropy (which is valid for bulk metal forming of initially textureless materials), the state of microstructure of final product and its flow properties as well as the thermo-mechanical aspects of the process were fully determined. The approach proposed and executed in this study has proven to be a sustainable and perhaps the only (computational) solution for

step size. A Hikari EBSD camera by Ametek-EDAX, in combination with the OIM software suite (OIM Data Collection and OIM Analysis v7.3) by EDAX-TSL, is used for data acquisition and analysis. Subsequently, at each point, GND density is calculated from kernel average misorientation (KAM), which is the average angular deviation between a point and its neighbors in a distance twice the step size as long as their misorientation does not exceed 5°. After mapping KAM values to GND density, over a representative material area with the size of $100 \times 100\,\mu$m, the average GND density is calculated.

comprehensive and simultaneous design of product and process. In summary:

- The theory of continuum finite strain for isotropic hypoelasto-viscoplasticity has been reformulated in the format of rate equations (without using accumulated strain scalars and tensors). This is the only feasible way for correct integration of a microstructural constitutive model based on microstructural state variables (e.g., dislocation densities). Moreover, integration of the microstructural constitutive model using various schemes has been explained in detail.
- The proposed method has shown to be computationally efficient and applicable in industrial scale for optimization of process parameters and tools with respect to properties and microstructure of final products. The cost of TMM implicit FE simulations is higher by orders of magnitude compared to their explicit counterparts. Moreover, the performance of TMM explicit FE simulations with the proposed stress-based return mapping for hypoelasto-viscoplasticity is considerably higher than those performed using strain-based return mapping.
- For the first time, an industrial metal forming process has been thermo-micro-mechanically simulated, and become validated not only by experimental force-displacement but also using measured microstructural state variables, i.e. dislocation density, at different points in the actual final product.

Acknowledgments

Authors appreciate the support received under the project “IGF-Vorhaben 18531N” in the framework of research program of “Integrierte Umform und Wärmebehandlungssimulation für Massivumformteile (InUWäM)” funded by the German federation of industrial research associations (AiF). The support provided by the project “Laserunterstütztes Kragenziehen hochfester Bleche” from the research association EFB e.V. funded under the number 18277N by AiF is as well gratefully acknowledged. The authors also wish to thank “Schondelmaier GmbH Presswerk” for performing experimental forging.

Supplementary materials

Supplementary materials associated with this article are available in the GitHub repository GitHub.com/SAHMotaman/TMM-FE-Simulation:

- Animations of warm forging simulation with demonstration of evolving variables (temperature, equivalent plastic strain rate, stress and MSVs).
- Fortran scripts of the microstructural solver including user-defined material subroutines in ABAQUS Explicit (VUMAT) and ABAQUS Standard/implicit (UMAT) with semi-implicit and fully-implicit constitutive integration schemes using both stress-based and strain-based return mapping algorithms.
- FE models of ABAQUS Standard and ABAQUS Explicit (CAE and INP formats) for uniaxial compression/upsetting test at different (true) strain rates.
- FE models of ABAQUS Standard and ABAQUS Explicit (CAE and INP formats) for cold and warm forging of bevel gear.

References

ABAQUS, 2014. ABAQUS 6.14 Users's Manual and Theory Guide. Dassault Systemes Simulia Corp, , Providence, RI, USA.
Altan, T., Ngaile, G., Shen, G., 2004. Cold and Hot Forging: Fundamentals and Applications. ASM International, Materials Park, OH ix, 341.
Álvarez Hostos, J.C., Bencomo, A.D., Puchi Cabrera, E.S., Guérin, J.-D., Dubar, L., 2018. Modeling the viscoplastic flow behavior of a 20MnCr5 steel grade deformed under hot-working conditions, employing a meshless technique. Int. J. Plast. 103, 119–142. doi:10.1016/j.ijplas.2018.01.005.
Aravas, N., 1987. On the numerical integration of a class of pressure-dependent plasticity models. Int. J. Numer. Meth. Eng. 24, 1395–1416. doi:10.1002/nme.1620240713.
Arsenlis, A., Parks, D., 1999. Crystallographic aspects of geometrically-necessary and statistically-stored dislocation density. Acta Mater. 47, 1597–1611. doi:10.1016/S1359-6454(99)00020-8.
Ashby, M.F., 1970. The deformation of plastically non-homogeneous materials. Philos. Mag. 21, 399–424. doi:10.1080/14786437008238426.
Belytschko, T., Liu, W.K., Moran, B., Elkhodary, K.I., 2014. Nonlinear Finite Elements for Continua and Structures. Hoboken, New Jersey; Wiley, Chichester, West Sussex, UK 1 online resource.
Berisha, B., Hora, P., Wahlen, A., Tong, L., 2010. A combined isotropic-kinematic hardening model for the simulation of warm forming and subsequent loading at room temperature. Int. J. Plast. 26, 126–140. doi:10.1016/j.ijplas.2009.06.001.
Bok, H.-H., Choi, J., Barlat, F., Suh, D.W., Lee, M.-G., 2014. Thermo-mechanical-metallurgical modeling for hot-press forming in consideration of the prior austenite deformation effect. Int. J. Plast. 58, 154–183. doi:10.1016/j.ijplas.2013.12.002.
Brnic, J., Turkalj, G., Lanc, D., Canadija, M., Brcic, M., Vukelic, G., 2014. Comparison of material properties: steel 20MnCr5 and similar steels. J. Construct. Steel Res. 95, 81–89. doi:10.1016/j.jcsr.2013.11.024.
Choi, C., Groseclose, A., Altan, T., 2012. Estimation of plastic deformation and abrasive wear in warm forging dies. J. Mater. Process. Technol. 212, 1742–1752. doi:10.1016/j.jmatprotec.2012.03.023.
Columbus, D., Grujicic, M., 2002. A comparative discrete-dislocation/nonlocal crystal-plasticity analysis of plane-strain mode I fracture. Mater. Sci. Eng. 323, 386–402. doi:10.1016/S0921-5093(01)01397-1.
de-Borst, R., Heeres, O.M., 2002. A unified approach to the implicit integration of standard, non-standard and viscous plasticity models. Int. J. Numer. Anal. Meth. Geomech. 26, 1059–1070. doi:10.1002/nag.234.
de-Borst, R., Verhoosel, C.V., Remmers, J.J.C., 2014. Nonlinear Finite Element Analysis of Solids and Structures. Wiley, Hoboken, N.J. 1 online resource.
de-Souza Neto, E., Peric, D., Owens, D., 2008. Computational Methods for Plasticity: Theory and Applications. Wiley, Chichester, UK 1 online resource (xxii, 791.
Doghri, I., 2000. Mechanics of Deformable Solids. Springer, Berlin XVIII-579.
Doherty, R.D., Hughes, D.A., Humphreys, F.J., Jonas, J.J., Jensen, D., Kassner, M.E., King, W.E., McNelley, T.R., McQueen, H.J., Rollett, A.D., 1997. Current issues in recrystallization: a review. Mater. Sci. Eng. 238, 219–274. doi:10.1016/S0921-5093(97)00424-3.
Dunne, F., 2011. Introduction to Computational Plasticity. Oxford University Press, Oxford 241 S.
Eringen, A., 1983. Theories of nonlocal plasticity. Int. J. Eng. Sci. 21, 741–751. doi:10.1016/0020-7225(83)90058-7.
Estrin, Y., Kubin, L.P., 1986. Local strain hardening and nonuniformity of plastic deformation. Acta Metall. 34, 2455–2464. doi:10.1016/0001-6160(86)90148-3.
Field, J.E., Walley, S.M., Proud, W.G., Goldrein, H.T., Siviour, C.R., 2004. Review of experimental techniques for high rate deformation and shock studies. Int. J. Impact Eng. 30, 725–775. doi:10.1016/j.ijimpeng.2004.03.005.
Follansbee, P.S., Kocks, U.F., 1988. A constitutive description of the deformation of copper based on the use of the mechanical threshold stress as an internal state variable. Acta Metall. 36, 81–93. doi:10.1016/0001-6160(88)90030-2.
Galindo-Nava, E.I., Rae, C., 2016. Microstructure-sensitive modelling of dislocation creep in polycrystalline FCC alloys: orowan theory revisited. Mater. Sci. Eng. 651, 116–126. doi:10.1016/j.msea.2015.10.088.
Gao, H., Huang, Y., 2001. Taylor-based nonlocal theory of plasticity. Int. J. Solids Struct. 38, 2615–2637. doi:10.1016/S0020-7683(00)00173-6.
Gao, H., Huang, Y., 2003. Geometrically necessary dislocation and size-dependent plasticity. Scr. Mater. 48, 113–118. doi:10.1016/S1359-6462(02)00329-9.
Green, A.E., Naghdi, P.M., 1965. A general theory of an elastic-plastic continuum. Arch. Rational Mech. Anal. 18, 251–281. doi:10.1007/BF00251666.
Green, A.E., Naghdi, P.M., 1971. Some remarks on elastic-plastic deformation at finite strain. Int. J. Eng. Sci. 9, 1219–1229. doi:10.1016/0020-7225(71)90086-3.
Guan, Y., Bai, X., Liu, M., Song, L., Zhao, G., 2015. Preform design in forging process of complex parts by using quasi-equipotential field and response surface methods. Int. J. Adv. Manuf. Technol. 79, 21–29. doi:10.1007/s00170-014-6775-6.
Hartley, P., Pillinger, I., 2006. Numerical simulation of the forging process. Comput. Methods Appl. Mech. Eng. 195, 6676–6690. doi:10.1016/j.cma.2005.03.013.
Heeres, O.M., Suiker, A.S., Borst, R. de, 2002. A comparison between the Perzyna viscoplastic model and the Consistency viscoplastic model. Eur. J. Mech. 21, 1–12. doi:10.1016/S0997-7538(01)01188-3.
Horstemeyer, M.F., Bammann, D.J., 2010. Historical review of internal state variable theory for inelasticity. Int. J. Plast. 26, 1310–1334. doi:10.1016/j.ijplas.2010.06.005.
Hughes, D., Hansen, N., Bammann, D., 2003. Geometrically necessary boundaries, incidental dislocation boundaries and geometrically necessary dislocations. Scr. Mater. 48, 147–153. doi:10.1016/S1359-6462(02)00358-5.
Hughes, T.J.R., Winget, J., 1980. Finite rotation effects in numerical integration of rate constitutive equations arising in large-deformation analysis. Int. J. Numer. Meth. Eng. 15, 1862–1867. doi:10.1002/nme.1620151210.
Johnson, G.C., Bammann, D.J., 1984. A discussion of stress rates in finite deformation problems. Int. J. Solids .Struct. 20, 725–737. doi:10.1016/0020-7683(84)90061-1.
Kassner, M.E., Geantil, P., Levine, L.E., 2013. Long range internal stresses in single-phase crystalline materials. Int. J. Plast. 45, 44–60. doi:10.1016/j.ijplas.2012.10.003.

Khan, A.S., Huang, S., 1995. Continuum Theory of Plasticity. John Wiley & Sons, Estados Unidos, p. 421.
Kim, H., Yagi, T., Yamanaka, M., 2000. FE simulation as a must tool in cold/warm forging process and tool design. J. Mater. Process. Technol. 98, 143–149. doi:10.1016/S0924-0136(99)00190-9.
Kröner, E., 1959. Allgemeine kontinuumstheorie der versetzungen und eigenspannungen. Arch. Ration. Mech. Anal. 4, 273–334. doi:10.1007/BF00281393.
Kumar, A., Hauser, F., Dorn, J., 1968. Viscous drag on dislocations in aluminum at high strain rates. Acta Metall. 16, 1189–1197. doi:10.1016/0001-6160(68)90054-0.
Lee, E.H., 1969. Elastic-plastic deformation at finite strains. J. Appl. Mech. 36, 1. doi:10.1115/1.3564580.
Lee, E.H., Liu, D.T., 1967. Finite-strain elastic—plastic theory with application to plane-wave analysis. J. Appl. Phys. 38, 19–27. doi:10.1063/1.1708953.
Lee, J.-J., Jung, U.-J., Park, G.-J., 2013. Shape optimization of the workpiece in the forging process using equivalent static loads. Finite Elem. Anal. Des. 69, 1–18. doi:10.1016/j.finel.2013.01.005.
Mecking, H., Kocks, U.F., 1981. Kinetics of flow and strain-hardening. Acta Metall. 29, 1865–1875. doi:10.1016/0001-6160(81)90112-7.
Motaman, S.A.H., Prahl, U., 2019. Microstructural constitutive model for polycrystal viscoplasticity in cold and warm regimes based on continuum dislocation dynamics. J. Mech. Phys. Solids 122, 205–243. doi:10.1016/j.jmps.2018.09.002.
Mourad, H.M., Bronkhorst, C.A., Addessio, F.L., Cady, C.M., Brown, D.W., Chen, S.R., Gray, G.T., 2014. Incrementally objective implicit integration of hypoelastic–viscoplastic constitutive equations based on the mechanical threshold strength model. Comput. Mech. 53, 941–955. doi:10.1007/s00466-013-0941-9.
Mughrabi, H., 1987. A two-parameter description of heterogeneous dislocation distributions in deformed metal crystals. Mater. Sci. Eng. 85, 15–31. doi:10.1016/0025-5416(87)90463-0.
Mughrabi, H., 2006. Dual role of deformation-induced geometrically necessary dislocations with respect to lattice plane misorientations and/or long-range internal stresses. Acta Mater. 54, 3417–3427. doi:10.1016/j.actamat.2006.03.047.
Nemat-Nasser, S., 1979. Decomposition of strain measures and their rates in finite deformation elastoplasticity. Int. J. Solids Struct. 15, 155–166. doi:10.1016/0020-7683(79)90019-2.
Ortiz, M., Popov, E.P., 1985. Accuracy and stability of integration algorithms for elastoplastic constitutive relations. Int. J. Numer. Meth. Eng. 21, 1561–1576. doi:10.1002/nme.1620210902.
Ou, H., Wang, P., Lu, B., Long, H., 2012. Finite element modelling and optimisation of net-shape metal forming processes with uncertainties. Comput. Struct. 90-91, 13–27. doi:10.1016/j.compstruc.2011.10.014.
Perzyna, P., 1966. Fundamental problems in viscoplasticity. In: Chernyi, G.G. (Ed.). In: Advances in Applied Mechanics, vol. 9. Academic Press, New York, pp. 243–377.
Puchi-Cabrera, E.S., Guérin, J.-D., Dubar, M., Staia, M.H., Lesage, J., Chicot, D., 2014. Constitutive description for the design of hot-working operations of a 20MnCr5 steel grade. Mater. Des. 62, 255–264. doi:10.1016/j.matdes.2014.05.011.
Puchi-Cabrera, E.S., Staia, M.H., Guérin, J.D., Lesage, J., Dubar, M., Chicot, D., 2013. Analysis of the work-hardening behavior of C–Mn steels deformed under hot-working conditions. Int. J. Plast. 51, 145–160. doi:10.1016/j.ijplas.2013.05.007.
Reina, C., Fokoua Djodom, L., Ortiz, M., Conti, S., 2018. Kinematics of elasto-plasticity: validity and limits of applicability of F=FeFp for general three-dimensional deformations. J. Mech. Phys. Solids 121, 99–113. doi:10.1016/j.jmps.2018.07.006.
Rice, J.R., 1970. On the structure of stress-strain relations for time-dependent plastic deformation in metals. J. Appl. Mech. 37, 728. doi:10.1115/1.3408603.
Rice, J.R., 1971. Inelastic constitutive relations for solids: an internal-variable theory and its application to metal plasticity. J. Mech. Phys. Solids 19, 433–455. doi:10.1016/0022-5096(71)90010-X.
Rosakis, P., Rosakis, A.J., Ravichandran, G., Hodowany, J., 2000. A thermodynamic internal variable model for the partition of plastic work into heat and stored energy in metals. J. Mech. Phys. Solids 48, 581–607. doi:10.1016/S0022-5096(99)00048-4.
Sedighi, M., Tokmechi, S., 2008. A new approach to preform design in forging process of complex parts. J. Mater. Process. Technol. 197, 314–324. doi:10.1016/j.jmatprotec.2007.06.043.
Sherby, O.D., Burke, P.M., 1968. Mechanical behavior of crystalline solids at elevated temperature. Progress Mater. Sci. 13, 323–390. doi:10.1016/0079-6425(68)90024-8.
Simo, J.C., Hughes, T.J.R., 1998. Computational Inelasticity. Springer, New York 1 online resource (xiv, 392).
Taylor, G.I., Quinney, H., 1934. The latent energy remaining in a metal after cold working. Proc. R. Soc. A 143, 307–326. doi:10.1098/rspa.1934.0004.
Truesdell, C., Noll, W., 1965. The non-linear field theories of mechanics. In: Truesdell, C., Noll, W., Antman, S.S. (Eds.), The Non-Linear Field Theories of Mechanics. Springer, Berlin Heidelberg, Berlin, Heidelberg, pp. 1–579.
Vazquez, V., Altan, T., 2000. Die design for flashless forging of complex parts. J. Mater. Process. Technol. 98, 81–89. doi:10.1016/S0924-0136(99)00308-8.
Voyiadjis, G.Z., Al-Rub, R.K.A., 2005. Gradient plasticity theory with a variable length scale parameter. Int. J. Solids Struct. 42, 3998–4029. doi:10.1016/j.ijsolstr.2004.12.010.
Wang, W.M., Sluys, L.J., Borst, R. de, 1997. Viscoplasticity for instabilities due to strain softening and strain-rate softening. Int. J. Numer. Meth. Engng. 40, 3839–3864 10.1002/(SICI)1097-0207(19971030)40:20<3839:AID-NME245>3.0.CO;2-6.
Xianghong, W., Guoqun, Z., Yiguo, L., Xinwu, M., 2006. Numerical simulation and die structure optimization of an aluminum rectangular hollow pipe extrusion process. Mater. Sci. Eng. 435-436, 266–274. doi:10.1016/j.msea.2006.06.114.
Zaera, R., Fernández-Sáez, J., 2006. An implicit consistent algorithm for the integration of thermoviscoplastic constitutive equations in adiabatic conditions and finite deformations. Int. J. Solids Struct. 43, 1594–1612. doi:10.1016/j.ijsolstr.2005.03.070.
Zehnder, A.T., 1991. A model for the heating due to plastic work. Mech. Res. Commun. 18, 23–28. doi:10.1016/0093-6413(91)90023-P.
Zhao, X., Zhao, G., Wang, G., Wang, T., 2002. Preform die shape design for uniformity of deformation in forging based on preform sensitivity analysis. J. Mater. Process. Technol. 128, 25–32. doi:10.1016/S0924-0136(02)00054-7.

3.3. Paper III

S.A.H. Motaman, F. Roters, C. Haase: Anisotropic polycrystal plasticity due to microstructural heterogeneity - A multi-scale experimental and numerical study on additively manufactured metallic materials.
Acta Materialia 185 (2020): 340–369, ISSN: 1359-6454.
doi: 10.1016/j.actamat.2019.12.003.

Acta Materialia 185 (2020) 340–369

Contents lists available at ScienceDirect

Acta Materialia

journal homepage: www.elsevier.com/locate/actamat

Full length article

Anisotropic polycrystal plasticity due to microstructural heterogeneity: A multi-scale experimental and numerical study on additively manufactured metallic materials

S. Amir H. Motaman[a,*], Franz Roters[b], Christian Haase[a,*]

[a] Institut für Eisenhüttenkunde, RWTH Aachen University, Intzestraße 1, 52072 Aachen, Germany
[b] Max-Planck-Institut für Eisenforschung GmbH, Max-Planck-Straße 1, 40237 Düsseldorf, Germany

ARTICLE INFO

Article history:
Received 17 July 2019
Revised 29 November 2019
Accepted 2 December 2019
Available online 3 December 2019

Keywords:
Anisotropic plasticity
Microstructural heterogeneity
Additive manufacturing
Powder bed fusion
High-manganese steel
Twinning-induced plasticity
Crystal plasticity modeling
Physics-based constitutive modeling
Representative volume element

ABSTRACT

Additively manufactured (AM) metallic parts exhibit substantially different microstructures compared to those that are conventionally produced. Characterization studies have revealed that the microstructure of as-built AM metallic materials is highly heterogeneous in many respects. The strongly anisotropic mechanical response under plastic deformation observed in AM metals, compared to their conventionally manufactured counterparts, lies in the aforementioned inherent microstructural disparities. In this study, we have focused on a high-manganese steel (HMnS) processed by laser powder bed fusion (LPBF), which exhibits twinning-induced plasticity (TWIP). The as-built microstructure is carefully characterized by electron backscatter diffraction (EBSD), transmission electron microscopy (TEM) and X-ray diffraction (XRD) techniques. To unfold the potential of metal additive manufacturing, it is essential to understand the microstructure of AM products and its connection with the mechanical properties by means of numerical modeling and simulation. The mechanical response of AM components under plastic deformation is highly complex and its simulation requires advanced modeling and numerical methods. In the present study, in order to simulate the anisotropic plasticity of the LPBF-HMnS, we used the full field method for computational polycrystal homogenization combined with physics-based crystal plasticity constitutive and statistical microstructure modeling. The impact of different process-induced microstructural heterogeneity characteristics on macroscopic strain hardening behavior of the material has been comprehensively and systematically investigated. Finally, it has been argued why the chosen AM material with the selected processing parameters and chemical composition represented an ideal candidate for a generic assessment of the anisotropic polycrystal plasticity due to microstructural heterogeneity.

1. Introduction

Metal additive manufacturing (AM) offers enormous potential for rapid production of net-shaped, geometrically complex, lightweight and customized metallic parts for aerospace, automotive, energy and biomedical applications without the need for expensive tools required in conventional manufacturing [1–4]. The metal AM technologies enable the production of fully dense bulk volumes in a layer-wise fashion by melting a powder or wire feedstock using a high power density source such as laser, electron beam or plasma arc, as opposed to conventional casting, subtractive or formative manufacturing processes. Metal AM technologies are divided into powder bed fusion (PBF) techniques, e.g. laser powder bed fusion (LPBF) often referred to as selective laser melting (SLM), and directed energy deposition (DED) processes, e.g. wire or powder laser directed energy deposition (LDED), also known as laser metal deposition (LMD) [3].

While geometrical aspects during AM are highly controllable, so far the biggest challenge is the tailoring of the microstructure and mechanical properties of AM products [1,2,5–8]. Therefore, establishing a quantitative linkage among process-microstructure-properties is imperative for design and optimization [9] and consequently essential for a widespread adoption of AM structurally critical load bearing components [8,10,11]. Given the complexity of metal AM processes and as-built/as-deposited/as-fabricated microstructures, multi-scale and multi-physics integrated computational materials engineering (ICME) seems to be a viable solution [1,6,8,10–13].

It is well known that the AM process parameters significantly influence the microstructure [1,7,14,15]. The localized melt pool

* Corresponding authors.
E-mail addresses: seyedamirhossein.motaman@iehk.rwth-aachen.de (S.A.H. Motaman), christian.haase@iehk.rwth-aachen.de (C. Haase).

https://doi.org/10.1016/j.actamat.2019.12.003
1359-6454/

shape and size, scanning strategy, epitaxial nucleation and growth, high thermal gradient, high cooling/heating rate, and thermal cycles resulting from the repeated deposition of newly molten layers result in the evolution of highly heterogeneous microstructure (strong texture, inhomogeneous grain morphology, heterogeneous dislocation substructure and elemental segregation) [1,5,15]. The profound anisotropic mechanical response under plastic deformation observed in AM metals, compared to their conventionally manufactured counterparts (with the same chemical composition but relatively homogenous microstructure), originates from these hierarchical microstructural heterogeneities [15–18]. The anisotropy in mechanical behavior is detrimental for applications involving multiaxial stress states.

In the last few years, the impact of process parameters on the development of microstructural heterogeneities [19–39] as well as the effect of process-induced microstructural heterogeneities on anisotropic mechanical properties of different metallic materials have been experimentally investigated for various AM processes [40–58]. However, even though the effect of AM process parameters on microstructural evolution has been explored through modeling and simulation [59–72], so far, literature lacks fine-scale in-depth investigations of the relationship between microstructural heterogeneities of AM metallic materials and their anisotropic mechanical properties.

High-manganese steels (HMnS) are characterized by outstanding mechanical properties, but so far their application has been impeded due to inherent limitations in conventional processing. AM provides an alternative to exploit the unique properties of HMnS due to strongly differing processing conditions [52,73,74]. In this work, a fully austenitic HMnS processed by LPBF is used. The outcome as-built microstructure is carefully characterized by electron backscatter diffraction (EBSD), transmission electron microscopy (TEM) and X-ray diffraction (XRD) techniques. In order to construct a representative volume element (RVE), the characterization data were statistically analyzed to derive a set of parameters, namely the microstructure descriptors, which adequately describe the microstructural heterogeneity characteristics. Subsequently, the generated RVE was used to simulate the anisotropic strain hardening behavior of the LPBF-HMnS by full field method for computational polycrystal homogenization using a spectral solver and a physics-based crystal plasticity constitutive model. Finally, the influence of different process-induced microstructural heterogeneity aspects on the overall polycrystal plasticity was systematically studied.

2. Experimental investigation

2.1. Material

In the present study, a fully austenitic high-Mn steel produced by LPBF process is used. The concept of HMnS is based on stabilizing the austenitic phase by high Mn content, typically between 15 and 30 wt%. Due to a low stacking fault energy (SFE) in the range of 10–50 mJ m^{-2}, multiple deformation mechanisms can be activated in addition to dislocation slip/glide [75–79]. Under uniaxial deformation at a quasi-static strain rate and room temperature, low SFE values ($\leq$18 mJ m^{-2}) coincide with the activation of transformation-induced plasticity (TRIP), while TWIP is triggered in the range between 12 and 50 mJ m^{-2} [80–85]. These additional deformation mechanisms together with the strong planarity of dislocation slip promote a high strain hardening (rate) [80,81,84,86–89]. Since active deformation mechanisms is a function of SFE and hence alloy composition, the mechanical properties can be roughly tailored by alloy screening, e.g. modifying Mn, C or Al contents [81,87,90]. Table 1 lists the chemical composition of the powder and as-built states of the investigated HMnS, which were determined by wet chemical analysis. Pre-alloyed steel and Al powder

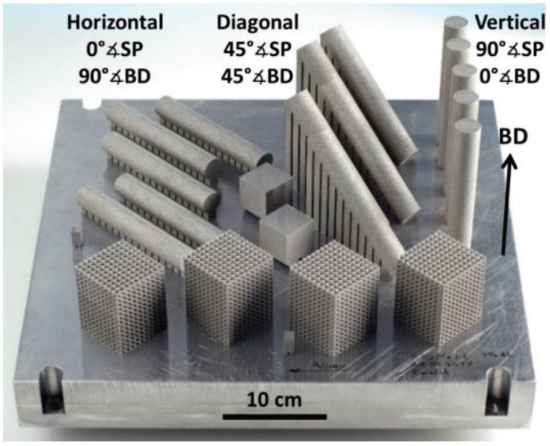

Fig. 1. AM specimens for microstructure characterization and uniaxial testing. Thin-walled support structures were employed at the bottom of each specimen which connects them to the substrate plate (SP).

were homogenized in a Turbula mixer for 1 h and then sieved to guarantee a homogeneous mixture with a powder size between 10 and 45 µm. Materials with similar chemical compositions which were conventionally produced by thermo-mechanical treatment have been experimentally and numerically investigated [91–93].

Specimens with a relative density of ca. 99.95% were produced using the process parameters presented in Table 2. During the LPBF process, the chemical composition was mainly altered due to evaporation of Mn (Table 1). Mn is highly vulnerable to evaporation due to its high vapor pressure [94,95]. Evaporation of Mn has led to reduction of SFE from 25.2 mJ m^{-2} (associated with 21 wt% Mn in the powder) to 20.2 mJ m^{-2} (associated with 18.5 wt% Mn in the bulk material) [87]. However, still the reduced SFE is within the range of slip and TWIP (without TRIP) under uniaxial deformation at a quasi-static strain rate and room temperature, provided that the alloying elements (most importantly C and Mn) are distributed uniformly [80–85]. Samples for microstructure characterization (10 mm^3 cubes), as well as for mechanical testing (cylindrical rods with 45 mm length and 6 mm diameter), were fabricated as shown in Fig. 1. In order to experimentally investigate the anisotropic flow behavior of the AM material, cylindrical specimens were 3D-printed with different (symmetry) axis orientation, 0°, 45° and 90° with respect to the substrate plane (SP) and build direction (BD): the horizontal, diagonal and vertical samples (Fig. 1).

2.2. Macroscopic plasticity

From the differently oriented rods shown in Fig. 1, dogbone-shaped cylindrical specimens with a gage length of 30 mm and section diameter of 6 mm were machined. The anisotropic plastic flow behavior of the material was then characterized by uniaxial tensile tests performed on a Z100 Zwick/Roell machine at (constant) room temperature ($T = 23$ °C), a constant quasi-static (true) strain rate ($\dot{\varepsilon} = 10^{-3}$ s^{-1}), and different loading axis (0°, 45° and 90° with respect to the BD). The corresponding flow (true stress–strain) curves and strain hardening (first derivative of stress with respect to strain) curves for the uniform elongation domain are plotted in Fig. 2. For each sample orientation three independent tensile tests with the same deformation parameters were carried out. The experimental scatter is negligible: the mean normalized absolute deviation is consistently less than 0.3%. Additionally, in order to investigate evolution of micro-state variables (MSVs) with strain, three interrupted tensile tests with load direction/axis (LD) along the BD (LD‖BD) were performed on three vertical specimens until engineering/nominal strains (ε^{eng}) of 12.5%, 25% and 37.5%.

Table 1
Chemical composition of different states of the investigated steel.

State	Fe	C [wt%]	Mn [wt%]	Cr [wt%]	Ni [wt%]	Al [wt%]	Si [wt%]	O [ppm]	S [ppm]	P [ppm]
Steel powder (X30Mn21)	Base	0.33	21.0	0.16	0.08	0.03	0.09	1073	51	<20
As-built (X30MnAl19-1)	Base	0.33	18.5	0.16	0.09	1.00	0.11	257	41	<20

Table 2
Process parameters/specifications.

Process	Energy source				Deposition parameters			Scanning strategy
	Type	wavelength [nm]	Power [W]	Spot diameter [µm]	Scanning speed [mm s^{-1}]	Hatch distance [µm]	Layer thickness [µm]	
LPBF	Yb-YAG fiber laser	1064	120	82	700	70	30	Bidirectional with 33° rotation in each layer

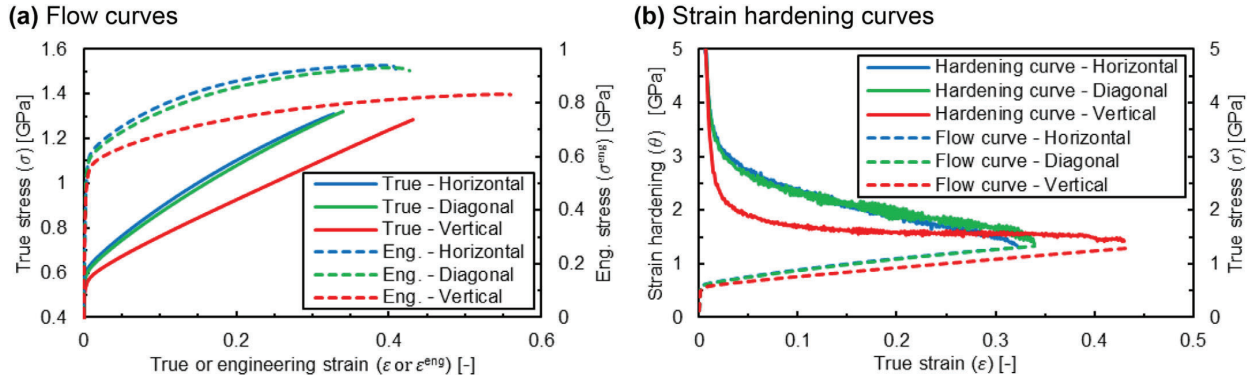

Fig. 2. Mechanical response of the investigated material under uniaxial tension at room temperature ($T = 23\,^{\circ}C$), constant quasi-static (true) strain rate $\dot{\varepsilon} = 10^{-3}$ s^{-1}, and different tensile LD: 90° (horizontal), 45° (diagonal) and 0° (vertical) with respect to the BD.

As shown in Fig. 2, although the variation in the initial yield/flow stress (σ_0) of the horizontal (LD⊥BD) and vertical (LD∥BD) samples is relatively small (weak anisotropy in the initial yield), there is a strong anisotropy in their (tensile) strain hardening ($\theta \equiv \frac{\partial \sigma}{\partial \varepsilon}$), leading to considerably different (yield/flow) true stresses (σ) at various strains (ε). Nevertheless, the difference between flow and strain hardening curves of the horizontal and diagonal (LD∠BD = 45°) samples is relatively small. Furthermore, in all the performed tensile tests, nearly no (macroscopic) strain localization/necking (post-uniform elongation) is observed (Fig. 2(a)), as the flow curves have barely reached the Considere criterion ($\theta = \sigma$) (Fig. 2(b)).

2.3. Microstructure

AM components having the same shape and size but manufactured by different process parameters have strikingly different microstructures. Fundamentally, the solidification microstructure depends on the local heat flow directions (as a result of temperature gradient) and competitive epitaxial grain growth in one of the six ⟨100⟩ preferred/easy growth directions in face-centered cubic (fcc) alloys [96]. In fact, the grain growth is favored when the maximum heat flow direction aligns closely with one of the preferred growth directions. This is the main reason behind the typical strong microstructural polarity along the BD observed in AM metallic products. Since the as-built microstructure consists of fully austenitic (fcc) grains (single-phase), the sources of microstructural heterogeneity are grain morphology and texture on the meso–scale as well as dislocation substructures and elemental micro-segregation on the micro-scale.

The applied scanning strategy involved rotation of the scan direction (SD) and the transverse direction (TD) in each AM layer by 33° around the BD (Table 2). Therefore, for a randomly chosen material cross section on a plane parallel or orthogonal to the BD, the difference between SD and TD is unclear. For this reason, in the following, sometimes instead of SD and/or TD (or any direction in the plane containing both), the terms scan/transverse direction (S/TD) or transverse/scan direction (T/SD) (so that T/SD ⊥ S/TD) is used. These terms refer to any direction on the plane orthogonal to the BD. The grain morphology (size, shape and shape-axes orientation) distribution of the as-built material was characterized by EBSD of relatively large areas on two orthogonal planes: parallel to the BD (designated by ∥BD) and orthogonal to the BD (designated by ⊥BD). The alternative approach for a more precise 3D characterization of the microstructure would be 3D-EBSD using a focused ion beam (FIB) automated serial sectioning technique [97–101]. Moreover, dislocation density and twin fraction in the as-built/undeformed material as well as their evolution with respect to strain using differently strained material states were also estimated by means of EBSD orientation maps on ∥BD and ⊥BD sections.

EBSD measurements of the as-built samples were carried out on a JEOL JSM 7000F field emission gun scanning electron microscope (FEG-SEM) using an EDAX-TSL Hikari EBSD camera. EBSD measurements of the deformed samples were performed using an Oxford Instruments NordlysNano EBSD detector on a Carl Zeiss GeminiSEM FEG-SEM with a 60 µm aperture. All EBSD measurements were conducted with an accelerating voltage of 20 kV, 30 nA probe current and 100 nm step size. XRD macro-texture measurements were performed on ∥BD and ⊥BD planes for the as-built material states. A Bruker D8 Advance X-ray diffractometer with a HI-STAR area detector operating at 30 kV and 25 mA with Fe-Kα radiation (wavelength of 1.93735 nm) was used to acquire incomplete (0°–85°) {100}, {110} and {111} pole figures. Samples

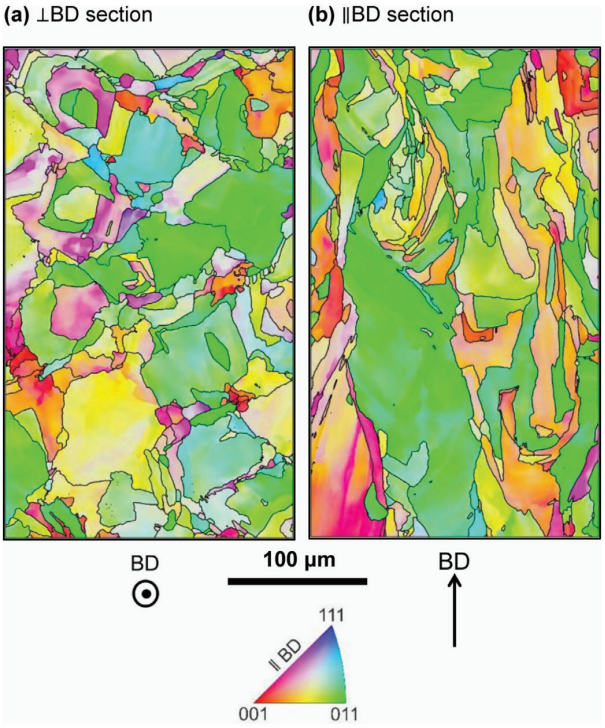

Fig. 3. EBSD IPF orientation maps of the as-built material on ∥BD and ⊥BD sections. Solid black lines indicate at least 10° misorientation across grain boundary.

for EBSD and XRD measurements were prepared by mechanical grinding (up to 1200 SiC grit paper), mechanical polishing (3 and 1 µm diamond suspension) and etching with a Nital (5%) solution. The mechanically polished samples were electropolished for 20 s at a voltage of 28 V at room temperature by a Struers LectroPol-5 electrolytic polishing machine using a Struers A2 electrolyte. For the analysis and noise reduction of microstructure characterization data acquired by EBSD and XRD, the open source MATLAB®-based MTEX toolbox [102–106] and DREAM.3D software [101,107–110] were used (see Appendix A). In addition, TEM measurements were conducted on a JEOL JEM-2100 microscope operating at 200 kV. TEM foils were electropolished at a voltage of 20 V at room temperature by a Struers Tenupol-5 double jet unit using an electrolyte composed of 10% perchloric acid and 90% acetic acid. TEM bright-field images and selective area diffraction pattern (SADP) were recorded with imaging plates (made by DITABIS AG) and digitalized using a DITABIS special scanner.

2.3.1. Grain morphology

EBSD inverse pole figure (IPF) orientation maps of ∥BD and ⊥BD sections of the as-built material are shown in Fig. 3. Grains are defined in such a way so that there is at least 10° misorientation across the grain boundaries. From the total area of each grain (A), the grain size or equivalent grain diameter ($d \equiv \sqrt{\frac{4}{\pi}A}$) is calculated. Grain size distributions (GSD) (number and area fractions) on ∥BD and ⊥BD sections are plotted in Fig. 4(a) and (b). In addition, the lognormal probability density/distribution function (PDF) which is often used to describe GSD in polycrystals [108,109,111,112], has been fitted to the grain size number fraction distribution, as shown in Fig. 4(a) and (b). As suggested by Figs. 3 and 4(a) and (b), there is a profound heterogeneity in GSD on both ∥BD and ⊥BD planes. However, the GSD heterogeneity on the ∥BD section is somewhat higher than that on the ⊥BD section. On the ∥BD section, 21.53% of the total number of grains take up only 0.97% of the total scanned area. Conversely, there is one large grain (number fraction of 0.51%) occupying 21.33% of the total area. Essentially, this tremendous heterogeneity in GSD should have a considerable effect on the mechanical response of the material [113–116].

The anisotropic shape of an arbitrary grain in the microstructure can be characterized by the ellipsoid model. In this context, three shape parameters are used, including grain size (equivalent diameter d), minimum aspect ratio ($m_{\min} \equiv {}^{c}/_{a}$) and maximum aspect ratio ($m_{\max} \equiv {}^{b}/_{a}$) [117]. Each ellipsoid can be described by three (principal) axes with the lengths a, b and c ($a \geq b \geq c$), aligned with a Cartesian orthonormal basis ($\hat{\boldsymbol{e}}_a, \hat{\boldsymbol{e}}_b, \hat{\boldsymbol{e}}_c$). In addition, the spatial orientation of the ellipsoid axes ($\hat{\boldsymbol{e}}_a, \hat{\boldsymbol{e}}_b, \hat{\boldsymbol{e}}_c$) with respect to the reference/global/sample/lab Cartesian coordinate system xyz having the orthonormal basis ($\hat{\boldsymbol{e}}_x, \hat{\boldsymbol{e}}_y, \hat{\boldsymbol{e}}_z$), can be described by the three Euler angles $\boldsymbol{\varphi}' \equiv \{\varphi_1', \Phi', \varphi_2'\}$ (Bunge/zxz notation) that represent three elemental rotations (see Appendix D). Thus, for a full characterization of grain morphology distribution by ellipsoid simplification, it is sufficient to determine the distribution of the aforementioned six variables using the PDF $\bar{\mathcal{F}}(d,\ m_{\min},\ m_{\max}, \boldsymbol{\varphi}')$.

Fig. 4(c) and (d) shows the grain shape (aspect ratio) distribution (in terms of grain number and area fractions) with (2D) ellipse fitting to the spatially resolved grains using the EBSD orientation maps of the ∥BD and ⊥BD sections of the as-built material (Fig. 3). The best-fit ellipse for a given grain is a section through the ellipsoid representation of that grain orthogonal to a semi-axis of the ellipsoid. Although semi-axes of the ellipse section have the same aspect ratio as the sliced ellipsoid, the dimensions must be less than or equal to the axes of the sectioned ellipsoid. Nevertheless, 2D orientation maps do not provide all the information to fully determine $\bar{\mathcal{F}}(d,\ m_{\min},\ m_{\max}, \boldsymbol{\varphi}')$, as they do not give a complete 3D geometry of the grain ensemble. As shown in Figs. 3 and 4(c) and (d), the section of grains on ∥BD plane are dominantly columnar, meaning that they are polarized (having an elongated shape with relatively low aspect ratio and low angle of the major principal axis) along the BD. In contrast, the sections of grains on ⊥BD plane are nearly equi-axed (aspect ratio close to 1). Therefore, it is plausible to assume that the mean aspect ratio on the ⊥BD section ($\bar{m}_{\perp BD}$) represents the average aspect ratio ${}^{\bar{c}}/_{\bar{b}}$ of (3D) ellipsoids, while the mean aspect ratio on the ∥BD section ($\bar{m}_{\parallel BD}$) contains both average aspect ratios $\bar{m}_{\min} \equiv {}^{\bar{c}}/_{\bar{a}}$ and $\bar{m}_{\max} \equiv {}^{\bar{b}}/_{\bar{a}}$ of ellipsoids ($\bar{m}_{\min} < \bar{m}_{\parallel BD} < \bar{m}_{\max}$). Hence, in this specific case, we assume that $\bar{m}_{\min}$ and $\bar{m}_{\max}$ differ from $\bar{m}_{\parallel BD}$ by half of the standard deviation of the fitted PDF: $\bar{m}_{\max/\min} = \bar{m}_{\parallel BD} \pm {}^{\sigma_{\parallel BD}}/_{2}$, meaning that $\bar{m}_{\min} \cong 0.3$ and $\bar{m}_{\max} \cong 0.5$.

By ellipse fitting to the grains analyzed from the 2D orientation maps of two orthogonal sections [118] and calculation of the angle between ellipses major or minor axes and a reference direction, we can obtain a rough estimate of the shape-axes orientation of grains in the 3D space. Grain shape-axes orientation distribution on the ∥BD and ⊥BD sections of the as-built material are shown in Fig. 4(e) and (f). As shown in Fig. 4(e) and (f), the (ellipse-fitted) axes of grain sections on the ⊥BD plane is nearly oriented randomly, while the major axes of grain sections on the ∥BD plane are almost aligned with the BD.

2.3.2. Crystallographic texture

In order to have a better representation of the crystallographic texture of the as-built material, XRD macro-texture measurements were carried out in addition to the EBSD micro-texture measurements. Since distributions of (2D) morphological characteristics on the ∥BD and ⊥BD sections are considerably different (Fig. 4), to ensure a representation of the underlying bulk texture (weight-averaged by grain volume) of the as-built material, XRD

(a) Grain size distribution: ⊥BD section

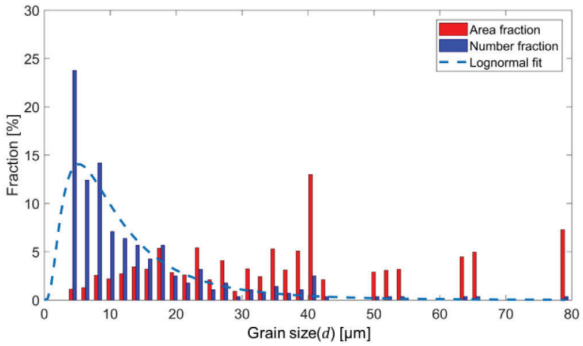

(b) Grain size distribution: ∥BD section

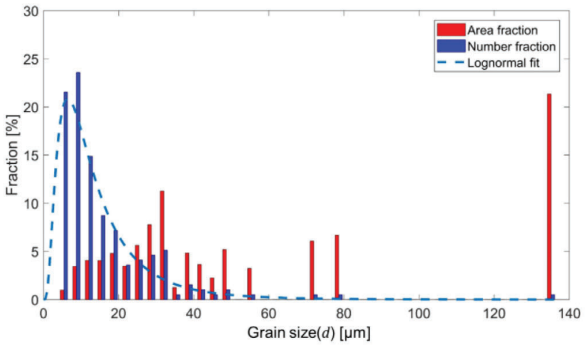

Mean grain size calculated from number fraction	$\bar{d} = 13.0$ μm	$\bar{d} = 15.3$ μm
Mean grain size calculated from area fraction	$\bar{d} = 36.1$ μm	$\bar{d} = 57.1$ μm
Mean of logarithmic values	$\mu_{\ln} = 2.248$	$\mu_{\ln} = 2.422$
Standard deviation of logarithmic values	$\sigma_{\ln} = 0.771$	$\sigma_{\ln} = 0.774$
Standard deviation	$\sigma = 11.5$	$\sigma = 12.8$

(c) Grain shape distribution: ⊥BD section

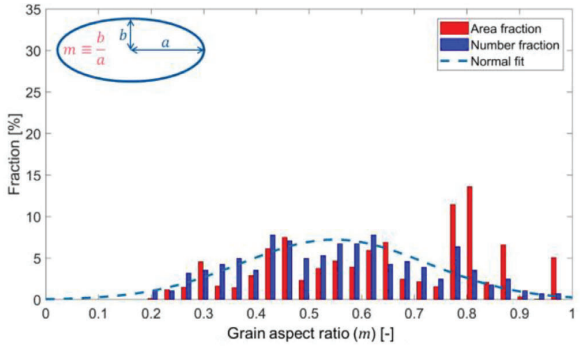

(d) Grain shape distribution: ∥BD section

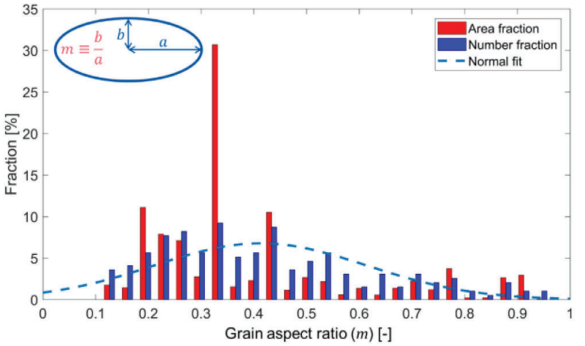

Mean aspect ratio calculated from number fraction	$\bar{m} = 0.547$	$\bar{m} = 0.411$
Mean aspect ratio calculated from area fraction	$\bar{m} = 0.627$	$\bar{m} = 0.385$
Standard deviation	$\sigma = 0.176$	$\sigma = 0.201$

(e) Grain shape-axes orientation distribution: ⊥BD section

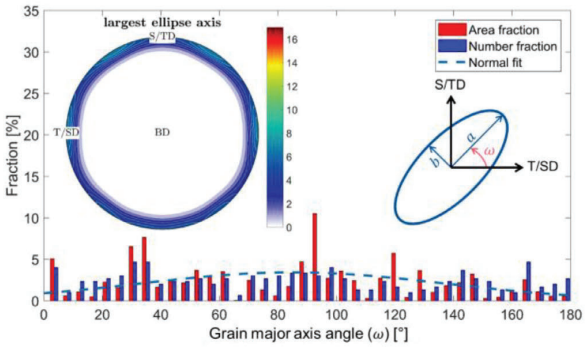

(f) Grain shape-axes orientation distribution: ∥BD section

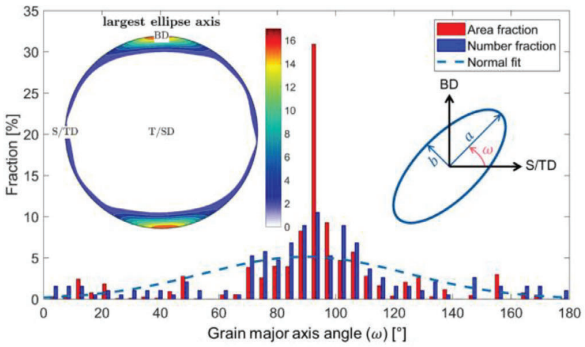

Mean angle calculated from number fraction	$\bar{\omega} = 85.07°$	$\bar{\omega} = 89.72°$
Mean angle calculated from area fraction	$\bar{\omega} = 79.90°$	$\bar{\omega} = 90.17°$
Standard deviation	$\sigma = 52.20$	$\sigma = 34.88$

Fig. 4. Grain morphology (size, shape and shape-axes orientation) distributions of the as-built material, evaluated from the EBSD orientation maps. The 2D pole figures plotted in (e) and (f) as their corresponding histogram represent the distributions of the angle of grain major axis (ω) on the respective section.

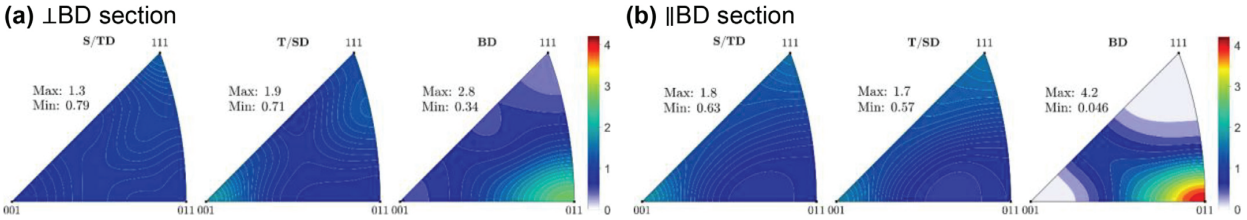

Fig. 5. Crystallographic orientation distribution in terms of IPFs evaluated from XRD-measured pole figure data of the as-built material on ∥BD and ⊥BD sections.

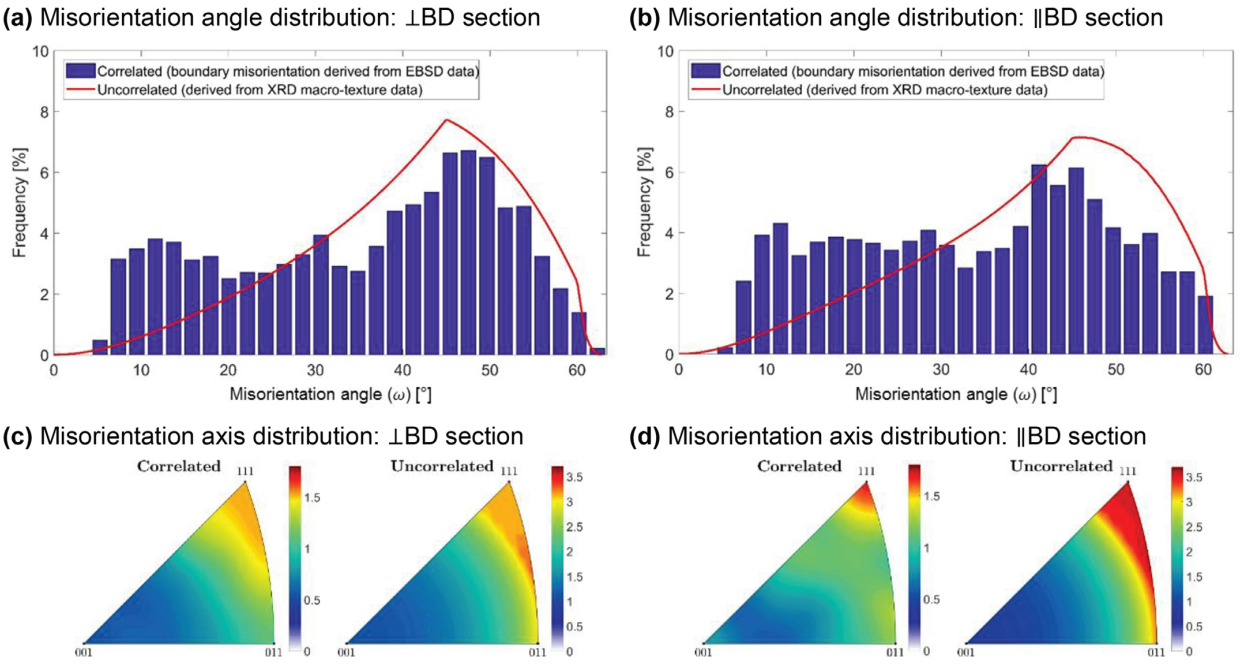

Fig. 6. Misorientation (angle and axis) distribution of the as-built material on ∥BD and ⊥BD sections.

macro-texture measurements were performed on both ∥BD and ⊥BD sections (the surfaces at which the X-ray incident beam hits the specimen). Crystallographic orientation distribution functions (ODFs) were calculated from the XRD pole figure measurements. The ODF is a PDF ($\breve{\mathcal{G}}(\boldsymbol{\varphi})$) representing the statistical distribution of the orientation of the crystallographic orthonormal basis ($\hat{\boldsymbol{e}}_{100}, \hat{\boldsymbol{e}}_{010}, \hat{\boldsymbol{e}}_{001}$) with respect to the reference Cartesian coordinate system *xyz* having the basis ($\hat{\boldsymbol{e}}_x, \hat{\boldsymbol{e}}_y, \hat{\boldsymbol{e}}_z$). This orientation relationship can be described in terms of three Bunge-Euler angles $\boldsymbol{\varphi} \equiv \{\varphi_1, \Phi, \varphi_2\}$ denoting three elemental rotations (see Appendix D). The corresponding IPFs evaluated from the XRD macro-texture measurement data of the as-built material on ∥BD and ⊥BD sections are plotted in Fig. 5. A relatively strong ⟨011⟩∥BD fiber texture was observed. Nevertheless, the intensity of ⟨011⟩∥BD is higher in the XRD measurements on ∥BD section than that on ⊥BD section.

Another texture related aspect of microstructural heterogeneity which needs to be considered is the misorientation distribution. The misorientation distribution function (MDF) represents the statistical distribution of grain boundary misorientation, typically described in axis-angle notation using the PDF $\breve{\mathcal{H}}(\boldsymbol{a}, \omega)$, where $\boldsymbol{a} \equiv \langle h, k, l \rangle$ denotes the misorientation (crystallographic rotation) axis and ω being the misorientation angle. While the MDF of a material is certainly connected to its ODF, the presence of morphological heterogeneities influencing the orientations of contiguous neighboring grains may have a strong effect on the MDF [119–126]. In the case of a random distribution of morphological characteristics (size, shape and shape-axes orientation), the MDF is fully dependent on the ODF. Therefore, with a random morphology, the (spatially-) correlated MDF or grain boundary misorientation distribution, which can be determined using EBSD orientation maps, coincides with the uncorrelated/Mackenzie MDF calculated by random sampling of orientations from the ODF [119,127]. Correlated and uncorrelated misorientation (angle-axis) distributions calculated, respectively using the EBSD orientation maps and XRD pole figure data associated with the ∥BD and ⊥BD sections of the as-built material are shown in Fig. 6. According to Fig. 6, the morphological heterogeneity has led to an appreciable deviation between correlated and uncorrelated misorientation angle-axis distributions on both ∥BD and ⊥BD sections. In the as-built material, grain boundaries with low angle misorientations have a higher frequency than in the case with identical macro-texture and random grain morphology.

2.3.3. Evolution of micro-state variables (MSVs)

It has been reported that as-built AM metallic materials contain relatively high dislocation density, which is formed due to thermally induced stresses during rapid solidification [16,39,128,129]. TEM images shown in Fig. 7 reveal heterogeneous cellular dislocation fractal pattern (having relatively thick walls with high

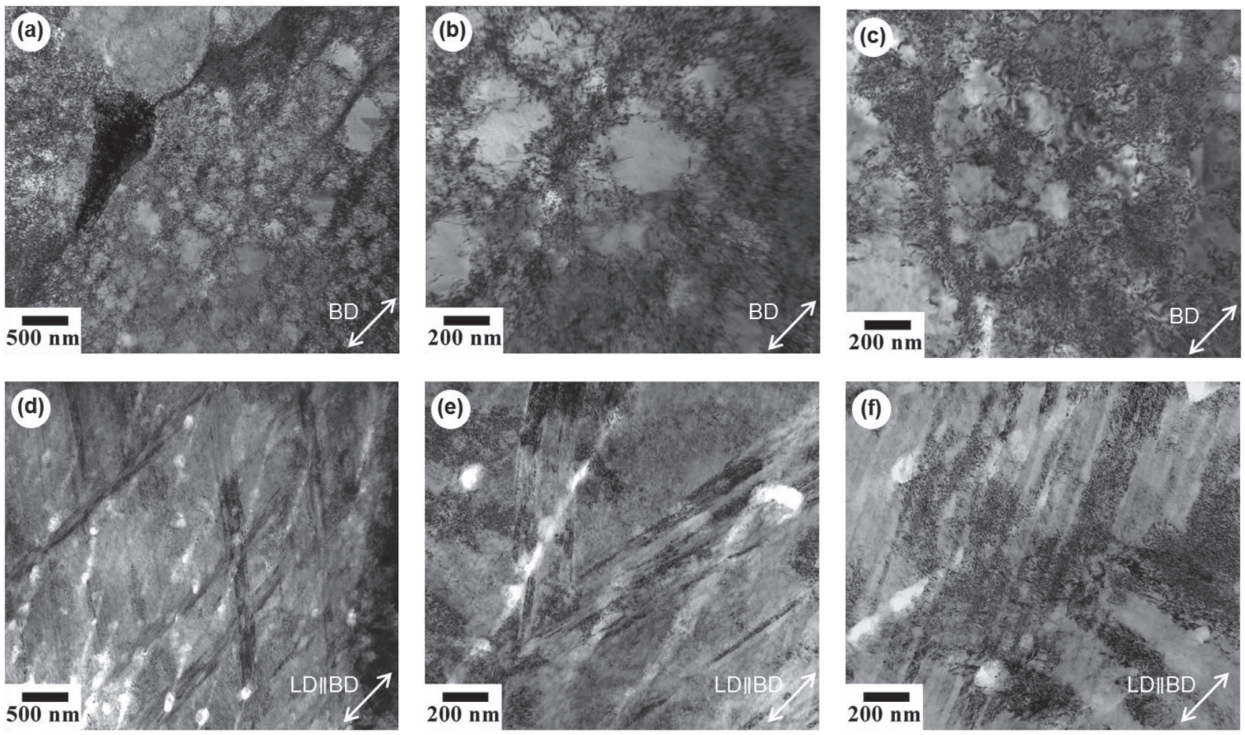

Fig. 7. Bright-field TEM images showing, (a–c) high-density cellular dislocation fractal pattern and incidental dislocation boundaries on the ‖BD section of the as-built material; and (d–f): twin substructure evolved at 50% strain under uniaxial tension along the BD (LD‖BD) at a quasi-static strain rate ($\dot{\bar{\varepsilon}} = 10^{-3}$ s^{-1}) and room temperature ($T = 23\,^{\circ}$C).

dislocation density) and twin substructure in the as-built and deformed material states. The observed cell block (dislocation) substructure resembles those that typically exist in conventionally-manufactured plastically-deformed materials [130]. Due to a negligible misorientation across neighboring cells, their boundaries are considered as incidental dislocation boundaries (IDBs) mostly comprised of (unipolar and dipolar) statistically stored dislocations (SSDs). In contrast, subgrain or geometrically necessary boundaries (GNBs) are made of highly concentrated (unipolar) geometrically necessary dislocations (GNDs) with a net Burgers vector accommodating localized lattice curvature, that often arises as a result of non-uniform plastic deformation [131–134].

As shown in Fig. 3, the as-built microstructure has a considerably high intra-granular misorientation, which is attributed to a high (initial) GND density [133–136]. We utilized the method proposed by Pantleon [137] for spatially resolving GND density on (2D) orientation maps at each slip system. This approach is based on curvature and dislocation density tensors with reduced number of components (implemented in the recent releases of MTEX). Furthermore, using the EBSD orientation maps of differently strained (uniaxial tension) samples on ‖BD and ⊥BD sections, twin boundaries were determined. The criterion used for characterization of ($\Sigma 3$) twin boundaries is based on the following definition valid for fcc crystals: $\langle 11\bar{1}\rangle_{\mathrm{mt}} = \langle \bar{5}\bar{1}1\rangle_{\mathrm{tw}}$, $\langle 1\bar{1}\bar{1}\rangle_{\mathrm{mt}} = \langle \bar{1}15\rangle_{\mathrm{tw}}$, $\langle 111\rangle_{\mathrm{mt}} = \langle \bar{1}\bar{5}\bar{1}\rangle_{\mathrm{tw}}$, where mt and tw denote matrix and twin, respectively. This corresponds precisely to a 60° misorientation about the $\langle 111\rangle$ axis within the austenitic matrix [138]. Backscatter Kikuchi pattern image quality maps were also used to help identifying twin boundaries [88,139,140]. The twins in materials with cubic crystal structure often appear in bundles/stacks of thin twins [141,142]. Hence, the image quality of the EBSD patterns decreases near these twin bundles. After the characterization of twin boundaries, twinned regions were identified from the matrix. Subsequently, the summation of the area of the twinned regions over the total scanned area rendered the twin (area) fraction. Fig. 8 shows the distributions of estimated GND density, twin boundaries and ε-martensite (hcp) on the EBSD orientation maps of ‖BD and ⊥BD sections of the as-built/undeformed and differently strained (uniaxial tension along the BD) vertical material samples. The evolution of the mean GND density and twin and ε-martensite (area) fractions with respect to strain calculated based on the analysis of EBSD orientation maps of ‖BD and ⊥BD sections of the as-built and differently strained (uniaxial tension along the BD) vertical material samples are shown in Fig. 9.

As shown in Figs. 8 and 9, in the regime of the adopted deformation parameters (strain, strain rate, temperature and triaxiality), the fraction of ε-martensite and hence the amplitude of TRIP effect at different strains is negligible (less than 1.5%). Moreover, in all the measurements, the area fraction associated with α'-martensite was almost zero (less than 0.05%). The highest ε-martensite area fraction was measured at 12.5% strain state on ‖BD section (1.2%), while by increasing strain, its value was reduced. Therefore, we assume that slip and twinning are the only (dominant) plastic deformation mechanisms that activate in the investigated material (at room temperature and quasi-static strain rates). Given the average values of ε-martensite fractions on ⊥BD and ‖BD sections (Fig. 9(c)), it is conceivable that the formation of ε-martensite in this material under the chosen deformation parameters is a stochastic event (not a direct function of macroscopic strain). This can be explained by considering the effect of elemental micro-segregation (distribution of alloying elements on the micro-scale) on the SFE. Depending on the process type and processing parameters, elemental micro-segregation in AM might be significant [52,73]. Moreover, since the SFE is an explicit function of chemical

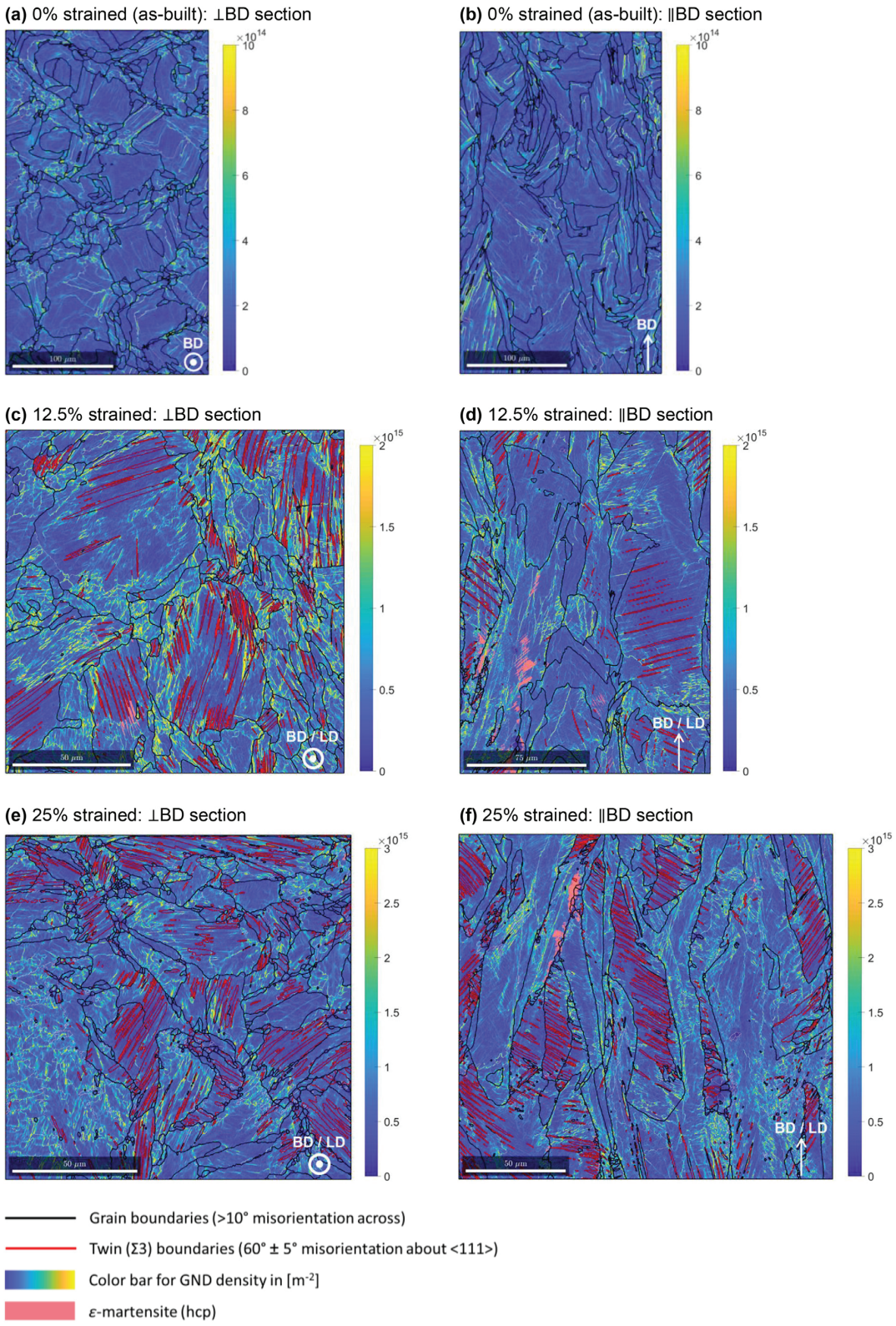

Fig. 8. Spatially resolved GND density, twin boundary and ε-martensite. Calculations are performed using the EBSD orientation maps of ∥BD and ⊥BD sections of the as-built/undeformed and differently strained (uniaxial tension along BD) vertical material samples. Note that the transformed (due to deformation) ε-martensite content is comparatively negligible in the regime of the adopted deformation parameters.

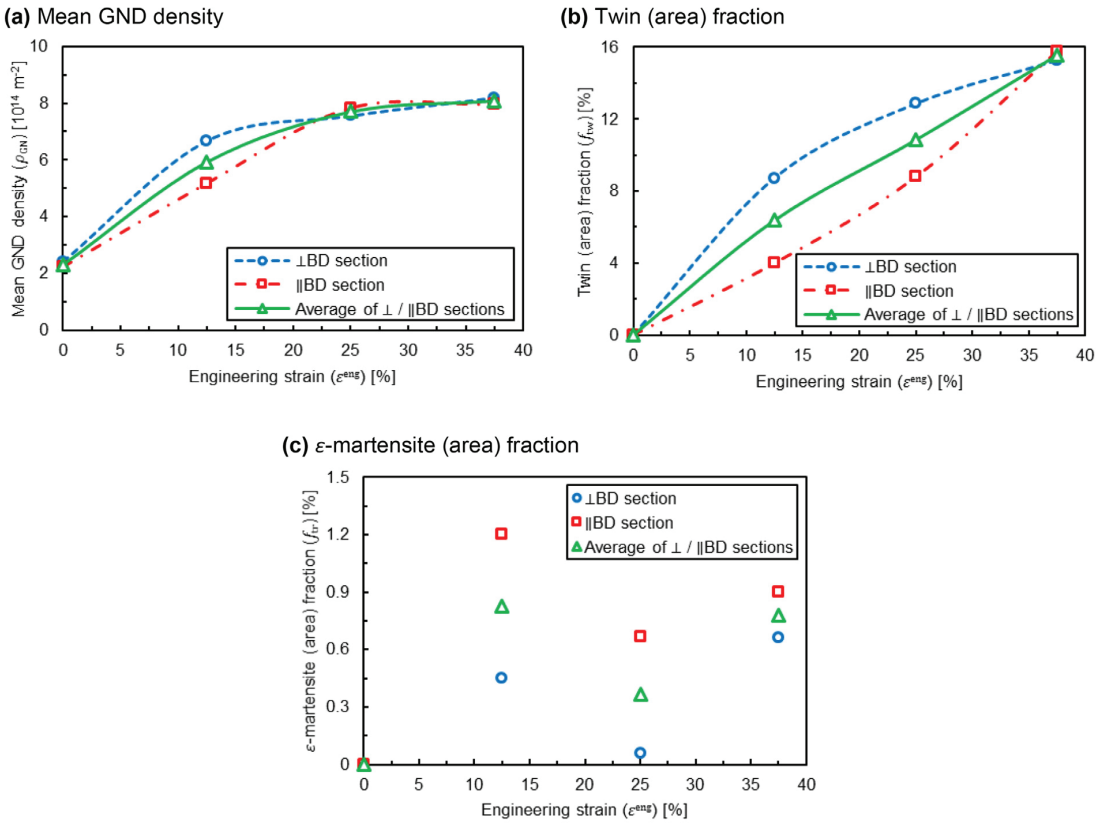

Fig. 9. Evolution of the mean GND density, twin (area) fraction and ε-martensite (area) fraction with respect to (engineering) strain (uniaxial tension along the BD) estimated by the analysis of EBSD orientation maps of ∥BD and ⊥BD sections of the as-built and differently strained vertical material samples.

composition, local variation of concentration of alloying elements results in a distribution of SFE (around the calculated mean value) on the micro-scale. Therefore, even in the so-called "TWIP steels", typically there are small local volumes with sufficiently low SFE and high dislocation density, in which TRIP occurs.

The GND density values estimated from the orientation maps on ∥BD and ⊥BD sections are similar. It seems that they converge to their average at relatively large strains. However, the twin fraction values estimated from the analysis of orientation maps of ∥BD sections are considerably lower than those of corresponding ⊥BD sections. This is attributed to the larger grain size and higher microstructural heterogeneity and polarity on ∥BD planes, as well as the limited scanned area. As a result, the twin area fraction calculated from ⊥BD sections is a better representative for twin volume fraction of the bulk of the material.

3. Continuum crystal plasticity modeling

In the present study, we adopted the full field (continuum) crystal plasticity modeling framework for computational polycrystal homogenization. In this context, the meso–scale microstructure is modeled as a periodic statistically representative volume element (RVE) of the polycrystalline aggregate. The externally imposed macroscopic boundary conditions in terms of homogenous rate of the deformation gradient tensor ($\dot{\bar{\mathbf{F}}}$) and the first Piola–Kirchhoff stress tensor ($\bar{\mathbf{P}}$) with complementary components (mutually exclusive) translate to pure deformation periodic boundary conditions on the RVE. The governing boundary value problem is then solved to fulfill the mechanical/stress equilibrium using a spectral method based on fast Fourier transform (FFT) by calculation of the deformation gradient at discretized space (integration pints) and time (time steps/increments) [143,144].

The crystal plasticity constitutive model developed in this study explicitly accounts for both dislocation slip and twinning as plastic deformation mechanisms along with their corresponding kinetics and associated deformation systems. A model based on the continuum theory of crystal finite strain/deformation is used to project the deformation gradient and stress tensors at material points on the respective deformation (slip/twin) systems in terms of (resolved) plastic shear strain rates and shear stresses. The mechanical response at the underlying deformation systems of each material point is evaluated by a physics-based constitutive model. The resulting sets of nonlinear partial differential equations (PDEs) are then integrated (using the general Euler method with adaptive damping factor), linearized (using the tangent-based iterative Newton–Raphson scheme) and solved by a self-consistent (semi-) implicit return mapping (predictor-corrector) algorithm implemented in the modular crystal plasticity code DAMASK [145]. The incrementally resolved fields (stress, strain, state variables) at the material points are then homogenized over the RVE to give the average macroscopic response.

3.1. Crystal finite strain modeling

The crystal plasticity modeling framework applied in the present study is based on the rigorous formalism of crystal hypoelasto-viscoplasticity (metallic materials) at finite strains, established in the last three decades of 20th century by the works

of Rice [146], Hill and Rice [147], Asaro and Rice [148], Peirce et al. [149,150], Asaro [151,152], Asaro and Needleman [153], Kalidindi et al. [154,155], and Kalidindi [156].

3.1.1. Kinematics

At single-crystal material points, the (total) deformation gradient tensor ($\mathbf{F}$) is multiplicatively decomposed into its elastic ($\mathbf{F}_e$) and isochoric plastic ($\mathbf{F}_p$) components/splits [148,157–160]:

$$\mathbf{F} \equiv \frac{\partial \boldsymbol{x}}{\partial \boldsymbol{x}_0} = \mathbf{F}_e\mathbf{F}_p; \quad J \equiv \det(\mathbf{F}) = \det(\mathbf{F}_e) > 0; \quad \det(\mathbf{F}_p) = 1; \tag{1}$$

where $\boldsymbol{x}$ is the spatial coordinate; subscript 0 represents the initial/undeformed/reference configuration; subscripts e and p denote elastic and plastic, respectively; and J is the Jacobian of the deformation map. The main postulate through the aforementioned elasto-plastic decomposition is that the crystal plastic deformation occurs by flow of material through the crystal lattice without distorting the lattice itself, while the material point undergoes lattice distortion (giving rise to lattice stresses) due to the elastic deformation gradient [147,148,157]. In this picture, the hypothetical configuration defined by the transformation $\mathbf{F}_p$ is referred to as the plastic/relaxed/unloaded/undistorted/unrotated/intermediate configuration. Accordingly, the (total) velocity gradient tensor ($\mathbf{L}$) can be expressed as [161]:

$$\mathbf{L} \equiv \frac{\partial \boldsymbol{v}}{\partial \boldsymbol{x}} = \dot{\mathbf{F}}\mathbf{F}^{-1} = \mathbf{L}_e + \mathbf{L}_p; \quad \boldsymbol{v} \equiv \frac{\partial \boldsymbol{x}}{\partial t};$$
$$\mathbf{L}_e \equiv \dot{\mathbf{F}}_e\mathbf{F}_e^{-1}; \quad \mathbf{L}_p \equiv \mathbf{F}_e\underline{\mathbf{L}}_p\mathbf{F}_e^{-1}; \quad \underline{\mathbf{L}}_p \equiv \dot{\mathbf{F}}_p\mathbf{F}_p^{-1}; \tag{2}$$

where $\boldsymbol{v}$ is the velocity vector; t is time; and the underline $\underline{\ }$ indicates the vector/tensor quantity in the plastic configuration. Furthermore, through the polar decomposition theorem, the non-singular elastic deformation gradient tensor is uniquely decomposed into the product of the orthogonal elastic rigid-body rotation tensor ($\mathbf{R}_e$) and the symmetric right elastic stretch tensor ($\mathbf{U}_e$):

$$\mathbf{F}_e = \mathbf{R}_e\mathbf{U}_e; \quad \mathbf{R}_e^{-1} = \mathbf{R}_e^{\mathrm{T}}; \quad \mathbf{U}_e = \mathbf{U}_e^{\mathrm{T}}; \quad \Rightarrow \ \mathbf{U}_e^2 = \mathbf{C}_e \equiv \mathbf{F}_e^{\mathrm{T}}\mathbf{F}_e; \tag{3}$$

where $\mathbf{C}_e$ is referred to as the elastic right Cauchy–Green deformation tensor. Therefore, the lattice rotation from the plastic configuration can be represented by $\mathbf{R}_e^{\mathrm{T}}$:

$$\mathbf{Q} = \mathbf{R}_e^{\mathrm{T}}; \quad \mathbf{Q}^{-1} = \mathbf{Q}^{\mathrm{T}}; \quad \mathbf{Q} \equiv \breve{\mathbf{Q}}(\boldsymbol{\varphi}); \quad \Rightarrow \ \boldsymbol{\varphi} = \breve{\mathbf{Q}}^{-1}\left(\mathbf{R}_e^{\mathrm{T}}\right); \tag{4}$$

where $\mathbf{Q}$ is the orientation matrix as a function of three Bunge–Euler angles $\boldsymbol{\varphi} \equiv (\varphi_1, \Phi, \varphi_2)$ (see Appendix D) at the arbitrary time t; and the sign $\breve{\ }$ denotes a function. Moreover, the initial orientation of the crystal lattice basis with respect to the reference frame is accommodated by initialization of the plastic deformation gradient by a virtual (initial) deformation (pure rotation) step [162]:

$$\mathbf{F}_{p0} \equiv \mathbf{Q}_0 \equiv \breve{\mathbf{Q}}(\boldsymbol{\varphi}_0); \quad \mathbf{F}_0 = \mathbf{F}_{e0}\mathbf{F}_{p0} = \mathbf{I};$$
$$\Rightarrow \ \mathbf{F}_{e0} = \mathbf{R}_{e0}\mathbf{U}_{e0} = \mathbf{R}_{e0} = \mathbf{Q}_0^{-1} = \mathbf{Q}_0^{\mathrm{T}}; \quad \mathbf{U}_{e0} \equiv \mathbf{I}; \tag{5}$$

where the index 0 represents the initial (virtual) step ($t = 0$); $\boldsymbol{\varphi}_0 \equiv (\varphi_{10}, \Phi_0, \varphi_{20})$ is the set of three Bunge-Euler angles describing the initial/undeformed crystallographic lattice orientation of the considered material point with respect to the frame of reference; and $\mathbf{I}$ is the (second-order) unit/identity tensor. The virtual deformation step by $\mathbf{F}_{p0} \equiv \mathbf{Q}_0$ guarantees that the lattice basis in the plastic configuration always coincides with the reference coordinate system.

3.1.2. Crystal plasticity

Inspired by Rice [146] and Kalidindi [156], the homogenized plastic velocity gradient at the considered "single-crystal" material point in the plastic configuration is approximated as follows:

$$\underline{\mathbf{L}}_p \cong \sum_{\alpha=1}^{N_{\mathrm{sl}}} \dot{\gamma}_{\mathrm{sl}}^{\alpha}\ \underline{\mathbf{Z}}_{\mathrm{sl}}^{\alpha} + \sum_{\beta=1}^{N_{\mathrm{tw}}} \dot{\gamma}_{\mathrm{tw}}^{\beta}\ \underline{\mathbf{Z}}_{\mathrm{tw}}^{\beta};$$
$$\underline{\mathbf{Z}}_{\mathrm{sl}}^{\alpha} = \mathbf{F}_e^{-1}\mathbf{Z}_{\mathrm{sl}}^{\alpha}\mathbf{F}_e; \quad \mathbf{Z}_{\mathrm{sl}}^{\alpha} \equiv \widehat{\boldsymbol{b}}_{\mathrm{sl}}^{\alpha} \otimes \widehat{\boldsymbol{n}}_{\mathrm{sl}}^{\alpha}; \quad \mathbf{Z}_{\mathrm{sl}}^{\alpha} \equiv \hat{\boldsymbol{b}}_{\mathrm{sl}}^{\alpha} \otimes \hat{\boldsymbol{n}}_{\mathrm{sl}}^{\alpha};$$
$$\underline{\mathbf{Z}}_{\mathrm{tw}}^{\beta} = \mathbf{F}_e^{-1}\mathbf{Z}_{\mathrm{tw}}^{\beta}\mathbf{F}_e; \quad \underline{\mathbf{Z}}_{\mathrm{tw}}^{\beta} \equiv \widehat{\boldsymbol{b}}_{\mathrm{tw}}^{\beta} \otimes \widehat{\boldsymbol{n}}_{\mathrm{tw}}^{\beta}; \quad \mathbf{Z}_{\mathrm{tw}}^{\beta} \equiv \hat{\boldsymbol{b}}_{\mathrm{tw}}^{\beta} \otimes \hat{\boldsymbol{n}}_{\mathrm{tw}}^{\beta}; \tag{6}$$

where subscripts sl and tw indicate that the corresponding quantities are associated with slip and twin, respectively; N is the number of deformation (slip/twin) systems; superscripts α and β are slip and twin systems indices, respectively; γ is the plastic shear strain; $\mathbf{Z}$ is the schmid tensor; $\boldsymbol{b}$ is the slip/twin Burgers vector; $\hat{\boldsymbol{b}}$ is the slip/twin Burgers direction (unit) vector (normalized slip/twin Burgers vector); $\hat{\boldsymbol{n}}$ is the slip/twin plane normal (unit) vector (see Appendix E); and the sign $\widehat{\ }$ indicates normalization ($\hat{\bullet} = \frac{\bullet}{|\bullet|}$). Eq. (6) only holds through the following assumptions [163]: (i) twins can be sheared by dislocation slip in a compatible manner to the parent/surrounding matrix; and (ii) any potentially different evolution of slip resistance within them is negligible.

3.1.3. Crystal elasticity

The mean elastic stiffness tensor in the plastic configuration ($\bar{\mathbb{C}}_e$) at the considered "single-crystal" material point is homogenized as follows to account for the contributions of twins and matrix [156,164]:

$$\bar{\mathbb{C}}_e = (1 - f_{\mathrm{tw}})\ \mathbb{C}_{e\ \mathrm{mt}} + \sum_{\beta=1}^{N_{\mathrm{tw}}} f_{\mathrm{tw}}^{\beta}\ \mathbb{C}_{e\ \mathrm{tw}}^{\beta}; \quad f_{\mathrm{tw}} = \sum_{\beta=1}^{N_{\mathrm{tw}}} f_{\mathrm{tw}}^{\beta};$$
$$\left[\mathbb{C}_{e\ \mathrm{tw}}^{\beta}\right]_{ijkl} = \left[\mathbb{C}_{e\ \mathrm{mt}}\right]_{pqrs}\left[\mathbf{T}_{\mathrm{mt-tw}}^{\beta}\right]_{ip}\left[\mathbf{T}_{\mathrm{mt-tw}}^{\beta}\right]_{jq}\left[\mathbf{T}_{\mathrm{mt-tw}}^{\beta}\right]_{kr}\left[\mathbf{T}_{\mathrm{mt-tw}}^{\beta}\right]_{ls};$$
$$\mathbf{T}_{\mathrm{tw}}^{\beta} = 2\widehat{\boldsymbol{n}}_{\mathrm{tw0}}^{\beta} \otimes \widehat{\boldsymbol{n}}_{\mathrm{tw0}}^{\beta} - \mathbf{I}; \tag{7}$$

where the bar $\bar{\ }$ denotes mean/homogenization; f represents volume fraction; $\mathbb{C}$ is the fourth-order stiffness tensor; subscript mt stands for matrix; $\mathbf{T}_{\mathrm{mt-tw}}^{\beta}$ represents the matrix transforming the lattice orientation in the parent matrix to the lattice orientation in the twinned region (twin system β) in the plastic configuration; and the square brackets [] is used to indicate index/component notation (see Appendix B). See Appendix F for more information regarding the entries of $\mathbb{C}_{e\ \mathrm{mt}}$ as well as the calculation of the average elastic moduli (shear modulus and Poisson's ratio) in case of cubic crystal symmetry.

According to the general/three-dimensional Hooke's law, the second Piola–Kirchhoff (nominal) stress tensor in the plastic configuration ($\underline{\mathbf{S}}$) is calculated by (double) contraction (inner product) of $\bar{\mathbb{C}}_e$with its work conjugate pair, the elastic Green-Lagrange (nominal) strain tensor in the plastic configuration ($\underline{\mathbf{E}}_e$):

$$\underline{\mathbf{S}} = \bar{\mathbb{C}}_e : \underline{\mathbf{E}}_e; \quad \underline{\mathbf{E}}_e = \frac{1}{2}(\mathbf{C}_e - \mathbf{I}). \tag{8}$$

Given Eq. (6) and considering the power conjugacy of the (asymmetric) Mandel stress ($\mathbf{M}$) and velocity gradient ($\mathbf{L}$) tensors [154,155,161]:

$$\dot{w}_p = \underline{\mathbf{M}} : \underline{\mathbf{L}}_p = \sum_{\alpha=1}^{N_{\mathrm{sl}}} \tau_{\mathrm{sl}}^{\alpha}\ \dot{\gamma}_{\mathrm{sl}}^{\alpha} + \sum_{\beta=1}^{N_{\mathrm{tw}}} \tau_{\mathrm{tw}}^{\beta}\ \dot{\gamma}_{\mathrm{tw}}^{\beta}; \quad \underline{\mathbf{M}} \equiv \underline{\mathbf{C}}_e\underline{\mathbf{S}};$$
$$\Rightarrow \tau_{\mathrm{sl}}^{\alpha} = \underline{\mathbf{M}} : \underline{\mathbf{Z}}_{\mathrm{sl}}^{\alpha} \cong \underline{\mathbf{S}} : \underline{\mathbf{Z}}_{\mathrm{sl}}^{\alpha}; \quad \tau_{\mathrm{tw}}^{\beta} = \underline{\mathbf{M}} : \underline{\mathbf{Z}}_{\mathrm{tw}}^{\beta} \cong \underline{\mathbf{S}} : \underline{\mathbf{Z}}_{\mathrm{tw}}^{\beta}; \tag{9}$$

where w is the volumetric deformation work at the considered material point; and τ is the resolved shear stress (RSS) at the corresponding deformation system. Generally, the deformation of metallic materials are categorized as crystal hypoelasto-viscoplasticity. Therefore, one typically assumes that elastic strains are very small compared to unity, so that $\mathbf{F}_e \approx \mathbf{I}$, leading to $\underline{\mathbf{C}}_e \equiv \mathbf{F}_e^{\mathrm{T}}\mathbf{F}_e \approx \mathbf{I}$, which entails the useful approximation of $\underline{\mathbf{M}} \approx \underline{\mathbf{S}}$.

3.2. Physics-based crystal plasticity constitutive modeling

The physics-based continuum constitutive model for single crystal plasticity presented in this section accounts for plastic de-

formation accommodated by both slip and twinning mechanisms. It has three nonlocal (internal) micro-state variables (MSVs): two types of dislocation density (unipolar and dipolar) and the twin (volume) fraction. The physics-based evolution of the MSVs and the respective kinetics are described in the following.

3.2.1. Kinetics of slip

In the framework of continuum dislocation dynamics, the notion of dislocation density as a MSV is used to describe the dislocation slip and its corresponding phenomena. In this context, however, the (total) dislocation density can be decomposed differently with respect to various properties of dislocations [165]. Here, following Blum et al. [166], the total dislocation density at slip system α is decomposed to unipolar and dipolar dislocation densities:

$$\rho_t^\alpha \equiv \rho_u^\alpha + \rho_d^\alpha; \quad \rho_x \equiv \sum_{\alpha=1}^{N_{\mathrm{sl}}} \rho_x^\alpha; \quad x \in \{t, u, d\}; \tag{10}$$

where ρ denotes dislocation density; subscripts t, u and d stand for total, unipolar and dipolar, respectively; and ρ without slip system superscript (α) is the sum of the corresponding dislocation density type (x) over all the slip systems at the considered material point.

Dislocations in dipolar configuration are considered immobile (zero slip velocity), while unipolar dislocations can be mobile and thus contribute to the plastic shear strain rate according to Orowan's equation [167,168]:

$$\dot{\gamma}_{\mathrm{sl}}^\alpha = b_{\mathrm{sl}} \rho_u^\alpha \bar{v}_{\mathrm{sl}\ u}^\alpha; \quad \bar{v}_{\mathrm{sl}\ u}^\alpha = v_{\mathrm{sl}\ u0} \exp\left(-\frac{\Delta G_{\mathrm{sl}}^\alpha}{k_B T}\right) \mathrm{sign}\left(\tau_{\mathrm{sl}}^\alpha\right);$$
$$\Delta G_{\mathrm{sl}}^\alpha = \Delta F_{\mathrm{sl}} \left(1 - \left(\frac{\tau_{\mathrm{sl\ eff}}^\alpha}{\tau_{\mathrm{sl}0}}\right)^{p_{\mathrm{sl}\ t}}\right)^{p_{\mathrm{sl}\ b}}; \quad \tau_{\mathrm{sl\ eff}}^\alpha = \left\langle \left|\tau_{\mathrm{sl}}^\alpha\right| - \tau_{\mathrm{sl\ cr}}^\alpha \right\rangle; \tag{11}$$

where b denotes the Burgers length (magnitude of Burgers vector: $|\boldsymbol{b}|$) (see Appendix E); $\Delta G_{\mathrm{sl}}^\alpha$ is the average Gibbs free energy difference (activation enthalpy) for bypassing short-range obstacles by mobile dislocations at slip system α; k_B is the Boltzmann constant; T is the absolute temperature; $v_{\mathrm{sl}\,u0}$ is the reference mean slip speed (magnitude of velocity vector) of unipolar dislocations (mean unipolar dislocation speed at high temperatures so that $T \gg \Delta G_{\mathrm{sl}}^\alpha / k_B$); ΔF_{sl} is the mean thermal activation energy (Helmholtz free energy) for slip without the aid of external stress ($0.05 \leq \frac{\Delta F_{\mathrm{sl}}}{\mu b_{\mathrm{sl}}^2} \leq 2$ [168]); $\bar{v}_{\mathrm{sl}\ u}^\alpha$ is the mean slip velocity of unipolar dislocations at slip system α; $\tau_{\mathrm{sl}0}$ is the maximum short-range slip resistance (in average), also known as Peierls stress or solid solution strength, which can be calculated using *ab initio*/first-principles methods based on density functional theory (DFT) [169–176]; $\tau_{\mathrm{sl\ eff}}^\alpha$ is the effective/viscous/rate-dependent/thermal/friction/over shear stress at slip system α; $p_{\mathrm{sl}\,t}$ and $p_{\mathrm{sl}\,b}$ are the constitutive exponents that respectively describe the shape of the top and bottom of the short-range obstacle force-distance profile and are constrained by: $0 < p_{\mathrm{sl}\,t} \leq 1$; $1 \leq p_{\mathrm{sl}\,b} \leq 2$; $\tau_{\mathrm{sl\ cr}}^\alpha$ is the mean critical/plastic/athermal/rate-independent/internal/back (resolved) shear stress to activate the slip at system α; and $\langle\ \rangle$ is the Macaulay brackets: $\langle \bullet \rangle = \frac{1}{2}(|\bullet| + \bullet)$.

By assuming $p_{\mathrm{sl}\ t} = p_{\mathrm{sl}\ b} = 1$, which corresponds to a so-called box-shaped or rectangular/square dislocation-obstacle interaction potential [177–180], Gibbs [181] proposed a simplified parameter-free version of Eq. (11) for the calculation of the Gibbs free energy difference for bypassing short-range obstacles by slipping dislocations:

$$p_{\mathrm{sl}\ t} = p_{\mathrm{sl}\ b} = 1;$$
$$\Rightarrow \Delta G_{\mathrm{sl}}^\alpha = \Delta F_{\mathrm{sl}} - \tau_{\mathrm{sl\ eff}}^\alpha \Delta V_{\mathrm{sl}}; \quad \Delta V_{\mathrm{sl}} \equiv -\frac{\partial \Delta G_{\mathrm{sl}}^\alpha}{\partial \tau_{\mathrm{sl\ eff}}^\alpha} = \frac{\Delta F_{\mathrm{sl}}}{\tau_{\mathrm{sl}0}}; \tag{12}$$

where ΔV_{sl} is the activation volume for slip, also known as apparent/operational activation volume. It contains information about the short-range obstacles to dislocation motion [182].

At the meso–scale material points, the critical shear stress at slip systems is assumed to be the maximum between intra-granular and inter-granular resistances. The intra-granular critical shear stress at slip system α ($\tau_{\rho\ \mathrm{cr}}^\alpha$) is the minimum shear stress at slip system α (in average) that needs to be overcome for bowed-out mobile dislocations to slip. $\tau_{\rho\ \mathrm{cr}}^\alpha$ is a function of (total) dislocation density (stored in grain interiors) and calculated by the generalized Taylor equation, which accounts for the anisotropic interactions between slip systems (latent hardening) [183,184]. The inter-granular critical shear stress ($\tau_{d\,\mathrm{cr}}$) is a function of effective grain size (d_{eff}) and calculated according to the Hall–Petch equation [185,186]. The scalar d_{eff} is defined to be the average of mean equivalent grain diameters, which are calculated using distributions based on number and area fractions. Therefore,

$$\tau_{\mathrm{sl\ cr}}^\alpha = \max\left\{\tau_{\rho\ \mathrm{cr}}^\alpha, \tau_{d\ \mathrm{cr}}\right\};$$
$$\tau_{\rho\ \mathrm{cr}}^\alpha = \mu b_{\mathrm{sl}} \sqrt{\sum_{\acute{\alpha}=1}^{N_{\mathrm{sl}}} [\mathbf{A}]^{\alpha\acute{\alpha}} \rho_t^{\acute{\alpha}}}; \quad \tau_{d\ \mathrm{cr}} = \frac{k_{\mathrm{HP}}}{\sqrt{d_{\mathrm{eff}}}}; \tag{13}$$

where μ is the shear modulus (see Appendix F); $[\mathbf{A}]^{\alpha\acute{\alpha}}$ is the slip interaction strength matrix entry representing strength of interaction between slip systems α and α' (see Appendix G); and k_{HP} is the Hall–Petch constant. Eq. (13) implies that with low dislocation density and low effective grain size (corresponding to high grain boundary area density), critical shear stress for the onset of plasticity is controlled by the Hall–Petch relationship (size effect).

The overall evolution (time rate) of unipolar and dipolar dislocation densities at slip system α is given by (the derivation is given in Appendix H):

$$\dot{\rho}_u^\alpha = \left(\frac{1}{\Lambda_{\mathrm{sl}}^\alpha} - 2h_{d\ \max}^\alpha \rho_u^\alpha\right) \frac{\left|\dot{\gamma}_{\mathrm{sl}}^\alpha\right|}{b_{\mathrm{sl}}};$$
$$\dot{\rho}_d^\alpha = 2\left(h_{d\ \max}^\alpha \rho_u^\alpha - h_{d\ \min} \rho_t^\alpha\right) \frac{\left|\dot{\gamma}_{\mathrm{sl}}^\alpha\right|}{b_{\mathrm{sl}}} - \frac{4\left|\bar{v}_{\mathrm{cl}\ d}^\alpha\right|}{h_{d\ \max}^\alpha - h_{d\ \min}} \rho_d^\alpha; \tag{14}$$

where $\Lambda_{\mathrm{sl}}^\alpha$ is the mean free path (MFP) for dislocation slip at system α; $h_{d\,\min}$ is the minimum height (slip plane spacing) of stable dislocation dipoles (in average); $h_{d\ \max}^\alpha$ is the maximum height of stable dipoles at slip system α (in average); and $|\bar{v}_{\mathrm{cl}\ d}^\alpha|$ is the average (out-of-plane) climb speed/rate of dipolar dislocations located at slip system α.

The upper bound of the dipole height is calculated as follows [166,187–189]:

$$h_{d\ \max}^\alpha = \frac{\mu b_{\mathrm{sl}}}{8\pi(1-\nu)\left|\tau_{\mathrm{sl}\ c}^\alpha\right|}; \quad h_{d\ \min} \leq h_{d\ \max}^\alpha \leq \Lambda_{\mathrm{sl}}^\alpha; \tag{15}$$

where ν is Poisson's ratio (see Appendix F). The mean climb velocity is a function of the average dipole height and temperature [187–189]:

$$\left|\bar{v}_{\mathrm{cl}\ d}^\alpha\right| \cong \frac{D_v V_{\mathrm{cl}} \xi^\alpha}{b_{\mathrm{sl}}^2 k_B T}; \quad D_v = D_{v0} \exp\left(-\frac{Q_v}{k_B T}\right);$$
$$\xi^\alpha = \frac{\mu b_{\mathrm{sl}}^2}{2\pi(1-\nu)\bar{h}_d^\alpha}; \quad \bar{h}_d^\alpha = \frac{h_{d\ \min} + h_{d\ \max}^\alpha}{2}; \tag{16}$$

where V_{cl} is the activation volume for climb, which can be calculated by atomistic simulations [190]; ξ^α is the average normal force (parallel to the slip plane normal) exerted over unit length of the dislocation line, under which dipole partners attract one another; Q_v is the mean thermal activation energy for vacancy diffusion; D_v is self-diffusivity or self/vacancy diffusion coefficient; D_{v0} is reference/pre-exponential self-diffusivity (vacancy diffusion

coefficient at high temperatures so that $T \gg {Q_v}/{k_B}$); and $\tilde{h}_d^\alpha$ is the average dipole height at slip system α. Q_v and D_{v0} can be calculated via *ab initio* molecular dynamics (AIMD) [191].

The notion of mean free path was first introduced by Kocks and co-workers [192,193]. The MFP for slip (or the slip MFP) at system α is known as the mean distance for slip of a mobile dislocation before its motion is impeded by an obstacle (dislocation accumulation/storage) [194]. However, more fundamentally, the slip MFP determines the mean (mobile) dislocation segment length and curvature, and therefore, controls the rate of dislocation multiplication (see Appendix H). The slip MFP has confining contributions due to various existing sources of obstacles (grain boundaries, forest dislocations and twin boundaries), which can be homogenized using the following harmonic mean/mixture law [195–197]:

$$\frac{1}{\Lambda_{\text{sl}}^\alpha} = \frac{1}{d_{\text{eff}}} + \frac{1}{\lambda_f^\alpha} + \frac{1}{\lambda_{\text{sl}-\text{tw}}^\alpha}; \tag{17}$$

where λ_f^α is the effective "forest" dislocations spacing at slip system α; and $\lambda_{\text{sl}-\text{tw}}^\alpha$ is the mean spacing among twin boundaries interacting with slipping mobile dislocation at slip system α.

The most significant contribution to the slip MFP arises from the interaction of mobile dislocations with forest dislocations, which are the dislocations of other systems that pierce their slip plane. The well-known relationship for the effective forest spacing ($\lambda_f \propto \frac{1}{\sqrt{\rho_t}}$) [177,193,194] can be generalized to account for the contribution of different slip systems (α') on the forest hardening [198] of a specific slip system (α) [199–201]:

$$\frac{1}{\lambda_f^\alpha} = \frac{1}{c_f}\sqrt{\sum_{\acute{\alpha}=1}^{N_{\text{sl}}} \left[\mathbf{B}_f\right]^{\alpha\acute{\alpha}} \rho_t^{\acute{\alpha}}}; \quad \left[\mathbf{B}_f\right]^{\alpha\acute{\alpha}} = \left|\widehat{\underline{\boldsymbol{n}}}_{\text{sl}}^\alpha \cdot \widehat{\underline{\boldsymbol{t}}}_e^{\acute{\alpha}}\right|; \quad \widehat{\underline{\boldsymbol{t}}}_e^{\acute{\alpha}} = \widehat{\underline{\boldsymbol{n}}}_{\text{sl}}^{\acute{\alpha}} \times \widehat{\underline{\boldsymbol{b}}}_{\text{sl}}^{\acute{\alpha}}; \tag{18}$$

where c_f is the constitutive coefficient associated with the forest interactions; $\mathbf{B}_f$ is the matrix detailing anisotropic forest interaction coefficients (forest projection matrix); and $\boldsymbol{t}_e$ is the edge dislocation (tangent) line vector.

In case of the occurrence of twinning, Fullman's stereological law [202] can be invoked to calculate the mean twin boundary spacing. The generalized/modified form of Fullman's relationship, accounting for anisotropic interaction of different twin systems on restricting the MFP for slip at system α, proposed by Allain et al. [89], is given by:

$$\frac{1}{\lambda_{\text{sl}-\text{tw}}^\alpha} = \frac{1}{c_{\text{sl}-\text{tw}}} \sum_{\beta=1}^{N_{\text{tw}}} \left[\mathbf{B}_{\text{sl}-\text{tw}}\right]^{\alpha\beta} \frac{f_{\text{tw}}^\beta}{s_{\text{tw}}(1-f_{\text{tw}})};$$

$$\left[\mathbf{B}_{\text{sl}-\text{tw}}\right]^{\alpha\beta} = \begin{cases} 0 & : \widehat{\underline{\boldsymbol{n}}}_{\text{sl}}^\alpha = \widehat{\underline{\boldsymbol{n}}}_{\text{tw}}^\beta \\ 1 & : \widehat{\underline{\boldsymbol{n}}}_{\text{sl}}^\alpha \neq \widehat{\underline{\boldsymbol{n}}}_{\text{tw}}^\beta \end{cases}; \tag{19}$$

where $c_{\text{sl}-\text{tw}}$ is a constitutive coefficient pertaining to the effective topology of twins and its impact on the slip resistance; s_{tw} is the mean twin thickness, which often decreases with decreasing SFE [142]; and $\mathbf{B}_{\text{sl}-\text{tw}}$ is the anisotropic slip-twin interaction matrix, defined based on the assumption that only a twin system (β), which is non-coplanar/secant with a specific slip system (α) confines its slip MFP.

3.2.2. Kinetics of twinning

We adopted the following principal relationships for the kinetics of twinning and the evolution of twin volume fraction based on the continuum formalism established by the works of Olson and Cohen [203], Remy [204], and Allain at al. [196]:

$$\dot{\gamma}_{\text{tw}}^\beta = \gamma_{\text{tw}} \dot{f}_{\text{tw}}^\beta;$$

$$\dot{f}_{\text{tw}}^\beta = (1-f_{\text{tw}}) V_{\text{tw}}^\beta \dot{n}_{\text{tw}}^\beta P_{\text{tw}}^\beta; \quad V_{\text{tw}}^\beta = \frac{\pi}{4}\left(\Lambda_{\text{tw}}^\beta\right)^2 s_{\text{tw}}; \tag{20}$$

where γ_{tw} is the characteristic plastic shear strain induced by twinning, which in case of cubic crystals is $\gamma_{\text{tw}}^{\text{cubic}} = {\sqrt{2}}/{2}$; V_{tw}^β is the average volume of twins on twin system β; $\dot{n}_{\text{tw}}^\beta$ is the average number density of twin stacking faults nucleated per unit time at twin system β; P_{tw}^β is the probability density for propagation/bowing-out of the corresponding twin nucleus to form a twin under the application of the homogenized RSS at twin system β (τ_{tw}^β); and $\Lambda_{\text{tw}}^\beta$ is the MFP for twinning at twin system β. The model used for calculation of $\dot{n}_{\text{tw}}^\beta$ in fcc crystals is presented in Appendix I. This model is based on a mechanism in which two full/perfect dislocations dissociate into fault pairs and react on the primary slip plane to produce three Shockley partial dislocations on successive parallel planes.

The twin propagation (from the existing twin stacking fault embryos) is a stochastic event, that requires sufficiently high local stress concentration (typically at dislocation pile-ups at grain boundaries), which can be maintained only if the mean RSS at the respective twin system is adequately high. We adopted the probabilistic treatment of the twin propagation process (based on its underlying physics) as a stochastic Poisson process described by the following cumulative PDF [163,205–208]:

$$P_{\text{tw}}^\beta = \exp\left(-\left(\frac{\langle \tau_{\text{tw}}^\beta \rangle}{\tau_{\text{tw cr}}}\right)^{-p_{\text{tw}}}\right); \quad p_{\text{tw}} > 0; \tag{21}$$

where p_{tw} is the constitutive exponent controlling the sigmoid shape of the associated cumulative PDF (P_{tw}^β), which is affected by the heterogeneity in elemental micro-segregation (distribution of alloying elements and its variance in lower scales); and $\tau_{\text{tw cr}}$ is the critical RSS (at twin systems) for twin propagation (the model for calculation of $\tau_{\text{tw cr}}$ in fcc crystals is given in Appendix I).

Finally, it is envisaged that the propagation of twins is mainly terminated at either grain boundaries or twin boundaries [209], which are non-coplanar with the propagating twin. As a result, the mean free path for twins at twin system β is given by the following harmonic mean relationship [89]:

$$\frac{1}{\Lambda_{\text{tw}}^\beta} = \frac{1}{c_{\text{tw}-\text{tw}}}\left(\frac{1}{d_{\text{eff}}} + \frac{1}{\lambda_{\text{tw}-\text{tw}}^\beta}\right);$$

$$\frac{1}{\lambda_{\text{tw}-\text{tw}}^\beta} = \sum_{\beta'=1}^{N_{\text{tw}}} \left[\mathbf{B}_{\text{tw}-\text{tw}}\right]^{\beta\beta'} \frac{f_{\text{tw}}^{\beta'}}{s_{\text{tw}}(1-f_{\text{tw}})};$$

$$\left[\mathbf{B}_{\text{tw}-\text{tw}}\right]^{\beta\beta'} = \begin{cases} 0 & : \widehat{\underline{\boldsymbol{n}}}_{\text{tw}}^\beta = \widehat{\underline{\boldsymbol{n}}}_{\text{tw}}^{\beta'} \\ 1 & : \widehat{\underline{\boldsymbol{n}}}_{\text{tw}}^\beta \neq \widehat{\underline{\boldsymbol{n}}}_{\text{tw}}^{\beta'} \end{cases}; \tag{22}$$

where $c_{\text{tw}-\text{tw}}$ is a constitutive coefficient associated with the effective topology of twins and its impact on the strength of twin-twin interaction; and $\mathbf{B}_{\text{tw}-\text{tw}}$ is the anisotropic twin-twin interaction coefficients matrix, which is defined using the same rule as for $\mathbf{B}_{\text{sl}-\text{tw}}$.

Further, the twin (lateral) growth/thickening phenomenon is observed to be the dominant twin (fraction) evolution mechanism in some materials (e.g. magnesium), particularly those with a low symmetry crystal structure (e.g. hcp lattice), as in those materials the threshold for twin nucleation and propagation is presumably higher than that for twin growth [205,210–214]. In the presented model for twin evolution, the twin growth mechanism is not considered through the adoption of a constant (mean) twin thickness (s_{tw}), which is reasonable in alloys with cubic crystal symmetry [141,142,215]. Nevertheless, by introducing a variable twin thickness with its respective kinetics relationship, the twin growth mechanism could be incorporated in the twinning model.

Table 3
Designation and features of the generated RVEs.

RVE character	Designation	Morphology (M)	Texture (T)
Experimental (E)	EM-ET	Experimental	Experimental
Half-random	EM-RT	Experimental	Random
	RM-ET	Random	Experimental
Random (R)	RM-RT	Random	Random

3.3. Microstructure modeling (RVE generation)

As mentioned earlier, a (single-phase) microstructure owns two main categories of (fairly distinctive) characteristics on the meso–scale: (grain) morphology and (crystallographic) texture. The results of the statistical analysis of the as-built microstructure (Section 2.3) were used to model the initial microstructure by means of generating a periodic statistically representative volume element in three dimensions. The main reasons for modeling the "experimental" RVE are, firstly, to fit the constitutive parameters associated with the investigated material, and secondly, to validate the applied three levels of continuum physics-based (crystal finite strain, constitutive and microstructure) modeling. Subsequently, RVEs with at least one random feature (morphology, texture or both) were generated for (case-) studying the impact of different aspects of microstructural heterogeneity on the overall anisotropic polycrystal plasticity.

The robust microstructure modeling formalism for generating 3D RVE using an integrated experimental–computational approach, established through the works of Saylor et al. [216], Deka et al. [217], and Groeber et al. [101,218,219], (implemented in the DREAM.3D code [107]), was used (see Appendices A and J). The applied automated methodology to generate RVEs with periodic boundaries is made up of four principal modules: (i) equivalent ellipsoidal grain generator (controlling grain size, shape and shape-axes orientation), (ii) constrained grain packer (controlling the spatial placement of grains), (iii) seed point generator-constrained Voronoi tessellation tool, and (iv) crystallographic orientation assigner (controlling the bulk texture and boundary misorientation). The RVE generation process termed as statistically induced realistic instantiations (SIRI) [218], which assembles the sequence of the aforementioned modules, produces a realistic model of the corresponding microstructure, based on its morphological and texture-related characteristics (for more detail see Appendix J).

As mentioned earlier, case-study "random" and "half-random" RVEs with at least one random/homogenous feature (morphology, texture or both) were constructed. The generated experimental and random RVEs with their corresponding features and designations are listed in Table 3. Through the analysis of the EBSD orientation maps (the average values of the ∥BD and ⊥BD sections taken from Fig. 4), the experimental morphological descriptors were determined. The grain size and shape descriptors used in the generation of volume elements with experimental and random grain morphologies are listed in Table 4. The grain shape-axes orientation as an input for the construction of grain structures with experimental and random morphologies, in terms of pole figures with respect to the ellipsoidal grain principal axes is shown in Fig. 10. It should be noted that the grain shape-axes orientation distribution used for generating the experimental (morphological) volume elements are derived from the experimental characterization of grain morphology on the orthogonal ∥BD and ⊥BD sections (Fig. 4(e) and (f)).

Table 4
The grain size and shape descriptors used for generating the volume elements with experimental and random grain morphologies.

Morphological descriptor	Experimental	Random
Mean grain size ($\bar{d}$) [μm]	14.15	14.15
Logarithmic grain size mean ($\mu_{\ln}$) [-]	2.335	2.57
Logarithmic grain size standard deviation ($\sigma_{\ln}$) [-]	0.772	0.4
Minimum grain size cut off ($d_{\min}$) [μm]	3	3
Maximum grain size cut off ($d_{\max}$) [μm]	70	35
Grain size bin step size (Δd_{bin}) [μm]	0.6	0.6
Average minimum aspect ratio ($\bar{m}_{\min}$) [-]	0.3	1
Average maximum aspect ratio ($\bar{m}_{\max}$) [-]	0.5	1

To construct the (fully-) experimental (EM-ET) RVE, the texture-related descriptors were analyzed from the superposition of the measured ODFs and (correlated) MDFs associated with the orthogonal ∥BD and ⊥BD sections of the as-built material (Figs. 5 and 6). They served as an input to the synthetic microstructure generator. Subsequently, a cubic RVE with periodic boundaries and a minimalistic grid resolution (GR) of $16 \times 16 \times 16 = 4096$ (voxels) was generated. Additionally, a volume element having a random morphology but with the same number of grains, mean grain size and grid resolution as its experimental counterpart was generated. Furthermore, in order to demonstrate the distribution of simulated field variables with a relatively high resolution, another experimental RVE containing 1321 grains with a grid resolution of $64^3 = 262144$ was generated. For this, the same input parameters as for the experimental RVE with GR $= 16^3$ were used. The volume elements with different grain morphology and grid resolution are shown in Fig. 11.

The maximum number of grains embedded in a morphological volume element is limited by the extent of morphological heterogeneities as well as the grid resolution (e.g., a GR $= 16^3$ cannot contain more than $16^3 = 4096$ grains). Moreover, the lower bound for the required number of grains inside an RVE is dependent on the overall microstructural heterogeneities (e.g., for modeling a single crystal material an RVE with a GR $= 1^3$ is sufficient). For each generated RVE in this study, all the microstructural heterogeneity characteristics of interest, as discussed earlier, have been sufficiently captured. Moreover, all the generated cubic volume elements have periodic boundaries. This means that the grains that are cut by a face of the volume element appear from the opposite

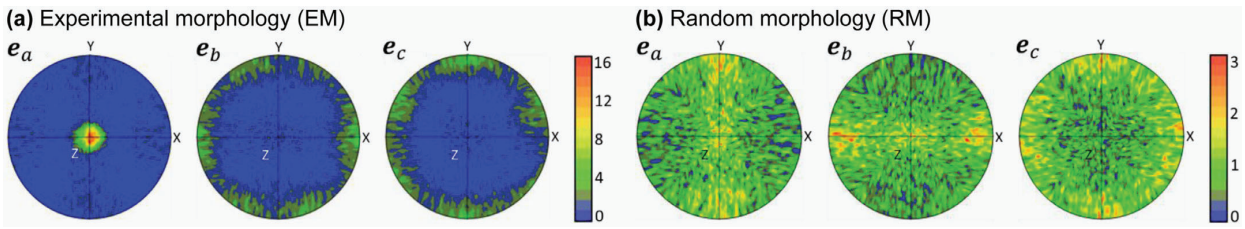

Fig. 10. The grain shape-axes orientation distribution as an input for generating the morphological grain structure, in terms of pole figures with respect to the ellipsoidal grain principal axes ($\boldsymbol{e}_a$, $\boldsymbol{e}_b$, $\boldsymbol{e}_c$).

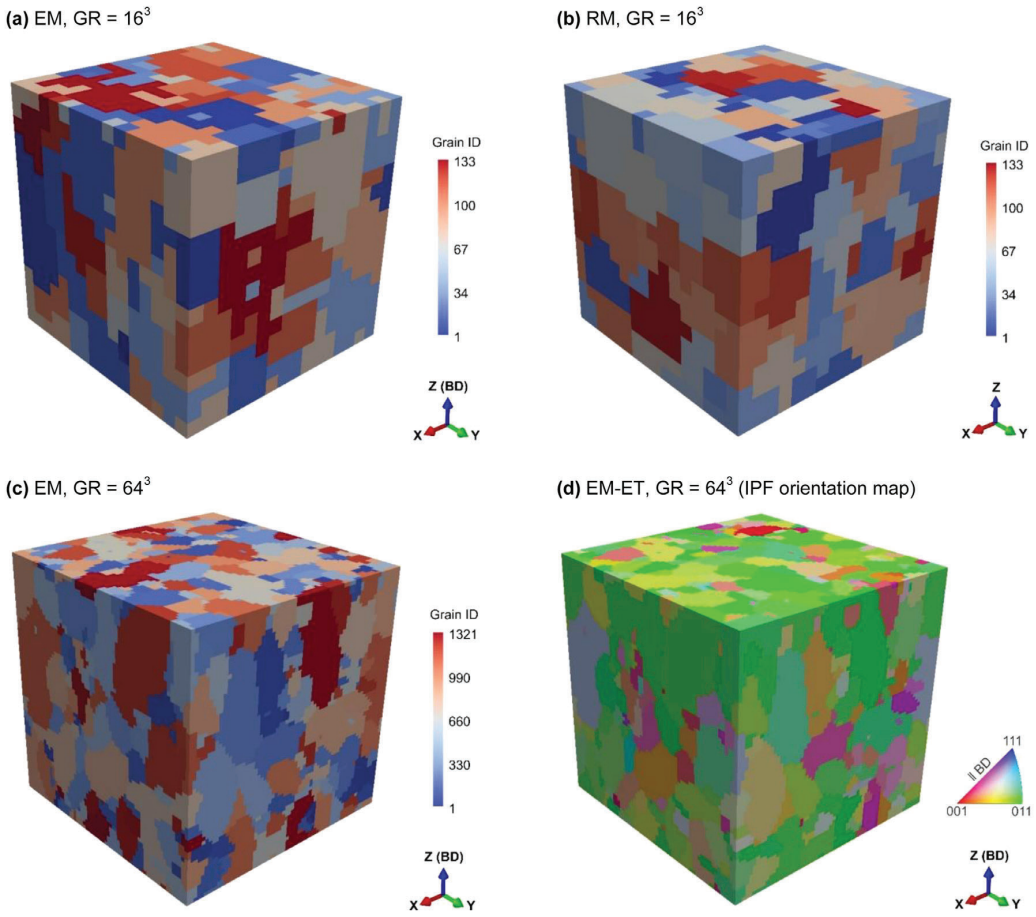

Fig. 11. The volume elements with different grain morphology and grid resolution (see Appendix A). Paraview software [220] was used for visualization of the RVEs.

parallel face, unless the respective face cuts the corresponding grain at its (grain) boundary.

In the construction of the half-random and random RVEs (RVEs with at least one random feature: morphology or texture), among the texture-related descriptors, the MDF is assumed to be random (uncorrelated: fully dependent on the ODF), since the correlated MDF is a both texture-related and morphological characteristic. Therefore, in case of randomness of one of the dualistic aspects of microstructural heterogeneity (grain morphology or texture), the MDF should be considered fully dependent on the ODF. As such, the experimental ODF (superposed ODFs associated with the measured macro-texture on ∥BD and ⊥BD planes (Fig. 5)) and a random ODF were used in an iterative procedure. This procedure involved random sampling and subsequent assignment of crystallographic orientations to the grains of the (random and experimental) volume elements, so that the outcome bulk texture (weight-averaged by grain volume) of the respective RVE fits to the desired ODF (in terms of IPFs within a tolerance). The IPFs associated with the bulk texture of the generated RVEs are shown in Fig. 12.

4. Crystal plasticity simulation

Homogenous external boundary conditions corresponding to displacement-controlled uniaxial tension at quasi-static strain rate of 10^{-3} s^{-1} and room temperature ($T = 23\,^{\circ}C$) along different axes were imposed on the generated RVEs. First, the experimental (EM-ET) and random (RM-RT) RVEs with grid resolution of 16^3 were used for identification of the constitutive parameters and validation of the modeling approach. Then, the experimental RVE with GR = 64^3 was utilized for demonstration of distribution of simulated resolved field variables. Lastly, the half-random (RM-ET and EM-RT) RVEs were used for studying the influence of different aspects of microstructural heterogeneity on the macroscopic anisotropic response of the polycrystalline aggregate under plastic deformation.

4.1. Constitutive parameters and validation

The (fully) experimental (EM-ET) RVE was set under homogenous external (displacement-controlled) uniaxial tension at quasi-static strain rate of $\dot{\bar{\varepsilon}} = 10^{-3}$ s^{-1} and room temperature $T = 23\,^{\circ}C$ along the X-axis (or any other direction in the X–Y plane), with an initial guess for the unknown constitutive parameters. Afterwards, the outcome homogenized flow curve was fitted to the experimental (true) stress–strain response associated with the horizontal (LD⊥BD) sample (Figs. 1 and 2). The (inverse) parameter fitting/calibration was carried out by an iterative updating of the aforementioned target constitutive parameters followed by subsequent simulations in order to minimize the deviation between the simulated homogenized response with its corresponding experimental counterpart. The fitted constitutive parameters as well as the material constants that were adopted from various sources are presented in Table 5. The (meso–scale) simulations

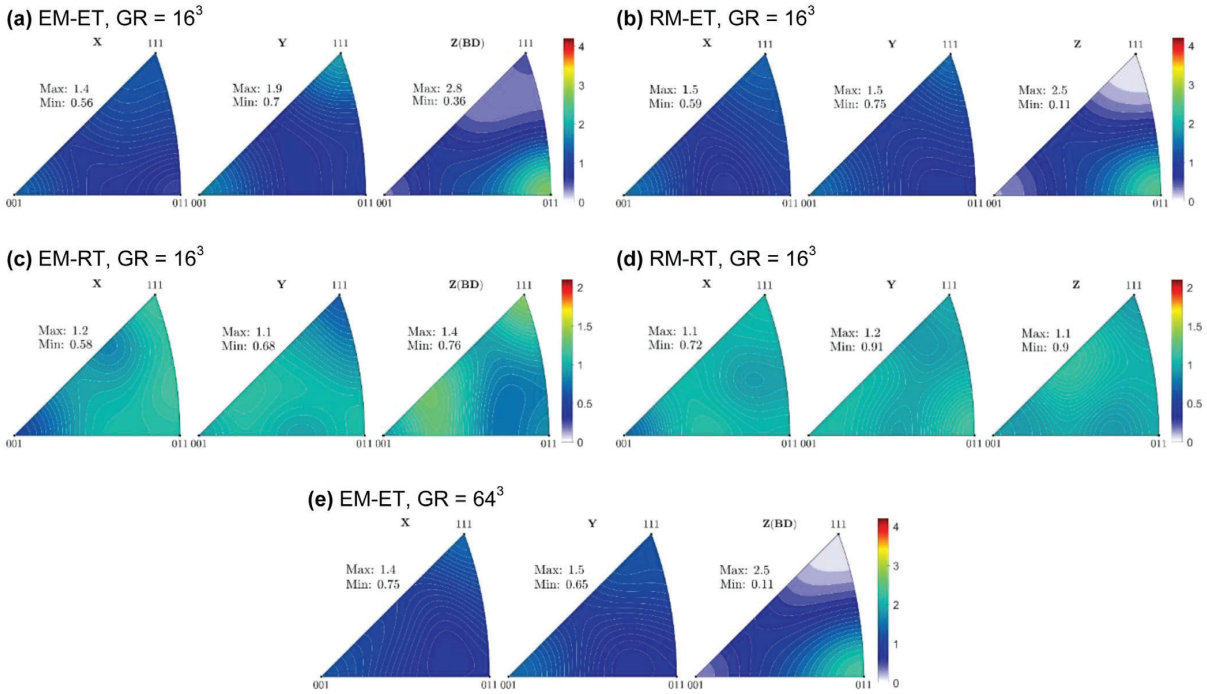

Fig. 12. The IPFs associated with the bulk texture of the constructed RVEs (see Appendix A).

Table 5
Constitutive parameters.

Category	Parameter	Symbol	Value[a]	Unit	Source
General	Crystal symmetry	-	fcc		(See Appendices E,F,G and I)
	Lattice constant	a_0	0.361	nm	[89,221,222] (see Appendix E)
	Elastic constants	C_{11}	175	GPa	[223](see Appendix F)
		C_{12}	115	GPa	
		C_{44}	135	GPa	
Initial MSVs	Initial unipolar dislocation density	ρ^{α}_{u0}	3×10^{13}	m^{-2}	Fitting (inspired by Fig. 9(a))
	Initial dipolar dislocation density	ρ^{α}_{d0}	10^{12}	m^{-2}	Fitting (inspired by Fig. 7(a-c))
	Initial twin volume fraction	f^{β}_{tw0}	0	-	Fig. 9(b)
Size effect	Effective grain size	d_{eff}	30	μm	Fig. 4(a) and (b)
	Hall-Petch constant	k_{HP}	145.4	MPa $\mu m^{\frac{1}{2}}$	[84] (assuming a Taylor factor of $M = 3.06$)
Slip kinetics	Thermal activation (Helmholtz free) energy for slip	ΔF_{sl}	0.9	eV	[224]
	Reference slip speed of unipolar dislocations	$v_{sl\ u0}$	5×10^{-7}	$m\,s^{-1}$	[224]
	Maximum short-range slip resistance	τ^{α}_{sl0}	44	MPa	Fitting (inspired by [224,225])
	Top shape parameter for short-range obstacle force-distance profile	$p_{sl\ t}$	1	-	Eq. (12)
	Bottom shape parameter for short-range obstacle force-distance profile	$p_{sl\ b}$	1	-	Eq. (12)
Recovery	Minimum stable dipole height	$h_{d\ min}$	6	b_{sl}	[166]
	Thermal activation energy for (climb) vacancy diffusion	Q_v	2.05	eV	Fitting (inspired by [226,227])
	Activation volume for climb	V_{cl}	1	b^3_{sl}	[166]
	Reference self-diffusion coefficient	D_{v0}	0.4	$cm^2\,s^{-1}$	[225]
Twinning kinetics	Parameter associated with twin propagation PDF	p_{tw}	3.5	-	Fitting
	Twin thickness	s_{tw}	0.2	μm	Fitting (Inspired by Fig. 7(d-f))
	Length of twin nucleus	l_{tw}	375	b_{sl}	Fitting (inspired by [228]) (see Appendix I)
	Activation volume for cross-slip	V_{cs}	15	b^3_{sl}	[229–231] (see Appendix I)
	Critical distance for proximity of repulsive partial dislocations to form twin's stacking fault nucleus	r_c	1	nm	[231] (see Appendix I)
	Stacking fault energy	Γ_{sf}	20.2	$mJ\,m^{-2}$	[86,89] (see Appendix I)
Mean free paths	Parameter associated with the forest interaction	$c_f \equiv c_{sl-sl}$	15	-	Fitting
	Parameter associated with the effective topology of twins and its impact on the slip resistance	c_{sl-tw}	10	-	Fitting
	Parameter associated with the effective topology of twins and its impact on the strength of twin-twin interaction	c_{tw-tw}	0.1	-	Fitting

[a] The listed values for most of the constitutive parameters are specific for the chosen austenitic high-manganese steel at room temperature with the chemical composition and processing details specified in Tables 1 and 2, respectively.

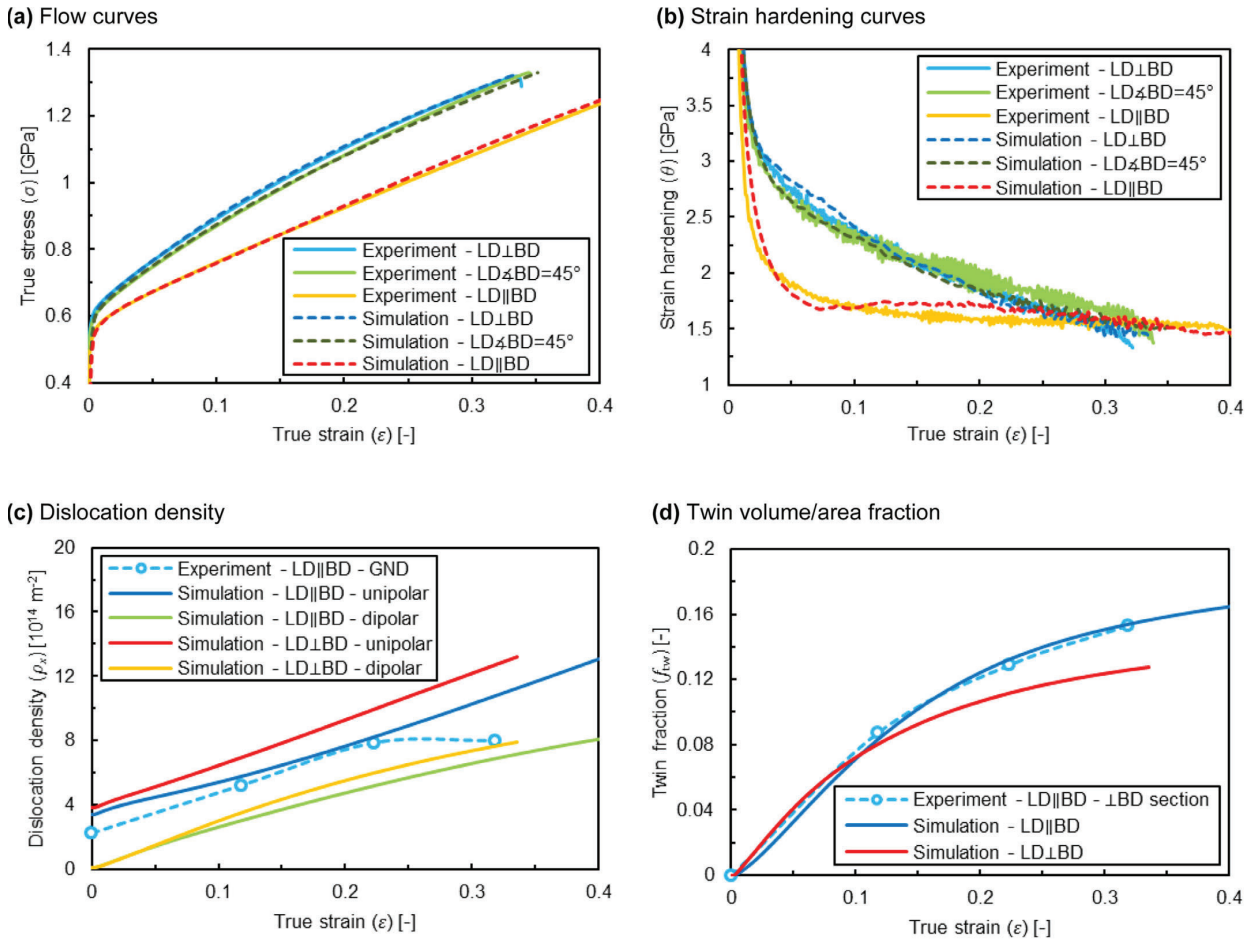

Fig. 13. Comparison among experimental and simulated homogenized true stress–strain (see Appendix K), strain hardening and the evolution of MSVs in the investigated material under uniaxial tension at $\dot{\bar{\varepsilon}} = 10^{-3}$ s^{-1} and $T = 23\,^{\circ}$C along different axes.

in this study have been exceptionally informed by independent experimental measurements and/or lower scale simulations.

Subsequently, homogenous external boundary conditions for displacement-controlled uniaxial tension at $\dot{\bar{\varepsilon}} = 10^{-3}$ s^{-1} and $T = 23\,^{\circ}$C along the axes corresponding to the vertical (LD∥BD) and diagonal (LD∡BD $= 45^{\circ}$) samples were imposed on the experimental RVE. The comparison among experimental and simulated homogenized true stress–strain (see Appendix K), strain hardening and the MSVs in the investigated material is shown in Fig. 13.

As shown in Fig. 13(a) and (b), the simplifying assumptions made in the crystal plasticity modeling (Section 3) are sufficient/valid for accurately capturing the complex anisotropic polycrystal plasticity, which is observed experimentally. The initial yield in the investigated material does not show notable anisotropy, while the anisotropy in strain hardening behavior of the polycrystalline aggregate is profound. Moreover, the simulated twin volume fraction (Fig. 13(d)) is consistent with the experimentally measured twin area fraction (on ⊥BD plane), where LD∥BD. The simulated unipolar dislocation density in the case of LD∥BD is close to the measured mean GND density (Fig. 8 and 9(a)) except for the relatively large strains. In principle, the unipolar dislocation density must be higher than the GND density in a sufficiently large volume, since GNDs are a subset of unipolar dislocations. There is a large difference between the measured mean GND density and the simulated unipolar dislocation density at $\bar{\varepsilon} = 0.32$. This is partly due to the sensitivity of GND density mapping to the frequency of unindexed points in the EBSD orientation maps, which is often high at large strains. In order to further validate the modeling approach, particularly the microstructure modeling (Section 3.3) method, the generated fully random (RM-RT) RVE was exposed to homogenous external uniaxial tension (at $\dot{\bar{\varepsilon}} = 10^{-3}$ s^{-1} and $T = 23\,^{\circ}$C) along the X and Z axes. The resulting simulated homogenized tensile true stress–strain and strain hardening curves are plotted against those of the experimental (EM-ET) RVE in Fig. 14. As expected, the plastic flow behavior of the modeled fully random microstructure (RM-RT RVE) is almost fully isotropic.

4.2. Case-study simulations

In Fig. 15, the simulated homogenized evolution of the stress, strain hardening and MSVs under uniaxial tension (at $\dot{\bar{\varepsilon}} = 10^{-3}$ s^{-1} and $T = 23\,^{\circ}$C) along different axes associated with the half-random RVEs (EM-RT and RM-ET) are compared to those of the experimental (EM-ET) RVE.

As shown in Fig. 15(a) and (b), any inhomogeneity of the discussed microstructural aspects in the polycrystalline aggregate contributes to its anisotropic response under plastic deformation. Fig. 15(a) and (b) implies that both morphological and texture

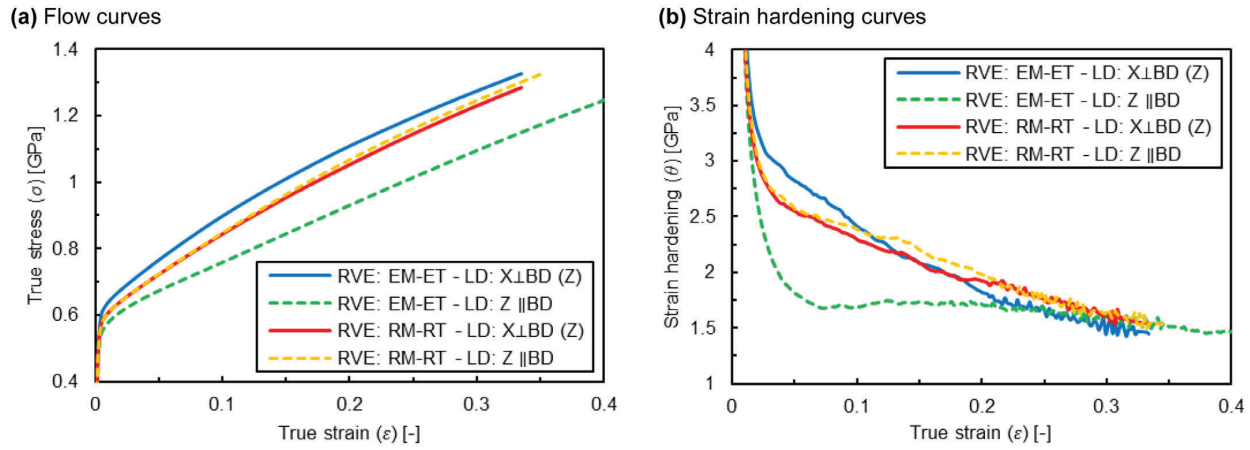

Fig. 14. Simulated homogenized true stress–strain and strain hardening curves of the fully random (RM-RT) RVE against those of fully experimental (EM-ET) RVE under uniaxial tension at $\dot{\bar{\varepsilon}} = 10^{-3}$ s^{-1} and $T = 23\,^{\circ}$C along different axes.

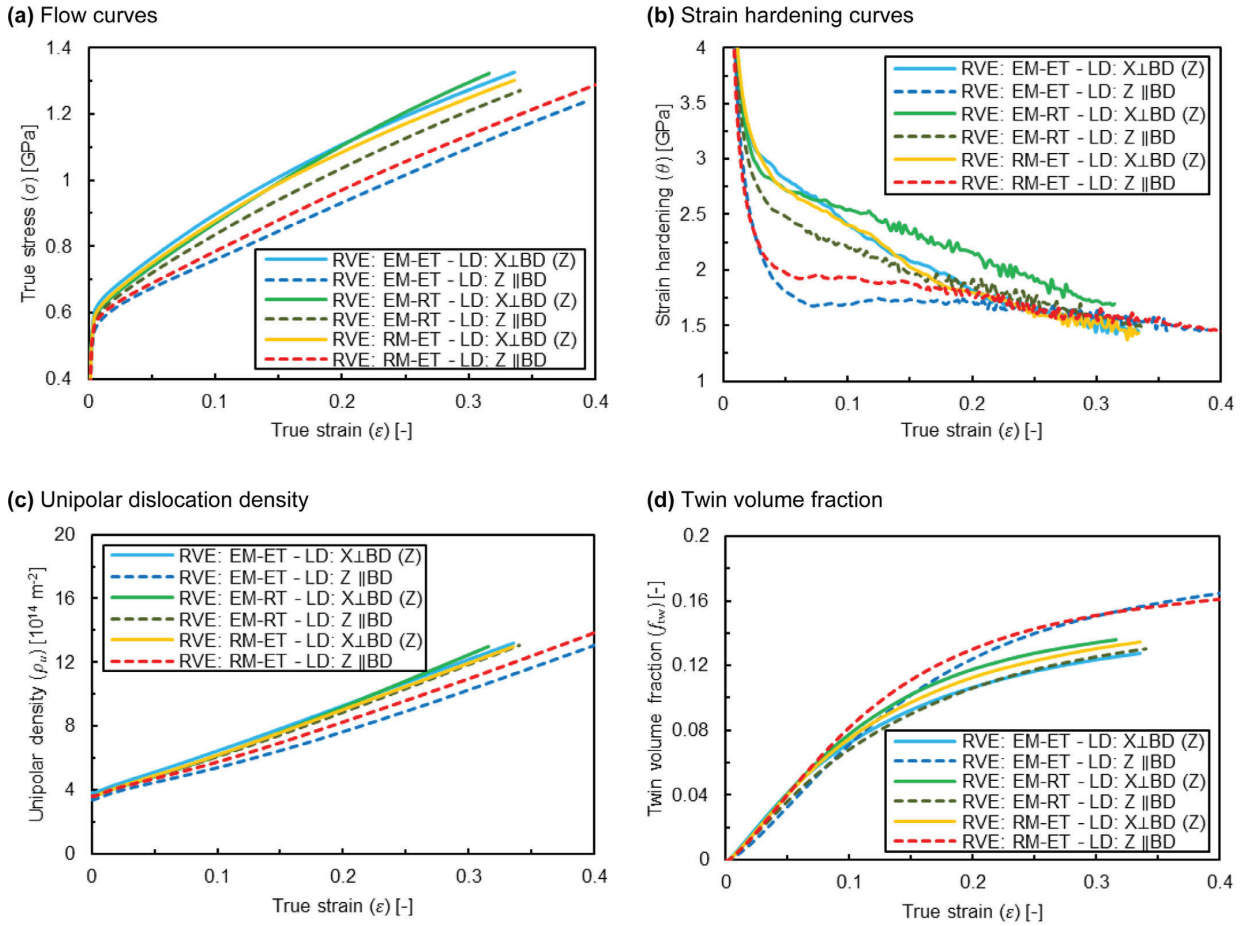

Fig. 15. Simulated homogenized evolution of the stress–strain, strain hardening and MSVs under uniaxial tension (at $\dot{\bar{\varepsilon}} = 10^{-3}$ s^{-1} and $T = 23\,^{\circ}$C) along different axes associated with the half-random RVEs (EM-RT and RM-ET) versus those of the fully experimental (EM-ET) RVE.

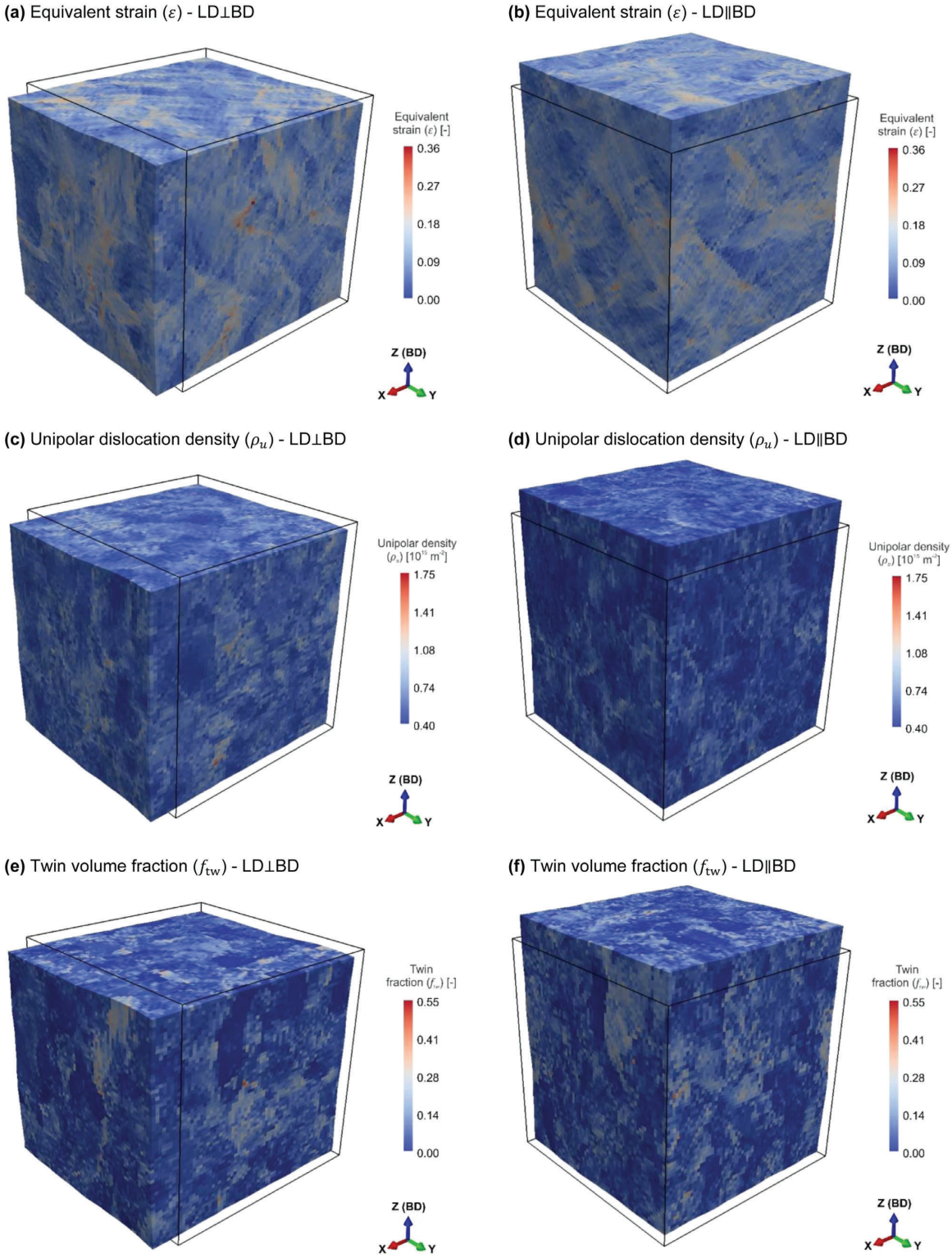

Fig. 16. Simulated resolved equivalent strain, unipolar dislocation density and twin volume fraction for the (fully) experimental RVE with GR = 64^3, deformed along different axes (LD⊥BD and LD∥BD) under uniaxial tension at $\dot{\bar{\varepsilon}} = 10^{-3}$ s^{-1} and $T = 23\,^{\circ}C$ until a true tensile strain $\bar{\varepsilon} = 0.095$, which corresponds to approximately $\varepsilon^{eng} = 10\%$ engineering tensile strain (visualized by Paraview [220]).

heterogeneities almost equally but differently affect the overall anisotropic plasticity. However, one might argue that texture has a slightly stronger impact on the anisotropic response of the material. The flow curves of the experimental RVE associated with two different tensile loading axes act as the bounds for those of the half-random RVEs, meaning that the strongest anisotropy pertains to the case in which both grain morphology and texture are polarized.

In the investigated material, the unique processing conditions of AM have led to a specific morphological heterogeneity, which corresponds to elongated relatively large grains whose major axis are oriented with low angle with respect to the BD (columnar grains). However, along the other two orthogonal directions on ⊥BD plane, the morphological properties are more homogenous (Fig. 4). By elimination of the texture-related effects through application of the EM-RT RVE, a parallel shift in the strain hardening curve when loaded along the BD (LD∥BD) and perpendicular to the BD (LD⊥BD) was observed (Fig. 15(b)). The polycrystal exhibited higher strain hardening while plastically deformed perpendicular to the BD compared to the case where LD∥BD. Therefore, a smaller grain size along a specific axis (compared to the other orthogonal axes) generally leads to a higher strain hardening (when the polycrystal is uniaxially defromed) along that axis. This phenomenon can be regarded as a size/Hall-Petch effect on the strain hardening anisotropy.

Furthermore, the studied material has a relatively strong ⟨011⟩∥BD initial fiber texture (Fig. 5), which was formed due to the specific processing conditions of AM. By excluding the effects of morphological heterogeneities using the RM-ET RVE, two disparate strain hardening behaviors along and perpendicular to the BD were witnessed (Fig. 15(b)), that can only be correlated to the inhomogeneous distribution of crystallographic orientation in the polycrystalline aggregate. The displacement-controlled tensile load along the BD rendered an almost constant strain hardening, while loading perpendicular to the BD resulted in a steep continuously decreasing strain hardening. Moreover, the strain hardening associated with loading the RM-ET RVE along the ∥BD is slightly higher than that of its experimental counterpart, again due to the aforementioned size effect. Nonetheless, both RM-ET and EM-ET RVEs yielded a similar evolution of the strain hardening perpendicular to the build direction (LD⊥BD).

The constant strain hardening associated with the RM-ET RVE, where LD∥BD, seems to be dominantly affected by twinning, as its corresponding twin fraction evolution curve serves as an upper bound to the rest of such curves plotted in Fig. 15(d). Conversely, the case of EM-RT RVE with LD∥BD, acts as the lower bound to the plotted twin fraction evolution curves. It highlights that, this specific experimental morphology suppresses the twin nucleation and propagation to a certain extent.

4.3. Distribution of field variables

The simulated spatial distribution of equivalent strain, unipolar dislocation density and twin volume fraction are demonstrated in Fig. 16 for the (fully) experimental RVE with GR = 64^3 (Fig. 11(c) and (d)), which are deformed along different axes (LD⊥BD and LD∥BD) until 10% engineering tensile strain. In this deformation state, the microstructure in terms of grain morphology and texture has not yet undergone considerable deformation-induced changes. Therefore, it is comparable to the initial microstructure, while the amount of deformation is sufficient for potential patterns (if any) to emerge with minimum interference.

As shown in Fig. 16(a) and (b), the equivalent strain distribution, where LD⊥BD is highly entropic (does not form any particular pattern). Contrastingly, in the case of LD∥BD, pronounced thick and long bands of localized strain have been formed and propagated across several grains (shear bands) on ∥BD planes with an angle close to 45° along the BD. The formation of the shear bands network is favored when there is a relatively homogenous boundary conditions on individual grains within the polycrystal loaded along a specific direction. Therefore, grain boundary misorientation and the morphological polarity with respect to the direction of the external load contribute to the formation of distinct inter-granular shear localization patterns. However, the main contributing factor to shear bands formation is the distribution of crystallographic orientation with respect to the direction of the external load. The reason lies within the curvature (second derivative of true stress with respect to true strain) of the strain hardening curve, which is dominantly controlled by the texture. In fact, a sufficiently strong texture combined with an external load direction favorable for activation of non-slip plastic deformation mechanisms (which assist dislocation slip) generally promotes a constant macroscopic strain hardening as a result of a certain distribution of the underlying shear localization. Furthermore, as suggested by Fig. 16(e) and (f), some grains with a favorable orientation have undergone heavy twinning, while some other grains are almost without twins.

5. Concluding remarks

5.1. Highlights

The anisotropic polycrystal plasticity due to microstructural heterogeneity has been experimentally and numerically investigated in an unprecedented detail. This systematic multi-scale analysis brought us to the following conclusions:

- The heterogeneous microstructure of polycrystalline metallic materials is very rich in details. It is evidenced that the modeling assumptions made in the three levels of the applied continuum physics-based modeling (crystal finite strain, constitutive and microstructure modeling) are generally sufficient for realization of a complex anisotropic polycrystal plasticity, as a result of interplay of numerous underlying phenomena that span over various length/time scales.
- Microstructure has a dual nature: grain morphology and crystallographic texture. By isolating the morphological and texture-related heterogeneities from one another via the generation of half-random RVEs, it was revealed that both morphology and texture almost equally affect the overall anisotropic strain hardening behavior.
- Grain morphology has a direct impact on deformation incompatibilities, stress and slip transfer at grain boundaries (grain boundary condition). Our key finding is that the morphological heterogeneities influence the anisotropic polycrystal plasticity through a size effect: a parallel shift of strain hardening (rate) curve.
- The curvature of the strain hardening curve (the second derivative of true stress with respect to true strain) is very sensitive to the crystallographic texture but almost independent from the grain morphology.
- The anisotropic evolution of twin volume fraction is more sensitive to crystallographic texture than grain morphology.
- Formation of distinct shear bands, combined with the high rate of twin nucleation and propagation, which are mainly regulated by the texture (crystallographic orientation and misorientation distributions), promotes an almost constant strain hardening rate.
- The identified correlation between microstructural heterogeneity and anisotropic plasticity enables process-based microstructure (morphology and texture) tailoring to control the mechanical properties of additively manufactured metallic components.

5.2. Suitability of the investigated material

Due to the following reasons, the selected metallic material with its specific chemical composition (Table 1) and additive manufacturing process parameters (Table 2) turned out to be an ideal candidate for the multi-scale experimental-numerical investigation of the anisotropic polycrystal plasticity due to microstructural heterogeneities:

- The single crystal constituents of the selected polycrystalline material are composed of a single phase with a high crystal symmetry (face-centered cubic), while they exhibit both dislocation slip and considerable amount of deformation twinning during plasticity. Therefore, the microstructural heterogeneities play a crucial role on the overall anisotropic response of the polycrystal under plastic deformation, especially more than for cases with lower crystal symmetry, or the instances that only show activation of dislocation slip and not twinning.
- According to the experimental investigation, there exists an appreciable heterogeneity in every respect of the as-built microstructure in terms of both grain morphology and crystallographic texture.
- Due to the additive manufacturing process parameters, particularly chosen for producing the studied material, the as-built state exhibits strong microstructural polarity and anisotropic plasticity only along two orthogonal directions (parallel and perpendicular to the build direction).
- Despite the almost isotropic (weakly anisotropic) initial yield in the investigated polycrystalline material, there is a strong anisotropy in its plasticity (strain hardening behavior), as the existing microstructural heterogeneities are process-induced. However, deformation-induced microstructural heterogeneities, such as those typically observed in cold-rolled sheets, often entail anisotropy in both the initial yield as well as the strain hardening response.
- Lastly, the as-built material, while loaded under displacement-controlled uniaxial tension, plastically deforms adequately before its fracture. This allows for an unambiguous investigation of its anisotropic plasticity behavior, including strain hardening over a wide range of plastic strain.

Declaration of Competing Interest

The authors declare that they have no known competing financial interests or personal relationships that could have appeared to influence the work reported in this paper.

Acknowledgments

The authors would like to thank the German Research Foundation (Deutsche Forschungsgemeinschaft, DFG) for the support of the depicted research within the Cluster of Excellence “Internet of Production” – CRD C2 “Enablers and Tools” and within the Collaborative Research Center (SFB) 761 “Steel – *ab initio*; quantum mechanics guided design of new Fe based materials”. The authors would also like to thank Patrick Köhnen, Frederike Brasche, Andrey Belyakov and Simon Ewald for the help with carrying out the experiments.

Appendix A. Supplementary materials

The Supplementary materials associated with this article, including the MTEX MATLAB scripts for analysis of EBSD and XRD data and the DREAM.3D pipelines for RVE generation, are available in the GitHub repository https://github.com/SAHMotaman/Microstructure-Analysis. Moreover, the characterization data will be made available on request.

Appendix B. Notation convention

The adopted notation convention includes the following:

- *Quantities*: Scalar quantities are written by italic letters, e.g. a, B; vector (first-order tensor) and first-order (row/column) matrix quantities are written by boldface and italic lower-case letters e.g. $\boldsymbol{a}$, $\boldsymbol{b}$; second-order tensor/matrix quantities are written by boldface upper-case letters e.g. $\mathbf{A}$, $\mathbf{B}$; and fourth-order tensor quantities are written by double-struck upper-case letters, e.g. $\mathbb{A}$, $\mathbb{B}$.
- *Index notation*: Square brackets [] is used to indicate index notation of tensorial and matrix quantities. Since all the coordinate systems are Cartesian, only covariant indices are used. Moreover, for brevity, Einstein's implicit summation is assumed over the repeated indices
- *Inner product*: Inner product (contraction) of two vectors is denoted by a dot, e.g. $\boldsymbol{a} \cdot \boldsymbol{b} = \delta_{ij}[\boldsymbol{a}]_i[\boldsymbol{b}]_j = [\boldsymbol{a}]_i[\boldsymbol{b}]_i = c$, where δ is the Kronecker delta. Inner product (double contraction) of two second-order tensors is denoted by a double-dot, e.g. $\mathbf{A} : \mathbf{B} = \delta_{ik}\delta_{jl}[\mathbf{A}]_{ij}[\mathbf{B}]_{kl} = [\mathbf{A}]_{ij}[\mathbf{B}]_{ij} = c$. Inner product (double contraction) of a fourth-order tensor with a second-order tensor is also denoted by a double-dot, e.g. $\mathbb{A} : \mathbf{B} = \mathbf{C}$, where $[\mathbf{C}]_{ij} = \delta_{km}\delta_{ln}[\mathbb{A}]_{ijkl}[\mathbf{B}]_{mn} = [\mathbb{A}]_{ijkl}[\mathbf{B}]_{kl}$.
- *Cross product*: Cross product of two vectors is denoted by a cross, e.g. $\boldsymbol{a} \times \boldsymbol{b} = \boldsymbol{c}$, so that $[\boldsymbol{c}]_k = \epsilon_{ijk}[\boldsymbol{a}]_i[\boldsymbol{b}]_j$, where ϵ is the Levi-Civita permutation symbol.
- *Outer product*: Outer/tensor/dyadic product of two vectors is denoted by a circled-cross, e.g. $\boldsymbol{a} \otimes \boldsymbol{b} = \mathbf{C}$, so that $[\mathbf{C}]_{ij} = [\boldsymbol{a}]_i[\boldsymbol{b}]_j$. Therefore, the tensorial quantities of different order can be expanded, i.e. $\boldsymbol{a} = [\boldsymbol{a}]_i\hat{\boldsymbol{e}}_i$, $\mathbf{A} = [\mathbf{A}]_{ij}\hat{\boldsymbol{e}}_i \otimes \hat{\boldsymbol{e}}_j$ and $\mathbb{A} = [\mathbb{A}]_{ijkl}\hat{\boldsymbol{e}}_i \otimes \hat{\boldsymbol{e}}_j \otimes \hat{\boldsymbol{e}}_k \otimes \hat{\boldsymbol{e}}_l$, where $\hat{\boldsymbol{e}}_i$ is the basis vector associated with the i–th dimension of the given Cartesian coordinate system.
- *Transformation*: Operation of a second-order tensor $\mathbf{A}$ on a vector $\boldsymbol{b}$, which transforms it to the vector $\boldsymbol{c}$ is represented by $\mathbf{A}\boldsymbol{b} = \boldsymbol{c}$, where $[\boldsymbol{c}]_i = [\mathbf{A}]_{ij}[\boldsymbol{b}]_j$. Action of a second-order tensor $\mathbf{A}$ on a second-order tensor $\mathbf{B}$, which transforms it to the second-order tensor $\mathbf{C}$, is expressed by $\mathbf{AB} = \mathbf{C}$, where $[\mathbf{C}]_{ik} = [\mathbf{A}]_{ij}[\mathbf{B}]_{jk}$.
- *Transpose*: The transpose of a second-order tensor $\mathbf{A}$ is denoted by $\mathbf{A}^{\mathrm{T}}$, so that $[\mathbf{A}^{\mathrm{T}}]_{ij} = [\mathbf{A}]_{ji}$.
- *Inverse*: The inverse of a second-order tensor $\mathbf{A}$ is denoted by $\mathbf{A}^{-1}$, so that $\mathbf{A}\mathbf{A}^{-1} = \mathbf{I}$, where $\mathbf{I}$ is the second-order unit/identity tensor ($[\mathbf{I}]_{ij} = \delta_{ij}$).
- *Norm*: The Euclidian norm of the vector $\boldsymbol{a}$ is denoted by $|\boldsymbol{a}|$, so that $|\boldsymbol{a}| = \sqrt{\boldsymbol{a} \cdot \boldsymbol{a}}$. The Euclidian norm of the second-order tensor $\mathbf{A}$ is denoted by $||\mathbf{A}||$, so that $||\mathbf{A}|| = \sqrt{\mathbf{A} : \mathbf{A}}$.

Appendix C. Nomenclature

Latin symbol	Description	
a	Lattice parameter/constant	[m]
A	Surface area	[m^2]
$\boldsymbol{a}$	A generic vector, or a crystallographic axis	
$\mathbf{A}$	Slip interaction strength matrix	[-]
b	Burgers length (magnitude of Burgers vector: $\|\boldsymbol{b}\|$)	[m]
$\boldsymbol{b}$	Burges vector	[m]
$\mathbf{B}$	Interaction coefficient/projection matrix	[-]
c	Constitutive coefficient	[-]
C	Elastic constant (component of elastic stiffness tensor)	[Pa]
$\mathbf{C}$	Right Cauchy-Green deformation tensor	[-]
$\mathbb{C}$	Fourth-order stiffness tensor	[Pa]
d	Grain size (equivalent diameter)	[m]
D	Diffusion coefficient	[m^2 s^{-1}]
$\mathbf{D}$	Rate of deformation tensor	[s^{-1}]
$\boldsymbol{e}$	Basis vector	[-]
$\mathbf{E}$	Green-Lagrange (nominal) strain tensor	[-]

f	Fraction	[-]
F	Helmholtz free energy	[J]
$\mathbf{F}$	Deformation gradient tensor	[-]
G	Gibbs free energy	[J]
h	Interplanar height/spacing/distance for two parallel slip planes	[m]
$\mathbf{I}$	Unit/identity (second-order) tensor	[-]
J	Jacobian of the deformation map	[-]
k	Constant	
l	Length	[m]
$\mathbf{L}$	Velocity gradient tensor	[s^{-1}]
m	Aspect ratio	[-]
M	Taylor factor	[-]
$\mathbf{M}$	Mandel stress tensor	[Pa]
n	Number density	[m^{-3}]
N	Number of (deformation systems)	[-]
$\boldsymbol{n}$	Deformation system's plane normal vector	[m]
p	Constitutive exponent	[-]
P	Probability	[-]
$\mathbf{P}$	First Piola-Kirchhoff stress tensor	[Pa]
Q	Thermal (activation) energy	[J]
$\mathbf{Q}$	Orientation matrix	[-]
r	Distance	[m]
$\mathbf{R}$	Polar (rigid-body) rotation tensor	[-]
s	Mean twin thickness	[m]
$\mathbf{S}$	Second Piola-Kirchhoff (nominal) stress tensor	[Pa]
t	Time (temporal coordinate)	[s]
T	Temperature	[K]
$\boldsymbol{t}$	Dislocation (tangent) line vector	[m]
$\mathbf{T}$	A generic second-order tensor or matrix	
$\boldsymbol{u}$	Displacement vector	[m]
$\mathbf{U}$	Right stretch tensor	[-]
v	Mean dislocation slip velocity/speed	[m s^{-1}]
V	Volume	[m^3]
$\boldsymbol{v}$	Velocity vector	[m s^{-1}]
$\mathbf{V}$	Left stretch tensor	[-]
w	Volumetric (deformation) work	[J m^{-3}]
$\mathbf{W}$	Spin tensor	[s^{-1}]
$\boldsymbol{x}$	Position vector (spatial coordinate)	[m]
$\mathbf{Z}$	Schmid tensor	[-]

Greek symbol	Description	
γ	(Resolved) plastic shear strain	[-]
Γ	Interfacial energy	[J m^{-2}]
ε	True/logarithmic (normal) strain	[-]
$\boldsymbol{\varepsilon}$	True/logarithmic strain tensor	[-]
θ	Strain hardening (rate)	[Pa]
λ	Effective/mean spacing	[m]
Λ	Mean free path	[m]
μ	Shear modulus, or mean value in a distribution	[Pa]
ν	Poisson's ratio	[-]
ξ	Normal force per unit dislocation line length	[N m^{-1}]
τ	Resolved shear stress	[Pa]
φ	Bunge-Euler angles	[rad]
$\boldsymbol{\varphi}$	Set of Bunge-Euler angles	[rad]
ρ	Dislocation density	[m^{-2}]
ϱ	Molar surface density	[mol m^{-2}]
σ	True stress, or standard deviation in a distribution	[Pa]
$\boldsymbol{\sigma}$	Cauchy/true stress tensor	[Pa]
ω	Misorientation angle, or a generic angle	[rad]

Subscript	Description
0	Reference/initial/undeformed
a	active
b	Bottom
B	Boltzmann
c	Capture(d)
cr	Critical
cl	Climb
cs	Cross-slip
d	Dipolar
e	Elastic, or edge dislocation
f	Forest dislocations
eff	Effective
HP	Hall-Petch
max	Maximum
min	Minimum
mt	Matrix
p	Plastic, partial, or passive
sf	Stacking fault
sl	Slip
t	Total, or top
tw	Twin
u	Unipolar
v	Vacancy

Superscript	Description
an	Annihilation
cl	Climb
d	Deviatoric/isochoric
eng	Engineering/nominal
g	Global
gn	Generation/multiplication/formation
h	Hydrostatic
l	Local
sp	Spontaneous
v	Volumetric
$\alpha, \acute{\alpha}$	Slip system index
$\beta,\ \beta'$	Twin system index

Operator	Description
$\parallel\bullet$	An axis/plane parallel to $\bullet$
$\perp\bullet$	An axis/plane perpendicular/orthogonal to $\bullet$
$\hat{\bullet}$	Normalized: $\hat{\bullet} = \frac{\bullet}{\lvert\bullet\rvert}$
$\bar{\bullet}$	Mean/homogenized (spatial and/or temporal)
$\breve{\bullet}$	Function
$\underset{\sim}{\bullet}$	plastic/relaxed/intermediate configuration
$\langle\bullet\rangle$	Macaulay brackets: $\langle\bullet\rangle = \frac{1}{2}(\lvert\bullet\rvert + \bullet)$, or notation for crystallographic axis

Abbreviation	Description
AM	Additive manufacturing, or additively manufactured
bcc	Body-centered cubic
BD	Build direction
DFT	Density functional theory
EBSD	Electron backscatter diffraction
fcc	Face-centered cubic
GND	Geometrically necessary dislocation
GR	Grid resolution
GSD	Grain size distribution
hcp	Hexagonal close packed
HMnS	High-manganese steel
IPF	Inverse pole figure
LD	Load direction/axis
LPBF	Laser powder bed fusion
MDF	Misorientation distribution function
MFP	Mean free path
MSV	Micro-state variable
ODF	Orientation distribution function
PDF	Probability density/distribution function
RSS	Resolved shear stress
RVE	Representative volume element
S/TD	Scan/transverse direction
SD	Scan direction
SEM	Scanning electron microscopy/microscope
SFE	Stacking fault energy
T/SD	Transverse/scan direction
TD	Transverse direction
TEM	Transmission electron microscopy/microscope
TRIP	Transformation-induced plasticity
TWIP	Twinning-induced plasticity
XRD	X-ray diffraction

Table 6
Deformation system families for cubic crystal lattice structures in terms of Miller indices of slip/twin Burgers and plane normal vectors.

Cubic lattice	Deformation system	Burgers family ($\underline{\boldsymbol{b}}_x$)*	Plane normal family ($\hat{\boldsymbol{n}}_x$)
fcc	Slip ($x=$ sl)	$\frac{a_0}{2}\langle 0\ 1\ \bar{1}\rangle$	$\frac{1}{\sqrt{3}}\{1\ 1\ 1\}$
	Twin ($x=$ tw)	$\frac{a_0}{2}\langle 1\ 1\ \bar{2}\rangle$	$\frac{1}{\sqrt{3}}\{1\ 1\ 1\}$
bcc	Slip ($x=$ sl)	$\frac{a_0}{2}\langle 1\ \bar{1}\ 1\rangle$	$\frac{1}{\sqrt{2}}\{0\ 1\ 1\}$
		$\frac{a_0}{2}\langle \bar{1}\ 1\ 1\rangle$	$\frac{1}{\sqrt{6}}\{2\ 1\ 1\}$
	Twin ($x=$ tw)	$\frac{a_0}{2}\langle \bar{1}\ 1\ 1\rangle$	$\frac{1}{\sqrt{6}}\{2\ 1\ 1\}$

* a_0 is the cubic lattice constant (equilibrium unit cell edge length) at the reference (room) temperature, which can be determined by DFT-based *ab initio* methods as a function of chemical composition [236].

Appendix D. Bunge–Euler angles and elemental rotations

Euler angles are used to describe a (passive) transformation/orientation matrix $\mathbf{Q}$ from a global/reference Cartesian frame (orthonormal basis in the Euclidean 3-space) $(\hat{\boldsymbol{e}}_1^g, \hat{\boldsymbol{e}}_2^g, \hat{\boldsymbol{e}}_3^g)$ to a local Cartesian basis denoted by $(\hat{\boldsymbol{e}}_1^l, \hat{\boldsymbol{e}}_2^l, \hat{\boldsymbol{e}}_3^l)$, so that $[\mathbf{Q}]_{ij} = \hat{\boldsymbol{e}}_i^l \cdot \hat{\boldsymbol{e}}_j^g$. This transformation is defined by a non-unique sequence of three elemental rotations that relate the reference frame to the local frame. In Bunge's/zxz notation, the coordinate transformation using Bunge's Euler angles $\boldsymbol{\varphi} \equiv \{\varphi_1, \Phi, \varphi_2\}$, includes the following passive rotations [154,233–235]:

(1) Rotation of the global basis $(\hat{\boldsymbol{e}}_1^g, \hat{\boldsymbol{e}}_2^g, \hat{\boldsymbol{e}}_3^g)$ about $\hat{\boldsymbol{e}}_3^g$ by the angle φ_1 $(0 \le \varphi_1 \le 2\pi)$ resulting in $(\hat{\boldsymbol{e}}_1^{(1)}, \hat{\boldsymbol{e}}_2^{(1)}, \hat{\boldsymbol{e}}_3^g)$, which is represented by:

$$\mathbf{Q}_{\varphi_1} \equiv \begin{bmatrix} \cos\varphi_1 & \sin\varphi_1 & 0 \\ -\sin\varphi_1 & \cos\varphi_1 & 0 \\ 0 & 0 & 1 \end{bmatrix}. \tag{23}$$

(2) Rotation of $(\hat{\boldsymbol{e}}_1^{(1)}, \hat{\boldsymbol{e}}_2^{(1)}, \hat{\boldsymbol{e}}_3^g)$ basis about $\hat{\boldsymbol{e}}_1^{(1)}$ by the angle Φ $(0 \le \Phi \le \pi)$ giving $(\hat{\boldsymbol{e}}_1^{(1)}, \hat{\boldsymbol{e}}_2^{(2)}, \hat{\boldsymbol{e}}_3^{(1)})$, which is expressed as:

$$\mathbf{Q}_{\Phi} \equiv \begin{bmatrix} 1 & 0 & 0 \\ 0 & \cos\Phi & \sin\Phi \\ 0 & -\sin\Phi & \cos\Phi \end{bmatrix}. \tag{24}$$

(3) Rotation of $(\hat{\boldsymbol{e}}_1^{(1)}, \hat{\boldsymbol{e}}_2^{(2)}, \hat{\boldsymbol{e}}_3^{(1)})$ basis about $\hat{\boldsymbol{e}}_3^{(1)}$ by the angle φ_2 $(0 \le \varphi_2 \le 2\pi)$ yielding $(\hat{\boldsymbol{e}}_1^{(2)}, \hat{\boldsymbol{e}}_2^{(3)}, \hat{\boldsymbol{e}}_3^{(1)})$, which is aligned with $(\hat{\boldsymbol{e}}_1^l, \hat{\boldsymbol{e}}_2^l, \hat{\boldsymbol{e}}_3^l)$ and represented by:

$$\mathbf{Q}_{\varphi_2} \equiv \begin{bmatrix} \cos\varphi_2 & \sin\varphi_2 & 0 \\ -\sin\varphi_2 & \cos\varphi_2 & 0 \\ 0 & 0 & 1 \end{bmatrix}. \tag{25}$$

At this point, we can write:

$$\boldsymbol{a}^l = \mathbf{Q}\boldsymbol{a}^g; \quad \mathbf{T}^l = \mathbf{Q}\mathbf{T}^g\mathbf{Q}^T; \quad \mathbf{Q} \equiv \mathbf{Q}_{\varphi_2}\mathbf{Q}_{\Phi}\mathbf{Q}_{\varphi_1}. \tag{26}$$

where $\boldsymbol{a}^g$ and $\boldsymbol{a}^l$ represent the same vector in the global and local Cartesian frames, respectively; and $\mathbf{T}^g$ and $\mathbf{T}^l$ represent the same second-order tensor in the global and local Cartesian frames, respectively.

Appendix E. Slip systems and Burgers vector in cubic crystals

Deformation system families for cubic crystal symmetries, fcc and body-centered cubic (bcc), in terms of Miller indices of slip/twin Burgers direction and plane normal vectors (in the reference frame) are presented in Table 6. In cubic crystals, each system has 12 members ($N_{\text{sl}}^{\text{cubic}} = N_{\text{tw}}^{\text{cubic}} = 12$). Moreover, the twin Burgers vector is the same as the Burgers vector of the respective partial dislocations ($\underline{\boldsymbol{b}}_{\text{tw}} = \underline{\boldsymbol{b}}_p$). Therefore, as Table 6 suggests, the following relationships regarding the Burgers length (magnitude of Burgers vector) for slip and twinning in cubic crystal symmetry is conceivable:

$$\frac{b_{\text{sl}}}{b_{\text{tw}}} = \frac{|\underline{\boldsymbol{b}}_{\text{sl}}|}{|\underline{\boldsymbol{b}}_{\text{tw}}|} = \sqrt{3}; \quad \begin{cases} b_{\text{sl}} = \frac{\sqrt{2}}{2}a_0;\ b_{\text{tw}} = \frac{\sqrt{6}}{6}a_0 & : \text{fcc} \\ b_{\text{sl}} = \frac{\sqrt{3}}{2}a_0;\ b_{\text{tw}} = \frac{1}{2}a_0 & : \text{bcc} \end{cases}. \tag{27}$$

Appendix F. Elastic stiffness and moduli for cubic crystals

Due to the symmetry of the elastic stiffness tensor $\mathbb{C}_{e\ \text{mt}}$, it only contains three independent components (elastic constants) in case of cubic (fcc/bcc) crystal symmetry [237]: C_{11}, C_{12} and C_{44} (represented in Voigt notation), which can be calculated using DFT-based *ab initio* methods [236]. Moreover, the average moduli, shear modulus (μ) and Poisson's ratio (ν), in cubic crystals are expressed as functions of the elastic constants based on the Voigt homogenization/approximation scheme [237–239]:

$$\mu = \frac{1}{5}(C_{11} - C_{12} + 3C_{44}); \quad \nu = \frac{C_{11} + 4C_{12} - 2C_{44}}{4C_{11} + 6C_{12} + 2C_{44}}. \tag{28}$$

Appendix G. Interaction strength matrix for cubic crystals

In cubic crystal symmetry, the interaction matrix $\mathbf{A}$ has $(N_{\text{sl}}^{\text{cubic}})^2 = 144$ components. The number of distinct entries is divided by two due to the diagonal symmetry of the matrix ($[\mathbf{A}]^{\alpha\acute{\alpha}} = [\mathbf{A}]^{\acute{\alpha}\alpha}$) and the occurrence of four $\langle 111\rangle$ (for fcc) or $\langle 110\rangle$ (for bcc) axes with ternary symmetry further divides it by twelve. As such, there are only six independent coefficients, which are associated with six distinct types of interactions [240,241]. Three of them account for forest interactions between non-coplanar slip systems, resulting in the formation of junctions or locks: for fcc, the orthogonal/Hirth lock [242], the sessile/Lomer–Cottrell lock [243,244], and the glissile junction [245,246]; and for bcc, mixed-symmetrical, mixed-asymmetrical and edge junctions [241]. There are two coplanar interactions for dislocations slipping on parallel slip planes with parallel Burgers vector [240,241]: the dipolar/self-interaction; or unparallel coplanar Burgers vectors: the cross-coplanar interaction. Finally, the strongest interaction, the collinear interaction [247], occurs between dislocations slipping on two slip planes that are cross-slip planes with respect to each other. For the description of dislocation reactions in fcc crystals, the Thompson tetrahedron is helpful [248]. Table 7 presents the geometrical relationships associated with the independent components of the slip–slip interaction matrix for fcc crystal structures, and their values estimated using discrete dislocation dynamics (DDD) simulations.

Appendix H. Dislocation density evolution

Following Blum et al. [166,251] and based on the superposition rule of dislocation density evolution [177,194], the overall evolution (time rate) of unipolar and dipolar dislocation density at each slip system in cold and warm regimes [165] is decomposed to the underlying dislocation processes as follows:

$$\begin{aligned} \dot{\rho}_u^{\alpha} &= \dot{\rho}_u^{\alpha\,\text{gn}} - \dot{\rho}_u^{\alpha\,\text{sp an}} - \dot{\rho}_d^{\alpha\,\text{gn}}; \\ \dot{\rho}_d^{\alpha} &= \dot{\rho}_d^{\alpha\,\text{gn}} - \dot{\rho}_d^{\alpha\,\text{sp an}} - \dot{\rho}_d^{\alpha\,\text{cl an}}; \end{aligned} \tag{29}$$

where superscripts gn, an, sp and cl stand for generation, annihilation, spontaneous and climb, respectively; $\dot{\rho}_u^{\alpha\,\text{gn}}$ and $\dot{\rho}_d^{\alpha\,\text{gn}}$ represent the generation (time) rates of unipolar and dipolar dislocation densities at slip system α, respectively; $\dot{\rho}_u^{\alpha\,\text{sp an}}$ and $\dot{\rho}_d^{\alpha\,\text{sp an}}$ denote the spontaneous annihilation rates of unipolar and dipolar dislocation densities at slip system α, respectively; and $\dot{\rho}_d^{\alpha\,\text{cl an}}$ represents the climb-assisted annihilation rate of dipolar dislocation density at slip system α.

Table 7
Independent components of the slip–slip interaction matrix for fcc crystals, and their values estimated using discrete dislocation dynamics simulations.

Junction type	Coplanar		Non-coplanar			
Plane normal	$\widehat{\underline{\boldsymbol{n}}}^{\alpha}_{\mathrm{sl}} = \widehat{\underline{\boldsymbol{n}}}^{\acute{\alpha}}_{\mathrm{sl}}$		$\widehat{\underline{\boldsymbol{n}}}^{\alpha}_{\mathrm{sl}} \neq \widehat{\underline{\boldsymbol{n}}}^{\acute{\alpha}}_{\mathrm{sl}}$			
Orientation relationship	$\widehat{\underline{\boldsymbol{b}}}^{\alpha}_{\mathrm{sl}} = \widehat{\underline{\boldsymbol{b}}}^{\acute{\alpha}}_{\mathrm{sl}}$	$\widehat{\underline{\boldsymbol{b}}}^{\alpha}_{\mathrm{sl}} \neq \widehat{\underline{\boldsymbol{b}}}^{\acute{\alpha}}_{\mathrm{sl}}$	$\widehat{\underline{\boldsymbol{b}}}^{\alpha}_{\mathrm{sl}} = \widehat{\underline{\boldsymbol{b}}}^{\acute{\alpha}}_{\mathrm{sl}}$	$\widehat{\underline{\boldsymbol{b}}}^{\alpha}_{\mathrm{sl}} \neq \widehat{\underline{\boldsymbol{b}}}^{\acute{\alpha}}_{\mathrm{sl}}$ $\widehat{\underline{\boldsymbol{b}}}^{\alpha}_{\mathrm{sl}} \cdot \widehat{\underline{\boldsymbol{b}}}^{\acute{\alpha}}_{\mathrm{sl}} = 0$	$\widehat{\underline{\boldsymbol{b}}}^{\alpha}_{\mathrm{sl}} \cdot \widehat{\underline{\boldsymbol{b}}}^{\acute{\alpha}}_{\mathrm{sl}} \neq 0$ $(\widehat{\underline{\boldsymbol{b}}}^{\alpha}_{\mathrm{sl}} \times \widehat{\underline{\boldsymbol{b}}}^{\acute{\alpha}}_{\mathrm{sl}}) \cdot (\widehat{\underline{\boldsymbol{n}}}^{\alpha}_{\mathrm{sl}} \times \widehat{\underline{\boldsymbol{n}}}^{\acute{\alpha}}_{\mathrm{sl}}) = 0$	$(\widehat{\underline{\boldsymbol{b}}}^{\alpha}_{\mathrm{sl}} \times \widehat{\underline{\boldsymbol{b}}}^{\acute{\alpha}}_{\mathrm{sl}}) \cdot (\widehat{\underline{\boldsymbol{n}}}^{\alpha}_{\mathrm{sl}} \times \widehat{\underline{\boldsymbol{n}}}^{\acute{\alpha}}_{\mathrm{sl}}) \neq 0$
Junction/lock	Dipolar/self	Cross-coplanar	Collinear	Orthogonal/Hirth	Glissile	Sessile/Lomer-Cottrell
$[\mathbf{A}]^{\alpha\acute{\alpha}}$	A_{dip}	A_{cop}	A_{col}	A_{ort}	A_{gls}	A_{ses}
Value [-]	0.122	0.122	0.625	0.070	0.137	0.122
Source	[249]	[240]	[250]	[240]	[250]	[250]

The generation/multiplication rate of unipolar dislocation density at slip system α ($\dot{\rho}_u^{\alpha\ \mathrm{gn}}$) is proportional to the average slip speed of (mobile) unipolar dislocations ($|\bar{v}^{\alpha}_{\mathrm{sl}\ u}|$) as well as the (mean) number density of unipolar dislocations ($n_u^{\alpha} \equiv \frac{1}{\Lambda^{\alpha}_{\mathrm{sl}}}\rho_u^{\alpha}$) as (potential) dislocation sources at slip system α. Therefore, considering Orowan's equation (Eq. (11)):

$$\dot{\rho}_u^{\alpha\ \mathrm{gn}} = \frac{1}{\Lambda^{\alpha}_{\mathrm{sl}}}\rho_u^{\alpha}\left|\bar{v}^{\alpha}_{\mathrm{sl}\ u}\right| = \frac{1}{b_{\mathrm{sl}}\Lambda^{\alpha}_{\mathrm{sl}}}\left|\dot{\gamma}^{\alpha}_{\mathrm{sl}}\right|. \tag{30}$$

To derive the rates of generation/formation of dipolar dislocations and spontaneous annihilation of dislocations, first we need to define the (parallel) encounter events. An encounter event takes place when an active (dislocation) partner (slipping unipolar dislocation) meets its passive oppositely signed pair (either unipolar or dipolar with opposite Burgers vector) residing on a parallel slip plane within a characteristic capture height h_c for that specific encounter. Thus, for the occurrence of an admissible encounter, the height/distance of the slip plane of the passive partner from its active pair (h) must fulfill the following constraint: $-h_c \leq h \leq h_c$. In order to describe the rate of an encounter reaction, one needs to define a differential capture/sample volume $\mathrm{d}V_c^{\alpha}$ (in which the encounter event occurs) slipped/swept by an active dislocation line (with a differential length) within the height of $2h_c = (h_c - (-h_c))$. Given this premise, we immediately find:

$$\mathrm{d}^2V_c^{\alpha} \equiv 2h_c\mathrm{d}l_a^{\alpha}\left|v^{\alpha}_{\mathrm{sl}\ a}\right|\mathrm{d}t; \qquad \mathrm{d}l_a^{\alpha} = V\mathrm{d}\rho_a^{\alpha}; \tag{31}$$

where subscripts c and a stand for captured (undergone a specific encounter) and active, respectively; $\mathrm{d}l_a^{\alpha}$ is a differential active dislocation line length at slip system α; V is the control volume (surrounding the meso–scale material point under consideration) in which (meso–scale) dislocation density is defined; and ρ_a^{α} represents the potential active population (dislocation density) at slip system α. Integrating both sides of Eq. (31) over ρ_a^{α} leads to:

$$\mathrm{d}V_c^{\alpha} = 2h_cV\mathrm{d}t\,\rho_a^{\alpha}\left|\bar{v}^{\alpha}_{\mathrm{sl}\ a}\right|; \qquad \left|\bar{v}^{\alpha}_{\mathrm{sl}\ a}\right| \equiv \frac{\int_{\rho_a^{\alpha}}\left|v^{\alpha}_{\mathrm{sl}\ a}\right|\mathrm{d}\rho_a^{\alpha}}{\rho_a^{\alpha}}. \tag{32}$$

Hence, given the fact that in each encounter event two dislocations (active and passive) with equal line lengths interact:

$$\dot{\rho}_{pc}^{\alpha} \equiv \frac{\mathrm{d}\rho_{pc}^{\alpha}}{\mathrm{d}t} \equiv \frac{\mathrm{d}l_{pc}^{\alpha}}{V\mathrm{d}t} \equiv \frac{\rho_p^{\alpha}\mathrm{d}V_c^{\alpha}}{V\mathrm{d}t} = 2h_c\rho_p^{\alpha}\rho_a^{\alpha}\left|\bar{v}^{\alpha}_{\mathrm{sl}\ a}\right|; \tag{33}$$

where ρ_p^{α} denotes the potential passive population at slip system α; and $\dot{\rho}_{pc}^{\alpha}$ represents the rate of captured passive dislocation density.

The type of the permissible encounters depends on the absolute slip plane spacing of the active and passive partners ($|h|$):

$$\begin{cases} \text{(unstable dipole) spontaneous annihilation} & : 0 \leq |h| \leq h_{d\,\min} \\ \text{(stable) dipole formation} & : h_{d\,\min} < |h| < h_{d\,\max} \\ \text{(unstable dipole) instantaneous dissociation} & : |h| \geq h_{d\,\max} \end{cases}. \tag{34}$$

Here, among the permissible encounter events, we only consider (stable) dipole generation and spontaneous annihilation. Furthermore, we assume an equal population of oppositely signed dislocations on each slip system. Consequently, given Eqs. (33) and (34) and Orowan's equation (Eq. (11)), the generation rate of dipolar dislocation density at slip system α ($\dot{\rho}_d^{\alpha\ \mathrm{gn}}$), in which both active and passive reacting partners are of unipolar type, can be conveniently expressed as:

$$\begin{aligned}\dot{\rho}_d^{\alpha\ \mathrm{gn}} &= 2\left(h_{d\ \max}^{\alpha} - h_{d\ \min}\right)\rho_u^{\alpha}\rho_u^{\alpha}\left|v^{\alpha}_{\mathrm{sl}\ u}\right| \\ &= \frac{2\left(h_{d\ \max}^{\alpha} - h_{d\ \min}\right)}{b_{\mathrm{sl}}}\rho_u^{\alpha}\left|\dot{\gamma}^{\alpha}_{\mathrm{sl}}\right|;\end{aligned} \tag{35}$$

It should be noted that since in generation of dipolar dislocations, unipolar dislocations react and transform, $\dot{\rho}_d^{\alpha\ \mathrm{gn}}$ must appear with a negative sign (sink term) and positive sign (source term) in $\dot{\rho}_u^{\alpha}$ and $\dot{\rho}_d^{\alpha}$ (Eq. (29)), respectively.

Analogously, the spontaneous annihilation rate of unipolar dislocation density at slip system α ($\dot{\rho}_d^{\alpha\ \mathrm{sp\ an}}$) again with both encountering partners being unipolar, is represented by:

$$\dot{\rho}_u^{\alpha\ \mathrm{sp\ an}} = 2h_{d\ \min}\rho_u^{\alpha}\rho_u^{\alpha}\left|v^{\alpha}_{\mathrm{sl}\ u}\right| = \frac{2h_{d\ \min}}{b_{\mathrm{sl}}}\rho_u^{\alpha}\left|\dot{\gamma}^{\alpha}_{\mathrm{sl}}\right|. \tag{36}$$

In spontaneous annihilation events, first an unstable narrow dislocation dipole is formed and then spontaneously (and instantly) disintegrated. In spontaneous annihilation of dipolar dislocations, the passive partners are stable dipoles. In such events, an active unipolar dislocation segment and a dislocation segment in dipolar configuration mutually annihilate. This releases the other (former) dipole segment from the corresponding dipole bound and transforms it to a unipolar dislocation segment supposedly with the same length as the incoming active unipolar dislocation. As a result, in the processes of spontaneous annihilation of dipolar dislocations, unipolar dislocations only act as catalysts and hence are not consumed. Therefore, $\dot{\rho}_u^{\alpha\ \mathrm{sp\ an}}$ only appears with a negative sign in $\dot{\rho}_d^{\alpha}$ (Eq. (29)). Consequently,

$$\dot{\rho}_d^{\alpha\ \mathrm{sp\ an}} = 2h_{d\ \min}\ \rho_d^{\alpha}\ \rho_u^{\alpha}\ \left|v^{\alpha}_{\mathrm{sl}\ u}\right| = \frac{2h_{d\ \min}}{b_{\mathrm{sl}}}\rho_d^{\alpha}\left|\dot{\gamma}^{\alpha}_{\mathrm{sl}}\right|. \tag{37}$$

In annihilation of dipolar dislocations by thermally-activated out-of-plane climb mechanism, two dipole partners mutually annihilate. Assuming that two attracting dipole partners with an initial dipole height h_d climb towards one another by the velocities $\pm\frac{v_{\mathrm{cl}\ d}}{2}$ (parallel to slip plane normal), annihilation by climb takes place when they travel the distance $h_d - h_{d\ \min}$. After elapsing time $\frac{h_d - h_{d\ \min}}{|v_{\mathrm{cl}\ d}|}$, the climb has reduced their slip plane spacing to $h_{d\,\min}$, at which they spontaneously annihilate one another. Given a control volume and at slip system α, there is a spectrum of (stable) dipole heights between $h_{d\ \min} < h_d^{\alpha} < h_{d\ \max}^{\alpha}$, which corresponds to an average dipole height $\bar{h}_d^{\alpha} = \frac{h_{d\ \min} + h_{d\ \max}^{\alpha}}{2}$ (Eq. (16)). Supposing that in each annihilation event by climb two dipolar dislocation segments mutually annihilate, the climb-assisted annihilation rate

of dipolar dislocation density reads:

$$\dot{\rho}_d^{\alpha\ \mathrm{cl\ an}} = 2\rho_d^{\alpha}\frac{\left|\bar{v}_{\mathrm{cl}\ d}^{\alpha}\right|}{\bar{h}_d^{\alpha} - h_{d\ \min}} = \frac{4\left|\bar{v}_{\mathrm{cl}\ d}^{\alpha}\right|}{h_{d\ \max}^{\alpha} - h_{d\ \min}}\rho_d^{\alpha}. \tag{38}$$

By inserting Eqs. (30), (35)–(38) into Eq. (29) and with some trivial rearrangement, we arrive at the compact expressions given by Eq. (14).

Appendix I. Twin nucleation model for fcc crystals

The nucleation of a twin stacking fault is a stochastic process, that requires sufficiently high local stress concentration, which can be maintained only if the mean RSS at the respective twin system is adequately high, while cross-slip (acting as another mechanism for relaxing the stress concentration) is an unfavorable competing mechanism [252–255]. Therefore, following Steinmetz et al. [256], we postulate the following relationship for calculation of $\dot{n}_{\mathrm{tw}}^{\beta}$:

$$\dot{n}_{\mathrm{tw}}^{\beta} = \dot{n}_{\mathrm{tw0}}P_{\mathrm{sf}}^{\beta}; \tag{39}$$

where P_{sf}^{β} is the probability density that cross-slip does not take place, which would allow a sufficient (local) dislocation accumulation rendering the stress concentration (at twin system β) necessary for dislocation dissociation/separation and the consequent stacking fault generation; and $\dot{n}_{\mathrm{tw0}}^{\beta}$ is the (reference) average number density of potential twin stacking fault nuclei per unit time at twin system β, which is given as:

$$\begin{aligned}\dot{n}_{\mathrm{tw0}}^{\beta} &= \frac{1}{l_{\mathrm{tw0}}}\left(\left|v_{\mathrm{sl}\ u}^{\alpha}\right|\rho_u^{\alpha}\rho_t^{\acute{\alpha}} + \left|v_{\mathrm{sl}\ u}^{\acute{\alpha}}\right|\rho_u^{\acute{\alpha}}\rho_t^{\alpha}\right)\\ &= \frac{1}{l_{\mathrm{tw}}}\left(\left|\dot{\gamma}_{\mathrm{sl}}^{\alpha}\right|\rho_t^{\acute{\alpha}} + \left|\dot{\gamma}_{\mathrm{sl}}^{\acute{\alpha}}\right|\rho_t^{\alpha}\right);\quad l_{\mathrm{tw}} = l_{\mathrm{tw0}}b_{\mathrm{sl}};\\ \underline{\hat{\boldsymbol{n}}}_{\mathrm{tw}}^{\beta} &= \underline{\hat{\boldsymbol{n}}}_{\mathrm{sl}}^{\alpha} = \underline{\hat{\boldsymbol{n}}}_{\mathrm{sl}}^{\acute{\alpha}};\quad 3\underline{\boldsymbol{b}}_{\mathrm{tw}}^{\beta} = \underline{\boldsymbol{b}}_{\mathrm{sl}}^{\alpha} + \underline{\boldsymbol{b}}_{\mathrm{sl}}^{\acute{\alpha}};\quad \alpha \neq \acute{\alpha};\end{aligned} \tag{40}$$

where l_{tw0} is the dimensionless mean length of twin nuclei as a multiple of slip Burgers length; and l_{tw} is the average length of twin nuclei (can be calculated by atomistic simulations). Eq. (40) is based on the twin nucleation mechanism in fcc crystals envisaged by Mahajan and Chin [232]. In this mechanism, two coplanar full $\frac{a}{2}\langle 01\bar{1}\rangle$ dislocations (where a is the lattice constant) of different Burgers vectors $\underline{\boldsymbol{b}}_{\mathrm{sl}}^{\alpha} \neq \underline{\boldsymbol{b}}_{\mathrm{sl}}^{\acute{\alpha}}$ split into fault pairs and react on the primary slip plane to emanate three $\frac{a}{6}\langle 11\bar{2}\rangle$ Shockley partial dislocations with identical Burgers vector $\underline{\boldsymbol{b}}_{\mathrm{tw}}^{\beta}$ on successive parallel {111} planes. This results in an ordered three-layer stacking fault arrangement that can produce a twin [215,232,254,256,257].

Inspired by the relationship proposed by Kubin et al. [258] for the frequency of cross-slip occurrence, we suggest the following equation for calculation of P_{sf}^{β}:

$$P_{\mathrm{sf}}^{\beta} = 1 - P_{\mathrm{cs}}^{\beta};\quad P_{\mathrm{cs}}^{\beta} = \exp\left(-\frac{V_{\mathrm{cs}}}{k_B T}\langle \tau_{\mathrm{sf\,cr}} - \langle \tau_{\mathrm{tw}}^{\beta}\rangle\rangle\right); \tag{41}$$

where P_{cs}^{β} is the probability for cross-slip occurrence at slip systems coplanar with the twin system β; V_{cs} is the activation volume for cross-slip [259,260], which can be calculated by atomistic simulations [229–231,261,262]; and $\tau_{\mathrm{sf\,cr}} > 0$ is the mean critical shear stress for dislocation dissociation (increases by increasing SFE). In fcc crystals, the critical shear stress to nucleate a three-layer stacking fault ($\tau_{\mathrm{sf\,cr}}$), that can serve as a twin embryo, is given as a threshold for bringing the respective repulsive partial dislocations within the critical distance r_c [226,232,263,264]:

$$\tau_{\mathrm{sf\ cr}} = \frac{\mu b_{\mathrm{tw}}}{2\pi}\left(\frac{1}{r_0 + r_c} + \frac{1}{2r_0}\right);\quad r_0 = \frac{\mu b_{\mathrm{tw}}^2}{8\pi\,\Gamma_{\mathrm{sf}}}\frac{2+\nu}{1-\nu}; \tag{42}$$

where r_0 is the equilibrium dissociation distance for Shockley partials in fcc crystals, in which the repulsive force due to the partial dislocations is balanced by the attractive force exerted by the stacking fault; and Γ_{sf} is the SFE.

In addition, the critical resolved shear stress (at twin systems) for twin propagation ($\tau_{\mathrm{tw\,cr}}$) in fcc crystals based on twin nucleation model proposed by Mahajan and Chin [232], is given by the following equation [253,256,265]:

$$\tau_{\mathrm{tw\ cr}} = \frac{\Gamma_{\mathrm{sf}}}{3b_{\mathrm{tw}}} + \frac{3\mu b_{\mathrm{tw}}}{l_{\mathrm{tw}}}. \tag{43}$$

The SFE (Γ_{sf}) for fcc alloys is calculated as follows [266,267]:

$$\Gamma_{\mathrm{sf}} = 2\varrho\,\Delta G^{\gamma\to\varepsilon} + 2\Gamma^{\gamma\to\varepsilon}; \tag{44}$$

where ϱ is the molar surface density along the close-packed {111} planes; $\Gamma^{\gamma\to\varepsilon}$ is the interfacial energy between the parent γ (-austenite) phase (fcc) and the transformed ε (-martensite) phase (hcp); and $\Delta G^{\gamma\to\varepsilon}$ is the effective molar Gibbs free energy difference for $\gamma \to \varepsilon$ phase transformation. The composition- and temperature-dependent $\Delta G^{\gamma\to\varepsilon}$ for different alloys can be calculated using thermodynamics-based models [81,87,90]. Alternatively, for a given alloying system, the SFE (Γ_{sf}) can be calculated using DFT-based *ab initio* methods based on either explicit/direct (supercell) approach [268–276] or axial next-nearest-neighbor Ising (ANNNI) model [277–284].

Appendix J. RVE generation procedure

The RVE generation procedure based on the statistically induced realistic instantiations (SIRI) algorithm [218] first generates bins of morphological features (grain size, shape, shape-axes orientation) using the associated PDFs derived from the input statistical morphological descriptors. Moreover, the PDF of the number of contiguous grains and its associated bins is fully dependently correlated to the grain size PDF, inspired from a statistical analysis of experimental 3D grain structure in polycrystals [285]. The algorithm then assigns the morphological bins to each other in a fairly random process; and creates grains, which will be later placed in a voxelized RVE (by satisfying the generated statistics concerning the contiguous neighboring grains and periodic boundaries) through an iterative process (grain packer) controlled by several constraints and preset tolerances. The number of grains in the RVE is determined based on its size, the morphological bins and the grain placement procedure. From the resultant voxelized representation of the grain aggregate, seed points for the Voronoi tessellation are generated. The constrained Voronoi tessellation tool creates a grain structure with an arbitrary grid/mesh resolution. After construction of the grain ensemble, the crystallographic orientations (Bunge-Euler triples), binned/sampled from the input ODF (by the number of grains), will be assigned to the tessellated grains through an iterative scheme, so that the resultant bulk (weight-averaged by grain volume) ODF and correlated MDF of the RVE match their input counterparts within the specified tolerance.

Appendix K. True stress and strain measures

For post-processing purposes, one needs to compute true (in current configuration) strain and stress tensors and their equivalent scalars. First, we need to consider the following polar decomposition of the non-singular (total) deformation gradient tensor (at material points and/or homogenized over RVE):

$$\mathbf{F} = \mathbf{VR};\quad \mathbf{V} = \mathbf{V}^{\mathrm{T}};\quad \mathbf{R}^{-1} = \mathbf{R}^{\mathrm{T}}; \tag{45}$$

where $\mathbf{V}$ is the symmetric left stretch tensor; and $\mathbf{R}$ is the orthogonal polar rotation tensor. The true conjugate pairs: the Cauchy/true stress tensor ($\boldsymbol{\sigma}$) and logarithmic/true strain tensor ($\boldsymbol{\varepsilon}$) (at material points and/or homogenized over a volume), are calculated from

the known **S** and **V**, respectively, as follows:

$$\mathbf{S} = J\mathbf{F}^{-1}\boldsymbol{\sigma}\mathbf{F}^{-\mathrm{T}} = \mathbf{F}_p^{-1}\underline{\mathbf{S}}\mathbf{F}_p^{-\mathrm{T}}; \quad \Rightarrow \quad \boldsymbol{\sigma} = \frac{1}{J}\mathbf{F}_e\underline{\mathbf{S}}\mathbf{F}_e^{\mathrm{T}} = \frac{1}{J}\mathbf{F}\mathbf{S}\mathbf{F}^{\mathrm{T}};$$
$$\dot{\boldsymbol{\varepsilon}} \equiv \mathbf{D} \equiv \mathrm{sym}(\mathbf{L}) \equiv \frac{1}{2}\left(\mathbf{L} + \mathbf{L}^{\mathrm{T}}\right) = \dot{\mathbf{V}}\mathbf{V}^{-1}; \quad \Rightarrow \quad \boldsymbol{\varepsilon} = \ln(\mathbf{V}); \tag{46}$$

where **D** is known as the rate of deformation. Consequently, the equivalent true stress and strain (at material points and/or homogenized over RVE) according to von Mises are calculated as follows [286]:

$$\sigma \equiv \sqrt{\frac{3}{2}}||\boldsymbol{\sigma}^d||; \quad \boldsymbol{\sigma}^d \equiv \boldsymbol{\sigma} - \boldsymbol{\sigma}^h; \quad \boldsymbol{\sigma}^h \equiv \sigma^h\mathbf{I}; \quad \sigma^h = \frac{1}{3}\mathbf{I} : \boldsymbol{\sigma};$$
$$\varepsilon \equiv \sqrt{\frac{2}{3}}||\boldsymbol{\varepsilon}^d||; \quad \boldsymbol{\varepsilon}^d \equiv \boldsymbol{\varepsilon} - \boldsymbol{\varepsilon}^v; \quad \boldsymbol{\varepsilon}^v \equiv \frac{1}{3}\varepsilon^v\mathbf{I}; \quad \varepsilon^v = \mathbf{I} : \boldsymbol{\varepsilon}; \tag{47}$$

where σ and ε are the equivalent (von Mises) stress and strain (scalars), respectively; and superscripts *d*, *h* and *v*, respectively represent deviatoric, hydrostatic and volumetric parts of the corresponding tensorial quantity.

References

[1] W.J. Sames, F.A. List, S. Pannala, R.R. Dehoff, S.S. Babu, The metallurgy and processing science of metal additive manufacturing, Int. Mater. Rev. 61 (2016) 315–360, doi:10.1080/09506608.2015.1116649.

[2] D.D. Gu, W. Meiners, K. Wissenbach, R. Poprawe, Laser additive manufacturing of metallic components, Int. Mater. Rev. 57 (2013) 133–164, doi:10.1179/1743280411Y.0000000014.

[3] T. DebRoy, H.L. Wei, J.S. Zuback, T. Mukherjee, J.W. Elmer, J.O. Milewski, A.M. Beese, et al., Additive manufacturing of metallic components – process, structure and properties, Prog. Mater. Sci. 92 (2018) 112–224, doi:10.1016/j.pmatsci.2017.10.001.

[4] D.L. Bourell, Perspectives on additive manufacturing, Annu. Rev. Mater. Res. 46 (2016) 1–18, doi:10.1146/annurev-matsci-070115-031606.

[5] E.W. Frazier, Metal additive manufacturing: a review, J Mater. Eng. Perform. 23 (2014) 1917–1928, doi:10.1007/s11665-014-0958-z.

[6] M. Seifi, A. Salem, J. Beuth, O. Harrysson, J.J. Lewandowski, Overview of materials qualification needs for metal additive manufacturing, JOM 68 (2016) 747–764, doi:10.1007/s11837-015-1810-0.

[7] D. Zhang, S. Sun, D. Qiu, M.A. Gibson, M.S. Dargusch, M. Brandt, M. Qian, et al., Metal alloys for fusion-based additive manufacturing, Adv. Eng. Mater. 20 (2018) 1700952, doi:10.1002/adem.201700952.

[8] W.E. King, A.T. Anderson, R.M. Ferencz, N.E. Hodge, C. Kamath, S.A. Khairallah, A.M. Rubenchik, Laser powder bed fusion additive manufacturing of metals; physics, computational, and materials challenges, Appl. Phys. Rev. 2 (2015) 41304, doi:10.1063/1.4937809.

[9] G.B. Olson, Computational design of hierarchically structured materials, Science 277 (1997) 1237–1242, doi:10.1126/science.277.5330.1237.

[10] J.J. Lewandowski, M. Seifi, Metal additive manufacturing, Annu. Rev. Mater. Res. 46 (2016) 151–186, doi:10.1146/annurev-matsci-070115-032024.

[11] J. Smith, W. Xiong, W. Yan, S. Lin, P. Cheng, O.L. Kafka, G.J. Wagner, et al., Linking process, structure, property, and performance for metal-based additive manufacturing, Comput. Mech. 57 (2016) 583–610, doi:10.1007/s00466-015-1240-4.

[12] D. Pal, N. Patil, K. Zeng, B. Stucker, An integrated approach to additive manufacturing simulations using physics based, coupled multiscale process modeling, J. Manuf. Sci. Eng. 136 (2014) 61022, doi:10.1115/1.4028580.

[13] M.M. Francois, A. Sun, W.E. King, N.J. Henson, D. Tourret, C.A. Bronkhorst, N.N. Carlson, et al., Modeling of additive manufacturing processes for metals, Curr. Opin. Solid State Mater. Sci. 21 (2017) 198–206, doi:10.1016/j.cossms.2016.12.001.

[14] D. Herzog, V. Seyda, E. Wycisk, C. Emmelmann, Additive manufacturing of metals, Acta Mater. 117 (2016) 371–392, doi:10.1016/j.actamat.2016.07.019.

[15] P.C. Collins, D.A. Brice, P. Samimi, I. Ghamarian, H.L. Fraser, Microstructural control of additively manufactured metallic materials, Annu. Rev. Mater. Res. 46 (2016) 63–91, doi:10.1146/annurev-matsci-070115-031816.

[16] Y.M. Wang, T. Voisin, J.T. McKeown, J. Ye, N.P. Calta, Z. Li, Z. Zeng, et al., Additively manufactured hierarchical stainless steels with high strength and ductility, Nat. Mater. 17 (2018) 63–71, doi:10.1038/nmat5021.

[17] L.E. Murr, S.M. Gaytan, D.A. Ramirez, E. Martinez, J. Hernandez, K.N. Amato, P.W. Shindo, et al., Metal fabrication by additive manufacturing using laser and electron beam melting technologies, J. Mater. Sci. Technol. 28 (2012) 1–14, doi:10.1016/S1005-0302(12)60016-4.

[18] B. Song, X. Zhao, S. Li, C. Han, Q. Wei, S. Wen, J. Liu, et al., Differences in microstructure and properties between selective laser melting and traditional manufacturing for fabrication of metal parts, Front. Mech. Eng. 10 (2015) 111–125, doi:10.1007/s11465-015-0341-2.

[19] S.S. Al-Bermani, M.L. Blackmore, W. Zhang, I. Todd, The origin of microstructural diversity, texture, and mechanical properties in electron beam melted Ti–6Al–4V, Metall. Mat. Trans. A 41 (2010) 3422–3434, doi:10.1007/s11661-010-0397-x.

[20] A.A. Antonysamy, J. Meyer, P.B. Prangnell, Effect of build geometry on the β-grain structure and texture in additive manufacture of Ti6Al4V by selective electron beam melting, Mater. Charact. 84 (2013) 153–168, doi:10.1016/j.matchar.2013.07.012.

[21] R.R. Dehoff, M.M. Kirka, F.A. List, K.A. Unocic, W.J. Sames, Crystallographic texture engineering through novel melt strategies via electron beam melting, Mater. Sci. Technol. 31 (2014) 939–944, doi:10.1179/1743284714Y.0000000697.

[22] M. Garibaldi, I. Ashcroft, M. Simonelli, R. Hague, Metallurgy of high-silicon steel parts produced using selective laser melting, Acta Mater. 110 (2016) 207–216, doi:10.1016/j.actamat.2016.03.037.

[23] F. Geiger, K. Kunze, T. Etter, Tailoring the texture of IN738LC processed by selective laser melting (SLM) by specific scanning strategies, Mater. Sci. Eng. A 661 (2016) 240–246, doi:10.1016/j.msea.2016.03.036.

[24] H. Helmer, A. Bauereiß, R.F. Singer, C. Körner, Grain structure evolution in inconel 718 during selective electron beam melting, Mater. Sci. Eng. A 668 (2016) 180–187, doi:10.1016/j.msea.2016.05.046.

[25] F. Liu, X. Lin, C. Huang, M. Song, G. Yang, J. Chen, W. Huang, The effect of laser scanning path on microstructures and mechanical properties of laser solid formed nickel-base superalloy inconel 718, J. Alloys Compd. 509 (2011) 4505–4509, doi:10.1016/j.jallcom.2010.11.176.

[26] L.L. Parimi, R.G. A., D. Clark, M.M. Attallah, Microstructural and texture development in direct laser fabricated IN718, Mater. Charact. 89 (2014) 102–111, doi:10.1016/j.matchar.2013.12.012.

[27] M.S. Pham, B. Dovgyy, P.A. Hooper, Twinning induced plasticity in austenitic stainless steel 316L made by additive manufacturing, Mater. Sci. Eng. A 704 (2017) 102–111, doi:10.1016/j.msea.2017.07.082.

[28] M. Simonelli, Y.Y. Tse, C. Tuck, On the texture formation of selective laser melted Ti–6Al–4V, Metall. Mat. Trans. A 45 (2014) 2863–2872, doi:10.1007/s11661-014-2218-0.

[29] A. Yadollahi, N. Shamsaei, S.M. Thompson, D.W. Seely, Effects of process time interval and heat treatment on the mechanical and microstructural properties of direct laser deposited 316L stainless steel, Mater. Sci. Eng. A 644 (2015) 171–183, doi:10.1016/j.msea.2015.07.056.

[30] L. Thijs, F. Verhaeghe, T. Craeghs, J. van Humbeeck, J.-P. Kruth, A study of the microstructural evolution during selective laser melting of Ti–6Al–4V, Acta Mater. 58 (2010) 3303–3312, doi:10.1016/j.actamat.2010.02.004.

[31] L. Thijs, K. Kempen, J.-P. Kruth, J. van Humbeeck, Fine-structured aluminium products with controllable texture by selective laser melting of pre-alloyed alsi10mg powder, Acta Mater. 61 (2013) 1809–1819, doi:10.1016/j.actamat.2012.11.052.

[32] T. Wang, Y.Y. Zhu, S.Q. Zhang, H.B. Tang, H.M. Wang, Grain morphology evolution behavior of titanium alloy components during laser melting deposition additive manufacturing, J. Alloys Compd. 632 (2015) 505–513, doi:10.1016/j.jallcom.2015.01.256.

[33] J. Wu, X.Q. Wang, W. Wang, M.M. Attallah, M.H. Loretto, Microstructure and strength of selectively laser melted alsi10mg, Acta Mater. 117 (2016) 311–320, doi:10.1016/j.actamat.2016.07.012.

[34] I. Yadroitsev, P. Krakhmalev, I. Yadroitsava, S. Johansson, I. Smurov, Energy input effect on morphology and microstructure of selective laser melting single track from metallic powder, J. Mater. Process. Technol. 213 (2013) 606–613, doi:10.1016/j.jmatprotec.2012.11.014.

[35] Q. Zhang, J. Chen, X. Lin, H. Tan, W.D. Huang, Grain morphology control and texture characterization of laser solid formed Ti6Al2Sn2Zr3Mo1.5Cr2Nb titanium alloy, J. Mater. Process. Technol. 238 (2016) 202–211, doi:10.1016/j.jmatprotec.2016.07.011.

[36] Y. Zhong, L. Liu, S. Wikman, D. Cui, Z. Shen, Intragranular cellular segregation network structure strengthening 316L stainless steel prepared by selective laser melting, J. Nucl. Mater. 470 (2016) 170–178, doi:10.1016/j.jnucmat.2015.12.034.

[37] X. Zhou, K. Li, D. Zhang, X. Liu, J. Ma, W. Liu, Z. Shen, Textures formed in a cocrmo alloy by selective laser melting, J. Alloys Compd. 631 (2015) 153–164, doi:10.1016/j.jallcom.2015.01.096.

[38] C. Haase, F. Tang, M.B. Wilms, A. Weisheit, B. Hallstedt, Combining thermodynamic modeling and 3D printing of elemental powder blends for high-throughput investigation of high-entropy alloys – towards rapid alloy screening and design, Mater. Sci. Eng. A 688 (2017) 180–189, doi:10.1016/j.msea.2017.01.099.

[39] P. Köhnen, M. Létang, M. Voshage, J. Henrich Schleifenbaum, C. Haase, Understanding the process-microstructure correlations for tailoring the mechanical properties of L-PBF produced austenitic advanced high strength steel, Addit. Manufac. (2019) 100914, doi:10.1016/j.addma.2019.100914.

[40] Y. Kok, X.P. Tan, P. Wang, M. Nai, N.H. Loh, E. Liu, S.B. Tor, Anisotropy and heterogeneity of microstructure and mechanical properties in metal additive manufacturing, Mater. Des. 139 (2018) 565–586, doi:10.1016/j.matdes.2017.11.021.

[41] Y. Zhu, X. Tian, J. Li, H. Wang, The anisotropy of laser melting deposition additive manufacturing ti–6.5al–3.5mo–1.5zr–0.3si titanium alloy, Mater. Des. 67 (2015) 538–542, doi:10.1016/j.matdes.2014.11.001.

[42] M. Tang, P.C. Pistorius, Anisotropic mechanical behavior of alsi10mg parts produced by selective laser melting, JOM 69 (2017) 516–522, doi:10.1007/s11837-016-2230-5.

[43] L.Y. Chen, J.C. Huang, C.H. Lin, C.T. Pan, S.Y. Chen, T.L. Yang, D.Y. Lin, et al., Anisotropic response of Ti–6Al–4V alloy fabricated by 3D printing selective laser melting, Mater. Sci. Eng. A 682 (2017) 389–395, doi:10.1016/j.msea.2016.11.061.
[44] B. AlMangour, D. Grzesiak, J.-M. Yang, Scanning strategies for texture and anisotropy tailoring during selective laser melting of TiC/316L stainless steel nanocomposites, J. Alloys Compd. 728 (2017) 424–435, doi:10.1016/j.jallcom.2017.08.022.
[45] S. Dadbakhsh, B. Vrancken, J.-P. Kruth, J. Luyten, J. van Humbeeck, Texture and anisotropy in selective laser melting of NiTi alloy, Mater. Sci. Eng. A 650 (2016) 225–232, doi:10.1016/j.msea.2015.10.032.
[46] L. Thijs, M.L. Montero Sistiaga, R. Wauthle, Q. Xie, J.-P. Kruth, J. van Humbeeck, Strong morphological and crystallographic texture and resulting yield strength anisotropy in selective laser melted tantalum, Acta Mater. 61 (2013) 4657–4668, doi:10.1016/j.actamat.2013.04.036.
[47] V.A. Popovich, E.V. Borisov, A.A. Popovich, V. Sufiiarov, D.V. Masaylo, L. Alzina, Functionally graded inconel 718 processed by additive manufacturing, Mater. Des. 114 (2017) 441–449, doi:10.1016/j.matdes.2016.10.075.
[48] T. Niendorf, S. Leuders, A. Riemer, H.A. Richard, T. Tröster, D. Schwarze, Highly anisotropic steel processed by selective laser melting, Metall. Mater. Trans. B 44 (2013) 794–796, doi:10.1007/s11663-013-9875-z.
[49] B.E. Carroll, T.A. Palmer, A.M. Beese, Anisotropic tensile behavior of Ti–6Al–4V components fabricated with directed energy deposition additive manufacturing, Acta Mater. 87 (2015) 309–320, doi:10.1016/j.actamat.2014.12.054.
[50] T. Maity, N. Chawake, J.T. Kim, J. Eckert, K.G. Prashanth, Anisotropy in local microstructure – does it affect the tensile properties of the SLM samples? Manufac. Lett. 15 (2018) 33–37, doi:10.1016/j.mfglet.2018.02.012.
[51] E. Chlebus, B. Kuźnicka, T. Kurzynowski, B. Dybała, Microstructure and mechanical behaviour of Ti–6Al–7Nb alloy produced by selective laser melting, Mater. Charact. 62 (2011) 488–495, doi:10.1016/j.matchar.2011.03.006.
[52] C. Haase, J. Bültmann, J. Hof, S. Ziegler, S. Bremen, C. Hinke, A. Schwedt, et al., Exploiting process-related advantages of selective laser melting for the production of high-manganese steel, Materials (Basel, Switzerland) 10 (2017), doi:10.3390/ma10010056.
[53] E. Liverani, S. Toschi, L. Ceschini, A. Fortunato, Effect of selective laser melting (SLM) process parameters on microstructure and mechanical properties of 316L austenitic stainless steel, J. Mater. Process. Technol. 249 (2017) 255–263, doi:10.1016/j.jmatprotec.2017.05.042.
[54] T.R. Smith, J.D. Sugar, C. San Marchi, J.M. Schoenung, Strengthening mechanisms in directed energy deposited austenitic stainless steel, Acta Mater. 164 (2019) 728–740, doi:10.1016/j.actamat.2018.11.021.
[55] S.-H. Sun, Y. Koizumi, S. Kurosu, Y.-P. Li, H. Matsumoto, A. Chiba, Build direction dependence of microstructure and high-temperature tensile property of Co–Cr–Mo alloy fabricated by electron beam melting, Acta Mater. 64 (2014) 154–168, doi:10.1016/j.actamat.2013.10.017.
[56] T. Tancogne-Dejean, C.C. Roth, U. Woy, D. Mohr, Probabilistic fracture of Ti–6Al–4V made through additive layer manufacturing, Int. J. Plast. 78 (2016) 145–172, doi:10.1016/j.ijplas.2015.09.007.
[57] T. Vilaro, C. Colin, J.D. Bartout, L. Nazé, M. Sennour, Microstructural and mechanical approaches of the selective laser melting process applied to a nickel-base superalloy, Mater. Sci. Eng. A 534 (2012) 446–451, doi:10.1016/j.msea.2011.11.092.
[58] Z. Wang, T.A. Palmer, A.M. Beese, Effect of processing parameters on microstructure and tensile properties of austenitic stainless steel 304L made by directed energy deposition additive manufacturing, Acta Mater. 110 (2016) 226–235, doi:10.1016/j.actamat.2016.03.019.
[59] J.A. Koepf, D. Soldner, M. Ramsperger, J. Mergheim, M. Markl, C. Körner, Numerical microstructure prediction by a coupled finite element cellular automaton model for selective electron beam melting, Comput. Mater. Sci. 162 (2019) 148–155, doi:10.1016/j.commatsci.2019.03.004.
[60] J. Kundin, A. Ramazani, U. Prahl, C. Haase, Microstructure evolution of binary and multicomponent manganese steels during selective laser melting, Metall and Mat Trans A 50 (2019) 2022–2040, doi:10.1007/s11661-019-05143-x.
[61] N. Raghavan, R. Dehoff, S. Pannala, S. Simunovic, M. Kirka, J. Turner, N. Carlson, et al., Numerical modeling of heat-transfer and the influence of process parameters on tailoring the grain morphology of IN718 in electron beam additive manufacturing, Acta Mater. 112 (2016) 303–314, doi:10.1016/j.actamat.2016.03.063.
[62] T.M. Rodgers, J.D. Madison, V. Tikare, Simulation of metal additive manufacturing microstructures using kinetic monte carlo, Comput. Mater. Sci. 135 (2017) 78–89, doi:10.1016/j.commatsci.2017.03.053.
[63] A. Zinoviev, O. Zinovieva, V. Ploshikhin, V. Romanova, R. Balokhonov, Evolution of grain structure during laser additive manufacturing. simulation by a cellular automata method, Mater. Des. 106 (2016) 321–329, doi:10.1016/j.matdes.2016.05.125.
[64] O. Zinovieva, A. Zinoviev, V. Ploshikhin, Three-dimensional modeling of the microstructure evolution during metal additive manufacturing, Comput. Mater. Sci. 141 (2018) 207–220, doi:10.1016/j.commatsci.2017.09.018.
[65] H.L. Wei, J.W. Elmer, T. DebRoy, Origin of grain orientation during solidification of an aluminum alloy, Acta Mater. 115 (2016) 123–131, doi:10.1016/j.actamat.2016.05.057.
[66] J.A. Koepf, M.R. Gotterbarm, M. Markl, C. Körner, 3D multi-layer grain structure simulation of powder bed fusion additive manufacturing, Acta Mater. 152 (2018) 119–126, doi:10.1016/j.actamat.2018.04.030.
[67] A. Rai, H. Helmer, C. Körner, Simulation of grain structure evolution during powder bed based additive manufacturing, Addit. Manufac. 13 (2017) 124–134, doi:10.1016/j.addma.2016.10.007.
[68] A. Rai, M. Markl, C. Körner, A coupled cellular automaton–lattice boltzmann model for grain structure simulation during additive manufacturing, Comput. Mater. Sci. 124 (2016) 37–48, doi:10.1016/j.commatsci.2016.07.005.
[69] Y. Lian, Z. Gan, C. Yu, D. Kats, W.K. Liu, G.J. Wagner, A cellular automaton finite volume method for microstructure evolution during additive manufacturing, Mater. Des. 169 (2019) 107672, doi:10.1016/j.matdes.2019.107672.
[70] Y. Lian, S. Lin, W. Yan, W.K. Liu, G.J. Wagner, A parallelized three-dimensional cellular automaton model for grain growth during additive manufacturing, Comput. Mech. 61 (2018) 543–558, doi:10.1007/s00466-017-1535-8.
[71] X. Li, W. Tan, Numerical investigation of effects of nucleation mechanisms on grain structure in metal additive manufacturing, Comput. Mater. Sci. 153 (2018) 159–169, doi:10.1016/j.commatsci.2018.06.019.
[72] S. Ghosh, M. Mahmoudi, L. Johnson, A. Elwany, R. Arroyave, D. Allaire, Uncertainty analysis of microsegregation during laser powder bed fusion, Modelling Simul. Mater. Sci. Eng. 27 (3) (2019), doi:10.1088/1361-651X/ab01bf.
[73] F. Kies, P. Köhnen, M.B. Wilms, F. Brasche, K.G. Pradeep, A. Schwedt, S. Richter, et al., Design of high-manganese steels for additive manufacturing applications with energy-absorption functionality, Mater. Des. 160 (2018) 1250–1264, doi:10.1016/j.matdes.2018.10.051.
[74] T. Niendorf, F. Brenne, Steel showing twinning-induced plasticity processed by selective laser melting—an additively manufactured high performance material, Mater. Charact. 85 (2013) 57–63, doi:10.1016/j.matchar.2013.08.010.
[75] G. Frommeyer, U. Brüx, P. Neumann, Supra-Ductile and high-strength manganese-trip/twip steels for high energy absorption purposes, ISIJ Int. 43 (2003) 438–446, doi:10.2355/isijinternational.43.438.
[76] O. Grässel, L. Krüger, G. Frommeyer, L. Meyer, High strength Fe–Mn–(Al, Si) trip/twip steels development—properties—application, Int. J. Plast. 16 (2000) 1391–1409, doi:10.1016/S0749-6419(00)00015-2.
[77] L. Krüger, L.W. Meyer, U. Brûx, G. Frommeyer, O. Grässel, Stress-deformation behaviour of high manganese (Al, Si) trip and twip steels, J. Phys. IV France 110 (2003) 189–194, doi:10.1051/jp4:20020692.
[78] K. Sato, M. Ichinose, Y. Hirotsu, Y. Inoue, Effects of deformation induced phase transformation and twinning on the mechanical properties of austenitic fe-Mn–Al alloys, ISIJ Int. 29 (1989) 868–877, doi:10.2355/isijinternational.29.868.
[79] D.T. Pierce, J.A. Jiménez, J. Bentley, D. Raabe, C. Oskay, J.E. Wittig, The influence of manganese content on the stacking fault and austenite/ε-martensite interfacial energies in Fe–Mn–(Al–Si) steels investigated by experiment and theory, Acta Mater. 68 (2014) 238–253, doi:10.1016/j.actamat.2014.01.001.
[80] A. Saeed-Akbari, L. Mosecker, A. Schwedt, W. Bleck, Characterization and prediction of flow behavior in high-manganese twinning induced plasticity steels, Metall and Mat Trans A 43 (2012) 1688–1704, doi:10.1007/s11661-011-0993-4.
[81] S. Allain, J.-P. Chateau, O. Bouaziz, S. Migot, N. Guelton, Correlations between the calculated stacking fault energy and the plasticity mechanisms in fe–mn–c alloys, Mater. Sci. Eng. A 387-389 (2004) 158–162, doi:10.1016/j.msea.2004.01.059.
[82] S. Martin, S. Wolf, U. Martin, L. Krüger, D. Rafaja, Deformation mechanisms in austenitic trip/twip steel as a function of temperature, Metall. Mat. Trans. A 47 (2016) 49–58, doi:10.1007/s11661-014-2684-4.
[83] H. Idrissi, L. Ryelandt, M. Veron, D. Schryvers, P.J. Jacques, Is there a relationship between the stacking fault character and the activated mode of plasticity of Fe–Mn-based austenitic steels? Scr. Mater. 60 (2009) 941–944, doi:10.1016/j.scriptamat.2009.01.040.
[84] J.-K. Kim, B.C. de Cooman, Stacking fault energy and deformation mechanisms in Fe–xMn–0.6C–yAl twip steel, Mater. Sci. Eng. A 676 (2016) 216–231, doi:10.1016/j.msea.2016.08.106.
[85] B.C. de Cooman, Y. Estrin, S.K. Kim, Twinning-induced plasticity (TWIP) steels, Acta Mater. 142 (2018) 283–362, doi:10.1016/j.actamat.2017.06.046.
[86] M. Linderov, C. Segel, A. Weidner, H. Biermann, A. Vinogradov, Deformation mechanisms in austenitic trip/twip steels at room and elevated temperature investigated by acoustic emission and scanning electron microscopy, Mater. Sci. Eng. A 597 (2014) 183–193, doi:10.1016/j.msea.2013.12.094.
[87] A. Dumay, J.-P. Chateau, S. Allain, S. Migot, O. Bouaziz, Influence of addition elements on the stacking-fault energy and mechanical properties of an austenitic Fe–Mn–C steel, Mater. Sci. Eng. A 483-484 (2008) 184–187, doi:10.1016/j.msea.2006.12.170.
[88] K. Renard, P.J. Jacques, On the relationship between work hardening and twinning rate in twip steels, Mater. Sci. Eng. A 542 (2012) 8–14, doi:10.1016/j.msea.2012.01.123.
[89] S. Allain, J.-P. Chateau, O. Bouaziz, A physical model of the twinning-induced plasticity effect in a high manganese austenitic steel, Mater. Sci. Eng. A 387–389 (2004) 143–147, doi:10.1016/j.msea.2004.01.060.
[90] A. Saeed-Akbari, J. Imlau, U. Prahl, W. Bleck, Derivation and variation in composition-dependent stacking fault energy maps based on subregular solution model in high-manganese steels, Metall. Mat. Trans. A 40 (2009) 3076–3090, doi:10.1007/s11661-009-0050-8.
[91] C. Haase, L.A. Barrales-Mora, F. Roters, D.A. Molodov, G. Gottstein, Applying the texture analysis for optimizing thermomechanical treatment of high manganese twinning-induced plasticity steel, Acta Mater. 80 (2014) 327–340, doi:10.1016/j.actamat.2014.07.068.
[92] C. Haase, M. Kühbach, L.A. Barrales-Mora, S.L. Wong, F. Roters, D.A. Molodov, G. Gottstein, Recrystallization behavior of a high-manganese steel, Acta Mater. 100 (2015) 155–168, doi:10.1016/j.actamat.2015.08.057.
[93] M. Diehl, M. Groeber, C. Haase, D.A. Molodov, F. Roters, D. Raabe, Identifying structure–property relationships through dream.3d representative volume el-

ements and damask crystal plasticity simulations, JOM 69 (2017) 848–855, doi:10.1007/s11837-017-2303-0.

[94] J. Günther, F. Brenne, M. Droste, M. Wendler, O. Volkova, H. Biermann, T. Niendorf, Design of novel materials for additive manufacturing – isotropic microstructure and high defect tolerance, Sci. Rep. 8 (2018) 1298, doi:10.1038/s41598-018-19376-0.

[95] A. Šalak, M. Selecká, Manganese in Powder Metallurgy Steels, CISP, Cambridge, England, 2012.

[96] H.L. Wei, J. Mazumder, T. DebRoy, Evolution of solidification texture during additive manufacturing, Sci. Rep. 5 (2015) 16446, doi:10.1038/srep16446.

[97] S. Zaefferer, S.I. Wright, D. Raabe, Three-Dimensional orientation microscopy in a focused ion beam–scanning electron microscope, Metall. Mat. Trans. A 39 (2008) 374–389, doi:10.1007/s11661-007-9418-9.

[98] W. Xu, M. Ferry, N. Mateescu, J.M. Cairney, F.J. Humphreys, Techniques for generating 3-D ebsd microstructures by fib tomography, Mater. Charact. 58 (2007) 961–967, doi:10.1016/j.matchar.2006.10.001.

[99] S. Ghosh, Y. Bhandari, M. Groeber, CAD-based reconstruction of 3D polycrystalline alloy microstructures from fib generated serial sections, Comput. Aided Des. 40 (2008) 293–310, doi:10.1016/j.cad.2007.11.003.

[100] Y. Bhandari, S. Sarkar, M. Groeber, M.D. Uchic, D.M. Dimiduk, S. Ghosh, 3D polycrystalline microstructure reconstruction from fib generated serial sections for Fe analysis, Comput. Mater. Sci. 41 (2007) 222–235, doi:10.1016/j.commatsci.2007.04.007.

[101] M. Groeber, A framework for automated analysis and simulation of 3D polycrystalline microstructures. Part 1, Acta Mater. 56 (2008) 1257–1273, doi:10.1016/j.actamat.2007.11.041.

[102] F. Bachmann, R. Hielscher, H. Schaeben, Grain detection from 2d and 3d EBSD data–specification of the MTEX algorithm, Ultramicroscopy 111 (2011) 1720–1733, doi:10.1016/j.ultramic.2011.08.002.

[103] F. Bachmann, R. Hielscher, H. Schaeben, Texture analysis with MTEX – free and open source software toolbox, SSP 160 (2010) 63–68, doi:10.4028/www.scientific.net/SSP.160.63.

[104] R. Hielscher, H. Schaeben, A novel pole figure inversion method, J. Appl. Crystallogr. 41 (2008) 1024–1037, doi:10.1107/S0021889808030112.

[105] G. Nolze, R. Hielscher, Orientations – perfectly colored, J. Appl. Crystallogr. 49 (2016) 1786–1802, doi:10.1107/S1600576716012942.

[106] G. Nolze, Euler angles and crystal symmetry, Cryst. Res. Technol. 50 (2015) 188–201, doi:10.1002/crat.201400427.

[107] M.A. Groeber, M.A. Jackson, DREAM.3D, Integr. Mater. 3 (2014) 3009, doi:10.1186/2193-9772-3-5.

[108] S.P. Donegan, J.C. Tucker, A.D. Rollett, K. Barmak, M. Groeber, Extreme value analysis of tail departure from log-normality in experimental and simulated grain size distributions, Acta Mater. 61 (2013) 5595–5604, doi:10.1016/j.actamat.2013.06.001.

[109] J.C. Tucker, L.H. Chan, G.S. Rohrer, M.A. Groeber, A.D. Rollett, Tail departure of log-normal grain size distributions in synthetic three-dimensional microstructures, Metall. Mat. Trans. A 43 (2012) 2810–2822, doi:10.1007/s11661-011-0851-4.

[110] I.M. Robertson, C.A. Schuh, J.S. Vetrano, N.D. Browning, D.P. Field, D.J. Jensen, M.K. Miller, et al., Towards an integrated materials characterization toolbox„ J. Mater. Res. 26 (2011) 1341–1383, doi:10.1557/jmr.2011.41.

[111] M. Fátima Vaz, M.A. Fortes, Grain size distribution, Scr. Metall. 22 (1988) 35–40, doi:10.1016/S0036-9748(88)80302-8.

[112] B. Roebuck, Measurement of grain size and size distribution in engineering materials, Mater. Sci. Technol. 16 (2013) 1167–1174, doi:10.1179/026708300101506911.

[113] B. Raeisinia, C.W. Sinclair, A representative grain size for the mechanical response of polycrystals, Mater. Sci. Eng. A 525 (2009) 78–82, doi:10.1016/j.msea.2009.06.045.

[114] K.J. Kurzydłowski, A model for the flow stress dependence on the distribution of grain size in polycrystals, Scr. Metall. Mater. 24 (1990) 879–883, doi:10.1016/0956-716X(90)90129-5.

[115] R.A. Masumura, P.M. Hazzledine, C.S. Pande, Yield stress of fine grained materials, Acta Mater. 46 (1998) 4527–4534, doi:10.1016/S1359-6454(98)00150-5.

[116] S. Berbenni, V. Favier, M. Berveiller, Impact of the grain size distribution on the yield stress of heterogeneous materials, Int. J. Plast. 23 (2007) 114–142, doi:10.1016/j.ijplas.2006.03.004.

[117] O. Ito, E.R. Fuller, Computer modelling of anisotropic grain microstructure in two dimensions, Acta Metall. Mater. 41 (1993) 191–198, doi:10.1016/0956-7151(93)90350-2.

[118] K.F. Mulchrone, K.R. Choudhury, Fitting an ellipse to an arbitrary shape, J. Struct. Geol. 26 (2004) 143–153, doi:10.1016/S0191-8141(03)00093-2.

[119] J.K. Mason, C.A. Schuh, The generalized Mackenzie distribution, Acta Mater. 57 (2009) 4186–4197, doi:10.1016/j.actamat.2009.05.016.

[120] V. Gertsman, A.P. Zhilyaev, A.I. Pshennichnyuk, R.Z. Valiev, Modelling of grain boundary misorientation spectrum in polycrystals with crystallographic texture, Acta Metall. Mater. 40 (1992) 1433–1441, doi:10.1016/0956-7151(92)90445-K.

[121] A. Garbacz, M.W. Grabski, The relationship between texture and CSL boundaries distribution in polycrystalline materials—I. the grain boundary misorientation distribution in random polycrystal, Acta Metall. Mater. 41 (1993) 469–473, doi:10.1016/0956-7151(93)90075-4.

[122] A. Garbacz, M.W. Grabski, The relationship between texture and csl boundaries distribution in polycrystalline materials—II. Analysis of the relationship between texture and coincidence grain boundary distribution, Acta Metall. Mater. 41 (1993) 475–483, doi:10.1016/0956-7151(93)90076-5.

[123] A.P. Zhilyaev, V. Gertsman, O.V. Mishin, A.I. Pshenichnyuk, I.V. Aleksandrov, R.Z. Valiev, Grain boundary misorientation spectra (GBMS) determined by real odf in F.C.C.-materials susceptible to annealing twinning, Acta Metall. Mater. 41 (1993) 2657–2665, doi:10.1016/0956-7151(93)90135-F.

[124] A. Morawiec, J.A. Szpunar, D.C. Hinz, Texture influence on the frequency of occurrence of CSL-boundaries in polycrystalline materials, Acta Metall. Mater. 41 (1993) 2825–2832, doi:10.1016/0956-7151(93)90097-C.

[125] J. Zhao, B.L. Adams, P.R. Morris, A comparison of measured and texture-estimated misorientation distributions in type 304 stainless steel tubing, Text. Microstruct. 8 (1988) 493–508, doi:10.1155/TSM.8-9.493.

[126] O.V. Mishin, V.Y. Gertsman, G. Gottstein, Distributions of orientations and misorientations in hot-rolled copper, Mater. Charact. 38 (1997) 39–48, doi:10.1016/S1044-5803(96)00130-1.

[127] J.K. Mackenzie, SECOND paper on statistics associated with the random disorientation of cubes, Biometrika 45 (1958) 229–240, doi:10.1093/biomet/45.1-2.229.

[128] L. Liu, Q. Ding, Y. Zhong, J. Zou, J. Wu, Y.-L. Chiu, J. Li, et al., Dislocation network in additive manufactured steel breaks strength–ductility trade-off, Mater. Today 21 (2018) 354–361, doi:10.1016/j.mattod.2017.11.004.

[129] K. Saeidi, X. Gao, Y. Zhong, Z.J. Shen, Hardened austenite steel with columnar sub-grain structure formed by laser melting, Mater. Sci. Eng. A 625 (2015) 221–229, doi:10.1016/j.msea.2014.12.018.

[130] H. Mughrabi, Dislocation wall and cell structures and long-range internal stresses in deformed metal crystals, Acta Metall. 31 (1983) 1367–1379, doi:10.1016/0001-6160(83)90007-X.

[131] D. Kuhlmann-Wilsdorf, N. Hansen, Geometrically necessary, incidental and subgrain boundaries, Scr. Metall. Mater. 25 (1991) 1557–1562, doi:10.1016/0956-716X(91)90451-6.

[132] D. Hughes, N. Hansen, D. Bammann, Geometrically necessary boundaries, incidental dislocation boundaries and geometrically necessary dislocations, Scr. Mater. 48 (2003) 147–153, doi:10.1016/S1359-6462(02)00358-5.

[133] J. Nye, Some geometrical relations in dislocated crystals, Acta Metall. 1 (1953) 153–162, doi:10.1016/0001-6160(53)90054-6.

[134] A. Arsenlis, D. Parks, Crystallographic aspects of geometrically-necessary and statistically-stored dislocation density, Acta Mater. 47 (1999) 1597–1611, doi:10.1016/S1359-6454(99)00020-8.

[135] M.F. Ashby, The deformation of plastically non-homogeneous materials, Philos. Mag. 21 (1970) 399–424, doi:10.1080/14786437008238426.

[136] H. Gao, Y. Huang, Geometrically necessary dislocation and size-dependent plasticity, Scr. Mater. 48 (2003) 113–118, doi:10.1016/S1359-6462(02)00329-9.

[137] W. Pantleon, Resolving the geometrically necessary dislocation content by conventional electron backscattering diffraction, Scr. Mater. 58 (2008) 994–997, doi:10.1016/j.scriptamat.2008.01.050.

[138] M. Niewczas, Chapter 75 Dislocations and Twinning in Face Centred Cubic Crystals, Elsevier, 2007, pp. 263–364.

[139] S. Dancette, L. Delannay, K. Renard, M.A. Melchior, P.J. Jacques, Crystal plasticity modeling of texture development and hardening in twip steels, Acta Mater. 60 (2012) 2135–2145, doi:10.1016/j.actamat.2012.01.015.

[140] D. Barbier, N. Gey, N. Bozzolo, S. Allain, M. Humbert, EBSD for analysing the twinning microstructure in fine-grained twip steels and its influence on work hardening, J. Microsc. 235 (2009) 67–78, doi:10.1111/j.1365-2818.2009.03182.x.

[141] I. Gutierrez-Urrutia, D. Raabe, Dislocation and twin substructure evolution during strain hardening of an Fe–22wt% Mn–0.6wt% c twip steel observed by electron channeling contrast imaging, Acta Mater. 59 (2011) 6449–6462, doi:10.1016/j.actamat.2011.07.009.

[142] Y. Zhang, N.R. Tao, K. Lu, Effect of stacking-fault energy on deformation twin thickness in Cu–Al alloys, Scr. Mater. 60 (2009) 211–213, doi:10.1016/j.scriptamat.2008.10.005.

[143] P. Eisenlohr, M. Diehl, R.A. Lebensohn, F. Roters, A spectral method solution to crystal elasto-viscoplasticity at finite strains, Int. J. Plast. 46 (2013) 37–53, doi:10.1016/j.ijplas.2012.09.012.

[144] P. Shanthraj, P. Eisenlohr, M. Diehl, F. Roters, Numerically robust spectral methods for crystal plasticity simulations of heterogeneous materials, Int. J. Plast. 66 (2015) 31–45, doi:10.1016/j.ijplas.2014.02.006.

[145] F. Roters, M. Diehl, P. Shanthraj, P. Eisenlohr, C. Reuber, S.L. Wong, T. Maiti, et al., DAMASK – the Düsseldorf advanced material simulation kit for modeling multi-physics crystal plasticity, thermal, and damage phenomena from the single crystal up to the component scale, Comput. Mater. Sci. 158 (2019) 420–478, doi:10.1016/j.commatsci.2018.04.030.

[146] J.R. Rice, Inelastic constitutive relations for solids, J. Mech. Phys. Solids 19 (1971) 433–455, doi:10.1016/0022-5096(71)90010-X.

[147] R. Hill, J.R. Rice, Constitutive analysis of elastic-plastic crystals at arbitrary strain, J. Mech. Phys. Solids 20 (1972) 401–413, doi:10.1016/0022-5096(72)90017-8.

[148] R.J. Asaro, J.R. Rice, Strain localization in ductile single crystals, J. Mech. Phys. Solids 25 (1977) 309–338, doi:10.1016/0022-5096(77)90001-1.

[149] D. Peirce, R.J. Asaro, A. Needleman, An analysis of nonuniform and localized deformation in ductile single crystals, Acta Metall. 30 (1982) 1087–1119, doi:10.1016/0001-6160(82)90005-0.

[150] D. Peirce, R.J. Asaro, A. Needleman, Material rate dependence and localized deformation in crystalline solids, Acta Metall. 31 (1983) 1951–1976, doi:10.1016/0001-6160(83)90014-7.

[151] R.J. Asaro, Crystal plasticity, J. Appl. Mech. 50 (1983) 921, doi:10.1115/1.3167205.
[152] R.J. Asaro, Micromechanics of crystals and polycrystals, Advances in Applied Mechanics, 23, Elsevier, 1983, pp. 1–115.
[153] R.J. Asaro, A. Needleman, Overview no. 42 texture development and strain hardening in rate dependent polycrystals, Acta Metall. 33 (1985) 923–953, doi:10.1016/0001-6160(85)90188-9.
[154] S.R. Kalidindi, C.A. Bronkhorst, L. Anand, Crystallographic texture evolution in bulk deformation processing of FCC metals, J. Mech. Phys. Solids 40 (1992) 537–569, doi:10.1016/0022-5096(92)80003-9.
[155] C.A. Bronkhorst, S.R. Kalidindi, L. Anand, Polycrystalline plasticity and the evolution of crystallographic texture in FCC metals, Phil. Trans. R. Soc. Lond. A 341 (1992) 443–477, doi:10.1098/rsta.1992.0111.
[156] S.R. Kalidindi, Incorporation of deformation twinning in crystal plasticity models, J. Mech. Phys. Solids 46 (1998) 267–290, doi:10.1016/S0022-5096(97)00051-3.
[157] C. Reina, L. Fokoua Djodom, M. Ortiz, S. Conti, Kinematics of elasto-plasticity, J. Mech. Phys. Solids 121 (2018) 99–113, doi:10.1016/j.jmps.2018.07.006.
[158] E.H. Lee, D.T. Liu, Finite-strain elastic—plastic theory with application to plane-wave analysis, J. Appl. Phys. 38 (1967) 19–27, doi:10.1063/1.1708953.
[159] E.H. Lee, Elastic-plastic deformation at finite strains, J. Appl. Mech. 36 (1969) 1, doi:10.1115/1.3564580.
[160] E. Kröner, Allgemeine kontinuumstheorie der versetzungen und eigenspannungen, Arch. Rational Mech. Anal. 4 (1959) 273–334, doi:10.1007/BF00281393.
[161] L. Anand, Constitutive equations for hot-working of metals, Int. J. Plast. 1 (1985) 213–231, doi:10.1016/0749-6419(85)90004-X.
[162] A. Ma, F. Roters, D. Raabe, A dislocation density based constitutive model for crystal plasticity fem including geometrically necessary dislocations, Acta Mater. 54 (2006) 2169–2179, doi:10.1016/j.actamat.2006.01.005.
[163] N. Jia, F. Roters, P. Eisenlohr, C. Kords, D. Raabe, Non-crystallographic shear banding in crystal plasticity fem simulations, Acta Mater. 60 (2012) 1099–1115, doi:10.1016/j.actamat.2011.10.047.
[164] P. van Houtte, Simulation of the rolling and shear texture of brass by the taylor theory adapted for mechanical twinning, Acta Metall. 26 (1978) 591–604, doi:10.1016/0001-6160(78)90111-6.
[165] S.A.H. Motaman, U. Prahl, Microstructural constitutive model for polycrystal viscoplasticity in cold and warm regimes based on continuum dislocation dynamics, J. Mech. Phys. Solids 122 (2019) 205–243, doi:10.1016/j.jmps.2018.09.002.
[166] W. Blum, P. Eisenlohr, F. Breutinger, Understanding creep—a review, Metall and Mat Trans A 33 (2002) 291–303, doi:10.1007/s11661-002-0090-9.
[167] E. Orowan, Zur kristallplastizitaet, Z. Physik 89 (1934) 605–613, doi:10.1007/BF01341478.
[168] U.F. Kocks, A.S. Argon, M.F. Ashby, Thermodynamics and kinetics of slip, Prog. Mater Sci. 19 (1975).
[169] G.P.M. Leyson, W.A. Curtin, L.G. Hector, C.F. Woodward, Quantitative prediction of solute strengthening in aluminium alloys, Nat. Mater. 9 (2010) 750–755, doi:10.1038/nmat2813.
[170] G. Leyson, L.G. Hector, W.A. Curtin, Solute strengthening from first principles and application to aluminum alloys, Acta Mater. 60 (2012) 3873–3884, doi:10.1016/j.actamat.2012.03.037.
[171] G. Leyson, L.G. Hector, W.A. Curtin, First-principles prediction of yield stress for basal slip in Mg–Al alloys, Acta Mater. 60 (2012) 5197–5203, doi:10.1016/j.actamat.2012.06.020.
[172] H. Zhang, B. Johansson, R. Ahuja, L. Vitos, First-principles study of solid-solution hardening in steel alloys, Comput. Mater. Sci. 55 (2012) 269–272, doi:10.1016/j.commatsci.2011.12.020.
[173] S. Vannarat, M.H.F. Sluiter, Y. Kawazoe, First-principles study of solute-dislocation interaction in aluminum-rich alloys, Phys. Rev. B 64 (2001) 94104, doi:10.1103/PhysRevB.64.224203.
[174] J.A. Yasi, L.G. Hector, D.R. Trinkle, First-principles data for solid-solution strengthening of magnesium, Acta Mater. 58 (2010) 5704–5713, doi:10.1016/j.actamat.2010.06.045.
[175] D. Ma, M. Friák, J. von Pezold, D. Raabe, J. Neugebauer, Computationally efficient and quantitatively accurate multiscale simulation of solid-solution strengthening by ab initio calculation, Acta Mater. 85 (2015) 53–66, doi:10.1016/j.actamat.2014.10.044.
[176] D. Ma, M. Friák, J. von Pezold, J. Neugebauer, D. Raabe, Ab initio study of compositional trends in solid solution strengthening in metals with low peierls stresses, Acta Mater. 98 (2015) 367–376, doi:10.1016/j.actamat.2015.07.054.
[177] U.F. Kocks, Laws for work-hardening and low-temperature creep, J. Eng. Mater. Technol. 98 (1976) 76, doi:10.1115/1.3443340.
[178] E. Nadgornyi, Dislocation dynamics and mechanical properties of crystals, Prog. Mater Sci. 31 (1988) 1–530, doi:10.1016/0079-6425(88)90005-9.
[179] D. Caillard, J.-L. Martin, Thermally Activated Mechanisms in Crystal Plasticity, first ed, Amsterdam, Pergamon, 2007.
[180] K. Ono, Temperature dependence of dispersed barrier hardening, J. Appl. Phys. 39 (1968) 1803–1806, doi:10.1063/1.1656434.
[181] G.B. Gibbs, Thermodynamic analysis of dislocation glide controlled by dispersed local obstacles, Mater. Sci. Eng. 4 (1969) 313–328, doi:10.1016/0025-5416(69)90026-3.
[182] W. Blum, Discussion, Scr. Mater. 146 (2018) 27–30, doi:10.1016/j.scriptamat.2017.10.029.
[183] G.I. Taylor, The mechanism of plastic deformation of crystals. part I. theoretical, proceedings of the royal society A: mathematical, Phys. Eng. Sci. 145 (1934) 362–387, doi:10.1098/rspa.1934.0106.
[184] P. Franciosi, M. Berveiller, A. Zaoui, Latent hardening in copper and aluminium single crystals, Acta Metall. 28 (1980) 273–283, doi:10.1016/0001-6160(80)90162-5.
[185] E.O. Hall, The deformation and ageing of mild steel, Proc. Phys. Soc. B 64 (1951) 747–753, doi:10.1088/0370-1301/64/9/303.
[186] N.J. Petch, The cleavage strength of polycrystals, J. Iron Steel Inst 174 (1953) 25–28.
[187] J.P. Hirth, J. Lothe, Theory of Dislocations, second ed, Krieger Pub. C, Malabar FL, 1982.
[188] R.W. Cahn, P. Haasen, Physical Metallurgy, forth ed., North-Holland, Amsterdam, New York, 1996.
[189] F. KROUPA, DISLOCATION dipoles and dislocation loops, J. Phys. Colloques 27 (1966) C3-154-C3-167, doi:10.1051/jphyscol:1966320.
[190] M. Kabir, T.T. Lau, D. Rodney, S. Yip, K.J. van Vliet, Predicting dislocation climb and creep from explicit atomistic details, Phys. Rev. Lett. 105 (2010) 95501, doi:10.1103/PhysRevLett.105.095501.
[191] D.G. Sangiovanni, O. Hellman, B. Alling, I.A. Abrikosov, Efficient and accurate determination of lattice-vacancy diffusion coefficients via non equilibrium ab initio molecular dynamics, Phys. Rev. B 93 (2016) 271, doi:10.1103/PhysRevB.93.094305.
[192] U.F. Kocks, A statistical theory of flow stress and work-hardening, Philos. Mag. 13 (1966) 541–566, doi:10.1080/14786436608212647.
[193] U.F. Kocks, H. Mecking, Physics and phenomenology of strain hardening, Prog. Mater Sci. 48 (2003) 171–273, doi:10.1016/S0079-6425(02)00003-8.
[194] E. Nes, Modelling of work hardening and stress saturation in fcc metals, Prog. Mater Sci. 41 (1997) 129–193, doi:10.1016/S0079-6425(97)00032-7.
[195] Y. Estrin, Dislocation theory based constitutive modelling, J. Mater. Process. Technol. 80–81 (1998) 33–39, doi:10.1016/S0924-0136(98)00208-8.
[196] S. Allain, J.-P. Chateau, O. Bouaziz, Constitutive model of the twip effect in a polycrystalline high manganese content austenitic steel, Steel Res. 73 (2002) 299–302, doi:10.1002/srin.200200212.
[197] O. Bouaziz, N. Guelton, Modelling of twip effect on work-hardening, Mater. Sci. Eng. A 319–321 (2001) 246–249, doi:10.1016/S0921-5093(00)02019-0.
[198] R. Madec, B. Devincre, L.P. Kubin, From dislocation junctions to forest hardening, Phys. Rev. Lett. 89 (2002) 255508, doi:10.1103/PhysRevLett.89.255508.
[199] B. Devincre, T. Hoc, L. Kubin, Dislocation mean free paths and strain hardening of crystals, Science 320 (2008) 1745–1748, doi:10.1126/science.1156101.
[200] A. Arsenlis, D.M. Parks, Modeling the evolution of crystallographic dislocation density in crystal plasticity, J. Mech. Phys. Solids 50 (2002) 1979–2009, doi:10.1016/S0022-5096(01)00134-X.
[201] A. Ma, F. Roters, A constitutive model for fcc single crystals based on dislocation densities and its application to uniaxial compression of aluminium single crystals, Acta Mater. 52 (2004) 3603–3612, doi:10.1016/j.actamat.2004.04.012.
[202] R.L. Fullman, Measurement of particle sizes in opaque bodies, Trans AIME 5 (1953) 447–452, doi:10.1007/BF03398971.
[203] G.B. Olson, M. Cohen, Kinetics of strain-induced martensitic nucleation, MTA 6 (1975) 791–795, doi:10.1007/BF02672301.
[204] L. Remy, Kinetics of f.c.c. deformation twinning and its relationship to stress–strain behaviour, Acta Metall. 26 (1978) 443–451, doi:10.1016/0001-6160(78)90170-0.
[205] I.J. Beyerlein, C.N. Tomé, A probabilistic twin nucleation model for hcp polycrystalline metals, Proc. R. Soc. A 466 (2010) 2517–2544, doi:10.1098/rspa.2009.0661.
[206] I.J. Beyerlein, R.J. McCabe, C.N. Tomé, Effect of microstructure on the nucleation of deformation twins in polycrystalline high-purity magnesium, J. Mech. Phys. Solids 59 (2011) 988–1003, doi:10.1016/j.jmps.2011.02.007.
[207] I.J. Beyerlein, L. Capolungo, P.E. Marshall, R.J. McCabe, C.N. Tomé, Statistical analyses of deformation twinning in magnesium, Philos. Mag. 90 (2010) 2161–2190, doi:10.1080/14786431003630835.
[208] J. Wang, I.J. Beyerlein, C.N. Tomé, An atomic and probabilistic perspective on twin nucleation in mg, Scr. Mater. 63 (2010) 741–746, doi:10.1016/j.scriptamat.2010.01.047.
[209] O. Bouaziz, S. Allain, C. Scott, Effect of grain and twin boundaries on the hardening mechanisms of twinning-induced plasticity steels, Scr. Mater. 58 (2008) 484–487, doi:10.1016/j.scriptamat.2007.10.050.
[210] F. Siska, L. Stratil, J. Cizek, A. Ghaderi, M. Barnett, Numerical analysis of twin thickening process in magnesium alloys, Acta Mater. 124 (2017) 9–16, doi:10.1016/j.actamat.2016.10.068.
[211] P.A. Lynch, M. Kunz, N. Tamura, M.R. Barnett, Time and spatial resolution of slip and twinning in a grain embedded within a magnesium polycrystal, Acta Mater. 78 (2014) 203–212, doi:10.1016/j.actamat.2014.06.030.
[212] H. El Kadiri, C.D. Barrett, J. Wang, C.N. Tomé, Why are {10$\bar{1}$2} twins profuse in magnesium? Acta Mater. 85 (2015) 354–361, doi:10.1016/j.actamat.2014.11.033.
[213] M. Ardeljan, I.J. Beyerlein, M. Knezevic, Effect of dislocation density-twin interactions on twin growth in AZ31 as revealed by explicit crystal plasticity finite element modeling, Int. J. Plast. 99 (2017) 81–101, doi:10.1016/j.ijplas.2017.09.002.
[214] C. Liu, P. Shanthraj, M. Diehl, F. Roters, S. Dong, J. Dong, W. Ding, et al., An integrated crystal plasticity-phase field model for spatially resolved twin nucleation, propagation, and growth in hexagonal materials, Int. J. Plast. 106 (2018) 203–227, doi:10.1016/j.ijplas.2018.03.009.

[215] J.W. Christian, S. Mahajan, Deformation twinning, Prog. Mater Sci. 39 (1995) 1–157, doi:10.1016/0079-6425(94)00007-7.
[216] D.M. Saylor, J. Fridy, B.S. El-Dasher, K.-Y. Jung, A.D. Rollett, Statistically representative three-dimensional microstructures based on orthogonal observation sections, Metall. Mat. Trans. A 35 (2004) 1969–1979, doi:10.1007/s11661-004-0146-0.
[217] D. Deka, D.S. Joseph, S. Ghosh, M.J. Mills, Crystal plasticity modeling of deformation and creep in polycrystalline Ti-6242, Metall. Mat. Trans. A 37 (2006) 1371–1388, doi:10.1007/s11661-006-0082-2.
[218] M. Groeber, A framework for automated analysis and simulation of 3D polycrystalline microstructures. Part 2, Acta Mater. 56 (2008) 1274–1287, doi:10.1016/j.actamat.2007.11.040.
[219] M. Groeber, S. Ghosh, M.D. Uchic, D.M. Dimiduk, Developing a robust 3-D characterization-representation framework for modeling polycrystalline materials, JOM 59 (2007) 32–36, doi:10.1007/s11837-007-0113-5.
[220] U. Ayachit, The Paraview Guide, Kitware, 2015 [Erscheinungsort nicht ermittelbar].
[221] S. Reeh, D. Music, T. Gebhardt, M. Kasprzak, T. Jäpel, S. Zaefferer, D. Raabe, et al., Elastic properties of face-centred cubic Fe–Mn–C studied by nanoindentation and ab initio calculations, Acta Mater. 60 (2012) 6025–6032, doi:10.1016/j.actamat.2012.07.038.
[222] C.M. Chu, H. Huang, P.W. Kao, D. Gan, Effect of alloying chemistry on the lattice constant of austenitic Fe–Mn–Al–C alloys, Scr. Metall. Mater. 30 (1994) 505–508, doi:10.1016/0956-716X(94)90611-4.
[223] D. Music, T. Takahashi, L. Vitos, C. Asker, I.A. Abrikosov, J.M. Schneider, Elastic properties of Fe–Mn random alloys studied by ab initio calculations, Appl. Phys. Lett. 91 (2007) 191904, doi:10.1063/1.2807677.
[224] I.-C. Jung, B.C. de Cooman, Temperature dependence of the flow stress of Fe–18Mn–0.6C–xAl twinning-induced plasticity steel, Acta Mater. 61 (2013) 6724–6735, doi:10.1016/j.actamat.2013.07.042.
[225] W.S. Choi, B.C. de Cooman, S. Sandlöbes, D. Raabe, Size and orientation effects in partial dislocation-mediated deformation of twinning-induced plasticity steel micro-pillars, Acta Mater. 98 (2015) 391–404, doi:10.1016/j.actamat.2015.06.065.
[226] G. Gottstein, Physical Foundations of Materials Science, Springer Berlin Heidelberg, Berlin, Heidelberg, 2004.
[227] A.M. Brown, M.F. Ashby, Correlations for diffusion constants, Acta Metall. 28 (1980) 1085–1101, doi:10.1016/0001-6160(80)90092-9.
[228] P.R. Thornton, T.E. Mitchell, Deformation twinning in alloys at low temperatures, Philos. Mag. 7 (1962) 361–375, doi:10.1080/14786436208212171.
[229] S.I. Rao, D.M. Dimiduk, J.A. El-Awady, T.A. Parthasarathy, M.D. Uchic, C. Woodward, Activated states for cross-slip at screw dislocation intersections in face-centered cubic nickel and copper via atomistic simulation, Acta Mater. 58 (2010) 5547–5557, doi:10.1016/j.actamat.2010.06.005.
[230] S. Rao, T.A. Parthasarathy, C. Woodward, Atomistic simulation of cross-slip processes in model fcc structures, Philos. Mag. A 79 (1998) 1167–1192, doi:10.1080/01418619908210354.
[231] Vegge, Rasmussen, Leffers, Pedersen, Jacobsen, Determination of the of rate cross slip of screw dislocations, Phys. Rev. Lett. 85 (2000) 3866–3869, doi:10.1103/PhysRevLett.85.3866.
[232] S. Mahajan, G.Y. Chin, Formation of deformation twins in f.c.c. crystals, Acta Metall. 21 (1973) 1353–1363, doi:10.1016/0001-6160(73)90085-0.
[233] H.J. Bunge, Three-dimensional texture analysis, Int. Mater. Rev. 32 (1987) 265–291, doi:10.1179/imr.1987.32.1.265.
[234] H.-J. Bunge, Texture Analysis in Materials Science: Mathematical Methods, Butterworths, London, 1982.
[235] D. Rowenhorst, A.D. Rollett, G.S. Rohrer, M. Groeber, M. Jackson, P.J. Konijnenberg, M. de Graef, Consistent representations of and conversions between 3D rotations, Modell. Simul. Mater. Sci. Eng. 23 (2015) 83501, doi:10.1088/0965-0393/23/8/083501.
[236] F. Giustino, Materials Modelling Using Density Functional theory: Properties and Predictions/Feliciano Giustino, Oxford University Press, Oxford, 2014.
[237] M. Jamal, S. Jalali Asadabadi, I. Ahmad, H.A. Rahnamaye Aliabad, Elastic constants of cubic crystals, Comput. Mater. Sci. 95 (2014) 592–599, doi:10.1016/j.commatsci.2014.08.027.
[238] G. Grimvall, Thermophysical Properties of Materials, Elsevier, Amsterdam, Netherlands, New York, 1999.
[239] D.N. Blaschke, Averaging of elastic constants for polycrystals, J. Appl. Phys. 122 (2017) 145110, doi:10.1063/1.4993443.
[240] L. Kubin, B. Devincre, T. Hoc, Modeling dislocation storage rates and mean free paths in face-centered cubic crystals, Acta Mater. 56 (2008) 6040–6049, doi:10.1016/j.actamat.2008.08.012.
[241] S. Queyreau, G. Monnet, B. Devincre, Slip systems interactions in α-iron determined by dislocation dynamics simulations, Int. J. Plast. 25 (2009) 361–377, doi:10.1016/j.ijplas.2007.12.009.
[242] J.P. Hirth, On dislocation interactions in the fcc lattice, J. Appl. Phys. 32 (1961) 700–706, doi:10.1063/1.1736074.
[243] A.H. Cottrell, Dislocations and Plastic Flow in Crystals, Clarendon Press, Oxford, 1953.
[244] W.M. Lomer, A dislocation reaction in the face-centred cubic lattice, Lond., Edinb. Dubl. Philos. Mag. J. Sci. 42 (1951) 1327–1331, doi:10.1080/14786444108561389.
[245] L. Dupuy, M.C. Fivel, A study of dislocation junctions in fcc metals by an orientation dependent line tension model, Acta Mater. 50 (2002) 4873–4885, doi:10.1016/S1359-6454(02)00356-7.
[246] E. Martínez, J. Marian, A. Arsenlis, M. Victoria, J.M. Perlado, Atomistically informed dislocation dynamics in fcc crystals, J. Mech. Phys. Solids 56 (2008) 869–895, doi:10.1016/j.jmps.2007.06.014.
[247] R. Madec, B. Devincre, L. Kubin, T. Hoc, D. Rodney, The role of collinear interaction in dislocation-induced hardening, Science 301 (2003) 1879–1882, doi:10.1126/science.1085477.
[248] N. Thompson, Dislocation nodes in face-centred cubic lattices, Proc. Phys. Soc. B 66 (1953) 481–492, doi:10.1088/0370-1301/66/6/304.
[249] B. Devincre, L. Kubin, T. Hoc, Collinear superjogs and the low-stress response of fcc crystals, Scr. Mater. 57 (2007) 905–908, doi:10.1016/j.scriptamat.2007.07.026.
[250] B. Devincre, L. Kubin, T. Hoc, Physical analyses of crystal plasticity by dd simulations, Scr. Mater. 54 (2006) 741–746, doi:10.1016/j.scriptamat.2005.10.066.
[251] W. Blum, P. Eisenlohr, Dislocation mechanics of creep, Mater. Sci. Eng. A 510–511 (2009) 7–13, doi:10.1016/j.msea.2008.04.110.
[252] J.A. Venables, Deformation twinning in face-centred cubic metals, Philos. Mag. 6 (1961) 379–396, doi:10.1080/14786436108235892.
[253] J. Venables, The nucleation and propagation of deformation twins, J. Phys. Chem. Solids 25 (1964) 693–700, doi:10.1016/0022-3697(64)90178-7.
[254] S. Kibey, J.B. Liu, D.D. Johnson, H. Sehitoglu, Predicting twinning stress in fcc metals, Acta Mater. 55 (2007) 6843–6851, doi:10.1016/j.actamat.2007.08.042.
[255] S. Mahajan, D.F. Williams, Deformation twinning in metals and alloys, Int. Metall. Rev. 18 (1973) 43–61, doi:10.1179/imtlr.1973.18.2.43.
[256] D.R. Steinmetz, T. Jäpel, B. Wietbrock, P. Eisenlohr, I. Gutierrez-Urrutia, A. Saeed-Akbari, T. Hickel, et al., Revealing the strain-hardening behavior of twinning-induced plasticity steels, Acta Mater. 61 (2013) 494–510, doi:10.1016/j.actamat.2012.09.064.
[257] L. Bracke, L. Kestens, J. Penning, Direct observation of the twinning mechanism in an austenitic Fe–Mn–C steel, Scr. Mater. 61 (2009) 220–222, doi:10.1016/j.scriptamat.2009.03.045.
[258] L.P. Kubin, G. Canova, M. Condat, B. Devincre, V. Pontikis, Y. Bréchet, Dislocation microstructures and plastic flow, SSP 23–24 (1992) 455–472, doi:10.4028/www.scientific.net/SSP.23-24.455.
[259] J. Bonneville, B. Escaig, J. Martin, A study of cross-slip activation parameters in pure copper, Acta Metall. 36 (1988) 1989–2002, doi:10.1016/0001-6160(88)90301-X.
[260] O. Couteau, T. Kruml, J.-L. Martin, About the activation volume for cross-slip in cu at high stresses, Acta Mater. 59 (2011) 4207–4215, doi:10.1016/j.actamat.2011.03.045.
[261] T. Rasmussen, K.W. Jacobsen, T. Leffers, O.B. Pedersen, S.G. Srinivasan, H. Jónsson, Atomistic determination of cross-slip pathway and energetics, Phys. Rev. Lett. 79 (1997) 3676–3679, doi:10.1103/PhysRevLett.79.3676.
[262] T. Vegge, T. Rasmussen, T. Leffers, O.B. Pedersen, K.W. Jacobsen, Atomistic simulations of cross-slip of jogged screw dislocations in copper, Philos. Mag. Lett. 81 (2001) 137–144, doi:10.1080/09500830010019040.
[263] T.S. Byun, On the stress dependence of partial dislocation separation and deformation microstructure in austenitic stainless steels, Acta Mater. 51 (2003) 3063–3071, doi:10.1016/S1359-6454(03)00117-4.
[264] A. Kelly, K.M. Knowles, Crystallography and Crystal Defects, second ed., Wiley, Chichester, West Sussex, 2012.
[265] H. Suzuki, C. Barrett, Deformation twinning in silver-gold alloys, Acta Metall. 6 (1958) 156–165, doi:10.1016/0001-6160(58)90002-6.
[266] P.H. Adler, G.B. Olson, W.S. Owen, Strain hardening of Hadfield manganese steel, MTA 17 (1986) 1725–1737, doi:10.1007/BF02817271.
[267] J.P. Hirth, Thermodynamics of stacking faults, Metall. Trans. 1 (1970) 2367–2374, doi:10.1007/BF03038365.
[268] C. Niu, C.R. LaRosa, J. Miao, M.J. Mills, M. Ghazisaeidi, Magnetically-driven phase transformation strengthening in high entropy alloys, Nat. Commun. 9 (2018) 1363, doi:10.1038/s41467-018-03846-0.
[269] Y.H. Zhang, Y. Zhuang, A. Hu, J.J. Kai, C.T. Liu, The origin of negative stacking fault energies and nano-twin formation in face-centered cubic high entropy alloys, Scr. Mater. 130 (2017) 96–99, doi:10.1016/j.scriptamat.2016.11.014.
[270] M. Beyramali Kivy, M. Asle Zaeem, Generalized stacking fault energies, ductilities, and twinnabilities of cocrfeni-based face-centered cubic high entropy alloys, Scr. Mater. 139 (2017) 83–86, doi:10.1016/j.scriptamat.2017.06.014.
[271] M. Jahnátek, J. Hafner, M. Krajčí, Shear deformation, ideal strength, and stacking fault formation of fcc metals, Phys. Rev. B (2009) 79, doi:10.1103/PhysRevB.79.224103.
[272] S.L. Shang, W.Y. Wang, Y. Wang, Y. Du, J.X. Zhang, A.D. Patel, Z.K. Liu, Temperature-dependent ideal strength and stacking fault energy of fcc ni: a first-principles study of shear deformation, J. Phys. Cond. Mat. Inst. Phys. J 24 (2012) 155402, doi:10.1088/0953-8984/24/15/155402.
[273] A.J. Zaddach, C. Niu, C.C. Koch, D.L. Irving, Mechanical properties and stacking fault energies of nifecrcomn high-entropy alloy, JOM 65 (2013) 1780–1789, doi:10.1007/s11837-013-0771-4.
[274] J. Ding, Q. Yu, M. Asta, R.O. Ritchie, Tunable stacking fault energies by tailoring local chemical order in CrCoNi medium-entropy alloys, Proc. Natl. Acad. Sci. USA 115 (2018) 8919–8924, doi:10.1073/pnas.1808660115.
[275] L. Vitos, J.-O. Nilsson, B. Johansson, Alloying effects on the stacking fault energy in austenitic stainless steels from first-principles theory, Acta Mater. 54 (2006) 3821–3826, doi:10.1016/j.actamat.2006.04.013.
[276] C. Brandl, P.M. Derlet, H. van Swygenhoven, General-stacking-fault energies in highly strained metallic environments, Phys. Rev. B 76 (2007) 44, doi:10.1103/PhysRevB.76.054124.

[277] S. Sandlöbes, M. Friák, S. Zaefferer, A. Dick, S. Yi, D. Letzig, Z. Pei, et al., The relation between ductility and stacking fault energies in mg and Mg–Y alloys, Acta Mater. 60 (2012) 3011–3021, doi:10.1016/j.actamat.2012.02.006.
[278] A. Reyes-Huamantinco, P. Puschnig, C. Ambrosch-Draxl, O.E. Peil, A.V. Ruban, Stacking-fault energy and anti-Invar effect in Fe–Mn alloy from first principles, Phys. Rev. B 86 (2012) 346, doi:10.1103/PhysRevB.86.060201.
[279] A. Dick, T. Hickel, J. Neugebauer, The effect of disorder on the concentration-dependence of stacking fault energies in Fe1–xMnx – a First principles study, Steel Res. Int. 80 (2009) 603–608, doi:10.2374/SRI09SP015.
[280] S. Zhao, G.M. Stocks, Y. Zhang, Stacking fault energies of face-centered cubic concentrated solid solution alloys, Acta Mater. 134 (2017) 334–345, doi:10.1016/j.actamat.2017.05.001.
[281] P. Denteneer, J.M. Soler, Energetics of point and planar defects in aluminium from first-principles calculations, Solid State Commun. 78 (1991) 857–861, doi:10.1016/0038-1098(91)90243-O.
[282] P.J.H. Denteneer, W. van Haeringen, Stacking-fault energies in semiconductors from first-principles calculations, J. Phys. C Solid State Phys. 20 (1987) L883–L887, doi:10.1088/0022-3719/20/32/001.
[283] X. Zhang, B. Grabowski, F. Körmann, A.V. Ruban, Y. Gong, R.C. Reed, T. Hickel, et al., Temperature dependence of the stacking-fault Gibbs energy for Al, Cu, and Ni, Phys. Rev. B 98 (2018) 2429, doi:10.1103/PhysRevB.98.224106.
[284] A. Abbasi, A. Dick, T. Hickel, J. Neugebauer, First-principles investigation of the effect of carbon on the stacking fault energy of Fe–C alloys, Acta Mater. 59 (2011) 3041–3048, doi:10.1016/j.actamat.2011.01.044.
[285] C. Zhang, M. Enomoto, A. Suzuki, T. Ishimaru, Characterization of three-dimensional grain structure in polycrystalline iron by serial sectioning, Metall and Mat Trans A 35 (2004) 1927–1933, doi:10.1007/s11661-004-0141-5.
[286] S.A.H. Motaman, K. Schacht, C. Haase, U. Prahl, Thermo-micro-mechanical simulation of metal forming processes, Int. J. Solids Struct. 178–179 (2019) 59–80, doi:10.1016/j.ijsolstr.2019.05.028.

3.4. Paper IV

S.A.H. Motaman, F. Kies, P. Köhnen, M. Létang, M. Lin, A. Molotnikov, C. Haase: Optimal design for metal additive manufacturing - An integrated computational materials engineering (ICME) approach.
JOM 72 (2020): 1092–1104, ISSN: 1543-1851.
doi: 10.1007/s11837-020-04028-4.

JOM, Vol. 72, No. 3, 2020
https://doi.org/10.1007/s11837-020-04028-4

THE 2ND ASIA-PACIFIC INTERNATIONAL CONFERENCE ON ADDITIVE MANUFACTURING (APICAM 2019)

Optimal Design for Metal Additive Manufacturing: An Integrated Computational Materials Engineering (ICME) Approach

S. AMIR H. MOTAMAN,[1,3] FABIAN KIES,[1] PATRICK KÖHNEN,[1] MAIKE LÉTANG,[1] MINGXUAN LIN,[1] ANDREY MOLOTNIKOV,[2] and CHRISTIAN HAASE[1,4]

1.—ICME Group, Steel Institute, RWTH Aachen University, Aachen, Germany. 2.—Centre for Additive Manufacturing, School of Engineering, RMIT University, Melbourne, VIC, Australia. 3.—e-mail: seyedamirhossein.motaman@iehk.rwth-aachen.de. 4.—e-mail: christian.haase@iehk.rwth-aachen.de

We present our latest results on linking the process–structure–properties–performance (PSPP) chain for metal additive manufacturing (AM), using a multi-scale and multi-physics integrated computational materials engineering (ICME) approach. The abundance of design parameters and the complex relationship between those and the performance of AM parts have so far impeded the widespread adoption of metal AM technologies for structurally critical load-bearing components. To unfold the full potential of metal AM, establishing a full quantitative PSPP linkage is essential. It will not only help in understanding the underlying physics but will also serve as a powerful and effective tool for optimal computational design. In this work, we illustrate an example of ICME-based PSPP linkage in metal AM, along with a hybrid physics-based data-driven strategy for its application in the optimal design of a component. Finally, we discuss our outlook for the improvement of each part in the computational linking of the PSPP chain.

INTRODUCTION

Metal additive manufacturing (AM) offers enormous potential for the rapid production of net-shaped, geometrically complex, lightweight, minimum-waste and customized metallic parts without the need for the expensive tools required in conventional casting, subtractive or formative manufacturing processes.[1–4] Typically, metal AM provides high degrees of freedom in all aspects of component design, including alloy selection, (macro-)structural geometry and microstructural features. Some alloying systems that otherwise would require expensive conventional processing can be readily used in AM, such as refractory alloys,[3] high-manganese steels[5–9] or titanium aluminides.[10] One of the central benefits of metal AM lies within its unrivalled flexibility in building highly customized and complex geometries of macroscopic structures.

Recent experimental studies have reported that unique microstructures are formed during AM, which are substantially influenced by the process parameters.[6,11–24] AM components having the same shape and size (macroscopic structure) but made using different process parameters possess strikingly different microstructures, and hence mechanical properties. Consequently, the AM process parameters can be controlled to tailor the microstructures. Therefore, one could simultaneously 3D-print the (macroscopic) structure as well as the desirable microstructure depending on the expected in-service performance of the specialized component.

The high dimensionality of design space, multi-objective design requirements, high sensitivity of the AM parts performance to the design, and extremely complex relationships between the design parameters and performance have so far impeded the widespread adoption of metal AM technologies for structurally critical load-bearing components. In this context, multi-scale and multi-physics integrated computational materials engineering (ICME)[25] for computational (bottom–up) linking of process–(micro)structure–properties–performance (PSPP)[26] is a viable solution.[1,27–34] The role of the

(Published online January 29, 2020)

microstructure is of particular importance, as it controls the material inherent mechanical properties but is often neglected in AM component design.

In this paper, we present a systematic ICME-based approach that can be used for comprehensive and optimal design for AM. Generally, in metal manufacturing, the design space consists of alloy composition, process parameters, and macroscopic geometry of the structure/component, with the design objective being the in-service performance of the final component. The performance depending on the thermo-chemo-mechanical (TCM) service load may include multiple functional aspects, such as specific energy absorption capacity, fatigue strength/life, high-temperature strength, creep resistance, erosion/wear resistance, and/or corrosion resistance. The TCM processing fields, microstructure, and (macroscopic) TCM material properties are treated as design internal/hidden variables, which are directly affected by the design parameters and determine the performance of the final product. The design elements and their interaction in metal additive manufacturing are shown in Fig. 1. It should be noted that, according to the selected metal manufacturing method (which can be various metal AM methods), the chosen alloy family and design criteria, certain constraints are imposed to each element in the design space. The pre-imposed constraints to the design space include the limitation in the chosen alloy family (corresponding to an allowable concentration of the principal element and each alloying element), process parameters which are constrained by the applied AM method (e.g., laser powder bed fusion; LPBF) and the utilized AM machine (e.g., power density of the energy source), and the component geometry which is limited due to the device it will be a part of (e.g., constraints on the component weight, shape and size). Therefore, a constrained subset of the design space is always under consideration. Moreover, the performance space is also constrained by a set of requirements corresponding to the design criteria and the expected/acceptable performance (range) of the final component under the service TCM loads (e.g., the tolerable minimum energy absorption capacity, which preserves the in-service functionality of an additively manufactured lattice structure).

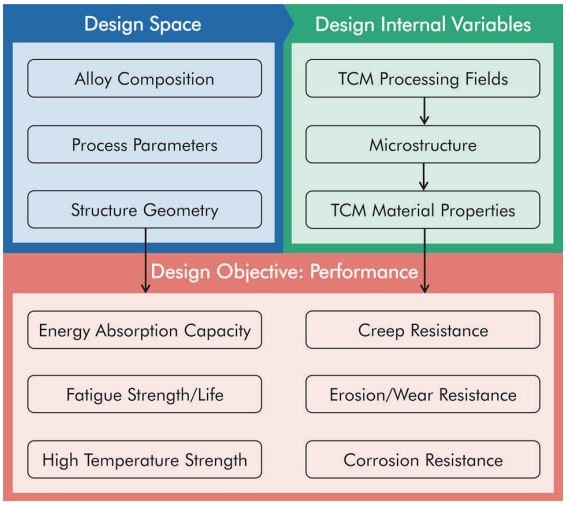

Fig. 1. The design elements and their interaction in metal additive manufacturing.

A polycrystal internal structure, i.e., microstructure, with respect to its hierarchal heterogeneity owns the following main distinctive attributes known as the *microstructural features*, which span across different length scales:

- *Meso-scale features* Distribution of grain morphology (size, shape and shape-axis orientation), crystallographic texture (orientation and misorientation), phases, twins, and micro-precipitates.
- *Submeso-scale/constitutive features* Distribution of alloying elements (elemental micro-segregation), dislocation density, porosity/micro-voids (and other defective inclusions), and nano-precipitates.

In our previous experimental-numerical study on high-manganese steel processed by LPBF,[35] it was shown that different aspects of microstructural heterogeneity, in particular grain morphology and crystallographic texture, influence the overall anisotropic mechanical properties, and can be captured using crystal plasticity modeling and computational polycrystal homogenization.

The emerging cross-disciplinary ICME toolset enables a physics-based and hence reliable linkage between process and performance. In this work, we outline an ICME-based strategy, which can be used to connect the AM processing conditions with structure–properties–performance of an AM component and will lead to a better understanding of their relationship. It is hypothesized that such an approach will allow exploiting the unique and flexible local processing conditions of AM for tailoring the local properties of AM components. The proposed framework is illustrated through a simple example, in which the crucial information obtained from the results of each simulation/calculation is passed on to the next one in the chain. This example consists of the following steps:

- Alloy selection for AM using CALPHAD and ab initio/first-principles calculations based on density functional theory (DFT).
- Finite element (FE) simulation of thermal field during AM.
- Simulation of microstructure evolution during AM (using the results of thermal field simulation), by phase field (PF) and kinetic Monte Carlo (KMC) models.
- Crystal plasticity (CP) simulation of macroscopic plastic flow properties by a physics-based constitutive model and using the full field method

for computational polycrystal homogenization through a fast Fourier transform-based (FFT-based) spectral solver.
- FE simulation of the performance of macroscopic structure using the CP simulation results.

In the present case study, single-phase austenitic high-manganese steel was selected as the model alloy and processed by LPBF to fabricate a lattice structure which is ultimately subjected to a service compressive load for an application corresponding to its specific energy absorption capacity (energy absorption capacity normalized by the weight of the structure).

ALLOY SELECTION

The design space is initially constrained by selecting a limited set of chemical compositions (within an alloy family) using rapid screening of alloy compositions based on the presumed (TCM) properties. The approach adopted for the present study combined CALPHAD and DFT calculations, as schematically illustrated in Fig. 2.

First, the compositional subspace is computationally screened by CALPHAD and thermodynamics-based models. In the present study, the aim was to design a single-phase face-centered cubic (fcc) high-manganese steel as the model alloy. Therefore, the vast compositional space was constrained to a subspace associated with the high-manganese steel family. Such an alloy remains single-phase during AM, which reduced the number of possible design internal variables in this case study. Further, in the selected alloy family, the activation of twinning-induced plasticity,[36–38] which is highly dependent on the microstructural heterogeneities, in particular crystallographic orientation distribution,[35] was used to promote a high strain hardening (rate) and hence energy absorption capacity (see "Mechanical Properties" and "Performance" sections). The PreCHiMn-04 database[39] was used for (thermodynamics-based phase stability) CALPHAD calculations within the Fe-Mn-Al-C chemistry subspace by Thermo-Calc software. Moreover, thermodynamics-based stacking fault energy (SFE) calculations were performed for the selected alloy family.[38,40,41] DFT-based ab initio calculations were subsequently performed to derive phase stabilities and energetic material properties, such as the SFE,[42–48] lattice and elastic constants,[49,50] and solid solution strength.[51–57] We selected an alloy with an SFE being sufficiently low to promote deformation twinning and, at the same time, sufficiently high to avoid martensitic phase transformation during deformation. Subsequently, alloys processed by different AM methods, with the elemental composition X30MnAl23-x (x = 0–2 wt.% Al) were experimentally screened.[6] The alloy X30MnAl23-1 was identified as single-phase fcc with high work-hardening capacity and, therefore, serves as a model alloy for the present ICME study. In addition, a similar methodology has also been successfully employed and validated for high-entropy alloys.[58–65]

THERMAL FIELD

The output of the alloy selection ("Alloy Selection" section) provided the required input for the work performed in this section, i.e., the thermo-physical properties of the alloy. The temperature (T) field in the melt pool and heat-affected zone play the most significant role in the formation of the as-built microstructure. The grain morphology, texture, segregation of solute elements, and the formation of primary precipitates are known to be affected by the temperature gradient near the solidification front and by the growth velocity. The development

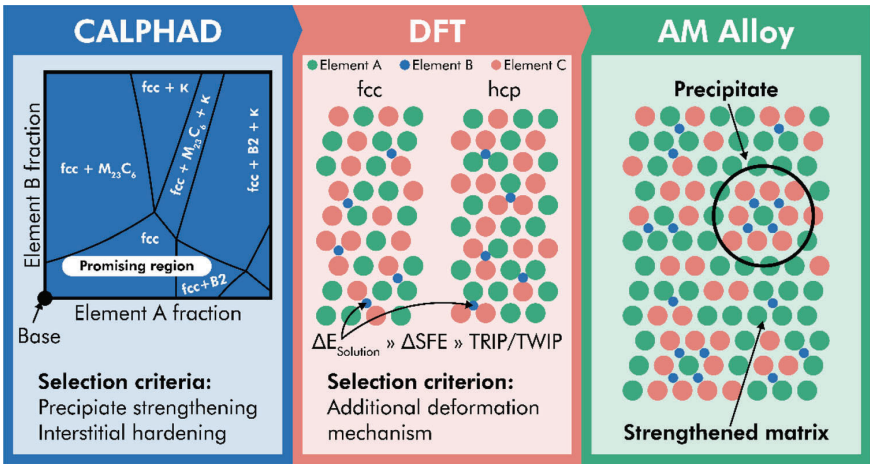

Fig. 2. The alloy selection approach. CALPHAD calculations are first performed to narrow the space of promising chemical compositions. More precise calculation of phase stabilities and energetic material properties are performed using DFT-based models.

of a stable melt pool depends on the interaction between the moving heat source (laser beam), the material in various states (powder, liquid, and solidified) and the ambient environment. In the past decade, FE-based transient thermal conduction models that originate from laser-welding applications have been employed to simulate the temperature evolution in AM processes.[66,67] More recently, comprehensive multi-physics models have been developed to simulate the thermal-fluid flow (heat and mass transfer) in the melt pool (using computational fluid dynamics) and the particle dynamics in the powder bed.[68–71] However, due to complex fluid–structural interactions and extremely high temperature gradients, the computational cost for such type of simulations is prohibitively high for large-scale applications. Therefore, in this work, we used the less demanding FE method (without consideration of fluid flow in the melt pool).

Our earlier work,[72] demonstrated an FE model for the simulation of melt pool geometry under different scan speeds during LPBF. The implicit thermal solver of FE software ABAQUS was used to numerically simulate the transient thermal field and melt pool geometry, using a moving semi-ellipsoidal volumetric heat flux defined by the (user-defined) subroutine DFLUX with a Gaussian heat source intensity profile. The temperature-dependent thermal conductivity was adopted from experimental measurements on a similar alloy.[73] Since the laser radiation interacts mostly with the liquid melt pool during LPBF,[74] an absorption coefficient of 0.41 for liquid iron irradiated by an Nd-YAG laser was chosen.[75] Five scanning tracks with a bi-directional scan strategy were modeled. The solution domain was decomposed to the powder bed and solidified material, which were approximated as homogenous and continuous fields. The thermo-physical properties of the material, including liquidus temperature (T_l), solidus temperature (T_s), specific heat capacity, and latent heat were calculated by Thermo-Calc using the PrecHiMn-04 database. The thermo-physical properties of the powder were determined based on those of the solid and the powder bed density, which was assumed to be a fraction (40%) of that of the bulk material.[76] The user-defined field subroutine (USDFLD) was used to define a state variable ($0 \leq \varphi \leq 1$), which was initialized with $\varphi = 0$ representing the powder. At each material/integration point, once the temperature reached the liquidus temperature ($T = T_l$), the state variable changed its value to $\varphi = 1$ denoting the non-powder (fully liquid or dense solid) state. For $T_s \leq T \leq T_l$, the powder density and heat conductivity were linearly interpolated between those of fully solid and liquid states. An example of the simulated temperature field and melt pool geometry during the bi-directional scanning in LPBF of a (rectangular) block structure is shown in Fig. 3.

MICROSTRUCTURE EVOLUTION

As mentioned earlier, the microstructure has distinctive features at the meso- and submeso-scales. Therefore, in order to sufficiently capture the (mechanical) material properties at the macro-scale, microstructure development needs to be simulated at both the meso- and submeso-scales. Here, elemental micro-segregation as a decisive submeso-structural aspect together with the grain structure at the meso-scale were simulated, respectively using FP and KMC models, based on the information delivered by the alloy selection ("Alloy Selection" section) and thermal field ("Thermal Field" section) calculations/simulations.

Elemental Segregation

Modeling of elemental micro-segregation during AM requires not only the thermo-physical properties ("Alloy Selection" section) but also the evolution of the temperature field over time during

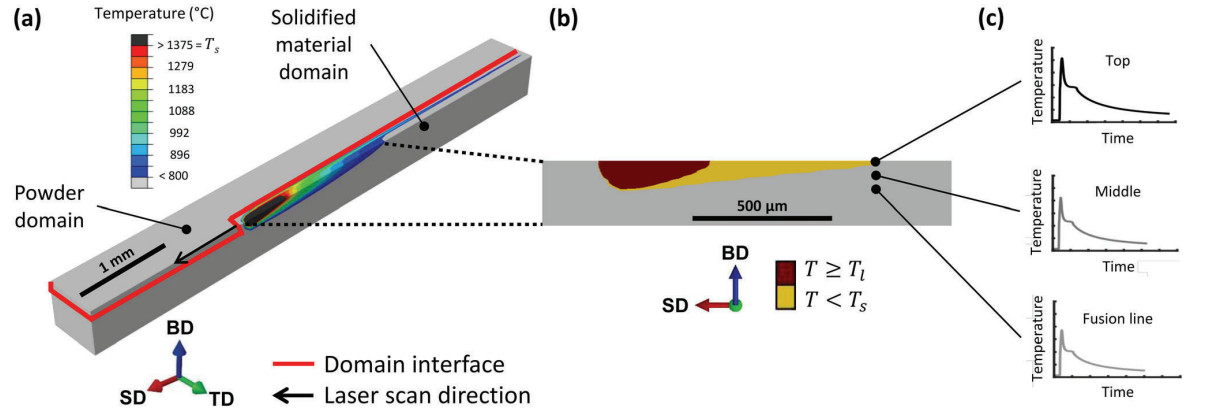

Fig. 3. (a) FE-simulated temperature field, (b) corresponding melt pool geometry, and (c) site-specific temperature evolution during LPBF of a block structure.

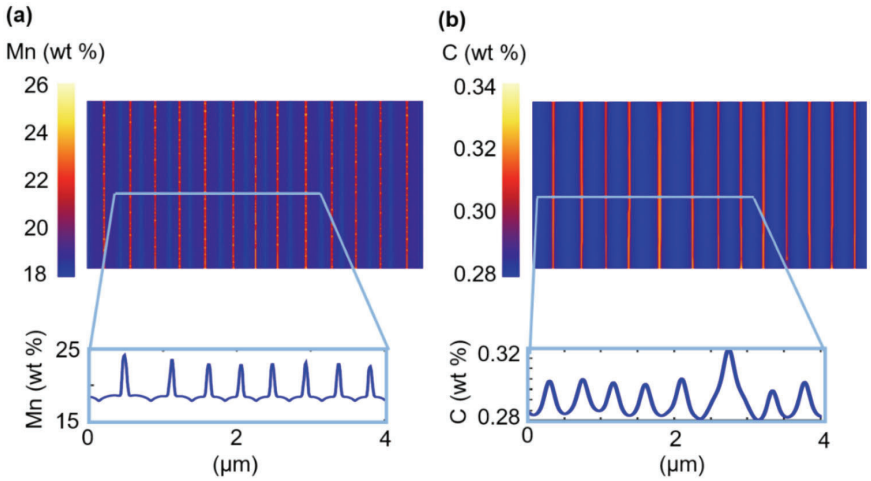

Fig. 4. PF-simulated micro-segregation pattern of (a) manganese and (b) carbon with the corresponding distribution profiles along an intercept line (perpendicular to the build direction).

solidification ("Thermal Field" section). The solidification simulations with a focus on elemental segregation were carried out using the phase-field software MICRESS® based on the multi-phase field approach.[77] PF and diffusion equations are derived from a free energy functional. Numerical minimization of the free energy of the multiphase system was performed using Thermo-Calc to simulate the solute partitioning and to evaluate the thermodynamics driving force for phase transformations. This method has been widely used to simulate the microstructure evolution during solidification. In addition to composition and temperature, order parameters (PF variables) were used, giving an extra degree of freedom. This parameter can vary continuously from 0 (absence) to 1 (existence) for different phases/grains, so that non-equilibrium processes can be investigated without the necessity to track the interface.[77,78]

A two-dimensional (2D) simulation was performed to study the relationship between the process parameters, the resulting thermal conditions, and the microstructure, including micro-segregation. The FE-simulated thermal field during the LPBF process was used as input. The vertical direction in the modeled (2D) domain is parallel to the build direction of the LPBF sample. The height of the simulated area was chosen in such a way that the total melt pool height is displayed. Since the solidification parameters in the melt pool are different in every position and only a one-dimensional temperature profile can be handled in MICRESS®, the melt pool width was not considered, resulting in a 70 × 10 μm simulation domain with a grid size of 0.0125 μm. Thermodynamics properties were determined using the Thermo-Calc (TCFE9 and MOBFE4) databases. An initial structure was defined by two phases, representing the solidified layer and the melt. Epitaxial growth was assumed. The height of the initial structure was set to 40 μm. This height corresponds to the existing substrate height in the modeled area, after lowering the substrate plane by 30 μm before adding a new powder layer and remelting. The melt was present in the area above the grains. The melt composition and starting structure were identical. At the boundaries of the simulated domain, insulating boundary conditions were defined. The time step size was automatically selected by the PF solver. The PF-simulated cellular segregation profiles of manganese and carbon (two main alloying elements in the selected alloying system) are shown in Fig. 4. Since carbon is a fast diffusive interstitial alloying element, the carbon profile appears smoother than that of manganese, which results from back-diffusion of the carbon from the enriched cell boundaries into the cells during solidification and cooling. On the other hand, the substitutional alloying element manganese, with slower diffusivity and lower back-diffusion, remained richer within the inter-dendritic regions. The temperature-dependent diffusion coefficients for all the elements are derived from the coupled Thermo-Calc mobility database MOBFE4.

Grain Structure

The melt pool dimension as derived from the thermal field simulation along with the process parameters (laser power, spot size, and scanning strategy) served as direct input for simulation of the mesoscopic grain structure formed during LPBF. The meso-scale microstructure (or simply meso-structure) evolution was simulated using a KMC model,[79] which is implemented in the open source SPPARKS Potts-KMC simulator software. After 10 deposited layers, from the center of the simulated volume, the grain structure shown in Fig. 5 was extracted as a representative volume element

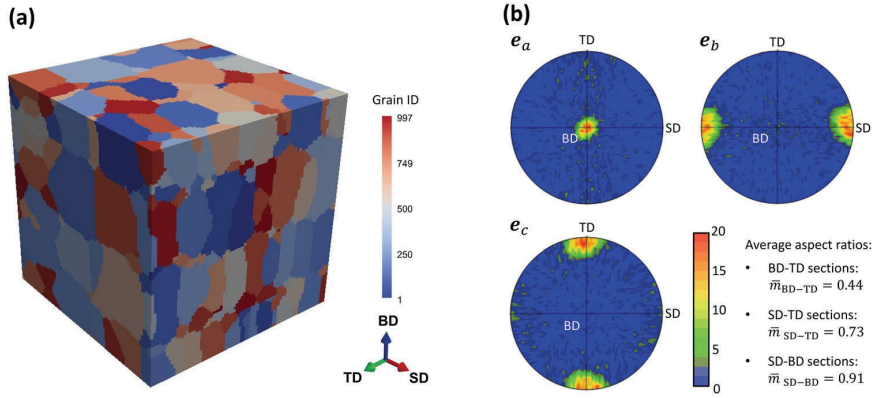

Fig. 5. (a) Grain structure as RVE extracted from the ensemble of grains after 10 additively deposited (LPBF) layers simulated using the KMC model.[79] (b) Mean grain shape (aspect ratio at orthogonal planes) and grain shape-axis orientation distribution in terms of pole figures with respect to ellipsoidal grain principal axes ($\boldsymbol{e}_a$, $\boldsymbol{e}_b$, $\boldsymbol{e}_c$), which were analyzed and plotted by DREAM.3D software.[80]

(RVE). As shown in Fig. 5, grain sections on the build direction (BD)-transverse direction (TD) plane and scan direction (SD)–TD plane are dominantly elongated towards BD and SD, respectively, whereas grain sections on the BD–SD plane are almost equiaxed. This is due to the specifically chosen AM process parameters including the bi-directional scanning pattern (without rotation or switching between SD and TD in each AM layer), and considering the fact that grain growth is favorable along the maximum local heat flow direction. This is in line with the typically observed grain shapes in AM meso-structures, as the grain sections on BD–TD sections are columnar, meaning that they are polarized (having an elongated shape with relatively low aspect ratio and low angle of the major principal axis) along BD. Here, the aspect ratio ($m \equiv {}^{b}/_{a}$, where $0 < m \leq 1$) for a given grain is defined as the length of minor axes (b) of the best-fit ellipse divided by its major axis length (a).

MECHANICAL PROPERTIES

The (as-built) AM microstructures have been shown to be highly polarized (strong crystallographic texture and strongly polarized grain morphology), heterogeneous and spatially non-uniform in every possible aspect compared to their traditionally manufactured counterparts.[35] These inherent microstructural disparities result in a highly anisotropic (macroscopic) plastic flow behavior. Macroscopic mechanical response/properties of such materials can be adequately captured by the full field method for computational polycrystal homogenization using RVE coupled with physics-based CP constitutive modeling.

The RVE extracted using the results of meso-structure simulation ("Grain Structure" section) was used in CP simulations to derive the macroscopic mechanical response of material in terms of homogenized (monotonic) flow curves. The polycrystalline aggregate was set under externally imposed macroscopic boundary conditions corresponding to displacement-controlled uniaxial load with a quasi-static (true) strain rate ($\dot{\bar{\varepsilon}} = 10^{-3}\,\mathrm{s}^{-1}$), which translates to pure deformation periodic boundary conditions on the RVE (Fig. 5). The governing boundary value problem is then solved using the physics-based CP model detailed in Ref. 35 to fulfill the mechanical equilibrium by the FFT-based spectral solver of the modular CP code DAMASK.[81] The applied CP constitutive model computes the mechanical response as well as evolution and anisotropic interaction of micro-state variables (MSVs) at deformation (slip/twin) systems of meso-scale grid/integration points (or simply meso-points) of the RVE, using physically motivated formulations that take submeso-scale/constitutive effects into account. The constitutive state variables are unipolar and dipolar dislocation densities, as well as twin volume fraction. The incrementally resolved fields (stress, strain and MSVs) at the meso-points are then homogenized over the mesoscopic RVE to give the macroscopic response.

Since the applied constitutive model is based on the underlying physics of crystal plastic deformation, most of the corresponding constitutive/sub-meso-structural parameters have a clear physical meaning and are adopted from various sources of independent experimental measurements and/or submeso-scale simulations (ab initio, atomistic and discrete dislocation dynamics) associated with the selected alloy composition (X30MnAl23-1). The effective grain size as a constant was determined from the grain size (number and volume fraction) distribution of the KMC-simulated grain ensemble. As mentioned in "Alloy Selection" section, the SFE, as another material constant, was calculated from the chemical composition of the material. The initial dislocation density was estimated as a function of the average cooling rate during solidification. Furthermore, the results of micro-segregation

simulations ("Elemental Segregation" section) have been used to calculate the variance in the submesoscale distribution of SFE and, subsequently, the parameters associated with the probability density of twin nucleation. The homogenized mechanical response in terms of (flow) stress and strain hardening ($\theta \equiv \frac{\partial \sigma}{\partial \varepsilon}$) along with the evolutions of twin (volume) fraction and (unipolar) dislocation density with strain are plotted in Fig. 6.

PERFORMANCE

The design objective of the present case study was obtaining the deformation behavior and the resulting specific energy absorption capacity of the f2cc,z lattice structure. FE simulations are a useful tool to assess the performance of structural parts under different loading conditions, and offer guidance in the selection of materials and geometrical features of components to optimize their performance.[82] FE models are constructed from computer-aided design (CAD) files which describe the geometry of the structural component. The imported geometry is then discretized using finite elements, and specific boundary conditions are applied corresponding to service loads. It is worth noting that the selection of FE type influences the accuracy of the predictions as well as the computation time.[83,84]

Here, we present a FE model of the f2cc,z lattice structure fabricated by LPBF of the alloy X30MnAl23-1 under compressive load (Fig. 7a). The geometry and boundary conditions were adapted from Refs. 6 and 24. The compression specimen consisted of five f2cc,z unit cells in each direction with 500-μm-diameter struts. The simulations were performed using the commercial FE package QForm VX and utilized tetrahedron elements. QForm VX employs an automatic remeshing algorithm as a function of the varying stress field, which allows obtaining an accurate prediction of the structural deformation behavior. The material behavior under plastic deformation was represented as flow curves (true stress response as a function of accumulated plastic strain) with different

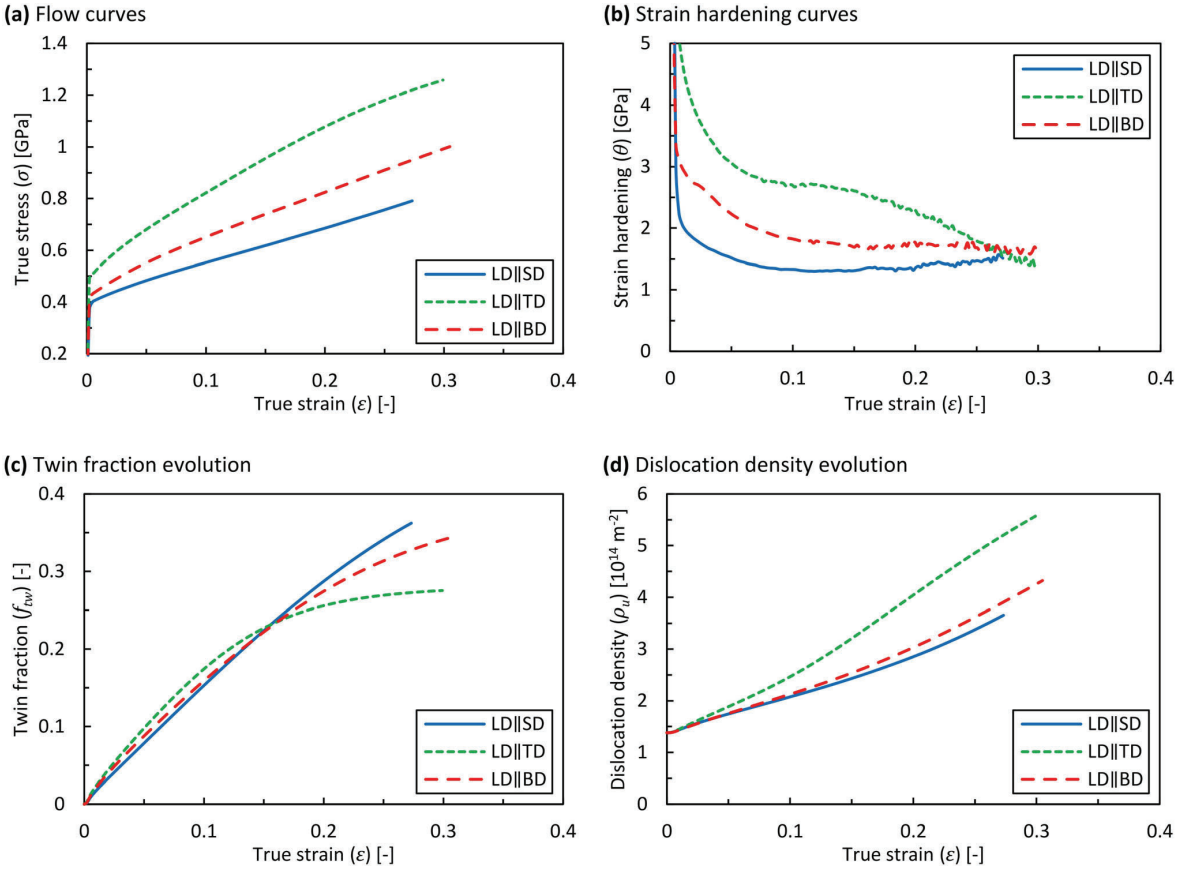

Fig. 6. Simulated homogenized (a) flow curves, (b) strain hardening curves, (c) evolution of twin (volume) fraction, and (d) evolution of (unipolar) dislocation density of/in the high-manganese steel processed by LPBF (using the RVE shown in Fig. 5) under uniaxial tension at $\dot{\varepsilon} = 10^{-3}\,s^{-1}$ and $T = 23°C$ along different axes.

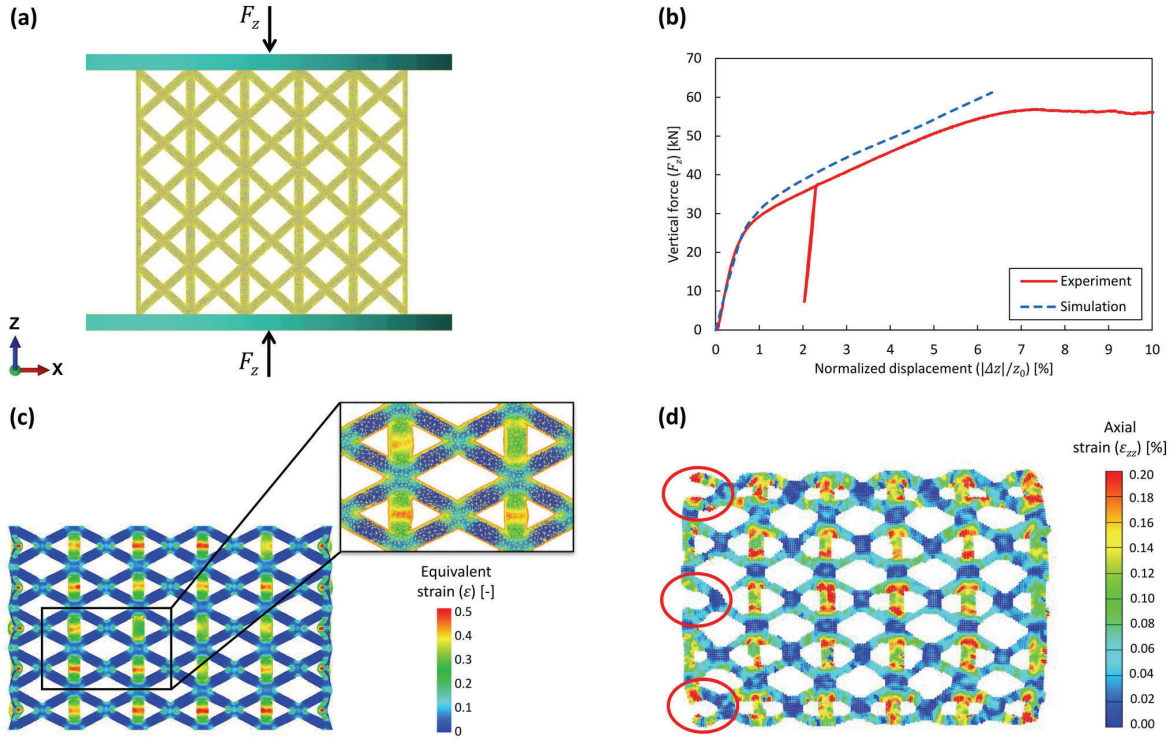

Fig. 7. FE simulation of a compression test of high-manganese steel lattice structure fabricated by LPBF. (a) The FE model of the f2cc,*z* lattice structure with a fine mesh using tetrahedron elements. (b) Comparison of the experimental and FE-simulated force-displacement responses of the lattice structure. (c) FE-simulated distribution of equivalent (von Mises) strain showing strain localization in the vertical ($\|Z$) struts. The magnified deformed area illustrates the increased density of tetrahedron elements to capture the localized deformation. (d) Experimentally measured (local) axial ($\|Z$) strain distribution using digital image correlation (DIC) at 10% normalized compressive displacement.

deformation parameters (combination of strain rate and loading axis), which were determined using the computational polycrystal homogenization approach described in "Mechanical Properties" section.

Most FE software packages provide the possibility of integrating advanced material models, and permit the user to trace the evolution of MSVs. Figure 7c shows an example of the local (equivalent) strain distribution in the lattice structure during compressive deformation measured using digital image correlation (DIC). The major deformation in the lattice structure is accommodated by the vertical ($\|Z$) struts,[24] as their axes are parallel to the loading direction ($\|$LD). Additional areas of high strain concentrations are observed at the strut junctions (Fig. 7c). These zones of (macro-scale) strain localization lead to failure of the struts in these regions. Similar observations have also been reported in Refs. 24 and 84. The comparison of FE-simulated and experimental force-displacement responses of the lattice structure (Fig. 7b) implies a reliable numerical prediction of the lattice structure performance for the elastic and elasto-plastic deformation regimes. However, simulation of the force-displacement response of the lattice structure in the deformation regimes after the onset of damage initiation (here, corresponding to the normalized compressive displacement of 6%) requires coupling the elasto-plastic constitutive model with a suitable ductile damage model. Incorporation of a damage model which accounts for the process-induced defects in the as-built structure, including internal pores/voids, surface roughness,[85] and deviations in the morphology of the struts, would also enhance the agreement between the simulated local strain distributions and those obtained from the corresponding DIC maps (Fig. 7c and d). In particular, Fig. 7d shows the failure in some (circled) of the struts at relatively early stages of deformation. The experimental result also shows variations in strut diameter and some minor bulging due to friction in the interfaces of the lattice structure and tools. Despite these differences, which become more pronounced with increased accumulation of the plastic strain and damage, the simulation was able to predict force-displacement responses (performance) of the lattice structure in the early stages of deformation where damage is not dominant. Nonetheless, the (simulated) force is slightly overestimated (Fig. 7b).

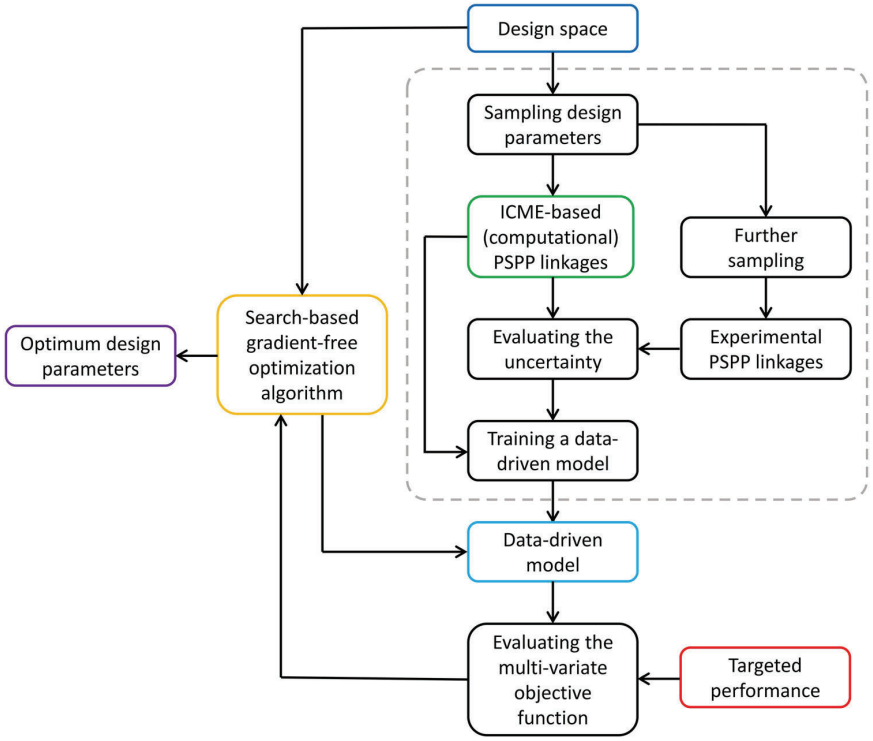

Fig. 8. Workflow of the proposed hybrid ICME-based data-driven method as a performance-oriented optimal design strategy for metal AM.

OPTIMAL DESIGN

Once the ICME-based PSPP linkage is established, the search–predict–optimize (SPO) cycle can be invoked for the optimal selection of design parameters from the design space, which consists of alloy composition, process parameters, and (macroscopic) structural geometry. However, a rigorous ICME-based PSPP linkage is quite (computationally) expensive and complex. Therefore, we propose an efficient hybrid ICME-based data-driven modeling as a performance-oriented optimal design strategy for metal AM, which its workflow is demonstrated in Fig. 8. It consists of the following steps:

I. Decomposition of the multi-dimensional design space into a finite number of domains according to the specific ranges of interest for each dimension; and sampling the design parameters from the aforementioned domains, using a design-of-experiments method.
II. Predicting the performance for design parameter combinations via the ICME-based PSPP linkage, as illustrated in Fig. 9.
III. Establishing experimental PSPP linkages for a few combinations of design parameters and evaluating the uncertainty in the ICME-based PSPP linkages.
IV. Training a data-driven model by the physics-based performance predictions associated with the sampled design parameters. Data-driven Gaussian process regression models, which are kernel-based and non-parametric, seem to be suitable candidates to emulate the ICME-based PSPP linkages. Such surrogate models, which are already implemented in MATLAB and Python, can be readily used.
V. Defining a multi-variate objective function for minimization based on the targeted performance features.
VI. Application of the trained data-driven model for performance optimization through the closed-loop SPO iterations using a search-based gradient-free optimization algorithm to minimize the multi-variate objective function.
VII. Validating and fine-tuning the “optimum” set of design parameters using ICME-based PSPP linkages followed by experimental verification of the performance associated with the outcome design parameters.

REMAINING CHALLENGES

Despite the fact that the demonstrated work covers all the ICME-based links in the PSPP chain, there are several remaining challenges. Enhanced

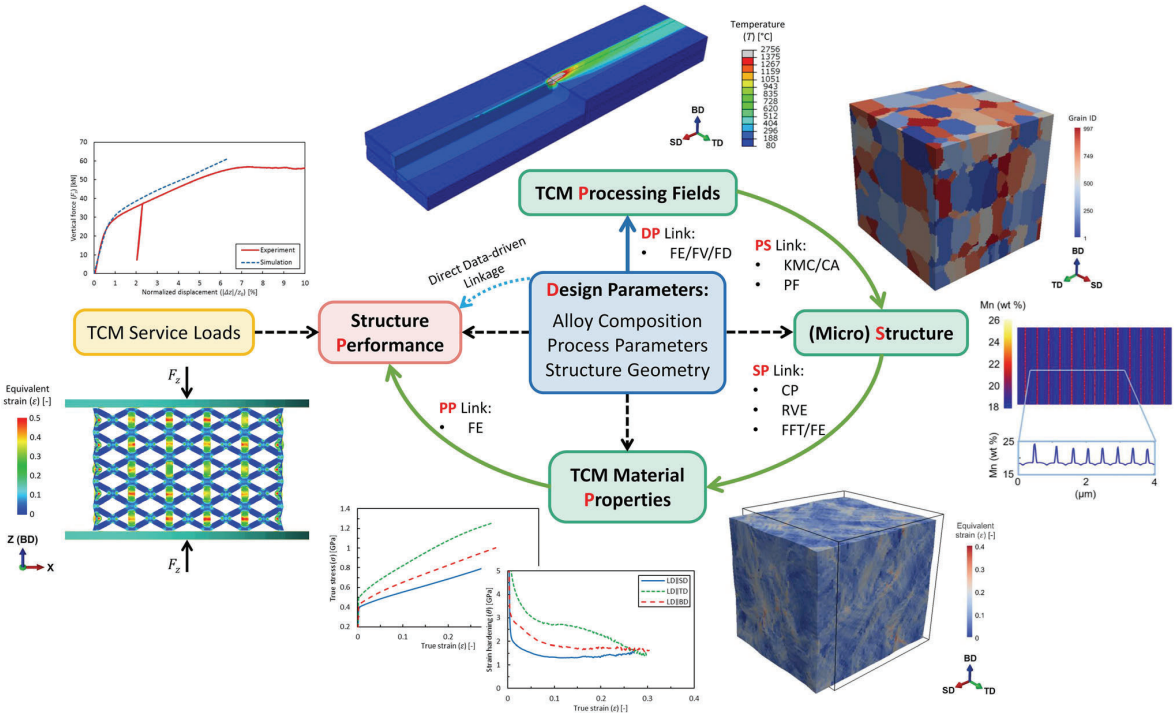

Fig. 9. Overview of the ICME-based PSPP linkage for performance (specific energy absorption capacity) prediction of a lattice structure, made of high-manganese steel, additively manufactured by LPBF.

accuracy in each link can be achieved by relaxing some of the initial assumptions and integration of more sophisticated models:

- *Process–structure (PS) link* convective melt pool dynamics and powder bed particle dynamics modeling can be used to inform/improve the presented relatively efficient and simple model for the simulation of thermal field during AM. The current model can be extended to include the effects of successive build layers and their associated cyclic heating of lower layers on the evolution of thermal field. Moreover, formation of macro-scale residual stresses during AM due to non-equilibrium cooling, which can be significant depending on the process parameters and structural geometry, is not currently considered. Finally, the applied microstructure evolution models do not account for the evolution of texture, phases, precipitates, micro-voids, and dislocation density. Therefore, there is a critical need for efficient and comprehensive microstructure evolution models which are coupled with the processing fields. The cellular automata models for microstructure evolution that are coupled with finite element/volume/difference thermal models seem to be promising.[86–93] These types of models have recently been applied for simulation of grain morphology and crystallographic texture during various metal AM processes.
- *Structure–properties SP link* the utilized model for the structure–properties linkage is robust and computationally efficient. However, it does not account for a number of physical phenomena that can be significant in some regimes. These physical phenomena are the deformation-twin thickening, dynamic/static pinning of dislocations, strain-path change, tension–compression asymmetry, slip transfer at microstructural interfaces and, most importantly, damage and fracture. Computationally expensive but advanced (continuum) gradient-based crystal plasticity constitutive models with dislocation fluxes[94,95] that are coupled with phase field models for damage[96] and twinning[97] can be used to inform/improve the applied more efficient model.
- *Properties–performance PP link* the model used for performance simulation takes the flow curves corresponding to different deformation parameters (combination of strain rate, temperature and loading axis) as input. These flow curves were provided from the SP simulations. However, since, generally, the macro-scale material points in the performance simulations are under complex multi-axial and cyclic loading conditions with different and varying deformation parameters, the applied modeling approach, which is not physics-based and history-dependent, may lead to inaccurate predictions. This inaccuracy

becomes significant when the mechanical response of the material is highly sensitive to deformation parameters, such as those observed in the highly anisotropic stress response in AM materials. One solution is the application of mean-field methods for computational polycrystal homogenization rendering the unique macro-scale material response as a function of evolving micro-state variables and multi-axial deformation parameters, e.g., self-consistent methods.[98–100] Moreover, nonlocal microstructural constitutive modeling at the macro-scale,[101] implemented in a thermo-micro-mechanical framework,[102] is also a viable solution. In this context, the applied mean-field/nonlocal constitutive model must adequately account for the microstructural features, such as grain morphology and crystallographic texture, which are known to control the macroscopic anisotropy in mechanical response of the polycrystalline aggregates. Such mean-field or nonlocal models can be informed by the results of full-field SP simulations. Furthermore, another important aspect which is currently neglected in the depicted PP link is damage. For a more precise and comprehensive performance simulation of the macroscopic structure, a physics-based continuum damage model, which accounts for defects such as surface roughness and voids,[103–108] should be coupled with the applied elasto-plastic constitutive model.

CONCLUDING REMARKS

A versatile ICME-based approach for optimal design for metal additive manufacturing has been introduced. The following concluding remarks can be made:

- Due to the vastness and multi-dimensionality of the design space and the highly complex relationship between the design parameters and outcome performance, the optimal design is only achievable computationally, as it will dramatically reduce time and effort in experimentation and provide accelerated pathways to explore the design space.
- We proposed a hybrid physics-based data-driven strategy for optimizing the performance of additively manufactured products by selecting the optimum design parameters from the design space. The physics-based ICME methods allow for the capturing of the prevalent physical mechanisms, whereas the combination with data-driven approaches enables computationally efficient acquisition of the PSPP linkages.
- The approach outlined in this paper will provide a roadmap for widespread adoption of load-bearing additively manufactured metallic components.

ACKNOWLEDGEMENTS

Open Access funding provided by Projekt DEAL. The authors would like to thank the German Research Foundation (Deutsche Forschungsgemeinschaft, DFG) for the support of the depicted research within the Cluster of Excellence “Internet of Production”—CRD C2 “Enablers and Tools” and within the Collaborative Research Center (SFB) 761 “Steel—ab initio; quantum mechanics guided design of new Fe based materials”. A.M. and C.H. would also like to acknowledge the support of the Australia-Germany Joint Research Co-operation Scheme (German Academic Exchange Service (DAAD)/Universities Australia, Project ID 57388267).

REFERENCES

1. W.J. Sames, F.A. List, S. Pannala, R.R. Dehoff, and S.S. Babu, *Int. Mater. Rev.* (2016). https://doi.org/10.1080/09506608.2015.1116649.
2. D.D. Gu, W. Meiners, K. Wissenbach, and R. Poprawe, *Int. Mater. Rev.* (2013). https://doi.org/10.1179/1743280411Y.0000000014.
3. T. DebRoy, H.L. Wei, J.S. Zuback, T. Mukherjee, J.W. Elmer, J.O. Milewski, A.M. Beese, A. Wilson-Heid, A. De, and W. Zhang, *Prog. Mater. Sci.* (2018). https://doi.org/10.1016/j.pmatsci.2017.10.001.
4. D.L. Bourell, *Annu. Rev. Mater. Res.* (2016). https://doi.org/10.1146/annurev-matsci-070115-031606.
5. C. Haase, J. Bültmann, J. Hof, S. Ziegler, S. Bremen, C. Hinke, A. Schwedt, U. Prahl, and W. Bleck, *Materials (Basel, Switzerland)* (2017). https://doi.org/10.3390/ma10010056.
6. F. Kies, P. Köhnen, M.B. Wilms, F. Brasche, K.G. Pradeep, A. Schwedt, S. Richter, A. Weisheit, J.H. Schleifenbaum, and C. Haase, *Mater. Des.* (2018). https://doi.org/10.1016/j.matdes.2018.10.051.
7. F. Kies, M.B. Wilms, N. Pirch, K.G. Pradeep, J.H. Schleifenbaum, and C. Haase, *Mater. Sci. Eng., A* (2019). https://doi.org/10.1016/j.msea.2019.138688.
8. T. Niendorf and F. Brenne, *Mater. Charact.* (2013). https://doi.org/10.1016/j.matchar.2013.08.010.
9. T. Niendorf, S. Leuders, A. Riemer, H.A. Richard, T. Tröster, and D. Schwarze, *Metall. Mater. Trans. B* (2013). https://doi.org/10.1007/s11663-013-9875-z.

10. L.E. Murr, S.M. Gaytan, A. Ceylan, E. Martinez, J.L. Martinez, D.H. Hernandez, B.I. Machado, D.A. Ramirez, F. Medina, and S. Collins, *Acta Mater.* (2010). https://doi.org/10.1016/j.actamat.2009.11.032.
11. A.A. Antonysamy, J. Meyer, and P.B. Prangnell, *Mater. Charact.* (2013). https://doi.org/10.1016/j.matchar.2013.07.012.
12. R.R. Dehoff, M.M. Kirka, F.A. List, K.A. Unocic, and W.J. Sames, *Mater. Sci. Technol.* (2014). https://doi.org/10.1179/1743284714Y.0000000697.
13. F. Geiger, K. Kunze, and T. Etter, *Mater. Sci. Eng., A* (2016). https://doi.org/10.1016/j.msea.2016.03.036.
14. H. Helmer, A. Bauereiß, R.F. Singer, and C. Körner, *Mater. Sci. Eng., A* (2016). https://doi.org/10.1016/j.msea.2016.05.046.
15. F. Liu, X. Lin, C. Huang, M. Song, G. Yang, J. Chen, and W. Huang, *J. Alloys Compd.* (2011). https://doi.org/10.1016/j.jallcom.2010.11.176.
16. L.L. Parimi, G.A. Ravi, D. Clark, and M.M. Attallah, *Mater. Charact.* (2014). https://doi.org/10.1016/j.matchar.2013.12.012.
17. M. Simonelli, Y.Y. Tse, and C. Tuck, *Metall. Mater. Trans. A* (2014). https://doi.org/10.1007/s11661-014-2218-0.
18. L. Thijs, F. Verhaeghe, T. Craeghs, J. van Humbeeck, and J.-P. Kruth, *Acta Mater.* (2010). https://doi.org/10.1016/j.actamat.2010.02.004.
19. L. Thijs, K. Kempen, J.-P. Kruth, and J. van Humbeeck, *Acta Mater.* (2013). https://doi.org/10.1016/j.actamat.2012.11.052.
20. T. Wang, Y.Y. Zhu, S.Q. Zhang, H.B. Tang, and H.M. Wang, *J. Alloys Compd.* (2015). https://doi.org/10.1016/j.jallcom.2015.01.256.
21. I. Yadroitsev, P. Krakhmalev, I. Yadroitsava, S. Johansson, and I. Smurov, *J. Mater. Process. Technol.* (2013). https://doi.org/10.1016/j.jmatprotec.2012.11.014.
22. Q. Zhang, J. Chen, X. Lin, H. Tan, and W.D. Huang, *J. Mater. Process. Technol.* (2016). https://doi.org/10.1016/j.jmatprotec.2016.07.011.
23. X. Zhou, K. Li, D. Zhang, X. Liu, J. Ma, W. Liu, and Z. Shen, *J. Alloys Compd.* (2015). https://doi.org/10.1016/j.jallcom.2015.01.096.
24. P. Köhnen, C. Haase, J. Bültmann, S. Ziegler, J.H. Schleifenbaum, and W. Bleck, *Mater. Des.* (2018). https://doi.org/10.1016/j.matdes.2018.02.062.
25. M.F. Horstemeyer, *Integrated Computational Materials Engineering (ICME) for Metals* (Hoboken: Wiley, 2018).
26. G.B. Olson, *Science* (1997). https://doi.org/10.1126/science.277.5330.1237.
27. M. Seifi, A. Salem, J. Beuth, O. Harrysson, and J.J. Lewandowski, *JOM* (2016). https://doi.org/10.1007/s11837-015-1810-0.
28. W. Yan, Y. Lian, C. Yu, O.L. Kafka, Z. Liu, W.K. Liu, and G.J. Wagner, *Comput. Methods Appl. Mech. Eng.* (2018). https://doi.org/10.1016/j.cma.2018.05.004.
29. W. Yan, S. Lin, O.L. Kafka, Y. Lian, C. Yu, Z. Liu, J. Yan, S. Wolff, H. Wu, E. Ndip-Agbor, M. Mozaffar, K. Ehmann, J. Cao, G.J. Wagner, and W.K. Liu, *Comput. Mech.* (2018). https://doi.org/10.1007/s00466-018-1539-z.
30. W. Yan, S. Lin, O.L. Kafka, C. Yu, Z. Liu, Y. Lian, S. Wolff, J. Cao, G.J. Wagner, and W.K. Liu, *Front. Mech. Eng.* (2018). https://doi.org/10.1007/s11465-018-0505-y.
31. J. Smith, W. Xiong, W. Yan, S. Lin, P. Cheng, O.L. Kafka, G.J. Wagner, J. Cao, and W.K. Liu, *Comput. Mech.* (2016). https://doi.org/10.1007/s00466-015-1240-4.
32. D. Pal, N. Patil, K. Zeng, and B. Stucker, *J. Manuf. Sci. Eng.* (2014). https://doi.org/10.1115/1.4028580.
33. M.M. Francois, A. Sun, W.E. King, N.J. Henson, D. Tourret, C.A. Bronkhorst, N.N. Carlson, C.K. Newman, T. Haut, J. Bakosi, J.W. Gibbs, V. Livescu, S.A. Vander Wiel, A.J. Clarke, M.W. Schraad, T. Blacker, H. Lim, T. Rodgers, S. Owen, F. Abdeljawad, J. Madison, A.T. Anderson, J.-L. Fattebert, R.M. Ferencz, N.E. Hodge, S.A. Khairallah, and O. Walton, *Curr. Opin. Solid State Mater. Sci.* (2017). https://doi.org/10.1016/j.cossms.2016.12.001.
34. L. Koschmieder, S. Hojda, M. Apel, R. Altenfeld, Y. Bami, C. Haase, M. Lin, A. Vuppala, G. Hirt, and G.J. Schmitz, *Integr. Mater. Manuf. Innov.* (2019). https://doi.org/10.1007/s40192-019-00138-3.
35. S.A.H. Motaman, F. Roters, and C. Haase, *Acta Mater.* (2020). https://doi.org/10.1016/j.actamat.2019.12.003.
36. B.C. de Cooman, Y. Estrin, and S.K. Kim, *Acta Mater.* (2018). https://doi.org/10.1016/j.actamat.2017.06.046.
37. A. Saeed-Akbari, L. Mosecker, A. Schwedt, and W. Bleck, *Metall. Mater. Trans. A* (2012). https://doi.org/10.1007/s11661-011-0993-4.
38. A. Saeed-Akbari, J. Imlau, U. Prahl, and W. Bleck, *Metall. Mater. Trans. A* (2009). https://doi.org/10.1007/s11661-009-0050-8.
39. B. Hallstedt, A.V. Khvan, B.B. Lindahl, M. Selleby, and S. Liu, *Calphad* (2017). https://doi.org/10.1016/j.calphad.2016.11.006.
40. A. Dumay, J.-P. Chateau, S. Allain, S. Migot, and O. Bouaziz, *Mater. Sci. Eng., A* (2008). https://doi.org/10.1016/j.msea.2006.12.170.
41. S. Allain, J.-P. Chateau, O. Bouaziz, S. Migot, and N. Guelton, *Mater. Sci. Eng., A* (2004). https://doi.org/10.1016/j.msea.2004.01.059.
42. A. Dick, T. Hickel, and J. Neugebauer, *Steel Res. Int.* (2009). https://doi.org/10.2374/SRI09SP015.
43. L. Vitos, J.-O. Nilsson, and B. Johansson, *Acta Mater.* (2006). https://doi.org/10.1016/j.actamat.2006.04.013.
44. C. Brandl, P.M. Derlet, and H. van Swygenhoven, *Phys. Rev. B* (2007). https://doi.org/10.1103/PhysRevB.76.054124.
45. A. Reyes-Huamantinco, P. Puschnig, C. Ambrosch-Draxl, O.E. Peil, and A.V. Ruban, *Phys. Rev. B* (2012). https://doi.org/10.1103/PhysRevB.86.060201.
46. A. Abbasi, A. Dick, T. Hickel, and J. Neugebauer, *Acta Mater.* (2011). https://doi.org/10.1016/j.actamat.2011.01.044.
47. X. Zhang, B. Grabowski, F. Körmann, A.V. Ruban, Y. Gong, R.C. Reed, T. Hickel, and J. Neugebauer, *Phys. Rev. B* (2018). https://doi.org/10.1103/PhysRevB.98.224106.
48. O. Güvenç, F. Roters, T. Hickel, and M. Bambach, *JOM* (2015). https://doi.org/10.1007/s11837-014-1192-8.
49. D. Music, T. Takahashi, L. Vitos, C. Asker, I.A. Abrikosov, and J.M. Schneider, *Appl. Phys. Lett.* (2007). https://doi.org/10.1063/1.2807677.
50. S. Reeh, D. Music, T. Gebhardt, M. Kasprzak, T. Jäpel, S. Zaefferer, D. Raabe, S. Richter, A. Schwedt, J. Mayer, B. Wietbrock, G. Hirt, and J.M. Schneider, *Acta Mater.* (2012). https://doi.org/10.1016/j.actamat.2012.07.038.
51. D. Ma, M. Friák, J. von Pezold, J. Neugebauer, and D. Raabe, *Acta Mater.* (2015). https://doi.org/10.1016/j.actamat.2015.07.054.
52. D. Ma, M. Friák, J. von Pezold, D. Raabe, and J. Neugebauer, *Acta Mater.* (2015). https://doi.org/10.1016/j.actamat.2014.10.044.
53. G.P.M. Leyson, L.G. Hector, and W.A. Curtin, *Acta Mater.* (2012). https://doi.org/10.1016/j.actamat.2012.06.020.
54. G.P.M. Leyson, L.G. Hector, and W.A. Curtin, *Acta Mater.* (2012). https://doi.org/10.1016/j.actamat.2012.03.037.
55. G.P.M. Leyson, W.A. Curtin, L.G. Hector, and C.F. Woodward, *Nat. Mater.* (2010). https://doi.org/10.1038/nmat2813.
56. H. Zhang, B. Johansson, R. Ahuja, and L. Vitos, *Comput. Mater. Sci.* (2012). https://doi.org/10.1016/j.commatsci.2011.12.020.
57. S. Vannarat, M.H.F. Sluiter, and Y. Kawazoe, *Phys. Rev. B* (2001). https://doi.org/10.1103/PhysRevB.64.224203.
58. C. Haase, F. Tang, M.B. Wilms, A. Weisheit, and B. Hallstedt, *Mater. Sci. Eng., A* (2017). https://doi.org/10.1016/j.msea.2017.01.099.
59. S. Ewald, F. Kies, S. Hermsen, M. Voshage, C. Haase, and J.H. Schleifenbaum, *Materials (Basel, Switzerland)* (2019). https://doi.org/10.3390/ma12101706.
60. F. Kies, Y. Ikeda, S. Ewald, J.H. Schleifenbaum, B. Hallstedt, F. Körmann, and C. Haase, *Scr. Mater.* (2019). https://doi.org/10.1016/j.scriptamat.2019.12.004.

61. Y. Ikeda, I. Tanaka, J. Neugebauer, and F. Körmann, *Phys. Rev. Mater.* (2019). https://doi.org/10.1103/PhysRevMaterials.3.113603.
62. Y. Ikeda, B. Grabowski, and F. Körmann, *Mater. Charact.* (2019). https://doi.org/10.1016/j.matchar.2018.06.019.
63. O.N. Senkov, J.D. Miller, D.B. Miracle, and C. Woodward, *Calphad* (2015). https://doi.org/10.1016/j.calphad.2015.04.009.
64. D. Miracle, J. Miller, O. Senkov, C. Woodward, M. Uchic, and J. Tiley, *Entropy* (2014). https://doi.org/10.3390/e16010494.
65. K.G. Pradeep, C.C. Tasan, M.J. Yao, Y. Deng, H. Springer, and D. Raabe, *Mater. Sci. Eng., A* (2015). https://doi.org/10.1016/j.msea.2015.09.010.
66. G. Vastola, G. Zhang, Q.X. Pei, and Y.-W. Zhang, *JOM* (2016). https://doi.org/10.1007/s11837-016-1890-5.
67. J. Yang and F. Wang, *Int. J. Adv. Manuf. Technol.* (2009). https://doi.org/10.1007/s00170-008-1785-x.
68. S.A. Khairallah and A. Anderson, *J. Mater. Process. Technol.* (2014). https://doi.org/10.1016/j.jmatprotec.2014.06.001.
69. T.T. Roehling, S.S.Q. Wu, S.A. Khairallah, J.D. Roehling, S.S. Soezeri, M.F. Crumb, and M.J. Matthews, *Acta Mater.* (2017). https://doi.org/10.1016/j.actamat.2017.02.025.
70. C. Panwisawas, C.L. Qiu, Y. Sovani, J.W. Brooks, M.M. Attallah, and H.C. Basoalto, *Scr. Mater.* (2015). https://doi.org/10.1016/j.scriptamat.2015.04.016.
71. C. Panwisawas, C. Qiu, M.J. Anderson, Y. Sovani, R.P. Turner, M.M. Attallah, J.W. Brooks, and H.C. Basoalto, *Comput. Mater. Sci.* (2017). https://doi.org/10.1016/j.commatsci.2016.10.011.
72. P. Köhnen, M. Létang, M. Voshage, J. Henrich Schleifenbaum, and C. Haase, *Addit. Manuf.* (2019). https://doi.org/10.1016/j.addma.2019.100914.
73. P. Lan and J. Zhang, *Steel Res. Int.* (2016). https://doi.org/10.1002/srin.201500022.
74. S.A. Khairallah, A.T. Anderson, A. Rubenchik, and W.E. King, *Acta Mater.* (2016). https://doi.org/10.1016/j.actamat.2016.02.014.
75. C. Suryanarayana, *Non-equilibrium Processing of Materials* (Oxford: Pergamon, 1999).
76. A.B. Spierings, N. Herres, and G. Levy, *Rapid Prototyp. J.* (2011). https://doi.org/10.1108/13552541111124770.
77. J. Eiken, B. Böttger, and I. Steinbach, *Phys. Rev. E* (2006). https://doi.org/10.1103/PhysRevE.73.066122.
78. B. Böttger, J. Eiken, and M. Apel, *Comput. Mater. Sci.* (2015). https://doi.org/10.1016/j.commatsci.2015.03.003.
79. T.M. Rodgers, J.D. Madison, and V. Tikare, *Comput. Mater. Sci.* (2017). https://doi.org/10.1016/j.commatsci.2017.03.053.
80. M.A. Groeber and M.A. Jackson, *Integr. Mater.* (2014). https://doi.org/10.1186/2193-9772-3-5.
81. F. Roters, M. Diehl, P. Shanthraj, P. Eisenlohr, C. Reuber, S.L. Wong, T. Maiti, A. Ebrahimi, T. Hochrainer, H.-O. Fabritius, S. Nikolov, M. Friák, N. Fujita, N. Grilli, K.G.F. Janssens, N. Jia, P.J.J. Kok, D. Ma, F. Meier, E. Werner, M. Stricker, D. Weygand, and D. Raabe, *Comput. Mater. Sci.* (2019). https://doi.org/10.1016/j.commatsci.2018.04.030.
82. O.C. Zienkiewicz, *The Finite Element Method for Solid and Structural Mechanics*, 6th ed. (Amsterdam: Elsevier, 2005).
83. M. Smith, Z. Guan, and W.J. Cantwell, *Int. J. Mech. Sci.* (2013). https://doi.org/10.1016/j.ijmecsci.2012.12.004.
84. B. Lozanovski, M. Leary, P. Tran, D. Shidid, M. Qian, P. Choong, and M. Brandt, *Mater. Des.* (2019). https://doi.org/10.1016/j.matdes.2019.107671.
85. C. de Formanoir, M. Suard, R. Dendievel, G. Martin, and S. Godet, *Addit. Manuf.* (2016). https://doi.org/10.1016/j.addma.2016.05.001.
86. J.A. Koepf, D. Soldner, M. Ramsperger, J. Mergheim, M. Markl, and C. Körner, *Comput. Mater. Sci.* (2019). https://doi.org/10.1016/j.commatsci.2019.03.004.
87. J.A. Koepf, M.R. Gotterbarm, M. Markl, and C. Körner, *Acta Mater.* (2018). https://doi.org/10.1016/j.actamat.2018.04.030.
88. O. Zinovieva, A. Zinoviev, and V. Ploshikhin, *Comput. Mater. Sci.* (2018). https://doi.org/10.1016/j.commatsci.2017.09.018.
89. Y. Lian, Z. Gan, C. Yu, D. Kats, W.K. Liu, and G.J. Wagner, *Mater. Des.* (2019). https://doi.org/10.1016/j.matdes.2019.107672.
90. Y. Lian, S. Lin, W. Yan, W.K. Liu, and G.J. Wagner, *Comput. Mech.* (2018). https://doi.org/10.1007/s00466-017-1535-8.
91. X. Li and W. Tan, *Comput. Mater. Sci.* (2018). https://doi.org/10.1016/j.commatsci.2018.06.019.
92. S. Chen, G. Guillemot, and C.-A. Gandin, *Acta Mater.* (2016). https://doi.org/10.1016/j.actamat.2016.05.011.
93. S. Chen, G. Guillemot, and C.-A. Gandin, *ISIJ Int.* (2014). https://doi.org/10.2355/isijinternational.54.401.
94. C. Reuber, P. Eisenlohr, F. Roters, and D. Raabe, *Acta Mater.* (2014). https://doi.org/10.1016/j.actamat.2014.03.012.
95. N. Grilli, K.G.F. Janssens, J. Nellessen, S. Sandlöbes, and D. Raabe, *Int. J. Plast.* (2018). https://doi.org/10.1016/j.ijplas.2017.09.015.
96. P. Shanthraj, L. Sharma, B. Svendsen, F. Roters, and D. Raabe, *Comput. Methods Appl. Mech. Eng.* (2016). https://doi.org/10.1016/j.cma.2016.05.006.
97. C. Liu, P. Shanthraj, M. Diehl, F. Roters, S. Dong, J. Dong, W. Ding, and D. Raabe, *Int. J. Plast.* (2018). https://doi.org/10.1016/j.ijplas.2018.03.009.
98. A. Molinari, G.R. Canova, and S. Ahzi, *Acta Metall.* (1987). https://doi.org/10.1016/0001-6160(87)90297-5.
99. R.A. Lebensohn and C.N. Tomé, *Acta Metall. Mater.* (1993). https://doi.org/10.1016/0956-7151(93)90130-K.
100. R.A. Lebensohn, C.N. Tomé, and P.P. CastaÑeda, *Philos. Mag.* (2007). https://doi.org/10.1080/14786430701432619.
101. S.A.H. Motaman and U. Prahl, *J. Mech. Phys. Solids* (2019). https://doi.org/10.1016/j.jmps.2018.09.002.
102. S.A.H. Motaman, K. Schacht, C. Haase, and U. Prahl, *Int. J. Solids Struct.* (2019). https://doi.org/10.1016/j.ijsolstr.2019.05.028.
103. A.L. Gurson, *J. Eng. Mater. Technol.* (1977). https://doi.org/10.1115/1.3443401.
104. V. Tvergaard, *Advances in Applied Mechanics*, Vol. 27 (Amsterdam: Elsevier, 1989), p. 83.
105. A. Needleman and V. Tvergaard, *J. Mech. Phys. Solids* (1987). https://doi.org/10.1016/0022-5096(87)90034-2.
106. Y. Hammi and M.F. Horstemeyer, *Int. J. Plast.* (2007). https://doi.org/10.1016/j.ijplas.2007.03.010.
107. C.F. Niordson, *Eur. J. Mech. A* (2008). https://doi.org/10.1016/j.euromechsol.2007.07.001.
108. N. Aravas and P. Ponte Castañeda, *Comput Methods Appl. Mech. Eng.* (2004). https://doi.org/10.1016/j.cma.2004.02.009.

4. Discussion

Given the computational power currently at disposal, the microstructural effects on the mechanical response of polycrystals can only be modeled and simulated in the continuum framework either at the macro-scale using the nonlocal microstructural modeling or at the meso-scale through the computational polycrystal homogenization (CPH) methods. In this thesis, both approaches are used to model the microstructural effects and demonstrate the applications with respect to the in-process behavior simulation of polycrystalline materials as well as the in-service performance prediction of polycrystalline components.

4.1. Macro-scale modeling and in-process application

Papers I and II present the microstructural modeling at macro-scale and its application in thermo-micro-mechanical/thermal-microstructural-mechanical (TMM) simulation of metal forming processes. Typically, in bulk metal forming processes, the initial billet contains an almost non-polarized initial microstructure due to the prior homogenization annealing heat treatment. The microstructure often remains mostly non-polarized during the closed-die bulk metal forming, owing to their specific class of boundary conditions. Moreover, since the loading mode in bulk metal forming is dominantly compressive, the porosity effect is usually negligible. Thereby, in the bulk metal forming processes where the polarity, composite, and porosity effects are assumed negligible/absent, modeling the size effect can sufficiently capture the in-process material behavior.

The meso- and submeso-size effects are coupled though the microstructural (continuum) constitutive modeling nonlocally at macro-scale (Paper I). The key postulate is that a differential meso-scale singularity (infinitesimal sharp interface associated with a disorientation) in the *polycrystal continuum* can be replaced by a fictitious *equivalent geometrically necessary dislocation (GND) density* as a diffuse interface that smoothly resolves the effective geometrical features and mechanical properties of the meso-interface. Accordingly, the microstructural size features at different length scales and their associated (meso- and submeso-size) effects are consistently unified.

In the microstructural model presented in Paper I, the statistical state of the microstructure (polycrystal discontinuities) is described by three micro-state variables (MSVs), which represent mesoscopically nonlocal dislocation densities. Thereby, the total dislocation content of the polycrystal is decomposed based on the mobility feature of dislocations (mobile/immobile) and their arrangement

(cell/wall), as well as the stability of dislocation submeso-structural and (equivalent) meso-structural boundaries. In this context, mobile dislocations have a *sufficient instantaneous mobility* to carry the crystal plastic strain by slipping inside the subcells. The subcell boundaries, which have a highly dynamic character during deformation in the cold regime and almost vanish in the warm regime, are mostly dipolar statistically stored dislocations (SSDs). It was postulated that the subcells (interiors), which collectively constitute almost all the polycrystal volume, have an instantaneous relatively low (submesoscopically local) dislocation density. However, the subcell volumes are under long-range internal stresses due to the nonlocal influence of the (relatively) immobile cell walls (geometrically necessary boundaries, GNBs).

Temporarily immobile dislocations in the cell interiors (cell immobile dislocations) mostly form/(accumulate at) unstable subcell boundaries. Due to their unstable character, these subcell boundaries are postulated to occupy all the subcell volumes in a relatively short time scale (relative to the imposed macroscopic strain rate). Therefore, cell mobile/immobile dislocations lack nonlocal effects because of their relatively uniform spatiotemporal distributions. However, the wall (immobile) dislocations, which are mainly geometrically necessary, existing in the relatively localized stable dislocation walls (GNBs) impose nonlocal effects by propagating long-range stresses inside the cells. Another important postulate made is that the intra-granular dislocation walls are nucleated in the cell interiors from the accumulates of cell immobile dislocations (at subcell boundaries) due to the nonuniformity of local plastic deformation (transformation of subcell boundaries to dislocation walls). The wall dislocations due to their nonlocality, relative immobility, and the associated long-range internal stresses are the main microstructural elements contributing to the higher stress response of single-constituent polycrystals compared to their defect-free single-crystal counterparts. In addition, like the fact that the cell immobile dislocations almost disappear in the warm regime, wall dislocations provide the driving force for recrystallization, and thus tend to vanish in the hot regime. Notice that the properly chosen wall terminology refers to the relative stability of dislocation walls in the cold and warm regimes.

In the presented model (Paper I), it was postulated that only adequately mobile segments of dislocations accommodate the crystal plasticity, and hence contribute to relaxing the internal stresses, whereas immobile segments of dislocations contribute to strain hardening. Through another postulate, the constitutive stress response is additively decomposed to the contributions of immobile dislo-

cations of cell and wall species corresponding to the (mean) short-range critical/threshold/back and long-range internal stresses, respectively. Both the short- and long-range contributions are calculated using the isotropic Taylor relation to render the macroscopic instantaneous plastic/athermal/rate-independent stress response (σ_p): $\sigma_p = MbG\tilde{\alpha}_c\sqrt{\rho_{ci}} + MbG\tilde{\alpha}_w\sqrt{\rho_{wi}}$; where M, b, and G are the Taylor factor, Burgers length, and shear modulus, respectively; $\tilde{\alpha}_c$ and $\tilde{\alpha}_w$ denote the mean dislocation interaction strengths associated with the local density and geometrical arrangement of immobile dislocations of cell and wall types, respectively; and ρ_{ci} and ρ_{wi} represent the cell and wall immobile dislocation densities (defined in a macroscopic representative material volume), respectively. This equation is unique in the sense that most of the published models do not consider such short/long-range decomposition, and simply use a familiar form of the following relation instead: $\sigma_p = MbG\tilde{\alpha}\sqrt{\rho_t}$; where ρ_t denotes the total dislocation density, meaning that if all the dislocation types are defined in the same control volume, $\rho_t \equiv \sum_i \rho_i$; where ρ_i is the i-th nonoverlapping independent dislocation type.

Furthermore, the temperature and strain rate dependence of the instantaneous viscous response and evolution of MSVs are incorporated phenomenologically using power-law relations. Moreover, for the first time a dislocation density-dependent explicit function for the plastic dissipation efficiency (the Taylor-Quinney coefficient or the fraction of inelastic power converted to heat) is proposed, and integrated in the constitutive model. The predictions of the microstructural constitutive model are consistent with the results of the displacement-controlled uniaxial compression tests at various (constant) temperatures and strain rates, the multistep compression experiments, and the measurements of (mean) GND density at different strain states.

It is worth noting that some of the definitions and decompositions in the presented microstructural model such as mobile/immobile, cell/wall, short-range/long-range, and local/nonlocal may not sound very rigorous and fundamental, meaning that there is a certain ambiguity associated with them. The presence of such ambiguities along with the numerous postulates made is inevitable, particularly in a microstructural model at macro-scale, which is supposed to adequately account for the hierarchical underlying physics of deformation, and accurately capture a large body of experimental measurements. Generally, in modeling of a physical system, larger length/time scale of the adopted theory leads to less rigorous postulates/definitions and thus higher ambiguity. The absence of the polarity and the porosity effects is another simplifying assumption made in the presented microstructural constitutive model. Thereby, mean dislocation

interaction strengths ($\tilde{\alpha}_c$ and $\tilde{\alpha}_w$) and constant Taylor factor ($M \cong 3.06$) were assumed, which are associated with the non-polarized meso-structure having (face-centered) cubic crystal symmetry. Moreover, the stress-reversal effect was neglected as the (displacement) boundary conditions associated with the uniaxial compression tests were monotonic.

The microstructural constitutive model was implemented in TMM explicit and implicit finite element (FE) frameworks as microstructural solvers via user-defined material subroutines in the standard FE software ABAQUS, which are coupled with the built-in thermal and mechanical solvers of the FE package. The implementation is detailed in Paper II. Subsequently, examples of complex bulk metal forming processes (industrial multi-step cold and warm forging of a bevel gear shaft) were thermo-micro-mechanically simulated. The approach was validated by comparing the predictions of the simulations with the experimental measurement of the force-displacement response of the warm forging process and GND density measurements of the final cold-forged part. It was revealed that the preheating of the initial billet has a substantial influence on the macroscopic GND density distribution in the final part. The presented approach and the corresponding TMM simulations are unprecedented and unique in that the sophisticated underlying dislocation structure are represented in the macroscopic length scale within a component after/during industrially complex multi-step metal forming processes.

4.2. Meso-scale modeling and in-service application

Papers III and IV deal with modeling of the primary microstructural effects (the size and polarity effects) at meso-scale using a physics-based crystal plasticity model, and its application in the optimal computational design of additively manufactured polycrystalline metallic materials. In Paper III, a meso-scale polycrystal plasticity model based on a full-field CPH scheme was presented, which consists of a physics-based crystal plasticity constitutive model, a crystal finite strain model, and a meso-structure model. The linearized crystal plasticity constitutive and finite strain models incrementally compute the constitutive mechanical response as well as the evolution and the anisotropic interactions of the MSVs at the underlying deformation (slip/twin) systems of each integration meso-point of the statistically representative volume element (SRVE). The crystal plasticity constitutive and finite strain models are based on physically motivated formulations that adequately account for the submeso-structural effects. The MSVs are (scalar) unipolar and dipolar dislocation densities at slip systems, and twin (volume) fraction at twin systems. In addition, statistically realistic models

of the polycrystalline meso-structure in terms of SRVEs (with different grid resolution) were generated based on the experimentally determined meso-structural (size, morphological, and crystallographic) descriptors.

In the framework of full-field CPH, in principle, the meso-structural features (including the meso-size) and their effects on the macroscopic mechanical response should be fully handled by the mesoscopic SRVE, while the submeso-structural aspects and their associated effects are reflected by the (physics-based) constitutive model. Such rigorous constitutive formulations involve gradient-based treatment in meso-scale continuum constitutive modeling of polycrystal plasticity by decomposing the (total) dislocation density into the underlying GND and SSD densities. The gradient-based models can be coupled with an interface model to account for (disorientation-dependent) slip transmission at grain boundaries as a function of interface opacity. Those highly nonlinear models locally (on the meso-scale) resolve the expected relatively high stress concentration in the vicinity of grain boundaries in the SRVE at the expense of the convergence rate leading to a longer computation time. Furthermore, due to their sensitivity to non-smoothness and geometrical contrasts, the gradient-based full-field simulations generally require higher grid resolution. Moreover, in the gradient-based full-field framework, in the case of twinning as a potential plastic deformation mechanism, the gradient-based constitutive model for dislocation-mediated plasticity must be coupled with a twinning model that resolves twins explicitly on the meso-scale. Coupling of the gradient-based dislocation slip and explicit twinning (continuum) constitutive models for large-strain full-field (3D) simulation of polycrystal plasticity is not currently practical as it becomes highly complex, demanding, nonlinear, and computationally expensive. Therefore, the approach adopted in the physics-based constitutive modeling detailed in Paper III is the rather simpler and more efficient (while effective) nonlocal treatment, in which some meso-structural features such as grain size and twins (size, shape, and orientation) are nonlocally incorporated in the governing constitutive formulation. In other words, the effect of stress concentration and strain localization due to the opacity of meso-structural interfaces is phenomenologically and nonlocally smeared all over the (intra-granular) meso-points of the SRVE.

The polycrystalline material studied in Paper III is an additively manufactured (single-phase) austenitic high-Mn steel exhibiting both slip and twinning in the cold regime. In the absence of composite effects and with a negligible porosity effect in the considered strain range and deformation parameters, the size and polarity effects were the only microstructural effects governing the mechanical

response of the investigated polycrystal. As typically observed in (as-built) additively manufactured metallic materials, the studied polycrystal contained a relatively polarized meso-structures, large meso-size, and small submeso-size. As a result, a relatively strong polarity and submeso-size, and weak meso-size effects were experimentally observed and numerically simulated.

The measured strongly anisotropic and nonlinear mechanical response of the polycrystal in a wide range of strain (at room temperature and a quasi-static strain rate) was consistently captured by the full-filed simulations with an unprecedented level of accuracy. The presented comparison between the experimental and the simulated (macroscopic) anisotropic mechanical responses is a strong irrefutable validation of the meso-scale full-field polycrystal plasticity along with the adopted underlying modeling approaches. Nevertheless, a physics-based crystal plasticity constitutive model can always be improved. For instance, the presented constitutive model can be enriched with formulations that account for the stress-reversal effect and the grain boundary plasticity resistance. Further, the introduced constitutive model consists of many underlying continuum models, which all are based on simplifying assumptions. Generalization of the underlying models by relaxing some of their constraints would lead to an enhancement of the accuracy and sophistication of the constitutive model. However, the presented validations have revealed that at least for the investigated polycrystalline material, the physics-based constitutive model along with all the underlying assumptions are quite sufficient for realization of the observed complex anisotropic polycrystal plasticity.

In addition to the proof of concept, systematic case-study simulations corresponding to different meso-structural polarity states were performed. Those case-study simulations, in which the morphological and crystallographic polarities were isolated from one another, provided new insights into the polarity effect. It was evidenced that the morphological and crystallographic polarities almost equally affect the anisotropic polycrystal plasticity and the associated mechanical response. Another key finding was that the morphological polarity affects the anisotropic strain hardening response of the polycrystal through a meso-size-like effect: a parallel shift of the strain hardening curve. Moreover, it was argued that the chosen specific Fe-Mn-Al-C alloy combined with the processing method/parameters selected for the study depicted in Paper III, represented an ideal polycrystalline material for a deep probe into the polarity effect on the strain hardening response. The fact the studied polycrystal contained a single constituent with a high crystal symmetry while exhibiting the activation of twinning (in

addition to dislocation slip) and large uniform elongation before fracture, allowed for a generic assessment of the the polarity effect.

Finally, Paper IV demonstrates that meso-scale modeling of polycrystal plasticity and microstructural effects plays the central role in the optimal design of specialized polycrystalline metallic materials under known service loads. In particular, the polycrystalline materials manufactured by unconventional metal processing techniques such as metal additive manufacturing processes are suitably subjected to the aforementioned paradigm of the optimal design. Owing to the proven robustness of the meso-scale full-field modeling of polycrystal plasticity in capturing the polarity effect, it can be invoked in the context of optimal design to exploit such a mysterious microstructural effect. Conventionally, the meso-structural polarity and the consequent anisotropy in the mechanical properties can be controlled to a certain extent through the deformation-based metal processing (i.e., metal forming) or directional solidification. However, given the flexibility of the metal additive manufacturing processes, almost every point in the meso-structural polarity space is conveniently accessible. Optimally, the meso-structure of a specialized additively manufactured metallic component, particularly with respect to polarity, can be designed in such a way to exhibit its highest load-bearing capacity in the direction where the service load is expected to be the maximum.

5. Summary and Outlook

In this thesis, the microstructural effects on the mechanical response of polycrystals are divided into four groups: size, polarity, composite, and porosity effects. The origins and a century of research on the modeling of the microstructural effects are reviewed. Furthermore, the primary microstructure effects, the size and polarity effects, are modeled for different polycrystalline metallic materials at two different length scales. First, the size effect was modeled using a macro-scale nonlocal microstructural model for (isotropic) polycrystal plasticity in the cold and warm regimes. Second, the polarity effect was modeled using a meso-scale full-field model for polycrystal plasticity to capture the anisotropic (macroscopic) mechanical response of a strongly (meso-structurally) polarized polycrystal. The macro-scale model was used to simulate industrial cold and warm forging processes of a bevel gear shaft made of a ferritic-pearlitic steel and predict its final microstructure and properties. The meso-scale model was applied for the optimal design of an additively manufactured lattice structure made of an austenitic high-Mn steel.

The concurrent modeling of all the quadruple microstructural effects at the macro-scale in a single framework is essential for the optimal (computational) design of structurally critical load-bearing components made of high-performance specialized polycrystalline metallic materials, particularly those manufactured by unconventional metal processing techniques such as metal additive manufacturing processes.

The integrated modeling approach, in which the parameters of (physics-based) constitutive models at each scale are estimated by simulations/calculations at lower scales, is inevitable for the simultaneous optimal design of (polycrystalline) materials and manufacturing processes. The good news is that from the subatomic scale(s) up to the meso-scale, the modeling approaches (based on quantum mechanics, density functional theory, molecular dynamics, discrete dislocation dynamics, phase-field micro-elasticity, continuum crystal plasticity, and polycrystal homogenization) are well developed. However, there is a big gap from the meso-scale to the macro-scale, meaning that there is no comprehensive physics-based constitutive model at the macro-scale accounting for all the microstructural effects. This gap is of paramount importance because without a proper and efficient meso-macro bridge, in general, it is not possible to strictly simulate the in-process behavior and in-service performance of macroscopic structures. Therefore, unless this gap is properly bridged by comprehensive *microstructural constitutive models*, the optimal design of macroscopic structures will not be realized.

I believe that this thesis will pave the way to pursue a unified general theory of (macro-scale) Continuum Microstructure Dynamics, based on which the aforementioned microstructural constitutive models can be developed. This theory is expected to comprehensively account for all the discussed interdependent microstructural effects, and sufficiently for all the aspects of microstructure evolution. The motivation behind this thesis is not to provide the final answer to the unification problem, but to offer a new perspective in the journey towards the ultimate answer.

References

[1] G.B. Olson, Computational Design of Hierarchically Structured Materials, Science 277 (1997) 1237–1242, doi: 10.1126/science.277.5330.1237.

[2] B.L. Adams, T. Olson, The mesostructure—properties linkage in polycrystals, Progress in Materials Science 43 (1998) 1–87, doi: 10.1016/S0079-6425(98)00002-4.

[3] H.-J. Bunge, Texture analysis in materials science: Mathematical methods, Butterworths, London, 1982.

[4] H.J. Bunge, Three-dimensional texture analysis, International Materials Reviews 32 (1987) 265–291, doi: 10.1179/imr.1987.32.1.265.

[5] H.J. Bunge, H. Weiland, Orientation Correlation in Grain and Phase Boundaries, Textures and Microstructures 7 (1988) 231–263, doi: 10.1155/TSM.7.231.
[6] G. Wassermann, J. Grewen, Texturen metallischer Werkstoffe, Springer, Berlin, Heidelberg, 1962.
[7] O. Engler, V. Randle, Introduction to texture analysis: Macrotexture, microtexture, and orientation mapping, 2nd ed., CRC Press, Boca Raton, Fla., 2010.
[8] M. Li, S. Ghosh, O. Richmond, H. Weiland, T.N. Rouns, Three dimensional characterization and modeling of particle reinforced metal matrix composites, Materials Science and Engineering: A 265 (1999) 153–173, doi: 10.1016/S0921-5093(98)01132-0.
[9] D.M. Saylor, J. Fridy, B.S. El-Dasher, K.-Y. Jung, A.D. Rollett, Statistically representative three-dimensional microstructures based on orthogonal observation sections, Metall and Mat Trans A 35 (2004) 1969–1979, doi: 10.1007/s11661-004-0146-0.
[10] M. Groeber, A framework for automated analysis and simulation of 3D polycrystalline microstructures.Part 1, Acta Materialia 56 (2008) 1257–1273, doi: 10.1016/j.actamat.2007.11.041.
[11] G. Lebon, D. Jou, J. Casas-Vázquez, Understanding Non-equilibrium Thermodynamics: Foundations, Applications, Frontiers, 1st ed., Springer-Verlag, s.l., 2008.
[12] D. Jou, J. Casas-Vásquez, G. Lebon, Extended Irreversible Thermodynamics, 4th ed., Springer Science+Business Media B.V, Dordrecht, 2010.
[13] D. Jou, J. Casas-Vázquez, G. Lebon, Extended irreversible thermodynamics revisited (1988-98), Physical review. E, Statistical physics, plasmas, fluids, and related interdisciplinary topics 62 (1999) 1035–1142, doi: 10.1088/0034-4885/62/7/201.
[14] I. Prigogine, Introduction to thermodynamics of irreversible processes, 3rd ed., Interscience Publ, New York, 1967.
[15] S. Kjelstrup, D. Bedeaux, Non-equilibrium thermodynamics of heterogeneous systems, World Scientific Pub. Co, Singapore, Hackensack, N.J, 2008.
[16] R. Balescu, Equilibrium and nonequilibrium statistical mechanics, Wiley, New York, 1975.
[17] D.N. Zubarev, P.E. Gray, Nonequilibrium statistical thermodynamics, Consultants Bureau, New York, 1974.
[18] L. Onsager, Reciprocal Relations in Irreversible Processes. I, Phys. Rev. 37 (1931) 405–426, doi: 10.1103/PhysRev.37.405.
[19] L. Onsager, Reciprocal Relations in Irreversible Processes. II, Phys. Rev. 38 (1931) 2265–2279, doi: 10.1103/PhysRev.38.2265.
[20] J. Meixner, Thermodynamische Theorie der elastischen Relaxation, Zeitschrift für Naturforschung A 9 (1954) 654–663, doi: 10.1515/zna-1954-7-812.
[21] J. Meixner, H.G. Reik, Thermodynamik der irreversiblen Prozesse, in: S. Flügge (Ed.), Prinzipien der Thermodynamik und Statistik, Springer Berlin Heidelberg, Berlin, Heidelberg, 1959, pp. 413–523.
[22] I. Prigogine, Le domaine de validité de la thermodynamique des phénomènes irréversibles, Physica 15 (1949) 272–284, doi: 10.1016/0031-8914(49)90056-7.
[23] M. Hillert, J. Ågren, Extremum principles for irreversible processes, Acta Materialia 54 (2006) 2063–2066, doi: 10.1016/j.actamat.2005.12.033.
[24] S.A.H. Motaman, F. Roters, C. Haase, Anisotropic polycrystal plasticity due to microstructural heterogeneity, Acta Materialia 185 (2020) 340–369, doi: 10.1016/j.actamat.2019.12.003.
[25] A. Reuss, Berechnung der Fließgrenze von Mischkristallen auf Grund der Plastizitätsbedingung für Einkristalle, Z. Angew. Math. Mech. 9 (1929) 49–58, doi: 10.1002/zamm.19290090104.
[26] R. Hill, The Elastic Behaviour of a Crystalline Aggregate, Z. Angew. Math. Mech. 65 (1952) 349–354, doi: 10.1088/0370-1298/65/5/307.
[27] A.V. Hershey, The elasticity of an isotropic aggregate of anisotropic cubic crystals, Journal of Applied mechanics-transactions of the ASME 21 (1954) 236–240.
[28] J.D. Eshelby, The determination of the elastic field of an ellipsoidal inclusion, and related problems, Proc. R. Soc. Lond. A 241 (1957) 376–396, doi: 10.1098/rspa.1957.0133.
[29] J.D. Eshelby, Elastic inclusions and inhomogeneities, in: Progress in Solid Mechanics, North-Holland Publ., 1961, pp. 87–140.
[30] G. Sachs, Zur Ableitung einer Fließbedingung, Z. V. d. I. 72 (1929) 734–736, doi: 10.1007/978-3-642-92045-5_12.

[31] G.I. Taylor, Plastic strain in metals, J. Inst. Metals (1938) 307–325.
[32] J.F.W. Bishop, R. Hill, CXXVIII. A theoretical derivation of the plastic properties of a polycrystalline face-centred metal, The London, Edinburgh, and Dublin Philosophical Magazine and Journal of Science 42 (1951) 1298–1307, doi: 10.1080/14786444108561385.
[33] J.F.W. Bishop, R. Hill, XLVI. A theory of the plastic distortion of a polycrystalline aggregate under combined stresses, The London, Edinburgh, and Dublin Philosophical Magazine and Journal of Science 42 (1951) 414–427, doi: 10.1080/14786445108561065.
[34] T.H. Lin, Analysis of elastic and plastic strains of a face-centred cubic crystal, Journal of the Mechanics and Physics of Solids 5 (1957) 143–149, doi: 10.1016/0022-5096(57)90058-3.
[35] E. Kröner, On the plastic deformation of polycrystals, Acta Metallurgica 9 (1961) 155–161.
[36] U.F. Kocks, The relation between polycrystal deformation and single-crystal deformation, Metall and Materi Trans 1 (1970) 1121–1143, doi: 10.1007/BF02900224.
[37] H.J. Bunge, Some applications of the Taylor theory of polycrystal plasticity, Krist. Techn. 5 (1970) 145–175, doi: 10.1002/crat.19700050112.
[38] F. Roters, P. Eisenlohr, L. Hantcherli, D.D. Tjahjanto, T.R. Bieler, D. Raabe, Overview of constitutive laws, kinematics, homogenization and multiscale methods in crystal plasticity finite-element modeling, Acta Materialia 58 (2010) 1152–1211, doi: 10.1016/j.actamat.2009.10.058.
[39] J. Segurado, R.A. Lebensohn, J. LLorca, Computational Homogenization of Polycrystals, in: Advances in Crystals and Elastic Metamaterials, Part 1, Elsevier, 2018, pp. 1–114.
[40] S. Nemat-Nasser, M. Hori, Micromechanics: Overall properties of heterogeneous materials / by S. Nemat-Nasser, M. Hori, North-Holland, Amsterdam, London, 1993.
[41] P. Kanouté, D.P. Boso, J.L. Chaboche, B.A. Schrefler, Multiscale Methods for Composites: A Review, Arch Computat Methods Eng 16 (2009) 31–75, doi: 10.1007/s11831-008-9028-8.
[42] J.R. Rice, Inelastic constitutive relations for solids, Journal of the Mechanics and Physics of Solids 19 (1971) 433–455, doi: 10.1016/0022-5096(71)90010-X.
[43] R. Hill, J.R. Rice, Constitutive analysis of elastic-plastic crystals at arbitrary strain, Journal of the Mechanics and Physics of Solids 20 (1972) 401–413, doi: 10.1016/0022-5096(72)90017-8.
[44] R.J. Asaro, J.R. Rice, Strain localization in ductile single crystals, Journal of the Mechanics and Physics of Solids 25 (1977) 309–338, doi: 10.1016/0022-5096(77)90001-1.
[45] D. Peirce, R.J. Asaro, A. Needleman, An analysis of nonuniform and localized deformation in ductile single crystals, Acta Metallurgica 30 (1982) 1087–1119, doi: 10.1016/0001-6160(82)90005-0.
[46] D. Peirce, R.J. Asaro, A. Needleman, Material rate dependence and localized deformation in crystalline solids, Acta Metallurgica 31 (1983) 1951–1976, doi: 10.1016/0001-6160(83)90014-7.
[47] R.J. Asaro, Crystal Plasticity, J. Appl. Mech. 50 (1983) 921, doi: 10.1115/1.3167205.
[48] R.J. Asaro, Micromechanics of Crystals and Polycrystals, in: Advances in Applied Mechanics Volume 23, Elsevier, 1983, pp. 1–115.
[49] S.R. Kalidindi, C.A. Bronkhorst, L. Anand, Crystallographic texture evolution in bulk deformation processing of FCC metals, Journal of the Mechanics and Physics of Solids 40 (1992) 537–569, doi: 10.1016/0022-5096(92)80003-9.
[50] C.A. Bronkhorst, S.R. Kalidindi, L. Anand, Polycrystalline plasticity and the evolution of crystallographic texture in FCC metals, Phil. Trans. R. Soc. Lond. A 341 (1992) 443–477, doi: 10.1098/rsta.1992.0111.
[51] S.R. Kalidindi, Incorporation of deformation twinning in crystal plasticity models, Journal of the Mechanics and Physics of Solids 46 (1998) 267–290, doi: 10.1016/S0022-5096(97)00051-3.
[52] M.M. Rashid, S. Nemat-Nasser, A constitutive algorithm for rate-dependent crystal plasticity, Computer Methods in Applied Mechanics and Engineering 94 (1992) 201–228, doi: 10.1016/0045-7825(92)90147-C.
[53] A.M. Cuitino, M. Ortiz, Computational modelling of single crystals, Modelling Simul. Mater. Sci. Eng. 1 (1993) 225–263, doi: 10.1088/0965-0393/1/3/001.
[54] R.A. Lebensohn, C.N. Tomé, A self-consistent anisotropic approach for the simulation of plastic deformation and texture development of polycrystals, Acta Metallurgica et Materialia 41 (1993) 2611–2624, doi: 10.1016/0956-7151(93)90130-K.

[55] A. Molinari, G.R. Canova, S. Ahzi, A self consistent approach of the large deformation polycrystal viscoplasticity, Acta Metallurgica 35 (1987) 2983–2994, doi: 10.1016/0001-6160(87)90297-5.
[56] M. Berveiller, A. Zaoui, An extension of the self-consistent scheme to plastically-flowing polycrystals, Journal of the Mechanics and Physics of Solids 26 (1978) 325–344, doi: 10.1016/0022-5096(78)90003-0.
[57] R.A. Lebensohn, C.N. Tomé, P.P. CastaÑeda, Self-consistent modelling of the mechanical behaviour of viscoplastic polycrystals incorporating intragranular field fluctuations, Philosophical Magazine 87 (2007) 4287–4322, doi: 10.1080/14786430701432619.
[58] R. Masson, M. Bornert, P. Suquet, A. Zaoui, An affine formulation for the prediction of the effective properties of nonlinear composites and polycrystals, Journal of the Mechanics and Physics of Solids 48 (2000) 1203–1227, doi: 10.1016/S0022-5096(99)00071-X.
[59] E. Kröner, Berechnung der elastischen Konstanten des Vielkristalls aus den Konstanten des Einkristalls, Z. Physik (Zeitschrift für Physik) 151 (1958) 504–518, doi: 10.1007/BF01337948.
[60] E. Kröner, Zur plastischen verformung des vielkristalls, Acta Metallurgica 9 (1961) 155–161, doi: 10.1016/0001-6160(61)90060-8.
[61] R. Hill, Continuum micro-mechanics of elastoplastic polycrystals, Journal of the Mechanics and Physics of Solids 13 (1965) 89–101, doi: 10.1016/0022-5096(65)90023-2.
[62] J.W. Hutchinson, Elastic-plastic behaviour of polycrystalline metals and composites, Proc. R. Soc. Lond. A 319 (1970) 247–272, doi: 10.1098/rspa.1970.0177.
[63] T. Mori, K. Tanaka, Average stress in matrix and average elastic energy of materials with misfitting inclusions, Acta Metallurgica 21 (1973) 571–574, doi: 10.1016/0001-6160(73)90064-3.
[64] M. Zecevic, W. Pantleon, R.A. Lebensohn, R.J. McCabe, M. Knezevic, Predicting intragranular misorientation distributions in polycrystalline metals using the viscoplastic self-consistent formulation, Acta Materialia 140 (2017) 398–410, doi: 10.1016/j.actamat.2017.08.056.
[65] Y. Liu, P. Gilormini, P. Ponte Castañeda, Variational self-consistent estimates for texture evolution in viscoplastic polycrystals, Acta Materialia 51 (2003) 5425–5437, doi: 10.1016/S1359-6454(03)00409-9.
[66] J.W. Hutchinson, Bounds and self-consistent estimates for creep of polycrystalline materials, Proc. R. Soc. Lond. A 348 (1976) 101–127, doi: 10.1098/rspa.1976.0027.
[67] G. deBotton, P. Ponte Castañeda, Variational estimates for the creep behaviour of polycrystals, Proc. R. Soc. Lond. A 448 (1995) 121–142, doi: 10.1098/rspa.1995.0009.
[68] M. Nebozhyn, Variational self-consistent estimates for cubic viscoplastic polycrystals, Journal of the Mechanics and Physics of Solids 49 (2001) 313–340, doi: 10.1016/S0022-5096(00)00037-5.
[69] Y. Liu, P. Ponte Castañeda, Homogenization estimates for the average behavior and field fluctuations in cubic and hexagonal viscoplastic polycrystals, Journal of the Mechanics and Physics of Solids 52 (2004) 1175–1211, doi: 10.1016/j.jmps.2003.08.006.
[70] P. Gilormini, M.V. Nebozhyn, P. Ponte Castañeda, Accurate estimates for the creep behavior of hexagonal polycrystals, Acta Materialia 49 (2001) 329–337, doi: 10.1016/S1359-6454(00)00319-0.
[71] R.A. Lebensohn, Y. Liu, P. Ponte Castañeda, On the accuracy of the self-consistent approximation for polycrystals: comparison with full-field numerical simulations, Acta Materialia 52 (2004) 5347–5361, doi: 10.1016/j.actamat.2004.07.040.
[72] M. Zecevic, R.A. Lebensohn, R.J. McCabe, M. Knezevic, Modeling of intragranular misorientation and grain fragmentation in polycrystalline materials using the viscoplastic self-consistent formulation, International Journal of Plasticity 109 (2018) 193–211, doi: 10.1016/j.ijplas.2018.06.004.
[73] J.R. Willis, Bounds and self-consistent estimates for the overall properties of anisotropic composites, Journal of the Mechanics and Physics of Solids 25 (1977) 185–202, doi: 10.1016/0022-5096(77)90022-9.
[74] P.P. CastaÑeda, Fully optimized second-order variational estimates for the macroscopic response and field statistics in viscoplastic crystalline composites, Proc. R. Soc. A 471 (2015) 20150665, doi: 10.1098/rspa.2015.0665.
[75] Y. Liu, P. Ponte Castañeda, Second-order theory for the effective behavior and field fluctuations in viscoplastic polycrystals, Journal of the Mechanics and Physics of Solids 52 (2004) 467–495, doi: 10.1016/S0022-5096(03)00078-4.
[76] P.P. CastaÑeda, M.V. Nebozhyn, Variational estimates of the self-consistent type for the effective behaviour of some model nonlinear polycrystals, Proc. R. Soc. A 453 (1997) 2715–2724, doi: 10.1098/rspa.1997.0144.

[77] O. Castelnau, R. Brenner, R. LEBENSOHN, The effect of strain heterogeneity on the work hardening of polycrystals predicted by mean-field approaches, Acta Materialia 54 (2006) 2745–2756, doi: 10.1016/j.actamat.2006.02.014.
[78] R.A. Lebensohn, M. Zecevic, M. Knezevic, R.J. McCabe, Average intragranular misorientation trends in polycrystalline materials predicted by a viscoplastic self-consistent approach, Acta Materialia 104 (2016) 228–236, doi: 10.1016/j.actamat.2015.10.035.
[79] A. Ostapovets, P. Šedá, A. Jäger, P. Lejček, New misorientation scheme for a visco-plastic self-consistent model: Equal channel angular pressing of magnesium single crystals, International Journal of Plasticity 29 (2012) 1–12, doi: 10.1016/j.ijplas.2011.07.006.
[80] D. Song, P. Ponte Castañeda, Fully optimized second-order homogenization estimates for the macroscopic response and texture evolution of low-symmetry viscoplastic polycrystals, International Journal of Plasticity 110 (2018) 272–293, doi: 10.1016/j.ijplas.2018.07.004.
[81] T. Mura, Micromechanics of defects in solids, Springer Netherlands, Dordrecht, 1987.
[82] H. Wang, P.D. Wu, C.N. Tomé, Y. Huang, A finite strain elastic–viscoplastic self-consistent model for polycrystalline materials, Journal of the Mechanics and Physics of Solids 58 (2010) 594–612, doi: 10.1016/j.jmps.2010.01.004.
[83] R.A. Lebensohn, C.N. Tomé, A self-consistent viscoplastic model, Materials Science and Engineering: A 175 (1994) 71–82, doi: 10.1016/0921-5093(94)91047-2.
[84] G.J. Weng, A Self-Consistent Scheme for the Relaxation Behavior of Metals, J. Appl. Mech. 48 (1981) 779–784, doi: 10.1115/1.3157733.
[85] G.J. Weng, A Unified, Self-Consistent Theory for the Plastic-Creep Deformation of Metals, J. Appl. Mech. 49 (1982) 728–734, doi: 10.1115/1.3162609.
[86] G.J. Weng, A self-consistent relation for the time-dependent creep of polycrystals, International Journal of Plasticity 9 (1993) 181–198, doi: 10.1016/0749-6419(93)90028-O.
[87] A. Molinari, S. Ahzi, R. Kouddane, On the self-consistent modeling of elastic-plastic behavior of polycrystals, Mechanics of Materials 26 (1997) 43–62, doi: 10.1016/S0167-6636(97)00017-3.
[88] P.A. Turner, C.N. Tomé, C.H. Woo, Self-consistent modelling of nonlinear visco-elastic polycrystals: An approximate scheme, Philosophical Magazine A 70 (1994) 689–711, doi: 10.1080/01418619408242256.
[89] P.A. Turner, C.N. Tomé, Self-consistent modeling of visco-elastic polycrystals: Application to irradiation creep and growth, Journal of the Mechanics and Physics of Solids 41 (1993) 1191–1211, doi: 10.1016/0022-5096(93)90090-3.
[90] C.N. Tomé, Self-consistent polycrystal models: a directional compliance criterion to describe grain interactions, Acta Metallurgica 7 (1999) 723–738, doi: 10.1088/0965-0393/7/5/305.
[91] S. Nemat-Nasser, M. Obata, Rate-dependent, finite elasto-plastic deformation of polycrystals, Proc. R. Soc. Lond. A 407 (1986) 343–375, doi: 10.1098/rspa.1986.0101.
[92] S.V. Harren, The finite deformation of rate-dependent polycrystals—I. A self-consistent framework, Journal of the Mechanics and Physics of Solids 39 (1991) 345–360, doi: 10.1016/0022-5096(91)90017-I.
[93] S.V. Harren, The finite deformation of rate-dependent polycrystals—II: A comparison of the self-consistent and Taylor methods, Journal of the Mechanics and Physics of Solids 39 (1991) 361–383, doi: 10.1016/0022-5096(91)90018-J.
[94] A. Molinari, L.S. Tóth, Tuning a self consistent viscoplastic model by finite element results—I. Modeling, Acta Metallurgica et Materialia 42 (1994) 2453–2458, doi: 10.1016/0956-7151(94)90324-7.
[95] A. Zaoui, Continuum Micromechanics: Survey, J. Eng. Mech. 128 (2002) 808–816, doi: 10.1061/(ASCE)0733-9399(2002)128:8(808).
[96] T. Iwakuma, S. Nemat-Nasser, Finite elastic-plastic deformation of polycrystalline metals, Proc. R. Soc. Lond. A 394 (1984) 87–119, doi: 10.1098/rspa.1984.0071.
[97] B. BUDIANSKY, T.T. Wu, Theoretical prediction of plastic strains of polycrystals, Proceedings of the 4th US National Congress of Applied Mechanics, Trans. of the ASME (1962) 1175–1185.
[98] H. Sabar, M. Berveiller, V. Favier, S. Berbenni, A new class of micro–macro models for elastic–viscoplastic heterogeneous materials, International Journal of Solids and Structures 39 (2002) 3257–3276, doi: 10.1016/S0020-7683(02)00256-1.
[99] P. LIPINSKI, M. Berveiller, Elastoplasticity of micro-inhomogeneous metals at large strains, International Journal of Plasticity 5 (1989) 149–172, doi: 10.1016/0749-6419(89)90027-2.

[100] A. Paquin, S. BERBENNI, V. FAVIER, X. Lemoine, M. Berveiller, Micromechanical modeling of the elastic–viscoplastic behavior of polycrystalline steels, International Journal of Plasticity 17 (2001) 1267–1302, doi: 10.1016/S0749-6419(00)00047-4.

[101] G.M. Brown, A self-consistent polycrystalline model for creep under combined stress states, Journal of the Mechanics and Physics of Solids 18 (1970) 367–381, doi: 10.1016/0022-5096(70)90015-3.

[102] D.R.S. Talbot, J.R. Willis, Some simple explicit bounds for the overall behaviour of nonlinear composites, International Journal of Solids and Structures 29 (1992) 1981–1987, doi: 10.1016/0020-7683(92)90188-Y.

[103] D.R.S. TALBOT, J.R. Willis, Variational Principles for Inhomogeneous Non-linear Media, IMA J Appl Math 35 (1985) 39–54, doi: 10.1093/imamat/35.1.39.

[104] J.R. Willis, Variational and Related Methods for the Overall Properties of Composites, in: Advances in Applied Mechanics Volume 21, Elsevier, 1981, pp. 1–78.

[105] J.R. Willis, On methods for bounding the overall properties of nonlinear composites, Journal of the Mechanics and Physics of Solids 39 (1991) 73–86, doi: 10.1016/0022-5096(91)90031-I.

[106] P.P. Castañeda, New variational principles in plasticity and their application to composite materials, Journal of the Mechanics and Physics of Solids 40 (1992) 1757–1788, doi: 10.1016/0022-5096(92)90050-C.

[107] P.P. Castañeda, P. Suquet, Nonlinear Composites, in: E. van der Giessen, T.Y. Wu (Eds.), Advances in applied mechanics, Academic P, San Diego, 1999, pp. 171–302.

[108] Z. Hashin, S. Shtrikman, Note on a variational approach to the theory of composite elastic materials, Journal of the Franklin Institute 271 (1961) 336–341, doi: 10.1016/0016-0032(61)90032-1.

[109] Z. Hashin, S. Shtrikman, On some variational principles in anisotropic and nonhomogeneous elasticity, Journal of the Mechanics and Physics of Solids 10 (1962) 335–342, doi: 10.1016/0022-5096(62)90004-2.

[110] Z. Hashin, S. Shtrikman, A variational approach to the theory of the elastic behaviour of multiphase materials, Journal of the Mechanics and Physics of Solids 11 (1963) 127–140, doi: 10.1016/0022-5096(63)90060-7.

[111] P.P. Castañeda, The effective mechanical properties of nonlinear isotropic composites, Journal of the Mechanics and Physics of Solids 39 (1991) 45–71, doi: 10.1016/0022-5096(91)90030-R.

[112] P.P. Castañeda, Exact second-order estimates for the effective mechanical properties of nonlinear composite materials, Journal of the Mechanics and Physics of Solids 44 (1996) 827–862, doi: 10.1016/0022-5096(96)00015-4.

[113] P.P. Castañeda, Second-order homogenization estimates for nonlinear composites incorporating field fluctuations: II—applications, Journal of the Mechanics and Physics of Solids 50 (2002) 759–782, doi: 10.1016/S0022-5096(01)00098-9.

[114] P.P. Castañeda, Second-order homogenization estimates for nonlinear composites incorporating field fluctuations: I—theory, Journal of the Mechanics and Physics of Solids 50 (2002) 737–757, doi: 10.1016/S0022-5096(01)00099-0.

[115] Y. Leroy, P. Ponte Castañeda, Bounds on the self-consistent approximation for nonlinear media and implications for the second-order method, Comptes Rendus de l'Académie des Sciences - Series IIB - Mechanics 329 (2001) 571–577, doi: 10.1016/S1620-7742(01)01369-1.

[116] P.P. CastaÑeda, M. Zaidman, The finite deformation of nonlinear composite materials—I. Instantaneous constitutive relations, International Journal of Solids and Structures 33 (1996) 1271–1286, doi: 10.1016/0020-7683(95)00099-2.

[117] M. Zaidman, P. Ponte Castañeda, The finite deformation of nonlinear composite materials—II. Evolution of the microstructure, International Journal of Solids and Structures 33 (1996) 1287–1303, doi: 10.1016/0020-7683(95)00100-X.

[118] P. Suquet, Overall properties of nonlinear composites: a modified secant moduli theory and its link with Ponte Castañeda's nonlinear variational procedure, Comptes rendus de l'Académie des sciences. Série II, Mécanique, physique, chimie, astronomie 320 (1995) 563–571.

[119] C. Miehe, Strain-driven homogenization of inelastic microstructures and composites based on an incremental variational formulation, Int. J. Numer. Meth. Engng 55 (2002) 1285–1322, doi: 10.1002/nme.515.

[120] P. van Houtte, On the equivalence of the relaxed Taylor theory and the Bishop-Hill theory for partially constrained plastic deformation of crystals, Materials Science and Engineering 55 (1982) 69–77, doi: 10.1016/0025-5416(82)90085-4.

[121] P. van Houtte, A Comprehensive Mathematical Formulation of an Extended Taylor–Bishop–Hill Model Featuring Relaxed Constraints, the Renouard–Wintenberger Theory and a Strain Rate Sensitivity Model, Textures and Microstructures 8 (1988) 313–350, doi: 10.1155/TSM.8-9.313.

[122] P. van Houtte, Deformation texture prediction, International Journal of Plasticity 21 (2005) 589–624, doi: 10.1016/j.ijplas.2004.04.011.

[123] U.F. Kocks, H. Chandra, Slip geometry in partially constrained deformation, Acta Metallurgica 30 (1982) 695–709, doi: 10.1016/0001-6160(82)90119-5.

[124] D.D. Tjahjanto, P. Eisenlohr, F. Roters, Relaxed grain cluster (RGC) homogenization scheme, Int J Mater Form 2 (2009) 939–942, doi: 10.1007/s12289-009-0619-1.

[125] D.D. Tjahjanto, P. Eisenlohr, F. Roters, A novel grain cluster-based homogenization scheme, Modelling Simul. Mater. Sci. Eng. 18 (2010) 15006, doi: 10.1088/0965-0393/18/1/015006.

[126] P. Eisenlohr, D.D. Tjahjanto, T. Hochrainer, F. Roters, D. Raabe, Texture prediction from a novel grain cluster-based homogenization scheme, Int J Mater Form 2 (2009) 523–526, doi: 10.1007/s12289-009-0561-2.

[127] M. Crumbach, M. Goerdeler, G. Gottstein, L. Neumann, H. Aretz, R. Kopp, Through-process texture modelling of aluminium alloys, Acta Materialia 12 (2004) S1-S18, doi: 10.1088/0965-0393/12/1/S01.

[128] M. Crumbach, M. Goerdeler, G. Gottstein, Modelling of recrystallisation textures in aluminium alloys: II. Model performance and experimental validation, Acta Materialia 54 (2006) 3291–3306, doi: 10.1016/j.actamat.2006.03.019.

[129] M. Crumbach, M. Goerdeler, G. Gottstein, Modelling of recrystallisation textures in aluminium alloys, Acta Materialia 54 (2006) 3275–3289, doi: 10.1016/j.actamat.2006.03.017.

[130] P. van Houtte, L. Delannay, S.R. Kalidindi, Comparison of two grain interaction models for polycrystal plasticity and deformation texture prediction, International Journal of Plasticity 18 (2002) 359–377, doi: 10.1016/S0749-6419(00)00102-9.

[131] P. van Houtte, L. Delannay, I. Samajdar, Quantitative Prediction of Cold Rolling Textures in Low-Carbon Steel by Means of the Lamel Model, Textures and Microstructures 31 (1999) 109–149, doi: 10.1155/TSM.31.109.

[132] D.D. Tjahjanto, P. Eisenlohr, F. Roters, Multiscale deep drawing analysis of dual-phase steels using grain cluster-based RGC scheme, Modelling Simul. Mater. Sci. Eng. 23 (2015) 45005, doi: 10.1088/0965-0393/23/4/045005.

[133] J. Gawad, A. van Bael, P. Eyckens, G. Samaey, P. van Houtte, D. Roose, Hierarchical multi-scale modeling of texture induced plastic anisotropy in sheet forming, Computational Materials Science 66 (2013) 65–83, doi: 10.1016/j.commatsci.2012.05.056.

[134] P. van Houtte, A.K. Kanjarla, A. van Bael, M. Seefeldt, L. Delannay, Multiscale modelling of the plastic anisotropy and deformation texture of polycrystalline materials, European Journal of Mechanics - A/Solids 25 (2006) 634–648, doi: 10.1016/j.euromechsol.2006.05.003.

[135] J.-C. Michel, P. Suquet, A model-reduction approach to the micromechanical analysis of polycrystalline materials, Comput Mech 57 (2016) 483–508, doi: 10.1007/s00466-015-1248-9.

[136] F. Fritzen, T. Böhlke, Three-dimensional finite element implementation of the nonuniform transformation field analysis, Int. J. Numer. Meth. Engng 84 (2010) 803–829, doi: 10.1002/nme.2920.

[137] J.C. Michel, P. Suquet, Nonuniform transformation field analysis, International Journal of Solids and Structures 40 (2003) 6937–6955, doi: 10.1016/S0020-7683(03)00346-9.

[138] F. Fritzen, M. Leuschner, Reduced basis hybrid computational homogenization based on a mixed incremental formulation, Computer Methods in Applied Mechanics and Engineering 260 (2013) 143–154, doi: 10.1016/j.cma.2013.03.007.

[139] J.-C. Michel, P. Suquet, NON-UNIFORM TRANSFORMATION FIELD ANALYSIS: A REDUCED MODEL FOR MULTISCALE NON-LINEAR PROBLEMS IN SOLID MECHANICS, in: U. Galvanetto, M.H. ALIABADI (Eds.), Multiscale modeling in solid mechanics: Computational approaches / editors Ugo Galvanetto, M.H. Ferri Aliabadi, IMPERIAL COLLEGE PRESS, London, 2010, pp. 159–206.

[140] J.-C. Michel, P. Suquet, A model-reduction approach in micromechanics of materials preserving the variational structure of constitutive relations, Journal of the Mechanics and Physics of Solids 90 (2016) 254–285, doi: 10.1016/j.jmps.2016.02.005.

[141] J.C. Michel, P. Suquet, Computational analysis of nonlinear composite structures using the nonuniform transformation field analysis, Computer Methods in Applied Mechanics and Engineering 193 (2004) 5477–5502, doi: 10.1016/j.cma.2003.12.071.

[142] F. Fritzen, T. Böhlke, Nonuniform transformation field analysis of materials with morphological anisotropy, Composites Science and Technology 71 (2011) 433–442, doi: 10.1016/j.compscitech.2010.12.013.

[143] F. Fritzen, T. Böhlke, Reduced basis homogenization of viscoelastic composites, Composites Science and Technology 76 (2013) 84–91, doi: 10.1016/j.compscitech.2012.12.012.

[144] G.J. Dvorak, Transformation field analysis of inelastic composite materials, Proc. R. Soc. Lond. A 437 (1992) 311–327, doi: 10.1098/rspa.1992.0063.

[145] G.J. Dvorak, Y.A. Bahei-El-Din, A.M. Wafa, The modeling of inelastic composite materials with the transformation field analysis, Int. J. Numer. Meth. Engng 2 (1994) 571–586, doi: 10.1088/0965-0393/2/3A/011.

[146] G.J. Dvorak, A.M. Wafa, Y.A. Bahei-El-Din, Implementation of the transformation field analysis for inelastic composite materials, Comput Mech 14 (1994) 201–228, doi: 10.1007/BF00370073.

[147] J. Fish, K. Shek, M. Pandheeradi, M.S. Shephard, Computational plasticity for composite structures based on mathematical homogenization: Theory and practice, Computer Methods in Applied Mechanics and Engineering 148 (1997) 53–73, doi: 10.1016/S0045-7825(97)00030-3.

[148] R. Largenton, J.-C. Michel, P. Suquet, Extension of the Nonuniform Transformation Field Analysis to linear viscoelastic composites in the presence of aging and swelling, Mechanics of Materials 73 (2014) 76–100, doi: 10.1016/j.mechmat.2014.02.004.

[149] M. Groeber, A framework for automated analysis and simulation of 3D polycrystalline microstructures. Part 2, Acta Materialia 56 (2008) 1274–1287, doi: 10.1016/j.actamat.2007.11.040.

[150] M.A. Groeber, M.A. Jackson, DREAM.3D, Integrating Materials 3 (2014) 3009, doi: 10.1186/2193-9772-3-5.

[151] L. Scheunemann, D. Balzani, D. Brands, J. Schröder, Construction of Statistically Similar RVEs, in: S. Conti, K. Hackl (Eds.), Analysis and computation of microstructure in finite plasticity, Springer, Cham, 2015, pp. 219–256.

[152] D. Brands, D. Balzani, L. Scheunemann, J. Schröder, H. Richter, D. Raabe, Computational modeling of dual-phase steels based on representative three-dimensional microstructures obtained from EBSD data, Arch Appl Mech 86 (2016) 575–598, doi: 10.1007/s00419-015-1044-1.

[153] S. Torquato, H.W. Haslach, Random Heterogeneous Materials: Microstructure and Macroscopic Properties, Applied Mechanics Reviews 55 (2002) B62-B63, doi: 10.1115/1.1483342.

[154] S. Yang, J. Dirrenberger, E. Monteiro, N. Ranc, Representative volume element size determination for viscoplastic properties in polycrystalline materials, International Journal of Solids and Structures 158 (2019) 210–219, doi: 10.1016/j.ijsolstr.2018.09.011.

[155] T. Kanit, S. Forest, I. Galliet, V. Mounoury, D. Jeulin, Determination of the size of the representative volume element for random composites: statistical and numerical approach, International Journal of Solids and Structures 40 (2003) 3647–3679, doi: 10.1016/S0020-7683(03)00143-4.

[156] D. Jeulin, T. Kanit, S. Forest, Representative Volume Element: A Statistical Point of View, in: D.J. Bergman, E. Inan (Eds.), Continuum models and discrete systems: Proceedings of the NATO Advanced Research Workshop on Continuum Models and Discrete Systems, Shoresh, Israel, 30 June-4 July, 2003, Kluwer, Dordrecht, 2004, pp. 21–27.

[157] S. RANGANATHAN, M. OSTOJASTARZEWSKI, Scaling function, anisotropy and the size of RVE in elastic random polycrystals, Journal of the Mechanics and Physics of Solids 56 (2008) 2773–2791, doi: 10.1016/j.jmps.2008.05.001.

[158] S. Bargmann, B. Klusemann, J. Markmann, J.E. Schnabel, K. Schneider, C. Soyarslan, J. Wilmers, Generation of 3D representative volume elements for heterogeneous materials, Progress in Materials Science 96 (2018) 322–384, doi: 10.1016/j.pmatsci.2018.02.003.

[159] I.M. Gitman, H. Askes, L.J. Sluys, Representative volume: Existence and size determination, Engineering Fracture Mechanics 74 (2007) 2518–2534, doi: 10.1016/j.engfracmech.2006.12.021.

[160] A. Brahme, M.H. Alvi, D. Saylor, J. Fridy, A.D. Rollett, 3D reconstruction of microstructure in a commercial purity aluminum, Scripta Materialia 55 (2006) 75–80, doi: 10.1016/j.scriptamat.2006.02.017.

[161] F. Roters, P. Eisenlohr, T.R. Bieler, D. Raabe, Crystal Plasticity Finite Element Methods, Wiley-VCH Verlag GmbH & Co. KGaA, Weinheim, Germany, 2010.

[162] R. Becker, Analysis of texture evolution in channel die compression—I. Effects of grain interaction, Acta Metallurgica et Materialia 39 (1991) 1211–1230, doi: 10.1016/0956-7151(91)90209-J.

[163] F. Barbe, L. Decker, D. Jeulin, G. Cailletaud, Intergranular and intragranular behavior of polycrystalline aggregates. Part 1: F.E. model, International Journal of Plasticity 17 (2001) 513–536, doi: 10.1016/S0749-6419(00)00061-9.

[164] D.P. Mika, P.R. Dawson, Polycrystal plasticity modeling of intracrystalline boundary textures, Acta Materialia 47 (1999) 1355–1369, doi: 10.1016/S1359-6454(98)00386-3.

[165] D.P. Mika, P.R. Dawson, Effects of grain interaction on deformation in polycrystals, Materials Science and Engineering: A 257 (1998) 62–76, doi: 10.1016/S0921-5093(98)00824-7.

[166] A.J. Beaudoin, K.K. Mathur, P.R. Dawson, G.C. Johnson, Three-dimensional deformation process simulation with explicit use of polycrystal plasticity models, International Journal of Plasticity 9 (1993) 833–860, doi: 10.1016/0749-6419(93)90054-T.

[167] A.J. Beaudoin, P.R. Dawson, K.K. Mathur, U.F. Kocks, A hybrid finite element formulation for polycrystal plasticity with consideration of macrostructural and microstructural linking, International Journal of Plasticity 11 (1995) 501–521, doi: 10.1016/S0749-6419(99)80003-5.

[168] C. Miehe, J. Schröder, J. Schotte, Computational homogenization analysis in finite plasticity Simulation of texture development in polycrystalline materials, Computer Methods in Applied Mechanics and Engineering 171 (1999) 387–418, doi: 10.1016/S0045-7825(98)00218-7.

[169] F. Delaire, J.L. Raphanel, C. Rey, Plastic heterogeneities of a copper multicrystal deformed in uniaxial tension: experimental study and finite element simulations, Acta Materialia 48 (2000) 1075–1087, doi: 10.1016/S1359-6454(99)00408-5.

[170] E.B. Marin, P.R. Dawson, Elastoplastic finite element analyses of metal deformations using polycrystal constitutive models, Computer Methods in Applied Mechanics and Engineering 165 (1998) 23–41, doi: 10.1016/S0045-7825(98)00033-4.

[171] E.B. Marin, P.R. Dawson, On modelling the elasto-viscoplastic response of metals using polycrystal plasticity, Computer Methods in Applied Mechanics and Engineering 165 (1998) 1–21, doi: 10.1016/S0045-7825(98)00034-6.

[172] R. A. Lebensohn, N-site modeling of a 3D viscoplastic polycrystal using Fast Fourier Transform, Acta Materialia 49 (2001) 2723–2737, doi: 10.1016/S1359-6454(01)00172-0.

[173] H. Moulinec, P. Suquet, A numerical method for computing the overall response of nonlinear composites with complex microstructure, Computer Methods in Applied Mechanics and Engineering 157 (1998) 69–94, doi: 10.1016/S0045-7825(97)00218-1.

[174] P. Eisenlohr, M. Diehl, R.A. Lebensohn, F. Roters, A spectral method solution to crystal elasto-viscoplasticity at finite strains, International Journal of Plasticity 46 (2013) 37–53, doi: 10.1016/j.ijplas.2012.09.012.

[175] A. Prakash, R.A. Lebensohn, Simulation of micromechanical behavior of polycrystals: finite elements versus fast Fourier transforms, Modelling Simul. Mater. Sci. Eng. 17 (2009) 64010, doi: 10.1088/0965-0393/17/6/064010.

[176] A.K. Kanjarla, R.A. Lebensohn, L. Balogh, C.N. Tomé, Study of internal lattice strain distributions in stainless steel using a full-field elasto-viscoplastic formulation based on fast Fourier transforms, Acta Materialia 60 (2012) 3094–3106, doi: 10.1016/j.actamat.2012.02.014.

[177] F. Grennerat, M. Montagnat, O. Castelnau, P. Vacher, H. Moulinec, P. Suquet, P. Duval, Experimental characterization of the intragranular strain field in columnar ice during transient creep, Acta Materialia 60 (2012) 3655–3666, doi: 10.1016/j.actamat.2012.03.025.

[178] J.C. Michel, H. Moulinec, P. Suquet, Effective properties of composite materials with periodic microstructure: a computational approach, Computer Methods in Applied Mechanics and Engineering 172 (1999) 109–143, doi: 10.1016/S0045-7825(98)00227-8.

[179] P. Suquet, H. Moulinec, O. Castelnau, M. Montagnat, N. Lahellec, F. Grennerat, P. Duval et al., Multi-scale modeling of the mechanical behavior of polycrystalline ice under transient creep, Procedia IUTAM 3 (2012) 76–90, doi: 10.1016/j.piutam.2012.03.006.

[180] M. Schneider, An FFT-based fast gradient method for elastic and inelastic unit cell homogenization problems, Computer Methods in Applied Mechanics and Engineering 315 (2017) 846–866, doi: 10.1016/j.cma.2016.11.004.

[181] M. Kabel, S. Fliegener, M. Schneider, Mixed boundary conditions for FFT-based homogenization at finite strains, Comput Mech 57 (2016) 193–210, doi: 10.1007/s00466-015-1227-1.

[182] V. Monchiet, G. Bonnet, Numerical homogenization of nonlinear composites with a polarization-based FFT iterative scheme, Computational Materials Science 79 (2013) 276–283, doi: 10.1016/j.commatsci.2013.04.035.

[183] S. Brisard, L. Dormieux, Combining Galerkin approximation techniques with the principle of Hashin and Shtrikman to derive a new FFT-based numerical method for the homogenization of composites, Computer Methods in Applied Mechanics and Engineering 217-220 (2012) 197–212, doi: 10.1016/j.cma.2012.01.003.

[184] S. Brisard, L. Dormieux, FFT-based methods for the mechanics of composites: A general variational framework, Computational Materials Science 49 (2010) 663–671, doi: 10.1016/j.commatsci.2010.06.009.

[185] D.J. Eyre, G.W. Milton, A fast numerical scheme for computing the response of composites using grid refinement, Eur. Phys. J. AP 6 (1999) 41–47, doi: 10.1051/epjap:1999150.

[186] P. Shanthraj, P. Eisenlohr, M. Diehl, F. Roters, Numerically robust spectral methods for crystal plasticity simulations of heterogeneous materials, International Journal of Plasticity 66 (2015) 31–45, doi: 10.1016/j.ijplas.2014.02.006.

[187] S. Lucarini, J. Segurado, On the accuracy of spectral solvers for micromechanics based fatigue modeling, Comput Mech 63 (2019) 365–382, doi: 10.1007/s00466-018-1598-1.

[188] R.A. Lebensohn, A. Needleman, Numerical implementation of non-local polycrystal plasticity using fast Fourier transforms, Journal of the Mechanics and Physics of Solids 97 (2016) 333–351, doi: 10.1016/j.jmps.2016.03.023.

[189] M.V. Upadhyay, L. Capolungo, V. Taupin, C. Fressengeas, R.A. Lebensohn, A higher order elasto-viscoplastic model using fast Fourier transforms: Effects of lattice curvatures on mechanical response of nanocrystalline metals, International Journal of Plasticity 83 (2016) 126–152, doi: 10.1016/j.ijplas.2016.04.007.

[190] A. Vidyasagar, A.D. Tutcuoglu, D.M. Kochmann, Deformation patterning in finite-strain crystal plasticity by spectral homogenization with application to magnesium, Computer Methods in Applied Mechanics and Engineering 335 (2018) 584–609, doi: 10.1016/j.cma.2018.03.003.

[191] R.A. Lebensohn, A.K. Kanjarla, P. Eisenlohr, An elasto-viscoplastic formulation based on fast Fourier transforms for the prediction of micromechanical fields in polycrystalline materials, International Journal of Plasticity 32-33 (2012) 59–69, doi: 10.1016/j.ijplas.2011.12.005.

[192] J.C. Michel, H. Moulinec, P. Suquet, A computational scheme for linear and non-linear composites with arbitrary phase contrast, Int. J. Numer. Meth. Engng 52 (2001) 139–160, doi: 10.1002/nme.275.

[193] K.S. Djaka, S. Berbenni, V. Taupin, R.A. Lebensohn, A FFT-based numerical implementation of mesoscale field dislocation mechanics: Application to two-phase laminates, International Journal of Solids and Structures 184 (2020) 136–152, doi: 10.1016/j.ijsolstr.2018.12.027.

[194] R.A. Lebensohn, A.D. Rollett, Spectral methods for full-field micromechanical modelling of polycrystalline materials, Computational Materials Science 173 (2020) 109336, doi: 10.1016/j.commatsci.2019.109336.

[195] J.S. Nagra, A. Brahme, R.A. Lebensohn, K. Inal, Efficient fast Fourier transform-based numerical implementation to simulate large strain behavior of polycrystalline materials, International Journal of Plasticity 98 (2017) 65–82, doi: 10.1016/j.ijplas.2017.07.001.

[196] H. Moulinec, P. Suquet, A fast numerical method for computing the linear and nonlinear mechanical properties of composites., Comptes rendus de l'Académie des sciences. Série II, Mécanique, physique, chimie, astronomie 318 (1994) 1417–1423.

[197] N. Lahellec, J.C. Michel, H. Moulinec, P. Suquet, Analysis of Inhomogeneous Materials at Large Strains using Fast Fourier Transforms, in: C. Miehe (Ed.), IUTAM symposium on computational mechanics of solid materials at large strains, Springer, Dordrecht, London, 2001, pp. 247–258.

[198] E. Arzt, Size effects in materials due to microstructural and dimensional constraints: a comparative review, Acta Materialia 46 (1998) 5611–5626, doi: 10.1016/S1359-6454(98)00231-6.

[199] R.W. Armstrong, The influence of polycrystal grain size on several mechanical properties of materials, Metall and Materi Trans 1 (1970) 1169–1176, doi: 10.1007/BF02900227.

[200] J. Gil Sevillano, I. Ocaña Arizcorreta, L.P. Kubin, Intrinsic size effects in plasticity by dislocation glide, Materials Science and Engineering: A 309-310 (2001) 393–405, doi: 10.1016/S0921-5093(00)01733-0.

[201] E. Orowan, Die erhhte Festigkeit dnner Fden, der Joff-Effekt und verwandte Erscheinungen vom Standpunkt der Griffithschen Bruchtheorie, Z. Physik 86 (1933) 195–213, doi: 10.1007/BF01343285.

[202] G.I. Taylor, The Mechanism of Plastic Deformation of Crystals. Part I. Theoretical, Proceedings of the Royal Society A: Mathematical, Physical and Engineering Sciences 145 (1934) 362–387, doi: 10.1098/rspa.1934.0106.

[203] L. BRAGG, A Theory of the Strength of Metals, Nature 149 (1942) 511–513, doi: 10.1038/149511a0.

[204] C. Zener, A Theoretical Criterion for the Initiation of Slip Bands, Phys. Rev. 69 (1946) 128–129, doi: 10.1103/PhysRev.69.128.2.

[205] E.O. Hall, Variation of Hardness of Metals with Grain Size, Nature 173 (1954) 948–949, doi: 10.1038/173948b0.

[206] E.O. Hall, The Deformation and Ageing of Mild Steel: III Discussion of Results, Proceedings of the Physical Society 64 (1951) 747.

[207] N.J. Petch, The cleavage strength of polycrystals, J. Iron Steel Inst. 174 (1953) 25–28.

[208] N.J. Petch, XVI. The ductile fracture of polycrystalline α-iron, Philosophical Magazine 1 (1956) 186–190, doi: 10.1080/14786435608238091.

[209] J.D. Eshelby, F.C. Frank, F.R.N. Nabarro, XLI. The equilibrium of linear arrays of dislocations, The London, Edinburgh, and Dublin Philosophical Magazine and Journal of Science 42 (1951) 351–364, doi: 10.1080/14786445108561060.

[210] G. Leibfried, Verteilung von Versetzungen im statischen Gleichgewicht, Z. Physik 130 (1951) 214–226, doi: 10.1007/BF01337695.

[211] M.A. Meyers, E. Ashworth, A model for the effect of grain size on the yield stress of metals, Philosophical Magazine A 46 (1982) 737–759, doi: 10.1080/01418618208236928.

[212] H. Conrad, S. Feuerstein, L. Rice, Effects of grain size on the dislocation density and flow stress of niobium, Materials Science and Engineering 2 (1967) 157–168, doi: 10.1016/0025-5416(67)90032-8.

[213] J.C.M. Li, Petch relation and grain boundary sources, Trans AIME 227 (1963) 239.

[214] H. Conrad, Effect of grain size on the lower yield and flow stress of iron and steel, Acta Metallurgica 11 (1963) 75–77.

[215] A.H. Cottrell, Theory of brittle fracture in steel and similar metals, Trans. Met. Soc. AIME 212 (1958).

[216] R. Armstrong, I. Codd, R.M. Douthwaite, N.J. Petch, The plastic deformation of polycrystalline aggregates, Philosophical Magazine 7 (1962) 45–58, doi: 10.1080/14786436208201857.

[217] E. Smith, P.J. Worthington, The effect of orientation on the grain size dependence of the yield strength of metals, Philosophical Magazine 9 (1964) 211–216, doi: 10.1080/14786436408229186.

[218] A. Navarro, E.R. de los Rios, An alternative model of the blocking of dislocations at grain boundaries, Philosophical Magazine A 57 (1988) 37–42, doi: 10.1080/01418618808204497.

[219] L.H. Friedman, D.C. Chrzan, Continuum analysis of dislocation pile-ups: Influence of sources, Philosophical Magazine A 77 (1998) 1185–1204, doi: 10.1080/01418619808214247.

[220] V. Bata, E.V. Pereloma, An alternative physical explanation of the Hall–Petch relation, Acta Materialia 52 (2004) 657–665, doi: 10.1016/j.actamat.2003.10.002.

[221] M.F. Ashby, The deformation of plastically non-homogeneous materials, Philosophical Magazine 21 (1970) 399–424, doi: 10.1080/14786437008238426.

[222] A.W. Thompson, M.I. Baskes, W.F. Flanagan, The dependence of polycrystal work hardening on grain size, Acta Metallurgica 21 (1973) 1017–1028, doi: 10.1016/0001-6160(73)90158-2.

[223] J.D. Meakin, N.J. Petch, Strain-hardening of polycrystals: The α-brasses, Philosophical Magazine 29 (1974) 1149–1156, doi: 10.1080/14786437408226599.

[224] Z.C. Cordero, B.E. Knight, C.A. Schuh, Six decades of the Hall–Petch effect – a survey of grain-size strengthening studies on pure metals, International Materials Reviews 61 (2016) 495–512, doi: 10.1080/09506608.2016.1191808.

[225] H. Margolin, M. Stefan Stanescu, Polycrystalline strengthening, Acta Metallurgica 23 (1975) 1411–1418, doi: 10.1016/0001-6160(75)90150-9.

[226] H.-H. Fu, D.J. Benson, M.A. Meyers, Analytical and computational description of effect of grain size on yield stress of metals, Acta Materialia 49 (2001) 2567–2582, doi: 10.1016/S1359-6454(01)00062-3.

[227] L.E. Murr, Yielding and grain-boundary ledges: Some comments on the Hall-Petch relation, Appl. Phys. Lett. 24 (1974) 533–536, doi: 10.1063/1.1655042.

[228] J.A. Wert, Comments on "An alternative physical explanation of the Hall–Petch relation", Scripta Materialia 50 (2004) 1487–1490, doi: 10.1016/j.scriptamat.2004.02.017.

[229] V. Bata, E.V. Pereloma, Reply to comment on "An alternate physical explanation of the Hall–Petch relation", Scripta Materialia 51 (2004) 927–929, doi: 10.1016/j.scriptamat.2004.06.035.

[230] J.P. Hirth, J. Lothe, Theory of dislocations, Krieger Pub. Co, Malabar FL, 1969.

[231] J.P. Hirth, The influence of grain boundaries on mechanical properties, MTA 3 (1972) 3047–3067, doi: 10.1007/BF02661312.

[232] J.C.M. Li, Y.T. Chou, The role of dislocations in the flow stress grain size relationships, Metall and Materi Trans 1 (1970) 747, doi: 10.1007/BF02900225.

[233] N. Hansen, Polycrystalline strengthening, MTA 16 (1985) 2167–2190, doi: 10.1007/BF02670417.

[234] G.J. Weng, A micromechanical theory of grain-size dependence in metal plasticity, Journal of the Mechanics and Physics of Solids 31 (1983) 193–203, doi: 10.1016/0022-5096(83)90021-2.

[235] A. Lasalmonie, J.L. Strudel, Influence of grain size on the mechanical behaviour of some high strength materials, J Mater Sci 21 (1986) 1837–1852, doi: 10.1007/BF00547918.

[236] C.S. Pande, R.A. Masumura, R.W. Armstrong, Pile-up based hall-petch relation for nanoscale materials, Nanostructured Materials 2 (1993) 323–331, doi: 10.1016/0965-9773(93)90159-9.

[237] X. Feaugas, H. Haddou, Grain-size effects on tensile behavior of nickel and AISI 316L stainless steel, Metall and Mat Trans A 34 (2003) 2329–2340, doi: 10.1007/s11661-003-0296-5.

[238] R.W. Armstrong, Y.T. Chou, R.M. Fisher, N. Louat, The limiting grain size dependence of the strength of a polycrystalline aggregate, Philosophical Magazine 14 (1966) 943–951, doi: 10.1080/14786436608244765.

[239] N. Hansen, The effect of grain size and strain on the tensile flow stress of aluminium at room temperature, Acta Metallurgica 25 (1977) 863–869, doi: 10.1016/0001-6160(77)90171-7.

[240] J.D. Campbell, K.J. Marsh, The effect of grain size on the delayed yielding of mild steel, Philosophical Magazine 7 (1962) 933–952, doi: 10.1080/14786436208212890.

[241] D. Kuhlmann-Wilsdorf, The theory of dislocation-based crystal plasticity, Philosophical Magazine A 79 (1999) 955–1008, doi: 10.1080/01418619908210342.

[242] G.E. Dieter, D. Bacon, Mechanical metallurgy, McGraw-Hill, London, 1988.

[243] M. Kato, Hall–Petch Relationship and Dislocation Model for Deformation of Ultrafine-Grained and Nanocrystalline Metals, Mater. Trans. 55 (2014) 19–24, doi: 10.2320/matertrans.MA201310.

[244] D. Liu, Y. He, B. Zhang, L. Shen, A continuum theory of stress gradient plasticity based on the dislocation pile-up model, Acta Materialia 80 (2014) 350–364, doi: 10.1016/j.actamat.2014.07.043.

[245] R.W. Armstrong, Dislocation Pile-Ups, Material Strength Levels, and Thermal Activation, Metall and Mat Trans A 47 (2016) 5801–5810, doi: 10.1007/s11661-015-3161-4.

[246] S.D. Antolovich, R.W. Armstrong, Plastic strain localization in metals: origins and consequences, Progress in Materials Science 59 (2014) 1–160, doi: 10.1016/j.pmatsci.2013.06.001.

[247] R.W. Armstrong, Theory of the tensile ductile-brittle behavior of poly-crystalline h.c.p. materials, with application to beryllium, Acta Metallurgica 16 (1968) 347–355, doi: 10.1016/0001-6160(68)90021-7.

[248] A.N. Stroh, CXI. Brittle fracture and yielding, The London, Edinburgh, and Dublin Philosophical Magazine and Journal of Science 46 (1955) 968–972, doi: 10.1080/14786440908520617.

[249] J.C.M. Li, G.C.T. Liu, Circular dislocation pile-ups, Philosophical Magazine 15 (1967) 1059–1063, doi: 10.1080/14786436708221653.

[250] D.A. Konstantinidis, E.C. Aifantis, On the "Anomalous" hardness of nanocrystalline materials, Nanostructured Materials 10 (1998) 1111–1118, doi: 10.1016/S0965-9773(98)00145-7.

[251] J.E. Carsley, J. Ning, W.W. Milligan, S.A. Hackney, E.C. Aifantis, A simple, mixtures-based model for the grain size dependence of strength in nanophase metals, Nanostructured Materials 5 (1995) 441–448, doi: 10.1016/0965-9773(95)00257-F.

[252] R.W. Armstrong, in: T.N. Baker (Ed.), Yield, Flow and Fracture of Polycrystals, Applied Science Publishers, UK, 1983, pp. 1–31.

[253] A.A.W. Thompson, Yielding in nickel as a function of grain or cell size, Acta Metallurgica 23 (1975) 1337–1342, doi: 10.1016/0001-6160(75)90142-X.

[254] M.R. Staker, D.L. Holt, The dislocation cell size and dislocation density in copper deformed at temperatures between 25 and 700°C, Acta Metallurgica 20 (1972) 569–579, doi: 10.1016/0001-6160(72)90012-0.

[255] D.A. Hughes, N. Hansen, Microstructure and strength of nickel at large strains, Acta Materialia 48 (2000) 2985–3004, doi: 10.1016/S1359-6454(00)00082-3.

[256] D. Kuhlmann-Wilsdorf, Theory of plastic deformation: - properties of low energy dislocation structures, Materials Science and Engineering: A 113 (1989) 1–41, doi: 10.1016/0921-5093(89)90290-6.

[257] D. Kuhlmann-Wilsdorf, J.H. van der Merwe, Theory of dislocation cell sizes in deformed metals, Materials Science and Engineering 55 (1982) 79–83, doi: 10.1016/0025-5416(82)90086-6.

[258] H. Mughrabi, Dislocation wall and cell structures and long-range internal stresses in deformed metal crystals, Acta Metallurgica 31 (1983) 1367–1379, doi: 10.1016/0001-6160(83)90007-X.

[259] H. Mughrabi, A two-parameter description of heterogeneous dislocation distributions in deformed metal crystals, Materials Science and Engineering 85 (1987) 15–31, doi: 10.1016/0025-5416(87)90463-0.

[260] H. Mughrabi, T. Ungár, Chapter 60 Long-Range internal stresses in deformed single-phase materials: The composite model and its consequences, in: 2002, pp. 343–411.

[261] D.J. Abson, J.J. Jonas, The Hall–Petch Relation and High-Temperature Subgrains, Metal Science Journal 4 (1970) 24–28, doi: 10.1179/msc.1970.4.1.24.

[262] N. Hansen, B. Ralph, The strain and grain size dependence of the flow stress of copper, Acta Metallurgica 30 (1982) 411–417, doi: 10.1016/0001-6160(82)90221-8.

[263] N. Hansen, Hall–Petch relation and boundary strengthening, Scripta Materialia 51 (2004) 801–806, doi: 10.1016/j.scriptamat.2004.06.002.

[264] D. Kuhlmann-Wilsdorf, Chapter 59 The LES theory of solid plasticity, in: F.R.N. Nabarro, M.S. Duesbery, J.P. Hirth (Eds.), Dislocations in solids, North-Holland Pub. Co, Amsterdam, New York, 2002, pp. 211–342.

[265] X. Feaugas, On the origin of the tensile flow stress in the stainless steel AISI 316L at 300 K: back stress and effective stress, Acta Materialia 47 (1999) 3617–3632, doi: 10.1016/S1359-6454(99)00222-0.

[266] G. Langford, M. Cohen, Strain hardening of iron by severe plastic deformation, Trans. ASM 62 (1969) 623–638.

[267] G. Langford, M. Cohen, Calculation of cell-size strengthening of wire-drawn iron, Metall and Materi Trans 1 (1970) 1478–1480, doi: 10.1007/BF02900287.

[268] G. Langford, M. Cohen, Microstructural analysis by high-voltage electron diffraction of severely drawn iron wires, MTA 6 (1975) 901–910, doi: 10.1007/BF02672314.

[269] A.W. Thompson, M.I. Baskes, The influence of grain size on the work hardening of face-center cubic polycrystals, Philosophical Magazine 28 (1973) 301–308, doi: 10.1080/14786437308217454.

[270] J. de Messemaeker, B. Verlinden, J. van Humbeeck, On the strength of boundaries in submicron IF steel, Materials Letters 58 (2004) 3782–3786, doi: 10.1016/j.matlet.2004.07.026.

[271] J. Gil Sevillano, P. van Houtte, E. Aernoudt, Large strain work hardening and textures, Progress in Materials Science 25 (1980) 69–134, doi: 10.1016/0079-6425(80)90001-8.

[272] B.L. Li, W.Q. Cao, Q. Liu, W. Liu, Flow stress and microstructure of the cold-rolled IF-steel, Materials Science and Engineering: A 356 (2003) 37–42, doi: 10.1016/S0921-5093(02)00889-4.

[273] S.V. Raj, G.M. Pharr, A compilation and analysis of data for the stress dependence of the subgrain size, Materials Science and Engineering 81 (1986) 217–237, doi: 10.1016/0025-5416(86)90265-X.

[274] D. Kuhlmann-Wilsdorf, Theory of workhardening 1934-1984, MTA 16 (1985) 2091–2108, doi: 10.1007/BF02670414.

[275] D. Gómez-García, B. Devincre, L.P. Kubin, Dislocation patterns and the similitude principle: 2.5D mesoscale simulations, Phys. Rev. Lett. 96 (2006) 125503, doi: 10.1103/PhysRevLett.96.125503.

[276] G. Ananthakrishna, D. Sahoo, A model based on nonlinear oscillations to explain jumps on creep curves, J. Phys. D: Appl. Phys. 14 (1981) 2081–2090, doi: 10.1088/0022-3727/14/11/015.

[277] D. Kuhlmann-Wilsdorf, Dislocation cells, redundant dislocations and the leds hypothesis, Scripta Materialia 34 (1996) 641–650, doi: 10.1016/1359-6462(95)00567-6.

[278] D. Kuhlmann-Wilsdorf, Technological high strain deformation of 'wavy glide' metals and LEDS, Phys. Stat. Sol. (a) 149 (1995) 225–241, doi: 10.1002/pssa.2211490116.

[279] M. Zaiser, P. Hähner, The flow stress of fractal dislocation arrangements, Materials Science and Engineering: A 270 (1999) 299–307, doi: 10.1016/S0921-5093(99)00270-1.

[280] M. Zaiser, S. Sandfeld, Scaling properties of dislocation simulations in the similitude regime, Modelling Simul. Mater. Sci. Eng. 22 (2014) 65012, doi: 10.1088/0965-0393/22/6/065012.

[281] P. Hähner, M. Zaiser, Dislocation dynamics and work hardening of fractal dislocation cell structures, Materials Science and Engineering: A 272 (1999) 443–454, doi: 10.1016/S0921-5093(99)00527-4.

[282] P. Hähner, K. Bay, M. Zaiser, Fractal Dislocation Patterning During Plastic Deformation, Physical review letters 81 (1998) 2470–2473, doi: 10.1103/PhysRevLett.81.2470.

[283] M. Zaiser, K. Bay, P. Hähner, Fractal analysis of deformation-induced dislocation patterns, Acta Materialia 47 (1999) 2463–2476, doi: 10.1016/S1359-6454(99)00096-8.

[284] P. Hähner, A theory of dislocation cell formation based on stochastic dislocation dynamics, Acta Materialia 44 (1996) 2345–2352, doi: 10.1016/1359-6454(95)00364-9.

[285] X. Feaugas, H. Haddou, Effects of grain size on dislocation organization and internal stresses developed under tensile loading in fcc metals, Phil. Mag. 87 (2007) 989–1018, doi: 10.1080/14786430601019441.

[286] M. Sauzay, L.P. Kubin, Scaling laws for dislocation microstructures in monotonic and cyclic deformation of fcc metals, Progress in Materials Science 56 (2011) 725–784, doi: 10.1016/j.pmatsci.2011.01.006.

[287] P. Franciosi, M. Berveiller, A. Zaoui, Latent hardening in copper and aluminium single crystals, Acta Metallurgica 28 (1980) 273–283, doi: 10.1016/0001-6160(80)90162-5.

[288] L. Kubin, B. Devincre, T. Hoc, Modeling dislocation storage rates and mean free paths in face-centered cubic crystals, Acta Materialia 56 (2008) 6040–6049, doi: 10.1016/j.actamat.2008.08.012.

[289] S. Queyreau, G. Monnet, B. Devincre, Slip systems interactions in α-iron determined by dislocation dynamics simulations, International Journal of Plasticity 25 (2009) 361–377, doi: 10.1016/j.ijplas.2007.12.009.

[290] B. Devincre, T. Hoc, L. Kubin, Dislocation mean free paths and strain hardening of crystals, Science (New York, N.Y.) 320 (2008) 1745–1748, doi: 10.1126/science.1156101.

[291] F.R.N. Nabarro, Z.S. Basinski, D.B. Holt, The plasticity of pure single crystals, Advances in Physics 13 (1964) 193–323, doi: 10.1080/00018736400101031.

[292] J.E. Bailey, P.B. Hirsch, The dislocation distribution, flow stress, and stored energy in cold-worked polycrystalline silver, Philosophical Magazine 5 (1960) 485–497, doi: 10.1080/14786436008238300.

[293] J.W. Edington, R.E. Smallman, The relationship between flow stress and dislocation density in deformed vanadium, Acta Metallurgica 12 (1964) 1313–1328, doi: 10.1016/0001-6160(64)90120-8.

[294] J.E. Bailey, The dislocation density, flow stress and stored energy in deformed polycrystalline copper, Philosophical Magazine 8 (1963) 223–236, doi: 10.1080/14786436308211120.

[295] R. Madec, B. Devincre, L.P. Kubin, From dislocation junctions to forest hardening, Phys. Rev. Lett. 89 (2002) 255508, doi: 10.1103/PhysRevLett.89.255508.

[296] R. Madec, L.P. Kubin, Second-order junctions and strain hardening in bcc and fcc crystals, Scripta Materialia 58 (2008) 767–770, doi: 10.1016/j.scriptamat.2007.12.032.

[297] B. Devincre, L. Kubin, T. Hoc, Physical analyses of crystal plasticity by DD simulations, Scripta Materialia 54 (2006) 741–746, doi: 10.1016/j.scriptamat.2005.10.066.

[298] V.V. Bulatov, L.L. Hsiung, M. Tang, A. Arsenlis, M.C. Bartelt, W. Cai, J.N. Florando et al., Dislocation multi-junctions and strain hardening, Nature 440 (2006) 1174–1178, doi: 10.1038/nature04658.

[299] R. Madec, B. Devincre, L. Kubin, T. Hoc, D. Rodney, The role of collinear interaction in dislocation-induced hardening, Science (New York, N.Y.) 301 (2003) 1879–1882, doi: 10.1126/science.1085477.

[300] G. Schoeck, R. Frydman, The Contribution of the Dislocation Forest to the Flow Stress, phys. stat. sol. (b) 53 (1972) 661–673, doi: 10.1002/pssb.2220530227.

[301] U.F. Kocks, A statistical theory of flow stress and work-hardening, Philosophical Magazine 13 (1966) 541–566, doi: 10.1080/14786436608212647.

[302] U.F. Kocks, H. Mecking, Physics and phenomenology of strain hardening, Progress in Materials Science 48 (2003) 171–273, doi: 10.1016/S0079-6425(02)00003-8.

[303] Y. Estrin, Dislocation theory based constitutive modelling, Journal of Materials Processing Technology 80-81 (1998) 33–39, doi: 10.1016/S0924-0136(98)00208-8.

[304] O. Bouaziz, N. Guelton, Modelling of TWIP effect on work-hardening, Materials Science and Engineering: A 319-321 (2001) 246–249, doi: 10.1016/S0921-5093(00)02019-0.

[305] S. Allain, J.-P. Chateau, O. Bouaziz, A physical model of the twinning-induced plasticity effect in a high manganese austenitic steel, Materials Science and Engineering: A 387-389 (2004) 143–147, doi: 10.1016/j.msea.2004.01.060.

[306] W.T. Read, XVI. Scattering of electrons by charged dislocations in semiconductors, The London, Edinburgh, and Dublin Philosophical Magazine and Journal of Science 46 (1955) 111–131, doi: 10.1080/14786440208520556.

[307] F. Roters, D. Raabe, G. Gottstein, Work hardening in heterogeneous alloys—a microstructural approach based on three internal state variables, Acta Materialia 48 (2000) 4181–4189, doi: 10.1016/S1359-6454(00)00289-5.

[308] U.F. Kocks, On the spacing of dispersed obstacles, Acta Metallurgica 14 (1966) 1629–1631, doi: 10.1016/0001-6160(66)90185-4.

[309] R.L. Fullman, Measurement of Particle Sizes in Opaque Bodies, Trans AIME 5 (1953) 447–452, doi: 10.1007/BF03398971.

[310] S.B. Biner, J.R. Morris, The effects of grain size and dislocation source density on the strengthening behaviour of polycrystals: a two-dimensional discrete dislocation simulation, Phil. Mag. 83 (2003) 3677–3690, doi: 10.1080/14786430310001599414.

[311] S.B. Biner, J.R. Morris, A two-dimensional discrete dislocation simulation of the effect of grain size on strengthening behaviour, Int. J. Numer. Meth. Engng 10 (2002) 617–635, doi: 10.1088/0965-0393/10/6/303.

[312] D.S. Balint, V.S. Deshpande, A. Needleman, E. van der Giessen, A discrete dislocation plasticity analysis of grain-size strengthening, Materials Science and Engineering: A 400-401 (2005) 186–190, doi: 10.1016/j.msea.2005.02.082.

[313] S. Lefebvre, B. Devincre, T. Hoc, Yield stress strengthening in ultrafine-grained metals: A two-dimensional simulation of dislocation dynamics, Journal of the Mechanics and Physics of Solids 55 (2007) 788–802, doi: 10.1016/j.jmps.2006.10.002.

[314] S. Lefebvre, B. Devincre, T. Hoc, Simulation of the Hall–Petch effect in ultra-fine grained copper, Materials Science and Engineering: A 400-401 (2005) 150–153, doi: 10.1016/j.msea.2005.02.067.

[315] D.S. Balint, V.S. Deshpande, A. Needleman, E. van der Giessen, Discrete dislocation plasticity analysis of the grain size dependence of the flow strength of polycrystals, International Journal of Plasticity 24 (2008) 2149–2172, doi: 10.1016/j.ijplas.2007.08.005.

[316] C.W. Sinclair, W.J. Poole, Y. Bréchet, A model for the grain size dependent work hardening of copper, Scripta Materialia 55 (2006) 739–742, doi: 10.1016/j.scriptamat.2006.05.018.

[317] Y. Estrin, H. Mecking, A unified phenomenological description of work hardening and creep based on one-parameter models, Acta Metallurgica 32 (1984) 57–70, doi: 10.1016/0001-6160(84)90202-5.

[318] L.E. Murr, S.S. Hecker, Quantitative evidence for dislocation emission from grain boundaries, Scripta Metallurgica 13 (1979) 167–171, doi: 10.1016/0036-9748(79)90286-2.

[319] C.W. Price, J.P. Hirth, A mechanism for the generation of screw dislocations from grain-boundary ledges, Materials Science and Engineering 9 (1972) 15–18, doi: 10.1016/0025-5416(72)90005-5.

[320] T. Narutani, J. Takamura, Grain-size strengthening in terms of dislocation density measured by resistivity, Acta Metallurgica et Materialia 39 (1991) 2037–2049, doi: 10.1016/0956-7151(91)90173-X.

[321] J.E. Flinn, D.P. Field, G.E. Korth, T.M. Lillo, J. Macheret, The flow stress behavior of OFHC polycrystalline copper, Acta Materialia 49 (2001) 2065–2074, doi: 10.1016/S1359-6454(01)00102-1.

[322] L.E. Murr, Some observations of grain boundary ledges and ledges as dislocation sources in metals and alloys, MTA 6 (1975) 505–513, doi: 10.1007/BF02658408.

[323] L.E. Murr, Strain-induced dislocation emission from grain boundaries in stainless steel, Materials Science and Engineering 51 (1981) 71–79, doi: 10.1016/0025-5416(81)90108-7.
[324] G. Buzzichelli, A. Mascanzoni, On the generation and motion of grain boundary dislocations in steel, Philosophical Magazine 24 (1971) 497–508, doi: 10.1080/14786437108217024.
[325] W.E. Carrington, D. McLean, Slip nuclei in silicon-iron, Acta Metallurgica 13 (1965) 493–499, doi: 10.1016/0001-6160(65)90099-4.
[326] P.J. Worthington, E. Smith, The formation of slip bands in polycrystalline 3% silicon iron in the pre-yield microstrain region, Acta Metallurgica 12 (1964) 1277–1281, doi: 10.1016/0001-6160(64)90112-9.
[327] K.J. Kurzydlowski, R.A. Varin, W. Zielinski, In situ investigation of the early stages of plastic deformation in an austenitic stainless steel, Acta Metallurgica 32 (1984) 71–78, doi: 10.1016/0001-6160(84)90203-7.
[328] A.W. Thompson, Effect of grain size on work hardening in nickel, Acta Metallurgica 25 (1977) 83–86, doi: 10.1016/0001-6160(77)90249-8.
[329] R.A. Rubio, S. Haouala, J. LLorca, Grain boundary strengthening of FCC polycrystals, J. Mater. Res. 34 (2019) 2263–2274, doi: 10.1557/jmr.2019.58.
[330] S. Haouala, S. Lucarini, J. LLorca, J. Segurado, Simulation of the Hall-Petch effect in FCC polycrystals by means of strain gradient crystal plasticity and FFT homogenization, Journal of the Mechanics and Physics of Solids (2019) 103755, doi: 10.1016/j.jmps.2019.103755.
[331] S. Haouala, J. Segurado, J. LLorca, An analysis of the influence of grain size on the strength of FCC polycrystals by means of computational homogenization, Acta Materialia 148 (2018) 72–85, doi: 10.1016/j.actamat.2018.01.024.
[332] T.L. Johnston, C.E. Feltner, Grain size effects in the strain hardening of polycrystals, Metall and Materi Trans 1 (1970) 45, doi: 10.1007/BF02900226.
[333] P. Hähner, L.P. Kubin, Coherent Propagative Structures in Plastic Deformation: A Theory of Lüders Bands in Polycrystals, SSP 23-24 (1992) 385–402, doi: 10.4028/www.scientific.net/SSP.23-24.385.
[334] L.P. Evers, D.M. Parks, W.A.M. Brekelmans, M.G.D. Geers, Crystal plasticity model with enhanced hardening by geometrically necessary dislocation accumulation, Journal of the Mechanics and Physics of Solids 50 (2002) 2403–2424, doi: 10.1016/S0022-5096(02)00032-7.
[335] L.P. Evers, W.A.M. Brekelmans, M.G.D. Geers, Scale dependent crystal plasticity framework with dislocation density and grain boundary effects, International Journal of Solids and Structures 41 (2004) 5209–5230, doi: 10.1016/j.ijsolstr.2004.04.021.
[336] U. Borg, A strain gradient crystal plasticity analysis of grain size effects in polycrystals, European Journal of Mechanics - A/Solids 26 (2007) 313–324, doi: 10.1016/j.euromechsol.2006.09.006.
[337] T.C. Lee, I.M. Robertson, H.K. Birnbaum, Interaction of dislocations with grain boundaries in Ni3Al, Acta Metallurgica et Materialia 40 (1992) 2569–2579, doi: 10.1016/0956-7151(92)90326-A.
[338] M. Ekh, M. Grymer, K. Runesson, T. Svedberg, Gradient crystal plasticity as part of the computational modelling of polycrystals, Int. J. Numer. Meth. Engng 72 (2007) 197–220, doi: 10.1002/nme.2015.
[339] S. Puri, A. Roy, A. Acharya, D. Dimiduk, Modeling dislocation sources and size effects at initial yield in continuum plasticity, JOMMS 4 (2009) 1603–1618, doi: 10.2140/jomms.2009.4.1603.
[340] K.S. Cheong, E.P. Busso, A. Arsenlis, A study of microstructural length scale effects on the behaviour of FCC polycrystals using strain gradient concepts, International Journal of Plasticity 21 (2005) 1797–1814, doi: 10.1016/j.ijplas.2004.11.001.
[341] S. Bargmann, M. Ekh, K. Runesson, B. Svendsen, Modeling of polycrystals with gradient crystal plasticity: A comparison of strategies, Phil. Mag. 90 (2010) 1263–1288, doi: 10.1080/14786430903334332.
[342] S. Berbenni, V. Taupin, R.A. Lebensohn, A fast Fourier transform-based mesoscale field dislocation mechanics study of grain size effects and reversible plasticity in polycrystals, Journal of the Mechanics and Physics of Solids (2019) 103808, doi: 10.1016/j.jmps.2019.103808.
[343] A. Acharya, A.J. Beaudoin, Grain-size effect in viscoplastic polycrystals at moderate strains, Journal of the Mechanics and Physics of Solids 48 (2000) 2213–2230, doi: 10.1016/S0022-5096(00)00013-2.
[344] T. Ohashi, M. Kawamukai, H. Zbib, A multiscale approach for modeling scale-dependent yield stress in polycrystalline metals, International Journal of Plasticity 23 (2007) 897–914, doi: 10.1016/j.ijplas.2006.10.002.

[345] D. Kuhlmann-Wilsdorf, N. Hansen, Geometrically necessary, incidental and subgrain boundaries, Scripta Metallurgica et Materialia 25 (1991) 1557–1562, doi: 10.1016/0956-716X(91)90451-6.

[346] D.A. Hughes, N. Hansen, D.J. Bammann, Geometrically necessary boundaries, incidental dislocation boundaries and geometrically necessary dislocations, Scripta Materialia 48 (2003) 147–153, doi: 10.1016/S1359-6462(02)00358-5.

[347] D.A. Hughes, Q. Liu, D.C. Chrzan, N. Hansen, Scaling of microstructural parameters, Acta Materialia 45 (1997) 105–112, doi: 10.1016/S1359-6454(96)00153-X.

[348] C. Hong, X. Huang, G. Winther, Dislocation content of geometrically necessary boundaries aligned with slip planes in rolled aluminium, Philosophical Magazine 93 (2013) 3118–3141, doi: 10.1080/14786435.2013.805270.

[349] D.A. Hughes, N. Hansen, Deformation structures developing on fine scales, Phil. Mag. 83 (2003) 3871–3893, doi: 10.1080/14786430310001605560.

[350] B. Bay, N. Hansen, D.A. Hughes, D. Kuhlmann-Wilsdorf, Overview no. 96 evolution of f.c.c. deformation structures in polyslip, Acta Metallurgica et Materialia 40 (1992) 205–219, doi: 10.1016/0956-7151(92)90296-Q.

[351] B. Bay, N. Hansen, D. Kuhlmann-Wilsdorf, Deformation structures in lightly rolled pure aluminium, Materials Science and Engineering: A 113 (1989) 385–397, doi: 10.1016/0921-5093(89)90325-0.

[352] B. Bay, N. Hansen, D. Kuhlmann-Wilsdorf, Microstructural evolution in rolled aluminium, Materials Science and Engineering: A 158 (1992) 139–146, doi: 10.1016/0921-5093(92)90002-I.

[353] N. Hansen, R.F. Mehl, A. Medalist, New discoveries in deformed metals, Metall and Mat Trans A 32 (2001) 2917–2935, doi: 10.1007/s11661-001-0167-x.

[354] N. Hansen, X. Huang, W. Pantleon, G. Winther, Grain orientation and dislocation patterns, Phil. Mag. 86 (2006) 3981–3994, doi: 10.1080/14786430600654446.

[355] D.A. Hughes, Scaling of deformation-induced microstructures in fcc metals, Scripta Materialia 47 (2002) 697–703, doi: 10.1016/S1359-6462(02)00186-0.

[356] D.A. Hughes, D.C. Chrzan, Q. Liu, N. Hansen, Scaling of Misorientation Angle Distributions, Phys. Rev. Lett. 81 (1998) 4664–4667, doi: 10.1103/PhysRevLett.81.4664.

[357] D.A. Hughes, N. Hansen, High angle boundaries formed by grain subdivision mechanisms, Acta Materialia 45 (1997) 3871–3886, doi: 10.1016/S1359-6454(97)00027-X.

[358] A. Godfrey, D.A. Hughes, Scaling of the spacing of deformation induced dislocation boundaries, Acta Materialia 48 (2000) 1897–1905, doi: 10.1016/S1359-6454(99)00474-7.

[359] A. Godfrey, D.A. Hughes, Physical parameters linking deformation microstructures over a wide range of length scale, Scripta Materialia 51 (2004) 831–836, doi: 10.1016/j.scriptamat.2004.06.019.

[360] W. Pantleon, N. Hansen, Disorientations in dislocation boundaries: formation and spatial correlation, Materials Science and Engineering: A 309-310 (2001) 246–250, doi: 10.1016/S0921-5093(00)01762-7.

[361] H. Gao, Y. Huang, Geometrically necessary dislocation and size-dependent plasticity, Scripta Materialia 48 (2003) 113–118, doi: 10.1016/S1359-6462(02)00329-9.

[362] A. Arsenlis, D.M. Parks, Crystallographic aspects of geometrically-necessary and statistically-stored dislocation density, Acta Materialia 47 (1999) 1597–1611, doi: 10.1016/S1359-6454(99)00020-8.

[363] J.F. Nye, Some geometrical relations in dislocated crystals, Acta Metallurgica 1 (1953) 153–162, doi: 10.1016/0001-6160(53)90054-6.

[364] W. Pantleon, Resolving the geometrically necessary dislocation content by conventional electron backscattering diffraction, Scripta Materialia 58 (2008) 994–997, doi: 10.1016/j.scriptamat.2008.01.050.

[365] E. Kröner, Der fundamentale Zusammenhang zwischen Versetzungsdichte und Spannungsfunktionen, Z. Physik 142 (1955) 463–475, doi: 10.1007/BF01375082.

[366] B.S. El-Dasher, B.L. Adams, A.D. Rollett, Viewpoint: experimental recovery of geometrically necessary dislocation density in polycrystals, Scripta Materialia 48 (2003) 141–145, doi: 10.1016/S1359-6462(02)00340-8.

[367] J.W. Kysar, Y. Saito, M.S. Oztop, D. Lee, W.T. Huh, Experimental lower bounds on geometrically necessary dislocation density, International Journal of Plasticity 26 (2010) 1097–1123, doi: 10.1016/j.ijplas.2010.03.009.

[368] M. Kleman, J. Friedel, Disclinations, dislocations, and continuous defects: A reappraisal, MRS Bull. 80 (2008) 61–115, doi: 10.1103/RevModPhys.80.61.

[369] C. Fressengeas, V. Taupin, L. Capolungo, An elasto-plastic theory of dislocation and disclination fields, International Journal of Solids and Structures 48 (2011) 3499–3509, doi: 10.1016/j.ijsolstr.2011.09.002.

[370] V. Taupin, L. Capolungo, C. Fressengeas, Disclination mediated plasticity in shear-coupled boundary migration, International Journal of Plasticity 53 (2014) 179–192, doi: 10.1016/j.ijplas.2013.08.002.

[371] V. Taupin, L. Capolungo, C. Fressengeas, M. Upadhyay, B. Beausir, A mesoscopic theory of dislocation and disclination fields for grain boundary-mediated crystal plasticity, International Journal of Solids and Structures 71 (2015) 277–290, doi: 10.1016/j.ijsolstr.2015.06.031.

[372] M.V. Upadhyay, L. Capolungo, V. Taupin, C. Fressengeas, Elastic constitutive laws for incompatible crystalline media: the contributions of dislocations, disclinations and G-disclinations, Phil. Mag. 93 (2013) 794–832, doi: 10.1080/14786435.2012.733829.

[373] S. Berbenni, V. Taupin, C. Fressengeas, L. Capolungo, A Fast Fourier Transform-Based Approach for Generalized Disclination Mechanics Within a Couple Stress Theory, in: H. Altenbach, S. Forest (Eds.), Generalized continua as models for classical and advanced materials, Springer, Switzerland, 2016, pp. 47–75.

[374] A.E. Romanov, V.I. Vladimirov, Disclinations in solids, Phys. Stat. Sol. (a) 78 (1983) 11–34, doi: 10.1002/pssa.2210780102.

[375] K.-H. Anthony, Die theorie der disklinationen, Arch. Rational Mech. Anal. 39 (1970) 43–88, doi: 10.1007/BF00281418.

[376] A. Acharya, C. Fressengeas, Coupled phase transformations and plasticity as a field theory of deformation incompatibility, Int J Fract 174 (2012) 87–94, doi: 10.1007/s10704-011-9656-0.

[377] A. Acharya, C. Fressengeas, Continuum Mechanics of the Interaction of Phase Boundaries and Dislocations in Solids, in: G.-Q.G. Chen, M. Grinfeld, R.J. Knops (Eds.), Differential Geometry and Continuum Mechanics, Springer International Publishing, Cham, 2015, pp. 123–165.

[378] S. Berbenni, V. Taupin, Fast Fourier transform-based micromechanics of interfacial line defects in crystalline materials, J. Micromech. Mol. Phys. 03 (2018) 1840007, doi: 10.1142/S2424913018400076.

[379] C. Fressengeas, V. Taupin, L. Capolungo, Continuous modeling of the structure of symmetric tilt boundaries, International Journal of Solids and Structures 51 (2014) 1434–1441, doi: 10.1016/j.ijsolstr.2013.12.031.

[380] R. deWit, Linear theory of static disclinations, in: J.A. Simmons, R. deWit, R. Bullough (Eds.), Fundamental Aspects of Dislocation Theory, NBS Spec. Publ. 317, National Bureau of Standards, Washington, DC, 1970, pp. 651–680.

[381] S. Berbenni, V. Taupin, K.S. Djaka, C. Fressengeas, A numerical spectral approach for solving elastostatic field dislocation and g-disclination mechanics, International Journal of Solids and Structures 51 (2014) 4157–4175, doi: 10.1016/j.ijsolstr.2014.08.009.

[382] J.C.M. Li, Disclination model of high angle grain boundaries, Surface Science 31 (1972) 12–26, doi: 10.1016/0039-6028(72)90251-8.

[383] K.K. Shih, J.C.M. Li, Energy of grain boundaries between cusp misorientations, Surface Science 50 (1975) 109–124, doi: 10.1016/0039-6028(75)90176-4.

[384] J.D. Clayton, D.L. McDowell, D.J. Bammann, Modeling dislocations and disclinations with finite micropolar elastoplasticity, International Journal of Plasticity 22 (2006) 210–256, doi: 10.1016/j.ijplas.2004.12.001.

[385] F.C. Frank, The resultant content of dislocations in an arbitrary intercrystalline boundary, Symposium on The Plastic Deformation of Crystalline Solids, Mellon Institute, Pittsburgh,(NAVEXOS-P-834) 150 (1950).

[386] B.A. Bilby, Types of dislocation source, in: Bristol Conference Report on Defects in Crystalline Solids, The Physical Society, London, 1955.

[387] J.W. Cahn, Y. Mishin, A. Suzuki, Duality of dislocation content of grain boundaries, Phil. Mag. 86 (2006) 3965–3980, doi: 10.1080/14786430500536909.

[388] A.P. Sutton, R.W. Balluffi, Interfaces in crystalline materials, Clarendon Press, Oxford, 2009.

[389] W.T. Read, W. Shockley, Dislocation Models of Crystal Grain Boundaries, Phys. Rev. 78 (1950) 275–289, doi: 10.1103/PhysRev.78.275.

[390] J.M. Burgers, Geometrical considerations concerning the structural irregularities to be assumed in a crystal, Proc. Phys. Soc. 52 (1940) 23–33, doi: 10.1088/0959-5309/52/1/304.

[391] D.G. Brandon, The structure of high-angle grain boundaries, Acta Metallurgica 14 (1966) 1479–1484, doi: 10.1016/0001-6160(66)90168-4.

[392] J.P. Hirth, R.W. Balluffi, On grain boundary dislocations and ledges, Acta Metallurgica 21 (1973) 929–942, doi: 10.1016/0001-6160(73)90150-8.

[393] J.P. Hirth, Defect structures in grain boundaries, Acta Metallurgica 22 (1974) 1023–1031, doi: 10.1016/0001-6160(74)90027-3.

[394] G.H. Bishop, B. Chalmers, A coincidence — Ledge — Dislocation description of grain boundaries, Scripta Metallurgica 2 (1968) 133–139, doi: 10.1016/0036-9748(68)90085-9.

[395] C.V. Di Leo, J.J. Rimoli, New perspectives on the grain-size dependent yield strength of polycrystalline metals, Scripta Materialia 166 (2019) 149–153, doi: 10.1016/j.scriptamat.2019.03.019.

[396] C.F.O. Dahlberg, J. Faleskog, Strain gradient plasticity analysis of the influence of grain size and distribution on the yield strength in polycrystals, European Journal of Mechanics - A/Solids 44 (2014) 1–16, doi: 10.1016/j.euromechsol.2013.09.004.

[397] W.M. Baldwin, Yield strength of metals as a function of grain size, Acta Metallurgica 6 (1958) 139–141, doi: 10.1016/0001-6160(58)90136-6.

[398] D.J. Dunstan, A.J. Bushby, The scaling exponent in the size effect of small scale plastic deformation, International Journal of Plasticity 40 (2013) 152–162, doi: 10.1016/j.ijplas.2012.08.002.

[399] D.J. Dunstan, A.J. Bushby, Grain size dependence of the strength of metals, International Journal of Plasticity 53 (2014) 56–65, doi: 10.1016/j.ijplas.2013.07.004.

[400] Y. Li, A.J. Bushby, D.J. Dunstan, The Hall-Petch effect as a manifestation of the general size effect, Proc. R. Soc. A 472 (2016) 20150890, doi: 10.1098/rspa.2015.0890.

[401] N. Ohno, D. Okumura, Higher-order stress and grain size effects due to self-energy of geometrically necessary dislocations, Journal of the Mechanics and Physics of Solids 55 (2007) 1879–1898, doi: 10.1016/j.jmps.2007.02.007.

[402] D.J. Lloyd, L.R. Morris, Luders band deformation in a fine grained aluminium alloy, Acta Metallurgica 25 (1977) 857–861, doi: 10.1016/0001-6160(77)90170-5.

[403] J.S. Hayes, R. Keyte, P.B. Prangnell, Effect of grain size on tensile behaviour of a submicron grained Al–3 wt-%Mg alloy produced by severe deformation, Materials Science and Technology 16 (2000) 1259–1263, doi: 10.1179/026708300101507479.

[404] Y.Z. Tian, S. Gao, L.J. Zhao, S. Lu, R. Pippan, Z.F. Zhang, N. Tsuji, Remarkable transitions of yield behavior and Lüders deformation in pure Cu by changing grain sizes, Scripta Materialia 142 (2018) 88–91, doi: 10.1016/j.scriptamat.2017.08.034.

[405] C.Y. Yu, P.W. Kao, C.P. Chang, Transition of tensile deformation behaviors in ultrafine-grained aluminum, Acta Materialia 53 (2005) 4019–4028, doi: 10.1016/j.actamat.2005.05.005.

[406] N. Kamikawa, X. Huang, N. Tsuji, N. Hansen, Strengthening mechanisms in nanostructured high-purity aluminium deformed to high strain and annealed, Acta Materialia 57 (2009) 4198–4208, doi: 10.1016/j.actamat.2009.05.017.

[407] D.J. Lloyd, S.A. Court, K.M. Gatenby, Lüders elongation in AI-Mg alloy AA5182, Materials Science and Technology 13 (1997) 660–666, doi: 10.1179/mst.1997.13.8.660.

[408] D.J. Lloyd, S.A. Court, Influence of grain size on tensile properties of Al-Mg alloys, Materials Science and Technology 19 (2003) 1349–1354, doi: 10.1179/026708303225006088.

[409] N. Tsuchida, Y. Tomota, K. Nagai, K. Fukaura, A simple relationship between Lüders elongation and work-hardening rate at lower yield stress, Scripta Materialia 54 (2006) 57–60, doi: 10.1016/j.scriptamat.2005.09.011.

[410] W.B. Morrison, The effect of grain size on the stress-strain relationship in low-carbon steel, ASM Trans 59 (1966).

[411] J.F. Butler, Lüders front propagation in low carbon steels, Journal of the Mechanics and Physics of Solids 10 (1962) 313–318, doi: 10.1016/0022-5096(62)90003-0.

[412] Z.C. Wang, P.B. Prangnell, Microstructure refinement and mechanical properties of severely deformed Al–Mg–Li alloys, Materials Science and Engineering: A 328 (2002) 87–97, doi: 10.1016/S0921-5093(01)01681-1.

[413] D.J. Lloyd, Deformation of fine-grained aluminium alloys, Metal Science 14 (1980) 193–198, doi: 10.1179/msc.1980.14.5.193.

[414] B.P. Kashyap, K. Tangri, On the Hall-Petch relationship and substructural evolution in type 316L stainless steel, Acta Metallurgica et Materialia 43 (1995) 3971–3981, doi: 10.1016/0956-7151(95)00110-H.

[415] N. Tsuji, Y. Ito, Y. Saito, Y. Minamino, Strength and ductility of ultrafine grained aluminum and iron produced by ARB and annealing, Scripta Materialia 47 (2002) 893–899, doi: 10.1016/S1359-6462(02)00282-8.

[416] D. Hull, Effect of grain size and temperature on slip, twinning and fracture in 3% silicon iron, Acta Metallurgica 9 (1961) 191–204, doi: 10.1016/0001-6160(61)90069-4.

[417] E.O. Hall, Yield Point Phenomena in Metals and Alloys, Springer US, Boston, MA, 1970.

[418] G.T. Hahn, A model for yielding with special reference to the yield-point phenomena of iron and related bcc metals, Acta Metallurgica 10 (1962) 727–738, doi: 10.1016/0001-6160(62)90041-X.

[419] D.V. Wilson, Role of Grain Boundaries in the Discontinuous Yielding of Low-Carbon Steels, Metal Science Journal 1 (1967) 40–47, doi: 10.1179/msc.1967.1.1.40.

[420] D.V. Wilson, Grain-size dependence of discontinuous yielding in strain-aged steels, Acta Metallurgica 16 (1968) 743–753, doi: 10.1016/0001-6160(68)90146-6.

[421] E.O. Hall, The Deformation and Ageing of Mild Steel: II Characteristics of the L ders Deformation, Proc. Phys. Soc. B 64 (1951) 742–747, doi: 10.1088/0370-1301/64/9/302.

[422] E.O. Hall, The Deformation and Ageing of Mild Steel, Proc. Phys. Soc. B 64 (1951) 747–753, doi: 10.1088/0370-1301/64/9/303.

[423] W. Sylwestrowicz, E.O. Hall, The Deformation and Ageing of Mild Steel, Proc. Phys. Soc. B 64 (1951) 495–502, doi: 10.1088/0370-1301/64/6/305.

[424] H. Conrad, K. Jung, Effect of grain size from millimeters to nanometers on the flow stress and deformation kinetics of Ag, Materials Science and Engineering: A 391 (2005) 272–284, doi: 10.1016/j.msea.2004.08.073.

[425] H. Conrad, Grain-size dependence of the flow stress of Cu from millimeters to nanometers, Metall and Mat Trans A 35 (2004) 2681–2695, doi: 10.1007/s11661-004-0214-5.

[426] M.A. Meyers, A. Mishra, D.J. Benson, Mechanical properties of nanocrystalline materials, Progress in Materials Science 51 (2006) 427–556, doi: 10.1016/j.pmatsci.2005.08.003.

[427] H. Conrad, Mechanisms for grain size hardening and softening in Zn, Acta Materialia 50 (2002) 5067–5078, doi: 10.1016/S1359-6454(02)00357-9.

[428] C.S. Pande, K.P. Cooper, Nanomechanics of Hall–Petch relationship in nanocrystalline materials, Progress in Materials Science 54 (2009) 689–706, doi: 10.1016/j.pmatsci.2009.03.008.

[429] J. Schiøtz, K.W. Jacobsen, A maximum in the strength of nanocrystalline copper, Science (New York, N.Y.) 301 (2003) 1357–1359, doi: 10.1126/science.1086636.

[430] J.R. Trelewicz, C.A. Schuh, The Hall–Petch breakdown in nanocrystalline metals: A crossover to glass-like deformation, Acta Materialia 55 (2007) 5948–5958, doi: 10.1016/j.actamat.2007.07.020.

[431] A.H. Chokshi, A. Rosen, J. Karch, H. Gleiter, On the validity of the hall-petch relationship in nanocrystalline materials, Scripta Metallurgica 23 (1989) 1679–1683, doi: 10.1016/0036-9748(89)90342-6.

[432] T.G. Nieh, J. Wadsworth, Hall-petch relation in nanocrystalline solids, Scripta Metallurgica et Materialia 25 (1991) 955–958, doi: 10.1016/0956-716X(91)90256-Z.

[433] J.R. Weertman, Hall-Petch strengthening in nanocrystalline metals, Materials Science and Engineering: A 166 (1993) 161–167, doi: 10.1016/0921-5093(93)90319-A.

[434] N. Wang, Z. Wang, K.T. Aust, U. Erb, Effect of grain size on mechanical properties of nanocrystalline materials, Acta Metallurgica et Materialia 43 (1995) 519–528, doi: 10.1016/0956-7151(94)00253-E.

[435] R. Song, D. Ponge, D. Raabe, J.G. Speer, D.K. Matlock, Overview of processing, microstructure and mechanical properties of ultrafine grained bcc steels, Materials Science and Engineering: A 441 (2006) 1–17, doi: 10.1016/j.msea.2006.08.095.

[436] K.S. Kumar, H. van Swygenhoven, S. Suresh, Mechanical behavior of nanocrystalline metals and alloys, Acta Materialia 51 (2003) 5743–5774, doi: 10.1016/j.actamat.2003.08.032.

[437] H. Conrad, Grain size dependence of the plastic deformation kinetics in Cu, Materials Science and Engineering: A 341 (2003) 216–228, doi: 10.1016/S0921-5093(02)00238-1.

[438] H. Conrad, J. Narayan, On the grain size softening in nanocrystalline materials, Scripta Materialia 42 (2000) 1025–1030, doi: 10.1016/S1359-6462(00)00320-1.

[439] R.A. Masumura, P.M. Hazzledine, C.S. Pande, Yield stress of fine grained materials, Acta Materialia 46 (1998) 4527–4534, doi: 10.1016/S1359-6454(98)00150-5.

[440] K.A. Padmanabhan, S. Sripathi, H. Hahn, H. Gleiter, Inverse Hall–Petch effect in quasi- and nanocrystalline materials, Materials Letters 133 (2014) 151–154, doi: 10.1016/j.matlet.2014.06.153.

[441] K.A. Padmanabhan, G.P. Dinda, H. Hahn, H. Gleiter, Inverse Hall–Petch effect and grain boundary sliding controlled flow in nanocrystalline materials, Materials Science and Engineering: A 452-453 (2007) 462–468, doi: 10.1016/j.msea.2006.10.084.

[442] H. Hahn, K.A. Padmanabhan, A model for the deformation of nanocrystalline materials, Philosophical Magazine B 76 (1997) 559–571, doi: 10.1080/01418639708241122.

[443] P.G. Sanders, J.A. Eastman, J.R. Weertman, Elastic and tensile behavior of nanocrystalline copper and palladium, Acta Materialia 45 (1997) 4019–4025, doi: 10.1016/S1359-6454(97)00092-X.

[444] V.G. Gryaznov, M.Y. Gutkin, A.E. Romanov, L.I. Trusov, On the yield stress of nanocrystals, J Mater Sci 28 (1993) 4359–4365, doi: 10.1007/BF01154943.

[445] P.G. Sanders, C.J. Youngdahl, J.R. Weertman, The strength of nanocrystalline metals with and without flaws, Materials Science and Engineering: A 234-236 (1997) 77–82, doi: 10.1016/S0921-5093(97)00185-8.

[446] R.W. Armstrong, 60 Years of Hall-Petch: Past to Present Nano-Scale Connections, Mater. Trans. 55 (2014) 2–12, doi: 10.2320/matertrans.MA201302.

[447] K. Lu, M.L. Sui, An explanation to the abnormal Hall-Petch relation in nanocrystalline materials, Scripta Metallurgica et Materialia 28 (1993) 1465–1470, doi: 10.1016/0956-716X(93)90576-E.

[448] T. SHEN, R. SCHWARZ, S. FENG, J. SWADENER, J. HUANG, M. Tang, J. ZHANG et al., Effect of solute segregation on the strength of nanocrystalline alloys: Inverse Hall–Petch relation, Acta Materialia 55 (2007) 5007–5013, doi: 10.1016/j.actamat.2007.05.018.

[449] G.J. Fan, H. Choo, P.K. Liaw, E.J. Lavernia, A model for the inverse Hall–Petch relation of nanocrystalline materials, Materials Science and Engineering: A 409 (2005) 243–248, doi: 10.1016/j.msea.2005.06.073.

[450] S. Takaki, K. Kawasaki, Y. Kimura, Mechanical properties of ultra fine grained steels, Journal of Materials Processing Technology 117 (2001) 359–363, doi: 10.1016/S0924-0136(01)00797-X.

[451] T. Christman, Grain boundary strengthening exponent in conventional and ultrafine microstructures, Scripta Metallurgica et Materialia 28 (1993) 1495–1500, doi: 10.1016/0956-716X(93)90581-C.

[452] S.N. Naik, S.M. Walley, The Hall–Petch and inverse Hall–Petch relations and the hardness of nanocrystalline metals, J Mater Sci 55 (2020) 2661–2681, doi: 10.1007/s10853-019-04160-w.

[453] H.S. Kim, Y. Estrin, M.B. Bush, Plastic deformation behaviour of fine-grained materials, Acta Materialia 48 (2000) 493–504, doi: 10.1016/S1359-6454(99)00353-5.

[454] A.S. Argon, S. Yip, The strongest size, Philosophical Magazine Letters 86 (2006) 713–720, doi: 10.1080/09500830600986091.

[455] A.E. Romanov, A.L. Kolesnikova, I.A. Ovid'ko, E.C. Aifantis, Disclinations in nanocrystalline materials: Manifestation of the relay mechanism of plastic deformation, Materials Science and Engineering: A 503 (2009) 62–67, doi: 10.1016/j.msea.2008.05.053.

[456] L. Lu, X. Chen, X. Huang, K. Lu, Revealing the maximum strength in nanotwinned copper, Science (New York, N.Y.) 323 (2009) 607–610, doi: 10.1126/science.1167641.

[457] S. Takeuchi, The mechanism of the inverse Hall-Petch relation of nanocrystals, Scripta Materialia 44 (2001) 1483–1487, doi: 10.1016/S1359-6462(01)00713-8.

[458] H.W. Song, S.R. Guo, Z.Q. Hu, A coherent polycrystal model for the inverse Hall-Petch relation in nanocrystalline materials, Nanostructured Materials 11 (1999) 203–210, doi: 10.1016/S0965-9773(99)00033-1.

[459] S.L. Thomas, K. Chen, J. Han, P.K. Purohit, D.J. Srolovitz, Reconciling grain growth and shear-coupled grain boundary migration, Nature communications 8 (2017) 1764, doi: 10.1038/s41467-017-01889-3.

[460] J.W. Cahn, Y. Mishin, A. Suzuki, Coupling grain boundary motion to shear deformation, Acta Materialia 54 (2006) 4953–4975, doi: 10.1016/j.actamat.2006.08.004.

[461] H. van Swygenhoven, Grain boundaries and dislocations, Science (New York, N.Y.) 296 (2002) 66–67, doi: 10.1126/science.1071040.

[462] H. van Swygenhoven, P.M. Derlet, Grain-boundary sliding in nanocrystalline fcc metals, Phys. Rev. B 64 (2001) 1225, doi: 10.1103/PhysRevB.64.224105.

[463] R.C. Gifkins, Grain-boundary sliding and its accommodation during creep and superplasticity, MTA 7 (1976) 1225–1232, doi: 10.1007/BF02656607.

[464] R. Raj, M.F. Ashby, On grain boundary sliding and diffusional creep, MTA 2 (1971) 1113–1127, doi: 10.1007/BF02664244.

[465] Y. Mishin, M. Asta, J. Li, Atomistic modeling of interfaces and their impact on microstructure and properties, Acta Materialia 58 (2010) 1117–1151, doi: 10.1016/j.actamat.2009.10.049.

[466] S. Berbenni, B. Paliwal, M. Cherkaoui, A micromechanics-based model for shear-coupled grain boundary migration in bicrystals, International Journal of Plasticity 44 (2013) 68–94, doi: 10.1016/j.ijplas.2012.11.011.

[467] M. Upmanyu, D.J. Srolovitz, A.E. Lobkovsky, J.A. Warren, W.C. Carter, Simultaneous grain boundary migration and grain rotation, Acta Materialia 54 (2006) 1707–1719, doi: 10.1016/j.actamat.2005.11.036.

[468] A. Basak, A. Gupta, Simultaneous grain boundary motion, grain rotation, and sliding in a tricrystal, Mechanics of Materials 90 (2015) 229–242, doi: 10.1016/j.mechmat.2015.01.012.

[469] M. Winning, G. Gottstein, L.S. Shvindlerman, On the mechanisms of grain boundary migration, Acta Materialia 50 (2002) 353–363, doi: 10.1016/S1359-6454(01)00343-3.

[470] M. Winning, G. Gottstein, L.S. Shvindlerman, Stress induced grain boundary motion, Acta Materialia 49 (2001) 211–219, doi: 10.1016/S1359-6454(00)00321-9.

[471] F. Mompiou, M. Legros, D. Caillard, Direct observation and quantification of grain boundary shear-migration coupling in polycrystalline Al, J Mater Sci 46 (2011) 4308–4313, doi: 10.1007/s10853-011-5369-z.

[472] F. Mompiou, M. Legros, D. Caillard, SMIG model: A new geometrical model to quantify grain boundary-based plasticity, Acta Materialia 58 (2010) 3676–3689, doi: 10.1016/j.actamat.2010.03.003.

[473] F. Mompiou, D. Caillard, M. Legros, Grain boundary shear–migration coupling—I. In situ TEM straining experiments in Al polycrystals, Acta Materialia 57 (2009) 2198–2209, doi: 10.1016/j.actamat.2009.01.014.

[474] S.V. Bobylev, N.F. Morozov, I.A. Ovid'ko, Cooperative grain boundary sliding and migration process in nanocrystalline solids, Physical review letters 105 (2010) 55504, doi: 10.1103/PhysRevLett.105.055504.

[475] C.M.F. Rae, D.A. Smith, On the mechanisms of grain boundary migration, Philosophical Magazine A 41 (1980) 477–492, doi: 10.1080/01418618008239327.

[476] V.A. Ivanov, Y. Mishin, Dynamics of grain boundary motion coupled to shear deformation: An analytical model and its verification by molecular dynamics, Phys. Rev. B 78 (2008) 927, doi: 10.1103/PhysRevB.78.064106.

[477] D. Farkas, A. Frøseth, H. van Swygenhoven, Grain boundary migration during room temperature deformation of nanocrystalline Ni, Scripta Materialia 55 (2006) 695–698, doi: 10.1016/j.scriptamat.2006.06.032.

[478] T. Gorkaya, D.A. Molodov, G. Gottstein, Stress-driven migration of symmetrical 〈100〉 tilt grain boundaries in Al bicrystals, Acta Materialia 57 (2009) 5396–5405, doi: 10.1016/j.actamat.2009.07.036.

[479] P. Ballo, N. Kioussis, G. Lu, Grain boundary sliding and migration: Effect of temperature and vacancies, Phys. Rev. B 64 (2001) 55, doi: 10.1103/PhysRevB.64.024104.

[480] N. Chandra, P. Dang, Atomistic simulation of grain boundary sliding and migration, J Mater Sci 34 (1999) 655–666, doi: 10.1023/A:1004531706998.

[481] J. Monk, B. Hyde, D. Farkas, The role of partial grain boundary dislocations in grain boundary sliding and coupled grain boundary motion, J Mater Sci 41 (2006) 7741–7746, doi: 10.1007/s10853-006-0552-3.

[482] D. MOLODOV, V. IVANOV, G. Gottstein, Low angle tilt boundary migration coupled to shear deformation, Acta Materialia 55 (2007) 1843–1848, doi: 10.1016/j.actamat.2006.10.045.

[483] H. Zhang, D. Du, D.J. Srolovitz, Effects of boundary inclination and boundary type on shear-driven grain boundary migration, Phil. Mag. 88 (2008) 243–256, doi: 10.1080/14786430701810764.

[484] D.A. Molodov, T. Gorkaya, G. Gottstein, Dynamics of grain boundaries under applied mechanical stress, J Mater Sci 46 (2011) 4318–4326, doi: 10.1007/s10853-010-5233-6.

[485] A.V. Sergueeva, N.A. Mara, A.K. Mukherjee, Grain boundary sliding in nanomaterials at elevated temperatures, J Mater Sci 42 (2007) 1433–1438, doi: 10.1007/s10853-006-0697-0.

[486] M. Guillope, J.P. Poirier, A model for stress-induced migration of tilt grain boundaries in crystals of NaCl structure, Acta Metallurgica 28 (1980) 163–167, doi: 10.1016/0001-6160(80)90065-6.

[487] S.E. Babcock, R.W. Balluffi, Grain boundary kinetics—II. In situ observations of the role of grain boundary dislocations in high-angle boundary migration, Acta Metallurgica 37 (1989) 2367–2376, doi: 10.1016/0001-6160(89)90034-5.

[488] S.E. Babcock, R.W. Balluffi, Grain boundary kinetics—I. In situ observations of coupled grain boundary dislocation motion, crystal translation and boundary displacement, Acta Metallurgica 37 (1989) 2357–2365, doi: 10.1016/0001-6160(89)90033-3.

[489] M. Jin, A.M. Minor, E.A. Stach, J.W. Morris, Direct observation of deformation-induced grain growth during the nanoindentation of ultrafine-grained Al at room temperature, Acta Materialia 52 (2004) 5381–5387, doi: 10.1016/j.actamat.2004.07.044.

[490] D.S. Gianola, S. van Petegem, M. Legros, S. Brandstetter, H. van Swygenhoven, K.J. Hemker, Stress-assisted discontinuous grain growth and its effect on the deformation behavior of nanocrystalline aluminum thin films, Acta Materialia 54 (2006) 2253–2263, doi: 10.1016/j.actamat.2006.01.023.

[491] M. Legros, D.S. Gianola, K.J. Hemker, In situ TEM observations of fast grain-boundary motion in stressed nanocrystalline aluminum films, Acta Materialia 56 (2008) 3380–3393, doi: 10.1016/j.actamat.2008.03.032.

[492] F. Mompiou, M. Legros, A. Boé, M. Coulombier, J.-P. Raskin, T. Pardoen, Inter- and intragranular plasticity mechanisms in ultrafine-grained Al thin films: An in situ TEM study, Acta Materialia 61 (2013) 205–216, doi: 10.1016/j.actamat.2012.09.051.

[493] A. Rajabzadeh, F. Mompiou, S. Lartigue-Korinek, N. Combe, M. Legros, D.A. Molodov, The role of disconnections in deformation-coupled grain boundary migration, Acta Materialia 77 (2014) 223–235, doi: 10.1016/j.actamat.2014.05.062.

[494] M. Shiga, W. Shinoda, Stress-assisted grain boundary sliding and migration at finite temperature: A molecular dynamics study, Philosophical Magazine A 70 (2004) 665, doi: 10.1103/PhysRevB.70.054102.

[495] A.J. Haslam, D. Moldovan, V. Yamakov, D. Wolf, S.R. Phillpot, H. Gleiter, Stress-enhanced grain growth in a nanocrystalline material by molecular-dynamics simulation, Acta Materialia 51 (2003) 2097–2112, doi: 10.1016/S1359-6454(03)00011-9.

[496] C.H. Li, E.H. Edwards, J. Washburn, E.R. Parker, Stress-induced movement of crystal boundaries, Acta Metallurgica 1 (1953) 223–229, doi: 10.1016/0001-6160(53)90062-5.

[497] M. Winning, A.D. Rollett, Transition between low and high angle grain boundaries, Acta Materialia 53 (2005) 2901–2907, doi: 10.1016/j.actamat.2005.03.005.

[498] D. Caillard, F. Mompiou, M. Legros, Grain-boundary shear-migration coupling. II. Geometrical model for general boundaries, Acta Materialia 57 (2009) 2390–2402, doi: 10.1016/j.actamat.2009.01.023.

[499] C. Molteni, N. Marzari, M.C. Payne, V. Heine, Sliding Mechanisms in Aluminum Grain Boundaries, Physical review letters 79 (1997) 869–872, doi: 10.1103/PhysRevLett.79.869.

[500] K. Zhang, J.R. Weertman, J.A. Eastman, Rapid stress-driven grain coarsening in nanocrystalline Cu at ambient and cryogenic temperatures, Scripta Metallurgica et Materialia 87 (2005) 61921, doi: 10.1063/1.2008377.

[501] T. Frolov, Y. Mishin, Thermodynamics of coherent interfaces under mechanical stresses. I. Theory, Phys. Rev. B 85 (2012) 1299, doi: 10.1103/PhysRevB.85.224106.

[502] T. Frolov, Y. Mishin, Thermodynamics of coherent interfaces under mechanical stresses. II. Application to atomistic simulation of grain boundaries, Phys. Rev. B 85 (2012) 444, doi: 10.1103/PhysRevB.85.224107.

[503] Z.T. Trautt, A. Adland, A. Karma, Y. Mishin, Coupled motion of asymmetrical tilt grain boundaries: Molecular dynamics and phase field crystal simulations, Acta Materialia 60 (2012) 6528–6546, doi: 10.1016/j.actamat.2012.08.018.

[504] Y. Wei, A.F. Bower, H. Gao, Enhanced strain-rate sensitivity in fcc nanocrystals due to grain-boundary diffusion and sliding, Acta Materialia 56 (2008) 1741–1752, doi: 10.1016/j.actamat.2007.12.028.

[505] H.A. Khater, A. Serra, R.C. Pond, J.P. Hirth, The disconnection mechanism of coupled migration and shear at grain boundaries, Acta Materialia 60 (2012) 2007–2020, doi: 10.1016/j.actamat.2012.01.001.

[506] Y. Mishin, A. Suzuki, B.P. Uberuaga, A.F. Voter, Stick-slip behavior of grain boundaries studied by accelerated molecular dynamics, Appl. Phys. A 75 (2007) 1, doi: 10.1103/PhysRevB.75.224101.

[507] A. Suzuki, Y.M. Mishin, Atomic Mechanisms of Grain Boundary Motion, MSF 502 (2005) 157–162, doi: 10.4028/www.scientific.net/MSF.502.157.

[508] J. Wang, A. Misra, J.P. Hirth, Shear response of $\Sigma 3\{112\}$ twin boundaries in face-centered-cubic metals, Phys. Rev. B 83 (2011) 643, doi: 10.1103/PhysRevB.83.064106.

[509] G.J. Tucker, J.A. Zimmerman, D.L. McDowell, Shear deformation kinematics of bicrystalline grain boundaries in atomistic simulations, Modelling Simul. Mater. Sci. Eng. 18 (2010) 15002, doi: 10.1088/0965-0393/18/1/015002.

[510] K.A. Padmanabhan, J. Schlipf, Model for grain boundary sliding and its relevance to optimal structural superplasticity Part 1—Theory, Materials Science and Technology 12 (1996) 391–399, doi: 10.1179/026708396790165920.

[511] J.C.M. Li, High-Angle Tilt Boundary—A Dislocation Core Model, Journal of Applied Physics 32 (1961) 525–541, doi: 10.1063/1.1736036.

[512] A. Rajabzadeh, M. Legros, N. Combe, F. Mompiou, D.A. Molodov, Evidence of grain boundary dislocation step motion associated to shear-coupled grain boundary migration, Phil. Mag. 93 (2013) 1299–1316, doi: 10.1080/14786435.2012.760760.

[513] A. Ask, S. Forest, B. Appolaire, K. Ammar, O.U. Salman, A Cosserat crystal plasticity and phase field theory for grain boundary migration, Journal of the Mechanics and Physics of Solids 115 (2018) 167–194, doi: 10.1016/j.jmps.2018.03.006.

[514] M. GURTIN, L. Anand, Nanocrystalline grain boundaries that slip and separate: A gradient theory that accounts for grain-boundary stress and conditions at a triple-junction, Journal of the Mechanics and Physics of Solids 56 (2008) 184–199, doi: 10.1016/j.jmps.2007.09.001.

[515] C.S. Pande, R.A. Masumura, Grain growth and deformation in nanocrystalline materials, Materials Science and Engineering: A 409 (2005) 125–130, doi: 10.1016/j.msea.2005.04.058.

[516] M.Y. Gutkin, I.A. Ovid'ko, C.S. Pande, Yield stress of nanocrystalline materials: role of grain-boundary dislocations, triple junctions and Coble creep, Phil. Mag. 84 (2004) 847–863, doi: 10.1080/14786430310001616063.

[517] I.A. Ovid'ko, Deformation of nanostructures, Science (New York, N.Y.) 295 (2002) 2386, doi: 10.1126/science.1071064.

[518] D. Moldovan, V. Yamakov, D. Wolf, S.R. Phillpot, Scaling behavior of grain-rotation-induced grain growth, Phys. Rev. Lett. 89 (2002) 206101, doi: 10.1103/PhysRevLett.89.206101.

[519] M. Murayama, J.M. Howe, H. Hidaka, S. Takaki, Atomic-level observation of disclination dipoles in mechanically milled, nanocrystalline Fe, Science (New York, N.Y.) 295 (2002) 2433–2435, doi: 10.1126/science.1067430.

[520] H. Fukutomi, T. Iseki, T. Endo, T. Kamijo, Sliding behavior of coincidence grain boundaries deviating from ideal symmetric tilt relationship, Acta Metallurgica et Materialia 39 (1991) 1445–1448, doi: 10.1016/0956-7151(91)90229-T.

[521] H. van Swygenhoven, M. Spaczer, A. CARO, D. Farkas, Competing plastic deformation mechanisms in nanophase metals, Phys. Rev. B 60 (1999) 22–25, doi: 10.1103/PhysRevB.60.22.

[522] M.Y. Gutkin, I.A. Ovid'ko, Grain boundary migration as rotational deformation mode in nanocrystalline materials, Appl. Phys. Lett. 87 (2005) 251916, doi: 10.1063/1.2147721.

[523] M. DAO, L. Lu, R. ASARO, J. DEHOSSON, E. Ma, Toward a quantitative understanding of mechanical behavior of nanocrystalline metals, Acta Materialia 55 (2007) 4041–4065, doi: 10.1016/j.actamat.2007.01.038.

[524] E. Bitzek, P.M. Derlet, P.M. Anderson, H. van Swygenhoven, The stress–strain response of nanocrystalline metals: A statistical analysis of atomistic simulations, Acta Materialia 56 (2008) 4846–4857, doi: 10.1016/j.actamat.2008.05.043.

[525] E.R. Homer, S.M. Foiles, E.A. Holm, D.L. Olmsted, Phenomenology of shear-coupled grain boundary motion in symmetric tilt and general grain boundaries, Acta Materialia 61 (2013) 1048–1060, doi: 10.1016/j.actamat.2012.10.005.

[526] Molteni, Francis, Payne, Heine, First principles simulation of grain boundary sliding, Physical review letters 76 (1996) 1284–1287, doi: 10.1103/PhysRevLett.76.1284.

[527] I.A. Ovid'ko, A.G. Sheinerman, Special strain hardening mechanism and nanocrack generation in nanocrystalline materials, Appl. Phys. Lett. 90 (2007) 171927, doi: 10.1063/1.2734393.

[528] I.A. Ovid'ko, A.G. Sheinerman, E.C. Aifantis, Stress-driven migration of grain boundaries and fracture processes in nanocrystalline ceramics and metals, Acta Materialia 56 (2008) 2718–2727, doi: 10.1016/j.actamat.2008.02.004.

[529] I.A. Ovid'ko, A.G. Sheinerman, Enhanced ductility of nanomaterials through optimization of grain boundary sliding and diffusion processes, Acta Materialia 57 (2009) 2217–2228, doi: 10.1016/j.actamat.2009.01.030.

[530] J. Schäfer, K. Albe, Competing deformation mechanisms in nanocrystalline metals and alloys: Coupled motion versus grain boundary sliding, Acta Materialia 60 (2012) 6076–6085, doi: 10.1016/j.actamat.2012.07.044.

[531] Z. Shan, E.A. Stach, J.M.K. Wiezorek, J.A. Knapp, D.M. Follstaedt, S.X. Mao, Grain boundary-mediated plasticity in nanocrystalline nickel, Science (New York, N.Y.) 305 (2004) 654–657, doi: 10.1126/science.1098741.

[532] J.W. Cahn, J.E. Taylor, A unified approach to motion of grain boundaries, relative tangential translation along grain boundaries, and grain rotation, Acta Materialia 52 (2004) 4887–4898, doi: 10.1016/j.actamat.2004.02.048.

[533] D.L. Olmsted, E.A. Holm, S.M. Foiles, Survey of computed grain boundary properties in face-centered cubic metals—II: Grain boundary mobility, Acta Materialia 57 (2009) 3704–3713, doi: 10.1016/j.actamat.2009.04.015.

[534] N. Combe, F. Mompiou, M. Legros, Heterogeneous disconnection nucleation mechanisms during grain boundary migration, Phys. Rev. Materials 3 (2019), doi: 10.1103/PhysRevMaterials.3.060601.

[535] J. Schäfer, K. Albe, Influence of solutes on the competition between mesoscopic grain boundary sliding and coupled grain boundary motion, Scripta Materialia 66 (2012) 315–317, doi: 10.1016/j.scriptamat.2011.11.031.

[536] J. Han, S.L. Thomas, D.J. Srolovitz, Grain-boundary kinetics: A unified approach, Progress in Materials Science 98 (2018) 386–476, doi: 10.1016/j.pmatsci.2018.05.004.

[537] A. Karma, Z.T. Trautt, Y. Mishin, Relationship between equilibrium fluctuations and shear-coupled motion of grain boundaries, Physical review letters 109 (2012) 95501, doi: 10.1103/PhysRevLett.109.095501.

[538] T.G. Langdon, Grain boundary sliding revisited: Developments in sliding over four decades, J Mater Sci 41 (2006) 597–609, doi: 10.1007/s10853-006-6476-0.

[539] T.J. Rupert, D.S. Gianola, Y. GAN, K.J. Hemker, Experimental observations of stress-driven grain boundary migration, Science (New York, N.Y.) 326 (2009) 1686–1690, doi: 10.1126/science.1178226.

[540] M.F. Ashby, Boundary defects, and atomistic aspects of boundary sliding and diffusional creep, Surface Science 31 (1972) 498–542, doi: 10.1016/0039-6028(72)90273-7.

[541] A. Rajabzadeh, F. Mompiou, M. Legros, N. Combe, Elementary mechanisms of shear-coupled grain boundary migration, Physical review letters 110 (2013) 265507, doi: 10.1103/PhysRevLett.110.265507.

[542] R. Hadian, B. Grabowski, C.P. Race, J. Neugebauer, Atomistic migration mechanisms of atomically flat, stepped, and kinked grain boundaries, Phys. Rev. B 94 (2016), doi: 10.1103/PhysRevB.94.165413.

[543] N. Combe, F. Mompiou, M. Legros, Disconnections kinks and competing modes in shear-coupled grain boundary migration, Phys. Rev. B 93 (2016), doi: 10.1103/PhysRevB.93.024109.

[544] H. Zhang, M.I. Mendelev, D.J. Srolovitz, Computer simulation of the elastically driven migration of a flat grain boundary, Acta Materialia 52 (2004) 2569–2576, doi: 10.1016/j.actamat.2004.02.005.

[545] H. Zhang, M. MENDELEV, D. SROLOVITZ, Mobility of ?5 tilt grain boundaries: Inclination dependence, Scripta Materialia 52 (2005) 1193–1198, doi: 10.1016/j.scriptamat.2005.03.012.

[546] T. Gorkaya, K.D. Molodov, D.A. Molodov, G. Gottstein, Concurrent grain boundary motion and grain rotation under an applied stress, Acta Materialia 59 (2011) 5674–5680, doi: 10.1016/j.actamat.2011.05.042.

[547] Y. QI, P. KRAJEWSKI, Molecular dynamics simulations of grain boundary sliding: The effect of stress and boundary misorientation, Acta Materialia 55 (2007) 1555–1563, doi: 10.1016/j.actamat.2006.10.016.

[548] L. Zhang, J. Han, Y. Xiang, D.J. Srolovitz, Equation of Motion for a Grain Boundary, Physical review letters 119 (2017) 246101, doi: 10.1103/PhysRevLett.119.246101.

[549] R.C. Pond, D.A. Smith, P.W.J. Southerden, On the role of grain boundary dislocations in high temperature creep, Philosophical Magazine A 37 (1978) 27–40, doi: 10.1080/01418617808239160.

[550] M. Weikamp, R. Spatschek, Effect of shear-coupled grain boundary motion on coherent precipitation, Phys. Rev. B 100 (2019), doi: 10.1103/PhysRevB.100.054103.

[551] K.D. Molodov, D.A. Molodov, Grain boundary mediated plasticity: On the evaluation of grain boundary migration - shear coupling, Acta Materialia 153 (2018) 336–353, doi: 10.1016/j.actamat.2018.04.057.

[552] N.C. Admal, G. Po, J. Marian, A unified framework for polycrystal plasticity with grain boundary evolution, International Journal of Plasticity 106 (2018) 1–30, doi: 10.1016/j.ijplas.2018.01.014.

[553] S.A.H. Motaman, U. Prahl, Microstructural constitutive model for polycrystal viscoplasticity in cold and warm regimes based on continuum dislocation dynamics, Journal of the Mechanics and Physics of Solids 122 (2019) 205–243, doi: 10.1016/j.jmps.2018.09.002.

[554] W.G. Johnston, J.J. Gilman, Dislocation Velocities, Dislocation Densities, and Plastic Flow in Lithium Fluoride Crystals, Journal of Applied Physics 30 (1959) 129–144, doi: 10.1063/1.1735121.

[555] G.A. Webster, A widely applicable dislocation model of creep, Philosophical Magazine 14 (1966) 775–783, doi: 10.1080/14786436608211971.

[556] Y. Bergström, A dislocation model for the stress-strain behaviour of polycrystalline α-Fe with special emphasis on the variation of the densities of mobile and immobile dislocations, Materials Science and Engineering 5 (1970) 193–200, doi: 10.1016/0025-5416(70)90081-9.

[557] U.F. Kocks, Laws for Work-Hardening and Low-Temperature Creep, J. Eng. Mater. Technol. 98 (1976) 76, doi: 10.1115/1.3443340.

[558] H. Mecking, U.F. Kocks, Kinetics of flow and strain-hardening, Acta Metallurgica 29 (1981) 1865–1875, doi: 10.1016/0001-6160(81)90112-7.

[559] D.J. Bammann, E.C. Aifantis, On a proposal for a continuum with microstructure, Acta Mechanica 45 (1982) 91–121, doi: 10.1007/BF01295573.

[560] Y. Estrin, L.P. Kubin, Local strain hardening and nonuniformity of plastic deformation, Acta Metallurgica 34 (1986) 2455–2464, doi: 10.1016/0001-6160(86)90148-3.

[561] R.A. Austin, D.L. McDowell, A dislocation-based constitutive model for viscoplastic deformation of FCC metals at very high strain rates, International Journal of Plasticity 27 (2011) 1–24, doi: 10.1016/j.ijplas.2010.03.002.

[562] A.S. Krausz, K. Krausz, Unified constitutive laws of plastic deformation, Academic Press, London, 1996.

[563] Y. Estrin, L.S. Tóth, A. Molinari, Y. Bréchet, A dislocation-based model for all hardening stages in large strain deformation, Acta Materialia 46 (1998) 5509–5522, doi: 10.1016/S1359-6454(98)00196-7.

[564] W.D. Nix, J.C. Gibeling, D.A. Hughes, Time-dependent deformation of metals, MTA 16 (1985) 2215–2226, doi: 10.1007/BF02670420.

[565] W. Blum, P. Eisenlohr, Dislocation mechanics of creep, Materials Science and Engineering: A 510-511 (2009) 7–13, doi: 10.1016/j.msea.2008.04.110.

[566] W. Blum, P. Eisenlohr, F. Breutinger, Understanding creep—a review, Metall and Mat Trans A 33 (2002) 291–303, doi: 10.1007/s11661-002-0090-9.

[567] A. Ma, F. Roters, A constitutive model for fcc single crystals based on dislocation densities and its application to uniaxial compression of aluminium single crystals, Acta Materialia 52 (2004) 3603–3612, doi: 10.1016/j.actamat.2004.04.012.

[568] A. Ma, F. Roters, D. Raabe, A dislocation density based constitutive model for crystal plasticity FEM including geometrically necessary dislocations, Acta Materialia 54 (2006) 2169–2179, doi: 10.1016/j.actamat.2006.01.005.

[569] A. Arsenlis, D.M. Parks, Modeling the evolution of crystallographic dislocation density in crystal plasticity, Journal of the Mechanics and Physics of Solids 50 (2002) 1979–2009, doi: 10.1016/S0022-5096(01)00134-X.

[570] A. Arsenlis, On the evolution of crystallographic dislocation density in non-homogeneously deforming crystals, Journal of the Mechanics and Physics of Solids 52 (2004) 1213–1246, doi: 10.1016/j.jmps.2003.12.007.

[571] A. Patra, D.L. McDowell, Crystal plasticity-based constitutive modelling of irradiated bcc structures, Philosophical Magazine 92 (2012) 861–887, doi: 10.1080/14786435.2011.634855.

[572] I.J. Beyerlein, C.N. Tomé, A dislocation-based constitutive law for pure Zr including temperature effects, International Journal of Plasticity 24 (2008) 867–895, doi: 10.1016/j.ijplas.2007.07.017.

[573] M. Monavari, M. Zaiser, Annihilation and sources in continuum dislocation dynamics, Mater Theory 2 (2018) 761, doi: 10.1186/s41313-018-0010-z.

[574] M. Monavari, S. Sandfeld, M. Zaiser, Continuum representation of systems of dislocation lines, Journal of the Mechanics and Physics of Solids 95 (2016) 575–601, doi: 10.1016/j.jmps.2016.05.009.

[575] L.P. Kubin, C. Fressengeas, G. Ananthakrishna, Chapter 57 Collective behaviour of dislocations in plasticity, in: F.R.N. Nabarro, M.S. Duesbery, J.P. Hirth (Eds.), Dislocations in solids, North-Holland Pub. Co, Amsterdam, New York, 2002, pp. 101–192.

[576] I. Groma, Link between the microscopic and mesoscopic length-scale description of the collective behavior of dislocations, Phys. Rev. B 56 (1997) 5807–5813, doi: 10.1103/PhysRevB.56.5807.

[577] N. Grilli, K.G.F. Janssens, J. Nellessen, S. Sandlöbes, D. Raabe, Multiple slip dislocation patterning in a dislocation-based crystal plasticity finite element method, International Journal of Plasticity 100 (2018) 104–121, doi: 10.1016/j.ijplas.2017.09.015.

[578] N. Grilli, K.G.F. Janssens, H. van Swygenhoven, Crystal plasticity finite element modelling of low cycle fatigue in fcc metals, Journal of the Mechanics and Physics of Solids 84 (2015) 424–435, doi: 10.1016/j.jmps.2015.08.007.

[579] I. Groma, G. Györgyi, B. Kocsis, Dynamics of coarse grained dislocation densities from an effective free energy, Philosophical Magazine 87 (2007) 1185–1199, doi: 10.1080/14786430600835813.

[580] T. Hochrainer, S. Sandfeld, M. Zaiser, P. Gumbsch, Continuum dislocation dynamics, Journal of the Mechanics and Physics of Solids 63 (2014) 167–178, doi: 10.1016/j.jmps.2013.09.012.

[581] T. Hochrainer, Multipole expansion of continuum dislocations dynamics in terms of alignment tensors, Phil. Mag. 95 (2015) 1321–1367, doi: 10.1080/14786435.2015.1026297.

[582] H. Askari, M.R. Maughan, N. Abdolrahim, D. Sagapuram, D.F. Bahr, H.M. Zbib, A stochastic crystal plasticity framework for deformation of micro-scale polycrystalline materials, International Journal of Plasticity 68 (2015) 21–33, doi: 10.1016/j.ijplas.2014.11.001.

[583] E. Nadgornyi, Dislocation dynamics and mechanical properties of crystals, Progress in Materials Science 31 (1988) 1–530, doi: 10.1016/0079-6425(88)90005-9.

[584] E. Nes, Modelling of work hardening and stress saturation in FCC metals, Progress in Materials Science 41 (1997) 129–193, doi: 10.1016/S0079-6425(97)00032-7.

[585] G. Gottstein, A.S. Argon, Dislocation theory of steady state deformation and its approach in creep and dynamic tests, Acta Metallurgica 35 (1987) 1261–1271, doi: 10.1016/0001-6160(87)90007-1.

[586] J. Deng, A. El-Azab, Temporal statistics and coarse graining of dislocation ensembles, Phil. Mag. 90 (2010) 3651–3678, doi: 10.1080/14786435.2010.497472.

[587] U. Essmann, H. Mughrabi, Annihilation of dislocations during tensile and cyclic deformation and limits of dislocation densities, Philosophical Magazine A 40 (1979) 731–756, doi: 10.1080/01418617908234871.

[588] B.L. Hansen, I.J. Beyerlein, C.A. Bronkhorst, E.K. Cerreta, D. Dennis-Koller, A dislocation-based multi-rate single crystal plasticity model, International Journal of Plasticity 44 (2013) 129–146, doi: 10.1016/j.ijplas.2012.12.006.

[589] M. Goerdeler, G. Gottstein, A microstructural work hardening model based on three internal state variables, Materials Science and Engineering: A 309-310 (2001) 377–381, doi: 10.1016/S0921-5093(00)01728-7.

[590] Y. Estrin, H. Braasch, Y. Brechet, A Dislocation Density Based Constitutive Model for Cyclic Deformation, J. Eng. Mater. Technol. 118 (1996) 441, doi: 10.1115/1.2805940.

[591] Y. Estrin, Dislocation-Density-Related Constitutive Modeling, in: Unified constitutive laws of plastic deformation, Academic Press, London, 1996, pp. 69–106.

[592] M. Zaiser, N. Nikitas, T. Hochrainer, E.C. Aifantis, Modelling size effects using 3D density-based dislocation dynamics, Philosophical Magazine 87 (2007) 1283–1306, doi: 10.1080/14786430600953764.

[593] K.-S. Cheong, E.P. Busso, Discrete dislocation density modelling of single phase FCC polycrystal aggregates, Acta Materialia 52 (2004) 5665–5675, doi: 10.1016/j.actamat.2004.08.044.

[594] P. Hähner, On the foundations of stochastic dislocation dynamics, Appl. Phys. A 62 (1996) 473–481, doi: 10.1007/BF01567120.

[595] D. Li, H. Zbib, X. Sun, M. Khaleel, Predicting plastic flow and irradiation hardening of iron single crystal with mechanism-based continuum dislocation dynamics, International Journal of Plasticity 52 (2014) 3–17, doi: 10.1016/j.ijplas.2013.01.015.

[596] L.S. Tóth, Y. Estrin, R. Lapovok, C. Gu, A model of grain fragmentation based on lattice curvature, Acta Materialia 58 (2010) 1782–1794, doi: 10.1016/j.actamat.2009.11.020.

[597] L.S. Tóth, A. Molinari, Y. Estrin, Strain Hardening at Large Strains as Predicted by Dislocation Based Polycrystal Plasticity Model, J. Eng. Mater. Technol 124 (2002) 71–77, doi: 10.1115/1.1421350.

[598] E.C. Aifantis, Gradient Deformation Models at Nano, Micro, and Macro Scales, J. Eng. Mater. Technol 121 (1999) 189–202, doi: 10.1115/1.2812366.

[599] R.J. Dorgan, G.Z. Voyiadjis, Nonlocal dislocation based plasticity incorporating gradients of hardening, Mechanics of Materials 35 (2003) 721–732, doi: 10.1016/S0167-6636(02)00202-8.

[600] G.M. Castelluccio, D.L. McDowell, Mesoscale cyclic crystal plasticity with dislocation substructures, International Journal of Plasticity 98 (2017) 1–26, doi: 10.1016/j.ijplas.2017.06.002.

[601] P. Hähner, Stochastic dislocation patterning during cyclic plastic deformation, Appl. Phys. A 63 (1996) 45–55, doi: 10.1007/BF01579745.

[602] R.A. Barrett, P.E. O'Donoghue, S.B. Leen, A dislocation-based model for high temperature cyclic viscoplasticity of 9–12Cr steels, Computational Materials Science 92 (2014) 286–297, doi: 10.1016/j.commatsci.2014.05.034.

[603] R.A. Barrett, P.E. O'Donoghue, S.B. Leen, A physically-based constitutive model for high temperature microstructural degradation under cyclic deformation, International Journal of Fatigue 100 (2017) 388–406, doi: 10.1016/j.ijfatigue.2017.03.018.

[604] K. Kitayama, C.N. Tomé, E.F. Rauch, J.J. Gracio, F. Barlat, A crystallographic dislocation model for describing hardening of polycrystals during strain path changes. Application to low carbon steels, International Journal of Plasticity 46 (2013) 54–69, doi: 10.1016/j.ijplas.2012.09.004.

[605] C.J. Hamelin, B.J. Diak, A.K. Pilkey, Multiscale modelling of the induced plastic anisotropy in bcc metals, International Journal of Plasticity 27 (2011) 1185–1202, doi: 10.1016/j.ijplas.2011.01.003.

[606] E.F. Rauch, J.J. Gracio, F. Barlat, Work-hardening model for polycrystalline metals under strain reversal at large strains, Acta Materialia 55 (2007) 2939–2948, doi: 10.1016/j.actamat.2007.01.003.

[607] B. Peeters, M. Seefeldt, C. Teodosiu, S.R. Kalidindi, P. van Houtte, E. Aernoudt, Work-hardening/softening behaviour of b.c.c. polycrystals during changing strain paths: I. An integrated model based on substructure and texture evolution, and its prediction of the stress–strain behaviour of an IF steel during two-stage strain paths, Acta Materialia 49 (2001) 1607–1619, doi: 10.1016/S1359-6454(01)00066-0.

[608] B. Peeters, S.R. Kalidindi, P. van Houtte, E. Aernoudt, A crystal plasticity based work-hardening/softening model for b.c.c. metals under changing strain paths, Acta Materialia 48 (2000) 2123–2133, doi: 10.1016/S1359-6454(00)00047-1.

[609] C. Reuber, P. Eisenlohr, F. Roters, D. Raabe, Dislocation density distribution around an indent in single-crystalline nickel, Acta Materialia 71 (2014) 333–348, doi: 10.1016/j.actamat.2014.03.012.

[610] W. Wen, M. Borodachenkova, C.N. Tomé, G. Vincze, E.F. Rauch, F. Barlat, J.J. Grácio, Mechanical behavior of Mg subjected to strain path changes: Experiments and modeling, International Journal of Plasticity 73 (2015) 171–183, doi: 10.1016/j.ijplas.2014.10.009.

[611] E.F. Rauch, J.J. Gracio, F. Barlat, G. Vincze, Modelling the plastic behaviour of metals under complex loading conditions, Modelling Simul. Mater. Sci. Eng. 19 (2011) 35009, doi: 10.1088/0965-0393/19/3/035009.

[612] H. Magnusson, R. Sandström, Creep Strain Modeling of 9 to 12 Pct Cr Steels Based on Microstructure Evolution, Metall and Mat Trans A 38 (2007) 2033–2039, doi: 10.1007/s11661-007-9256-9.

[613] H.S. Leung, P.S.S. Leung, B. Cheng, A.H.W. Ngan, A new dislocation-density-function dynamics scheme for computational crystal plasticity by explicit consideration of dislocation elastic interactions, International Journal of Plasticity 67 (2015) 1–25, doi: 10.1016/j.ijplas.2014.09.009.

[614] H.S. Leung, A.H.W. Ngan, Dislocation-density function dynamics – An all-dislocation, full-dynamics approach for modeling intensive dislocation structures, Journal of the Mechanics and Physics of Solids 91 (2016) 172–203, doi: 10.1016/j.jmps.2016.03.008.

[615] J. PONTES, D. WALGRAEF, E. AIFANTIS, On dislocation patterning, International Journal of Plasticity 22 (2006) 1486–1505, doi: 10.1016/j.ijplas.2005.07.011.

[616] D.-F. Li, B.J. Golden, N.P. O'Dowd, Multiscale modelling of mechanical response in a martensitic steel: A micromechanical and length-scale-dependent framework for precipitate hardening, Acta Materialia 80 (2014) 445–456, doi: 10.1016/j.actamat.2014.08.012.

[617] K.-S. Cheong, E.P. Busso, Effects of lattice misorientations on strain heterogeneities in FCC polycrystals, Journal of the Mechanics and Physics of Solids 54 (2006) 671–689, doi: 10.1016/j.jmps.2005.11.003.

[618] D.-F. Li, R.A. Barrett, P.E. O'Donoghue, N.P. O'Dowd, S.B. Leen, A multi-scale crystal plasticity model for cyclic plasticity and low-cycle fatigue in a precipitate-strengthened steel at elevated temperature, Journal of the Mechanics and Physics of Solids 101 (2017) 44–62, doi: 10.1016/j.jmps.2016.12.010.

[619] D.-F. Li, R.A. Barrett, P.E. O'Donoghue, C.J. Hyde, N.P. O'Dowd, S.B. Leen, Micromechanical finite element modelling of thermo-mechanical fatigue for P91 steels, International Journal of Fatigue 87 (2016) 192–202, doi: 10.1016/j.ijfatigue.2015.11.025.

[620] P.E.J. Rivera-Díaz-del-Castillo, M. Huang, Dislocation annihilation in plastic deformation, Acta Materialia 60 (2012) 2606–2614, doi: 10.1016/j.actamat.2012.01.027.

[621] E.I. Galindo-Nava, J. Sietsma, P.E.J. Rivera-Díaz-del-Castillo, Dislocation annihilation in plastic deformation, Acta Materialia 60 (2012) 2615–2624, doi: 10.1016/j.actamat.2012.01.028.

[622] M. Huang, P.E.J. Rivera-Díaz-del-Castillo, O. Bouaziz, S. van der Zwaag, A constitutive model for high strain rate deformation in FCC metals based on irreversible thermodynamics, Mechanics of Materials 41 (2009) 982–988, doi: 10.1016/j.mechmat.2009.05.007.

[623] M. Huang, P.E.J. Rivera-Díaz-del-Castillo, O. Bouaziz, S. van der Zwaag, Modelling the steady state deformation stress under various deformation conditions using a single irreversible thermodynamics based formulation, Acta Materialia 57 (2009) 3431–3438, doi: 10.1016/j.actamat.2009.03.023.

[624] S. Allain, J.-P. Chateau, O. Bouaziz, Constitutive model of the TWIP effect in a polycrystalline high manganese content austenitic steel, Steel Research 73 (2002) 299–302, doi: 10.1002/srin.200200212.

[625] D.R. Steinmetz, T. Jäpel, B. Wietbrock, P. Eisenlohr, I. Gutierrez-Urrutia, A. Saeed-Akbari, T. Hickel et al., Revealing the strain-hardening behavior of twinning-induced plasticity steels, Acta Materialia 61 (2013) 494–510, doi: 10.1016/j.actamat.2012.09.064.

[626] L. Remy, Kinetics of f.c.c. deformation twinning and its relationship to stress-strain behaviour, Acta Metallurgica 26 (1978) 443–451, doi: 10.1016/0001-6160(78)90170-0.

[627] I.J. Beyerlein, C.N. Tomé, A probabilistic twin nucleation model for HCP polycrystalline metals, Proc. R. Soc. A 466 (2010) 2517–2544, doi: 10.1098/rspa.2009.0661.

[628] I.J. Beyerlein, L. Capolungo, P.E. Marshall, R.J. McCabe, C.N. Tomé, Statistical analyses of deformation twinning in magnesium, Philosophical Magazine 90 (2010) 2161–2190, doi: 10.1080/14786431003630835.

[629] I.J. Beyerlein, R.J. McCabe, C.N. Tomé, Effect of microstructure on the nucleation of deformation twins in polycrystalline high-purity magnesium, Journal of the Mechanics and Physics of Solids 59 (2011) 988–1003, doi: 10.1016/j.jmps.2011.02.007.

[630] J. Wang, I.J. Beyerlein, C.N. Tomé, An atomic and probabilistic perspective on twin nucleation in Mg, Scripta Materialia 63 (2010) 741–746, doi: 10.1016/j.scriptamat.2010.01.047.

[631] M. Zecevic, M. Knezevic, I.J. Beyerlein, C.N. Tomé, An elasto-plastic self-consistent model with hardening based on dislocation density, twinning and de-twinning: Application to strain path changes in HCP metals, Materials Science and Engineering: A 638 (2015) 262–274, doi: 10.1016/j.msea.2015.04.066.

[632] S. Mahajan, G.Y. Chin, Formation of deformation twins in f.c.c. crystals, Acta Metallurgica 21 (1973) 1353–1363, doi: 10.1016/0001-6160(73)90085-0.

[633] J.W. Christian, S. Mahajan, Deformation twinning, Progress in Materials Science 39 (1995) 1–157, doi: 10.1016/0079-6425(94)00007-7.

[634] J.A. Venables, Deformation twinning in face-centred cubic metals, Philosophical Magazine 6 (1961) 379–396, doi: 10.1080/14786436108235892.

[635] J.A. Venables, The nucleation and propagation of deformation twins, Journal of Physics and Chemistry of Solids 25 (1964) 693–700, doi: 10.1016/0022-3697(64)90178-7.

[636] Q. Yu, Z.-W. Shan, J. Li, X. Huang, L. Xiao, J. Sun, E. Ma, Strong crystal size effect on deformation twinning, Nature 463 (2010) 335–338, doi: 10.1038/nature08692.

[637] F. Siska, L. Stratil, J. Cizek, A. Ghaderi, M. Barnett, Numerical analysis of twin thickening process in magnesium alloys, Acta Materialia 124 (2017) 9–16, doi: 10.1016/j.actamat.2016.10.068.

[638] A. Ghaderi, M.R. Barnett, Sensitivity of deformation twinning to grain size in titanium and magnesium, Acta Materialia 59 (2011) 7824–7839, doi: 10.1016/j.actamat.2011.09.018.

[639] M.A. Meyers, O. Vöhringer, V.A. Lubarda, The onset of twinning in metals, Acta Materialia 49 (2001) 4025–4039, doi: 10.1016/S1359-6454(01)00300-7.

[640] N. Stanford, U. Carlson, M.R. Barnett, Deformation Twinning and the Hall–Petch Relation in Commercial Purity Ti, Metall and Mat Trans A 39 (2008) 934–944, doi: 10.1007/s11661-007-9442-9.

[641] M. Niewczas, Chapter 75 Dislocations and Twinning in Face Centred Cubic Crystals, in: Elsevier, 2007, pp. 263–364.

[642] M.A. Meyers, L.E. Murr, A model for the formation of annealing twins in F.C.C. metals and alloys, Acta Metallurgica 26 (1978) 951–962, doi: 10.1016/0001-6160(78)90046-9.

[643] Q. Yu, L. Qi, K. Chen, R.K. Mishra, J. Li, A.M. Minor, The nanostructured origin of deformation twinning, Nano letters 12 (2012) 887–892, doi: 10.1021/nl203937t.

[644] H. Wang, P.D. Wu, J. Wang, C.N. Tomé, A crystal plasticity model for hexagonal close packed (HCP) crystals including twinning and de-twinning mechanisms, International Journal of Plasticity 49 (2013) 36–52, doi: 10.1016/j.ijplas.2013.02.016.

[645] M.H. Yoo, J.K. Lee, Deformation twinning in h.c.p. metals and alloys, Philosophical Magazine A 63 (1991) 987–1000, doi: 10.1080/01418619108213931.

[646] J. Wang, J.P. Hirth, C.N. Tomé, ($1\bar{0}12$) Twinning nucleation mechanisms in hexagonal-close-packed crystals, Acta Materialia 57 (2009) 5521–5530, doi: 10.1016/j.actamat.2009.07.047.

[647] J. Wang, R.G. Hoagland, J.P. Hirth, L. Capolungo, I.J. Beyerlein, C.N. Tomé, Nucleation of a ($1\bar{0}12$) twin in hexagonal close-packed crystals, Scripta Materialia 61 (2009) 903–906, doi: 10.1016/j.scriptamat.2009.07.028.

[648] L. Wang, Y. Yang, P. Eisenlohr, T.R. Bieler, M.A. Crimp, D.E. Mason, Twin Nucleation by Slip Transfer across Grain Boundaries in Commercial Purity Titanium, Metall and Mat Trans A 41 (2010) 421–430, doi: 10.1007/s11661-009-0097-6.

[649] H. Fan, S. Aubry, A. Arsenlis, J.A. El-Awady, Grain size effects on dislocation and twinning mediated plasticity in magnesium, Scripta Materialia 112 (2016) 50–53, doi: 10.1016/j.scriptamat.2015.09.008.

[650] L. Leclercq, L. Capolungo, D. Rodney, Atomic-Scale Comparison Between Twin Growth Mechanisms in Magnesium, Materials Research Letters 2 (2014) 152–159, doi: 10.1080/21663831.2014.880548.

[651] H. Fan, S. Aubry, A. Arsenlis, J.A. El-Awady, The role of twinning deformation on the hardening response of polycrystalline magnesium from discrete dislocation dynamics simulations, Acta Materialia 92 (2015) 126–139, doi: 10.1016/j.actamat.2015.03.039.

[652] A. Serra, D.J. Bacon, A new model for {10 1 2} twin growth in hcp metals, Philosophical Magazine A 73 (1996) 333–343, doi: 10.1080/01418619608244386.

[653] M. Knezevic, A. Levinson, R. Harris, R.K. Mishra, R.D. Doherty, S.R. Kalidindi, Deformation twinning in AZ31: Influence on strain hardening and texture evolution, Acta Materialia 58 (2010) 6230–6242, doi: 10.1016/j.actamat.2010.07.041.

[654] S.-G. Hong, S.H. Park, C.S. Lee, Role of {10–12} twinning characteristics in the deformation behavior of a polycrystalline magnesium alloy, Acta Materialia 58 (2010) 5873–5885, doi: 10.1016/j.actamat.2010.07.002.

[655] Y. Jin, B. Lin, M. Bernacki, G.S. Rohrer, A.D. Rollett, N. Bozzolo, Annealing twin development during recrystallization and grain growth in pure nickel, Materials Science and Engineering: A 597 (2014) 295–303, doi: 10.1016/j.msea.2014.01.018.

[656] S.G. Song, G.T. Gray, Structural interpretation of the nucleation and growth of deformation twins in Zr and Ti—I. Application of the coincidence site lattice (CSL) theory to twinning problems in h.c.p. structures, Acta Metallurgica et Materialia 43 (1995) 2325–2337, doi: 10.1016/0956-7151(94)00433-1.

[657] J.W. Christian, Deformation by moving interfaces, MTA 13 (1982) 509–538, doi: 10.1007/BF02644415.

[658] H. Somekawa, T. Mukai, Hall–Petch relation for deformation twinning in solid solution magnesium alloys, Materials Science and Engineering: A 561 (2013) 378–385, doi: 10.1016/j.msea.2012.10.040.

[659] C.S. Pande, B.B. Rath, M.A. Imam, Effect of annealing twins on Hall–Petch relation in polycrystalline materials, Materials Science and Engineering: A 367 (2004) 171–175, doi: 10.1016/j.msea.2003.09.100.

[660] M. Schneider, E.P. George, T.J. Manescau, T. Záležák, J. Hunfeld, A. Dlouhý, G. Eggeler et al., Analysis of strengthening due to grain boundaries and annealing twin boundaries in the CrCoNi medium-entropy alloy, International Journal of Plasticity 124 (2020) 155–169, doi: 10.1016/j.ijplas.2019.08.009.

[661] A. Jain, O. Duygulu, D.W. Brown, C.N. Tomé, S.R. Agnew, Grain size effects on the tensile properties and deformation mechanisms of a magnesium alloy, AZ31B, sheet, Materials Science and Engineering: A 486 (2008) 545–555, doi: 10.1016/j.msea.2007.09.069.

[662] S. Kibey, J.B. Liu, D.D. Johnson, H. Sehitoglu, Predicting twinning stress in fcc metals, Acta Materialia 55 (2007) 6843–6851, doi: 10.1016/j.actamat.2007.08.042.

[663] H. Suzuki, C.S. Barrett, Deformation twinning in silver-gold alloys, Acta Metallurgica 6 (1958) 156–165, doi: 10.1016/0001-6160(58)90002-6.

[664] J.E. Burke, The formation of annealing twins, JOM 2 (1950) 1324–1328, doi: 10.1007/BF03399157.

[665] J.R. Cahoon, Q. Li, N.L. Richards, Microstructural and processing factors influencing the formation of annealing twins, Materials Science and Engineering: A 526 (2009) 56–61, doi: 10.1016/j.msea.2009.07.021.

[666] H.C.H. Carpenter, The formation of twinned metallic crystals, Proc. R. Soc. Lond. A 113 (1926) 161–182, doi: 10.1098/rspa.1926.0144.

[667] S. Dash, N. Brown, An investigation of the origin and growth of annealing twins, Acta Metallurgica 11 (1963) 1067–1075, doi: 10.1016/0001-6160(63)90195-0.

[668] R.L. Fullman, J.C. Fisher, Formation of Annealing Twins During Grain Growth, Journal of Applied Physics 22 (1951) 1350–1355, doi: 10.1063/1.1699865.

[669] H. Gleiter, The formation of annealing twins, Acta Metallurgica 17 (1969) 1421–1428, doi: 10.1016/0001-6160(69)90004-2.

[670] P.J. Goodhew, Annealing twin formation by boundary dissociation, Metal Science 13 (1979) 108–112, doi: 10.1179/msc.1979.13.3-4.108.

[671] S. Mahajan, Formation of annealing twins in f.c.c. crystals, Acta Materialia 45 (1997) 2633–2638, doi: 10.1016/S1359-6454(96)00336-9.

[672] C.S. Pande, M.A. Imam, B.B. Rath, Study of annealing twins in fcc metals and alloys, MTA 21 (1990) 2891–2896, doi: 10.1007/BF02647209.

[673] V. Randle, P.R. Rios, Y. Hu, Grain growth and twinning in nickel, Scripta Materialia 58 (2008) 130–133, doi: 10.1016/j.scriptamat.2007.09.016.

[674] C. Liu, P. Shanthraj, M. Diehl, F. Roters, S. Dong, J. Dong, W. Ding et al., An integrated crystal plasticity–phase field model for spatially resolved twin nucleation, propagation, and growth in hexagonal materials, International Journal of Plasticity 106 (2018) 203–227, doi: 10.1016/j.ijplas.2018.03.009.

[675] M. Ardeljan, I.J. Beyerlein, M. Knezevic, Effect of dislocation density-twin interactions on twin growth in AZ31 as revealed by explicit crystal plasticity finite element modeling, International Journal of Plasticity 99 (2017) 81–101, doi: 10.1016/j.ijplas.2017.09.002.

[676] L. Capolungo, P.E. Marshall, R.J. McCabe, I.J. Beyerlein, C.N. Tomé, Nucleation and growth of twins in Zr: A statistical study, Acta Materialia 57 (2009) 6047–6056, doi: 10.1016/j.actamat.2009.08.030.

[677] M. Ardeljan, R.J. McCabe, I.J. Beyerlein, M. Knezevic, Explicit incorporation of deformation twins into crystal plasticity finite element models, Computer Methods in Applied Mechanics and Engineering 295 (2015) 396–413, doi: 10.1016/j.cma.2015.07.003.

[678] A. Khosravani, D.T. Fullwood, B.L. Adams, T.M. Rampton, M.P. Miles, R.K. Mishra, Nucleation and propagation of {101¯2} twins in AZ31 magnesium alloy, Acta Materialia 100 (2015) 202–214, doi: 10.1016/j.actamat.2015.08.024.

[679] H. Qiao, M.R. Barnett, P.D. Wu, Modeling of twin formation, propagation and growth in a Mg single crystal based on crystal plasticity finite element method, International Journal of Plasticity 86 (2016) 70–92, doi: 10.1016/j.ijplas.2016.08.002.

[680] E.I. Galindo-Nava, P.E.J. Rivera-Díaz-del-Castillo, Understanding martensite and twin formation in austenitic steels: A model describing TRIP and TWIP effects, Acta Materialia 128 (2017) 120–134, doi: 10.1016/j.actamat.2017.02.004.

[681] F.J. Humphreys, M. Hatherly, Recrystallization and related annealing phenomena, 2nd ed., Elsevier, Amsterdam, 2004.

[682] R.D. Doherty, D.A. Hughes, F.J. Humphreys, J.J. Jonas, D.J. Jensen, M.E. Kassner, W.E. King et al., Current issues in recrystallization, Materials Science and Engineering: A 238 (1997) 219–274, doi: 10.1016/S0921-5093(97)00424-3.

[683] K. Huang, R.E. Logé, A review of dynamic recrystallization phenomena in metallic materials, Materials & Design 111 (2016) 548–574, doi: 10.1016/j.matdes.2016.09.012.

[684] H.J. McQueen, Development of dynamic recrystallization theory, Materials Science and Engineering: A 387-389 (2004) 203–208, doi: 10.1016/j.msea.2004.01.064.

[685] D.G. Cram, H.S. Zurob, Y.J.M. Brechet, C.R. Hutchinson, Modelling discontinuous dynamic recrystallization using a physically based model for nucleation, Acta Materialia 57 (2009) 5218–5228, doi: 10.1016/j.actamat.2009.07.024.

[686] S. Gourdet, F. Montheillet, A model of continuous dynamic recrystallization, Acta Materialia 51 (2003) 2685–2699, doi: 10.1016/S1359-6454(03)00078-8.

[687] R.D. Doherty, J.A. Szpunar, Kinetics of sub-grain coalescence—A reconsideration of the theory, Acta Metallurgica 32 (1984) 1789–1798, doi: 10.1016/0001-6160(84)90235-9.

[688] J.E. Bailey, P.B. Hirsch, The recrystallization process in some polycrystalline metals, Proc. R. Soc. Lond. A 267 (1962) 11–30, doi: 10.1098/rspa.1962.0080.

[689] R.W. Cahn, A New Theory of Recrystallization Nuclei, MEKU 63 (1950) 323–336, doi: 10.1088/0370-1298/63/4/302.

[690] G. Gottstein, D.A. Molodov, L.S. Shvindlerman, Grain Boundary Migration in Metals: Recent Developments, Interface Science 6 (1998) 7–22, doi: 10.1023/A:1008641617937.

[691] G. Gottstein, L.S. Shvindlerman, Grain boundary migration in metals: Thermodynamics, kinetics, applications / Günter Gottstein, Lasar S. Shvindlerman, 2nd ed., Taylor & Francis, Boca Raton, 2010.

[692] W. Johnson, R. Mehl, Reaction kinetics in processes of nucleation and growth, Trans. Metall. Soc. AIME 135 (1939) 416–442.

[693] A.N. Kolmogorov, A statistical theory for the recrystallization of metals, Izv. Akad. Nauk USSR Ser. Fiz. Mat. Nauk (1937) 355–415.

[694] T. Furu, K. Marthinsen, E. Nes, Modelling recrystallisation, Materials Science and Technology 6 (1990) 1093–1102, doi: 10.1179/mst.1990.6.11.1093.

[695] C.E. Krill, L. Helfen, D. Michels, H. Natter, A. Fitch, O. Masson, R. Birringer, Size-dependent grain-growth kinetics observed in nanocrystalline Fe, Phys. Rev. Lett. 86 (2001) 842–845, doi: 10.1103/PhysRevLett.86.842.

[696] P.R. Rios, F. Siciliano Jr, H.R.Z. Sandim, R.L. Plaut, A.F. Padilha, Nucleation and growth during recrystallization, Mat. Res. 8 (2005) 225–238, doi: 10.1590/S1516-14392005000300002.

[697] R.W. Cahn, Recrystallization of single crystals after plastic bending, Journal of the Institute of Metals 76 (1949) 121.

[698] J.E. Burke, D. Turnbull, Recrystallization and grain growth, Progress in Metal Physics 3 (1952) 220–292, doi: 10.1016/0502-8205(52)90009-9.

[699] K. Lücke, K. Detert, A quantitative theory of grain-boundary motion and recrystallization in metals in the presence of impurities, Acta Metallurgica 5 (1957) 628–637, doi: 10.1016/0001-6160(57)90109-8.

[700] P. Cotterill, Mould P. R., Recrystallization and grain growth in metals, Krieger Pub Co (1976).

[701] A.R. Jones, B. Ralph, Hansen N., Subgrain coalescence and the nucleation of recrystallization at grain boundaries in aluminium, Proc. R. Soc. Lond. A 368 (1979) 345–357, doi: 10.1098/rspa.1979.0134.

[702] E.A. Holm, M.A. Miodownik, A.D. Rollett, On abnormal subgrain growth and the origin of recrystallization nuclei, Acta Materialia 51 (2003) 2701–2716, doi: 10.1016/S1359-6454(03)00079-X.

[703] R.D. Doherty, R.W. Cahn, Nucleation of new grains in recrystallization of cold-worked metals, Journal of the Less Common Metals 28 (1972) 279–296, doi: 10.1016/0022-5088(72)90131-2.

[704] A.D. Rollett, D.J. Srolovitz, R.D. Doherty, M.P. Anderson, Computer simulation of recrystallization in non-uniformly deformed metals, Acta Metallurgica 37 (1989) 627–639, doi: 10.1016/0001-6160(89)90247-2.

[705] M.L. Kronberg, F.H. Wilson, Secondary Recrystallization in Copper, JOM 1 (1949) 501–514, doi: 10.1007/BF03398387.

[706] H.J. McQueen, J.J. Jonas, Recovery and Recrystallization during High Temperature Deformation, in: H. Herman, R.J. Arsenault (Eds.), Treatise on materials science and technology, Academic Press, New York, London, 1975, pp. 393–493.

[707] U. Köster, Recrystallization Involving a Second Phase, Metal Science 8 (1974) 151–160, doi: 10.1179/msc.1974.8.1.151.

[708] P.R. Rios, Modeling time dependence of the average interface migration rate in site-saturated recrystallization, Metall and Mat Trans A 28 (1997) 939–946, doi: 10.1007/s11661-997-0224-1.

[709] H.P. Stüwe, A.F. Padilha, F. Siciliano, Competition between recovery and recrystallization, Materials Science and Engineering: A 333 (2002) 361–367, doi: 10.1016/S0921-5093(01)01860-3.

[710] I.L. Dillamore, C.J.E. Smith, T.W. Watson, Oriented Nucleation in the Formation of Annealing Textures in Iron, Metal Science Journal 1 (1967) 49–54, doi: 10.1179/msc.1967.1.1.49.

[711] R.D. Doherty, Recrystallization and texture, Progress in Materials Science 42 (1997) 39–58, doi: 10.1016/S0079-6425(97)00007-8.

[712] A. Galiyev, R. Kaibyshev, G. Gottstein, Correlation of plastic deformation and dynamic recrystallization in magnesium alloy ZK60, Acta Materialia 49 (2001) 1199–1207, doi: 10.1016/S1359-6454(01)00020-9.

[713] T. Sakai, A. Belyakov, R. Kaibyshev, H. Miura, J.J. Jonas, Dynamic and post-dynamic recrystallization under hot, cold and severe plastic deformation conditions, Progress in Materials Science 60 (2014) 130–207, doi: 10.1016/j.pmatsci.2013.09.002.

[714] M.E. Kassner, S.R. Barrabes, New developments in geometric dynamic recrystallization, Materials Science and Engineering: A 410-411 (2005) 152–155, doi: 10.1016/j.msea.2005.08.052.

[715] P.A. Beck, The Formation of Recrystallization Nuclei, Journal of Applied Physics 20 (1949) 633–634, doi: 10.1063/1.1698446.

[716] P.A. Beck, P.R. Sperry, Strain Induced Grain Boundary Migration in High Purity Aluminum, Journal of Applied Physics 21 (1950) 150–152, doi: 10.1063/1.1699614.

[717] A. Dehghan-Manshadi, P.D. Hodgson, Dependency of Recrystallization Mechanism to the Initial Grain Size, Metall and Mat Trans A 39 (2008) 2830–2840, doi: 10.1007/s11661-008-9656-5.

[718] J.J. Jonas, X. Quelennec, L. Jiang, É. Martin, The Avrami kinetics of dynamic recrystallization, Acta Materialia 57 (2009) 2748–2756, doi: 10.1016/j.actamat.2009.02.033.

[719] H.J. McQueen, C.A.C. Imbert, Dynamic recrystallization: plasticity enhancing structural development, Journal of Alloys and Compounds 378 (2004) 35–43, doi: 10.1016/j.jallcom.2003.10.067.

[720] W. Roberts, B. Ahlblom, A nucleation criterion for dynamic recrystallization during hot working, Acta Metallurgica 26 (1978) 801–813, doi: 10.1016/0001-6160(78)90030-5.

[721] W. Roberts, H. Boden, B. Ahlblom, Dynamic recrystallization kinetics, Metal Science 13 (2013) 195–205, doi: 10.1179/msc.1979.13.3-4.195.

[722] R. Sandström, R. Lagneborg, A model for hot working occurring by recrystallization, Acta Metallurgica 23 (1975) 387–398, doi: 10.1016/0001-6160(75)90132-7.

[723] T. Sakai, J.J. Jonas, Overview no. 35 Dynamic recrystallization: Mechanical and microstructural considerations, Acta Metallurgica 32 (1984) 189–209, doi: 10.1016/0001-6160(84)90049-X.

[724] T. Sakai, Dynamic recrystallization microstructures under hot working conditions, Journal of Materials Processing Technology 53 (1995) 349–361, doi: 10.1016/0924-0136(95)01992-N.

[725] R.L. Goetz, V. Seetharaman, Modeling Dynamic Recrystallization Using Cellular Automata, Scripta Materialia 38 (1998) 405–413, doi: 10.1016/S1359-6462(97)00500-9.

[726] R. Ding, Z.X. Guo, Coupled quantitative simulation of microstructural evolution and plastic flow during dynamic recrystallization, Acta Materialia 49 (2001) 3163–3175, doi: 10.1016/S1359-6454(01)00233-6.

[727] B. Derby, The dependence of grain size on stress during dynamic recrystallisation, Acta Metallurgica et Materialia 39 (1991) 955–962, doi: 10.1016/0956-7151(91)90295-C.

[728] U. Andrade, M.A. Meyers, K.S. Vecchio, A.H. Chokshi, Dynamic recrystallization in high-strain, high-strain-rate plastic deformation of copper, Acta Metallurgica et Materialia 42 (1994) 3183–3195, doi: 10.1016/0956-7151(94)90417-0.

[729] C.M. Sellars, J.A. Whiteman, Recrystallization and grain growth in hot rolling, Metal Science 13 (1979) 187–194, doi: 10.1179/msc.1979.13.3-4.187.

[730] G. Zhou, Z. Li, D. Li, Y. Peng, H.S. Zurob, P. Wu, A polycrystal plasticity based discontinuous dynamic recrystallization simulation method and its application to copper, International Journal of Plasticity 91 (2017) 48–76, doi: 10.1016/j.ijplas.2017.01.001.

[731] M. Bernacki, R.E. Logé, T. Coupez, Level set framework for the finite-element modelling of recrystallization and grain growth in polycrystalline materials, Scripta Materialia 64 (2011) 525–528, doi: 10.1016/j.scriptamat.2010.11.032.

[732] G. Abrivard, E.P. Busso, S. Forest, B. Appolaire, Phase field modelling of grain boundary motion driven by curvature and stored energy gradients. Part I: theory and numerical implementation, Phil. Mag. 92 (2012) 3618–3642, doi: 10.1080/14786435.2012.713135.

[733] G. Abrivard, E.P. Busso, S. Forest, B. Appolaire, Phase field modelling of grain boundary motion driven by curvature and stored energy gradients. Part II: Application to recrystallisation, Phil. Mag. 92 (2012) 3643–3664, doi: 10.1080/14786435.2012.717726.

[734] D. Raabe, R.C. Becker, Coupling of a crystal plasticity finite-element model with a probabilistic cellular automaton for simulating primary static recrystallization in aluminium, Acta Metallurgica 8 (2000) 445–462, doi: 10.1088/0965-0393/8/4/304.

[735] M. Bernacki, H. Resk, T. Coupez, R.E. Logé, Finite element model of primary recrystallization in polycrystalline aggregates using a level set framework, Philosophical Magazine A 17 (2009) 64006, doi: 10.1088/0965-0393/17/6/064006.

[736] W.G. Burgers, Crystal growth in the solid state (Recrystallization), Physica 15 (1949) 92–106, doi: 10.1016/0031-8914(49)90031-2.

[737] M. Upmanyu, R.W. Smith, D.J. Srolovitz, Atomistic Simulation of Curvature Driven Grain Boundary Migration, Interface Science 6 (1998) 41–58, doi: 10.1023/A:1008608418845.

[738] J.W. Cahn, Y. Mishin, Recrystallization initiated by low-temperature grain boundary motion coupled to stress, IJMR 100 (2009) 510–515, doi: 10.3139/146.110066.

[739] P.A. Beck, P.R. Sperry, H. Hu, The Orientation Dependence of the Rate of Grain Boundary Migration, Journal of Applied Physics 21 (1950) 420–425, doi: 10.1063/1.1699676.

[740] J.E. Taylor, J.W. Cahn, C.A. Handwerker, Overview No. 98 I—Geometric models of crystal growth, Acta Metallurgica et Materialia 40 (1992) 1443–1474, doi: 10.1016/0956-7151(92)90090-2.

[741] J.W. Cahn, J.E. Taylor, Overview no. 113 surface motion by surface diffusion, Acta Metallurgica et Materialia 42 (1994) 1045–1063, doi: 10.1016/0956-7151(94)90123-6.

[742] R.D. Doherty, The Deformed State and Nucleation of Recrystallization, Metal Science 8 (1974) 132–142, doi: 10.1179/msc.1974.8.1.132.

[743] J.C.M. Li, Possibility of Subgrain Rotation during Recrystallization, Journal of Applied Physics 33 (1962) 2958–2965, doi: 10.1063/1.1728543.

[744] J.J. Jonas, C.M. Sellars, W.J.M. Tegart, Strength and structure under hot-working conditions, Metallurgical Reviews 14 (1969) 1–24, doi: 10.1179/mtlr.1969.14.1.1.

[745] Y.B. Chun, S.H. Ahn, D.H. Shin, S.K. Hwang, Combined effects of grain size and recrystallization on the tensile properties of cryorolled pure vanadium, Materials Science and Engineering: A 508 (2009) 253–258, doi: 10.1016/j.msea.2009.01.003.

[746] G. Gottstein, D.A. Molodov, L.S. Shvindlerman, D.J. Srolovitz, M. Winning, Grain boundary migration: misorientation dependence, Current Opinion in Solid State and Materials Science 5 (2001) 9–14, doi: 10.1016/S1359-0286(00)00030-9.

[747] S.G. Kim, Y.B. Park, Grain boundary segregation, solute drag and abnormal grain growth, Acta Materialia 56 (2008) 3739–3753, doi: 10.1016/j.actamat.2008.04.007.

[748] M. Hillert, On the theory of normal and abnormal grain growth, Acta Metallurgica 13 (1965) 227–238, doi: 10.1016/0001-6160(65)90200-2.

[749] A.D. Rollett, D.J. Srolovitz, M.P. Anderson, Simulation and theory of abnormal grain growth—anisotropic grain boundary energies and mobilities, Acta Metallurgica 37 (1989) 1227–1240, doi: 10.1016/0001-6160(89)90117-X.

[750] C.J. Simpson, K.T. Aust, W.C. Winegard, The four stages of grain growth, Metallurgical Transactions 2 (1971) 987–991, doi: 10.1007/BF02664229.

[751] D. Fan, L.-Q. Chen, Computer simulation of grain growth using a continuum field model, Acta Materialia 45 (1997) 611–622, doi: 10.1016/S1359-6454(96)00200-5.

[752] M.P. Anderson, D.J. Srolovitz, G.S. Grest, P.S. Sahni, Computer simulation of grain growth—I. Kinetics, Acta Metallurgica 32 (1984) 783–791, doi: 10.1016/0001-6160(84)90151-2.

[753] D.J. Srolovitz, G.S. Grest, M.P. Anderson, A.D. Rollett, Computer simulation of recrystallization—II. Heterogeneous nucleation and growth, Acta Metallurgica 36 (1988) 2115–2128, doi: 10.1016/0001-6160(88)90313-6.

[754] D.J. Srolovitz, M.P. Anderson, G.S. Grest, P.S. Sahni, Computer simulation of grain growth-III. Influence of a particle dispersion, Acta Metallurgica 32 (1984) 1429–1438, doi: 10.1016/0001-6160(84)90089-0.

[755] G.S. Grest, D.J. Srolovitz, M.P. Anderson, Computer simulation of grain growth—IV. Anisotropic grain boundary energies, Acta Metallurgica 33 (1985) 509–520, doi: 10.1016/0001-6160(85)90093-8.

[756] D.J. Srolovitz, G.S. Grest, M.P. Anderson, Computer simulation of grain growth—V. Abnormal grain growth, Acta Metallurgica 33 (1985) 2233–2247, doi: 10.1016/0001-6160(85)90185-3.

[757] L. de Pari, W.Z. Misiolek, Theoretical predictions and experimental verification of surface grain structure evolution for AA6061 during hot rolling, Acta Materialia 56 (2008) 6174–6185, doi: 10.1016/j.actamat.2008.08.050.

[758] F.J. Humphreys, Modelling mechanisms and microstructures of recrystallisation, Materials Science and Technology 8 (1992) 135–144, doi: 10.1179/mst.1992.8.2.135.

[759] A. Khawam, D.R. Flanagan, Solid-state kinetic models: basics and mathematical fundamentals, The journal of physical chemistry. B 110 (2006) 17315–17328, doi: 10.1021/jp062746a.

[760] H.J. McQueen, N.D. Ryan, Constitutive analysis in hot working, Materials Science and Engineering: A 322 (2002) 43–63, doi: 10.1016/S0921-5093(01)01117-0.

[761] F. Chen, H. Zhu, H. Zhang, Z. Cui, Mesoscale Modeling of Dynamic Recrystallization: Multilevel Cellular Automaton Simulation Framework, Metall and Mat Trans A 51 (2020) 1286–1303, doi: 10.1007/s11661-019-05620-3.

[762] J.S. Nagra, A. Brahme, J. Lévesque, R. Mishra, R.A. Lebensohn, K. Inal, A new micromechanics based full field numerical framework to simulate the effects of dynamic recrystallization on the formability of HCP metals, International Journal of Plasticity 125 (2020) 210–234, doi: 10.1016/j.ijplas.2019.09.011.

[763] T. Takaki, Y. Hisakuni, T. Hirouchi, A. Yamanaka, Y. Tomita, Multi-phase-field simulations for dynamic recrystallization, Computational Materials Science 45 (2009) 881–888, doi: 10.1016/j.commatsci.2008.12.009.

[764] T. Takaki, T. Hirouchi, Y. Hisakuni, A. Yamanaka, Y. Tomita, Multi-Phase-Field Model to Simulate Microstructure Evolutions during Dynamic Recrystallization, Mater. Trans. 49 (2008) 2559–2565, doi: 10.2320/matertrans.MB200805.

[765] T. Takaki, C. Yoshimoto, A. Yamanaka, Y. Tomita, Multiscale modeling of hot-working with dynamic recrystallization by coupling microstructure evolution and macroscopic mechanical behavior, International Journal of Plasticity 52 (2014) 105–116, doi: 10.1016/j.ijplas.2013.09.001.

[766] M. Zecevic, R.A. Lebensohn, R.J. McCabe, M. Knezevic, Modelling recrystallization textures driven by intragranular fluctuations implemented in the viscoplastic self-consistent formulation, Acta Materialia 164 (2019) 530–546, doi: 10.1016/j.actamat.2018.11.002.

[767] E.P. Busso, A continuum theory for dynamic recrystallization with microstructure-related length scales, International Journal of Plasticity 14 (1998) 319–353, doi: 10.1016/S0749-6419(98)00008-4.

[768] W.W. Mullins, Two-Dimensional Motion of Idealized Grain Boundaries, Journal of Applied Physics 27 (1956) 900–904, doi: 10.1063/1.1722511.

[769] J. Zhang, W. Ludwig, Y. Zhang, H.H.B. Sørensen, D.J. Rowenhorst, A. Yamanaka, P.W. Voorhees et al., Grain Boundary Mobilities in Polycrystals, Acta Materialia (2020), doi: 10.1016/j.actamat.2020.03.044.

[770] E.A. Holm, S.M. Foiles, How grain growth stops: a mechanism for grain-growth stagnation in pure materials, Science (New York, N.Y.) 328 (2010) 1138–1141, doi: 10.1126/science.1187833.

[771] J. Zhang, Y. Zhang, W. Ludwig, D. Rowenhorst, P.W. Voorhees, H.F. Poulsen, Three-dimensional grain growth in pure iron. Part I. statistics on the grain level, Acta Materialia 156 (2018) 76–85, doi: 10.1016/j.actamat.2018.06.021.

[772] H.-K. Kim, S.G. Kim, W. Dong, I. Steinbach, B.-J. Lee, Phase-field modeling for 3D grain growth based on a grain boundary energy database, Biometrika 22 (2014) 34004, doi: 10.1088/0965-0393/22/3/034004.

[773] I.M. McKenna, M.P. Gururajan, P.W. Voorhees, Phase field modeling of grain growth: effect of boundary thickness, triple junctions, misorientation, and anisotropy, J Mater Sci 44 (2009) 2206–2217, doi: 10.1007/s10853-008-3196-7.

[774] A.E. Johnson, P.W. Voorhees, A phase-field model for grain growth with trijunction drag, Acta Materialia 67 (2014) 134–144, doi: 10.1016/j.actamat.2013.12.012.

[775] A.D. Rollett, G. Gottstein, L.S. Shvindlerman, D.A. Molodov, Grain boundary mobility – a brief review, MEKU 95 (2004) 226–229, doi: 10.3139/146.017938.

[776] G. Gottstein, L.S. Shvindlerman, B. Zhao, Thermodynamics and kinetics of grain boundary triple junctions in metals: Recent developments, Scripta Materialia 62 (2010) 914–917, doi: 10.1016/j.scriptamat.2010.03.017.

[777] E.A. Lazar, J.K. Mason, R.D. MacPherson, D.J. Srolovitz, A more accurate three-dimensional grain growth algorithm, Acta Materialia 59 (2011) 6837–6847, doi: 10.1016/j.actamat.2011.07.052.

[778] H. Gleiter, The mechanism of grain boundary migration, Acta Metallurgica 17 (1969) 565–573, doi: 10.1016/0001-6160(69)90115-1.

[779] S.B. Lee, D.Y. Yoon, N.M. Hwang, M.F. Henry, Grain boundary faceting and abnormal grain growth in nickel, Metall and Mat Trans A 31 (2000) 985–994, doi: 10.1007/s11661-000-0040-3.

[780] S. FOILES, J. HOYT, Computation of grain boundary stiffness and mobility from boundary fluctuations, Acta Materialia 54 (2006) 3351–3357, doi: 10.1016/j.actamat.2006.03.037.

[781] C.P. Race, J. von Pezold, J. Neugebauer, Role of the mesoscale in migration kinetics of flat grain boundaries, Phys. Rev. B 89 (2014), doi: 10.1103/PhysRevB.89.214110.

[782] C.P. Race, R. Hadian, J. von Pezold, B. Grabowski, J. Neugebauer, Mechanisms and kinetics of the migration of grain boundaries containing extended defects, Phys. Rev. B 92 (2015), doi: 10.1103/PhysRevB.92.174115.

[783] Z.T. Trautt, Y. Mishin, Grain boundary migration and grain rotation studied by molecular dynamics, Acta Materialia 60 (2012) 2407–2424, doi: 10.1016/j.actamat.2012.01.008.

[784] H. Zhang, M. Upmanyu, D.J. Srolovitz, Curvature driven grain boundary migration in aluminum: molecular dynamics simulations, Acta Materialia 53 (2005) 79–86, doi: 10.1016/j.actamat.2004.09.004.

[785] U. Czubayko, V.G. Sursaeva, G. Gottstein, L.S. Shvindlerman, Influence of triple junctions on grain boundary motion, Acta Materialia 46 (1998) 5863–5871, doi: 10.1016/S1359-6454(98)00241-9.

[786] D. Mattissen, D.A. Molodov, L.S. Shvindlerman, G. Gottstein, Drag effect of triple junctions on grain boundary and grain growth kinetics in aluminium, Acta Materialia 53 (2005) 2049–2057, doi: 10.1016/j.actamat.2005.01.016.

[787] J.W. Cahn, J.D. Pan, R.W. Balluffi, Diffusion induced grain boundary migration, Scripta Metallurgica 13 (1979) 503–509, doi: 10.1016/0036-9748(79)90078-4.

[788] A.H. King, Diffusion induced grain boundary migration, International Materials Reviews 32 (1987) 173–189, doi: 10.1179/095066087790150304.

[789] R.W. Balluffi, Grain boundary diffusion mechanisms in metals, MTB 13 (1982) 527–553, doi: 10.1007/BF02650011.

[790] D.A. Smith, A.H. King, On the mechanism of diffusion-induced boundary migration, Philosophical Magazine A 44 (1981) 333–340, doi: 10.1080/01418618108239536.

[791] C.Y. Ma, E. Rabkin, W. Gust, S.E. Hsu, On the kinetic behavior and driving force of diffusion induced grain boundary migration, Acta Metallurgica et Materialia 43 (1995) 3113–3124, doi: 10.1016/0956-7151(95)00011-J.

[792] L.A. Barrales-Mora, D.A. Molodov, Capillarity-driven shrinkage of grains with tilt and mixed boundaries studied by molecular dynamics, Acta Materialia 120 (2016) 179–188, doi: 10.1016/j.actamat.2016.08.060.

[793] R.W. Balluffi, J.W. Cahn, Mechanism for diffusion induced grain boundary migration, Acta Metallurgica 29 (1981) 493–500, doi: 10.1016/0001-6160(81)90073-0.

[794] P. Feltham, Grain growth in metals, Acta Metallurgica 5 (1957) 97–105, doi: 10.1016/0001-6160(57)90136-0.

[795] F.J. Humphreys, Recrystallization mechanisms in two-phase alloys, Metal Science 13 (1979) 136–145, doi: 10.1179/msc.1979.13.3-4.136.

[796] F.J. Humphreys, The nucleation of recrystallization at second phase particles in deformed aluminium, Acta Metallurgica 25 (1977) 1323–1344, doi: 10.1016/0001-6160(77)90109-2.

[797] E.I. Galindo-Nava, P.E.J. Rivera-Díaz-del-Castillo, Grain size evolution during discontinuous dynamic recrystallization, Scripta Materialia 72-73 (2014) 1–4, doi: 10.1016/j.scriptamat.2013.09.020.

[798] N.A. Fleck, J.W. Hutchinson, A phenomenological theory for strain gradient effects in plasticity, Journal of the Mechanics and Physics of Solids 41 (1993) 1825–1857, doi: 10.1016/0022-5096(93)90072-N.

[799] N.A. Fleck, J.W. Hutchinson, Strain Gradient Plasticity, in: Elsevier, 1997, pp. 295–361.

[800] N.A. Fleck, J.W. Hutchinson, A reformulation of strain gradient plasticity, Journal of the Mechanics and Physics of Solids 49 (2001) 2245–2271, doi: 10.1016/S0022-5096(01)00049-7.

[801] W.D. Nix, H. Gao, Indentation size effects in crystalline materials, Journal of the Mechanics and Physics of Solids 46 (1998) 411–425, doi: 10.1016/S0022-5096(97)00086-0.

[802] M.E. Gurtin, L. Anand, A theory of strain-gradient plasticity for isotropic, plastically irrotational materials. Part I: Small deformations, Journal of the Mechanics and Physics of Solids 53 (2005) 1624–1649, doi: 10.1016/j.jmps.2004.12.008.

[803] M.E. Gurtin, L. Anand, A theory of strain-gradient plasticity for isotropic, plastically irrotational materials. Part II: Finite deformations, International Journal of Plasticity 21 (2005) 2297–2318, doi: 10.1016/j.ijplas.2005.01.006.

[804] M. GURTIN, A gradient theory of small-deformation isotropic plasticity that accounts for the Burgers vector and for dissipation due to plastic spin, Journal of the Mechanics and Physics of Solids 52 (2004) 2545–2568, doi: 10.1016/j.jmps.2004.04.010.

[805] E.C. Aifantis, Strain gradient interpretation of size effects, in: Z.P. Bažant, Y.D.S. Rajapakse (Eds.), Fracture Scaling, Kluwer Academic Publishers, Dordrecht, 1999, pp. 299–314.

[806] P. Gudmundson, A unified treatment of strain gradient plasticity, Journal of the Mechanics and Physics of Solids 52 (2004) 1379–1406, doi: 10.1016/j.jmps.2003.11.002.

[807] P. Fredriksson, P. Gudmundson, Size-dependent yield strength of thin films, International Journal of Plasticity 21 (2005) 1834–1854, doi: 10.1016/j.ijplas.2004.09.005.

[808] P. Fredriksson, P. Gudmundson, Competition between interface and bulk dominated plastic deformation in strain gradient plasticity, Mechanics of Materials 15 (2007) S61-S69, doi: 10.1088/0965-0393/15/1/S06.

[809] N.A. Fleck, J.R. Willis, A mathematical basis for strain-gradient plasticity theory—Part I, Journal of the Mechanics and Physics of Solids 57 (2009) 161–177, doi: 10.1016/j.jmps.2008.09.010.

[810] N.A. Fleck, J.R. Willis, A mathematical basis for strain-gradient plasticity theory. Part II, Journal of the Mechanics and Physics of Solids 57 (2009) 1045–1057, doi: 10.1016/j.jmps.2009.03.007.

[811] I. Vardoulakis, E.C. Aifantis, A gradient flow theory of plasticity for granular materials, Acta Mech 87 (1991) 197–217, doi: 10.1007/BF01299795.

[812] R.K. Abu Al-Rub, G.Z. Voyiadjis, D.J. Bammann, A thermodynamic based higher-order gradient theory for size dependent plasticity, International Journal of Solids and Structures 44 (2007) 2888–2923, doi: 10.1016/j.ijsolstr.2006.08.034.

[813] N.A. Fleck, J.R. Willis, Bounds and estimates for the effect of strain gradients upon the effective plastic properties of an isotropic two-phase composite, Journal of the Mechanics and Physics of Solids 52 (2004) 1855–1888, doi: 10.1016/j.jmps.2004.02.001.

[814] N.A. Fleck, J.R. Willis, Strain gradient plasticity: energetic or dissipative?, Acta Mech Sinica 31 (2015) 465–472, doi: 10.1007/s10409-015-0468-8.

[815] J.Y. Shu, N.A. Fleck, The prediction of a size effect in microindentation, International Journal of Solids and Structures 35 (1998) 1363–1383, doi: 10.1016/S0020-7683(97)00112-1.

[816] G.Z. Voyiadjis, G. Pekmezi, B. Deliktas, Nonlocal gradient-dependent modeling of plasticity with anisotropic hardening, International Journal of Plasticity 26 (2010) 1335–1356, doi: 10.1016/j.ijplas.2010.01.015.

[817] G.Z. Voyiadjis, Y. Song, Strain gradient continuum plasticity theories: Theoretical, numerical and experimental investigations, International Journal of Plasticity 121 (2019) 21–75, doi: 10.1016/j.ijplas.2019.03.002.

[818] N.A. Fleck, G.M. Muller, M.F. Ashby, J.W. Hutchinson, Strain gradient plasticity, Acta Metallurgica et Materialia 42 (1994) 475–487, doi: 10.1016/0956-7151(94)90502-9.

[819] C. Polizzotto, A unified residual-based thermodynamic framework for strain gradient theories of plasticity, International Journal of Plasticity 27 (2011) 388–413, doi: 10.1016/j.ijplas.2010.07.001.

[820] C. Polizzotto, G. Borino, A thermodynamics-based formulation of gradient-dependent plasticity, European Journal of Mechanics - A/Solids 17 (1998) 741–761, doi: 10.1016/S0997-7538(98)80003-X.

[821] C. Polizzotto, Interfacial energy effects within the framework of strain gradient plasticity, International Journal of Solids and Structures 46 (2009) 1685–1694, doi: 10.1016/j.ijsolstr.2008.12.010.

[822] C. Polizzotto, Strain gradient plasticity, strengthening effects and plastic limit analysis, International Journal of Solids and Structures 47 (2010) 100–112, doi: 10.1016/j.ijsolstr.2009.09.019.

[823] C. Polizzotto, A nonlocal strain gradient plasticity theory for finite deformations, International Journal of Plasticity 25 (2009) 1280–1300, doi: 10.1016/j.ijplas.2008.09.009.

[824] C. Polizzotto, Unified thermodynamic framework for nonlocal/gradient continuum theories, European Journal of Mechanics - A/Solids 22 (2003) 651–668, doi: 10.1016/S0997-7538(03)00075-5.

[825] L. Bardella, Size effects in phenomenological strain gradient plasticity constitutively involving the plastic spin, International Journal of Engineering Science 48 (2010) 550–568, doi: 10.1016/j.ijengsci.2010.01.003.

[826] L. Bardella, A. Panteghini, Modelling the torsion of thin metal wires by distortion gradient plasticity, Journal of the Mechanics and Physics of Solids 78 (2015) 467–492, doi: 10.1016/j.jmps.2015.03.003.

[827] N.A. Fleck, J.W. Hutchinson, J.R. Willis, Strain gradient plasticity under non-proportional loading, Proc. R. Soc. A 470 (2014) 20140267, doi: 10.1098/rspa.2014.0267.

[828] S.H. Chen, T.C. Wang, A new deformation theory with strain gradient effects, International Journal of Plasticity 18 (2002) 971–995, doi: 10.1016/S0749-6419(01)00020-1.

[829] N.A. Fleck, J.W. Hutchinson, J.R. Willis, Guidelines for Constructing Strain Gradient Plasticity Theories, J. Appl. Mech. 82 (2015) 20140267, doi: 10.1115/1.4030323.

[830] L.H. Poh, R.H.J. Peerlings, M.G.D. Geers, S. Swaddiwudhipong, An implicit tensorial gradient plasticity model – Formulation and comparison with a scalar gradient model, International Journal of Solids and Structures 48 (2011) 2595–2604, doi: 10.1016/j.ijsolstr.2011.05.019.

[831] K.L. Nielsen, C.F. Niordson, A numerical basis for strain-gradient plasticity theory, Journal of the Mechanics and Physics of Solids 63 (2014) 113–127, doi: 10.1016/j.jmps.2013.09.018.

[832] C.F. Niordson, J.W. Hutchinson, Non-uniform plastic deformation of micron scale objects, Int. J. Numer. Meth. Engng 56 (2003) 961–975, doi: 10.1002/nme.593.

[833] C.F. Niordson, J.W. Hutchinson, On lower order strain gradient plasticity theories, European Journal of Mechanics - A/Solids 22 (2003) 771–778, doi: 10.1016/S0997-7538(03)00069-X.

[834] C. NIORDSON, Size-effects in plane strain sheet-necking, Journal of the Mechanics and Physics of Solids 52 (2004) 2431–2454, doi: 10.1016/j.jmps.2004.05.009.

[835] I. Tsagrakis, E.C. Aifantis, Recent Developments in Gradient Plasticity—Part I: Formulation and Size Effects, J. Eng. Mater. Technol 124 (2002) 352–357, doi: 10.1115/1.1479695.

[836] H. Gao, Huang Y., W.D. Nix, J.W. Hutchinson, Mechanism-based strain gradient plasticity-I. Theory, Journal of the Mechanics and Physics of Solids 47 (1999) 1239–1263, doi: 10.1016/S0022-5096(98)00103-3.

[837] H. Gao, Y. Huang, Taylor-based nonlocal theory of plasticity, International Journal of Solids and Structures 38 (2001) 2615–2637, doi: 10.1016/S0020-7683(00)00173-6.

[838] Y. Huang, H. Gao, W.D. Nix, J.W. Hutchinson, Mechanism-based strain gradient plasticity—II. Analysis, Journal of the Mechanics and Physics of Solids 48 (2000) 99–128, doi: 10.1016/S0022-5096(99)00022-8.

[839] C.-S. Han, H. Gao, Y. Huang, W.D. Nix, Mechanism-based strain gradient crystal plasticity—I. Theory, Journal of the Mechanics and Physics of Solids 53 (2005) 1188–1203, doi: 10.1016/j.jmps.2004.08.008.

[840] C.-S. Han, H. Gao, Y. Huang, W.D. Nix, Mechanism-based strain gradient crystal plasticity—II. Analysis, Journal of the Mechanics and Physics of Solids 53 (2005) 1204–1222, doi: 10.1016/j.jmps.2005.01.004.

[841] K.E. Aifantis, J.R. Willis, The role of interfaces in enhancing the yield strength of composites and polycrystals, Journal of the Mechanics and Physics of Solids 53 (2005) 1047–1070, doi: 10.1016/j.jmps.2004.12.003.

[842] K.E. Aifantis, W.A. Soer, J.T.M. de Hosson, J.R. Willis, Interfaces within strain gradient plasticity: Theory and experiments, Acta Materialia 54 (2006) 5077–5085, doi: 10.1016/j.actamat.2006.06.040.

[843] K.E. Aifantis, J.R. Willis, Scale effects induced by strain-gradient plasticity and interfacial resistance in periodic and randomly heterogeneous media, Mechanics of Materials 38 (2006) 702–716, doi: 10.1016/j.mechmat.2005.06.010.

[844] J.W. Hutchinson, Plasticity at the micron scale, International Journal of Solids and Structures 37 (2000) 225–238, doi: 10.1016/S0020-7683(99)00090-6.

[845] E.C. Aifantis, Update on a class of gradient theories, Mechanics of Materials 35 (2003) 259–280, doi: 10.1016/S0167-6636(02)00278-8.

[846] R.K.A. Al-Rub, G.Z. Voyiadjis, Determination of the Material Intrinsic Length Scale of Gradient Plasticity Theory, Int J Mult Comp Eng 2 (2004) 377–400, doi: 10.1615/IntJMultCompEng.v2.i3.30.

[847] R.K. Abu Al-Rub, G.Z. Voyiadjis, Analytical and experimental determination of the material intrinsic length scale of strain gradient plasticity theory from micro- and nano-indentation experiments, International Journal of Plasticity 20 (2004) 1139–1182, doi: 10.1016/j.ijplas.2003.10.007.

[848] R.K. Abu Al-Rub, G.Z. Voyiadjis, A physically based gradient plasticity theory, International Journal of Plasticity 22 (2006) 654–684, doi: 10.1016/j.ijplas.2005.04.010.

[849] G.Z. Voyiadjis, R.K.A. Al-Rub, Gradient plasticity theory with a variable length scale parameter, International Journal of Solids and Structures 42 (2005) 3998–4029, doi: 10.1016/j.ijsolstr.2004.12.010.

[850] X. Qiu, Y. Huang, Y. Wei, H. Gao, K.C. Hwang, The flow theory of mechanism-based strain gradient plasticity, Mechanics of Materials 35 (2003) 245–258, doi: 10.1016/S0167-6636(02)00274-0.

[851] X. Qiu, Y. Huang, W.D. Nix, K.C. Hwang, H. Gao, Effect of intrinsic lattice resistance in strain gradient plasticity, Acta Materialia 49 (2001) 3949–3958, doi: 10.1016/S1359-6454(01)00299-3.

[852] K.C. Hwang, H. Jiang, Y. Huang, H. Gao, N. Hu, A finite deformation theory of strain gradient plasticity, Journal of the Mechanics and Physics of Solids 50 (2002) 81–99, doi: 10.1016/S0022-5096(01)00020-5.

[853] K.C. Hwang, Y. Guo, H. Jiang, Y. Huang, Z. Zhuang, The finite deformation theory of Taylor-based nonlocal plasticity, International Journal of Plasticity 20 (2004) 831–839, doi: 10.1016/j.ijplas.2003.08.001.

[854] M.X. Shi, Y. Huang, K.C. Hwang, Plastic flow localization in mechanism-based strain gradient plasticity, International Journal of Mechanical Sciences 42 (2000) 2115–2131, doi: 10.1016/S0020-7403(00)00009-6.

[855] H. Jiang, Y. Huang, Z. Zhuang, K.C. Hwang, Fracture in mechanism-based strain gradient plasticity, Journal of the Mechanics and Physics of Solids 49 (2001) 979–993, doi: 10.1016/S0022-5096(00)00070-3.

[856] Y. Huang, S. Qu, K.C. Hwang, M. Li, H. Gao, A conventional theory of mechanism-based strain gradient plasticity, International Journal of Plasticity 20 (2004) 753–782, doi: 10.1016/j.ijplas.2003.08.002.

[857] Z. Xue, Y. Huang, M. Li, Particle size effect in metallic materials, Acta Materialia 50 (2002) 149–160, doi: 10.1016/S1359-6454(01)00325-1.

[858] H. Yuan, J. Chen, Identification of the intrinsic material length in gradient plasticity theory from micro-indentation tests, International Journal of Solids and Structures 38 (2001) 8171–8187, doi: 10.1016/S0020-7683(01)00121-4.

[859] H. Yuan, J. Chen, Analysis of size effects based on a symmetric lower-order gradient plasticity model, Computational Materials Science 19 (2000) 143–157, doi: 10.1016/S0927-0256(00)00149-X.

[860] Z.P. Bažant, Z. Guo, Size effect and asymptotic matching approximations in strain-gradient theories of micro-scale plasticity, International Journal of Solids and Structures 39 (2002) 5633–5657, doi: 10.1016/S0020-7683(02)00368-2.

[861] V.P. Smyshlyaev, N.A. Fleck, Bounds and estimates for the overall plastic behaviour of composites with strain gradient effects, Proc. R. Soc. Lond. A 451 (1995) 795–810, doi: 10.1098/rspa.1995.0156.

[862] G.Z. Voyiadjis, B. Deliktas, Formulation of strain gradient plasticity with interface energy in a consistent thermodynamic framework, International Journal of Plasticity 25 (2009) 1997–2024, doi: 10.1016/j.ijplas.2008.12.014.

[863] G.Z. Voyiadjis, B. Deliktas, Mechanics of strain gradient plasticity with particular reference to decomposition of the state variables into energetic and dissipative components, International Journal of Engineering Science 47 (2009) 1405–1423, doi: 10.1016/j.ijengsci.2009.05.013.

[864] G.Z. Voyiadjis, D. Faghihi, Thermo-mechanical strain gradient plasticity with energetic and dissipative length scales, International Journal of Plasticity 30-31 (2012) 218–247, doi: 10.1016/j.ijplas.2011.10.007.

[865] G.Z. Voyiadjis, D. Faghihi, Gradient plasticity for thermo-mechanical processes in metals with length and time scales, Phil. Mag. 93 (2013) 1013–1053, doi: 10.1080/14786435.2012.740576.

[866] G.Z. Voyiadjis, D. Faghihi, Y. Zhang, A theory for grain boundaries with strain-gradient plasticity, International Journal of Solids and Structures 51 (2014) 1872–1889, doi: 10.1016/j.ijsolstr.2014.01.020.

[867] G.Z. Voyiadjis, Y. Song, Effect of passivation on higher order gradient plasticity models for non-proportional loading: energetic and dissipative gradient components, Phil. Mag. 97 (2017) 318–345, doi: 10.1080/14786435.2016.1260783.

[868] G.Z. Voyiadjis, Y. Song, T. Park, Higher-Order Thermomechanical Gradient Plasticity Model With Energetic and Dissipative Components, J. Eng. Mater. Technol 139 (2017) 475, doi: 10.1115/1.4035293.

[869] L.H. Poh, Scale transition of a higher order plasticity model – A consistent homogenization theory from meso to macro, Journal of the Mechanics and Physics of Solids 61 (2013) 2692–2710, doi: 10.1016/j.jmps.2013.09.004.

[870] L.H. Poh, V.T. Phan, Numerical implementation and validation of a consistently homogenized higher order plasticity model, Int. J. Numer. Meth. Engng 106 (2016) 454–483, doi: 10.1002/nme.5129.

[871] L.H. Poh, R.H.J. Peerlings, M.G.D. Geers, S. Swaddiwudhipong, Homogenization towards a grain-size dependent plasticity theory for single slip, Journal of the Mechanics and Physics of Solids 61 (2013) 913–927, doi: 10.1016/j.jmps.2013.01.002.

[872] S.P. Lele, L. Anand, A small-deformation strain-gradient theory for isotropic viscoplastic materials, Phil. Mag. 88 (2008) 3655–3689, doi: 10.1080/14786430802087031.

[873] S.P. Lele, L. Anand, A large-deformation strain-gradient theory for isotropic viscoplastic materials, International Journal of Plasticity 25 (2009) 420–453, doi: 10.1016/j.ijplas.2008.04.003.

[874] D. Liu, D.J. Dunstan, Material length scale of strain gradient plasticity: A physical interpretation, International Journal of Plasticity 98 (2017) 156–174, doi: 10.1016/j.ijplas.2017.07.007.

[875] H. Mughrabi, On the current understanding of strain gradient plasticity, Materials Science and Engineering: A 387-389 (2004) 209–213, doi: 10.1016/j.msea.2004.01.086.

[876] A.G. Evans, J.W. Hutchinson, A critical assessment of theories of strain gradient plasticity, Acta Materialia 57 (2009) 1675–1688, doi: 10.1016/j.actamat.2008.12.012.

[877] C.F.O. Dahlberg, M. Boåsen, Evolution of the length scale in strain gradient plasticity, International Journal of Plasticity 112 (2019) 220–241, doi: 10.1016/j.ijplas.2018.08.016.

[878] A.C. Eringen, Nonlocal Continuum Mechanics and Some Applications, in: A.O. Barut (Ed.), Nonlinear Equations in Physics and Mathematics, Springer Netherlands, Dordrecht, 1978, pp. 271–318.

[879] A.C. Eringen, Theories of nonlocal plasticity, International Journal of Engineering Science 21 (1983) 741–751, doi: 10.1016/0020-7225(83)90058-7.

[880] A.C. Eringen, On nonlocal plasticity, International Journal of Engineering Science 19 (1981) 1461–1474, doi: 10.1016/0020-7225(81)90072-0.

[881] L. Strömberg, M. Ristinmaa, FE-formulation of a nonlocal plasticity theory, Computer Methods in Applied Mechanics and Engineering 136 (1996) 127–144, doi: 10.1016/0045-7825(96)00997-8.

[882] S.A.H. Motaman, K. Schacht, C. Haase, U. Prahl, Thermo-micro-mechanical simulation of metal forming processes, International Journal of Solids and Structures 178-179 (2019) 59–80, doi: 10.1016/j.ijsolstr.2019.05.028.

[883] N.C. Admal, G. Po, J. Marian, Diffuse-interface polycrystal plasticity: expressing grain boundaries as geometrically necessary dislocations, Mater Theory 1 (2017) 3643, doi: 10.1186/s41313-017-0006-0.

[884] M.E. Gurtin, A gradient theory of single-crystal viscoplasticity that accounts for geometrically necessary dislocations, Journal of the Mechanics and Physics of Solids 50 (2002) 5–32, doi: 10.1016/S0022-5096(01)00104-1.

[885] M. Kuroda, V. Tvergaard, On the formulations of higher-order strain gradient crystal plasticity models, Journal of the Mechanics and Physics of Solids 56 (2008) 1591–1608, doi: 10.1016/j.jmps.2007.07.015.

[886] A. Acharya, J.L. Bassani, Lattice incompatibility and a gradient theory of crystal plasticity, Journal of the Mechanics and Physics of Solids 48 (2000) 1565–1595, doi: 10.1016/S0022-5096(99)00075-7.

[887] M.E. Gurtin, The Burgers vector and the flow of screw and edge dislocations in finite-deformation single-crystal plasticity, Journal of the Mechanics and Physics of Solids 54 (2006) 1882–1898, doi: 10.1016/j.jmps.2006.03.003.

[888] M.E. Gurtin, On the plasticity of single crystals: free energy, microforces, plastic-strain gradients, Journal of the Mechanics and Physics of Solids 48 (2000) 989–1036, doi: 10.1016/S0022-5096(99)00059-9.

[889] A. Needleman, Computational mechanics at the mesoscale, Acta Materialia 48 (2000) 105–124, doi: 10.1016/S1359-6454(99)00290-6.

[890] J.L. Bassani, Incompatibility and a simple gradient theory of plasticity, Journal of the Mechanics and Physics of Solids 49 (2001) 1983–1996, doi: 10.1016/S0022-5096(01)00037-0.

[891] V.P. Smyshlyaev, N.A. Fleck, The role of strain gradients in the grain size effect for polycrystals, Journal of the Mechanics and Physics of Solids 44 (1996) 465–495, doi: 10.1016/0022-5096(96)00009-9.

[892] M.E. Gurtin, L. Anand, S.P. Lele, Gradient single-crystal plasticity with free energy dependent on dislocation densities, Journal of the Mechanics and Physics of Solids 55 (2007) 1853–1878, doi: 10.1016/j.jmps.2007.02.006.

[893] A. Menzel, On the continuum formulation of higher gradient plasticity for single and polycrystals, Journal of the Mechanics and Physics of Solids 48 (2000) 1777–1796, doi: 10.1016/S0022-5096(99)00024-1.

[894] K. Shizawa, H.M. Zbib, A thermodynamical theory of gradient elastoplasticity with dislocation density tensor. I: Fundamentals, International Journal of Plasticity 15 (1999) 899–938, doi: 10.1016/S0749-6419(99)00018-2.

[895] L. Bardella, Some remarks on the strain gradient crystal plasticity modelling, with particular reference to the material length scales involved, International Journal of Plasticity 23 (2007) 296–322, doi: 10.1016/j.ijplas.2006.05.004.

[896] L. BARDELLA, A. GIACOMINI, Influence of material parameters and crystallography on the size effects describable by means of strain gradient plasticity, Journal of the Mechanics and Physics of Solids 56 (2008) 2906–2934, doi: 10.1016/j.jmps.2008.04.001.

[897] C.F. Niordson, J.W. Kysar, Computational strain gradient crystal plasticity, Journal of the Mechanics and Physics of Solids 62 (2014) 31–47, doi: 10.1016/j.jmps.2013.08.014.

[898] E. Bayerschen, A.T. McBride, B.D. Reddy, T. Böhlke, Review on slip transmission criteria in experiments and crystal plasticity models, J Mater Sci 51 (2016) 2243–2258, doi: 10.1007/s10853-015-9553-4.

[899] T.R. Bieler, P. Eisenlohr, C. Zhang, H.J. Phukan, M.A. Crimp, Grain boundaries and interfaces in slip transfer, Current Opinion in Solid State and Materials Science 18 (2014) 212–226, doi: 10.1016/j.cossms.2014.05.003.

[900] M.d. Koning, R. Miller, V.V. Bulatov, F.F. Abraham, Modelling grain-boundary resistance in intergranular dislocation slip transmission, Philosophical Magazine A 82 (2002) 2511–2527, doi: 10.1080/01418610208240050.

[901] M. de Koning, R.J. Kurtz, V.V. Bulatov, C.H. Henager, R.G. Hoagland, W. Cai, M. Nomura, Modeling of dislocation–grain boundary interactions in FCC metals, Journal of Nuclear Materials 323 (2003) 281–289, doi: 10.1016/j.jnucmat.2003.08.008.

[902] J.D. Livingston, B. Chalmers, Multiple slip in bicrystal deformation, Acta Metallurgica 5 (1957) 322–327, doi: 10.1016/0001-6160(57)90044-5.

[903] J. Luster, M.A. Morris, Compatibility of deformation in two-phase Ti-Al alloys: Dependence on microstructure and orientation relationships, Metall and Mat Trans A 26 (1995) 1745–1756, doi: 10.1007/BF02670762.

[904] W.A.T. Clark, R.H. Wagoner, Z.Y. Shen, T.C. Lee, I.M. Robertson, H.K. Birnbaum, On the criteria for slip transmission across interfaces in polycrystals, Scripta Metallurgica et Materialia 26 (1992) 203–206, doi: 10.1016/0956-716X(92)90173-C.

[905] Z. Shen, R.H. Wagoner, W.A.T. Clark, Dislocation and grain boundary interactions in metals, Acta Metallurgica 36 (1988) 3231–3242, doi: 10.1016/0001-6160(88)90058-2.

[906] E. Werner, W. Prantl, Slip transfer across grain and phase boundaries, Acta Metallurgica et Materialia 38 (1990) 533–537, doi: 10.1016/0956-7151(90)90159-E.

[907] L. Patriarca, W. Abuzaid, H. Sehitoglu, H.J. Maier, Slip transmission in bcc FeCr polycrystal, Materials Science and Engineering: A 588 (2013) 308–317, doi: 10.1016/j.msea.2013.08.050.

[908] T.C. Lee, I.M. Robertson, H.K. Birnbaum, Prediction of slip transfer mechanisms across grain boundaries, Scripta Metallurgica 23 (1989) 799–803, doi: 10.1016/0036-9748(89)90534-6.

[909] I. Tiba, T. Richeton, C. Motz, H. Vehoff, S. BERBENNI, Incompatibility stresses at grain boundaries in Ni bicrystalline micropillars analyzed by an anisotropic model and slip activity, Acta Materialia 83 (2015) 227–238, doi: 10.1016/j.actamat.2014.09.033.

[910] J. Kacher, B.P. Eftink, B. Cui, I.M. Robertson, Dislocation interactions with grain boundaries, Current Opinion in Solid State and Materials Science 18 (2014) 227–243, doi: 10.1016/j.cossms.2014.05.004.

[911] J. Kacher, A.M. Minor, Twin boundary interactions with grain boundaries investigated in pure rhenium, Acta Materialia 81 (2014) 1–8, doi: 10.1016/j.actamat.2014.08.013.

[912] X. Hong, A. Godfrey, W. Liu, Challenges in the prediction of twin transmission at grain boundaries in a magnesium alloy, Scripta Materialia 123 (2016) 77–80, doi: 10.1016/j.scriptamat.2016.05.044.

[913] J.P. Hirth, R.C. Pond, J. Lothe, Disconnections in tilt walls, Acta Materialia 54 (2006) 4237–4245, doi: 10.1016/j.actamat.2006.05.017.

[914] S. Haouala, R. Alizadeh, T.R. Bieler, J. Segurado, J. LLorca, Effect of slip transmission at grain boundaries in Al bicrystals, International Journal of Plasticity 126 (2020) 102600, doi: 10.1016/j.ijplas.2019.09.006.

[915] Z. Shen, R.H. Wagoner, W.A.T. Clark, Dislocation pile-up and grain boundary interactions in 304 stainless steel, Scripta Metallurgica 20 (1986) 921–926, doi: 10.1016/0036-9748(86)90467-9.

[916] Z. Li, C. Hou, M. Huang, C. Ouyang, Strengthening mechanism in micro-polycrystals with penetrable grain boundaries by discrete dislocation dynamics simulation and Hall–Petch effect, Computational Materials Science 46 (2009) 1124–1134, doi: 10.1016/j.commatsci.2009.05.021.

[917] Y. SHEN, P. ANDERSON, Transmission of a screw dislocation across a coherent, slipping interface, Acta Materialia 54 (2006) 3941–3951, doi: 10.1016/j.actamat.2006.04.026.

[918] Y. SHEN, P. ANDERSON, Transmission of a screw dislocation across a coherent, non-slipping interface, Journal of the Mechanics and Physics of Solids 55 (2007) 956–979, doi: 10.1016/j.jmps.2006.11.005.

[919] T. Tsuru, Y. Shibutani, T. Hirouchi, A predictive model for transferability of plastic deformation through grain boundaries, AIP Advances 6 (2016) 15004, doi: 10.1063/1.4939819.

[920] D.E. Spearot, M.D. Sangid, Insights on slip transmission at grain boundaries from atomistic simulations, Current Opinion in Solid State and Materials Science 18 (2014) 188–195, doi: 10.1016/j.cossms.2014.04.001.

[921] D.J. Dingley, R.C. Pond, On the interaction of crystal dislocations with grain boundaries, Acta Metallurgica 27 (1979) 667–682, doi: 10.1016/0001-6160(79)90018-X.

[922] J. Kacher, I.M. Robertson, Quasi-four-dimensional analysis of dislocation interactions with grain boundaries in 304 stainless steel, Acta Materialia 60 (2012) 6657–6672, doi: 10.1016/j.actamat.2012.08.036.

[923] T.C. Lee, I.M. Robertson, H.K. Birnbaum, An In Situ transmission electron microscope deformation study of the slip transfer mechanisms in metals, MTA 21 (1990) 2437–2447, doi: 10.1007/BF02646988.

[924] T.C. Lee, I.M. Robertson, H.K. Birnbaum, TEM in situ deformation study of the interaction of lattice dislocations with grain boundaries in metals, Philosophical Magazine A 62 (1990) 131–153, doi: 10.1080/01418619008244340.

[925] M.P. Dewald, W.A. Curtin, Multiscale modelling of dislocation/grain-boundary interactions: I. Edge dislocations impinging on $\Sigma 11$ (1 1 3) tilt boundary in Al, Modelling Simul. Mater. Sci. Eng. 15 (2007) S193-S215, doi: 10.1088/0965-0393/15/1/S16.

[926] M.P. Dewald, W.A. Curtin, Multiscale modelling of dislocation/grain boundary interactions. II. Screw dislocations impinging on tilt boundaries in Al, Phil. Mag. 87 (2007) 4615–4641, doi: 10.1080/14786430701297590.

[927] A. Hunter, B. Leu, I.J. Beyerlein, A review of slip transfer, J Mater Sci 53 (2018) 5584–5603, doi: 10.1007/s10853-017-1844-5.

[928] J.D. Clayton, Mesoscale models of interface mechanics in crystalline solids: a review, J Mater Sci 53 (2018) 5515–5545, doi: 10.1007/s10853-017-1596-2.

[929] J. Wang, A. Misra, R.G. Hoagland, J.P. Hirth, Slip transmission across fcc/bcc interfaces with varying interface shear strengths, Acta Materialia 60 (2012) 1503–1513, doi: 10.1016/j.actamat.2011.11.047.

[930] A. Ma, F. Roters, D. Raabe, On the consideration of interactions between dislocations and grain boundaries in crystal plasticity finite element modeling – Theory, experiments, and simulations, Acta Materialia 54 (2006) 2181–2194, doi: 10.1016/j.actamat.2006.01.004.

[931] A. Ma, F. Roters, D. Raabe, Studying the effect of grain boundaries in dislocation density based crystal-plasticity finite element simulations, International Journal of Solids and Structures 43 (2006) 7287–7303, doi: 10.1016/j.ijsolstr.2006.07.006.

[932] A. Acharya, A. ROY, Size effects and idealized dislocation microstructure at small scales: Predictions of a Phenomenological model of Mesoscopic Field Dislocation Mechanics: Part I, Journal of the Mechanics and Physics of Solids 54 (2006) 1687–1710, doi: 10.1016/j.jmps.2006.01.009.

[933] İ. Özdemir, T. Yalçinkaya, Modeling of dislocation–grain boundary interactions in a strain gradient crystal plasticity framework, Comput Mech 54 (2014) 255–268, doi: 10.1007/s00466-014-0982-8.

[934] P.R.M. van Beers, G.J. McShane, V.G. Kouznetsova, M.G.D. Geers, Grain boundary interface mechanics in strain gradient crystal plasticity, Journal of the Mechanics and Physics of Solids 61 (2013) 2659–2679, doi: 10.1016/j.jmps.2013.08.011.

[935] C.J. Bayley, W.A.M. Brekelmans, M.G.D. Geers, A comparison of dislocation induced back stress formulations in strain gradient crystal plasticity, International Journal of Solids and Structures 43 (2006) 7268–7286, doi: 10.1016/j.ijsolstr.2006.05.011.

[936] N.M. Cordero, S. Forest, E.P. Busso, S. BERBENNI, M. CHERKAOUI, Grain size effects on plastic strain and dislocation density tensor fields in metal polycrystals, Computational Materials Science 52 (2012) 7–13, doi: 10.1016/j.commatsci.2011.02.043.

[937] İ. Ertürk, J.A.W. van Dommelen, M.G.D. Geers, Energetic dislocation interactions and thermodynamical aspects of strain gradient crystal plasticity theories, Journal of the Mechanics and Physics of Solids 57 (2009) 1801–1814, doi: 10.1016/j.jmps.2009.08.003.

[938] M. GURTIN, A theory of grain boundaries that accounts automatically for grain misorientation and grain-boundary orientation, Journal of the Mechanics and Physics of Solids 56 (2008) 640–662, doi: 10.1016/j.jmps.2007.05.002.

[939] A. Acharya, Jump condition for GND evolution as a constraint on slip transmission at grain boundaries, Philosophical Magazine 87 (2007) 1349–1359, doi: 10.1080/14786430600951537.

[940] M. GURTIN, A. Needleman, Boundary conditions in small-deformation, single-crystal plasticity that account for the Burgers vector, Journal of the Mechanics and Physics of Solids 53 (2005) 1–31, doi: 10.1016/j.jmps.2004.06.006.

[941] J.R. Mayeur, I.J. Beyerlein, C.A. Bronkhorst, H.M. Mourad, Incorporating interface affected zones into crystal plasticity, International Journal of Plasticity 65 (2015) 206–225, doi: 10.1016/j.ijplas.2014.08.013.

[942] P. Cermelli, M.E. Gurtin, Geometrically necessary dislocations in viscoplastic single crystals and bicrystals undergoing small deformations, International Journal of Solids and Structures 39 (2002) 6281–6309, doi: 10.1016/S0020-7683(02)00491-2.

[943] W.M. Ashmawi, M.A. Zikry, Prediction of Grain-Boundary Interfacial Mechanisms in Polycrystalline Materials, J. Eng. Mater. Technol 124 (2002) 88–96, doi: 10.1115/1.1421611.

[944] M. Ekh, S. Bargmann, M. Grymer, Influence of grain boundary conditions on modeling of size-dependence in polycrystals, Acta Mechanica 218 (2011) 103–113, doi: 10.1007/s00707-010-0403-9.

[945] S. Wulfinghoff, E. Bayerschen, T. Böhlke, A gradient plasticity grain boundary yield theory, International Journal of Plasticity 51 (2013) 33–46, doi: 10.1016/j.ijplas.2013.07.001.

[946] T. Pardoen, T.J. Massart, Interface controlled plastic flow modelled by strain gradient plasticity theory, Comptes Rendus Mécanique 340 (2012) 247–260, doi: 10.1016/j.crme.2012.02.008.

[947] D. Gottschalk, A. McBride, B.D. Reddy, A. Javili, P. Wriggers, C.B. Hirschberger, Computational and theoretical aspects of a grain-boundary model that accounts for grain misorientation and grain-boundary orientation, Computational Materials Science 111 (2016) 443–459, doi: 10.1016/j.commatsci.2015.09.048.

[948] S. Puri, A. Das, A. Acharya, Mechanical response of multicrystalline thin films in mesoscale field dislocation mechanics, Journal of the Mechanics and Physics of Solids 59 (2011) 2400–2417, doi: 10.1016/j.jmps.2011.06.009.

[949] S. Puri, A. Roy, Plastic deformation of multicrystalline thin films: Grain size distribution vs. grain orientation, Computational Materials Science 52 (2012) 20–24, doi: 10.1016/j.commatsci.2011.03.001.

[950] T. Richeton, L.T. Le, T. Chauve, M. Bernacki, S. BERBENNI, M. Montagnat, Modelling the transport of geometrically necessary dislocations on slip systems: application to single- and multi-crystals of ice, Proc. Phys. Soc. B 25 (2017) 25010, doi: 10.1088/1361-651X/aa5341.

[951] A. ROY, A. Acharya, Size effects and idealized dislocation microstructure at small scales: Predictions of a Phenomenological model of Mesoscopic Field Dislocation Mechanics: Part II, Journal of the Mechanics and Physics of Solids 54 (2006) 1711–1743, doi: 10.1016/j.jmps.2006.01.012.

[952] A. ROY, S. Puri, A. Acharya, Phenomenological mesoscopic field dislocation mechanics, lower-order gradient plasticity, and transport of mean excess dislocation density, Acta Metallurgica 15 (2007) S167-S180, doi: 10.1088/0965-0393/15/1/S14.

[953] V. Taupin, S. BERBENNI, C. Fressengeas, Size effects on the hardening of channel-type microstructures: A field dislocation mechanics-based approach, Acta Materialia 60 (2012) 664–673, doi: 10.1016/j.actamat.2011.10.033.

[954] L.P. Evers, W.A.M. Brekelmans, M.G.D. Geers, Non-local crystal plasticity model with intrinsic SSD and GND effects, Journal of the Mechanics and Physics of Solids 52 (2004) 2379–2401, doi: 10.1016/j.jmps.2004.03.007.

[955] O. Rezvanian, M.A. Zikry, A.M. Rajendran, Statistically stored, geometrically necessary and grain boundary dislocation densities: microstructural representation and modelling, Proc. R. Soc. A 463 (2007) 2833–2853, doi: 10.1098/rspa.2007.0020.

[956] A. Gupta, D.J. Steigmann, Plastic flow in solids with interfaces, Math. Meth. Appl. Sci. 35 (2012) 1799–1824, doi: 10.1002/mma.1611.

[957] L. Bardella, A deformation theory of strain gradient crystal plasticity that accounts for geometrically necessary dislocations, Journal of the Mechanics and Physics of Solids 54 (2006) 128–160, doi: 10.1016/j.jmps.2005.08.003.

[958] H. Lim, M.G. Lee, J.H. Kim, B.L. Adams, R.H. Wagoner, Simulation of polycrystal deformation with grain and grain boundary effects, International Journal of Plasticity 27 (2011) 1328–1354, doi: 10.1016/j.ijplas.2011.03.001.

[959] H. Lim, S. Subedi, D.T. Fullwood, B.L. Adams, R.H. Wagoner, A Practical Meso-Scale Polycrystal Model to Predict Dislocation Densities and the Hall–Petch Effect, Mater. Trans. 55 (2014) 35–38, doi: 10.2320/matertrans.MA201305.

[960] A.J. Beaudoin, A. Acharya, S.R. Chen, D.A. Korzekwa, M.G. Stout, Consideration of grain-size effect and kinetics in the plastic deformation of metal polycrystals, Acta Materialia 48 (2000) 3409–3423, doi: 10.1016/S1359-6454(00)00136-1.

[961] M.E. Gurtin, A finite-deformation, gradient theory of single-crystal plasticity with free energy dependent on the accumulation of geometrically necessary dislocations, International Journal of Plasticity 26 (2010) 1073–1096, doi: 10.1016/j.ijplas.2010.02.002.

[962] M.E. Gurtin, B.D. Reddy, Gradient single-crystal plasticity within a Mises–Hill framework based on a new formulation of self- and latent-hardening, Journal of the Mechanics and Physics of Solids 68 (2014) 134–160, doi: 10.1016/j.jmps.2014.01.002.

[963] M.E. Gurtin, A finite-deformation, gradient theory of single-crystal plasticity with free energy dependent on densities of geometrically necessary dislocations, International Journal of Plasticity 24 (2008) 702–725, doi: 10.1016/j.ijplas.2007.07.014.

[964] J.Y. Shu, N.A. Fleck, Strain gradient crystal plasticity, Journal of the Mechanics and Physics of Solids 47 (1999) 297–324, doi: 10.1016/S0022-5096(98)00081-7.

[965] V. Levkovitch, B. Svendsen, On the large-deformation- and continuum-based formulation of models for extended crystal plasticity, International Journal of Solids and Structures 43 (2006) 7246–7267, doi: 10.1016/j.ijsolstr.2006.05.010.

[966] M. Kuroda, Interfacial microscopic boundary conditions associated with backstress-based higher-order gradient crystal plasticity theory, JOMMS 12 (2017) 193–218, doi: 10.2140/jomms.2017.12.193.

[967] M. Ghorbani Moghaddam, A. Achuthan, B.A. Bednarcyk, S.M. Arnold, E.J. Pineda, Grain size-dependent crystal plasticity constitutive model for polycrystal materials, Materials Science and Engineering: A 703 (2017) 521–532, doi: 10.1016/j.msea.2017.07.087.

[968] L.H. Poh, R.H.J. Peerlings, The plastic rotation effect in an isotropic gradient plasticity model for applications at the meso scale, International Journal of Solids and Structures 78-79 (2016) 57–69, doi: 10.1016/j.ijsolstr.2015.09.017.

[969] L.H. Poh, R.H.J. Peerlings, M.G.D. Geers, S. Swaddiwudhipong, Towards a homogenized plasticity theory which predicts structural and microstructural size effects, Journal of the Mechanics and Physics of Solids 61 (2013) 2240–2259, doi: 10.1016/j.jmps.2013.06.004.

[970] S. BERBENNI, V. FAVIER, M. Berveiller, Impact of the grain size distribution on the yield stress of heterogeneous materials, International Journal of Plasticity 23 (2007) 114–142, doi: 10.1016/j.ijplas.2006.03.004.

[971] S. BERBENNI, V. FAVIER, M. Berveiller, Micro–macro modelling of the effects of the grain size distribution on the plastic flow stress of heterogeneous materials, Computational Materials Science 39 (2007) 96–105, doi: 10.1016/j.commatsci.2006.02.019.

[972] B. Raeisinia, C.W. Sinclair, A representative grain size for the mechanical response of polycrystals, Materials Science and Engineering: A 525 (2009) 78–82, doi: 10.1016/j.msea.2009.06.045.

[973] K.J. Kurzydłowski, A model for the flow stress dependence on the distribution of grain size in polycrystals, Scripta Metallurgica et Materialia 24 (1990) 879–883, doi: 10.1016/0956-716X(90)90129-5.

[974] B. Raeisinia, C.W. Sinclair, W.J. Poole, C.N. Tomé, On the impact of grain size distribution on the plastic behaviour of polycrystalline metals, Modelling Simul. Mater. Sci. Eng. 16 (2008) 25001, doi: 10.1088/0965-0393/16/2/025001.

[975] Y. Liu, J. Zhou, X. Ling, Impact of grain size distribution on the multiscale mechanical behavior of nanocrystalline materials, Materials Science and Engineering: A 527 (2010) 1719–1729, doi: 10.1016/j.msea.2009.11.033.

[976] F. Lavergne, R. Brenner, K. Sab, Effects of grain size distribution and stress heterogeneity on yield stress of polycrystals: A numerical approach, Computational Materials Science 77 (2013) 387–398, doi: 10.1016/j.commatsci.2013.04.061.

[977] S.P. Joshi, K.T. Ramesh, B.Q. Han, E.J. Lavernia, Modeling the constitutive response of bimodal metals, Metall and Mat Trans A 37 (2006) 2397–2404, doi: 10.1007/BF02586214.

[978] E.N. Borodin, A.E. Mayer, Influence of structure of grain boundaries and size distribution of grains on the yield strength at quasistatic and dynamical loading, Modelling Simul. Mater. Sci. Eng. 4 (2017) 85040, doi: 10.1088/2053-1591/aa8514.

[979] B. ZHU, R. ASARO, P. KRYSL, K. ZHANG, J. Weertman, Effects of grain size distribution on the mechanical response of nanocrystalline metals: Part II, Acta Materialia 54 (2006) 3307–3320, doi: 10.1016/j.actamat.2006.03.022.

[980] K.J. Kurzydlowski, J.J. Bucki, A method for grain size and grain size uniformity estimation - applications to polycrystalline materials, Scripta Metallurgica et Materialia 27 (1992) 117–120, doi: 10.1016/0956-716X(92)90330-H.

[981] K.J. Kurzydłowski, J.J. Bucki, Flow stress dependence on the distribution of grain size in polycrystals, Acta Metallurgica et Materialia 41 (1993) 3141–3146, doi: 10.1016/0956-7151(93)90044-S.

[982] K.J. Kurzydłowski, B. Ralph, J.J. Bucki, A. Garbacz, The grain boundary character distribution effect on the flow stress of polycrystals: The influence of crystal lattice texture, Materials Science and Engineering: A 205 (1996) 127–132, doi: 10.1016/0921-5093(95)09886-0.

[983] T. Yu, H. Shi, Effects of grain size distribution on the creep damage evolution of polycrystalline materials, J. Phys. D: Appl. Phys. 43 (2010) 165401, doi: 10.1088/0022-3727/43/16/165401.

[984] A. Abel, H. Muir, The Bauschinger effect and discontinuous yielding, Phil. Mag. 26 (1972) 489–504, doi: 10.1080/14786437208227444.

[985] P.S. Bate, D.V. Wilson, Analysis of the bauschinger effect, Acta Metallurgica 34 (1986) 1097–1105, doi: 10.1016/0001-6160(86)90220-8.

[986] Y. Xiang, J.J. Vlassak, Bauschinger and size effects in thin-film plasticity, Acta Materialia 54 (2006) 5449–5460, doi: 10.1016/j.actamat.2006.06.059.

[987] R.E. Stoltz, R.M. Pelloux, The Bauschinger effect in precipitation strengthened aluminum alloys, MTA 7 (1976) 1295–1306, doi: 10.1007/BF02658814.

[988] J.H. Schmitt, E.L. Shen, J.L. Raphanel, A parameter for measuring the magnitude of a change of strain path: Validation and comparison with experiments on low carbon steel, International Journal of Plasticity 10 (1994) 535–551, doi: 10.1016/0749-6419(94)90013-2.

[989] L.E. Levine, M.R. Stoudt, A. Creuziger, T.Q. Phan, R. Xu, M.E. Kassner, Basis for the Bauschinger effect in copper single crystals: changes in the long-range internal stress with reverse deformation, J Mater Sci 54 (2019) 6579–6585, doi: 10.1007/s10853-018-03295-6.

[990] I.J. Beyerlein, C.N. Tomé, Modeling transients in the mechanical response of copper due to strain path changes, International Journal of Plasticity 23 (2007) 640–664, doi: 10.1016/j.ijplas.2006.08.001.

[991] A. Abel, Historical perspectives and some of the main features of the Bauschinger effect, Materials forum (Rushcutters Bay) 10 (1987) 11–26.

[992] T. Hasegawa, T. Yakou, S. Karashima, Deformation behaviour and dislocation structures upon stress reversal in polycrystalline aluminium, Materials Science and Engineering 20 (1975) 267–276, doi: 10.1016/0025-5416(75)90159-7.

[993] H. Mughrabi, The cyclic hardening and saturation behaviour of copper single crystals, Materials Science and Engineering 33 (1978) 207–223, doi: 10.1016/0025-5416(78)90174-X.

[994] O.B. Pedersen, L.M. Brown, W.M. Stobbs, The bauschinger effect in copper, Acta Metallurgica 29 (1981) 1843–1850, doi: 10.1016/0001-6160(81)90110-3.

[995] M.G. Stout, A.D. Rollett, Large-strain Bauschinger effects in fcc metals and alloys, MTA 21 (1990) 3201–3213, doi: 10.1007/BF02647315.

[996] Y. Xiang, J.J. Vlassak, Bauschinger effect in thin metal films, Scripta Materialia 53 (2005) 177–182, doi: 10.1016/j.scriptamat.2005.03.048.

[997] R.C. Daniel, G.T. Horne, The Bauschinger effect and cyclic hardening in copper, MTB 2 (1971) 1161–1172, doi: 10.1007/BF02664248.

[998] N. Christodoulou, O.T. Woo, S.R. MacEwen, Effect of stress reversals on the work hardening behaviour of polycrystalline copper, Acta Metallurgica 34 (1986) 1553–1562, doi: 10.1016/0001-6160(86)90100-8.

[999] E.F. Rauch, J.J. Gracio, F. Barlat, A.B. Lopes, J. Ferreira Duarte, Hardening behavior and structural evolution upon strain reversal of aluminum alloys, Scripta Materialia 46 (2002) 881–886, doi: 10.1016/S1359-6462(02)00073-8.

[1000] S. Queyreau, B. Devincre, Bauschinger effect in precipitation-strengthened materials: A dislocation dynamics investigation, Philosophical Magazine Letters 89 (2009) 419–430, doi: 10.1080/09500830903005433.

[1001] A. Aran, M. Demirkol, A. Karabulut, Bauschinger effect in precipitation-strengthened aluminium alloy 2024, Materials Science and Engineering 89 (1987) L35-L39, doi: 10.1016/0025-5416(87)90271-0.

[1002] R. Sowerby, D.K. Uko, Y. Tomita, A review of certain aspects of the Bauschinger effect in metals, Materials Science and Engineering 41 (1979) 43–58, doi: 10.1016/0025-5416(79)90043-0.

[1003] J.D. Atkinson, L.M. Brown, W.M. Stobbs, The work-hardening of copper-silica: IV. The Bauschinger effect and plastic relaxation, Philosophical Magazine 30 (1974) 1247–1280, doi: 10.1080/14786437408207280.

[1004] S.N. Buckley, K.M. Entwistle, The bauschinger effect in super-pure aluminum single crystals and polycrystals, Acta Metallurgica 4 (1956) 352–361, doi: 10.1016/0001-6160(56)90023-2.

[1005] Z. Hu, E.F. Rauch, C. Teodosiu, Work-hardening behavior of mild steel under stress reversal at large strains, International Journal of Plasticity 8 (1992) 839–856, doi: 10.1016/0749-6419(92)90006-X.

[1006] J.R. Hancock, J.C. Grosskreutz, Mechanisms of fatigue hardening in copper single crystals, Acta Metallurgica 17 (1969) 77–97, doi: 10.1016/0001-6160(69)90130-8.

[1007] G.D. Moan, J.D. Embury, A study of the bauschinger effect in AlCu alloys, Acta Metallurgica 27 (1979) 903–914, doi: 10.1016/0001-6160(79)90125-1.

[1008] C.H. Caceres, J.R. Griffiths, P. Reiner, The influence of microstructure on the Bauschinger effect in an Al・Si・Mg casting alloy, Acta Materialia 44 (1996) 15–23, doi: 10.1016/1359-6454(95)00171-6.

[1009] D. Gould, P.B. Hirsch, F.J. Humphreys, The Bauschinger effect, work-hardening and recovery in dispersion-hardened copper crystals, Phil. Mag. 30 (1974) 1353–1377, doi: 10.1080/14786437408207287.

[1010] A.A. Mamun, R.J. Moat, J. Kelleher, P.J. Bouchard, Origin of the Bauschinger effect in a polycrystalline material, Materials Science and Engineering: A 707 (2017) 576–584, doi: 10.1016/j.msea.2017.09.091.

[1011] E. Demir, D. Raabe, Mechanical and microstructural single-crystal Bauschinger effects: Observation of reversible plasticity in copper during bending, Acta Materialia 58 (2010) 6055–6063, doi: 10.1016/j.actamat.2010.07.023.

[1012] J.K. Mahato, P.S. De, A. Sarkar, A. Kundu, P.C. Chakraborti, Effect of deformation mode and grain size on Bauschinger behavior of annealed copper, International Journal of Fatigue 83 (2016) 42–52, doi: 10.1016/j.ijfatigue.2015.04.023.

[1013] J.N. Hu, A.C.F. Cocks, Effect of creep on the Bauschinger effect in a polycrystalline austenitic stainless steel, Scripta Materialia 128 (2017) 100–104, doi: 10.1016/j.scriptamat.2016.10.005.

[1014] H. Mughrabi, Deformation-induced long-range internal stresses and lattice plane misorientations and the role of geometrically necessary dislocations, Philosophical Magazine 86 (2006) 4037–4054, doi: 10.1080/14786430500509054.

[1015] H. Mughrabi, Dual role of deformation-induced geometrically necessary dislocations with respect to lattice plane misorientations and/or long-range internal stresses☆, Acta Materialia 54 (2006) 3417–3427, doi: 10.1016/j.actamat.2006.03.047.

[1016] H. Biermann, T. Ungár, T. Pfannenmüller, G. Hoffmann, A. Borbély, H. Mughrabi, Local variations of lattice parameter and long-range internal stresses during cyclic deformation of polycrystalline copper, Acta Metallurgica et Materialia 41 (1993) 2743–2753, doi: 10.1016/0956-7151(93)90143-G.

[1017] E. Orowan, Internal stresses and fatigue in metals, in: G.M. Rassweiler, W.L. Grube (Eds.), General motors symposium, Elsevier, Amsterdam, 1959, p. 59.

[1018] M.E. Kassner, M.-T. Pérez-Prado, K.S. Vecchio, M.A. Wall, Determination of internal stresses in cyclically deformed copper single crystals using convergent-beam electron diffraction and dislocation dipole separation measurements, Acta Materialia 48 (2000) 4247–4254, doi: 10.1016/S1359-6454(00)00284-6.

[1019] H. Mughrabi, The long-range internal stress field in the dislocation wall structure of persistent slip bands, Phys. Stat. Sol. (a) 104 (1987) 107–120, doi: 10.1002/pssa.2211040108.

[1020] M. Sauzay, Analytical modelling of intragranular backstresses due to deformation induced dislocation microstructures, International Journal of Plasticity 24 (2008) 727–745, doi: 10.1016/j.ijplas.2007.07.004.

[1021] H. Mughrabi, Dislocation clustering and long-range internal stresses in monotonically and cyclically deformed metal crystals, Rev. Phys. Appl. (Paris) 23 (1988) 367–379, doi: 10.1051/rphysap:01988002304036700.

[1022] M. Sauzay, H. Brillet, I. Monnet, M. Mottot, F. Barcelo, B. Fournier, A. Pineau, Cyclically induced softening due to low-angle boundary annihilation in a martensitic steel, Materials Science and Engineering: A 400-401 (2005) 241–244, doi: 10.1016/j.msea.2005.02.092.

[1023] T. Hasegawa, T. Yakou, U.F. Kocks, Forward and reverse rearrangements of dislocations in tangled walls, Materials Science and Engineering 81 (1986) 189–199, doi: 10.1016/0025-5416(86)90262-4.

[1024] M.E. Kassner, P. Geantil, L.E. Levine, B.C. Larson, Backstress, the Bauschinger Effect and Cyclic Deformation, MSF 604-605 (2008) 39–51, doi: 10.4028/www.scientific.net/MSF.604-605.39.

[1025] J.C.M. Li, Some elastic properties of an edge dislocation wall, Acta Metallurgica 8 (1960) 563–574, doi: 10.1016/0001-6160(60)90111-5.

[1026] F. Mompiou, D. Caillard, M. Legros, H. Mughrabi, In situ TEM observations of reverse dislocation motion upon unloading in tensile-deformed UFG aluminium, Acta Materialia 60 (2012) 3402–3414, doi: 10.1016/j.actamat.2012.02.049.

[1027] W.Z. Han, A. Vinogradov, C.R. Hutchinson, On the reversibility of dislocation slip during cyclic deformation of Al alloys containing shear-resistant particles, Acta Materialia 59 (2011) 3720–3736, doi: 10.1016/j.actamat.2011.03.007.

[1028] H. Mori, H. Fujita, Behaviors of Individual Dislocations in Cu-9 at % Al Alloys under Reverse Stress, J. Phys. Soc. Jpn. 38 (1975) 1342–1348, doi: 10.1143/JPSJ.38.1342.

[1029] A.W. Sleeswyk, M.R. James, D.H. Plantinga, W.S.T. Maathuis, Reversible strain in cyclic plastic deformation, Acta Metallurgica 26 (1978) 1265–1271, doi: 10.1016/0001-6160(78)90011-1.

[1030] L. Song, B. Wu, L. Zhang, X. Du, Y. Wang, C. Esling, M.-J. Philippe, Detwinning-related Bauschinger effect of an extruded magnesium alloy AZ31B, Materials Characterization 148 (2019) 63–70, doi: 10.1016/j.matchar.2018.12.005.

[1031] L. Wu, A. Jain, D.W. Brown, G.M. Stoica, S.R. Agnew, B. Clausen, D.E. Fielden et al., Twinning–detwinning behavior during the strain-controlled low-cycle fatigue testing of a wrought magnesium alloy, ZK60A, Acta Materialia 56 (2008) 688–695, doi: 10.1016/j.actamat.2007.10.030.

[1032] L. Wang, G. Huang, Q. Quan, P. Bassani, E. Mostaed, M. Vedani, F. Pan, The effect of twinning and detwinning on the mechanical property of AZ31 extruded magnesium alloy during strain-path changes, Materials & Design 63 (2014) 177–184, doi: 10.1016/j.matdes.2014.05.056.

[1033] M.J. Szczerba, S. Kopacz, M.S. Szczerba, Experimental studies on detwinning of face-centered cubic deformation twins, Acta Materialia 104 (2016) 52–61, doi: 10.1016/j.actamat.2015.11.025.

[1034] S.J. McCormack, W. Wen, E.V. Pereloma, C.N. Tomé, A.A. Gazder, A.A. Saleh, On the first direct observation of de-twinning in a twinning-induced plasticity steel, Acta Materialia 156 (2018) 172–182, doi: 10.1016/j.actamat.2018.06.029.

[1035] Q. Yu, J. Zhang, Y. Jiang, Direct observation of twinning–detwinning–retwinning on magnesium single crystal subjected to strain-controlled cyclic tension–compression in [0 0 0 1] direction, Philosophical Magazine Letters 91 (2011) 757–765, doi: 10.1080/09500839.2011.617713.

[1036] H. Wang, P.D. Wu, J. Wang, Modelling the role of slips and twins in magnesium alloys under cyclic shear, Computational Materials Science 96 (2015) 214–218, doi: 10.1016/j.commatsci.2014.09.015.

[1037] B.M. Morrow, R.J. McCabe, E.K. Cerreta, C.N. Tomé, In-Situ TEM Observation of Twinning and Detwinning During Cyclic Loading in Mg, Metall and Mat Trans A 45 (2014) 36–40, doi: 10.1007/s11661-013-1765-0.

[1038] M.G.D. Geers, W.A.M. Brekelmans, C.J. Bayley, Second-order crystal plasticity: internal stress effects and cyclic loading, Philosophical Magazine 15 (2007) S133-S145, doi: 10.1088/0965-0393/15/1/S12.

[1039] M. Zecevic, M. Knezevic, A dislocation density based elasto-plastic self-consistent model for the prediction of cyclic deformation, International Journal of Plasticity 72 (2015) 200–217, doi: 10.1016/j.ijplas.2015.05.018.

[1040] E.C. Aifantis, On the Microstructural Origin of Certain Inelastic Models, J. Eng. Mater. Technol 106 (1984) 326–330, doi: 10.1115/1.3225725.

[1041] G. Proust, C.N. Tomé, G.C. Kaschner, Modeling texture, twinning and hardening evolution during deformation of hexagonal materials, Acta Materialia 55 (2007) 2137–2148, doi: 10.1016/j.actamat.2006.11.017.

[1042] T. Yalcinkaya, W.A.M. Brekelmans, M.G.D. Geers, A composite dislocation cell model to describe strain path change effects in BCC metals, Modelling Simul. Mater. Sci. Eng. 17 (2009) 64008, doi: 10.1088/0965-0393/17/6/064008.

[1043] J. Hu, B. Chen, D.J. Smith, P.E.J. Flewitt, A.C.F. Cocks, On the evaluation of the Bauschinger effect in an austenitic stainless steel—The role of multi-scale residual stresses, International Journal of Plasticity 84 (2016) 203–223, doi: 10.1016/j.ijplas.2016.05.009.

[1044] M. Zecevic, Y.P. Korkolis, T. Kuwabara, M. Knezevic, Dual-phase steel sheets under cyclic tension–compression to large strains, Journal of the Mechanics and Physics of Solids 96 (2016) 65–87, doi: 10.1016/j.jmps.2016.07.003.

[1045] S.A. El-Naaman, K.L. Nielsen, C.F. Niordson, An investigation of back stress formulations under cyclic loading, Mechanics of Materials 130 (2019) 76–87, doi: 10.1016/j.mechmat.2019.01.005.

[1046] C. Mareau, V. Favier, B. Weber, A. Galtier, M. Berveiller, Micromechanical modeling of the interactions between the microstructure and the dissipative deformation mechanisms in steels under cyclic loading, International Journal of Plasticity 32-33 (2012) 106–120, doi: 10.1016/j.ijplas.2011.12.004.

[1047] Y. Li, V. Aubin, C. Rey, P. Bompard, Polycrystalline numerical simulation of variable amplitude loading effects on cyclic plasticity and microcrack initiation in austenitic steel 304L, International Journal of Fatigue 42 (2012) 71–81, doi: 10.1016/j.ijfatigue.2011.07.003.

[1048] H. Qiao, S.R. Agnew, P.D. Wu, Modeling twinning and detwinning behavior of Mg alloy ZK60A during monotonic and cyclic loading, International Journal of Plasticity 65 (2015) 61–84, doi: 10.1016/j.ijplas.2014.08.010.

[1049] G. Fribourg, Y. Bréchet, A. Deschamps, A. Simar, Microstructure-based modelling of isotropic and kinematic strain hardening in a precipitation-hardened aluminium alloy, Acta Materialia 59 (2011) 3621–3635, doi: 10.1016/j.actamat.2011.02.035.

[1050] C. Déprés, M. Fivel, L. Tabourot, A dislocation-based model for low-amplitude fatigue behaviour of face-centred cubic single crystals, Scripta Materialia 58 (2008) 1086–1089, doi: 10.1016/j.scriptamat.2008.02.027.

[1051] P. Evrard, V. Aubin, S. Degallaix, D. Kondo, Formulation of a new single crystal law for modeling the cyclic softening, Mechanics Research Communications 35 (2008) 589–594, doi: 10.1016/j.mechrescom.2008.06.001.

[1052] A. Cruzado, J. LLorca, J. Segurado, Modeling cyclic deformation of inconel 718 superalloy by means of crystal plasticity and computational homogenization, International Journal of Solids and Structures 122-123 (2017) 148–161, doi: 10.1016/j.ijsolstr.2017.06.014.

[1053] M. Shenoy, Y. Tjiptowidjojo, D. McDowell, Microstructure-sensitive modeling of polycrystalline IN 100, International Journal of Plasticity 24 (2008) 1694–1730, doi: 10.1016/j.ijplas.2008.01.001.

[1054] M. SHENOY, J. ZHANG, D.L. McDowell, Estimating fatigue sensitivity to polycrystalline Ni-base superalloy microstructures using a computational approach, Fat Frac Eng Mat Struct 30 (2007) 889–904, doi: 10.1111/j.1460-2695.2007.01159.x.

[1055] L.M. Brown, A discussion of the structure and behaviour of dipole walls in cyclic plasticity, Phil. Mag. 84 (2004) 2501–2520, doi: 10.1080/14786430410001699791.

[1056] J. Bretschneider, C. Holste, B. Tippelt, Cyclic plasticity of nickel single crystals at elevated temperatures, Acta Materialia 45 (1997) 3775–3783, doi: 10.1016/S1359-6454(97)00030-X.

[1057] Z.S. Basinski, S.J. Basinski, Fundamental aspects of low amplitude cyclic deformation in face-centred cubic crystals, Progress in Materials Science 36 (1992) 89–148, doi: 10.1016/0079-6425(92)90006-S.

[1058] L.M. Brown, Dislocation plasticity in persistent slip bands, Materials Science and Engineering: A 285 (2000) 35–42, doi: 10.1016/S0921-5093(00)00662-6.

[1059] L.M. Brown, Dislocation bowing and passing in persistent slip bands, Phil. Mag. 86 (2006) 4055–4068, doi: 10.1080/14786430500501689.

[1060] L.M. Brown, A dipole model for the cross-slip of screw dislocations in fee metals, Philosophical Magazine A 82 (2002) 1691–1711, doi: 10.1080/01418610208235684.

[1061] B. Gong, Z. Wang, Z. Wang, Cyclic deformation behavior and dislocation structures of [001] copper single crystals—I Cyclic stress-strain response and surface feature, Acta Materialia 45 (1997) 1365–1377, doi: 10.1016/S1359-6454(96)00288-1.

[1062] M.S. Pham, S.R. Holdsworth, K.G.F. Janssens, E. Mazza, Cyclic deformation response of AISI 316L at room temperature, International Journal of Plasticity 47 (2013) 143–164, doi: 10.1016/j.ijplas.2013.01.017.

[1063] M.S. Pham, C. Solenthaler, K.G.F. Janssens, S.R. Holdsworth, Dislocation structure evolution and its effects on cyclic deformation response of AISI 316L stainless steel, Materials Science and Engineering: A 528 (2011) 3261–3269, doi: 10.1016/j.msea.2011.01.015.

[1064] B. Tippelt, J. Breitschneider, P. Hähner, The Dislocation Microstructure of Cyclically Deformed Nickel Single Crystals at Different Temperatures, Phys. Stat. Sol. (a) 163 (1997) 11–26, doi: 10.1002/1521-396X(199709)163:1%3C11:AID-PSSA11%3E3.0.CO;2-X.

[1065] E.E. Laufer, W.N. Roberts, Dislocations and persistent slip bands in fatigued copper, Philosophical Magazine 14 (1966) 65–78, doi: 10.1080/14786436608218989.

[1066] A. Weidner, R. Beyer, C. Blochwitz, C. Holste, A. Schwab, W. Tirschler, Slip activity of persistent slip bands in polycrystalline nickel, Materials Science and Engineering: A 435-436 (2006) 540–546, doi: 10.1016/j.msea.2006.07.039.

[1067] C. Schiller, D. WALGRAEF, Numerical simulation of persistent slip band formation, Acta Metallurgica 36 (1988) 563–574, doi: 10.1016/0001-6160(88)90089-2.

[1068] P. Lukáš, M. Klesnil, J. Krejčí, Dislocations and Persistent Slip Bands in Copper Single Crystals Fatigued at Low Stress Amplitude, phys. stat. sol. (b) 27 (1968) 545–558, doi: 10.1002/pssb.19680270212.

[1069] P. Lukáš, M. Klesnil, J. Krejčí, P. Ryš, Substructure of Persistent Slip Bands in Cyclically Deformed Copper, phys. stat. sol. (b) 15 (1966) 71–82, doi: 10.1002/pssb.19660150105.

[1070] A. Schwab, J. Bretschneider, C. Buque, C. Blochwitz, C. Holste, Application of electron channelling contrast to the investigation of strain localization effects in cyclically deformed fcc crystals, Philosophical Magazine Letters 74 (1996) 449–454, doi: 10.1080/095008396179986.

[1071] J. Ahmed, A.J. Wilkinson, S.G. Roberts, Characterizing dislocation structures in bulk fatigued copper single crystals using electron channelling contrast imaging (ECCI), Philosophical Magazine Letters 76 (1997) 237–246, doi: 10.1080/095008397178986.

[1072] U. Holzwarth, U. Essmann, Temperature-induced rearrangement of the dislocation pattern of Persistent Slip Bands in copper single crystals, Appl. Phys. A 58 (1994) 197–210, doi: 10.1007/BF00324376.

[1073] J. ZHANG, Y. JIANG, An experimental study of the formation of typical dislocation patterns in polycrystalline copper under cyclic shear, Acta Materialia 55 (2007) 1831–1842, doi: 10.1016/j.actamat.2006.10.044.

[1074] U. Essmann, K. Differt, Dynamic model of the wall structure in persistent slip bands of fatigued metals II. The wall spacing and the temperature dependence of the yield stress in saturation, Materials Science and Engineering: A 208 (1996) 56–68, doi: 10.1016/0921-5093(95)10063-6.

[1075] R. Kwadjo, L.M. Brown, Cyclic hardening of magnesium single crystals, Acta Metallurgica 26 (1978) 1117–1132, doi: 10.1016/0001-6160(78)90139-6.

[1076] L. Buchinger, S. Stanzl, C. Laird, Dislocation structures in copper single crystals fatigued at low amplitudes, Philosophical Magazine A 50 (1985) 275–298, doi: 10.1080/01418618408244227.

[1077] C. Watanabe, K. Kanmuri, M. Kato, S. Onaka, T. Fujii, Rearrangement of fatigue dislocation structure in copper single crystals associated with reduction in the plastic strain amplitude, Philosophical Magazine A 82 (2002) 1317–1330, doi: 10.1080/01418610208235674.

[1078] C.E. Feltner, C. Laird, Factors influencing dislocation structures in fatigued metals, Transactions of the Metallurgical Society of AIME 242 (1968) 1253–1260.

[1079] A. Plumtree, Cyclic stress–strain response and substructure, International Journal of Fatigue 23 (2001) 799–805, doi: 10.1016/S0142-1123(01)00037-8.

[1080] A.T. Winter, O.R. Pedersen, K.V. Rasmussen, Dislocation microstructures in fatigued copper polycrystals, Acta Metallurgica 29 (1981) 735–748, doi: 10.1016/0001-6160(81)90117-6.

[1081] P. Li, S.X. Li, Z.G. Wang, Z.F. Zhang, Fundamental factors on formation mechanism of dislocation arrangements in cyclically deformed fcc single crystals, Progress in Materials Science 56 (2011) 328–377, doi: 10.1016/j.pmatsci.2010.12.001.

[1082] R.L. Segall, P.G. Partridge, P.B. Hirsch, The Dislocation Distribution in Face-centred Cubic Metals after Fatigue, Phil. Mag. 6 (1961) 1493–1513, doi: 10.1080/00318086.1961.11643279.

[1083] C.C. Tasan, M. Diehl, D. Yan, C. Zambaldi, P. Shanthraj, F. Roters, D. Raabe, Integrated experimental–simulation analysis of stress and strain partitioning in multiphase alloys, Acta Materialia 81 (2014) 386–400, doi: 10.1016/j.actamat.2014.07.071.

[1084] G.R. Canova, H.R. Wenk, A. Molinari, Deformation modelling of multi-phase polycrystals: case of a quartz-mica aggregate, Acta Metallurgica et Materialia 40 (1992) 1519–1530, doi: 10.1016/0956-7151(92)90095-V.

[1085] M. Delincé, Y. Bréchet, J.D. Embury, M.G.D. Geers, P.J. Jacques, T. Pardoen, Structure–property optimization of ultrafine-grained dual-phase steels using a microstructure-based strain hardening model, Acta Materialia 55 (2007) 2337–2350, doi: 10.1016/j.actamat.2006.11.029.

[1086] J. Pagenkopf, A. Butz, M. Wenk, D. Helm, Virtual testing of dual-phase steels: Effect of martensite morphology on plastic flow behavior, Materials Science and Engineering: A 674 (2016) 672–686, doi: 10.1016/j.msea.2016.07.118.

[1087] C.C. Tasan, J.P.M. Hoefnagels, M. Diehl, D. Yan, F. Roters, D. Raabe, Strain localization and damage in dual phase steels investigated by coupled in-situ deformation experiments and crystal plasticity simulations, International Journal of Plasticity 63 (2014) 198–210, doi: 10.1016/j.ijplas.2014.06.004.

[1088] M. Diehl, D. An, P. Shanthraj, S. Zaefferer, F. Roters, D. Raabe, Crystal plasticity study on stress and strain partitioning in a measured 3D dual phase steel microstructure, Phys Mesomech 20 (2017) 311–323, doi: 10.1134/S1029959917030079.

[1089] H. Lyu, A. Ruimi, H.M. Zbib, A dislocation-based model for deformation and size effect in multi-phase steels, International Journal of Plasticity 72 (2015) 44–59, doi: 10.1016/j.ijplas.2015.05.005.

[1090] R. Pokharel, A. Patra, D.W. Brown, B. Clausen, S.C. Vogel, G.T. Gray, An analysis of phase stresses in additively manufactured 304L stainless steel using neutron diffraction measurements and crystal plasticity finite element simulations, International Journal of Plasticity 121 (2019) 201–217, doi: 10.1016/j.ijplas.2019.06.005.

[1091] C.T. Sun, R.S. Vaidya, Prediction of composite properties from a representative volume element, Composites Science and Technology 56 (1996) 171–179, doi: 10.1016/0266-3538(95)00141-7.

[1092] S.-H. Choi, E.-Y. Kim, W. Woo, S.H. Han, J.H. Kwak, The effect of crystallographic orientation on the micromechanical deformation and failure behaviors of DP980 steel during uniaxial tension, International Journal of Plasticity 45 (2013) 85–102, doi: 10.1016/j.ijplas.2012.11.013.

[1093] F. Rieger, T. Böhlke, Microstructure based prediction and homogenization of the strain hardening behavior of dual-phase steel, Arch Appl Mech 85 (2015) 1439–1458, doi: 10.1007/s00419-014-0974-3.

[1094] S. Cai, M.R. Daymond, R.A. Holt, Modeling the room temperature deformation of a two-phase zirconium alloy, Acta Materialia 57 (2009) 407–419, doi: 10.1016/j.actamat.2008.09.020.

[1095] J.H. Kim, D. Kim, F. Barlat, M.-G. Lee, Crystal plasticity approach for predicting the Bauschinger effect in dual-phase steels, Materials Science and Engineering: A 539 (2012) 259–270, doi: 10.1016/j.msea.2012.01.092.

[1096] K. Yoshida, R. Brenner, B. Bacroix, S. Bouvier, Micromechanical modeling of the work-hardening behavior of single- and dual-phase steels under two-stage loading paths, Materials Science and Engineering: A 528 (2011) 1037–1046, doi: 10.1016/j.msea.2010.10.078.

[1097] J. Kadkhodapour, A. Butz, S. Ziaei-Rad, S. Schmauder, A micro mechanical study on failure initiation of dual phase steels under tension using single crystal plasticity model, International Journal of Plasticity 27 (2011) 1103–1125, doi: 10.1016/j.ijplas.2010.12.001.

[1098] G.J. Weng, The overall elastoplastic stress-strain relations of dual-phase metals, Journal of the Mechanics and Physics of Solids 38 (1990) 419–441, doi: 10.1016/0022-5096(90)90007-Q.

[1099] D. Cédat, O. Fandeur, C. Rey, D. Raabe, Polycrystal model of the mechanical behavior of a Mo–TiC30 vol.% metal–ceramic composite using a three-dimensional microstructure map obtained by dual beam focused ion beam scanning electron microscopy, Acta Materialia 60 (2012) 1623–1632, doi: 10.1016/j.actamat.2011.11.055.

[1100] E. Busso, Gradient-dependent deformation of two-phase single crystals, Journal of the Mechanics and Physics of Solids 48 (2000) 2333–2361, doi: 10.1016/S0022-5096(00)00006-5.

[1101] S.-B. Lee, R.A. Lebensohn, A.D. Rollett, Modeling the viscoplastic micromechanical response of two-phase materials using Fast Fourier Transforms, International Journal of Plasticity 27 (2011) 707–727, doi: 10.1016/j.ijplas.2010.09.002.

[1102] J.a.U.o.O.U. Christian, The Theory of Transformations in Metals and Alloys, 1976.

[1103] K. Barmak, A Commentary on: "Reaction Kinetics in Processes of Nucleation and Growth"*, Metall and Materi Trans 49 (2018) 3616–3680, doi: 10.1007/s11663-010-9421-1.

[1104] M. Avrami, Granulation, Phase Change, and Microstructure Kinetics of Phase Change. III, The Journal of Chemical Physics 9 (1941) 177–184, doi: 10.1063/1.1750872.

[1105] M. Avrami, Kinetics of Phase Change. II Transformation-Time Relations for Random Distribution of Nuclei, The Journal of Chemical Physics 8 (1940) 212–224, doi: 10.1063/1.1750631.

[1106] M. Avrami, Kinetics of Phase Change. I General Theory, The Journal of Chemical Physics 7 (1939) 1103–1112, doi: 10.1063/1.1750380.

[1107] D.A. Porter, K.E. Easterling, M. Sherif, Phase Transformations in Metals and Alloys, Third Edition (Revised Reprint), 3rd ed., CRC Press, Hoboken, 2009.

[1108] H.I. Aaronson, M. Enomoto, J.K. Lee, Mechanisms of Diffusional Phase Transformations in Metals and Alloys, Taylor and Francis, Hoboken, 2010.

[1109] E. Pereloma, D.V. Edmonds, Phase transformation in steels: Fundamentals and diffusion-controlled transformations, Woodhead Pub, Oxford, 2012.

[1110] S.E. Offerman, N.H. van Dijk, J. Sietsma, S. Grigull, E.M. Lauridsen, L. Margulies, H.F. Poulsen et al., Grain nucleation and growth during phase transformations, Science (New York, N.Y.) 298 (2002) 1003–1005, doi: 10.1126/science.1076681.

[1111] K.C. Russell, Grain boundary nucleation kinetics, Acta Metallurgica 17 (1969) 1123–1131, doi: 10.1016/0001-6160(69)90057-1.

[1112] M.R. Plichta, W.A.T. Clark, H.I. Aaronson, The nucleation kinetics, crystallography, and mechanism of the massive transformation, MTA 15 (1984) 427–435, doi: 10.1007/BF02644966.

[1113] H.I. Aaronson, Atomic mechanisms of diffusional nucleation and growth and comparisons with their counterparts in shear transformations, MTA 24 (1993) 241–276, doi: 10.1007/BF02657313.

[1114] C. Zener, Kinetics of the decomposition of austenite, Trans AIME 167 (1946).

[1115] W.F. Lange, M. Enomoto, H.I. Aaronson, The kinetics of ferrite nucleation at austenite grain boundaries in Fe-C alloys, MTA 19 (1988) 427–440, doi: 10.1007/BF02649256.

[1116] S.J. JONES, H.K.D.H. BHADESHIA, KINETICS OF THE SIMULTANEOUS DECOMPOSITION OF AUSTENITE INTO SEVERAL TRANSFORMATION PRODUCTS, Acta Materialia 45 (1997) 2911–2920, doi: 10.1016/S1359-6454(96)00392-8.

[1117] M. Hillert, Solute drag in grain boundary migration and phase transformations, Acta Materialia 52 (2004) 5289–5293, doi: 10.1016/j.actamat.2004.07.032.

[1118] N. Saunders, A.P. Miodownik, CALPHAD (calculation of phase diagrams): A comprehensive guide, Pergamon, Oxford, New York, 1998.

[1119] K.C. Russell, Nucleation in solids: The induction and steady state effects, Advances in Colloid and Interface Science 13 (1980) 205–318, doi: 10.1016/0001-8686(80)80003-0.

[1120] R.W. Balluffi, R.A. Kemper, S.M. Allen, W.C. Carter, Kinetics of materials, Wiley-Interscience, Hoboken, N.J, 2005.

[1121] J.W. Cahn, The kinetics of grain boundary nucleated reactions, Acta Metallurgica 4 (1956) 449–459, doi: 10.1016/0001-6160(56)90041-4.

[1122] J.B. Leblond, J. Devaux, A new kinetic model for anisothermal metallurgical transformations in steels including effect of austenite grain size, Acta Metallurgica 32 (1984) 137–146, doi: 10.1016/0001-6160(84)90211-6.

[1123] F. Liu, F. Sommer, C. Bos, E.J. Mittemeijer, Analysis of solid state phase transformation kinetics: models and recipes, International Materials Reviews 52 (2007) 193–212, doi: 10.1179/174328007X160308.

[1124] F. Liu, F. Sommer, E.J. Mittemeijer, An analytical model for isothermal and isochronal transformation kinetics, J Mater Sci 39 (2004) 1621–1634, doi: 10.1023/B:JMSC.0000016161.79365.69.

[1125] J. Málek, T. Mitsuhashi, J.M. Criado, Kinetic analysis of solid-state processes, J. Mater. Res. 16 (2001) 1862–1871, doi: 10.1557/JMR.2001.0255.

[1126] R.A. Ramos, P.A. Rikvold, M.A. Novotny, Test of the Kolmogorov-Johnson-Mehl-Avrami picture of metastable decay in a model with microscopic dynamics, Phys. Rev. B 59 (1999) 9053–9069, doi: 10.1103/PhysRevB.59.9053.

[1127] B. Scharifker, G. Hills, Theoretical and experimental studies of multiple nucleation, Electrochimica Acta 28 (1983) 879–889, doi: 10.1016/0013-4686(83)85163-9.

[1128] K. Sekimoto, Evolution of the domain structure during the nucleation-and-growth process with non-conserved order parameter, Physica A: Statistical Mechanics and its Applications 135 (1986) 328–346, doi: 10.1016/0378-4371(86)90146-9.

[1129] J. Šesták, G. Berggren, Study of the kinetics of the mechanism of solid-state reactions at increasing temperatures, Thermochimica Acta 3 (1971) 1–12, doi: 10.1016/0040-6031(71)85051-7.

[1130] E. Feulvarch, J.M. Bergheau, J.B. Leblond, An implicit finite element algorithm for the simulation of diffusion with phase changes in solids, Int. J. Numer. Meth. Engng 78 (2009) 1492–1512, doi: 10.1002/nme.2537.

[1131] E.J. Mittemeijer, Analysis of the kinetics of phase transformations, J Mater Sci 27 (1992) 3977–3987, doi: 10.1007/BF01105093.

[1132] E.J. Mittemeijer, F. Sommer, Solid state phase transformation kinetics: a modular transformation model, MEKU 93 (2002) 352–361, doi: 10.3139/146.020352.

[1133] A.T.W. Kempen, F. Sommer, E.J. Mittemeijer, Determination and interpretation of isothermal and non-isothermal transformation kinetics; the effective activation energies in terms of nucleation and growth, J Mater Sci 37 (2002) 1321–1332, doi: 10.1023/A:1014556109351.

[1134] A.T.W. Kempen, F. Sommer, E.J. Mittemeijer, The kinetics of the austenite–ferrite phase transformation of Fe-Mn: differential thermal analysis during cooling, Acta Materialia 50 (2002) 3545–3555, doi: 10.1016/S1359-6454(02)00149-0.

[1135] F. Liu, S.J. Song, F. Sommer, E.J. Mittemeijer, Evaluation of the maximum transformation rate for analyzing solid-state phase transformation kinetics, Acta Materialia 57 (2009) 6176–6190, doi: 10.1016/j.actamat.2009.08.046.

[1136] F. Liu, F. Sommer, E.J. Mittemeijer, Analysis of the kinetics of phase transformations; roles of nucleation index and temperature dependent site saturation, and recipes for the extraction of kinetic parameters, J Mater Sci 42 (2007) 573–587, doi: 10.1007/s10853-006-0802-4.

[1137] J. Sietsma, S. van der Zwaag, A concise model for mixed-mode phase transformations in the solid state, Acta Materialia 52 (2004) 4143–4152, doi: 10.1016/j.actamat.2004.05.027.

[1138] M. MILITZER, M. MECOZZI, J. Sietsma, S. VANDERZWAAG, Three-dimensional phase field modelling of the austenite-to-ferrite transformation, Acta Materialia 54 (2006) 3961–3972, doi: 10.1016/j.actamat.2006.04.029.

[1139] C. Bos, F. Sommer, E.J. Mittemeijer, A kinetic Monte Carlo method for the simulation of massive phase transformations, Acta Materialia 52 (2004) 3545–3554, doi: 10.1016/j.actamat.2004.04.008.

[1140] B.J. Kooi, Extension of the Johnson-Mehl-Avrami-Kolmogorov theory incorporating anisotropic growth studied by Monte Carlo simulations, Phys. Rev. B 73 (2006) 355, doi: 10.1103/PhysRevB.73.054103.

[1141] I. Steinbach, Phase-Field Model for Microstructure Evolution at the Mesoscopic Scale, Annu. Rev. Mater. Res. 43 (2013) 89–107, doi: 10.1146/annurev-matsci-071312-121703.

[1142] A. Kwiatkowski da Silva, D. Ponge, Z. Peng, G. Inden, Y. Lu, A. Breen, B. Gault et al., Phase nucleation through confined spinodal fluctuations at crystal defects evidenced in Fe-Mn alloys, Nature communications 9 (2018) 1137, doi: 10.1038/s41467-018-03591-4.

[1143] J.W. Cahn, On spinodal decomposition, Acta Metallurgica 9 (1961) 795–801, doi: 10.1016/0001-6160(61)90182-1.

[1144] I. Steinbach, M. Apel, Multi phase field model for solid state transformation with elastic strain, Physica D: Nonlinear Phenomena 217 (2006) 153–160, doi: 10.1016/j.physd.2006.04.001.

[1145] L. Zhang, I. Steinbach, Phase-field model with finite interface dissipation: Extension to multi-component multi-phase alloys, Acta Materialia 60 (2012) 2702–2710, doi: 10.1016/j.actamat.2012.02.032.

[1146] H. Garcke, B. Nestler, B. Stoth, A MultiPhase Field Concept: Numerical Simulations of Moving Phase Boundaries and Multiple Junctions, SIAM J. Appl. Math. 60 (1999) 295–315, doi: 10.1137/S0036139998334895.

[1147] K. Thornton, J. Ågren, P.W. Voorhees, Modelling the evolution of phase boundaries in solids at the meso- and nano-scales, Acta Materialia 51 (2003) 5675–5710, doi: 10.1016/j.actamat.2003.08.008.

[1148] K.A. Jackson, J.D. Hunt, Lamellar and Rod Eutectic Growth, in: P. Pelce (Ed.), Dynamics of Curved Fronts, Elsevier Science, Burlington, 2012, pp. 363–376.

[1149] G.B. Olson, M. Cohen, A mechanism for the strain-induced nucleation of martensitic transformations, Journal of the Less Common Metals 28 (1972) 107–118, doi: 10.1016/0022-5088(72)90173-7.

[1150] M. Zecevic, M.V. Upadhyay, E. Polatidis, T. Panzner, H. van Swygenhoven, M. Knezevic, A crystallographic extension to the Olson-Cohen model for predicting strain path dependence of martensitic transformation, Acta Materialia 166 (2019) 386–401, doi: 10.1016/j.actamat.2018.12.060.

[1151] G.B. Olson, M. Cohen, Kinetics of strain-induced martensitic nucleation, MTA 6 (1975) 791–795, doi: 10.1007/BF02672301.

[1152] Y. Tomita, T. Iwamoto, Constitutive modeling of trip steel and its application to the improvement of mechanical properties, International Journal of Mechanical Sciences 37 (1995) 1295–1305, doi: 10.1016/0020-7403(95)00039-Z.

[1153] M. Mansourinejad, M. Ketabchi, Modification of Olson–Cohen model for predicting stress-state dependency of martensitic transformation, Materials Science and Technology 33 (2017) 1948–1954, doi: 10.1080/02670836.2017.1342016.

[1154] T. Iwamoto, T. Tsuta, Y. Tomita, Investigation on deformation mode dependence of strain-induced martensitic transformation in trip steels and modelling of transformation kinetics, International Journal of Mechanical Sciences 40 (1998) 173–182, doi: 10.1016/S0020-7403(97)00047-7.

[1155] H.N. Han, C.G. Lee, C.-S. Oh, T.-H. Lee, S.-J. Kim, A model for deformation behavior and mechanically induced martensitic transformation of metastable austenitic steel, Acta Materialia 52 (2004) 5203–5214, doi: 10.1016/j.actamat.2004.07.031.

[1156] G.W. Greenwood, Johnson R. H., The deformation of metals under small stresses during phase transformations, Proc. R. Soc. Lond. A 283 (1965) 403–422, doi: 10.1098/rspa.1965.0029.

[1157] F. Lecroisey, A. Pineau, Martensitic transformations induced by plastic deformation in the Fe-Ni-Cr-C system, Metall and Materi Trans 3 (1972) 391–400, doi: 10.1007/BF02642042.

[1158] H. Kim, J. Lee, F. Barlat, D. Kim, M.-G. Lee, Experiment and modeling to investigate the effect of stress state, strain and temperature on martensitic phase transformation in TRIP-assisted steel, Acta Materialia 97 (2015) 435–444, doi: 10.1016/j.actamat.2015.06.023.

[1159] A.M. Beese, D. Mohr, Effect of stress triaxiality and Lode angle on the kinetics of strain-induced austenite-to-martensite transformation, Acta Materialia 59 (2011) 2589–2600, doi: 10.1016/j.actamat.2010.12.040.

[1160] L.E. Murr, K.P. Staudhammer, S.S. Hecker, Effects of Strain State and Strain Rate on Deformation-Induced Transformation in 304 Stainless Steel: Part II. Microstructural Study (1982), doi: 10.1007/BF02644428.

[1161] S.S. Hecker, M.G. Stout, K.P. Staudhammer, J.L. Smith, Effects of Strain State and Strain Rate on Deformation-Induced Transformation in 304 Stainless Steel: Part I. Magnetic Measurements and Mechanical Behavior, MTA 13 (1982) 619–626, doi: 10.1007/BF02644427.

[1162] G.N. Haidemenopoulos, N. Aravas, I. Bellas, Kinetics of strain-induced transformation of dispersed austenite in low-alloy TRIP steels, Materials Science and Engineering: A 615 (2014) 416–423, doi: 10.1016/j.msea.2014.07.099.

[1163] J. Talonen, H. Hänninen, Formation of shear bands and strain-induced martensite during plastic deformation of metastable austenitic stainless steels, Acta Materialia 55 (2007) 6108–6118, doi: 10.1016/j.actamat.2007.07.015.

[1164] J. Talonen, H. Hänninen, P. Nenonen, G. Pape, Effect of strain rate on the strain-induced $\gamma \rightarrow \alpha'$-martensite transformation and mechanical properties of austenitic stainless steels, Metall and Mat Trans A 36 (2005) 421–432, doi: 10.1007/s11661-005-0313-y.

[1165] L. Kaufman, M. Cohen, Thermodynamics and kinetics of martensitic transformations, Progress in Metal Physics 7 (1958) 165–246, doi: 10.1016/0502-8205(58)90005-4.

[1166] M.S. Wechsler, Lieberman D. S., Read T. A., On the theory of the formation of martensite, Trans AIME 197 (1953) 1503–1515.

[1167] A.L. Roitburd, Martensitic Transformation as a Typical Phase Transformation in Solids, in: H. Ehrenreich, F. Seitz, D. Turnbull (Eds.), Solid state physics: Advances in research and applications, Academic Press, New York, 1978, pp. 317–390.

[1168] S.R. Pati, M. Cohen, Nucleation of the isothermal martensitic transformation, Acta Metallurgica 17 (1969) 189–199, doi: 10.1016/0001-6160(69)90058-3.

[1169] E.S. Machlin, M. Cohen, Isothermal Mode of the Martensitic Transformation, JOM 4 (1952) 489–500, doi: 10.1007/BF03397714.

[1170] J.C. Fisher, Application of nucleation theory to isothermal martensite, Acta Metallurgica 1 (1953) 32–35, doi: 10.1016/0001-6160(53)90007-8.

[1171] A. Borgenstam, M. Hillert, Activation energy for isothermal martensite in ferrous alloys, Acta Materialia 45 (1997) 651–662, doi: 10.1016/S1359-6454(96)00186-3.

[1172] G. Ghosh, G.B. Olson, Computational thermodynamics and the kinetics of martensitic transformation, JPE 22 (2001) 199–207, doi: 10.1361/105497101770338653.

[1173] G. Ghosh, G.B. Olson, Kinetics of F.C.C. → B.C.C. heterogeneous martensitic nucleation—I. The critical driving force for athermal nucleation, Acta Metallurgica et Materialia 42 (1994) 3361–3370, doi: 10.1016/0956-7151(94)90468-5.

[1174] G. Ghosh, G.B. Olson, Kinetics of F.c.c. → b.c.c. heterogeneous martensitic nucleation—II. Thermal activation, Acta Metallurgica et Materialia 42 (1994) 3371–3379, doi: 10.1016/0956-7151(94)90469-3.

[1175] J.R.C. Guimarães, P.R. Rios, Initial nucleation kinetics of martensite transformation, J Mater Sci 43 (2008) 5206–5210, doi: 10.1007/s10853-008-2753-4.
[1176] J.R. Patel, M. Cohen, Criterion for the action of applied stress in the martensitic transformation, Acta Metallurgica 1 (1953) 531–538, doi: 10.1016/0001-6160(53)90083-2.
[1177] I.-W. Chen, Y.-H. Chiao, K. Tsuzaki, Statistics of martensitic nucleation, Acta Metallurgica 33 (1985) 1847–1859, doi: 10.1016/0001-6160(85)90007-0.
[1178] G.B. Olson, K. Tsuzaki, M. Cohen, Statistical Aspects of Martensitic Nucleation, MRS Proc. 57 (1985) 124, doi: 10.1557/PROC-57-129.
[1179] H.K.D.H. BHADESHIA, D.V. Edmonds, The mechanism of bainite formation in steels, Acta Metallurgica 28 (1980) 1265–1273, doi: 10.1016/0001-6160(80)90082-6.
[1180] R.G. Stringfellow, D.M. Parks, G.B. Olson, A constitutive model for transformation plasticity accompanying strain-induced martensitic transformations in metastable austenitic steels, Acta Metallurgica et Materialia 40 (1992) 1703–1716, doi: 10.1016/0956-7151(92)90114-T.
[1181] G.B. Olson, M. Cohen, Stress-assisted isothermal martensitic transformation: Application to TRIP steels, MTA 13 (1982) 1907–1914, doi: 10.1007/BF02645934.
[1182] G.B. Olson, M. Cohen, A general mechanism of martensitic nucleation: Part I. General concepts and the FCC → HCP transformation, MTA 7 (1976) 1897–1904, doi: 10.1007/BF02659822.
[1183] R.E. Cech, D. Turnbull, Heterogeneous Nucleation of the Martensite Transformation, JOM 8 (1956) 124–132, doi: 10.1007/BF03377656.
[1184] J.S. Bowles, J.K. Mackenzie, The crystallography of martensite transformations I, Acta Metallurgica 2 (1954) 129–137, doi: 10.1016/0001-6160(54)90102-9.
[1185] J.K. Mackenzie, J.S. Bowles, The crystallography of martensite transformations II, Acta Metallurgica 2 (1954) 138–147, doi: 10.1016/0001-6160(54)90103-0.
[1186] J.S. Bowles, J.K. Mackenzie, The crystallography of martensite transformations III. Face-centred cubic to body-centred tetragonal transformations, Acta Metallurgica 2 (1954) 224–234, doi: 10.1016/0001-6160(54)90163-7.
[1187] J.K. Mackenzie, J.S. Bowles, The crystallography of martensite transformations—IV body-centred cubic to orthorhombic transformations, Acta Metallurgica 5 (1957) 137–149, doi: 10.1016/0001-6160(57)90018-4.
[1188] V. Raghavan, M. Cohen, A nucleation model for martensitic transformations in iron-base alloys, Acta Metallurgica 20 (1972) 333–338, doi: 10.1016/0001-6160(72)90025-9.
[1189] V. Raghavan, M. Cohen, Measurement and interpretation of isothermal martensitic kinetics, MTA 2 (1971) 2409–2418, doi: 10.1007/BF02814878.
[1190] W.G. Burgers, On the process of transition of the cubic-body-centered modification into the hexagonal-close-packed modification of zirconium, Physica 1 (1934) 561–586, doi: 10.1016/S0031-8914(34)80244-3.
[1191] A.J. Bogers, W.G. Burgers, Partial dislocations on the {110} planes in the B.C.C. lattice and the transition of the F.C.C. into the B.C.C. lattice, Acta Metallurgica 12 (1964) 255–261, doi: 10.1016/0001-6160(64)90194-4.
[1192] G.B. Olson, M. Cohen, A Perspective on Martensitic Nucleation, Annu. Rev. Mater. Sci. 11 (1981) 1–32, doi: 10.1146/annurev.ms.11.080181.000245.
[1193] G.B. Olson, M. Cohen, A general mechanism of martensitic nucleation: Part II. FCC → BCC and other martensitic transformations, MTA 7 (1976) 1905–1914, doi: 10.1007/BF02659823.
[1194] R.F. Bunshah, R.F. Mehl, Rate of propagation of martensite, Trans AIME 197 (1953) 1251–1258.
[1195] H.C. Shin, T.K. Ha, Y.W. Chang, Kinetics of deformation induced martensitic transformation in a 304 stainless steel, Scripta Materialia 45 (2001) 823–829, doi: 10.1016/S1359-6462(01)01101-0.
[1196] G.B. Olson, M. Cohen, A general mechanism of martensitic nucleation: Part III. Kinetics of martensitic nucleation, MTA 7 (1976) 1915–1923, doi: 10.1007/BF02659824.
[1197] Z. Nishiyama, Martensitic Transformation, Elsevier Science, Oxford, 1978.
[1198] I. Tamura, Deformation-induced martensitic transformation and transformation-induced plasticity in steels, Metal Science 16 (1982) 245–253, doi: 10.1179/030634582790427316.
[1199] E.C. Bain, Dunkirk N. Y., The nature of martensite, Trans AIME 70 (1924) 25–47.

[1200] J.A. Venables, The martensite transformation in stainless steel, Philosophical Magazine 7 (1962) 35–44, doi: 10.1080/14786436208201856.

[1201] E. Pereloma, D.V. Edmonds, Phase transformation in steels: Diffusionless transformations, high strength steels, modelling and advanced analytical techniques, Woodhead Pub, Cambridge, 2012.

[1202] H.C. Ling, W.S. Owen, A model of the thermoelastic growth of martensite, Acta Metallurgica 29 (1981) 1721–1736, doi: 10.1016/0001-6160(81)90006-7.

[1203] J.C. Fisher, J.H. Hollomon, D. Turnbull, Kinetics of the austenite→martensite transformation, JOM 1 (1949) 691–700, doi: 10.1007/BF03398922.

[1204] H.K.D.H. BHADESHIA, A rationalisation of shear transformations in steels, Acta Metallurgica 29 (1981) 1117–1130, doi: 10.1016/0001-6160(81)90063-8.

[1205] J.M. Diani, D.M. Parks, Effects of strain state on the kinetics of strain-induced martensite in steels, Journal of the Mechanics and Physics of Solids 46 (1998) 1613–1635, doi: 10.1016/S0022-5096(98)00001-5.

[1206] M. CHERKAOUI, M. Berveiller, H. Sabar, Micromechanical modeling of martensitic transformation induced plasticity (TRIP) in austenitic single crystals, International Journal of Plasticity 14 (1998) 597–626, doi: 10.1016/S0749-6419(99)80000-X.

[1207] T.-H. Lee, H.-Y. Ha, J.-Y. Kang, J. Moon, C.-H. Lee, S.-J. Park, An intersecting-shear model for strain-induced martensitic transformation, Acta Materialia 61 (2013) 7399–7410, doi: 10.1016/j.actamat.2013.08.046.

[1208] S. Dash, N. Brown, Nucleation and growth of martensite in fe-32.3% Ni alloy, Acta Metallurgica 14 (1966) 595–603, doi: 10.1016/0001-6160(66)90067-8.

[1209] S. Takaki, H. Nakatsu, Y. Tokunaga, Effects of Austenite Grain Size on epsilon Martensitic Transformation in Fe-15mass%Mn Alloy, Mater. Trans., JIM 34 (1993) 489–495, doi: 10.2320/matertrans1989.34.489.

[1210] M. Berveiller, F.D. Fischer (Eds.), Mechanics of Solids with Phase Changes, Springer Vienna, Vienna, s.l., 1997.

[1211] A. Ma, A. Hartmaier, A study of deformation and phase transformation coupling for TRIP-assisted steels, International Journal of Plasticity 64 (2015) 40–55, doi: 10.1016/j.ijplas.2014.07.008.

[1212] S. Gupta, A. Ma, A. Hartmaier, Mechanical twinning induced alteration in the kinetics of martensitic phase transformation in TRIP-maraging steels, International Journal of Solids and Structures 155 (2018) 213–224, doi: 10.1016/j.ijsolstr.2018.07.021.

[1213] M. CHERKAOUI, M. Berveiller, X. Lemoine, Couplings between plasticity and martensitic phase transformation: overall behavior of polycrystalline TRIP steels, International Journal of Plasticity 16 (2000) 1215–1241, doi: 10.1016/S0749-6419(00)00008-5.

[1214] S.L. Wong, M. Madivala, U. Prahl, F. Roters, D. Raabe, A crystal plasticity model for twinning- and transformation-induced plasticity, Acta Materialia 118 (2016) 140–151, doi: 10.1016/j.actamat.2016.07.032.

[1215] K. Bhattacharya, Comparison of the geometrically nonlinear and linear theories of martensitic transformation, Continuum Mech. Thermodyn. 5 (1993) 205–242, doi: 10.1007/BF01126525.

[1216] R.F. Kubler, M. Berveiller, P. Buessler, Semi phenomenological modelling of the behavior of TRIP steels, International Journal of Plasticity 27 (2011) 299–327, doi: 10.1016/j.ijplas.2010.05.002.

[1217] V.I. Levitas, Thermomechanical theory of martensitic phase transformations in inelastic materials, International Journal of Solids and Structures 35 (1998) 889–940, doi: 10.1016/S0020-7683(97)00089-9.

[1218] V. Levitas, Critical thought experiment to choose the driving force for interface propagation in inelastic materials, International Journal of Plasticity 18 (2002) 1499–1525, doi: 10.1016/S0749-6419(02)00027-X.

[1219] V.I. Levitas, A.V. Idesman, G.B. Olson, Continuum modeling of strain-induced martensitic transformation at shear-band intersections, Acta Materialia 47 (1998) 219–233, doi: 10.1016/S1359-6454(98)00314-0.

[1220] V.I. Levitas, V.A. Levin, K.M. Zingerman, E.I. Freiman, Displacive phase transitions at large strains: phase-field theory and simulations, Phys. Rev. Lett. 103 (2009) 25702, doi: 10.1103/PhysRevLett.103.025702.

[1221] V.I. Levitas, I.B. Ozsoy, Micromechanical modeling of stress-induced phase transformations. Part 1. Thermodynamics and kinetics of coupled interface propagation and reorientation, International Journal of Plasticity 25 (2009) 239–280, doi: 10.1016/j.ijplas.2008.02.004.

[1222] V.I. Levitas, I.B. Ozsoy, Micromechanical modeling of stress-induced phase transformations. Part 2. Computational algorithms and examples, International Journal of Plasticity 25 (2009) 546–583, doi: 10.1016/j.ijplas.2008.02.005.

[1223] D.D. Tjahjanto, S. Turteltaub, A.S.J. Suiker, Crystallographically based model for transformation-induced plasticity in multiphase carbon steels, Continuum Mech. Thermodyn. 19 (2008) 399–422, doi: 10.1007/s00161-007-0061-x.

[1224] R. Mahnken, M. Wolff, A. Schneidt, M. Böhm, Multi-phase transformations at large strains – Thermodynamic framework and simulation, International Journal of Plasticity 39 (2012) 1–26, doi: 10.1016/j.ijplas.2012.05.009.

[1225] S. Turteltaub, A. SUIKER, Transformation-induced plasticity in ferrous alloys, Journal of the Mechanics and Physics of Solids 53 (2005) 1747–1788, doi: 10.1016/j.jmps.2005.03.004.

[1226] V.G. Kouznetsova, M.G.D. Geers, A multi-scale model of martensitic transformation plasticity, Mechanics of Materials 40 (2008) 641–657, doi: 10.1016/j.mechmat.2008.02.004.

[1227] M.-G. Lee, S.-J. Kim, H.N. Han, Crystal plasticity finite element modeling of mechanically induced martensitic transformation (MIMT) in metastable austenite, International Journal of Plasticity 26 (2010) 688–710, doi: 10.1016/j.ijplas.2009.10.001.

[1228] C.L. Magee, H.W. Paxton, Transformation kinetics, microplasticity and aging of martensite in Fe–31Ni, Trans. Met. Soc. AIME 242 (1968) 1741–1749.

[1229] D.P. Koistinen, R.E. Marburger, A general equation prescribing the extent of the austenite–martensite transformations in pure iron-carbon alloys and plain carbon steels, Acta Metallurgica 7 (1959) 59–60.

[1230] F.D. Fischer, G. Reisner, A criterion for the martensitic transformation of a microregion in an elastic–plastic material, Acta Materialia 46 (1998) 2095–2102, doi: 10.1016/S1359-6454(97)00374-1.

[1231] F.D. Fischer, G. Reisner, E. Werner, K. Tanaka, G. Cailletaud, T. Antretter, A new view on transformation induced plasticity (TRIP), International Journal of Plasticity 16 (2000) 723–748, doi: 10.1016/S0749-6419(99)00078-9.

[1232] F.D. Fischer, Q.-P. Sun, K. Tanaka, Transformation-Induced Plasticity (TRIP), Applied Mechanics Reviews 49 (1996) 317–364, doi: 10.1115/1.3101930.

[1233] M. Fischlschweiger, G. Cailletaud, T. Antretter, A mean-field model for transformation induced plasticity including backstress effects for non-proportional loadings, International Journal of Plasticity 37 (2012) 53–71, doi: 10.1016/j.ijplas.2012.04.001.

[1234] F. Marketz, F.D. Fischer, A mesoscale study on the thermodynamic effect of stress on martensitic transformation, Metall and Mat Trans A 26 (1995) 267–278, doi: 10.1007/BF02664665.

[1235] F. Marketz, F.D. Fischer, Micromechanical modelling of stress-assisted martensitic transformation, Modelling Simul. Mater. Sci. Eng. 2 (1994) 1017–1046, doi: 10.1088/0965-0393/2/5/006.

[1236] J.M. Diani, H. Sabar, M. Berveiller, Micromechanical modelling of the transformation induced plasticity (TRIP) phenomenon in steels, International Journal of Engineering Science 33 (1995) 1921–1934, doi: 10.1016/0020-7225(95)00045-Y.

[1237] A.S.J. Suiker, S. Turteltaub, Computational modelling of plasticity induced by martensitic phase transformations, Int. J. Numer. Meth. Engng 63 (2005) 1655–1693, doi: 10.1002/nme.1327.

[1238] J.M. Ball, R.D. James, Fine phase mixtures as minimizers of energy, Arch. Rational Mech. Anal. 100 (1987) 13–52, doi: 10.1007/BF00281246.

[1239] C.Y. Sun, N. Guo, M.W. Fu, S.W. Wang, Modeling of slip, twinning and transformation induced plastic deformation for TWIP steel based on crystal plasticity, International Journal of Plasticity 76 (2016) 186–212, doi: 10.1016/j.ijplas.2015.08.003.

[1240] R.J. Wasilewski, On the nature of the martensitic transformation, MTA 6 (1975) 1405–1418, doi: 10.1007/BF02641933.

[1241] M. Watanabe, C.M. Wayman, Crystallography of the martensite transformation in Fe−Al−C alloys, Metall and Materi Trans 2 (1971) 2229–2236, doi: 10.1007/BF02917555.

[1242] A.A. Lebedev, V.V. Kosarchuk, Influence of phase transformations on the mechanical properties of austenitic stainless steels, International Journal of Plasticity 16 (2000) 749–767, doi: 10.1016/S0749-6419(99)00085-6.

[1243] H. Wang, Y. Jeong, B. Clausen, Y. Liu, R.J. McCabe, F. Barlat, C.N. Tomé, Effect of martensitic phase transformation on the behavior of 304 austenitic stainless steel under tension, Materials Science and Engineering: A 649 (2016) 174–183, doi: 10.1016/j.msea.2015.09.108.

[1244] J.B. Leblond, J. Devaux, J.C. Devaux, Mathematical modelling of transformation plasticity in steels I: Case of ideal-plastic phases, International Journal of Plasticity 5 (1989) 551–572, doi: 10.1016/0749-6419(89)90001-6.

[1245] H. HALLBERG, P. HAKANSSON, M. RISTINMAA, A constitutive model for the formation of martensite in austenitic steels under large strain plasticity, International Journal of Plasticity 23 (2007) 1213–1239, doi: 10.1016/j.ijplas.2006.11.002.

[1246] H. Hallberg, P. Håkansson, M. Ristinmaa, Thermo-mechanically coupled model of diffusionless phase transformation in austenitic steel, International Journal of Solids and Structures 47 (2010) 1580–1591, doi: 10.1016/j.ijsolstr.2010.02.019.

[1247] R. Mahnken, A. Schneidt, A thermodynamics framework and numerical aspects for transformation-induced plasticity at large strains, Arch Appl Mech 80 (2010) 229–253, doi: 10.1007/s00419-009-0308-z.

[1248] R. Mahnken, A. Schneidt, T. Antretter, Macro modelling and homogenization for transformation induced plasticity of a low-alloy steel, International Journal of Plasticity 25 (2009) 183–204, doi: 10.1016/j.ijplas.2008.03.005.

[1249] R. Mahnken, A. Schneidt, S. Tschumak, H.J. Maier, On the simulation of austenite to bainite phase transformation, Computational Materials Science 50 (2011) 1823–1829, doi: 10.1016/j.commatsci.2010.12.032.

[1250] R.P. Garrett, S. Xu, J. Lin, T.A. Dean, A model for predicting austenite to bainite phase transformation in producing dual phase steels, International Journal of Machine Tools and Manufacture 44 (2004) 831–837, doi: 10.1016/j.ijmachtools.2004.01.004.

[1251] F.D. Fischer, E.R. Oberaigner, K. Tanaka, F. Nishimura, Transformation induced plasticity revised an updated formulation, International Journal of Solids and Structures 35 (1998) 2209–2227, doi: 10.1016/S0020-7683(97)00134-0.

[1252] M. Wolff, M. Böhm, M. Dalgic, I. Hüßler, Evaluation of models for TRIP and stress-dependent transformation behaviour for the martensitic transformation of the steel 100Cr6, Computational Materials Science 43 (2008) 108–114, doi: 10.1016/j.commatsci.2007.07.040.

[1253] M. Wolff, M. Böhm, B. Suhr, Comparison of different approaches to transformation-induced plasticity in steel, Mat.-wiss. u. Werkstofftech. 40 (2009) 454–459, doi: 10.1002/mawe.200900476.

[1254] M. Wolff, M. Böhm, D. Helm, Material behavior of steel – Modeling of complex phenomena and thermodynamic consistency, International Journal of Plasticity 24 (2008) 746–774, doi: 10.1016/j.ijplas.2007.07.005.

[1255] P.J. Jacques, Q. Furnémont, F. Lani, T. Pardoen, F. Delannay, Multiscale mechanics of TRIP-assisted multiphase steels: I. Characterization and mechanical testing, Acta Materialia 55 (2007) 3681–3693, doi: 10.1016/j.actamat.2007.02.029.

[1256] F. Lani, Q. Furnémont, T. van Rompaey, F. Delannay, P.J. Jacques, T. Pardoen, Multiscale mechanics of TRIP-assisted multiphase steels: II. Micromechanical modelling, Acta Materialia 55 (2007) 3695–3705, doi: 10.1016/j.actamat.2007.02.015.

[1257] Y. Tomita, T. Iwamoto, Computational prediction of deformation behavior of TRIP steels under cyclic loading, International Journal of Mechanical Sciences 43 (2001) 2017–2034, doi: 10.1016/S0020-7403(01)00026-1.

[1258] A.V. Idesman, V.I. Levitas, E. Stein, Elastoplastic materials with martensitic phase transition and twinning at finite strains: Numerical solution with the finite element method, Computer Methods in Applied Mechanics and Engineering 173 (1999) 71–98, doi: 10.1016/S0045-7825(98)00258-8.

[1259] V.I. Levitas, A.V. Idesman, G.B. Olson, E. Stein, Numerical modelling of martensitic growth in an elastoplastic material, Philosophical Magazine A 82 (2002) 429–462, doi: 10.1080/01418610208239609.

[1260] V.I. Levitas, A.V. Idesman, D.L. Preston, Microscale simulation of martensitic microstructure evolution, Phys. Rev. Lett. 93 (2004) 105701, doi: 10.1103/PhysRevLett.93.105701.

[1261] V.I. Levitas, D.-W. Lee, Athermal resistance to interface motion in the phase-field theory of microstructure evolution, Phys. Rev. Lett. 99 (2007) 245701, doi: 10.1103/PhysRevLett.99.245701.

[1262] M.-G. Lee, S.-J. Kim, H.N. Han, W.C. Jeong, Implicit finite element formulations for multi-phase transformation in high carbon steel, International Journal of Plasticity 25 (2009) 1726–1758, doi: 10.1016/j.ijplas.2008.11.010.

[1263] S.H. LEE, J.-Y. Kang, H.N. Han, K.H. OH, H.-C. LEE, D.-W. SUH, S.-J. Kim, Variant Selection in Mechanically-induced Martensitic Transformation of Metastable Austenitic Steel, ISIJ Int. 45 (2005) 1217–1219, doi: 10.2355/isijinternational.45.1217.

[1264] S. Meftah, F. Barbe, L. Taleb, F. Sidoroff, Parametric numerical simulations of TRIP and its interaction with classical plasticity in martensitic transformation, European Journal of Mechanics - A/Solids 26 (2007) 688–700, doi: 10.1016/j.euromechsol.2006.10.004.

[1265] A.S.J. Suiker, S. Turteltaub, Numerical modelling of transformation-induced damage and plasticity in metals, Metall and Mat Trans A 15 (2007) S147-S166, doi: 10.1088/0965-0393/15/1/S13.

[1266] L. Taleb, F. Sidoroff, A micromechanical modeling of the Greenwood–Johnson mechanism in transformation induced plasticity, International Journal of Plasticity 19 (2003) 1821–1842, doi: 10.1016/S0749-6419(03)00020-2.

[1267] L. TALEB, S. PETIT, New investigations on transformation induced plasticity and its interaction with classical plasticity, International Journal of Plasticity 22 (2006) 110–130, doi: 10.1016/j.ijplas.2005.03.012.

[1268] L. TALEB, Experimental analysis of transformation plasticity, International Journal of Plasticity 17 (2001) 1–20, doi: 10.1016/S0749-6419(99)00090-X.

[1269] D.D. Tjahjanto, S. Turteltaub, A.S.J. Suiker, S. van der Zwaag, Modelling of the effects of grain orientation on transformation-induced plasticity in multiphase carbon steels, MTA 14 (2006) 617–636, doi: 10.1088/0965-0393/14/4/006.

[1270] D.D. Tjahjanto, A.S.J. Suiker, S. Turteltaub, P.E.J. Rivera Diaz del Castillo, S. van der Zwaag, Micromechanical predictions of TRIP steel behavior as a function of microstructural parameters, Computational Materials Science 41 (2007) 107–116, doi: 10.1016/j.commatsci.2007.03.005.

[1271] S. Manchiraju, P.M. Anderson, Coupling between martensitic phase transformations and plasticity: A microstructure-based finite element model, International Journal of Plasticity 26 (2010) 1508–1526, doi: 10.1016/j.ijplas.2010.01.009.

[1272] M. CHERKAOUI, M. Berveiller, Moving inelastic discontinuities and applications to martensitic phase transition, Arch Appl Mech 70 (2000) 159–181, doi: 10.1007/s004199900055.

[1273] J. Shi, S. Turteltaub, E. van der Giessen, Analysis of grain size effects on transformation-induced plasticity based on a discrete dislocation–transformation model, Journal of the Mechanics and Physics of Solids 58 (2010) 1863–1878, doi: 10.1016/j.jmps.2010.07.021.

[1274] S. Turteltaub, A.S.J. Suiker, A multiscale thermomechanical model for cubic to tetragonal martensitic phase transformations, International Journal of Solids and Structures 43 (2006) 4509–4545, doi: 10.1016/j.ijsolstr.2005.06.065.

[1275] C.Y. Sun, G. Fang, L.P. Lei, P. Zeng, Micromechanics model of martensitic transformation-induced plasticity, Journal of Materials Processing Technology 201 (2008) 226–231, doi: 10.1016/j.jmatprotec.2007.11.136.

[1276] C.Y. Sun, G. Fang, L.P. Lei, P. Zeng, Micro-thermomechanical constitutive model of transformation induced plasticity and its application on armour steel, Materials Science and Engineering: A 499 (2009) 18–22, doi: 10.1016/j.msea.2007.11.100.

[1277] E.R. Oberaigner, M. Fischlschweiger, A statistical mechanics approach describing martensitic phase transformation, Mechanics of Materials 43 (2011) 467–475, doi: 10.1016/j.mechmat.2011.06.001.

[1278] K. Nagayama, T. Terasaki, K. Tanaka, F.D. Fischer, T. Antretter, G. Cailletaud, F. Azzouz, Mechanical properties of a Cr–Ni–Mo–Al–Ti maraging steel in the process of martensitic transformation, Materials Science and Engineering: A 308 (2001) 25–37, doi: 10.1016/S0921-5093(00)01999-7.

[1279] K.F. Hane, T.W. Shield, Symmetry and microstructure in martensites, Philosophical Magazine A 78 (1998) 1215–1252, doi: 10.1080/01418619808239984.

[1280] R.D. James, K.F. Hane, Martensitic transformations and shape-memory materials, Acta Materialia 48 (2000) 197–222, doi: 10.1016/S1359-6454(99)00295-5.

[1281] T. Reti, Z. Fried, I. Felde, Computer simulation of steel quenching process using a multi-phase transformation model, Computational Materials Science 22 (2001) 261–278, doi: 10.1016/S0927-0256(01)00240-3.

[1282] J.B. Leblond, Mathematical modelling of transformation plasticity in steels II: Coupling with strain hardening phenomena, International Journal of Plasticity 5 (1989) 573–591, doi: 10.1016/0749-6419(89)90002-8.

[1283] F.S. Ham, Stress-Assisted Precipitation on Dislocations, Journal of Applied Physics 30 (1959) 915–926, doi: 10.1063/1.1735262.

[1284] E.S.K. Menon, H.I. Aaronson, Overview no. 57 Morphology, crystallography and kinetics of sympathetic nucleation, Acta Metallurgica 35 (1987) 549–563, doi: 10.1016/0001-6160(87)90179-9.

[1285] C. Zener, Theory of Growth of Spherical Precipitates from Solid Solution, Journal of Applied Physics 20 (1949) 950–953, doi: 10.1063/1.1698258.

[1286] F. Drolet, K.R. Elder, M. Grant, J.M. Kosterlitz, Phase-field modeling of eutectic growth, Physical review. E, Statistical physics, plasmas, fluids, and related interdisciplinary topics 61 (2000) 6705–6720, doi: 10.1103/physreve.61.6705.

[1287] Elder, Drolet, Kosterlitz, Grant, Stochastic eutectic growth, Physical review letters 72 (1994) 677–680, doi: 10.1103/PhysRevLett.72.677.

[1288] J.-B. Leblond, J.-M. Bergheau, R. Lacroix, D. Huin, Implementation and application of some nonlinear models of diffusion/reaction in solids, Finite Elements in Analysis and Design 132 (2017) 8–26, doi: 10.1016/j.finel.2017.04.004.

[1289] J.-B. Brunac, D. Huin, J.-B. Leblond, Numerical Implementation and Application of an Extended Model for Diffusion and Precipitation of Chemical Elements in Metallic Matrices, Oxid Met 73 (2010) 565–589, doi: 10.1007/s11085-010-9193-7.

[1290] D.E. Coates, Diffusion-controlled precipitate growth in ternary systems I, MTA 3 (1972) 1203–1212, doi: 10.1007/BF02642453.

[1291] D.E. Coates, Diffusion controlled precipitate growth in ternary systems: II, MTA 4 (1973) 1077–1086, doi: 10.1007/BF02645611.

[1292] I.M. Lifshitz, V.V. Slyozov, The kinetics of precipitation from supersaturated solid solutions, Journal of Physics and Chemistry of Solids 19 (1961) 35–50, doi: 10.1016/0022-3697(61)90054-3.

[1293] A. Deschamps, M. MILITZER, W.J. Poole, Precipitation Kinetics and Strengthening of a Fe-0.8wt%Cu Alloy, ISIJ Int. 41 (2001) 196–205, doi: 10.2355/isijinternational.41.196.

[1294] M. Hillert, G.R. Purdy, Chemically induced grain boundary migration, Acta Metallurgica 26 (1978) 333–340, doi: 10.1016/0001-6160(78)90132-3.

[1295] M. Hillert, On the driving force for diffusion induced grain boundary migration, Scripta Metallurgica 17 (1983) 237–240, doi: 10.1016/0036-9748(83)90105-9.

[1296] G. Meyrick, On the initiation of discontinuous precipitation, Scripta Metallurgica 10 (1976) 649–653, doi: 10.1016/0036-9748(76)90198-8.

[1297] J.D. Robson, Modeling competitive continuous and discontinuous precipitation, Acta Materialia 61 (2013) 7781–7790, doi: 10.1016/j.actamat.2013.09.017.

[1298] I.G. Solorzano, G.R. Purdy, Interlamellar spacing in discontinuous precipitation, Metall and Mat Trans A 15 (1984) 1055–1063, doi: 10.1007/BF02644697.

[1299] M. Hillert, An improved model for discontinuous precipitation, Acta Metallurgica 30 (1982) 1689–1696, doi: 10.1016/0001-6160(82)90190-0.

[1300] J.M. Shapiro, J.S. Kirkaldy, The kinetics of discontinuous precipitation in copper-indium alloys, Acta Metallurgica 16 (1968) 1239–1252, doi: 10.1016/0001-6160(68)90005-9.

[1301] G.R. Purdy, N. Lange, ON THE INITIAL STAGES OF DISCONTINUOUS PRECIPITATION REACTIONS, in: P. Haasen, V. Gerold, R. Wagner, M.F. Ashby (Eds.), Decomposition of alloys, the early stages: Proceedings of the 2nd Acta-scripta metallurgica conference, Sonnenberg, Germany, 19-23 September 1983, Pergamon Press, Oxford, New York, Paris (etc), 1984, pp. 214–220.

[1302] M. Hillert, On theories of growth during discontinuous precipitation, Metall and Materi Trans 3 (1972) 2729–2741, doi: 10.1007/BF02652840.

[1303] D.B. Williams, E.P. Butler, Grain boundary discontinuous precipitation reactions, International Metals Reviews 26 (1981) 153–183, doi: 10.1179/imtr.1981.26.1.153.

[1304] L.M. Klinger, Y.J.M. Brechet, G.R. Purdy, On velocity and spacing selection in discontinuous precipitation—I. Simplified analytical approach, Acta Materialia 45 (1997) 5005–5013, doi: 10.1016/S1359-6454(97)00171-7.

[1305] R.A. Fournelle, J.B. Clark, The genesis of the cellular precipitation reaction, Metall and Materi Trans 3 (1972) 2757–2767, doi: 10.1007/BF02652842.

[1306] D. Duly, Y. Brechet, Nucleation mechanism of discontinuous precipitation in Mg・Al alloys and relation with the morphology, Acta Metallurgica et Materialia 42 (1994) 3035–3043, doi: 10.1016/0956-7151(94)90400-6.

[1307] D. Duly, Y. Brechet, B. Chenal, Macroscopic kinetics of discontinuous precipitation in a Mg-8.5 wt% Al alloy, Acta Metallurgica et Materialia 40 (1992) 2289–2300, doi: 10.1016/0956-7151(92)90147-7.

[1308] D. Duly, M.C. Cheynet, Y. Brechet, Morphology and chemical nanoanalysis of discontinuous precipitation in Mg・Al alloys—I. Regular growth, Acta Metallurgica et Materialia 42 (1994) 3843–3854, doi: 10.1016/0956-7151(94)90450-2.

[1309] D. Duly, J.P. Simon, Y. Brechet, On the competition between continuous and discontinuous precipitations in binary Mg・Al alloys, Acta Metallurgica et Materialia 43 (1995) 101–106, doi: 10.1016/0956-7151(95)90266-X.

[1310] K.N. Braszczyńska-Malik, Discontinuous and continuous precipitation in magnesium–aluminium type alloys, Journal of Alloys and Compounds 477 (2009) 870–876, doi: 10.1016/j.jallcom.2008.11.008.

[1311] C.R. Hutchinson, J.F. Nie, S. Gorsse, Modeling the precipitation processes and strengthening mechanisms in a Mg-Al-(Zn) AZ91 alloy, Metall and Mat Trans A 36 (2005) 2093–2105, doi: 10.1007/s11661-005-0330-x.

[1312] F.K. LeGoues, Y.W. Lee, H.I. Aaronson, Influence of crystallography upon critical nucleus shapes and kinetics of homogeneous F.C.C.-F.C.C. nucleation—II. The non-classical regime, Acta Metallurgica 32 (1984) 1837–1843, doi: 10.1016/0001-6160(84)90241-4.

[1313] F.K. LeGoues, H.I. Aaronson, Y.W. Lee, Influence of crystallography upon critical nucleus shapes and kinetics of homogeneous f.c.c.-f.c.c. nucleation—III. The influence of elastic strain energy, Acta Metallurgica 32 (1984) 1845–1853, doi: 10.1016/0001-6160(84)90242-6.

[1314] S. Celotto, TEM study of continuous precipitation in Mg–9 wt%Al–1 wt%Zn alloy, Acta Materialia 48 (2000) 1775–1787, doi: 10.1016/S1359-6454(00)00004-5.

[1315] J.F. Nie, B.C. Muddle, H.I. Aaronson, S.P. Ringer, J.P. Hirth, On the roles of clusters during intragranular nucleation in the absence of static defects, Metall and Mat Trans A 33 (2002) 1649–1658, doi: 10.1007/s11661-002-0174-6.

[1316] S.P. Ringer, K. Hono, Microstructural Evolution and Age Hardening in Aluminium Alloys, Materials Characterization 44 (2000) 101–131, doi: 10.1016/S1044-5803(99)00051-0.

[1317] L. Rougier, A. Jacot, C.-A. Gandin, P. Di Napoli, P.-Y. Théry, D. Ponsen, V. Jaquet, Numerical simulation of precipitation in multicomponent Ni-base alloys, Acta Materialia 61 (2013) 6396–6405, doi: 10.1016/j.actamat.2013.07.018.

[1318] B. Dutta, E. Valdes, C.M. Sellars, Mechanism and kinetics of strain induced precipitation of Nb(C,N) in austenite, Acta Metallurgica et Materialia 40 (1992) 653–662, doi: 10.1016/0956-7151(92)90006-Z.

[1319] J.D. Robson, Modelling the overlap of nucleation, growth and coarsening during precipitation, Acta Materialia 52 (2004) 4669–4676, doi: 10.1016/j.actamat.2004.06.024.

[1320] R. Wagner, R. Kampmann, P.W. Voorhees, Homogeneous Second-Phase Precipitation, in: N. Setter (Ed.), Electroceramic-based MEMS: Fabrication-technology and applications, Springer Science+Business Media, New York, 2005.

[1321] R. Kampmann, R. Wagner, Kinetics of Precipitation in Metastabile Binary Alloys-Theory and Application to Cu 1.9 at.% Ti and Ni 14 at.% Al., in: P. Haasen, V. Gerold, R. Wagner, M.F. Ashby (Eds.), Decomposition of alloys, the early stages: Proceedings of the 2nd Acta-scripta metallurgica conference, Sonnenberg, Germany, 19-23 September 1983, Pergamon Press, Oxford, New York, Paris (etc), 1984, pp. 91–103.

[1322] M. Bonvalet, T. Philippe, X. Sauvage, D. Blavette, Modeling of precipitation kinetics in multicomponent systems: Application to model superalloys, Acta Materialia 100 (2015) 169–177, doi: 10.1016/j.actamat.2015.08.041.

[1323] Dee, Patterns produced by precipitation at a moving reaction front, Physical review letters 57 (1986) 275–278, doi: 10.1103/PhysRevLett.57.275.

[1324] J.D. Robson, P.B. Prangnell, Modelling Al3Zr dispersoid precipitation in multicomponent aluminium alloys, Materials Science and Engineering: A 352 (2003) 240–250, doi: 10.1016/S0921-5093(02)00894-8.

[1325] J.D. Robson, P.B. Prangnell, Dispersoid precipitation and process modelling in zirconium containing commercial aluminium alloys, Acta Materialia 49 (2001) 599–613, doi: 10.1016/S1359-6454(00)00351-7.

[1326] J.D. Robson, A new model for prediction of dispersoid precipitation in aluminium alloys containing zirconium and scandium, Acta Materialia 52 (2004) 1409–1421, doi: 10.1016/j.actamat.2003.11.023.

[1327] H.B. Aaron, G.R. Kotler, Second phase dissolution, Metallurgical Transactions 2 (1971) 393–408, doi: 10.1007/BF02663326.

[1328] M. Nicolas, A. Deschamps, Characterisation and modelling of precipitate evolution in an Al–Zn–Mg alloy during non-isothermal heat treatments, Acta Materialia 51 (2003) 6077–6094, doi: 10.1016/S1359-6454(03)00429-4.

[1329] S. Kumar, D. Ramkrishna, On the solution of population balance equations by discretization—III. Nucleation, growth and aggregation of particles, Chemical Engineering Science 52 (1997) 4659–4679, doi: 10.1016/S0009-2509(97)00307-2.

[1330] J.A. Marqusee, J. Ross, Theory of Ostwald ripening: Competitive growth and its dependence on volume fraction, The Journal of Chemical Physics 80 (1984) 536–543, doi: 10.1063/1.446427.

[1331] M.J. Anderson, C. Panwisawas, Y. Sovani, R.P. Turner, J.W. Brooks, H.C. Basoalto, Mean-field modelling of the intermetallic precipitate phases during heat treatment and additive manufacture of Inconel 718, Acta Materialia 156 (2018) 432–445, doi: 10.1016/j.actamat.2018.07.002.

[1332] X. Li, N. Saunders, A.P. Miodownik, The coarsening kinetics of γ' particles in nickel-based alloys, Metall and Mat Trans A 33 (2002) 3367–3373, doi: 10.1007/s11661-002-0325-9.

[1333] P. Maugis, M. Gouné, Kinetics of vanadium carbonitride precipitation in steel: A computer model, Acta Materialia 53 (2005) 3359–3367, doi: 10.1016/j.actamat.2005.03.036.

[1334] O.R. Myhr, Ø. Grong, Modelling of non-isothermal transformations in alloys containing a particle distribution, Acta Materialia 48 (2000) 1605–1615, doi: 10.1016/S1359-6454(99)00435-8.

[1335] Z. Mao, C.K. Sudbrack, K.E. Yoon, G. Martin, D.N. Seidman, The mechanism of morphogenesis in a phase-separating concentrated multicomponent alloy, Nature materials 6 (2007) 210–216, doi: 10.1038/nmat1845.

[1336] S. Björklund, L.F. Donaghey, M. Hillert, The effect of alloying elements on the rate of ostwald ripening of cementite in steel, Acta Metallurgica 20 (1972) 867–874, doi: 10.1016/0001-6160(72)90079-X.

[1337] J.E. Morral, G.R. Purdy, Particle coarsening in binary and multicomponent alloys, Scripta Metallurgica et Materialia 30 (1994) 905–908, doi: 10.1016/0956-716X(94)90413-8.

[1338] T. Philippe, P.W. Voorhees, Ostwald ripening in multicomponent alloys, Acta Materialia 61 (2013) 4237–4244, doi: 10.1016/j.actamat.2013.03.049.

[1339] T. Philippe, D. Blavette, P.W. Voorhees, Critical nucleus composition in a multicomponent system, The Journal of Chemical Physics 141 (2014) 124306, doi: 10.1063/1.4896222.

[1340] C. SUDBRACK, R. NOEBE, D. SEIDMAN, Compositional pathways and capillary effects during isothermal precipitation in a nondilute Ni–Al–Cr alloy, Acta Materialia 55 (2007) 119–130, doi: 10.1016/j.actamat.2006.08.009.

[1341] C. Booth-Morrison, Y. Zhou, R.D. Noebe, D.N. Seidman, On the nanometer scale phase separation of a low-supersaturation Ni–Al–Cr alloy, Phil. Mag. 90 (2010) 219–235, doi: 10.1080/14786430902806660.

[1342] M.J. Whelan, On the Kinetics of Precipitate Dissolution, Metal Science Journal 3 (1969) 95–97, doi: 10.1179/msc.1969.3.1.95.

[1343] H.B. Aaron, On the Kinetics of Precipitate Dissolution, Metal Science Journal 2 (1968) 192–193, doi: 10.1179/030634568790443170.

[1344] H. B. Aaron, Precipitate dissolution and its dependence on growth mode, Acta Metallurgica 17 (1969) 407–418, doi: 10.1016/0001-6160(69)90021-2.

[1345] Q. Chen, N. Ma, K. Wu, Y. Wang, Quantitative phase field modeling of diffusion-controlled precipitate growth and dissolution in Ti–Al–V, Scripta Materialia 50 (2004) 471–476, doi: 10.1016/j.scriptamat.2003.10.032.

[1346] D.H. Bratland, Ø. Grong, H. Shercliff, O.R. Myhr, S. Tjøtta, Overview No. 124 Modelling of precipitation reactions in industrial processing, Acta Materialia 45 (1997) 1–22, doi: 10.1016/S1359-6454(96)00100-0.

[1347] B.I. BjØrneklett, Ø. Grong, O.R. Myhr, A.O. Kluken, Additivity and isokinetic behaviour in relation to particle dissolution, Acta Materialia 46 (1998) 6257–6266, doi: 10.1016/S1359-6454(98)00260-2.

[1348] Ø. Grong, O.R. Myhr, Additivity and isokinetic behaviour in relation to diffusion controlled growth, Acta Materialia 48 (2000) 445–452, doi: 10.1016/S1359-6454(99)00360-2.

[1349] Ø. Grong, H.R. Shercliff, Microstructural modelling in metals processing, Progress in Materials Science 47 (2002) 163–282, doi: 10.1016/S0079-6425(00)00004-9.

[1350] J. Svoboda, F.D. Fischer, Generalization of the Lifshitz–Slyozov–Wagner coarsening theory to non-dilute multi-component systems, Acta Materialia 79 (2014) 304–314, doi: 10.1016/j.actamat.2014.05.042.

[1351] M. Fisk, J. Andersson, R. Du Rietz, S. Haas, S. Hall, Precipitate evolution in the early stages of ageing in Inconel 718 investigated using small-angle x-ray scattering, Materials Science and Engineering: A 612 (2014) 202–207, doi: 10.1016/j.msea.2014.06.036.

[1352] M.J. Anderson, A. Rowe, J. Wells, H.C. Basoalto, Application of a multi-component mean field model to the coarsening behaviour of a nickel-based superalloy, Acta Materialia 114 (2016) 80–96, doi: 10.1016/j.actamat.2016.05.024.

[1353] J.Z. Zhu, T. Wang, A.J. Ardell, S.H. Zhou, Z.K. Liu, L.Q. Chen, Three-dimensional phase-field simulations of coarsening kinetics of γ' particles in binary Ni–Al alloys, Acta Materialia 52 (2004) 2837–2845, doi: 10.1016/j.actamat.2004.02.032.

[1354] J. Svoboda, F.D. Fischer, P. Fratzl, E. Kozeschnik, Modelling of kinetics in multi-component multi-phase systems with spherical precipitates, Materials Science and Engineering: A 385 (2004) 166–174, doi: 10.1016/j.msea.2004.06.018.

[1355] E. Kozeschnik, J. Svoboda, P. Fratzl, F.D. Fischer, Modelling of kinetics in multi-component multi-phase systems with spherical precipitates, Materials Science and Engineering: A 385 (2004) 157–165, doi: 10.1016/j.msea.2004.06.016.

[1356] Q. Chen, J. Jeppsson, J. Ågren, Analytical treatment of diffusion during precipitate growth in multi-component systems, Acta Materialia 56 (2008) 1890–1896, doi: 10.1016/j.actamat.2007.12.037.

[1357] P.W. Voorhees, M.E. Glicksman, Solution to the multi-particle diffusion problem with applications to Ostwald ripening—I. Theory, Acta Metallurgica 32 (1984) 2001–2011, doi: 10.1016/0001-6160(84)90180-9.

[1358] P.W. Voorhees, M.E. Glicksman, Solution to the multi-particle diffusion problem with applications to ostwald ripening—II. Computer simulations, Acta Metallurgica 32 (1984) 2013–2030, doi: 10.1016/0001-6160(84)90181-0.

[1359] K.G. Wang, M.E. Glicksman, K. Rajan, Length scales in phase coarsening: Theory, simulation, and experiment, Computational Materials Science 34 (2005) 235–253, doi: 10.1016/j.commatsci.2004.11.005.

[1360] H. Basoalto, M. Anderson, An extension of mean-field coarsening theory to include particle coalescence using nearest-neighbour functions, Acta Materialia 117 (2016) 122–134, doi: 10.1016/j.actamat.2016.07.007.

[1361] I.J. Moore, M.G. Burke, E.J. Palmiere, Modelling the nucleation, growth and coarsening kinetics of γ'' (D022) precipitates in the Ni-base Alloy 625, Acta Materialia 119 (2016) 157–166, doi: 10.1016/j.actamat.2016.08.027.

[1362] E. Kozeschnik, J. Svoboda, F.D. Fischer, Shape factors in modeling of precipitation, Materials Science and Engineering: A 441 (2006) 68–72, doi: 10.1016/j.msea.2006.08.088.

[1363] J. Svoboda, F.D. Fischer, P.H. Mayrhofer, A model for evolution of shape changing precipitates in multicomponent systems, Acta Materialia 56 (2008) 4896–4904, doi: 10.1016/j.actamat.2008.06.016.

[1364] S.N. Samaras, Modelling of microstructure evolution during precipitation processes: a population balance approach of the KWN model, Progress in Materials Science 14 (2006) 1271–1292, doi: 10.1088/0965-0393/14/8/001.

[1365] H.I. Aaronson, J.B. Clark, Influence of continuous precipitation upon the growth kinetics of the cellular reaction in an Al-Ag alloy, Acta Metallurgica 16 (1968) 845–855, doi: 10.1016/0001-6160(68)90104-1.

[1366] M.J. Stowell, Precipitate nucleation: does capillarity theory work?, Materials Science and Technology 18 (2002) 139–144, doi: 10.1179/026708301125000348.

[1367] E. Clouet, C. Hin, D. Gendt, M. Nastar, F. Soisson, Kinetic Monte Carlo Simulations of Precipitation, Adv. Eng. Mater. 8 (2006) 1210–1214, doi: 10.1002/adem.200600183.

[1368] R. Duddu, D.L. Chopp, P. Voorhees, B. Moran, Diffusional evolution of precipitates in elastic media using the extended finite element and the level set methods, Journal of Computational Physics 230 (2011) 1249–1264, doi: 10.1016/j.jcp.2010.11.002.

[1369] E. Vincent, C.S. Becquart, C. Pareige, P. Pareige, C. Domain, Precipitation of the FeCu system: A critical review of atomic kinetic Monte Carlo simulations, Journal of Nuclear Materials 373 (2008) 387–401, doi: 10.1016/j.jnucmat.2007.06.016.

[1370] F. Soisson, A. Barbu, G. Martin, Monte Carlo simulations of copper precipitation in dilute iron-copper alloys during thermal ageing and under electron irradiation, Acta Materialia 44 (1996) 3789–3800, doi: 10.1016/1359-6454(95)00447-5.

[1371] F. Soisson, G. Martin, Monte Carlo simulations of the decomposition of metastable solid solutions: Transient and steady-state nucleation kinetics, Phys. Rev. B 62 (2000) 203–214, doi: 10.1103/PhysRevB.62.203.

[1372] Y.Z. Ji, A. Issa, T.W. Heo, J.E. Saal, C. Wolverton, L.-Q. Chen, Predicting β' precipitate morphology and evolution in Mg–RE alloys using a combination of first-principles calculations and phase-field modeling, Acta Materialia 76 (2014) 259–271, doi: 10.1016/j.actamat.2014.05.002.

[1373] V. Vaithyanathan, C. Wolverton, L.Q. Chen, Multiscale modeling of θ' precipitation in Al–Cu binary alloys, Acta Materialia 52 (2004) 2973–2987, doi: 10.1016/j.actamat.2004.03.001.

[1374] S.Y. Hu, J. Murray, H. Weiland, Z.K. Liu, L.Q. Chen, Thermodynamic description and growth kinetics of stoichiometric precipitates in the phase-field approach, Calphad 31 (2007) 303–312, doi: 10.1016/j.calphad.2006.08.005.

[1375] V. Fallah, J. Stolle, N. Ofori-Opoku, S. Esmaeili, N. Provatas, Phase-field crystal modeling of early stage clustering and precipitation in metal alloys, Phys. Rev. B 86 (2012), doi: 10.1103/PhysRevB.86.134112.

[1376] J.P. Simmons, Y. Wen, C. Shen, Y.Z. Wang, Microstructural development involving nucleation and growth phenomena simulated with the Phase Field method, Materials Science and Engineering: A 365 (2004) 136–143, doi: 10.1016/j.msea.2003.09.019.

[1377] J.P. Simmons, C. Shen, Y. Wang, Phase field modeling of simultaneous nucleation and growth by explicitly incorporating nucleation events, Scripta Materialia 43 (2000) 935–942, doi: 10.1016/S1359-6462(00)00517-0.

[1378] J.W. Martin, Precipitation hardening, 2nd ed., Butterworth-Heinemann, Oxford, 1998.

[1379] Z. Guo, W. Sha, Quantification of Precipitation Hardening and Evolution of Precipitates, Mater. Trans. 43 (2002) 1273–1282, doi: 10.2320/matertrans.43.1273.

[1380] N.F. Mott, F.R.N. Nabarro, An attempt to estimate the degree of precipitation hardening, with a simple model, Proc. Phys. Soc. 52 (1940) 86–89, doi: 10.1088/0959-5309/52/1/312.

[1381] E. Orowan, in: Symposium on internal stresses in metals and alloys, Institute of Metals, 1948, p. 451.

[1382] J.C. Fisher, E.W. Hart, R.H. Pry, The hardening of metal crystals by precipitate particles, Acta Metallurgica 1 (1953) 336–339, doi: 10.1016/0001-6160(53)90109-6.

[1383] J. Friedel, Dislocations: International Series of Monographs on Solid State Physics, Elsevier Science, Burlington, 1964.

[1384] J. Friedel, Les Dislocations, Gauthier-Villars, Paris, 1956.

[1385] U.F. Kocks, STATISTICAL TREATMENT OF PENETRABLE OBSTACLES, Can. J. Phys. 45 (1967) 737–755, doi: 10.1139/p67-056.

[1386] M.F. Ashby, Work hardening of dispersion-hardened crystals, Philosophical Magazine 14 (1966) 1157–1178, doi: 10.1080/14786436608224282.

[1387] M.F. Ashby, Results and consequences of a recalculation of the frank-read and the orowan stress, Acta Metallurgica 14 (1966) 679–681, doi: 10.1016/0001-6160(66)90074-5.

[1388] R. Ebeling, M.F. Ashby, Dispersion hardening of copper single crystals, Phil. Mag. 13 (1966) 805–834, doi: 10.1080/14786436608212698.

[1389] A.J.E. Foreman, M.J. Makin, Dislocation movement through random arrays of obstacles, Philosophical Magazine 14 (1966) 911–924, doi: 10.1080/14786436608244762.
[1390] A.J.E. Foreman, M.J. Makin, DISLOCATION MOVEMENT THROUGH RANDOM ARRAYS OF OBSTACLES, Can. J. Phys. 45 (1967) 511–517, doi: 10.1139/p67-044.
[1391] P.B. Hirsch, F.J. Humphreys, Plastic deformation of two-phase alloys containing small nondeformable particles, Phys. Strength Plast. (1969) 189-216.
[1392] P.B. Hirsch, F.J. Humphreys, The deformation of single crystals of copper and copper-zinc alloys containing alumina particles - I. Macroscopic properties and workhardening theory, Proc. R. Soc. Lond. A 318 (1970) 45–72, doi: 10.1098/rspa.1970.0133.
[1393] F.J. Humphreys, P.B. Hirsch, The deformation of single crystals of copper and copper-zinc alloys containing alumina particles - II. Microstructure and dislocation-particle interactions, Proc. R. Soc. Lond. A 318 (1970) 73–92, doi: 10.1098/rspa.1970.0134.
[1394] L.M. Brown, W.M. Stobbs, The work-hardening of copper-silica, Philosophical Magazine 23 (1971) 1201–1233, doi: 10.1080/14786437108217406.
[1395] G. Monnet, Investigation of precipitation hardening by dislocation dynamics simulations, Phil. Mag. 86 (2006) 5927–5941, doi: 10.1080/14786430600860985.
[1396] D.J. Bacon, U.F. Kocks, R.O. Scattergood, The effect of dislocation self-interaction on the orowan stress, Philosophical Magazine 28 (1973) 1241–1263, doi: 10.1080/14786437308227997.
[1397] R.O. Scattergood, D.J. Bacon, The Orowan mechanism in anisotropic crystals, Philosophical Magazine 31 (1975) 179–198, doi: 10.1080/14786437508229295.
[1398] P.M. Hazzledine, P.B. Hirsch, A coplanar Orowan loops model for dispersion hardening, Philosophical Magazine 30 (1974) 1331–1351, doi: 10.1080/14786437408207286.
[1399] L. Proville, B. Bakó, Dislocation depinning from ordered nanophases in a model fcc crystal: From cutting mechanism to Orowan looping, Acta Materialia 58 (2010) 5565–5571, doi: 10.1016/j.actamat.2010.06.018.
[1400] T. Hatano, Dynamics of a dislocation bypassing an impenetrable precipitate: The Hirsch mechanism revisited, Philosophical Magazine 74 (2006) 7, doi: 10.1103/PhysRevB.74.020102.
[1401] A.J. Ardell, J.C. Huang, Antiphase boundary energies and the transition from shearing to looping in alloys strengthened by ordered precipitates, Philosophical Magazine Letters 58 (1988) 189–197, doi: 10.1080/09500838808214752.
[1402] J.F. Nie, Effects of precipitate shape and orientation on dispersion strengthening in magnesium alloys, Scripta Materialia 48 (2003) 1009–1015, doi: 10.1016/S1359-6462(02)00497-9.
[1403] G. Monnet, S. Naamane, B. Devincre, Orowan strengthening at low temperatures in bcc materials studied by dislocation dynamics simulations, Acta Materialia 59 (2011) 451–461, doi: 10.1016/j.actamat.2010.09.039.
[1404] J.F. Nie, B.C. Muddle, Microstructural design of high-strength aluminum alloys, JPE 19 (1998) 543–551, doi: 10.1361/105497198770341734.
[1405] J.F. Nie, B.C. Muddle, I.J. Polmear, The Effect of Precipitate Shape and Orientation on Dispersion Strengthening in High Strength Aluminium Alloys, MSF 217-222 (1996) 1257–1262, doi: 10.4028/www.scientific.net/MSF.217-222.1257.
[1406] S. Queyreau, G. Monnet, B. Devincre, Orowan strengthening and forest hardening superposition examined by dislocation dynamics simulations, Acta Materialia 58 (2010) 5586–5595, doi: 10.1016/j.actamat.2010.06.028.
[1407] E. Arzt, M.F. Ashby, Threshold stresses in materials containing dispersed particles, Scripta Metallurgica 16 (1982) 1285–1290, doi: 10.1016/0036-9748(82)90484-7.
[1408] E.W. Hart, Theory of dispersion hardening in metals, Acta Metallurgica 20 (1972) 275–289, doi: 10.1016/0001-6160(72)90190-3.
[1409] B. Reppich, On the attractive particle–dislocation interaction in dispersion-strengthened material, Acta Materialia 46 (1998) 61–67, doi: 10.1016/S1359-6454(97)00234-6.
[1410] J. Rösler, E. Arzt, The kinetics of dislocation climb over hard particles—I. Climb without attractive particle-dislocation interaction, Acta Metallurgica 36 (1988) 1043–1051, doi: 10.1016/0001-6160(88)90158-7.

[1411] E. Arzt, J. Rösler, The kinetics of dislocation climb over hard particles—II. Effects of an attractive particle-dislocation interaction, Acta Metallurgica 36 (1988) 1053–1060, doi: 10.1016/0001-6160(88)90159-9.

[1412] J. Rösler, E. Arzt, A new model-based creep equation for dispersion strengthened materials, Acta Metallurgica et Materialia 38 (1990) 671–683, doi: 10.1016/0956-7151(90)90223-4.

[1413] E. Arzt, D.S. Wilkinson, Threshold stresses for dislocation climb over hard particles: The effect of an attractive interaction, Acta Metallurgica 34 (1986) 1893–1898, doi: 10.1016/0001-6160(86)90247-6.

[1414] L.M. Brown, D.R. Clarke, Work hardening due to internal stresses in composite materials, Acta Metallurgica 23 (1975) 821–830, doi: 10.1016/0001-6160(75)90198-4.

[1415] F.J. Humphreys, P.N. Kalu, Dislocation-particle interactions during high temperature deformation of two-phase aluminium alloys, Acta Metallurgica 35 (1987) 2815–2829, doi: 10.1016/0001-6160(87)90281-1.

[1416] F.J. Humphreys, P.B. Hirsch, Work-hardening and recovery of dispersion hardened alloys, Phil. Mag. 34 (1976) 373–390, doi: 10.1080/14786437608222029.

[1417] F.J. Humphreys, Local lattice rotations at second phase particles in deformed metals, Acta Metallurgica 27 (1979) 1801–1814, doi: 10.1016/0001-6160(79)90071-3.

[1418] F.J. Humphreys, P.N. Kalu, The plasticity of particle-containing polycrystals, Acta Metallurgica et Materialia 38 (1990) 917–930, doi: 10.1016/0956-7151(90)90164-C.

[1419] L.M. Brown, Precipitation and Dispersion Hardening, in: Strength of Metals and Alloys, Elsevier, 1979, pp. 1551–1571.

[1420] J.F. Nie, B.C. Muddle, Strengthening of an Al–Cu–Sn alloy by deformation-resistant precipitate plates, Acta Materialia 56 (2008) 3490–3501, doi: 10.1016/j.actamat.2008.03.028.

[1421] L.H. Friedman, D.C. Chrzan, Scaling Theory of the Hall-Petch Relation for Multilayers, Physical review letters 81 (1998) 2715–2718, doi: 10.1103/PhysRevLett.81.2715.

[1422] J. Wang, A. Misra, An overview of interface-dominated deformation mechanisms in metallic multilayers, Current Opinion in Solid State and Materials Science 15 (2011) 20–28, doi: 10.1016/j.cossms.2010.09.002.

[1423] J. Wang, R.G. Hoagland, J.P. Hirth, A. Misra, Atomistic modeling of the interaction of glide dislocations with "weak" interfaces, Acta Materialia 56 (2008) 5685–5693, doi: 10.1016/j.actamat.2008.07.041.

[1424] J. Wang, R.G. Hoagland, J.P. Hirth, A. Misra, Atomistic simulations of the shear strength and sliding mechanisms of copper–niobium interfaces, Acta Materialia 56 (2008) 3109–3119, doi: 10.1016/j.actamat.2008.03.003.

[1425] P.M. Anderson, T. Foecke, P.M. Hazzledine, Dislocation-Based Deformation Mechanisms in Metallic Nanolaminates, MRS Bull. 24 (1999) 27–33, doi: 10.1557/S0883769400051514.

[1426] A. Misra, J.P. Hirth, R.G. Hoagland, Length-scale-dependent deformation mechanisms in incoherent metallic multilayered composites, Acta Materialia 53 (2005) 4817–4824, doi: 10.1016/j.actamat.2005.06.025.

[1427] M. Damadam, S. Shao, G. Ayoub, H.M. Zbib, Recent advances in modeling of interfaces and mechanical behavior of multilayer metallic/ceramic composites, J Mater Sci 53 (2018) 5604–5617, doi: 10.1007/s10853-017-1704-3.

[1428] S. Shao, A. Misra, H. Huang, J. Wang, Micro-scale modeling of interface-dominated mechanical behavior, J Mater Sci 53 (2018) 5546–5561, doi: 10.1007/s10853-017-1662-9.

[1429] S.J. Wang, G. Liu, D.Y. Xie, Q. Lei, B.P. Ramakrishnan, J. Mazumder, J. Wang et al., Plasticity of laser-processed nanoscale Al Al2Cu eutectic alloy, Acta Materialia 156 (2018) 52–63, doi: 10.1016/j.actamat.2018.06.038.

[1430] G. Dehm, B.N. Jaya, R. Raghavan, C. Kirchlechner, Overview on micro- and nanomechanical testing: New insights in interface plasticity and fracture at small length scales, Acta Materialia 142 (2018) 248–282, doi: 10.1016/j.actamat.2017.06.019.

[1431] N.A. Mara, N. Li, A. Misra, J. Wang, Interface-Driven Plasticity in Metal–Ceramic Nanolayered Composites: Direct Validation of Multiscale Deformation Modeling via In Situ Indentation in TEM, JOM 68 (2016) 143–150, doi: 10.1007/s11837-015-1542-1.

[1432] J. Wang, R.F. Zhang, C.Z. Zhou, I.J. Beyerlein, A. Misra, Interface dislocation patterns and dislocation nucleation in face-centered-cubic and body-centered-cubic bicrystal interfaces, International Journal of Plasticity 53 (2014) 40–55, doi: 10.1016/j.ijplas.2013.07.002.

[1433] J. Wang, C. Zhou, I.J. Beyerlein, S. Shao, Modeling Interface-Dominated Mechanical Behavior of Nanolayered Crystalline Composites, JOM 66 (2014) 102–113, doi: 10.1007/s11837-013-0808-8.

[1434] J. Wang, Q. Zhou, S. Shao, A. Misra, Strength and plasticity of nanolaminated materials, Materials Research Letters 5 (2017) 1–19, doi: 10.1080/21663831.2016.1225321.

[1435] L.W. Yang, C. Mayer, N. Chawla, J. LLorca, J.M. Molina-Aldareguía, Deformation mechanisms of ultra-thin Al layers in Al/SiC nanolaminates as a function of thickness and temperature, Phil. Mag. 96 (2016) 3336–3355, doi: 10.1080/14786435.2016.1219075.

[1436] F. Akasheh, H.M. Zbib, J.P. Hirth, R.G. Hoagland, A. Misra, Dislocation dynamics analysis of dislocation intersections in nanoscale metallic multilayered composites, Journal of Applied Physics 101 (2007) 84314, doi: 10.1063/1.2721093.

[1437] F. Akasheh, H.M. Zbib, J.P. Hirth, R.G. Hoagland, A. Misra, Interactions between glide dislocations and parallel interfacial dislocations in nanoscale strained layers, Journal of Applied Physics 102 (2007) 34314, doi: 10.1063/1.2757082.

[1438] R.G. Hoagland, R.J. Kurtz, C.H. Henager, Slip resistance of interfaces and the strength of metallic multilayer composites, Scripta Materialia 50 (2004) 775–779, doi: 10.1016/j.scriptamat.2003.11.059.

[1439] A. Misra, J.P. Hirth, H. Kung, Single-dislocation-based strengthening mechanisms in nanoscale metallic multilayers, Philosophical Magazine A 82 (2002) 2935–2951, doi: 10.1080/01418610208239626.

[1440] R.G. Hoagland, T.E. Mitchell, J.P. Hirth, H. Kung, On the strengthening effects of interfaces in multilayer fee metallic composites, Philosophical Magazine A 82 (2002) 643–664, doi: 10.1080/01418610208243194.

[1441] R.G. Hoagland, J.P. Hirth, A. Misra, On the role of weak interfaces in blocking slip in nanoscale layered composites, Phil. Mag. 86 (2006) 3537–3558, doi: 10.1080/14786430600669790.

[1442] S.I. Rao, P.M. Hazzledine, Atomistic simulations of dislocation–interface interactions in the Cu-Ni multilayer system, Philosophical Magazine A 80 (2000) 2011–2040, doi: 10.1080/01418610008212148.

[1443] A. Misra, J.P. Hirth, R.G. Hoagland, J.D. Embury, H. Kung, Dislocation mechanisms and symmetric slip in rolled nano-scale metallic multilayers, Acta Materialia 52 (2004) 2387–2394, doi: 10.1016/j.actamat.2004.01.029.

[1444] A. Misra, H. Krug, Deformation Behavior of Nanostructured Metallic Multilayers, Adv. Eng. Mater. 3 (2001) 217–222, doi: 10.1002/1527-2648(200104)3:4<217:AID-ADEM217>3.0.CO;2-5.

[1445] A. Misra, M.J. Demkowicz, J. Wang, R.G. Hoagland, The multiscale modeling of plastic deformation in metallic nanolayered composites, JOM 60 (2008) 39–42, doi: 10.1007/s11837-008-0047-6.

[1446] G. Langford, Deformation of pearlite, MTA 8 (1977) 861–875, doi: 10.1007/BF02661567.

[1447] J.D. Embury, J.P. Hirth, On dislocation storage and the mechanical response of fine scale microstructures, Acta Metallurgica et Materialia 42 (1994) 2051–2056, doi: 10.1016/0956-7151(94)90030-2.

[1448] G. Liu, D. Xie, S. Wang, A. Misra, J. Wang, Mesoscale crystal plasticity modeling of nanoscale Al–Al2Cu eutectic alloy, International Journal of Plasticity 121 (2019) 134–152, doi: 10.1016/j.ijplas.2019.06.008.

[1449] P.M. Anderson, C. Li, Hall-Petch relations for multilayered materials, Nanostructured Materials 5 (1995) 349–362, doi: 10.1016/0965-9773(95)00250-I.

[1450] N. Abdolrahim, H.M. Zbib, D.F. Bahr, Multiscale modeling and simulation of deformation in nanoscale metallic multilayer systems, International Journal of Plasticity 52 (2014) 33–50, doi: 10.1016/j.ijplas.2013.04.002.

[1451] J. Wang, A. Misra, Strain hardening in nanolayered thin films, Current Opinion in Solid State and Materials Science 18 (2014) 19–28, doi: 10.1016/j.cossms.2013.10.003.

[1452] J. Gil Sevillano, Substructure and strengthening of heavily deformed single and two-phase metallic materials, J. Phys. III France 1 (1991) 967–988, doi: 10.1051/jp3:1991168.

[1453] K.F. Gan, A.H.W. Ngan, The unusual size effect of eutectic Sn/Pb alloys in the micro regime: Experiments and modeling, Acta Materialia 151 (2018) 282–292, doi: 10.1016/j.actamat.2018.04.005.

[1454] S. Lei, J.Y. Zhang, J.J. Niu, G. Liu, X. Zhang, J. Sun, Intrinsic size-controlled strain hardening behavior of nanolayered Cu/Zr micropillars, Scripta Materialia 66 (2012) 706–709, doi: 10.1016/j.scriptamat.2011.12.032.

[1455] X. Hu, P. van Houtte, M. Liebeherr, A. Walentek, M. Seefeldt, H. Vandekinderen, Modeling work hardening of pearlitic steels by phenomenological and Taylor-type micromechanical models, Acta Materialia 54 (2006) 1029–1040, doi: 10.1016/j.actamat.2005.10.030.

[1456] M. Dollar, I.M. Bernstein, A.W. Thompson, Influence of deformation substructure on flow and fracture of fully pearlitic steel, Acta Metallurgica 36 (1988) 311–320, doi: 10.1016/0001-6160(88)90008-9.

[1457] M.W. Kapp, A. Hohenwarter, S. Wurster, B. Yang, R. Pippan, Anisotropic deformation characteristics of an ultrafine- and nanolamellar pearlitic steel, Acta Materialia 106 (2016) 239–248, doi: 10.1016/j.actamat.2015.12.037.

[1458] C.R. Mayer, L.W. Yang, S.S. Singh, J. LLorca, J.M. Molina-Aldareguia, Y.L. Shen, N. Chawla, Anisotropy, size, and aspect ratio effects on micropillar compression of Al SiC nanolaminate composites, Acta Materialia 114 (2016) 25–32, doi: 10.1016/j.actamat.2016.05.018.

[1459] W.D. Nix, Yielding and strain hardening of thin metal films on substrates, Scripta Materialia 39 (1998) 545–554, doi: 10.1016/S1359-6462(98)00195-X.

[1460] J.D. Embury, R.M. Fisher, The structure and properties of drawn pearlite, Acta Metallurgica 14 (1966) 147–159, doi: 10.1016/0001-6160(66)90296-3.

[1461] T.E. Mitchell, Y.C. Lu, A.J.G. Jr., M. Nastasi, H. Kung, Structure and Mechanical Properties of Copper/Niobium Multilayers, Journal of the American Ceramic Society 80 (1997) 1673–1676, doi: 10.1111/j.1151-2916.1997.tb03037.x.

[1462] H.M. Zbib, C.T. Overman, F. Akasheh, D. Bahr, Analysis of plastic deformation in nanoscale metallic multilayers with coherent and incoherent interfaces, International Journal of Plasticity 27 (2011) 1618–1639, doi: 10.1016/j.ijplas.2011.03.006.

[1463] M.A. Phillips, B.M. Clemens, W.D. Nix, A model for dislocation behavior during deformation of Al/Al3Sc (fcc/L12) metallic multilayers, Acta Materialia 51 (2003) 3157–3170, doi: 10.1016/S1359-6454(03)00127-7.

[1464] J.Y. Zhang, S. Lei, Y. Liu, J.J. Niu, Y. Chen, G. Liu, X. Zhang et al., Length scale-dependent deformation behavior of nanolayered Cu/Zr micropillars, Acta Materialia 60 (2012) 1610–1622, doi: 10.1016/j.actamat.2011.12.001.

[1465] D. Bhattacharyya, N.A. Mara, P. Dickerson, R.G. Hoagland, A. Misra, Compressive flow behavior of Al–TiN multilayers at nanometer scale layer thickness, Acta Materialia 59 (2011) 3804–3816, doi: 10.1016/j.actamat.2011.02.036.

[1466] T.H. Courtney, Mechanical behavior of materials, 2nd ed., Waveland Press, Long Grove, Ill., 2005.

[1467] H. Gleiter, E. Hornbogen, Precipitation hardening by coherent particles, Materials Science and Engineering 2 (1968) 285–302, doi: 10.1016/0025-5416(68)90047-5.

[1468] A.J. Ardell, Precipitation hardening, MTA 16 (1985) 2131–2165, doi: 10.1007/BF02670416.

[1469] A.S. Argon, Strengthening mechanisms in crystal plasticity, Oxford University Press, Oxford, 2012.

[1470] L.M. Brown, R.K. Ham, Dislocation-particle interactions, in: A. Kelly, R.B. Nicholson (Eds.), Strengthening methods in crystals, Elsevier, Amsterdam, 1971, pp. 9–135.

[1471] E. Nembach, Particle strengthening of metals and alloys, Wiley, New York, 1997.

[1472] T. Gladman, Precipitation hardening in metals, Materials Science and Technology 15 (1999) 30–36, doi: 10.1179/026708399773002782.

[1473] A. Kelly, M.E. Fine, The strength of an alloy containing zones, Acta Metallurgica 5 (1957) 365–367, doi: 10.1016/0001-6160(57)90003-2.

[1474] S.D. Harkness, J.J. Hren, An investigation of strengthening by spherical coherent G. P. Zones, Metallurgical Transactions 1 (1970) 43–49, doi: 10.1007/BF02819240.

[1475] P.B. Hirsch, A. Kelly, Stacking-fault strengthening, Philosophical Magazine 12 (1965) 881–900, doi: 10.1080/14786436508228118.

[1476] E. Nembach, Precipitation hardening caused by a difference in shear modulus between particle and matrix, Phys. Stat. Sol. (a) 78 (1983) 571–581, doi: 10.1002/pssa.2210780223.

[1477] A. Melander, P.Å. Persson, The strength of a precipitation hardened AlZnMg alloy, Acta Metallurgica 26 (1978) 267–278, doi: 10.1016/0001-6160(78)90127-X.

[1478] K.C. Russell, L.M. Brown, A dispersion strengthening model based on differing elastic moduli applied to the iron-copper system, Acta Metallurgica 20 (1972) 969–974, doi: 10.1016/0001-6160(72)90091-0.

[1479] R.W. Weeks, S.R. Pati, M.F. Ashby, P. Barrand, The elastic interaction between a straight dislocation and a bubble or a particle, Acta Metallurgica 17 (1969) 1403–1410, doi: 10.1016/0001-6160(69)90002-9.

[1480] G. Knowles, P.M. Kelly, Effect of Second-Phase Particles on the Mechanical Properties of Steel, The Iron and Steel Institute, London, England (1971) 9.

[1481] V. Gerold, H. Haberkorn, On the Critical Resolved Shear Stress of Solid Solutions Containing Coherent Precipitates, phys. stat. sol. (b) 16 (1966) 675–684, doi: 10.1002/pssb.19660160234.

[1482] H. Gleiter, DIE ERHOHUNG DER KRITISCHEN SCHUBSPANNUNG DURCH DIE AUSSCHEIDUNG VON VERSPANNTEN KOHARENTEN TEILCHEN, Zeitschrift für Angewandte Physik 23 (1967) 108.

[1483] V. Gerold, H.-M. Pham, Precipitation hardening by misfitting particles and its comparison with experiments, Scripta Metallurgica 13 (1979) 895–898, doi: 10.1016/0036-9748(79)90182-0.

[1484] P. Guyot, Hardening by ordered coherent precipitates related to the statistical theory, Philosophical Magazine 24 (1971) 987–993, doi: 10.1080/14786437108217063.

[1485] H. Gleiter, E. Hornbogen, Theorie der Wechselwirkung von Versetzungen mit kohärenten geordneten Zonen (I), phys. stat. sol. (b) 12 (1965) 235–250, doi: 10.1002/pssb.19650120122.

[1486] J.L. CASTAGNÉ, DURCISSEMENT PAR DES PRÉCIPITÉS ORDONNÉS, J. Phys. Colloques 27 (1966) C3-233-C3-239, doi: 10.1051/jphyscol:1966331.

[1487] A.J. Ardell, Order hardening: comparison between revised theory and experiment, Metal Science 14 (1980) 221–224, doi: 10.1179/030634580790426463.

[1488] W. Huther, B. Reppich, Interaction of dislocations with coherent, stress-free, ordered particles, Z. Metallkde 69 (1978) 628–634.

[1489] S. Spigarelli, Microstructure-based assessment of creep rupture strength in 9Cr steels, International Journal of Pressure Vessels and Piping 101 (2013) 64–71, doi: 10.1016/j.ijpvp.2012.10.005.

[1490] R.A. Barrett, P.E. O'Donoghue, S.B. Leen, A physically-based high temperature yield strength model for 9Cr steels, Materials Science and Engineering: A 730 (2018) 410–424, doi: 10.1016/j.msea.2018.05.086.

[1491] P.M. Kelly, The quantitative relationship between micro-structure and properties in two-phase alloys, Int. Metall. Rev. 18 (1973) 31–36.

[1492] N. Büttner, K.-D. Fusenig, E. Nembach, On the additivity of precipitation and solid solution hardening in under-and over-aged single crystals of (Au)-Co, Acta Metallurgica 35 (1987) 845–854, doi: 10.1016/0001-6160(87)90161-1.

[1493] E. Nembach, M. Martin, Superposition of solid solution and particle strengthening in (Cu・Au)・Co single crystals, Acta Metallurgica 28 (1980) 1069–1075, doi: 10.1016/0001-6160(80)90090-5.

[1494] U.F. Kocks, Kinetics of solution hardening, MTA 16 (1985) 2109–2129, doi: 10.1007/BF02670415.

[1495] A.W. Zhu, A. Csontos, E.A. Starke, Computer experiment on superposition of strengthening effects of different particles, Acta Materialia 47 (1999) 1713–1721, doi: 10.1016/S1359-6454(99)00077-4.

[1496] L.A. Gypen, A. Deruyttere, Multi-component solid solution hardening, J Mater Sci 12 (1977) 1028–1033, doi: 10.1007/BF00540987.

[1497] U. Lagerpusch, V. Mohles, E. Nembach, On the additivity of solid solution and dispersion strengthening, Materials Science and Engineering: A 319-321 (2001) 176–178, doi: 10.1016/S0921-5093(01)00937-6.

[1498] R.W. Kozar, A. Suzuki, W.W. Milligan, J.J. Schirra, M.F. Savage, T.M. Pollock, Strengthening Mechanisms in Polycrystalline Multimodal Nickel-Base Superalloys, Metall and Mat Trans A 40 (2009) 1588–1603, doi: 10.1007/s11661-009-9858-5.

[1499] T.J. Koppenaal, D. Kuhlmann-Wilsdorf, THE EFFECT OF PRESTRESSING ON THE STRENGTH OF NEUTRON-IRRADIATED COPPER SINGLE CRYSTALS, Appl. Phys. Lett. 4 (1964) 59–61, doi: 10.1063/1.1753962.

[1500] L.M. Cheng, W.J. Poole, J.D. Embury, D.J. Lloyd, The influence of precipitation on the work-hardening behavior of the aluminum alloys AA6111 and AA7030, Metall and Mat Trans A 34 (2003) 2473–2481, doi: 10.1007/s11661-003-0007-2.

[1501] E. Nembach, Synergetic effects in the superposition of strengthening mechanisms, Acta Metallurgica et Materialia 40 (1992) 3325–3330, doi: 10.1016/0956-7151(92)90045-G.

[1502] Y. Dong, T. Nogaret, W.A. Curtin, Scaling of Dislocation Strengthening by Multiple Obstacle Types, Metall and Mat Trans A 41 (2010) 1954–1960, doi: 10.1007/s11661-010-0229-z.

[1503] A. Deschamps, Y. Brechet, Influence of predeformation and agEing of an Al–Zn–Mg alloy—II. Modeling of precipitation kinetics and yield stress, Acta Materialia 47 (1998) 293–305, doi: 10.1016/S1359-6454(98)00296-1.

[1504] F. Fazeli, W.J. Poole, C.W. Sinclair, Modeling the effect of Al3Sc precipitates on the yield stress and work hardening of an Al–Mg–Sc alloy, Acta Materialia 56 (2008) 1909–1918, doi: 10.1016/j.actamat.2007.12.039.

[1505] A. de Vaucorbeil, W.J. Poole, C.W. Sinclair, The superposition of strengthening contributions in engineering alloys, Materials Science and Engineering: A 582 (2013) 147–154, doi: 10.1016/j.msea.2013.06.032.

[1506] R.C. Picu, R. Li, Z. Xu, Strain rate sensitivity of thermally activated dislocation motion across fields of obstacles of different kind, Materials Science and Engineering: A 502 (2009) 164–171, doi: 10.1016/j.msea.2008.10.046.

[1507] M. Hiratani, V.V. Bulatov, Solid-solution hardening by point-like obstacles of different kinds, Philosophical Magazine Letters 84 (2004) 461–470, doi: 10.1080/09500830410001726969.

[1508] B. Reppich, W. Kühlein, G. Meyer, D. Puppel, M. Schulz, G. Schumann, Duplex γ' particle hardening of the superalloy Nimonic PE 16, Materials Science and Engineering 83 (1986) 45–63, doi: 10.1016/0025-5416(86)90173-4.

[1509] J.C. Huang, A.J. Ardell, Addition rules and the contribution of δ' precipitates to strengthening of aged Al・Li・Cu alloys, Acta Metallurgica 36 (1988) 2995–3006, doi: 10.1016/0001-6160(88)90182-4.

[1510] U.F. Kocks, A.S. Argon, Ashby M. F., Thermodynamics and kinetics of slip, Progress in Materials Science 19 (1975).

[1511] F. McClintock, S. Kaplan, C. Berg, Ductile fracture by hole growth in shear bands, Int J Fract 2 (1966), doi: 10.1007/BF00184558.

[1512] F.A. McClintock, A Criterion for Ductile Fracture by the Growth of Holes, J. Appl. Mech. 35 (1968) 363–371, doi: 10.1115/1.3601204.

[1513] J.R. Rice, D.M. Tracey, On the ductile enlargement of voids in triaxial stress fields∗, Journal of the Mechanics and Physics of Solids 17 (1969) 201–217, doi: 10.1016/0022-5096(69)90033-7.

[1514] D.M. Tracey, Strain-hardening and interaction effects on the growth of voids in ductile fracture, Engineering Fracture Mechanics 3 (1971) 301–315, doi: 10.1016/0013-7944(71)90040-3.

[1515] R.J. Green, A plasticity theory for porous solids, International Journal of Mechanical Sciences 14 (1972) 215–224, doi: 10.1016/0020-7403(72)90063-X.

[1516] J.W. Rudnicki, J.R. Rice, Conditions for the localization of deformation in pressure-sensitive dilatant materials, Journal of the Mechanics and Physics of Solids 23 (1975) 371–394, doi: 10.1016/0022-5096(75)90001-0.

[1517] R.M. McMeeking, Finite deformation analysis of crack tip opening in elastic-plastic materials and implications for fracture initiation, 1976.

[1518] J.W. Hancock, A.C. Mackenzie, On the mechanisms of ductile failure in high-strength steels subjected to multi-axial stress-states, Journal of the Mechanics and Physics of Solids 24 (1976) 147–160, doi: 10.1016/0022-5096(76)90024-7.

[1519] S. Shima, M. Oyane, Plasticity theory for porous metals, International Journal of Mechanical Sciences 18 (1976) 285–291, doi: 10.1016/0020-7403(76)90030-8.

[1520] A.L. Gurson, Continuum Theory of Ductile Rupture by Void Nucleation and Growth, J. Eng. Mater. Technol. 99 (1977) 2, doi: 10.1115/1.3443401.

[1521] H. Yamamoto, Conditions for shear localization in the ductile fracture of void-containing materials, Int J Fract 14 (1978) 347–365, doi: 10.1007/BF00015989.

[1522] A. Needleman, N. Triantafyllidis, Void Growth and Local Necking in Biaxially Stretched Sheets, J. Eng. Mater. Technol. 100 (1978) 164, doi: 10.1115/1.3443466.

[1523] A. Needleman, J.R. Rice, Limits to Ductility Set by Plastic Flow Localization, in: D.P. Koistinen, N.-M. Wang (Eds.), Mechanics of sheet metal forming: Material behavior and deformation analysis, Springer, [Place of publication not identified], 1978, pp. 237–267.

[1524] A.A. Benzerga, J.-B. Leblond, Ductile Fracture by Void Growth to Coalescence, in: Advances in Applied Mechanics Volume 44, Elsevier, 2010, pp. 169–305.

[1525] J. Besson, Continuum Models of Ductile Fracture: A Review, International Journal of Damage Mechanics 19 (2010) 3–52, doi: 10.1177/1056789509103482.

[1526] B. BUDIANSKY, J.W. Hutchinson, S. SLUTSKY, Void Growth and Collapse in Viscous Solids, in: H.G. Hopkins, M.J. Sewell, R. Hill (Eds.), Mechanics of solids: The Rodney Hill 60th anniversary volume, Pergamon, Oxford, 1982, pp. 13–45.

[1527] G. Huber, Y. Brechet, T. Pardoen, Predictive model for void nucleation and void growth controlled ductility in quasi-eutectic cast aluminium alloys, Acta Materialia 53 (2005) 2739–2749, doi: 10.1016/j.actamat.2005.02.037.

[1528] G. Le Roy, J.D. Embury, G. Edwards, M.F. Ashby, A model of ductile fracture based on the nucleation and growth of voids, Acta Metallurgica 29 (1981) 1509–1522, doi: 10.1016/0001-6160(81)90185-1.

[1529] N.A. Fleck, J.W. Hutchinson, V. Tvergaard, Softening by void nucleation and growth in tension and shear, Journal of the Mechanics and Physics of Solids 37 (1989) 515–540, doi: 10.1016/0022-5096(89)90027-6.

[1530] W.M. Garrison, N.R. Moody, Ductile fracture, Journal of Physics and Chemistry of Solids 48 (1987) 1035–1074, doi: 10.1016/0022-3697(87)90118-1.

[1531] M.F. Horstemeyer, M.M. Matalanis, A.M. Sieber, M.L. Botos, Micromechanical finite element calculations of temperature and void configuration effects on void growth and coalescence, International Journal of Plasticity 16 (2000) 979–1015, doi: 10.1016/S0749-6419(99)00076-5.

[1532] M.F. Horstemeyer, J. Lathrop, A.M. Gokhale, M. Dighe, Modeling stress state dependent damage evolution in a cast Al–Si–Mg aluminum alloy, Theoretical and Applied Fracture Mechanics 33 (2000) 31–47, doi: 10.1016/S0167-8442(99)00049-X.

[1533] S.M. Keralavarma, S. Hoelscher, A.A. Benzerga, Void growth and coalescence in anisotropic plastic solids, International Journal of Solids and Structures 48 (2011) 1696–1710, doi: 10.1016/j.ijsolstr.2011.02.020.

[1534] H. Klöcker, V. Tvergaard, Growth and coalescence of non-spherical voids in metals deformed at elevated temperature, International Journal of Mechanical Sciences 45 (2003) 1283–1308, doi: 10.1016/j.ijmecsci.2003.09.018.

[1535] R. Becker, A. Needleman, O. Richmond, V. Tvergaard, Void growth and failure in notched bars, Journal of the Mechanics and Physics of Solids 36 (1988) 317–351, doi: 10.1016/0022-5096(88)90014-2.

[1536] N. Aravas, R.M. McMeeking, Microvoid growth and failure in the ligament between a hole and a blunt crack tip, Int J Fract 29 (1985) 21–38, doi: 10.1007/BF00020674.

[1537] S. Aoki, K. Kishimoto, A. Takeya, M. Sakata, Effects of microvoids on crack blunting and initiation in ductile materials, Int J Fract 24 (1984) 267–278, doi: 10.1007/BF00020741.

[1538] J. Koplik, A. Needleman, Void growth and coalescence in porous plastic solids, International Journal of Solids and Structures 24 (1988) 835–853, doi: 10.1016/0020-7683(88)90051-0.

[1539] J. Faleskog, X. Gao, C.F. Shih, Cell model for nonlinear fracture analysis – I. Micromechanics calibration, Int J Fract 89 (1998) 355–373, doi: 10.1023/A:1007421420901.

[1540] D. Kwon, R.J. Asaro, A study of void nucleation, growth, and coalescence in spheroidized 1518 steel, MTA 21 (1990) 117–134, doi: 10.1007/BF02656430.

[1541] D. Lassance, F. Scheyvaerts, T. Pardoen, Growth and coalescence of penny-shaped voids in metallic alloys, Engineering Fracture Mechanics 73 (2006) 1009–1034, doi: 10.1016/j.engfracmech.2005.12.004.

[1542] D. Lassance, D. FABREGUE, F. Delannay, T. Pardoen, Micromechanics of room and high temperature fracture in 6xxx Al alloys, Progress in Materials Science 52 (2007) 62–129, doi: 10.1016/j.pmatsci.2006.06.001.

[1543] L. Lecarme, C. Tekoglu, T. Pardoen, Void growth and coalescence in ductile solids with stage III and stage IV strain hardening, International Journal of Plasticity 27 (2011) 1203–1223, doi: 10.1016/j.ijplas.2011.01.004.

[1544] A. Molinari, T.W. Wright, A physical model for nucleation and early growth of voids in ductile materials under dynamic loading, Journal of the Mechanics and Physics of Solids 53 (2005) 1476–1504, doi: 10.1016/j.jmps.2005.02.010.

[1545] M.A. Meyers, C. Taylor Aimone, Dynamic fracture (spalling) of metals, Progress in Materials Science 28 (1983) 1–96, doi: 10.1016/0079-6425(83)90003-8.

[1546] L. Morin, J.-B. Leblond, A.A. Benzerga, D. Kondo, A unified criterion for the growth and coalescence of microvoids, Journal of the Mechanics and Physics of Solids 97 (2016) 19–36, doi: 10.1016/j.jmps.2016.01.013.

[1547] A. Needleman, V. Tvergaard, An analysis of ductile rupture in notched bars, Journal of the Mechanics and Physics of Solids 32 (1984) 461–490, doi: 10.1016/0022-5096(84)90031-0.

[1548] C.F. Niordson, Void growth to coalescence in a non-local material, European Journal of Mechanics - A/Solids 27 (2008) 222–233, doi: 10.1016/j.euromechsol.2007.07.001.

[1549] T. Pardoen, I. Doghri, F. Delannay, Experimental and numerical comparison of void growth models and void coalescence criteria for the prediction of ductile fracture in copper bars, Acta Materialia 46 (1998) 541–552, doi: 10.1016/S1359-6454(97)00247-4.

[1550] T. Pardoen, J.W. Hutchinson, An extended model for void growth and coalescence, Journal of the Mechanics and Physics of Solids 48 (2000) 2467–2512, doi: 10.1016/S0022-5096(00)00019-3.

[1551] T. Pardoen, J.W. Hutchinson, Micromechanics-based model for trends in toughness of ductile metals, Acta Materialia 51 (2003) 133–148, doi: 10.1016/S1359-6454(02)00386-5.

[1552] G.P. Potirniche, M.F. Horstemeyer, G.J. Wagner, P.M. Gullett, A molecular dynamics study of void growth and coalescence in single crystal nickel, International Journal of Plasticity 22 (2006) 257–278, doi: 10.1016/j.ijplas.2005.02.001.

[1553] G.P. Potirniche, J.L. Hearndon, M.F. Horstemeyer, X.W. Ling, Lattice orientation effects on void growth and coalescence in fcc single crystals, International Journal of Plasticity 22 (2006) 921–942, doi: 10.1016/j.ijplas.2005.06.003.

[1554] A.R. Ragab, Application of an extended void growth model with strain hardening and void shape evolution to ductile fracture under axisymmetric tension, Engineering Fracture Mechanics 71 (2004) 1515–1534, doi: 10.1016/S0013-7944(03)00216-9.

[1555] F. Scheyvaerts, P.R. Onck, C. Tekog˘lu, T. Pardoen, The growth and coalescence of ellipsoidal voids in plane strain under combined shear and tension, Journal of the Mechanics and Physics of Solids 59 (2011) 373–397, doi: 10.1016/j.jmps.2010.10.003.

[1556] A. Srivastava, A. Needleman, Void growth versus void collapse in a creeping single crystal, Journal of the Mechanics and Physics of Solids 61 (2013) 1169–1184, doi: 10.1016/j.jmps.2013.01.006.

[1557] S.K. Yerra, C. Tekog˜lu, F. Scheyvaerts, L. Delannay, P. van Houtte, T. Pardoen, Void growth and coalescence in single crystals, International Journal of Solids and Structures 47 (2010) 1016–1029, doi: 10.1016/j.ijsolstr.2009.12.019.

[1558] P.F. Thomason, A three-dimensional model for ductile fracture by the growth and coalescence of microvoids, Acta Metallurgica 33 (1985) 1087–1095, doi: 10.1016/0001-6160(85)90202-0.

[1559] P.F. Thomason, Ductile fracture by the growth and coalescence of microvoids of non-uniform size and spacing, Acta Metallurgica et Materialia 41 (1993) 2127–2134, doi: 10.1016/0956-7151(93)90382-3.

[1560] V. Tvergaard, A. Needleman, Analysis of the cup-cone fracture in a round tensile bar, Acta Metallurgica 32 (1984) 157–169, doi: 10.1016/0001-6160(84)90213-X.

[1561] V. Tvergaard, Material Failure by Void Growth to Coalescence, in: Advances in Applied Mechanics Volume 27, Elsevier, 1989, pp. 83–151.

[1562] V. Tvergaard, J.W. Hutchinson, Two mechanisms of ductile fracture: void by void growth versus multiple void interaction, International Journal of Solids and Structures 39 (2002) 3581–3597, doi: 10.1016/S0020-7683(02)00168-3.

[1563] T. WRIGHT, K. RAMESH, Dynamic void nucleation and growth in solids: A self-consistent statistical theory, Journal of the Mechanics and Physics of Solids 56 (2008) 336–359, doi: 10.1016/j.jmps.2007.05.012.

[1564] Z.L. Zhang, C. Thaulow, J. Ødegård, A complete Gurson model approach for ductile fracture, Engineering Fracture Mechanics 67 (2000) 155–168, doi: 10.1016/S0013-7944(00)00055-2.

[1565] S. Osovski, A. Srivastava, J.C. Williams, A. Needleman, Grain boundary crack growth in metastable titanium β alloys, Acta Materialia 82 (2015) 167–178, doi: 10.1016/j.actamat.2014.08.062.

[1566] S. Osovski, A. Needleman, A. Srivastava, Intergranular fracture prediction and microstructure design, Int J Fract 216 (2019) 135–148, doi: 10.1007/s10704-019-00347-z.

[1567] A.A. Benzerga, J.-B. Leblond, A. Needleman, V. Tvergaard, Ductile failure modeling, Int J Fract 201 (2016) 29–80, doi: 10.1007/s10704-016-0142-6.

[1568] A. Molkeri, A. Srivastava, S. Osovski, A. Needleman, Influence of Grain Size Distribution on Ductile Intergranular Crack Growth Resistance, J. Appl. Mech. 87 (2020) 14132, doi: 10.1115/1.4045073.

[1569] A. Needleman, V. Tvergaard, An analysis of dynamic, ductile crack growth in a double edge cracked specimen, Int J Fract 49 (1991) 41–67, doi: 10.1007/BF00013502.

[1570] I. Barsoum, J. Faleskog, Micromechanical analysis on the influence of the Lode parameter on void growth and coalescence, International Journal of Solids and Structures 48 (2011) 925–938, doi: 10.1016/j.ijsolstr.2010.11.028.

[1571] Y. Zhu, M.D. Engelhardt, R. Kiran, Combined effects of triaxiality, Lode parameter and shear stress on void growth and coalescence, Engineering Fracture Mechanics 199 (2018) 410–437, doi: 10.1016/j.engfracmech.2018.06.008.

[1572] B. Selvarajou, S.P. Joshi, A.A. Benzerga, Void growth and coalescence in hexagonal close packed crystals, Journal of the Mechanics and Physics of Solids 125 (2019) 198–224, doi: 10.1016/j.jmps.2018.12.012.

[1573] C.C. Chu, A. Needleman, Void Nucleation Effects in Biaxially Stretched Sheets, J. Eng. Mater. Technol 102 (1980) 249–256, doi: 10.1115/1.3224807.

[1574] S.H. Goods, L.M. Brown, Overview No. 1, Acta Metallurgica 27 (1979) 1–15, doi: 10.1016/0001-6160(79)90051-8.

[1575] A. Needleman, A Continuum Model for Void Nucleation by Inclusion Debonding, J. Appl. Mech. 54 (1987) 525, doi: 10.1115/1.3173064.

[1576] M. Saje, J. Pan, A. Needleman, Void nucleation effects on shear localization in porous plastic solids, Int J Fract 19 (1982) 163–182, doi: 10.1007/BF00017128.

[1577] M.N. Shabrov, A. Needleman, An analysis of inclusion morphology effects on void nucleation, International Journal of Plasticity 10 (2002) 163–183, doi: 10.1088/0965-0393/10/2/305.

[1578] V. Tvergaard, Effect of yield surface curvature and void nucleation on plastic flow localization, Journal of the Mechanics and Physics of Solids 35 (1987) 43–60, doi: 10.1016/0022-5096(87)90027-5.

[1579] X.-P. Xu, A. Needleman, Void nucleation by inclusion debonding in a crystal matrix, Materials Science and Engineering: A 1 (1993) 111–132, doi: 10.1088/0965-0393/1/2/001.

[1580] X.-P. Xu, A. Needleman, The influence of nucleation criterion on shear localization in rate-sensitive porous plastic solids, International Journal of Plasticity 8 (1992) 315–330, doi: 10.1016/0749-6419(92)90052-E.

[1581] L. Xia, Ductile crack growth—II. Void nucleation and geometry effects on macroscopic fracture behavior, Journal of the Mechanics and Physics of Solids 43 (1995) 1953–1981, doi: 10.1016/0022-5096(95)00063-O.

[1582] A.S. Argon, J. Im, R. Safoglu, Cavity formation from inclusions in ductile fracture, MTA 6 (1975) 825–837, doi: 10.1007/BF02672306.

[1583] U. Borg, C.F. Niordson, J.W. Kysar, Size effects on void growth in single crystals with distributed voids, International Journal of Plasticity 24 (2008) 688–701, doi: 10.1016/j.ijplas.2007.07.015.

[1584] C.L. Hom, R.M. McMeeking, Void Growth in Elastic-Plastic Materials, J. Appl. Mech. 56 (1989) 309–317, doi: 10.1115/1.3176085.

[1585] Y. Huang, Accurate Dilatation Rates for Spherical Voids in Triaxial Stress Fields, J. Appl. Mech. 58 (1991) 1084–1086, doi: 10.1115/1.2897686.

[1586] J. Kim, X. Gao, T.S. Srivatsan, Modeling of void growth in ductile solids: effects of stress triaxiality and initial porosity, Engineering Fracture Mechanics 71 (2004) 379–400, doi: 10.1016/S0013-7944(03)00114-0.

[1587] M. Kuna, D.Z. Sun, Three-dimensional cell model analyses of void growth in ductile materials, Int J Fract 81 (1996) 235–258, doi: 10.1007/BF00039573.

[1588] R.A. Lebensohn, J.P. Escobedo, E.K. Cerreta, D. Dennis-Koller, C.A. Bronkhorst, J.F. Bingert, Modeling void growth in polycrystalline materials, Acta Materialia 61 (2013) 6918–6932, doi: 10.1016/j.actamat.2013.08.004.

[1589] V. Tvergaard, Influence of voids on shear band instabilities under plane strain conditions, Int J Fract 17 (1981) 389–407, doi: 10.1007/BF00036191.

[1590] V.A. Lubarda, M.S. Schneider, D.H. Kalantar, B.A. Remington, M.A. Meyers, Void growth by dislocation emission, Acta Materialia 52 (2004) 1397–1408, doi: 10.1016/j.actamat.2003.11.022.

[1591] Y.-S. Lee, P.R. Dawson, Modeling ductile void growth in viscoplastic materials—Part I: Void growth model, Mechanics of Materials 15 (1993) 21–34, doi: 10.1016/0167-6636(93)90076-4.

[1592] A. Needleman, V. Tvergaard, J.W. Hutchinson, Void Growth in Plastic Solids, in: A.S. Argon (Ed.), Topics in Fracture and Fatigue, Springer New York, New York, NY, 1992, pp. 145–178.

[1593] T.L. O'Regan, D.F. Quinn, M.A. Howe, P.E. McHugh, Void growth simulations in single crystals, Comput Mech 20 (1997) 115–121, doi: 10.1007/s004660050226.

[1594] V.C. Orsini, M.A. Zikry, Void growth and interaction in crystalline materials, International Journal of Plasticity 17 (2001) 1393–1417, doi: 10.1016/S0749-6419(00)00091-7.

[1595] G. Perrin, J.-B. Leblond, Accelerated void growth in porous ductile solids containing two populations of cavities, International Journal of Plasticity 16 (2000) 91–120, doi: 10.1016/S0749-6419(99)00049-2.

[1596] J. Segurado, J. LLorca, An analysis of the size effect on void growth in single crystals using discrete dislocation dynamics, Acta Materialia 57 (2009) 1427–1436, doi: 10.1016/j.actamat.2008.11.031.

[1597] J. Segurado, J. LLorca, Discrete dislocation dynamics analysis of the effect of lattice orientation on void growth in single crystals, International Journal of Plasticity 26 (2010) 806–819, doi: 10.1016/j.ijplas.2009.10.009.

[1598] E.T. Seppälä, J. Belak, R.E. Rudd, Effect of stress triaxiality on void growth in dynamic fracture of metals: A molecular dynamics study, Phys. Rev. B 69 (2004) 253, doi: 10.1103/PhysRevB.69.134101.

[1599] K. Siruguet, J.-B. Leblond, Effect of void locking by inclusions upon the plastic behavior of porous ductile solids—I: theoretical modeling and numerical study of void growth, International Journal of Plasticity 20 (2004) 225–254, doi: 10.1016/S0749-6419(03)00018-4.

[1600] O.P. Søvik, C. Thaulow, GROWTH OF SPHEROIDAL VOIDS IN ELASTIC-PLASTIC SOLIDS, Fatigue & Fracture of Engineering Materials & Structures 20 (1997) 1731–1744, doi: 10.1111/j.1460-2695.1997.tb01525.x.

[1601] A. Srivastava, A. Needleman, Porosity evolution in a creeping single crystal, Modelling Simul. Mater. Sci. Eng. 20 (2012) 35010, doi: 10.1088/0965-0393/20/3/035010.

[1602] A. Srivastava, A. Needleman, Effect of crystal orientation on porosity evolution in a creeping single crystal, Mechanics of Materials 90 (2015) 10–29, doi: 10.1016/j.mechmat.2015.01.015.

[1603] S. Traiviratana, E.M. Bringa, D.J. Benson, M.A. Meyers, Void growth in metals: Atomistic calculations, Acta Materialia 56 (2008) 3874–3886, doi: 10.1016/j.actamat.2008.03.047.

[1604] V. Tvergaard, C. Niordson, Nonlocal plasticity effects on interaction of different size voids, International Journal of Plasticity 20 (2004) 107–120, doi: 10.1016/S0749-6419(03)00036-6.

[1605] M. Worswick, Void growth and constitutive softening in a periodically voided solid, Journal of the Mechanics and Physics of Solids 38 (1990) 601–625, doi: 10.1016/0022-5096(90)90025-Y.

[1606] A. Needleman, Void Growth in an Elastic-Plastic Medium, J. Appl. Mech. 39 (1972) 964, doi: 10.1115/1.3422899.

[1607] A.A. Benzerga, J. Besson, A. Pineau, Coalescence-Controlled Anisotropic Ductile Fracture, J. Eng. Mater. Technol 121 (1999) 221–229, doi: 10.1115/1.2812369.

[1608] A. Benzerga, Micromechanics of coalescence in ductile fracture, Journal of the Mechanics and Physics of Solids 50 (2002) 1331–1362, doi: 10.1016/S0022-5096(01)00125-9.

[1609] A.A. Benzerga, J. Besson, R. Batisse, A. Pineau, Synergistic effects of plastic anisotropy and void coalescence on fracture mode in plane strain, Computer Methods in Applied Mechanics and Engineering 10 (2002) 73–102, doi: 10.1088/0965-0393/10/1/306.

[1610] A.A. Benzerga, J.-B. Leblond, Effective Yield Criterion Accounting for Microvoid Coalescence, J. Appl. Mech. 81 (2014) 2, doi: 10.1115/1.4024908.

[1611] J. Faleskog, C.F. Shih, Micromechanics of coalescence—I. Synergistic effects of elasticity, plastic yielding and multi-size-scale voids, Journal of the Mechanics and Physics of Solids 45 (1997) 21–50, doi: 10.1016/S0022-5096(96)00078-6.

[1612] J.-B. Leblond, G. Mottet, A theoretical approach of strain localization within thin planar bands in porous ductile materials, Comptes Rendus Mécanique 336 (2008) 176–189, doi: 10.1016/j.crme.2007.11.008.

[1613] A.A. Benzerga, J. Besson, A. Pineau, Anisotropic ductile fracture, Acta Materialia 52 (2004) 4623–4638, doi: 10.1016/j.actamat.2004.06.020.

[1614] A.A. Benzerga, J. Besson, A. Pineau, Anisotropic ductile fracture, Acta Materialia 52 (2004) 4639–4650, doi: 10.1016/j.actamat.2004.06.019.

[1615] K. Nahshon, J.W. Hutchinson, Modification of the Gurson Model for shear failure, European Journal of Mechanics - A/Solids 27 (2008) 1–17, doi: 10.1016/j.euromechsol.2007.08.002.

[1616] C. MCVEIGH, F. VERNEREY, W. Liu, B. Moran, G. OLSON, An interactive micro-void shear localization mechanism in high strength steels, Journal of the Mechanics and Physics of Solids 55 (2007) 225–244, doi: 10.1016/j.jmps.2006.08.002.

[1617] L. Morin, J.-B. Leblond, A.A. Benzerga, Coalescence of voids by internal necking: Theoretical estimates and numerical results, Journal of the Mechanics and Physics of Solids 75 (2015) 140–158, doi: 10.1016/j.jmps.2014.11.009.

[1618] T. Pardoen, D. Dumont, A. Deschamps, Y. Brechet, Grain boundary versus transgranular ductile failure, Journal of the Mechanics and Physics of Solids 51 (2003) 637–665, doi: 10.1016/S0022-5096(02)00102-3.

[1619] T. Pardoen, Y. Brechet, Influence of microstructure-driven strain localization on the ductile fracture of metallic alloys, Phil. Mag. 84 (2004) 269–297, doi: 10.1080/14786430310001610366.

[1620] T. Pardoen, Numerical simulation of low stress triaxiality ductile fracture, Computers & Structures 84 (2006) 1641–1650, doi: 10.1016/j.compstruc.2006.05.001.

[1621] S. Nemat-Nasser, T. Okinaka, V. Nesterenko, M. Liu, Dynamic void collapse in crystals: Computational modelling and experiments, Philosophical Magazine A 78 (1998) 1151–1174, doi: 10.1080/01418619808239981.

[1622] K.L. Nielsen, J. Dahl, V. Tvergaard, Collapse and coalescence of spherical voids subject to intense shearing: studied in full 3D, Int J Fract 177 (2012) 97–108, doi: 10.1007/s10704-012-9757-4.

[1623] K. Solanki, M.F. Horstemeyer, M.I. Baskes, H. Fang, Multiscale study of dynamic void collapse in single crystals, Mechanics of Materials 37 (2005) 317–330, doi: 10.1016/j.mechmat.2003.08.014.

[1624] K. Siruguet, J.-B. Leblond, Effect of void locking by inclusions upon the plastic behavior of porous ductile solids—part II: theoretical modeling and numerical study of void coalescence, International Journal of Plasticity 20 (2004) 255–268, doi: 10.1016/S0749-6419(03)00019-6.

[1625] P.F. Thomason, Ductile fracture of metals, 1st ed., Pergamon Press, Oxford [England], New York, 1990.

[1626] C. Tekoğlu, J.-B. Leblond, T. Pardoen, A criterion for the onset of void coalescence under combined tension and shear, Journal of the Mechanics and Physics of Solids 60 (2012) 1363–1381, doi: 10.1016/j.jmps.2012.02.006.

[1627] M.E. Torki, C. Tekoğlu, J.-B. Leblond, A.A. Benzerga, Theoretical and numerical analysis of void coalescence in porous ductile solids under arbitrary loadings, International Journal of Plasticity 91 (2017) 160–181, doi: 10.1016/j.ijplas.2017.02.011.

[1628] P.F. Thomason, Three-dimensional models for the plastic limit-loads at incipient failure of the inter-void matrix in ductile porous solids, Acta Metallurgica 33 (1985) 1079–1085, doi: 10.1016/0001-6160(85)90201-9.

[1629] P.F. Thomason, A VIEW ON DUCTILE-FRACTURE MODELLING, Fatigue & Fracture of Engineering Materials & Structures 21 (1998) 1105–1122, doi: 10.1046/j.1460-2695.1998.00077.x.

[1630] A.W. Thompson, Modeling of local strains in ductile fracture, MTA 18 (1987) 1877–1886, doi: 10.1007/BF02647017.

[1631] M.E. Torki, A.A. Benzerga, J.-B. Leblond, On Void Coalescence Under Combined Tension and Shear, J. Appl. Mech. 82 (2015) 81, doi: 10.1115/1.4030326.

[1632] V. Tvergaard, A. Needleman, Nonlocal effects on localization in a void-sheet, International Journal of Solids and Structures 34 (1997) 2221–2238, doi: 10.1016/S0020-7683(96)00140-0.

[1633] V. Tvergaard, Bifurcation into a localized mode from non-uniform periodic deformations around a periodic pattern of voids, Journal of the Mechanics and Physics of Solids 69 (2014) 112–122, doi: 10.1016/j.jmps.2014.05.002.

[1634] V. Tvergaard, Effect of stress-state and spacing on voids in a shear-field, International Journal of Solids and Structures 49 (2012) 3047–3054, doi: 10.1016/j.ijsolstr.2012.06.008.

[1635] L. Xue, Constitutive modeling of void shearing effect in ductile fracture of porous materials, Engineering Fracture Mechanics 75 (2008) 3343–3366, doi: 10.1016/j.engfracmech.2007.07.022.

[1636] Z.L. Zhang, E. Niemi, A new failure criterion for the Gurson-Tvergaard dilational constitutive model, Int J Fract 70 (1995) 321–334, doi: 10.1007/BF00032450.

[1637] K.L. Nielsen, V. Tvergaard, Ductile shear failure or plug failure of spot welds modelled by modified Gurson model, Engineering Fracture Mechanics 77 (2010) 1031–1047, doi: 10.1016/j.engfracmech.2010.02.031.

[1638] V. Tvergaard, Behaviour of voids in a shear field, Int J Fract 158 (2009) 41–49, doi: 10.1007/s10704-009-9364-1.

[1639] K.L. Nielsen, V. Tvergaard, Effect of a shear modified Gurson model on damage development in a FSW tensile specimen, International Journal of Solids and Structures 46 (2009) 587–601, doi: 10.1016/j.ijsolstr.2008.09.011.

[1640] C. Tekoğlu, J.W. Hutchinson, T. Pardoen, On localization and void coalescence as a precursor to ductile fracture, Philosophical transactions. Series A, Mathematical, physical, and engineering sciences 373 (2015), doi: 10.1098/rsta.2014.0121.

[1641] M.E. Torki, A.A. Benzerga, A mechanism of failure in shear bands, Extreme Mechanics Letters 23 (2018) 67–71, doi: 10.1016/j.eml.2018.06.008.

[1642] J. Hure, P.O. Barrioz, Theoretical estimates for flat voids coalescence by internal necking, European Journal of Mechanics - A/Solids 60 (2016) 217–226, doi: 10.1016/j.euromechsol.2016.08.001.

[1643] S.M. Keralavarma, S. Chockalingam, A criterion for void coalescence in anisotropic ductile materials, International Journal of Plasticity 82 (2016) 159–176, doi: 10.1016/j.ijplas.2016.03.003.

[1644] Z.G. Liu, W.H. Wong, T.F. Guo, Void behaviors from low to high triaxialities: Transition from void collapse to void coalescence, International Journal of Plasticity 84 (2016) 183–202, doi: 10.1016/j.ijplas.2016.05.008.

[1645] R. Becker, R.E. Smelser, O. Richmond, The effect of void shape on the development of damage and fracture in plane-strain tension, Journal of the Mechanics and Physics of Solids 37 (1989) 111–129, doi: 10.1016/0022-5096(87)90007-X.

[1646] L. Banks-Sills, B. Budiansky, On void collapse in viscous solids, Mechanics of Materials 1 (1982) 209–218, doi: 10.1016/0167-6636(82)90014-X.

[1647] L. Flandi, J.-B. Leblond, A new model for porous nonlinear viscous solids incorporating void shape effects – I: Theory, European Journal of Mechanics - A/Solids 24 (2005) 537–551, doi: 10.1016/j.euromechsol.2005.03.003.

[1648] L. Flandi, J.-B. Leblond, A new model for porous nonlinear viscous solids incorporating void shape effects – II: Numerical validation, European Journal of Mechanics - A/Solids 24 (2005) 552–571, doi: 10.1016/j.euromechsol.2005.03.004.

[1649] M. Gărăjeu, J.C. Michel, P. Suquet, A micromechanical approach of damage in viscoplastic materials by evolution in size, shape and distribution of voids, Computer Methods in Applied Mechanics and Engineering 183 (2000) 223–246, doi: 10.1016/S0045-7825(99)00220-0.

[1650] A.A. Benzerga, J. Besson, Plastic potentials for anisotropic porous solids, European Journal of Mechanics - A/Solids 20 (2001) 397–434, doi: 10.1016/S0997-7538(01)01147-0.

[1651] F. Pastor, J. Pastor, D. Kondo, Limit analysis of hollow spheres or spheroids with Hill orthotropic matrix, Comptes Rendus Mécanique 340 (2012) 120–129, doi: 10.1016/j.crme.2011.11.011.

[1652] L. Morin, K. Madou, J.-B. Leblond, D. Kondo, A new technique for finite element limit-analysis of Hill materials, with an application to the assessment of criteria for anisotropic plastic porous solids, International Journal of Engineering Science 74 (2014) 65–79, doi: 10.1016/j.ijengsci.2013.08.006.

[1653] V. Tvergaard, B. Nyvang Legarth, Effects of anisotropy and void shape on cavitation instabilities, International Journal of Mechanical Sciences 152 (2019) 81–87, doi: 10.1016/j.ijmecsci.2018.12.014.
[1654] V. Tvergaard, Effect of initial void shape on ductile failure in a shear field, Mechanics of Materials 90 (2015) 2–9, doi: 10.1016/j.mechmat.2014.11.001.
[1655] V. Tvergaard, On localization in ductile materials containing spherical voids, International Journal of Fracture 18 (1982) 237–252, doi: 10.1007/BF00015686.
[1656] V. Tvergaard, Material failure by void coalescence in localized shear bands, International Journal of Solids and Structures 18 (1982) 659–672, doi: 10.1016/0020-7683(82)90046-4.
[1657] V. Tvergaard, Ductile fracture by cavity nucleation between larger voids, Journal of the Mechanics and Physics of Solids 30 (1982) 265–286, doi: 10.1016/0022-5096(82)90033-3.
[1658] J.M. Duva, A constitutive description of nonlinear materials containing voids, Mechanics of Materials 5 (1986) 137–144, doi: 10.1016/0167-6636(86)90029-3.
[1659] J.B. Leblond, G. Perrin, P. Suquet, Exact results and approximate models for porous viscoplastic solids, International Journal of Plasticity 10 (1994) 213–235, doi: 10.1016/0749-6419(94)90001-9.
[1660] J.C. Michel, P. Suquet, The constitutive law of nonlinear viscous and porous materials, Journal of the Mechanics and Physics of Solids 40 (1992) 783–812, doi: 10.1016/0022-5096(92)90004-L.
[1661] M. Haghi, L. Anand, A constitutive model for isotropic, porous, elastic-viscoplastic metals, Mechanics of Materials 13 (1992) 37–53, doi: 10.1016/0167-6636(92)90034-B.
[1662] M. Gărăjeu, P. Suquet, Effective properties of porous ideally plastic or viscoplastic materials containing rigid particles, Journal of the Mechanics and Physics of Solids 45 (1997) 873–902, doi: 10.1016/S0022-5096(96)00128-7.
[1663] A.C.F. Cocks, Inelastic deformation of porous materials, Journal of the Mechanics and Physics of Solids 37 (1989) 693–715, doi: 10.1016/0022-5096(89)90014-8.
[1664] J.-B. Leblond, L. Morin, Gurson's Criterion and Its Derivation Revisited, J. Appl. Mech. 81 (2014) 2, doi: 10.1115/1.4026112.
[1665] S. Yi, W. Duo, A lower bound approach to the yield loci of porous materials, Acta Mech Sinica 5 (1989) 237–243, doi: 10.1007/BF02487985.
[1666] J.-B. Leblond, G. Perrin, J. Devaux, An improved Gurson-type model for hardenable ductile metals, European Journal of Mechanics - A/Solids 14 (1995) 499–527.
[1667] G. Rousselier, Ductile fracture models and their potential in local approach of fracture, Nuclear Engineering and Design 105 (1987) 97–111, doi: 10.1016/0029-5493(87)90234-2.
[1668] P. Sofronis, R.M. McMeeking, Creep of Power-Law Material Containing Spherical Voids, J. Appl. Mech. 59 (1992) S88-S95, doi: 10.1115/1.2899512.
[1669] J.B. Stewart, O. Cazacu, Analytical yield criterion for an anisotropic material containing spherical voids and exhibiting tension–compression asymmetry, International Journal of Solids and Structures 48 (2011) 357–373, doi: 10.1016/j.ijsolstr.2010.10.009.
[1670] P.M. Suquet, Overall potentials and extremal surfaces of power law or ideally plastic composites, Journal of the Mechanics and Physics of Solids 41 (1993) 981–1002, doi: 10.1016/0022-5096(93)90051-G.
[1671] B. Tanguy, J. Besson, An extension of the Rousselier model to viscoplastic temperature dependent materials, Int J Fract 116 (2002) 81–101, doi: 10.1023/A:1020192527733.
[1672] J.M. Duva, J.W. Hutchinson, Constitutive potentials for dilutely voided nonlinear materials, Mechanics of Materials 3 (1984) 41–54, doi: 10.1016/0167-6636(84)90013-9.
[1673] A. Benallal, R. Desmorat, M. Fournage, An assessment of the role of the third stress invariant in the Gurson approach for ductile fracture, European Journal of Mechanics - A/Solids 47 (2014) 400–414, doi: 10.1016/j.euromechsol.2014.02.009.
[1674] P. Francescato, J. Pastor, B. Riveill-Reydet, Ductile failure of cylindrically porous materials. Part I: plane stress problem and experimental results, European Journal of Mechanics - A/Solids 23 (2004) 181–190, doi: 10.1016/j.euromechsol.2003.12.001.
[1675] Y.X. Gan, J.W. Kysar, Cylindrical void in a rigid-ideally plastic single crystal III: Hexagonal close-packed crystal, International Journal of Plasticity 23 (2007) 592–619, doi: 10.1016/j.ijplas.2006.06.001.
[1676] Y. GAN, J. KYSAR, T. MORSE, Cylindrical void in a rigid-ideally plastic single crystal II: Experiments and simulations, International Journal of Plasticity 22 (2006) 39–72, doi: 10.1016/j.ijplas.2005.01.009.

[1677] J. KYSAR, Y. GAN, G. MENDEZARZUZA, Cylindrical void in a rigid-ideally plastic single crystal. Part I: Anisotropic slip line theory solution for face-centered cubic crystals, International Journal of Plasticity 21 (2005) 1481–1520, doi: 10.1016/j.ijplas.2004.07.007.

[1678] J. Pastor, P. Francescato, M. Trillat, E. Loute, G. Rousselier, Ductile failure of cylindrically porous materials. Part II: other cases of symmetry, European Journal of Mechanics - A/Solids 23 (2004) 191–201, doi: 10.1016/j.euromechsol.2003.12.002.

[1679] A. Mbiakop, A. Constantinescu, K. Danas, A model for porous single crystals with cylindrical voids of elliptical cross-section, International Journal of Solids and Structures 64-65 (2015) 100–119, doi: 10.1016/j.ijsolstr.2015.03.017.

[1680] U. Borg, J.W. Kysar, Strain gradient crystal plasticity analysis of a single crystal containing a cylindrical void, International Journal of Solids and Structures 44 (2007) 6382–6397, doi: 10.1016/j.ijsolstr.2007.02.032.

[1681] M. Subramani, C. Czarnota, S. Mercier, A. Molinari, Dynamic response of ductile materials containing cylindrical voids, International Journal of Fracture 222 (2020) 197–218, doi: 10.1007/s10704-020-00441-7.

[1682] M. Gologanu, J.-B. Leblond, J. Devaux, Approximate models for ductile metals containing non-spherical voids—Case of axisymmetric prolate ellipsoidal cavities, Journal of the Mechanics and Physics of Solids 41 (1993) 1723–1754, doi: 10.1016/0022-5096(93)90029-F.

[1683] M. Gologanu, J.-B. Leblond, J. Devaux, Approximate Models for Ductile Metals Containing Non-spherical Voids—Case of Axisymmetric Oblate Ellipsoidal Cavities, J. Eng. Mater. Technol 116 (1994) 290–297, doi: 10.1115/1.2904290.

[1684] M. Gologanu, J.-B. Leblond, G. Perrin, J. Devaux, Recent Extensions of Gurson's Model for Porous Ductile Metals, in: P. Suquet (Ed.), Continuum micromechanics, Springer, Wien, New York, 1997, pp. 61–130.

[1685] B.J. Lee, M.E. Mear, Axisymmetric deformation of power-law solids containing a dilute concentration of aligned spheroidal voids, Journal of the Mechanics and Physics of Solids 40 (1992) 1805–1836, doi: 10.1016/0022-5096(92)90052-4.

[1686] P. Suquet, On bounds for the overall potential of power law materials containing voids with an arbitrary shape, Mechanics Research Communications 19 (1992) 51–58.

[1687] Y.P. Qiu, G.J. Weng, Plastic potential and yield function of porous materials with aligned and randomly oriented spheroidal voids, International Journal of Plasticity 9 (1993) 271–290, doi: 10.1016/0749-6419(93)90038-R.

[1688] S.M. Keralavarma, A.A. Benzerga, An approximate yield criterion for anisotropic porous media, Comptes Rendus Mécanique 336 (2008) 685–692, doi: 10.1016/j.crme.2008.07.008.

[1689] S.M. Keralavarma, A.A. Benzerga, A constitutive model for plastically anisotropic solids with non-spherical voids, Journal of the Mechanics and Physics of Solids 58 (2010) 874–901, doi: 10.1016/j.jmps.2010.03.007.

[1690] V. Monchiet, C. Gruescu, E. Charkaluk, D. Kondo, Approximate yield criteria for anisotropic metals with prolate or oblate voids, Comptes Rendus Mécanique 334 (2006) 431–439, doi: 10.1016/j.crme.2006.06.001.

[1691] V. Monchiet, E. Charkaluk, D. Kondo, An improvement of Gurson-type models of porous materials by using Eshelby-like trial velocity fields, Comptes Rendus Mécanique 335 (2007) 32–41, doi: 10.1016/j.crme.2006.12.002.

[1692] V. Monchiet, O. Cazacu, E. Charkaluk, D. Kondo, Macroscopic yield criteria for plastic anisotropic materials containing spheroidal voids, International Journal of Plasticity 24 (2008) 1158–1189, doi: 10.1016/j.ijplas.2007.08.008.

[1693] K.C. Yee, M.E. Mear, Effect of void shape on the macroscopic response of non-linear porous solids, International Journal of Plasticity 12 (1996) 45–68, doi: 10.1016/S0749-6419(95)00044-5.

[1694] Z. LI, H. Huang, Combined effects of void shape and void size - oblate spheroidal microvoid embedded in infinite non-linear solid, International Journal of Plasticity 21 (2005) 625–650, doi: 10.1016/j.ijplas.2004.05.006.

[1695] Z. Li, P. Steinmann, RVE-based studies on the coupled effects of void size and void shape on yield behavior and void growth at micron scales, International Journal of Plasticity 22 (2006) 1195–1216, doi: 10.1016/j.ijplas.2005.07.004.

[1696] L. Morin, J.-B. Leblond, V. Tvergaard, Application of a model of plastic porous materials including void shape effects to the prediction of ductile failure under shear-dominated loadings, Journal of the Mechanics and Physics of Solids 94 (2016) 148–166, doi: 10.1016/j.jmps.2016.04.032.

[1697] N. Aravas, P. Ponte Castañeda, Numerical methods for porous metals with deformation-induced anisotropy, Computer Methods in Applied Mechanics and Engineering 193 (2004) 3767–3805, doi: 10.1016/j.cma.2004.02.009.

[1698] M. Kailasam, P.P. Castañeda, A general constitutive theory for linear and nonlinear particulate media with microstructure evolution, Journal of the Mechanics and Physics of Solids 46 (1998) 427–465, doi: 10.1016/S0022-5096(97)00095-1.

[1699] M. Agoras, P. Ponte Castañeda, Iterated linear comparison bounds for viscoplastic porous materials with "ellipsoidal" microstructures, Journal of the Mechanics and Physics of Solids 61 (2013) 701–725, doi: 10.1016/j.jmps.2012.11.003.

[1700] M. Agoras, P. Ponte Castañeda, Anisotropic finite-strain models for porous viscoplastic materials with microstructure evolution, International Journal of Solids and Structures 51 (2014) 981–1002, doi: 10.1016/j.ijsolstr.2013.11.025.

[1701] P.P. Castañeda, M. Zaidman, Constitutive models for porous materials with evolving microstructure, Journal of the Mechanics and Physics of Solids 42 (1994) 1459–1497, doi: 10.1016/0022-5096(94)90005-1.

[1702] K. Danas, P. Ponte Castañeda, A finite-strain model for anisotropic viscoplastic porous media: I – Theory, European Journal of Mechanics - A/Solids 28 (2009) 387–401, doi: 10.1016/j.euromechsol.2008.11.002.

[1703] K. Danas, P. Ponte Castañeda, Influence of the Lode parameter and the stress triaxiality on the failure of elasto-plastic porous materials, International Journal of Solids and Structures 49 (2012) 1325–1342, doi: 10.1016/j.ijsolstr.2012.02.006.

[1704] K. Danas, N. Aravas, Numerical modeling of elasto-plastic porous materials with void shape effects at finite deformations, Composites Part B: Engineering 43 (2012) 2544–2559, doi: 10.1016/j.compositesb.2011.12.011.

[1705] M. Kailasam, P.P. CastaÑeda, J.R. Willis, The effect of particle size, shape, distribution and their evolution on the constitutive response of nonlinearly viscous composites. I. Theory, Philosophical Transactions of the Royal Society of London. Series A: Mathematical, Physical and Engineering Sciences 355 (1997) 1835–1852, doi: 10.1098/rsta.1997.0092.

[1706] R.A. Lebensohn, C.N. Tomé, P.J. Maudlin, A selfconsistent formulation for the prediction of the anisotropic behavior of viscoplastic polycrystals with voids, Journal of the Mechanics and Physics of Solids 52 (2004) 249–278, doi: 10.1016/S0022-5096(03)00114-5.

[1707] R.A. Lebensohn, M.I. Idiart, P.P. CastaÑeda, P.-G. Vincent, Dilatational viscoplasticity of polycrystalline solids with intergranular cavities, Phil. Mag. 91 (2011) 3038–3067, doi: 10.1080/14786435.2011.561811.

[1708] J.-B. Leblond, M. Gologanu, External estimate of the yield surface of an arbitrary ellipsoid containing a confocal void, Comptes Rendus Mécanique 336 (2008) 813–819, doi: 10.1016/j.crme.2008.10.006.

[1709] K. Madou, J.-B. Leblond, A Gurson-type criterion for porous ductile solids containing arbitrary ellipsoidal voids—I: Limit-analysis of some representative cell, Journal of the Mechanics and Physics of Solids 60 (2012) 1020–1036, doi: 10.1016/j.jmps.2011.11.008.

[1710] K. Madou, J.-B. Leblond, A Gurson-type criterion for porous ductile solids containing arbitrary ellipsoidal voids—II: Determination of yield criterion parameters, Journal of the Mechanics and Physics of Solids 60 (2012) 1037–1058, doi: 10.1016/j.jmps.2012.01.010.

[1711] K. Madou, J.-B. Leblond, Numerical studies of porous ductile materials containing arbitrary ellipsoidal voids – I: Yield surfaces of representative cells, European Journal of Mechanics - A/Solids 42 (2013) 480–489, doi: 10.1016/j.euromechsol.2013.06.004.

[1712] K. Madou, J.-B. Leblond, L. Morin, Numerical studies of porous ductile materials containing arbitrary ellipsoidal voids – II: Evolution of the length and orientation of the void axes, European Journal of Mechanics - A/Solids 42 (2013) 490–507, doi: 10.1016/j.euromechsol.2013.06.005.

[1713] L. Morin, J.-B. Leblond, D. Kondo, A Gurson-type criterion for plastically anisotropic solids containing arbitrary ellipsoidal voids, International Journal of Solids and Structures 77 (2015) 86–101, doi: 10.1016/j.ijsolstr.2015.05.021.

[1714] D. Song, P. Ponte Castañeda, A finite-strain homogenization model for viscoplastic porous single crystals, Journal of the Mechanics and Physics of Solids 107 (2017) 560–579, doi: 10.1016/j.jmps.2017.06.008.

[1715] D. Song, P. Ponte Castañeda, A finite-strain homogenization model for viscoplastic porous single crystals: II – Applications, Journal of the Mechanics and Physics of Solids 107 (2017) 580–602, doi: 10.1016/j.jmps.2017.06.003.

[1716] D. Song, P. Ponte Castañeda, A multi-scale homogenization model for fine-grained porous viscoplastic polycrystals, Journal of the Mechanics and Physics of Solids 115 (2018) 102–122, doi: 10.1016/j.jmps.2018.03.001.

[1717] D. Song, P. Ponte Castañeda, A multi-scale homogenization model for fine-grained porous viscoplastic polycrystals: II – Applications to FCC and HCP materials, Journal of the Mechanics and Physics of Solids 115 (2018) 77–101, doi: 10.1016/j.jmps.2018.03.002.

[1718] A. Mbiakop, A. Constantinescu, K. Danas, An analytical model for porous single crystals with ellipsoidal voids, Journal of the Mechanics and Physics of Solids 84 (2015) 436–467, doi: 10.1016/j.jmps.2015.07.011.

[1719] D. Song, M. Agoras, P. Ponte Castañeda, The evolution of pore shape and orientation in plastically deforming metals: Implications for macroscopic response and shear localization, Mechanics of Materials 90 (2015) 47–68, doi: 10.1016/j.mechmat.2015.01.011.

[1720] R. Becker, The effect of porosity distribution on ductile failure, Journal of the Mechanics and Physics of Solids 35 (1987) 577–599, doi: 10.1016/0022-5096(87)90018-4.

[1721] U. Borg, C.F. Niordson, N.A. Fleck, V. Tvergaard, A viscoplastic strain gradient analysis of materials with voids or inclusions, International Journal of Solids and Structures 43 (2006) 4906–4916, doi: 10.1016/j.ijsolstr.2005.05.022.

[1722] D. Fabrègue, T. Pardoen, A constitutive model for elastoplastic solids containing primary and secondary voids, Journal of the Mechanics and Physics of Solids 56 (2008) 719–741, doi: 10.1016/j.jmps.2007.07.008.

[1723] S. Ghosh, K. Lee, P. Raghavan, A multi-level computational model for multi-scale damage analysis in composite and porous materials, International Journal of Solids and Structures 38 (2001) 2335–2385, doi: 10.1016/S0020-7683(00)00167-0.

[1724] G. Perrin, J.B. Leblond, Analytical study of a hollow sphere made of plastic porous material and subjected to hydrostatic tension-application to some problems in ductile fracture of metals, International Journal of Plasticity 6 (1990) 677–699, doi: 10.1016/0749-6419(90)90039-H.

[1725] M.F. Horstemeyer, S. Ramaswamy, On Factors Affecting Localization and Void Growth in Ductile Metals: A Parametric Study, International Journal of Damage Mechanics 9 (2000) 5–28, doi: 10.1177/105678950000900102.

[1726] M. HUSSEIN, U. BORG, C. NIORDSON, V. DESHPANDE, Plasticity size effects in voided crystals, Journal of the Mechanics and Physics of Solids 56 (2008) 114–131, doi: 10.1016/j.jmps.2007.05.004.

[1727] V. Monchiet, G. Bonnet, A Gurson-type model accounting for void size effects, International Journal of Solids and Structures 50 (2013) 320–327, doi: 10.1016/j.ijsolstr.2012.09.005.

[1728] C.F. Niordson, V. Tvergaard, A homogenized model for size-effects in porous metals, Journal of the Mechanics and Physics of Solids 123 (2019) 222–233, doi: 10.1016/j.jmps.2018.09.004.

[1729] V. Tvergaard, A. Needleman, Three dimensional microstructural effects on plane strain ductile crack growth, International Journal of Solids and Structures 43 (2006) 6165–6179, doi: 10.1016/j.ijsolstr.2005.05.057.

[1730] J. WEN, The modified Gurson model accounting for the void size effect, International Journal of Plasticity 21 (2005) 381–395, doi: 10.1016/j.ijplas.2004.01.004.

[1731] K.S. Zhang, J.B. Bai, D. François, Ductile fracture of materials with high void volumefraction, International Journal of Solids and Structures 36 (1999) 3407–3425, doi: 10.1016/S0020-7683(98)00157-7.

[1732] L. Xia, Ductile crack growth-I. A numerical study using computational cells with microstructurally-based length scales, Journal of the Mechanics and Physics of Solids 43 (1995) 233–259, doi: 10.1016/0022-5096(94)00064-C.

[1733] C. Tekog˘lu, T. Pardoen, A micromechanics based damage model for composite materials, International Journal of Plasticity 26 (2010) 549–569, doi: 10.1016/j.ijplas.2009.09.002.

[1734] B. Liu, Y. Huang, M. Li, K.C. Hwang, C. Liu, A study of the void size effect based on the Taylor dislocation model, International Journal of Plasticity 21 (2005) 2107–2122, doi: 10.1016/j.ijplas.2005.03.016.

[1735] K. Danas, P. Ponte Castañeda, A finite-strain model for anisotropic viscoplastic porous media: II – Applications, European Journal of Mechanics - A/Solids 28 (2009) 402–416, doi: 10.1016/j.euromechsol.2008.11.003.

[1736] J. Besson, C. Guillemer-Neel, An extension of the Green and Gurson models to kinematic hardening, Mechanics of Materials 35 (2003) 1–18, doi: 10.1016/S0167-6636(02)00169-2.

[1737] O. Cazacu, J.B. Stewart, Analytic plastic potential for porous aggregates with matrix exhibiting tension–compression asymmetry, Journal of the Mechanics and Physics of Solids 57 (2009) 325–341, doi: 10.1016/j.jmps.2008.10.010.

[1738] J. Besson, D. Steglich, W. Brocks, Modeling of plane strain ductile rupture, International Journal of Plasticity 19 (2003) 1517–1541, doi: 10.1016/S0749-6419(02)00022-0.

[1739] S. Kweon, B. Sagsoy, A.A. Benzerga, Constitutive relations and their time integration for anisotropic elasto-plastic porous materials, Computer Methods in Applied Mechanics and Engineering 310 (2016) 495–534, doi: 10.1016/j.cma.2016.06.005.

[1740] R.A. Lebensohn, O. Cazacu, Effect of single-crystal plastic deformation mechanisms on the dilatational plastic response of porous polycrystals, International Journal of Solids and Structures 49 (2012) 3838–3852, doi: 10.1016/j.ijsolstr.2012.08.019.

[1741] K.-C. Liao, J. Pan, S.C. Tang, Approximate yield criteria for anisotropic porous ductile sheet metals, Mechanics of Materials 26 (1997) 213–226, doi: 10.1016/S0167-6636(97)00033-1.

[1742] D.-A. Wang, J. Pan, S.-D. Liu, An Anisotropic Gurson Yield Criterion for Porous Ductile Sheet Metals with Planar Anisotropy, International Journal of Damage Mechanics 13 (2004) 7–33, doi: 10.1177/1056789504039010.

[1743] A. Srivastava, B. Revil-Baudard, O. Cazacu, A. Needleman, A model for creep of porous crystals with cubic symmetry, International Journal of Solids and Structures 110-111 (2017) 67–79, doi: 10.1016/j.ijsolstr.2017.02.002.

[1744] S. Ha, K. Kim, Void growth and coalescence in f.c.c. single crystals, International Journal of Mechanical Sciences 52 (2010) 863–873, doi: 10.1016/j.ijmecsci.2010.03.001.

[1745] X. Han, J. Besson, S. Forest, B. Tanguy, S. Bugat, A yield function for single crystals containing voids, International Journal of Solids and Structures 50 (2013) 2115–2131, doi: 10.1016/j.ijsolstr.2013.02.005.

[1746] J. Paux, L. Morin, R. Brenner, D. Kondo, An approximate yield criterion for porous single crystals, European Journal of Mechanics - A/Solids 51 (2015) 1–10, doi: 10.1016/j.euromechsol.2014.11.004.

[1747] T. Schacht, N. Untermann, E. Steck, The influence of crystallographic orientation on the deformation behaviour of single crystals containing microvoids, International Journal of Plasticity 19 (2003) 1605–1626, doi: 10.1016/S0749-6419(02)00038-4.

[1748] A. Pineau, A.A. Benzerga, T. Pardoen, Failure of metals I, Acta Materialia 107 (2016) 424–483, doi: 10.1016/j.actamat.2015.12.034.

[1749] A. Pineau, T. Pardoen, Failure of Metals, in: I. Milne, R.O. Ritchie, B. Karihaloo (Eds.), Comprehensive structural integrity, Elsevier/Pergamon, Amsterdam, Boston, 2003, pp. 684–797.

[1750] F.M. Beremin, A. Pineau, F. Mudry, J.-C. Devaux, Y. D'Escatha, P. Ledermann, A local criterion for cleavage fracture of a nuclear pressure vessel steel, MTA 14 (1983) 2277–2287, doi: 10.1007/BF02663302.

[1751] J.J. Lewandowski, A.W. Thompson, Microstructural effects on the cleavage fracture stress of fully pearlitic eutectoid steel, MTA 17 (1986) 1769–1786, doi: 10.1007/BF02817275.

[1752] J.H. Chen, R. Cao, Micromechanism of cleavage fracture of metals: A comprehensive microphysical model for cleavage cracking in metals, Elsevier Butterworth-Heinemann, Amsterdam, Boston, 2015.

[1753] C.J. McMahon, M. Cohen, Initiation of cleavage in polycrystalline iron, Acta Metallurgica 13 (1965) 591–604, doi: 10.1016/0001-6160(65)90121-5.

[1754] T. Lin, A.G. Evans, R.O. Ritchie, Stochastic modeling of the independent roles of particle size and grain size in transgranular cleavage fracture, Metall and Mat Trans A 18 (1987) 641–651, doi: 10.1007/BF02649480.

[1755] Y. Qiao, A.S. Argon, Cleavage crack-growth-resistance of grain boundaries in polycrystalline Fe–2%Si alloy: experiments and modeling, Mechanics of Materials 35 (2003) 129–154, doi: 10.1016/S0167-6636(02)00194-1.

[1756] Y. Qiao, A.S. Argon, Cleavage cracking resistance of high angle grain boundaries in Fe–3%Si alloy, Mechanics of Materials 35 (2003) 313–331, doi: 10.1016/S0167-6636(02)00284-3.

[1757] Y. Qiao, X. Kong, An energy analysis of the grain boundary behavior in cleavage cracking in Fe–3wt.%Si alloy, Materials Letters 58 (2004) 3156–3160, doi: 10.1016/j.matlet.2004.05.063.

[1758] A. Pineau, Crossing grain boundaries in metals by slip bands, cleavage and fatigue cracks, Philosophical transactions. Series A, Mathematical, physical, and engineering sciences 373 (2015), doi: 10.1098/rsta.2014.0131.

[1759] M. KROON, Micromechanics of cleavage fracture initiation in ferritic steels by carbide cracking, Journal of the Mechanics and Physics of Solids 53 (2005) 171–196, doi: 10.1016/j.jmps.2004.05.008.

[1760] F. Mudry, A local approach to cleavage fracture, Nuclear Engineering and Design 105 (1987) 65–76, doi: 10.1016/0029-5493(87)90230-5.

[1761] S.R. Bordet, A.D. Karstensen, D.M. Knowles, C.S. Wiesner, A new statistical local criterion for cleavage fracture in steel. Part I: model presentation, Engineering Fracture Mechanics 72 (2005) 435–452, doi: 10.1016/j.engfracmech.2004.02.009.

[1762] S.R. Bordet, A.D. Karstensen, D.M. Knowles, C.S. Wiesner, A new statistical local criterion for cleavage fracture in steel. Part II: application to an offshore structural steel, Engineering Fracture Mechanics 72 (2005) 453–474, doi: 10.1016/j.engfracmech.2004.02.010.

[1763] G. Bernauer, W. Brocks, W. Schmitt, Modifications of the Beremin model for cleavage fracture in the transition region of a ferritic steel, Engineering Fracture Mechanics 64 (1999) 305–325, doi: 10.1016/S0013-7944(99)00076-4.

[1764] J.P. Petti, R.H. Dodds, Ductile tearing and discrete void effects on cleavage fracture under small-scale yielding conditions, International Journal of Solids and Structures 42 (2005) 3655–3676, doi: 10.1016/j.ijsolstr.2004.11.015.

[1765] N.P. O'Dowd, Y. Lei, E.P. Busso, Prediction of cleavage failure probabilities using the Weibull stress, Engineering Fracture Mechanics 67 (2000) 87–100, doi: 10.1016/S0013-7944(00)00051-5.

[1766] L. Xia, C.F. Shih, Ductile crack growth—III. Transition to cleavage fracture incorporating statistics, Journal of the Mechanics and Physics of Solids 44 (1996) 603–639, doi: 10.1016/0022-5096(95)00086-0.

[1767] A. Pineau, Modeling ductile to brittle fracture transition in steels—micromechanical and physical challenges, Int J Fract 150 (2008) 129–156, doi: 10.1007/s10704-008-9232-4.

[1768] D.A. Curry, J.F. Knott, Effect of microstructure on cleavage fracture toughness of quenched and tempered steels, Metal Science 13 (1979) 341–345, doi: 10.1179/msc.1979.13.6.341.

[1769] J.R. Rice, R. Thomson, Ductile versus brittle behaviour of crystals, Philosophical Magazine 29 (1974) 73–97, doi: 10.1080/14786437408213555.

[1770] J.H. Chen, Q. Wang, G.Z. Wang, Z. LI, Fracture behavior at crack tip — a new framework for cleavage mechanism of steel, Acta Materialia 51 (2003) 1841–1855, doi: 10.1016/S1359-6454(02)00581-5.

[1771] G.T. Hahn, The Influence of Microstructure on Brittle Fracture Toughness, Metall and Mat Trans A 15 (1984) 947–959, doi: 10.1007/BF02644685.

[1772] A. Pineau, Global and Local Approaches of Fracture — Transferability of Laboratory Test Results to Components, in: A.S. Argon (Ed.), Topics in Fracture and Fatigue, Springer New York, New York, NY, 1992, pp. 197–234.

[1773] A. Pineau, Development of the Local Approach to Fracture over the Past 25 years: Theory and Applications, Int J Fract 138 (2006) 139–166, doi: 10.1007/s10704-006-0035-1.

[1774] A.G. Evans, Statistical aspects of cleavage fracture in steel, MTA 14 (1983) 1349–1355, doi: 10.1007/BF02664818.

[1775] D.P. Fairchild, D.G. Howden, W.A.T. Clark, The mechanism of brittle fracture in a microalloyed steel: Part I. Inclusion-induced cleavage, Metall and Mat Trans A 31 (2000) 641–652, doi: 10.1007/s11661-000-0007-4.

[1776] D.P. Fairchild, D.G. Howden, W.A.T. Clark, The mechanism of brittle fracture in a microalloyed steel: Part II. Mechanistic modeling, Metall and Mat Trans A 31 (2000) 653–667, doi: 10.1007/s11661-000-0008-3.

[1777] E. Smith, Cleavage fracture in mild steel, Int J Fract 4 (1968), doi: 10.1007/BF00188940.

[1778] G.A. Francfort, J.-J. Marigo, Revisiting brittle fracture as an energy minimization problem, Journal of the Mechanics and Physics of Solids 46 (1998) 1319–1342, doi: 10.1016/S0022-5096(98)00034-9.

[1779] B. Bourdin, G.A. Francfort, J.-J. Marigo, Numerical experiments in revisited brittle fracture, Journal of the Mechanics and Physics of Solids 48 (2000) 797–826, doi: 10.1016/S0022-5096(99)00028-9.

[1780] J.F. Knott, Fundamentals of fracture mechanics, Butterworths, London, 1981.

[1781] E. Orowan, Fracture and strength of solids, Philosophical Magazine 12 (1949) 185–232, doi: 10.1088/0034-4885/12/1/309.

[1782] A.N. Stroh, The formation of cracks as a result of plastic flow, Proc. R. Soc. Lond. A 223 (1954) 404–414, doi: 10.1098/rspa.1954.0124.

[1783] M. Diehl, M. Wicke, P. Shanthraj, F. Roters, A. Brueckner-Foit, D. Raabe, Coupled Crystal Plasticity–Phase Field Fracture Simulation Study on Damage Evolution Around a Void, JOM 69 (2017) 872–878, doi: 10.1007/s11837-017-2308-8.

[1784] A. Neimitz, J. Galkiewicz, I. Dzioba, The ductile-to-cleavage transition in ferritic Cr–Mo–V steel: A detailed microscopic and numerical analysis, Engineering Fracture Mechanics 77 (2010) 2504–2526, doi: 10.1016/j.engfracmech.2010.06.003.

[1785] I. Dzioba, M. Gajewski, A. Neimitz, Studies of fracture processes in Cr–Mo–V ferritic steel with various types of microstructures, International Journal of Pressure Vessels and Piping 87 (2010) 575–586, doi: 10.1016/j.ijpvp.2010.07.012.

[1786] J. Hohe, V. Friedmann, J. Wenck, D. Siegele, Assessment of the role of micro defect nucleation in probabilistic modeling of cleavage fracture, Engineering Fracture Mechanics 75 (2008) 3306–3327, doi: 10.1016/j.engfracmech.2007.08.008.